

THE SYSTEM-STRUCTURAL ANALYSIS OF A THERMODYNAMIC EFFICIENCY OF THE TECHNOLOGICAL SCHEMES OF REFRIGERATING AND HEAT PUMPS INSTALLATIONS

D. Kh. Kharlampidi

Department of modeling and identification of thermal processes
A. N. Podgorny Institute for Mechanical Engineering Problems of the NAS of Ukraine
Ukraine, Kharkov, 61046, Dmitry Pozharsky st. 2/10
Tel/fax (0572)94-27-94;(0572)94-46-35;
E-Mail: kharlampidi@ipmach.kharkov.ua

Abstract

On the basis of methods of modern applied thermodynamics, the technique of the system-structural analysis of thermodynamic efficiency refrigerating and heat pump installations has been developed. With use of coefficients of structural bond the analysis of influence of interelement connections in technological schemes of vapor compression refrigerating and heat pumps installations on thermodynamic efficiency has been realized. The influence of structural complexity of the technological schemes of heat pump installations on thermodynamic efficiency has been estimated. For this purpose for the first time in the thermodynamic analysis, the criterion of complexity of the scheme has been proposed. The system objective laws of irreversibility losses in the schemes of vapor compression refrigerating and heat pumps installations have been found. The technique of definition of componential irreversibility losses in vapor compression refrigeration cycle has been developed.

KEYWORDS

Heat pump installation, vapor compression cycle, coefficient of structural bond, irreversibility losses.

INTRODUCTION

Currently, the elements of refrigerating machines (RM) and heat pump installations (HPU) in some cases have reached the «a technical limit» when perfection of designs of the independent elements any more does not give essential to increase of efficiency of all installation. Meanwhile, opportunities perfection of the structures of technological schemes is still have not limitation. Development of the methods, that allow to find of different technological schemes the one scheme that has more efficiency, represents an actual problem. Thereby, at designing of RM or HPU can excluding from consideration those schemes, in which perfection of the elements does not essential influences on increase of efficiency of all installation.

One of directions of structural researches is the system - structural analysis that have a purpose finding of system characteristics of irreversibility losses in various technological schemes of energy conversion installations. In the present work for the first time the attempt is undertaken to create the technique of the system - structural analysis of vapor compression refrigeration machines and heat pumps.

THE ANALYSIS OF THE IRREVERSIBILITY LOSSES IN THE ELEMENTS OF REFRIGERATION MACHINE AND HEAT PUMP INSTALLATION

Thermodynamic non-equivalence exergy and exergy losses directly depends from the structure of the technological schemes of installation [1]. Therefore, for various technological schemes of RM and HPU takes place the specific character of the irreversibility losses. The same element having an identical design, but included in different technological schemes or part of the concrete scheme has a various level exergy

losses [2]. Thus, perfection of element without taking into account the structure of the technological scheme in which the element to have disposition cannot to increase of efficiency of all system. Exergy losses in a elements of vapor compression RM or HPU are interconnected. Any change of losses, for example, their increase in one element will necessarily cause change in the other element interconnected to it, and, this change at all does not mean increase of exergy losses in this element, and sometimes, even on the contrary (though and it is rare), losses can decrease. In other words, irreversibility of one of elements can be reduced by irreversibility of another element. This effect in energy conversion installation is not a paradox, and is a typical symptom of integrative properties of the system.

For the estimate the influence of change of a parameter of one process on the value of irreversible losses in the element, and for estimating the influence of these losses on the losses in all system of the coefficients of structural bonds are used [1–3].

For the analysis of influence of losses from irreversibility in technical systems of any complexity J. Bayer was used a following coefficient of structural bonds [1, 2]

$$\pi_{ik} = \left(\frac{\partial E_D^{\text{sum}}}{\partial x_{ik}} \right) / \left(\frac{\partial E_{Dk}}{\partial x_{ik}} \right), \quad (1)$$

where E_{Dk} – exergy losses in element; E_D^{sum} – overall exergy losses in all system; x_{ik} – the parameter influencing on the exergy losses.

Structural coefficients specify opportunities and a direction of increase of efficiency of all system as a whole, allow to estimate force of interelement connections, and to find the symptoms of system laws of irreversibility losses in a technological schemes of energy conversion installations. Value $\pi_{i,k}$ can change from $\pi_{i,k} \approx 0$ up to $\pi_{i,k} \geq 1$. Those elements, for which $\pi_{i,k} \geq 1$ should be subject to constructive perfection. In this case, there is a reserve for reduction of total irreversibility losses in system by means of decreasing of losses in several elements. If $0 < \pi_{i,k} < 1$ the reduction of irreversibility in one element of the scheme will be compensated by means of increasing in irreversibility in other elements of system. Therefore, decreasing of exergy losses in element will not influence on the increasing of efficiency of all installation, as structural communications between elements in this case have high rigidity.

A parameter x_{ik} depends from the constructive parameters of installation. Such parameter can be the value hydraulic resistance of the evaporator, the condenser, the pipelines, and value of the minimal temperature difference in condenser or evaporator. In this case, the input data is a refrigeration capacity of installations. Other approach to the structural analysis is estimating quality of structural communications and character of distribution of irreversibility losses at a variation of regime - constructive characteristics of the equipment for the refrigerant loop with known type of the compressor. For the variation of a parameter x_{ik} the surface of the evaporator or the condenser, diameters of pipelines, and also the value superheat and subcooling in cycle can be chosen.

For research of influence of local irreversibility E_{Dk} on total losses in installation E_{Dk}^{sum} it is necessary to know, how other parameters of processes in a cycle will react to change of losses in an element. It is necessary to explain it. For example, reduction of hydraulic resistance in evaporator will change the data of the minimal temperature difference in it. On the one hand, exergy losses in compressor depend not only on the compressor isentropic efficiency, but also from the value of the minimal temperature difference in evaporator and condenser, and from hydraulic resistances in a refrigerant loop. On the other hand, than more the irreversible a process in compressor than more increasing the exergy loss in the compressor and exergy loss in the condenser.

Let's to consider a technique of calculation of refrigeration cycle that is deformed because of influence of thermal-hydraulic irreversibility. Recommendations of work [4], and the approach that used for calculation of cycle in the program «Refrigeration Utilities» has been in a basis of a technique.

If in a first approximation for formation of the real cycle to neglect hydraulic resistances in processes of condensation and evaporation, and resistances in pipelines, then the refrigeration cycle in $P - i$ diagram have been shown dotted line (fig. 1). This cycle is base for calculation of a new cycle (the following calculation stage) in that a processes deformed by thermal-hydraulic irreversibility.

On the first stage (fig. 1 a) a non-isobaric processes of condensation, evaporation, processes in pipeline of refrigerant loop and also non- isentropic process in the compressor has been calculated for base cycle (point 3 and point 7 are fixed).

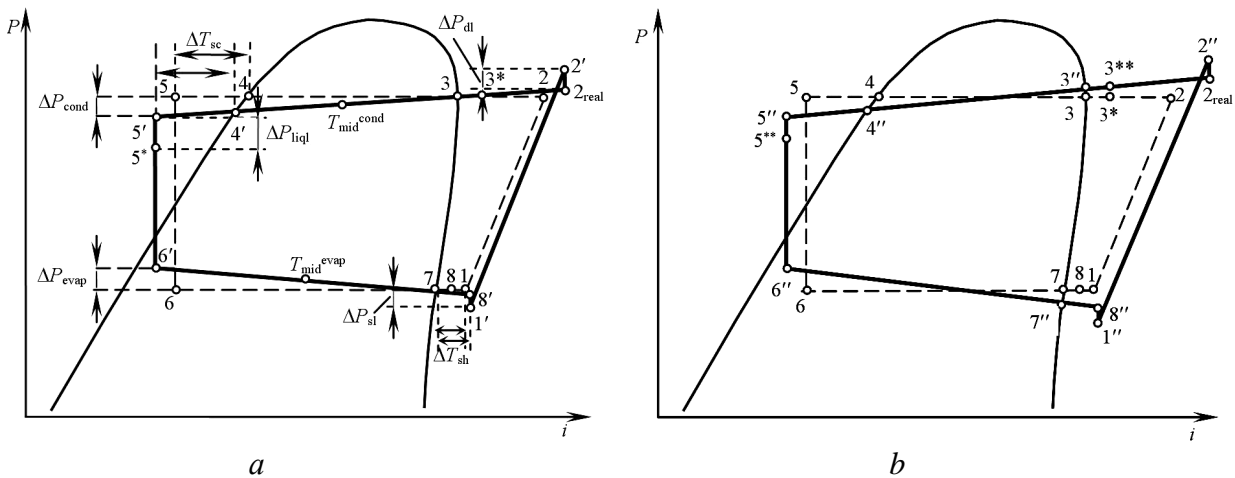


Fig. 1. Stages of calculation of real refrigeration cycle: *a* – first stage; *b* – second stage. ΔP_{cond} – pressure drop in condenser; ΔP_{evap} – pressure drop in evaporator; ΔP_{sl} – pressure drop in suction line; ΔP_{dl} – pressure drop in discharge line; ΔP_{liq} – pressure drop in liquid line; ΔT_{sh} – superheating; ΔT_{sc} – subcooling; $T_{\text{mid}}^{\text{cond}}$, $T_{\text{mid}}^{\text{evap}}$ – average temperatures of condensation and evaporation in non-isobaric processes

Dissipation energy that caused by forces of viscosity in a stream and friction on the internal surfaces of elements is the reason of a thermodynamic non-equilibrium statuses of a refrigerant, and consequently the irreversibility processes of evaporation and condensation. Thereby, the processes 3 – 4' and 6' – 7 represent of a direct lines only conditionally. However, if point 3 and point 4', and also point 6' and 7 are fixed on the basis of cycle calculation and hydraulic calculation of the evaporator and the condenser then by virtue of linear character of the pressure drop by Darcy's law, with a sufficient a substantiation it is possible to consider processes 3 – 4' and 6' – 7 represent as a real processes.

The second stage (fig. 1 b) calculation of a real cycle consists in procedure of a recalculation of parameters in the point 3 and point 7. This procedure takes into account increasing of condensation temperature on the value that equivalently to change of average temperature in this process caused by losses of pressure drop in the condenser, and decreasing of evaporation temperature on the value that equivalently to change of average temperature in evaporation process caused by pressure drop in the evaporator.

Let's explain it on an example. By results of calculation of a cycle after the first stage it is possible to conclude that hydraulic resistance in the evaporator does not effect on the change of compression work in the compressor. On the first stage of cycle calculation the point 7 is considered fixed and from it should be postponed the ΔP_{evap} in order that to fix next point in position 6'. However, as show on fig. 1, the average temperature in process 6' – 7 has risen in comparison with a base cycle on some $\Delta T_{\text{evap}}'$. Thus, the temperature of low potential of heat source in evaporator will not a correlated with the minimal temperature of difference, that is assigned at designing. Therefore, in the second stage of cycle calculation the temperature in point 7 is necessary to reduce by the value $\Delta T_{\text{evap}}' = T_6 - T_{\text{mid}}^{\text{evap}}$. Similarly it is necessary to act for calculation of process non-isobaric condensation, i.e. temperature in the point 3 should be increased by value $\Delta T_{\text{cond}}' = T_4 - T_{\text{mid}}^{\text{cond}}$.

The calculation of parameters of a thermodynamic cycle and constructive characteristics of a refrigerant loop a realized with the help of techniques [4–6]. The Martinally equations for calculation of pressure losses in evaporation process are used [6]. The thermalphysical properties of refrigerant by means of software «Refrigeration Utilities» are calculated.

The irreversibility losses in heat exchangers and pipelines include the losses because of heat exchange $E_{Dk}^{\Delta T}$ and losses because of hydraulic resistance $E_{Dk}^{\Delta P}$

$$E_{Dk} = E_{Dk}^{\Delta T} + E_{Dk}^{\Delta P}. \quad (2)$$

The losses because of dissipation energy in pipelines of refrigerant loop $E_{Dk}^{\Delta P}$, and the regulating valves a calculated from the equation

$$E_{Dk}^{\Delta P} = m_r T_d (S_j - S_j^{\Delta P}), \quad (3)$$

where $S_{j,и} S_j^{\Delta P}$ – the entropy of a refrigerant at the end of process in points of the base and deformed cycle; m_r – mass charge of refrigerant; T_d – ambient temperature.

The exergy losses because of heat exchange $E_{Dk}^{\Delta T}$ in the evaporator, the condenser, in the intermediate cooler of superheated vapor, and the pipelines of the equipment are determined from the equation

$$E_{Dk}^{\Delta T} = m_r T_d \left[(S_{j+1} - S_j) - \frac{(i_{j+1} - i_j)}{T_m} \right], \quad (4)$$

where T_m – the average logarithmic temperature of the heat-carrier in the heat exchangers; S_{j+1}, S_j – the entropy of a refrigerant in the end and in the beginning of process that considered; i_{j+1} and i_j – the enthalpy of a refrigerant in the end and in the beginning of the process of a thermodynamic cycle.

The entropy generation because of hydraulic resistance in the evaporator a calculated from the equation [7]

$$\Delta S_{evap}^{\Delta P} = m_r \left(S_{j+1}'' - S_j - 2.0 \frac{i_{j+1}'' - i_j}{T_{j+1}'' + T_j} \right), \quad (5)$$

where S'', i'' и T'' – entropy, enthalpy and temperature of a refrigerant in saturated vapor state.

The entropy generation because of hydraulic resistance in the condenser

$$\Delta S_{cond}^{\Delta P} = m_r \left(S_{j+1}' - S_j'' + 2.0 \frac{i_j'' - i_{j+1}'}{T_j'' + T_j'} \right) + m_r \left(-R \cdot \ln \left(1.0 - \frac{\Delta P_{dl}}{P_{dis}} \right) \right), \quad (6)$$

where S', i' and T' – entropy, enthalpy and temperature of a refrigerant in liquid state; ΔP_{dl} – hydraulic resistance in condenser in the zone cooling of superheated vapor; P_{dis} – discharge pressure in the cycle; R - a universal gas constant.

The exergy losses in the compressor a calculated from the equations

$$E_{Dcomp} = m_r T_d \left[(S_{j+1} - S_j) - \frac{Q_{comp}}{T_d} \right]. \quad (7)$$

$$Q_{comp} = m_r (i_{j+1} - i_j) - N_{comp}, \quad (8)$$

where N_{comp} – supply power of compressor.

Irreversibility losses in throttling valve

$$E_{Dexp} = m_r T_d (S_{j+1} - S_j). \quad (9)$$

The exergy losses in suction line – liquid line heat exchanger (SL-LL) a calculated from the equation

$$E_{Dsl}^{\Delta T} = m_r T_d [(S_{j+1} - S_j) - (S'_i - S_{i+1})], \quad (10)$$

where S_{i+1} , S_i – the entropy of a refrigerant in the end and in the start of process for a return stream in the SL-LL heat exchanger.

The exergy losses in the condenser, that caused by irreversibility of process in the compressor (losses due to interference of elements), calculating from the next equations

$$E'_{Dcond} = m_r [(T_{mid} - T_d)(S_{is} - S_{real})], \quad (11)$$

$$T_{mid} = (i_{is} - i_{real}) / (S_{is} - S_{real}). \quad (12)$$

where i_{is} , i_{real} , S_{is} , S_{real} – the enthalpy and entropy in the end isentropic and the real processes in the compressor; T_{mid} – the average thermodynamic temperature of real process in compressor.

For calculation of structural coefficient the main condition is variation only one parameter all other variables are conditionally fixed, i.e. not exposed to special influence on them [1].

The hydraulic resistance on the part of a refrigerant for various elements HPU as a varied parameter in the present work has been chose. The hydraulic resistance of the evaporator and the condenser a change due to a variation of a parameter $z = L_i / (d_i N_k)$, where L_i – length of tube, d_i – internal diameter, N_i – number of columns in a heat exchanger Calculations are lead at the following input data. Evaporation temperature as a first approximation $T_{evap} = 271$ K, condensation temperature $T_{cond} = 330$ K. Average temperature coolant in evaporator $T_s = 283$ K. Average temperature of the heat-carrier in condenser HPU $T_w = 320$ K; Refrigeration capacity HPU $Q_0 = 7,65$ kWt. Refrigerant R22. $T_d = 272$ K.

The dependences on fig. 2 and fig. 3 showing influence change of hydraulic resistance in the evaporator and the condenser on distribution exergy losses in elements HPU.

In table 1 value of various kinds of exergy losses in the evaporator and the condenser at a variation of size of hydraulic resistance of evaporator ΔP_{evap} are presented.

Table 1 Distribution of various kinds of exergy losses in HPU at variation ΔP_{evap}

Kind of loss	Exergy losses						
	0,1	0,2	0,3	0,4	0,5	0,6	0,7
ΔP_{evap} , bar							
$E_{Dsl}^{\Delta P}$, kWt	0,08227	0,08323	0,08416	0,08509	0,086	0,08693	0,08784
$E_{Devap}^{\Delta P}$, kWt	0,01613	0,03246	0,04942	0,0646	0,08246	0,09776	0,11434
$E_{Dcond}^{\Delta P}$, kWt	0,0029	0,0029	0,0029	0,0029	0,0029	0,00289	0,00289
$E_{Dsl}^{\Delta T}$, kWt	0,02609	0,02659	0,02657	0,02794	0,02654	0,02791	0,02928
$E_{Devap}^{\Delta T}$, kWt	0,35278	0,37056	0,38711	0,40224	0,41905	0,43445	0,4486
$E_{Dcond}^{\Delta T}$, kWt	0,51129	0,55065	0,53327	0,51453	0,49686	0,56422	0,54642
E'_{Dcond} , kWt	0,22561	0,22863	0,23074	0,23562	0,23861	0,24349	0,24509

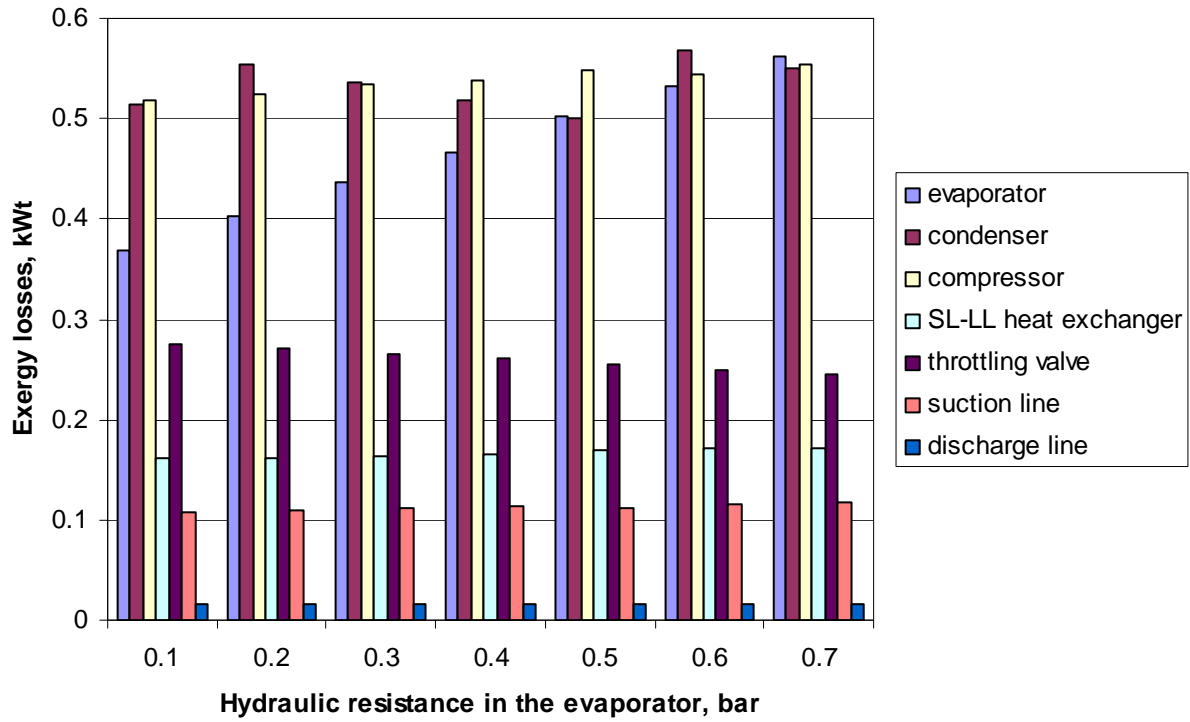


Fig. 2. Influence of hydraulic resistance in evaporator on exergy losses in HPU

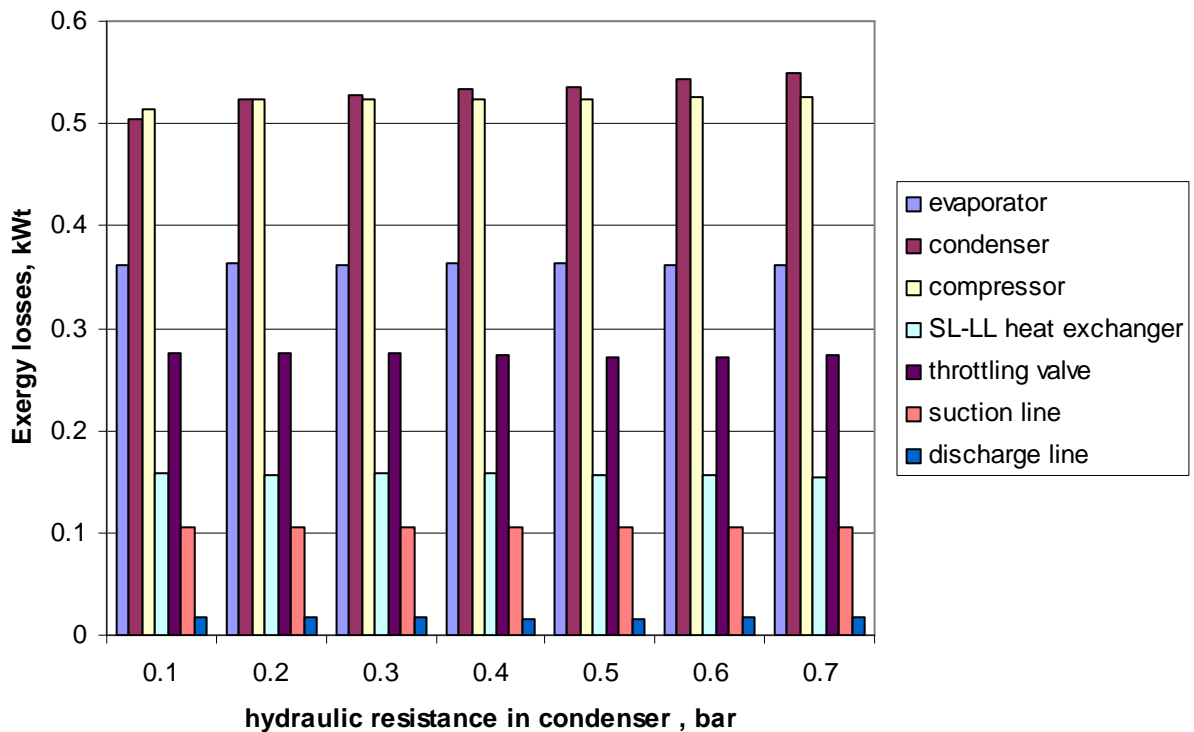


Fig. 3. Influence of hydraulic resistance in condenser on exergy losses in elements of HPU

Sometimes in the results of the exergy analysis is expediently to change the structure of technological scheme. In this case, the search of new structure of technological scheme must be formalized. For objective appraisal of a level of structural complexity of technological schemes of a refrigeration machines and heat pumps the Taubman criterion of complexity D are used [2]

$$D = D_i(2\bar{m} + \bar{p}). \quad (13)$$

where \bar{p} – the total number of interactions of heat engineering systems with an environment (condenser, evaporator, compressor, auxiliary heat exchangers); \bar{m} – the total number of technological communications between elements of system; D_i – the total complexity of all elements of system.

Let's consider the some complicated schemes of one-stage and two-stage cycles. The one-stage scheme with SL-LL heat exchanger ($D = 15$). The two-stage scheme with incomplete intermediate cooling heat exchanger and unitary throttling ($D = 17$). The two-stage scheme with incomplete intermediate cooling parallel throttling and subcooling of a liquid refrigerant in economizer ($D = 22$). The two-stage scheme with intermediate injection vapor in suction line in the second stage of compression ($D = 18$). Neglect complexity of elements ($D_i = \text{const}$).

On fig. 4. the influences of irreversibility losses in the evaporator and the condenser on the total of irreversibility losses in HPU E_{Dk}^{sum} for the technological schemes that having a different level of structural complexity is presented.

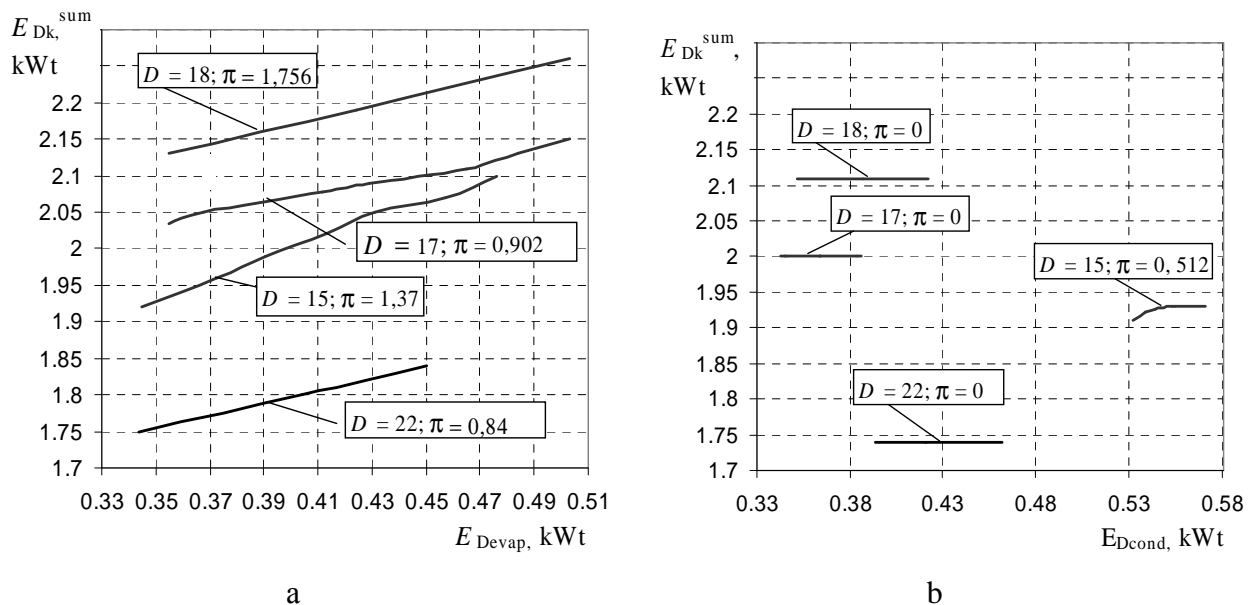


Fig. 4. Influences of exergy losses in evaporator and condenser on the total exergy losses in HPU at variation hydraulic resistance for technological schemes different structural complexity a – evaporator; b – condenser

The more are subject to influence of hydraulic resistances on the part of a refrigerant in the evaporator are the two-stage schemes with intermediate injection in suction line in the second stage of compression ($\pi = 1,756$) and the one-stage schemes with SL-LL heat exchanger ($\pi = 1,37$). For such schemes is impossible to use the internally finned-tubes evaporators. These type of evaporators can be used in schemes having the big rigidity of structural communications, and namely in the two-stage scheme with economizer ($\pi = 0,84$) or in the two-stage scheme with incomplete intermediate cooling and unitary throttling ($\pi = 0,902$). In these schemes a coefficient of structural bond $0 < \pi < 1$.

With increase the structural complexity of the technological scheme of two-stage heat pumps the coefficient of structural bonds also increases.

Using this technique the rational constructive characteristics of heat exchanger surfaces of the evaporator and the condenser and also a constructive parameters of the pipelines in depending from a level of structural complexity of the technological scheme RM or HPU has been chosen.

References

1. Brodyansky V. M. Exergy method and it applications / Brodyansky V. M., Fratsher V., Mychalic C. Moscow: Energoatomizdat, 1988. – 288 p.
2. Taubman E. I. Analysis and synthesis heat engineering system. Moscow: Energoatomizdat, 1983. – 176 p.
3. Boer D. Exergy and structural analysis of an absorption cooling cycle and the effect of efficiency parameters // *Int. J. of Thermodynamics*. 2005. Vol. 8 (4). Pp. 191–198.
4. Bratuta E. G., Kharlampidi D. Kh., Sherstyk V.G. Influences of non-isobaric processes condensation and evaporation on the energy efficiency refrigeration machines and heat pumps // *Eastern-European Journal of Enterprise Technologies*. 2006. Vol. 3/3(21). Pp. 91–93.
5. Bratuta E. G., Sherstyk V.G, Kharlampidi D.Kh. Analysis of influences Анализ влияния hydraulic resistance pipelines of refrigeration machine on the energy efficiency// *Integrative Technologies and Energy -Saving*. 2007. No.1. Pp.16–23.
6. Kim Y. J., Park I. S. Development of Performance-Analysis Program for Vapor-Compression Cycle based on Thermodynamic Analysis // *J. of Industrial and Engineering Chemistry*. 2000.Vol. 6 (6). Pp. 385–394.
7. Kalaiselvam S., Saravanan R. Exergy analysis of scroll compressors working with R22, R407C, and R417 as refrigerant for HVAC system // *Thermal science*. 2009. Vol. 13. Pp. 175–184.

TEMPERATURE DISTRIBUTION PREDICTION FOR TWO-PHASE HOT PLATE UNDER CONTACT THERMAL RESISTANCE TEST CONDITIONS

N. Koneva

A.V. Luikov Heat & Mass Transfer Institute NAS Belarus

P. Brovka str. 15, 220072, Minsk, Belarus

Tel: +(37517) 2842244/Fax:+(37517) 2922513; E-mail: nsk@hmti.ac.by

Abstract

Reproducible characteristics, small gradients and instrumental circuit play important role in system performance during procedure of the contact resistance testing on hot plates. Paper describes the study of temperature distribution and thermal control peculiarities of heat pipe based hot plates. Thermal control principle of evaporation-condensation circle provides a self-compensation to environmental parameter fluctuations and accurate surface temperature simulation conditions. Two-phase hot plate provides the important requirements for heat flux and surface temperature sensors testing: uniform and unidirectional heat transfer between the testing sample and heat source, high rate of heat transfer from the surface to the sensor and contact resistance.

KEYWORDS

Contact thermal resistance, heat pipe, thermal control, temperature of surface, uniform temperature distribution.

INTRODUCTION

Improvement of the solid and immersing thermostatic units for contact test methods go towards the elimination of variety of systematic errors during the experiments. The influence of thermal resistance onto the budget of uncertainty is well investigated on the referenced and measured temperature values only in solid hot plates. Most hot plates for sample testing by thermal contact have to reproduce of conditions exploitation. Heat pipe heat transfer as well its high value of effective thermal resistance provides the accurate repeatable reference temperature conditions. By using the highest thermal conductivity of two-phase hot plate it is possible to predict the contact heat flux and surface temperature sensor characteristics. Moreover, closed evaporation-condensation cycle realizes better thermostatic function. Two-phase hot plate gradually attains thermal equilibrium in the response to change the external test conditions. Thus it is possible to study the heat transfer in contact temperature sensor under specific test conditions. Peculiarity of heat pipe based hot plate method include: narrow operation temperature range due to heat transfer limitation factors, has limitation for power of heat supplies in the system. Two-phase hot plates due to specific organization and control of the multiple thermal resistances and heat transfer mechanism create a thermally compensation conditions for contact thermal resistance tested on their surfaces.

ACCURATE SURFACE TEMPERATURE SIMULATION

Temperature determination in isothermal devices

The main aim of hot plate is accurate control of superficial and spatial temperature in conditions of contact with additional thermal resistances, of isolation material samples, heat flux and surface temperature sensors [1, 2]. The better the heat transfer from the heat source to the sample the smaller the uncertainty in the measurement and the faster a stable end temperature is reached. Test unit is used for study of the heat exchange between sample and the surrounding surface and to other parts to be exposed to the environment. The unit also produces the uniform superficial and/or spatial temperature conditions to study the time response of any type sensors and any flow rate of the surrounding of the medium. In the Luikov heat and mass transfer institute the series of isothermal devices have been successfully created and tested [3, 4]. Among them the two new prototypes of two-phase hot plate (Fig.1.) with different thermal control loop for study samples in the intermediate temperature range.

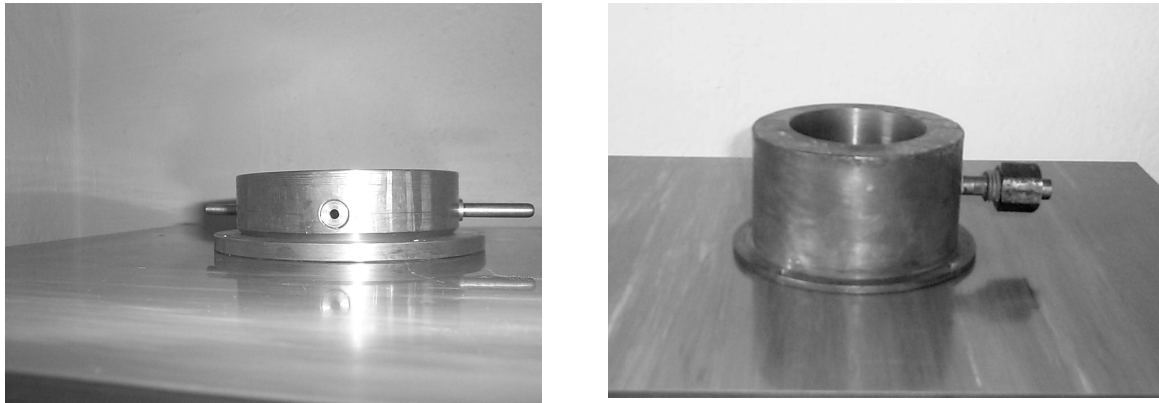


Fig. 1. Examples of two-phase units for contact thermal resistance testing

Hot plate has the parametric stabilization of two different types. Regulation both the minimal operation temperature difference, measured across the plate ΔT_e , and evaporation-condensation heat transfer present in the system. The device maintains the different saturation temperatures T_{ref} . The heat pipe in steady state conditions with correspondent thermal resistances and temperature measurement points presented on Fig.2. By measuring the temperature difference between vapour channel and evaporator ΔT_e the temperature difference for condenser has been evaluated ΔT_c since the design symmetry of thermal resistances.

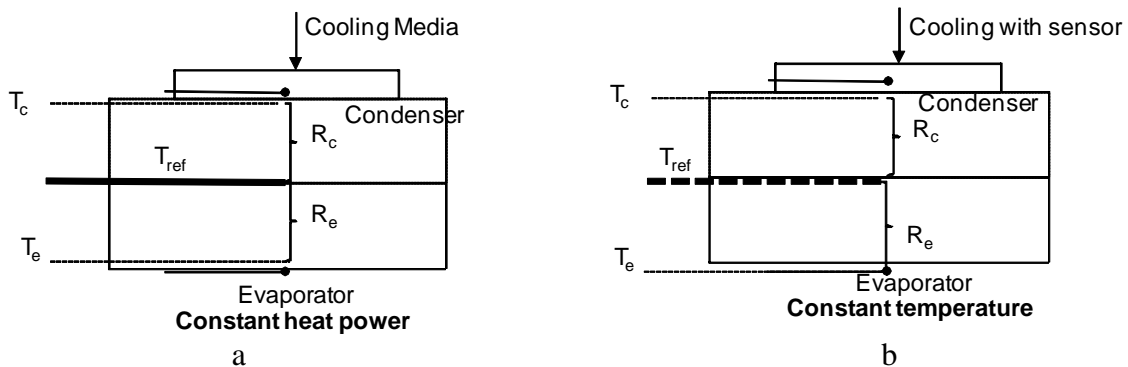


Fig. 2. Sample under constant heat power (a) and constant temperature (b) test conditions

In heat pipe hot plate the temperature uniformity for condenser T_c has minimal dependence from temperature distribution of heat sources. Procedure of temperature determination for hot plate includes examination the thermal conditions in steady state. The stability factor eq. (1) describes the repeatable temperature thermal characteristics under different test conditions:

$$K_S = R_{after}/R_{before} = (\Delta T_{after}/\Delta T_{before}) (Q_{before}/Q_{after}) \quad (1)$$

In case when equivalent heat pipe thermal resistance R_{after} has small variations from R_{before} and $(\Delta T_{after} \approx \Delta T_{before})$ leads to condition $(Q_{before} \approx Q_{after})$.

Temperature distribution prediction in steady state conditions

The results of spatial temperature distribution simulation shown on the Fig.3 indicates the uniform temperature fields for two-phase hot plate which is better than the non-uniform field for solid body isothermal devices. The geometry for simulation of both plates was: $d = 100$ mm, $h = 18$ mm. For three types of tested plate: with high thermal conductivity ($\lambda = 100$ W/(m·K)), heat conductive sample ($\lambda = 20$

W/(m·K)) and thermal isolation ($\lambda = 0.1$ W/(m·K)) the contact thermal resistance should be tested. Heating region in temperature conditions of $T_c = 150$ °C characterized by maximum temperature gradient ($\Delta T_b/l = 10.5$ °C/cm).

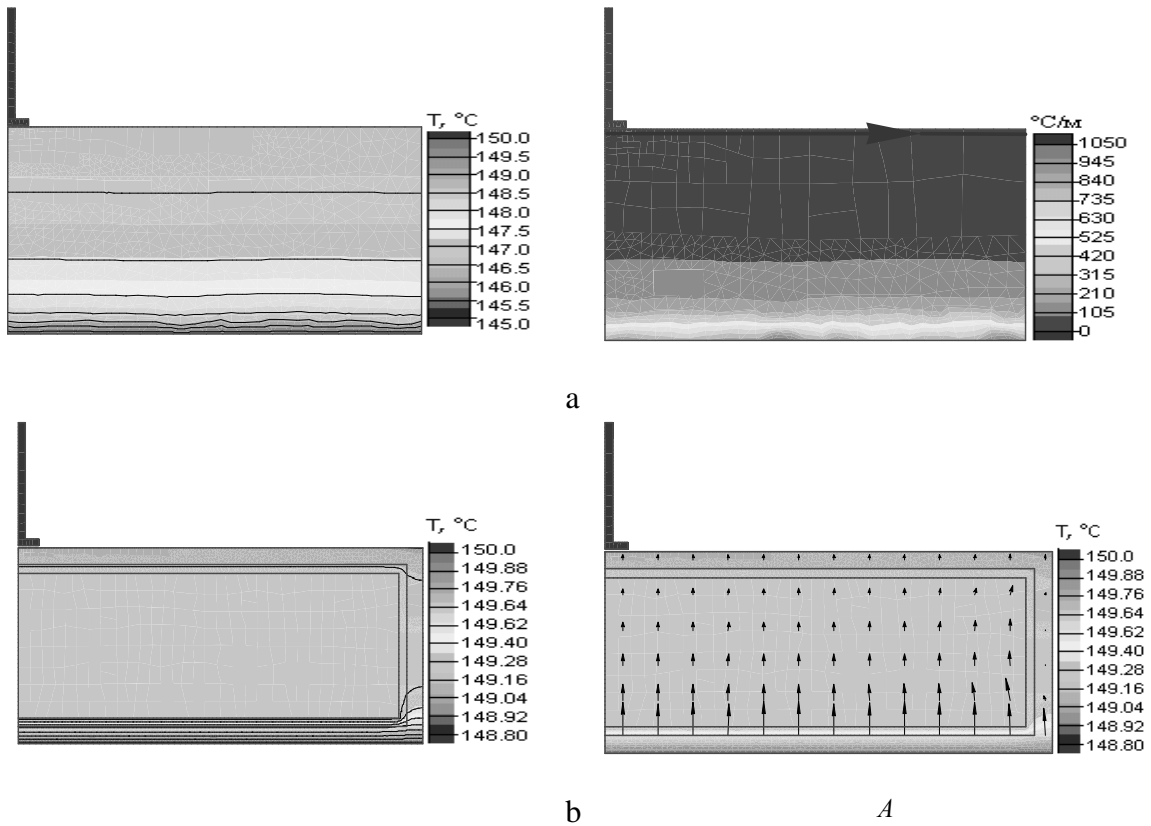


Fig. 3. Temperature distribution (left) and gradients (right) of solid plate (a) and two-phase (b) hot plate under steady state before and after sample testing (free convection $T_f = 20$ °C, $\alpha = 6$ W/m²·K)

The external effect from cooling media having temperature T_f to surface temperature prediction T_s is lower due to lowest thermal resistance ΣR of two-phase hot plate between cooling media and external thermal resistance at the condenser. Non-uniform distribution of temperature differences ΔT is located in thin regions of condenser and evaporator (Fig.3, b). Thus, the vapor temperature T_{ref} measured by accurate sensor is used to estimate the condenser temperature $T_s = T_c$. Test conditions for two-phase hot plate in case of axial one-dimensional heat flow have to be defined by eq.2.

$$\beta = \frac{T_s - T_f}{T_{ref} - T_s} = \frac{R_{konv}}{R_{HP}} \quad (2)$$

In test conditions with contact thermal resistance of the hot plate (Fig. 2) the heat transfer stability factor will change according to the eq.3.

$$\dot{q}A = \frac{T'_s - T_f}{T_{ref} - T_s} = \frac{R_{konv}}{R_{HP} + R_s} \quad (3)$$

Testing procedure allows determining the sensor heat dissipation value in ideal and real conditions of use. Temperature in the contact region of the hot plate surface T'_s compares with vapor temperature T_{ref} and with predicted surface temperature T_s . The calculation model has been used to predict the temperature distribution for all contact types of thermal resistances connection to the hot plate [5]. The Fig.4 demonstrates the typical temperature distribution of the previously described hot plates under the presence of additional contact resistance R_s .

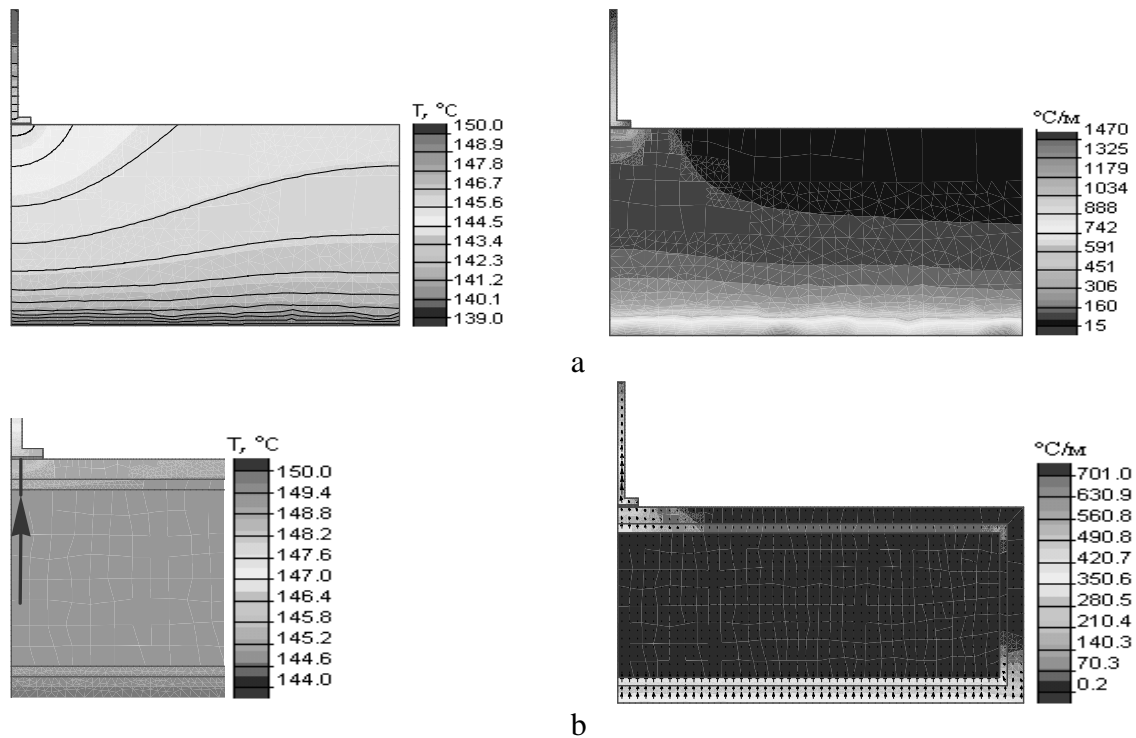


Fig. 4. Temperature distribution (left) and gradients (right) with tested sensor in a cross section plane in the same conditions for solid thermostat (a) and two phase hot plate (b)

As shown on Fig.4,b. the small region with non-uniform temperature distribution exist in condenser that should determine the correction value to the measured responsively of the contact sensor. In presented test conditions the heat pipe hot plate temperature distribution is estimated with lower value of uncertainty. First, because the thermal conductivity of traditional hot plate is smaller than α_{hp} , the contact resistance impact is smaller at heat flux which keeps $q = \text{const}$. Second, the average thermal resistance of material R_m between temperatures registered by sensor T_s and reference temperature T_{ref} is much higher for traditional hot plate than for heat pipe. Moreover, the two-phase hot plate temperature T_{ref} is independent from sensor location at the condenser surface and one inside the unit.

Accurate prediction of the temperature difference, condenser temperature T_c and temperature T_s require thermal resistance symmetry. Thermal interfaces at evaporator and condenser have equal and minimal thickness, including capillary structure saturated with liquid. Improved thermal control of the system requires a fundamental understanding of the fluid flow and heat transfer that occurs in the unit [6]. To achieve and maintain the predicted spatial and superficial temperature distribution the two-phase hot plate uses two types of thermal control circuits. The measurement circuit for heat pipe has to be based on open or closed type.

Optimum selection of measurement circuit for hot plate thermal parameters is based on temperature specific application, on thermometers classification by range, by sensitivity and stability. For instance, primary industry requirements are the temperature range, durability, the easy calibration and stability. Primary biomedical requirements are temperature range, precision and multi-point sensing.

THERMAL CONTROL OF SET POINT TEMPERATURE

Temperature control with feedback

The closed loop under constant power heat supply conditions was used to maintain the thermal equilibrium of heat pipe. According to this, the hot plate first temperature sensor in vapor used as input temperature value and the feedback to heater controller sets the temperature T_e . The second temperature sensor monitors the vapor output temperature. The heater controller maintains the set point of heat pipe. When the heat power is dynamically adjusted the closed loop does not provide the quick and stable thermal equilibrium. Reproducibility of the output temperature value is associated with estimation of all possible uncertainties. Temperature distribution estimation method has negligible uncertainty values due to vapor homogeneity, due to a reduced number of temperature sensors. In addition the condenser temperature T_c estimation method has negligible uncertainty due to thin material layer between reference thermometer and sensor, due to uniform surface temperature distribution at condenser surface and quick self-adjustment to ambient conditions.

Advanced temperature measurement circuit

The thermal control system should provide the data for the thermal resistance estimation of the heat pipe at steady state. Multy-function heater generates a constant heat power Q or constant evaporator output temperature T_e by heat power adjustment. Having the evaporator heat power value Q it is possible to estimate ΔT_e and thermal resistance of heat pipe. For experimental study of thermal control peculiarities the measurement system is supplied with two temperature sensors. The first sensor which is located at heat source and measures the value of T_e can be used as control input value to achieve the desired outlet temperature of external evaporator surface. The second sensor is placed in the middle of the vapour channel and measures the T_{ref} value, that travels closer to the thermodynamic equilibrium point.

Typically the passive control loop sets the input value T_e without taking into account the signal from output side. Such measures are not enough for precision output control; behaviour of the system is not accurately predictable. In real measurement procedure the disturbance from environment and from the additional thermal load at condenser have a negative effect on preset output temperature T_e and in T_{ref} . The benefit from the using the value ΔT_e is the self-feedback control to any external disturbances of system. The precise measurement of ΔT_e guarantee the estimation of the ΔT_c and output temperature value of the condenser T_c . The platinum resistance thermometers are used for precise temperature difference measuring of ΔT_e and ΔT_c ; every temperature sensor has a fixed position. Self-adjustment function of the heat pipe consists of variation of correspondent internal thermal resistances R_e and R_c . To estimate the local temperature gradients the hot plate is divided into several zones according to liquid phase distribution and set temperatures.

CONCLUSIONS

Thermal performance, measurement methods and uncertainties budget and temperature distribution prediction method for the heat-pipe hot plate has been discussed. Such device can simulate of real conditions of contact thermal resistance testing. Two-phase construction permits the use of varying number of sensors. Temperature distribution modeling under the contact thermal resistance test conditions shows that condenser is most suitable region for the accurate surface temperature estimation. It is important for sample testing to maintain the thermal resistance symmetry and spatial temperature uniformity of the hot plates. The axial temperature uniformity inside the hot plate is produced by closed evaporation-condensation circle and maximum vapor volume. Radial non-uniform temperature distribution within condenser region is caused by hot plate liquid transport characteristics and test sample and sensor contact resistance. Accurate temperature determination of every test samples on hot plate provide is temperature extrapolation method T_c with low uncertainty value. For both two-phase a hot plate with different thermal control circuits the reference temperature T_{ref} is measured in vapor channel by accurate temperature sensors. For accurate estimation of the temperature differences ΔT_e and ΔT_c platinum thermal resistance thermometers are required. Advanced thermal control is organized for further detailed study of the dynamic spatial and surface

temperature distribution. It is an appropriate method for surface measurements in microscopy based platform for detailed studies temperature dependent phase-change phenomena in biological and medical samples and specific testing of geological, semiconductor, photovoltaic, and other materials. The surface temperature estimation method based on contact thermometry is chosen for non-contact thermometry further investigation.

Acknowledgments

The author expresses her gratitude to the Istituto di Nazionale Ricerca Metrologica (INRiM, Italy), for the fellowship and Piedmont Region Administration of Italy, for partially funding the work done.

References

1. Michalski L. *Temperature Measurement*, Joan Wiley & Sons Ltd., New York, 1996, P. 400.
2. Koneva N., Drahn. U. Survey of surface temperature measurement techniques and calibrating devices. *Preprints of the A.V. Luikov Heat and Mass Transfer Institute NAS of Belarus*. 2005. Minsk. Preprint No 2. P.
3. Konev S., Chishik S., Domorod L., Koneva N., An isothermal heating microscope platform// *Annual proceedings: Heat-mass transfer. Minsk, Belarus*. 2008. Pp. 442-445. (in Russian).
4. Rosso L., Koneva N., Fericola V., Development of a Heat-Pipe-Based Hot Plate for surface-temperature measurements // *International Journal of Thermophysics*. 2009. Vol. 30. Pp. 257–264.
5. Bardon J. P., Cassagne B. *Techniques de l'Ingenier, traite Mesures et Controle*. R2. 732
6. Dunn P., Reay D. A. *Heat pipes*. 3rd ed. Pergamon Press. 1982.

HEAT PIPES WITH THE POROUS COMPOSITE STRUCTURES FUNCTIONING AT ANY ORIENTATION

A. G. Kostornov, A. A. Shapoval, A. L. Moroz, I. V. Shapoval

Department of permeable materials
Frantsevich Institute for Problems of Materials Science
Ukrainian National Academy of Sciences,
Tel/fax: 044-424-15-71; E-mail: ash48@rambler.ru

Abstract

Some researches results of heat pipes characteristics are presented in the report. Such pipes (HP) are intended for operation at any orientation in a gravitational field. The improvement of heat pipe operation in gravitational counteraction conditions is achieved by means of composite capillary structures in which design the best properties of fiber and powder materials are synthesized in a certain way. The characteristics of pipes, especially their thermal resistance, are investigated in all various heat pipes positions concerning horizon.

KEYWORDS

Heat pipes, composite capillary structures, gravitation, thermal resistance, orientation.

INTRODUCTION

Heat transfer parameters in the heat pipes (HP) heating zones and especially their limited heat fluxes, while working in usual (ground) conditions, essentially depend on orientation (disposition) of HP in space. From the experience of HP using researches and practice it is known, that the real height of the liquid capillary raising well moistening porous capillary structures (CS) does not exceed the values of 0.5 m. The length of a HP heating zone is a part of the specified value (0.5 m). The improvement of the HP parameters at their operation in gravitational force counteraction conditions is an important thermophysical and technological problem. Partially the decision of this problem is found in contour heat pipes development. It is necessary to note, that difficult and expensive technologies are needed for the contour heat pipes manufacturing.

The authors know only few researches, in which parameters and characteristics of porous capillary structures were specially investigated during HP working in difficult conditions of gravitational force counteraction.

PROBLEMS OF THE PERFECT CAPILLARY STRUCTURES CREATION FOR HEAT PIPES

The construction of HP capillary structure are very important for the effective HP functioning. The HP capillary structure must carry out two main functions: 1) hydrodynamical function (operational liquid-heat-carrier transportation at HP various disposition in a gravitational field deterioration); 2) thermophysical function (high-heat-intensity in HP heating and cooling zones). Total influence of hydrodynamical and thermophysical factors on heat transfer processes has often opposite character, i.e. the improvement of hydrodynamic processes leads to the deterioration of their thermal physics.

The wire mesh layers were used as capillary structures by HP developers in their first HP designs. Such application was based on the wire mesh materials availability, because of their serial industrial production. However, from the previous experience of heat pipe production, mesh materials have unsatisfactory thermophysical and operational characteristics. In particular, the pore size distribution, typical for mesh materials, leads to the unstable process of two-phase heat transfer (boiling) in HP heating zones as well as it imposes significant limitations on the quantities of the discharged heat fluxes. In addition to this, mesh materials at manufacturing TT are usually stacked in multiple layers that leads to the formation of local and relatively big heat emission resistances (R , K/W), including contact thermal resistances.

Metal-powder capillary structures (MPCS) guarantee better results in comparison with mesh CS [1, 2]. MPCS, unlike mesh CS, possess certain pore size distributions that guarantee stable boiling in the HP heating zone. Also powder CS guarantee relatively great values of the height of a liquids-heat-carriers capillary lifting in HP. However, CS powder also has some disadvantages. They are: 1) the presence of a relatively large number of closed (deadlock) pores; 2) the deterioration of CS permeability, because of the increased hydraulic resistance, caused by the characteristic properties of the metal-powder structures; 3) the presence of the so-called «heat hysteresis», arising during periodic increasing and reduction of heat flows brought to HP. The heat hysteresis worsens the heat pipes operation.

Metal-fiber capillary structures (MFCS), developed and studied in Frantsevich Institute for Problems of Materials Science of the Ukrainian National Academy of science, are practically deprived of the above mentioned weaknesses. There is no deadlock pores in MFCS owing to characteristic structure properties, that excludes undesirable heat hysteresis in such CS. The metal-fiber CS guarantee high hydrodynamical characteristics: the high permeability and the satisfactory height of capillary liquid lifting in HP. Also MFCS possess high thermophysical parameters of heat pipes, for example: the potential of HP functioning in the modes of stable liquid boiling in heating zones, high heat transfer intensity in heating and cooling zones, high limiting values of critical heat fluxes in heating zones.

Also MFCS have good physical-mechanical and operational characteristics. MFCS manufacturing techniques guarantee stable and reproducing parameters, the large resource of operation, high reliability of functioning, the capability of plastic deformation in a constructive necessity. Last feature of the HP with MFCS is an important factor for the heat pipes practical use in real systems and devices of the modern equipment.

COMPOSITE CAPILLARY STRUCTURES AND CHARACTERISTICS

The complex researches and development, carried out in The Institute for Problems of Materials Science made it possible to create composite fiber-powder capillary structures [3]. Positive qualities and properties of the capillary structures, made on the basis of the fibrous and powder materials synthesis, are effectively combined in such CS.

The cycle of heat pipe characteristic researches with composite porous capillary structures has shown, that such HP at work in "normal" conditions of space disposition practically are better than pipes with "usual" fiber porous capillary structures. In "difficult" conditions (zone of heating pipes located above a zone of cooling) "new" HP guarantee stable functioning at the increased values of heat flows (up to the values of $Q = 20-25$ W).

We have developed and created a set of pilot heat pipes (9 pieces) with composite capillary structures for the experimental researches. Some characteristics of pilot HP are presented in Table 1.

Table 1. Characteristics of pilot capillary structures and heat pipes

Number HP	CS Structure	CS Porosity Θ , %	Thickness of CS δ , mm
HP 1	Fibre \varnothing 50 microns,	71	1.0
HP 2	Powder 80 microns	74	1.0
HP 3	Fibre \varnothing 30 microns,	79	1.0
HP 4	Powder 40 microns	78	1.0
HP 5	Fibre \varnothing 50 microns,	85	0.8
HP 6	Powder 80 microns	85	0.8
HP 7	Fibre \varnothing 30 microns,	83	0.8
HP 8	Powder 40 microns	85	0.8
HP 9	Fibre \varnothing 50 microns	82	0.8

THE EXPERIMENTAL EQUIPMENT FOR THE RESEARCHES OF HEAT PIPE CHARACTERISTICS WITH COMPOSITE CAPILLARY STRUCTURES. THE TECHNIQUE OF THE RESEARCHES

A special stand is developed for thermophysical researches of HP parameters (Fig. 1). The angle of HP inclination was being changed by 180° relatively to the horizon. The pilot heat pipe was heated by the special heater. Heat removal from a condensation zone was carried out by the liquid cooling. We measured the temperatures on HP length by standard microthermocouples.

The structure of the experimental stand contains: the system of supply, regulation and measurement of a power (heat flow), the system of precision temperature measurement in HP control spots, system of maintenance and measurement of the heat-evacuation parameters, as well as some auxiliary systems.

The test procedure of HP researches was standard and consisted of the following: 1) pilot HP preparation to the tests; the installation of thermocouples on a HP surface (at the 5–7 control spots); the subsequent fastening of heating and cooling devices: 2) HP installation in researching positions ("A" – HP heating "from below"; "B" – HP is located horizontally; "C" – HP heating "from above"); 3) the power supply to HP by turning on an electro-heater. Thus, values of brought heat flow Q were changing in the range of 0–70 W, by means of the laboratory autotransformer, with great advance of 10 W. At the HP installation in position "a zone of heating – above" we were changing a heat flow in the range of 0–25 W, with great advance of 5 W; 4) we were waiting for a stationary heat mode (the thermocouples were fixed at some instant state) and measured the following values: 1) the heat flow (Q , W); 2) the temperatures of HP surface in 5–7 spots (t , $^\circ\text{C}$). Then we rated the values of a the thermal resistance R_{HP} (K/W) for pilot HP.



Fig. 1. The general view of the stand for HP researches

We tested all pipes in 3 characteristic positions concerning a line of a horizon: 1) HP heating zone – "below"; 2) HP heating zone is located horizontally; 3) HP heating zone of TT – "above". The main characteristics of pilot HP is following: 1) the HP-shells, fibrous and powders are made from a stainless steel (type 09X18H10T); the pipe-length: $L = 300\text{mm}$, external diameter of the shell: $\varnothing = 10\text{ mm}$; the liquid-heat-carrier – ethanol.

THE RESEARCHES RESULTS OF HEAT PIPES WITH SYNTHESIZED COMPOSITE CAPILLARY STRUCTURES

The results of our experiments are represented in the form of graphic dependences of temperature in a control spots of a transport zone on a surface of the HP-shell from the time of the tests. Also there was a

representation of findings in the form of thermal resistance R_{HP} dependence on a heat flow, at the angle variation of HP-inclination. The dependences of thermal resistance R_{HP} on a heat flow and on the angle of HP-inclination are presented in Figs. 2, 3.

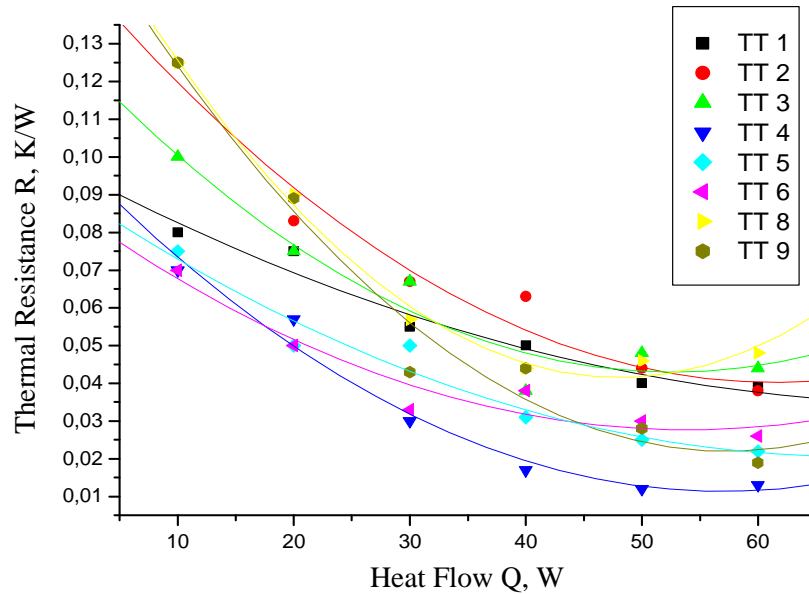


Fig. 2. Thermal resistance of heat pipes with composite and fiber CS at HP “below”-heating

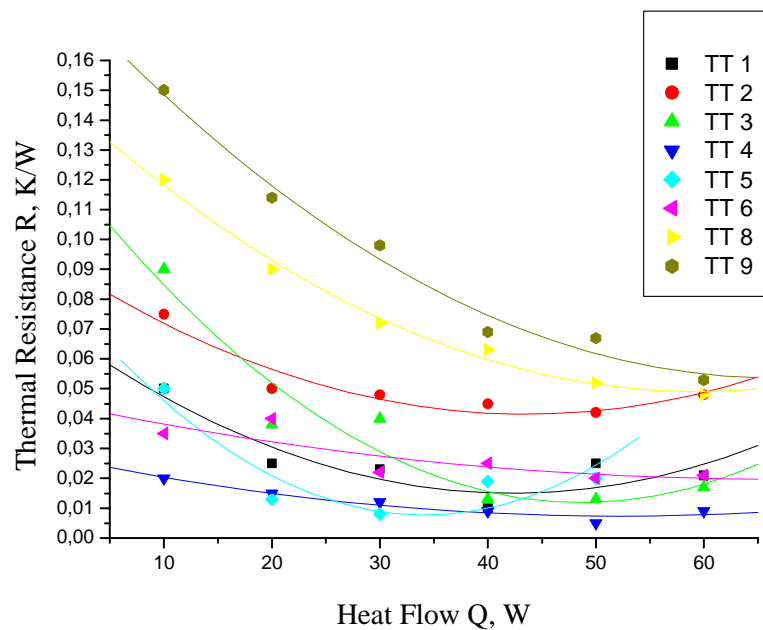


Fig. 3. Thermal resistance of heat pipes with composite and fiber CS at HP “horizontal” heating

We did not aim to make the experimental studies of the maximal heat flows, which our heat pipes could transmit. For an estimation of limiting heat flows Q_{max} we used known in the literature [4, 5] formulas. The results of calculations have confirmed the following fact: the high-porous structures guarantee big maximal heat flows at the HP-positions closed to horizontal. The capillary structures with average porosity ($\Theta \cong 40\%$), in comparison with high-porous CS, function better in position «HP heating – above». It is necessary to note, that calculations under known formulas were made in a view of assumptions about full saturation by the liquid of HP capillary structure. The CS partial drainage in real conditions of the HP with high-porous CS functioning could take place in that case when HP heating zone is situated above a cooling zone.

It is known, that speed of liquid flowing through the capillary structures is characterized by viscosity factor of permeability K (m^2). The fibrous structures differ from other CS types (for example, powder CS) because of the absence of the deadlock pores interfering longitudinal movement of a liquid. As a result the permeability indexes for the fibrous high-porous CS ($Q > 70\%$) reach the values of $K = 80-100m^2$. The specified values are greater in comparison with the values typical for powder structures ($K = 5-30 m^2$).

Thus, in horizontal position fibrous CS transport a liquid to the heating zone much more quickly in comparison with powder and mesh CS. The fibrous CS with extremely high porosity can't always guarantee the values of a capillary raising height of liquid (H , m) while HP working against forces of gravitation (in position "HP heating – above"). The large-scale pores of high-porous CS are easily drained, and capillary forces keep a liquid in such pores. The structure synthesis of positive properties of two different capillary structure types in one composite structure is capable to guarantee good characteristics of the created heat pipes while working in horizontal HP position as well as in conditions of gravitational force counteraction.

The researches results confirmed this statement. In positions "A" (angle of HP bank $\varphi = -90^\circ$, HP heating – "from below") and "B" ($\varphi = +90^\circ$, horizontal HP position) heat pipes with composite CS were working steadily and guaranteed the temperature level of a transport zone in a range similar to the range of temperatures of HP N1 with fibrous CS.

In position "C" (angle of HP bank $\varphi = +90^\circ$, HP heating TT – "from above") HP No. 2 and HP No. 3 guaranteed the higher values of removed heat flow ($Q_{max} = 20$ W) in comparison with value $Q_{max} = 10$ W, typical for HP No. 1. The last fact is caused by the presence of the powder parts in composite structure. The powder components have essentially smaller pores. The last fact, accordingly, guaranteed the best capillary liquid elevation in HP heating zone.

Similar results are received on the other HP researches (Figs. 2–4). Researches of the influence of HP developed characteristics with composite CS on thermal resistances R_{HP} have shown, that HP thermal resistance descends a little while heat flow Q increasing. Such results are explained because of the heat transfer intensity increasing in heating and cooling zones.

CONCLUSIONS

The researches results for developed HP with capillary structures of new types permit to assert the following.

1. In horizontal position and in position of "HP heating – below" the ethanol heat pipes with composite CS in transferred heat flow range of $Q = 0-70$ W function steadily and guarantee the low values of thermal resistance R_{HP} and high thermophysical characteristics. Such heat pipes not concede to HP with metal-fibrous capillary structures.
2. In the position of "HP heating – above" (the most difficult position for HP functioning) heat pipes in transferred heat flow range of $Q = 0-20$ W also work steadily and guarantee satisfactory values of thermal resistance R_{HP} . Thus, they transfer the heat flows with greater values (\sim in 2 times) in comparison with mono-fibrous HP.

References

1. Kostornov A.G. *Materials Technology of a Disperse and Porous Metals and Alloys. Vol. 2*, Kiev: Naukova dumka, 2003. – 550 p. (in Russian).
2. Belov S.V. *Porous Metals in Mechanical Engineering*, Mechanical engineering, Moscow, 1981. – 247 p. (in Russian).
3. Pat. 49874. Ukraine. The way of manufacturing of a non-tight layered materials from a metal fibre and powder / A.G. Kostornov, A.L. Moroz. Bulletin No. 10, 10.15.2002 (in Ukrainian).
4. Chi S.W. *Heat Pipe Theory and Practice*, Hemisphere Publishing Corporation, Washington, London, 1980. – 206 p.
5. Ivanovskij M.N., Sorokin V.P. et al. *Physical Fundamentals of a Heat Pipes*, Moscow: Atomizdat 1978. – 256 p. (in Russian).

CRITICAL POINT SHIFT IN FLUIDS EMBEDDED WITH NANOSTRUCTURED MATERIALS

D. N. Nikitin, B. V. Kosoy, V. A. Mazur
Engineering Thermodynamics Department
Odessa State Academy of Refrigeration
1/3 Dvoryanskaya Str., Odessa, 65082 Ukraine
e-mail: mazur@paco.net

Abstract

The main goal of the present research is to study the effect of nanoparticle doping on the critical point shift of classical fluids embedded with nanostructured materials (fullerenes and carbon nanotubes). The novel approach to study of nanostructured materials behavior in disordered media is based on the concept of structure similarity of nano- and near-critical fluids that exhibit enhanced thermal conductivity. The systems toluene + fullerene (carbon nanotubes) were analyzed to estimate the critical point shift in pure component from low temperature experimental data in liquid state. The obtained results present useful information for scientists and engineers working in the field of emerging nanotechnology applications. Computer modeling proved a possible azeotropy appearance in the zeotropic blends with nanoparticles that could be considered as a replacement for the conventional refrigerant R134a. There is no doubt that extension of existing knowledge on thermodynamic and phase behavior of nanofluids will guide to reliable engineering recipes resolving the actual problems of modern nanotechnologies.

KEYWORDS

Refrigerants, zeotropic blends, critical point shift, azeotropy, nanostructured materials.

INTRODUCTION

Nanofluids (NF), i.e. fluids embedded with nanostructured materials, have recently become a subject of growing scientific interest due to reports of greatly enhanced thermal properties. Key features of NF include thermal conductivity exceeding those of conventional suspensions, a nonlinear relationship between thermophysical properties and concentration for NF containing carbon nanotubes, and a significant increase in critical heat flux in boiling heat transfer. The exploitation of NF phenomena will allow to create a new class of efficient working and heat transfer media for wide range of technological application and bring such benefits like energy efficiency (e.g. improving heat transfer, reducing pumping power), lower operating costs, smaller/lighter systems (small heat exchangers) and cleaner environment (e.g. reducing heat transfer fluid inventory) [1].

The principal aim of this work is to study the effect of nanoparticle doping on the critical point shift of classical fluids embedded with nanostructured materials (fullerenes and carbon nanotubes). Since the diameter of nanoparticle is quite small, the nanostructured materials have specific properties and critical point of conventional fluids is shifted by adding nanoparticles. In present study the interplay between ballistic nature of heat transport in the nanoparticles and clustering effects in classic fluid is suggested as most credible scenario of NF thermal behaviour. The novel approach to study of nanostructured materials behaviour in disordered media is based on the idea of structure similarity of nano- and near-critical fluids that exhibit enhanced thermal conductivity. The systems toluene + fullerene (carbon nanotubes) are studied to estimate the critical point shift in pure component from low temperature experimental data in liquid state.

CRITICAL POINT SHIFT IN THE NANOFUIDS

Critical point defines thermodynamic behavior of substance in wide range of parameters of state. Adding of nanoparticles renormalizes the intermolecular interactions between fluid components embedded with nanostructured materials and shifts phase equilibria in the nanofluids. No direct experimental data are

available in literature to make conclusion about critical point shift. An assessment of nanoparticle doping on critical point shift of pure substances is possible to perform from experimental pressure – density – temperature ($P - \rho - T$) data. In this study we have used $P - \rho - T$ data for toluene embedded with single walled polydisperse carbon nanotubes (CNT) [2] and fullerenes [3]. The nanotube diameter varied from 0.4 to 2 nm, the tube length varied from 1 to 30 μm , and the nanotube concentration of 0.02 g/l [2].

It is hypothesized that the toluene with small impurities obeys the corresponding state (CS) principle. The rationale for this assumption is based on the two-parametric presentation of data [2], [3] by the Tait equation of state. We suggest that thermodynamic surfaces of reference fluid (toluene) and nanofluid with small nanoparticle concentration are coincided in reduced form. The compressibility factor (Z) of nanofluid is defined via scaled pure reference fluid properties

$$Z = Z(\rho_{Cnf}/\rho, T/T_{Cnf}), \quad (1)$$

where critical point parameters of nanofluid (ρ_{Cnf}, T_{Cnf}) are calculated from available experimental data in liquid phase far from critical point. To estimate the critical point parameters of system reference fluid (toluene) – nanoparticles (e.g., CNT) the fundamental equation of state in reduced form for toluene [4] was used. The results of our calculations are in good agreement with the data from [2] and [3]. As example, Figs. 2 and 3 illustrate the isotherm behavior of pure toluene and nanotube solution at different temperatures. The uncertainties in density for the equation of state are less 0.05% in the liquid phase in the temperature range 290 ... 330 K. The critical density shift from the low temperature data [2, 3] is about 4% both toluene – CNT and toluene – fullerene systems.

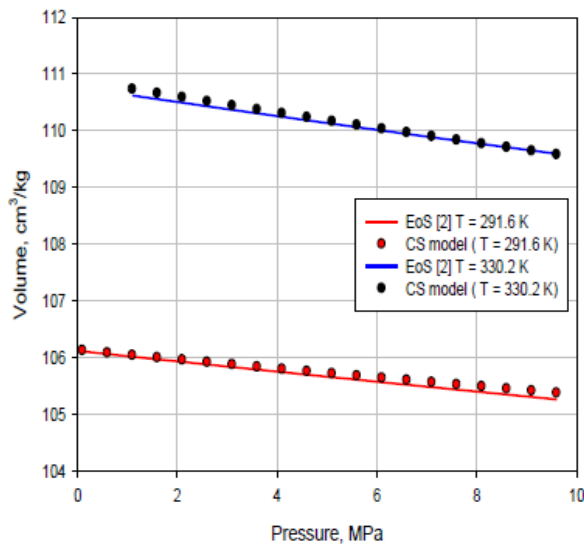


Fig. 1. The isotherms of pure toluene

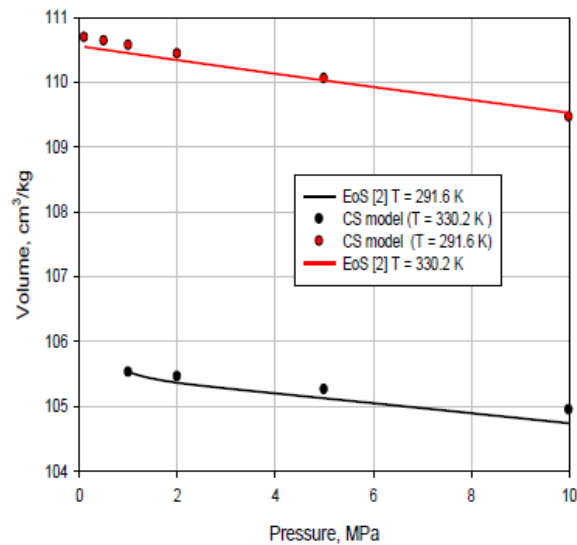


Fig. 2. The isotherms of toluene + CNT

Critical temperature shift restored from data [2, 3] doesn't exceed 7 K at given volume concentration (φ). To compute the thermodynamic properties of the nanofluids under investigation in the range 0 ... 5% volume concentrations of nanoparticles (np) the density of nanofluid (nf) calculated via reference fluid density (rf) by standard relation:

$$\rho_{nf} = (1 - \varphi)\rho_{rf} + \varphi\rho_{np} \quad (2)$$

The growth of volume concentration tends to increase the nanofluid critical temperature. The extrapolation data [2, 3] to nanoparticle volume fraction $\phi = 5\%$ predicts the temperature shift about 50 K at the same critical density.

Properties of nano-structured materials are specified by the intermolecular energy interaction competition between the nanoparticles and reference fluid. The ratio of a nanofluid physical property (F_{nf}) to that of the reference fluid (F_{rf}) at small ϕ can be expressed as a linear function of volume concentration. For instance, of critical temperature shift of reference fluid is written as

$$T_{C_{nf}} / T_{C_{rf}} = 1 + \alpha\phi + O(\phi)^2. \quad (3)$$

The effective thermal conductivities of liquids embedded with nanostructured materials are also found to obey the scaling law in eq. (3).

Coefficient α depends on nature of the nanoparticles and should be restored from experimental data. Other nanoparticles, e.g., Al_2O_3 , CuO , Fe_3O_4 due to higher density should increase the critical temperature shift. Nanoparticle addition promotes the aggregation of molecular structures into clusters in vicinity of critical state and significantly enhances the thermal conductivity of nanofluids due to changes in thermodynamic parameters of state in the phase diagram. Fig. 3 illustrates the results of nanoparticle volume fraction influence on thermodynamic properties (speed of sound) of toluene.

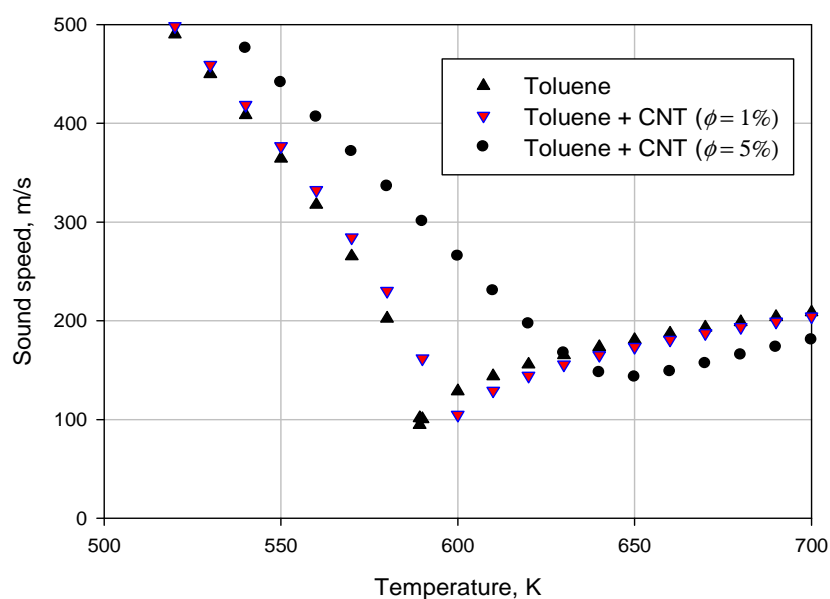


Fig. 3. Sound speed along isobar $P = 4$ MPa of toluene and toluene embedded with CNT

The shift of critical point parameters also changes the picture of phase behavior in binary mixtures and requires more detailed analysis unavailable in literature.

AZEOTROPY IN REFRIGERANT BLENDS WITH EMBEDDED NANOMATERIALS

A theoretical analysis of the topology of phase diagrams is a very useful tool for understanding the phenomena of phase equilibrium that are observed in multicomponent systems. The pioneering work of van Konynenburg and Scott [5] demonstrated that the van der Waals one-fluid model has wide possibilities of qualitative reproducing the main types of phase diagrams of binary fluids. The proposed classification was successful, and is now used as a basis for describing the different types of phase behavior in binary mixtures. A more rigorous classification of the typical characteristics of equilibrium surfaces and phase

diagrams of binary mixtures is given in the work of Varchenko [6], in which it is proved that the number of topologically different rearrangements is eight. At present, the topological analysis of equilibrium surfaces of binary fluid systems contains 26 singularities and 56 scenarios of evolution of the p – T diagrams [7].

To describe the thermodynamic properties and phase equilibria in the mixtures we use the one-fluid model of the SRK equation of state [8]

$$p = \frac{RT}{v-b} - \frac{a(T)}{v(v+b)}, \quad (4)$$

where R is the universal gas constant and v is the molar volume; the model parameters a and b depend on the molar composition of x_i and x_j with respect to the components i and j . The respective model parameters a and b are determined by quadratic dependences on composition and classical combining rules for the different pairs of interacting molecules a_{ij} and b_{ij} :

$$a = \sum_{i=1}^N \sum_{j=1}^N x_i x_j \sqrt{a_{ii} a_{jj}} (1 - k_{ij}), \quad (5)$$

$$b = \sum_{i=1}^N \sum_{j=1}^N x_i x_j \frac{(b_{ii} + b_{jj})}{2} (1 - l_{ij}), \quad (6)$$

$$a_{ii} = 0.4274 \frac{R^2 T_c^2}{P_{c,ii}}, \quad b_{ii} = 0.866 \frac{RT_{c,ii}}{P_{c,ii}}, \quad (7)$$

Global phase diagrams of binary fluids represent the boundaries between different types of phase behaviour in a dimensionless parameter space. The dimensionless coordinates depend on the model of equation of state; however, usually they are represented by analogy with the coordinates introduced by van Konynenburg and Scott for the van der Waals model [5]:

$$\begin{aligned} Z_1 &= (a_{22} - a_{11}) / (a_{22} + a_{11}), \\ Z_2 &= (a_{22} - 2a_{12} + a_{11}) / (a_{22} + a_{11}), \\ Z_3 &= (b_{22} - b_{11}) / (b_{22} + b_{11}), \\ Z_4 &= (b_{22} - 2b_{12} + b_{11}) / (b_{22} + b_{11}). \end{aligned} \quad (8)$$

Global phase diagrams for all realistic models have an extremely similar structure, particularly for the case of molecules of the same size. For example, the global phase diagrams of such different models as the Redlich–Kwong [8] or the Lennard-Jones binary fluid [9] are almost identical, including such sensitive phenomena as the presence of closed immiscibility regions. Accordingly, most of assumptions and conclusions based on the above mentioned models of phase behavior can be transferred to other cases. Algorithms of global phase diagrams construction are described in literature [11, 12]. To predict the

conventional phase diagrams the computational schemes [13] of phase equilibria calculations were realized in MATLAB.

The azeotropic boundaries are straight lines in the (Z_1, Z_2) -plane that cross at a single point in the vicinity of the centre for equal sized molecules. It opens the opportunity for obtaining the series of inequalities to separate azeotropic and zeotropic regions of the global phase diagram. Selection criterion for azeotrope for the SRK one fluid equation of state for binary mixture in global phase diagram variables was derived previously [14]:

$$Z_2 = \mp Z_1 - 0.67(1 \pm Z_1) \left(\frac{1 - Z_4}{1 \pm Z_3} - 1 \right), \quad (9)$$

where the upper signs «+» or «-» correspond to the value of the composition of critical azeotropic point at $x_c = 0$, the lower at $x_c = 1$. According to equation (9), in the Z_1 – Z_2 plane, at fixed values Z_3 and Z_4 , the boundary that separates the zeotropic and azeotropic states is a straight line. If a characteristic point is located in the northern or southern quadrants then azeotropy phenomena should appear in the binary mixture. Nanoparticles shift the critical point if added to the low-boiling component and thereby for substances with neighbor critical temperatures $a_{22} \approx a_{11}$ and $Z_1 \rightarrow 0$. It results to drastic phase behavior transformations from zeotropic to azeotropic state.

Here we consider phase behavior of the R1234yf – R161 zeotropic blend and R1234yf – R161 – Fe_3O_4 nanoparticles as most likely azeotropic system that are recognized as low global warming potential (GWP) refrigerants to replace the R134a refrigerant. The equation of state parameters for low-boiling component R1234yf were taken from [15]: $T_C = 367.85$ K, $P_C = 3.382$ MPa, and $\omega = 0.280$. For the equation of state parameters R161 corresponding values are as follows: $T_C = 375.35$ K, $P_C = 4.7$ MPa, and $\omega = 0.210$ [16]. The binary interaction parameters were fitted by the Lorentz-Berthelot combination rule ($k_{ij} = l_{ij} = 0$). Figs. 4 and 5 show the results of phase equilibria calculations for different temperatures in the pressure – composition and pressure – temperature diagrams. The R1234yf doped with the Fe_3O_4 nanoparticles increases the critical temperature of pure low-boiling component till 371 K. This shift conduces to transformation from zeotropic state (Fig. 4) to azeotropic state (Fig. 6).

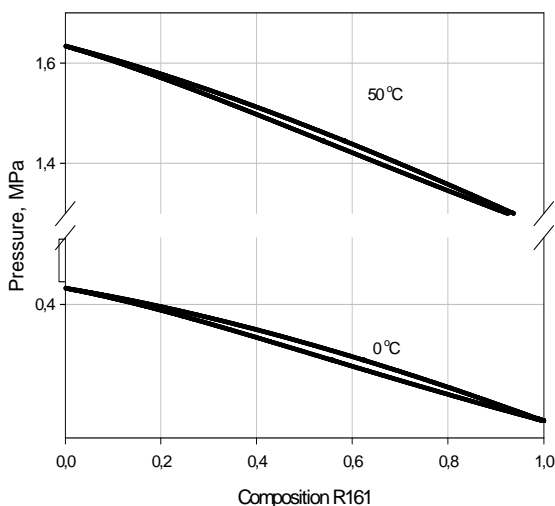


Fig. 4. $P - x,y$ diagram of the R1234yf – R161 binary blend at different temperatures

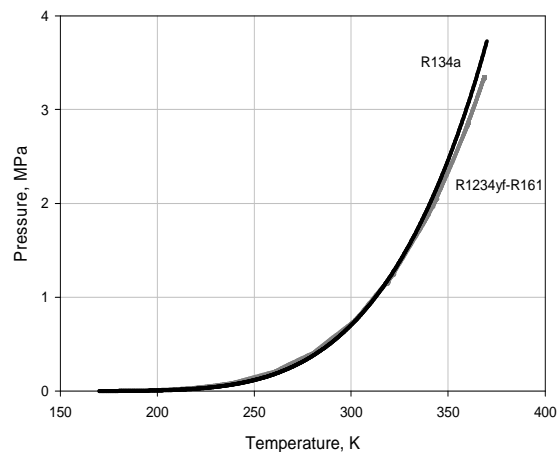


Fig. 5. $P - T$ diagram of the R134a and the R1234yf – R161 binary blend

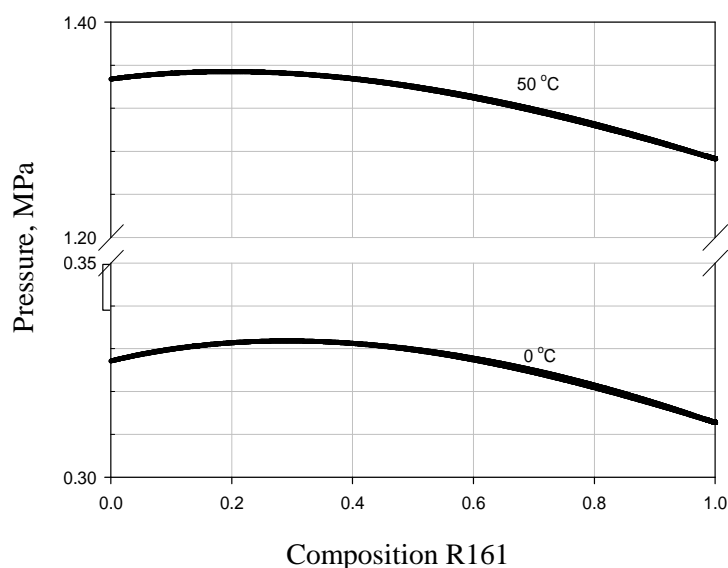


Fig. 6. P - x,y diagram of the R1234yf – R161 – Fe_3O_4 nanoparticles blend at different temperatures

CONCLUSION

This study is one of the first attempts to establish and demonstrate multiple links existing between the critical point shift in classical fluids and phase equilibria phenomena in mixtures embedded with nanostructured materials. From the very beginning of these efforts the obtained results serve very useful information for scientists and engineers working in the field of emerging nanotechnology applications. As an example, phase behavior of systems R1234yf – R161 and R1234yf – R161 – nanoparticles that are recognized as low GWP refrigerants has been studied. Computer modeling has shown a possible azeotropy appearance in the zeotropic blends with nanoparticles that can pretend to be replacement of conventional refrigerant R134a. There is no doubt that extension of our knowledge about thermodynamic and phase behaviour of nanofluids will lead to the creation of reliable engineering recipes for solving the actual problems of nanotechnologies.

References

1. Saidura R., Leong K.Y., Mohammad H.A. A Review on Applications and Challenges of Nanofluids // *Renewable and Sustainable Energy Reviews*. 2011. Vol. 15. Pp 1646–1668.
2. Adamenko I., Bulavin L., Korolovich V., Moroz K., Prylutsky Yu. Thermophysical properties of carbon nanotubes in toluene under high pressure // *J. of Molecular Liquids*. 2009. Vol. 150. Pp 1–3.
3. Adamenko I., Bulavin L., Moroz K., Prylutsky Yu., Scharf P. Equation of state for C_{60} toluene solution // *J. of Molecular Liquids*. 2003. Vol. 105, Nos. 2–3. Pp 149–155.
4. Lemmon E.W., Span R. Short fundamental equations of state for 20 industrial fluids // *J. Chem. Eng. Data*. 2006. Vol. 51. Pp 785–850.
5. van Konynenburg P.H., Scott R.L. Critical lines and phase equilibria in binary van der Waals mixtures // *Philos. Trans. R. Soc. Lond. Ser. A*. 1980. Vol. 298. Pp.495–540.
6. Varchenko A.N. Evolution of convex hulls and phase transition in thermodynamics // *J. Sov. Math.* 1990. Vol. 52(4). Pp 305–325.
7. Aicardi F., Valentin P., Ferrand E. On the classification of generic phenomena in one-parameter families of thermodynamic binary mixtures // *Phys. Chem. Chem. Phys.* 2002. Vol. 4. Pp 884–895.

8. Redlich O., Kwong J.N.S. On the thermodynamics of solutions: V. An equation of state: fugacities of gaseous solutions // *Chem. Rev.* 1949. Vol. 44. Pp 233–244; Soave G. Equilibrium constants from a modified redlich-kwong equation of state // *Chem. Eng. Sci.* 1972. Vol. 27. Pp 1197–1203.
9. Mazur V., Boshkov L., Murakhovsky V., Global phase behavior in binary Lennard-Jones mixtures // *Phys. Lett.* 1984. Vol. 104A. Pp. 415–418.
10. Deiters U.K., Pegg J.L. Systematic investigation of the phase behavior of binary fluid mixtures. I. Calculations based on the Redlich-Kwong equation of state // *J. Chem. Phys.* 1989. Vol. 90. Pp 6632–6641.
11. Patel K.S., Sunol A.K. Automatic generation of global phase equilibrium diagrams for binary mixtures // *Computers and Chemical Engineering*. 2009. Vol. 3 (11). Pp 1793–1804.
12. Cismondi M., Michelsen M. L. Global phase equilibrium calculations: Critical lines, critical end points and liquid–liquid–vapour equilibrium in binary mixtures // *J. of Supercritical Fluids*. 2007. Vol.39. Pp. 287–295.
13. Michelsen L., Mollerup J. *Thermodynamic Models, Fundamentals and Computational Aspects*. Lyngby (Denmark): Department of Chemical Engineering, Technical University of Denmark. 2002.
14. Artemenko S., Mazur V. Azeotropy in the natural and synthetic refrigerant mixtures // *International Journal of Refrigeration*. 2007. Vol. 30 (5). Pp 831–839.
15. Tanaka K., Higashi Y. Thermodynamic properties of HFO-1234yf (2,3,3,3-tetrafluoropropene // *3rd IIR Conference on Thermophysical Properties and Transfer Processes of Refrigerants*, Boulder, CO, USA. Paper 136, 2009.
16. Calm J., Hourahan G. Refrigerant Data Summary // *Engineered Systems*. 2001. Vol. 18 (11). Pp 74–88.

ASSESSMENT OF THE POSSIBILITY OF EXTRACTION AND UTILISATION OF GEOTHERMAL ENERGY FOR SUPPLYING ORC POWER PLANT/HEAT AND POWER PLANT

Wladyslaw Nowak, Aleksander A. Stachel

Department of Heat Engineering
West-Pomeranian University of Technology
al. Piastow 17, PL 70-310 Szczecin, Poland,
e-mail: andrzej.stachel@zut.edu.pl

Abstract

In the paper presented is the assessment of the possibility of utilisation of geothermal energy for supplying power plant/heat and power plant operating according to the low temperature Organic Rankine Cycle. The unit is supplied with heat acquired from the rocks by means of the underground closed heat exchanger installed at a high depth. In the paper discussed is the construction of the geothermal heat exchanger as well as principles of operation of the Organic Rankine Cycle power/heat and power unit. Additionally presented are basic relations enabling determination of the amount of extracted and utilized geothermal energy. The starting point for accomplished analysis was the thermal-hydraulic characteristics of the geothermal exchanger, which was developed based on the in-house analytical calculation model of the closed underground heat exchanger. Utilising the presented in the paper relations accomplished were calculations enabling assessment of operation of geothermal heat and power plant operating with different organic fluids and supplied with the network water of different temperatures at the outflow from the exchanger.

KEYWORDS

Geothermal energy, utilisation of geothermal energy, underground closed geothermal heat exchanger, low-temperature power plant, ORC.

INTRODUCTION

In Poland among the so called renewable sources of energy the geothermal and geothermic resources are regarded as those of high potential [1–3].

Practical implementation of geothermal energy is related to the extraction of water to the Earth's surface from the so called geothermal basins, which is very often highly mineralized. That is possible on the predominant part of the country. Due to the rather moderate temperature of extracted water energy contained there can be used first of all for heating purposes, which is discussed in detail in the available literature [1–5].

The second source of energy, namely the geothermic energy, can be acquired by means of special installations enabling introduction into the Earth's crust of water, which is going to act as the energy carrier. That water will remove heat from surrounding rocks and transport it to the surface. It is estimated that in Poland the possibilities for extraction of geothermic energy regard the depths of 2000–5000 m and are greater than the possibilities of acquisition of geothermal energy. The heat obtained in such a way can be used for heating purposes (heat from the depths of 2–3 km), as well as for production of electricity (heat from the depths 3–5 km) [3, 6–11].

In acquisition of geothermic energy there can be used two basic types of extraction installations, namely the open and closed systems.

One of the most interesting designs of the closed systems is the concept developed at the Technical University of Berlin of a so called underground closed geothermal heat exchanger, UCGHE in brief [11, 12]. The heat exchanger is composed of a set of pipelines located at a significant depth, through which the fluid removing heat from the rocks is pumped and subsequently transporting it to the Earth's surface, where it is transferred to the installation utilizing the heat obtained in such a way, Fig. 1. The heat exchanger features a significant independence from the localization as well as the possibility of a long term operation at relatively small power of circulation pumps. An important feature of the design is flexible way of its operation.

Additionally the exchanger enables extraction of geothermic energy in all those places where due to geological reasoning the open systems cannot be applied.

A major drawback of the UCGHE heat exchangers are significant investment costs and necessity of harnessing of difficult processes related to drilling and installation of sealed pipeline systems at large depths. It is estimated that the present technical advancement permits to develop the UCGHE situated at the depth of up to 5 km with a horizontal length of up to 15 km [12].

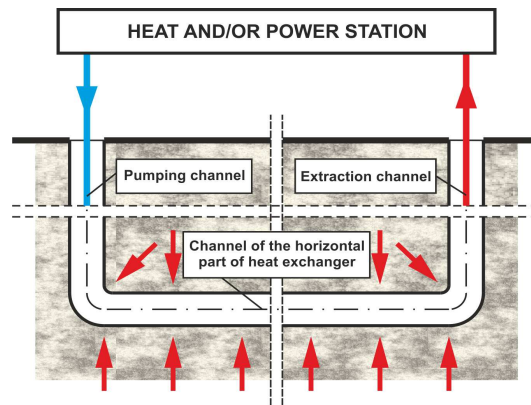


Fig. 1. Schematic of installation with a underground closed geothermal heat exchanger

It results from the up to date works that the exchangers of that type, situated at significant depths and acquiring the heat from the rocks, can be a source of energy applicable for supplying thermal plants as well as power plants [8, 9, 13]. Therefore the actions undertaken by the authors, of which the partial results are presented below, are aimed at the assessment of the possibility of application of the underground closed geothermal heat exchanger for supplying the power/heat and power plants equipped with the low-temperature installation operating according to the Organic Rankine Cycle.

1. UNDERGROUND CLOSED GEOTHERMAL HEAT EXCHANGER AS A SOURCE OF ENERGY FOR THE ORC PLANT

Due to specificity of extraction of geothermic energy an important issue in the analysis of that process is assessment of operation of such heat exchanger carried out with the view to extract and utilize thermal energy of the rocks.

In the considered case for the assessment of operations of the underground closed geothermal heat exchanger own analytical calculation model has been applied, where the transient heat conduction in the surrounding bed rock was considered [6, 8, 14, 15]. The model is derived at the following assumptions:

- Exchanger consists of three elements connected in series encompassing a vertical pumping channel, a horizontal channel, connecting the vertical channels, and a vertical extraction channel. For each of those elements there have been applied relevant calculation procedures including the fact that the overall heat transfer coefficient from the bed to the heat carrier is variable in time and uniform for the entire heat exchanger.

- Bed temperature at remote location from the extraction channel as well as the pumping channel varies linearly with depth, in line with the relation:

$$T_s(h) = a + bh. \quad (1)$$

- Temperature of the rock surrounding the horizontal part of the exchanger is constant and depending on the depth of channel location:

$$T_{sH}(h = H) = a + bH. \quad (2)$$

- Elementary rate of heat transferred from the bed to the heat carrier flowing in the heat exchanger can be determined utilizing the overall heat transfer coefficient k_z :

$$d\dot{Q} = k_z(\tau)[T_s(h) - T_p(h)]dA. \quad (3)$$

– Elementary rate of heat taken up by the heat carrier in the exchanger is given by:

$$d\dot{Q} = l_i \dot{W}_i dT_{pi}. \quad (4)$$

In the model utilised were relations enabling calculation of variable in time overall heat transfer coefficient or the overall thermal resistance from the rocks to the heat carrier. It has been assumed that the overall heat transfer coefficient k_z can be determined for the relation postulated by [16, 17]:

$$\frac{1}{k_z} = \frac{1}{\alpha} + \frac{D_1}{2} \sum_{i=1}^n \frac{1}{\lambda_i} \ln \frac{D_{i+1}}{D_i} + \frac{D_1}{2\lambda_s} \ln \frac{4\sqrt{a_s t}}{D_{n+1}} \quad (5)$$

or

$$\frac{1}{k_z} \cong \frac{1}{\alpha} + \frac{D_1}{2\lambda_s} \ln \frac{4\sqrt{a_s t}}{D_1}. \quad (5a)$$

Similar information can be obtained from the expression due to Djadkin and Gendler [1]:

$$k_z = \frac{k'_z}{1 + \text{Bi} \ln(1 + \sqrt{\gamma \text{Fo}})}, \quad (6)$$

where:

$$\frac{1}{k'_z} = \frac{1}{\alpha} + \frac{D_1}{2} \sum_{i=1}^n \frac{1}{\lambda_i} \ln \frac{D_{i+1}}{D_i}. \quad (6a)$$

Expression (5a) regards the deep drills where thermal resistance of pipelines can be neglected. Importance of particular quantities constituting the above expressions have been presented in detail in [8] and [15].

Developed calculation model of the underground closed geothermal heat exchanger enables calculation of temperature field in particular elements of heat exchanger as well as carry out the analysis and assessment of the influence of characteristic quantities of subsequent constituent elements on the reduced temperature difference of network water at the outflow from the exchanger [9, 15]:

$$\Theta_{1H,2L,3H} = \frac{T_{SH} - T_{p3H}}{T_{SH} - T_{p10}} = \phi + \Theta_{1H,2L} \cdot \exp(-kN_3) - \frac{\phi}{N_3} \cdot [1 - \exp(-kN_3)]. \quad (7)$$

The diagram developed in such a way, presenting the general course of curves depicting the temperature field of subsequent constituent elements of the UCGHE for different values of heat transfer units N_{ij} is presented in Fig. 2.

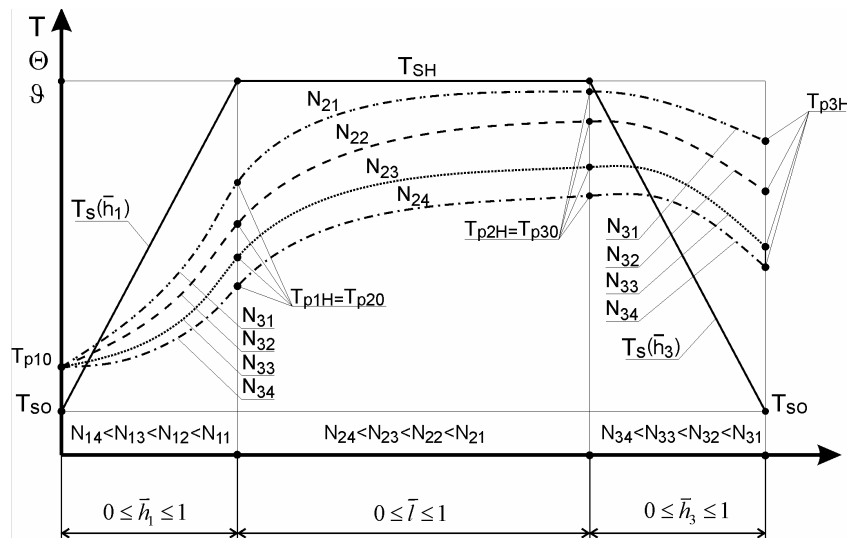


Fig. 2. Fluid temperature distribution in UCGHE for different values of N , if $k = 1$ [15]

On the extent of the rate of geothermic energy extracted from the rock and possible for utilization in the heat receiving system (heat plant, power plant) there decides the rate of heat carrier together with its temperature at inlet and outlet from the UCGHE, which results from the relation:

$$\dot{Q}_g = \dot{m}_g c_g (T_{gw} - T_{gz}) \quad [\text{kW}]. \quad (8)$$

It ought to be stressed that due to practical possibilities of utilisation an important quantity is temperature of water at outflow from the UCGHE, where its value is a function of:

- inlet water temperature to the exchanger (dependent on the kind of the heat receivers),
- temperature in the bed rock (significantly distant from the exchanger),
- extent of the rate of heat flowing through the exchanger,
- depth of location of geothermal exchanger and its geometrical dimensions.

Additionally, it stems from the conducted analysis that of significant importance on the temperature of water leaving the UCGHE are heat transfer conditions in the third element of the exchanger, i.e. in the outflow channel [8].

Presently used drilling techniques can be realized in temperatures not exceeding 175 °C [11, 12], and therefore the above temperature of the heat source should be assumed as a limiting upper temperature. Consequently, in the case of the power plant operating in the temperature range of 120 + 170 °C water can be assumed as a working medium. In case of temperatures lower than 120 °C, low-boiling point fluids should be used as a heat carrier and the working fluid.

In effect of application of the calculation model we can develop thermal-hydraulic characteristics of UCGHE enabling calculation of the rate of heat acquired from the geothermal heat (geothermal power) in function of the parameters resulting from the following relation, that is in function of volumetric flow rate of water flowing through the exchanger and its temperatures at pumping and extraction locations [6]:

$$\dot{Q}_g = f(\dot{V}_g, T_{gz}, \Delta T), \quad (9)$$

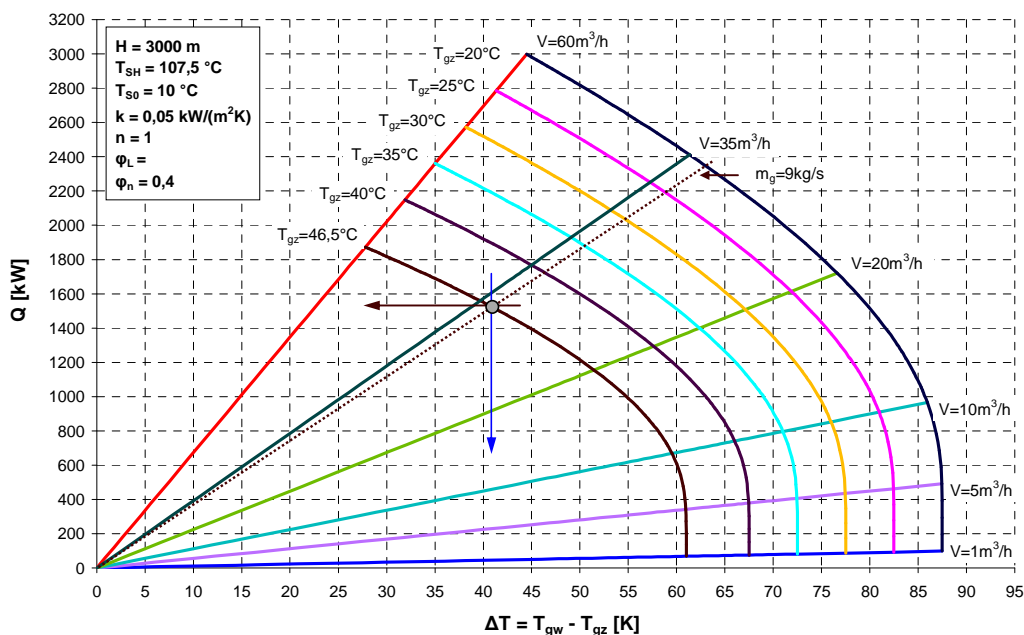


Fig. 3. Sample thermal-hydraulic characteristics of the underground closed geothermal heat exchanger

A sample characteristics presented in Fig. 3 has been elaborated for the exchanger featuring a horizontal channel of 3000 m, placed at the depth of 3 km. Temperature of the rock bed at the foundation of exchanger is 107.6 °C, whereas the transport fluid circulating in the exchanger is water. The characteristic serves as a basis for further calculations of the low-temperature ORC installation supplied with geothermal energy.

2. ORC POWER PLANT COOPERATING WITH UCGHE

In the analysis it has been assumed that geothermic energy received from the bed rock is supplied by means of the flow rate of network water to the low-temperature ORC installation, a schematic of which is presented in Fig. 4.

The flow rate of network water heated in the geothermal exchanger flows into the evaporator, where it transfers heat to the organic working fluid rendering its evaporation. Water leaving the evaporator is split into two flow rates of which the first one (m_{g1}) is directed to the counter-current heater of the working fluid, whereas the second one (m_{g2}) to the receivers of technological heat or heating installations (central heating, preparation of hot water). Subsequently both flow rates are recombined and pumped back to the geothermal heat exchanger, where water again heated in the heat exchange process with the bed rock.

The saturated vapour, produced in the low-temperature cycle of the power plant, is directed to the steam turbine, where it undergoes isentropic expansion to the condensation pressure. Next the expanded vapour flows to the condenser, where after initial cooling its condensation takes place. The working fluid in the liquid state is pumped to the heater where it is isobarically heated from condensation temperature to evaporation temperature, and subsequently to the evaporator where it evaporates as a result of supplied heat by water heater in the geothermal heat exchanger.

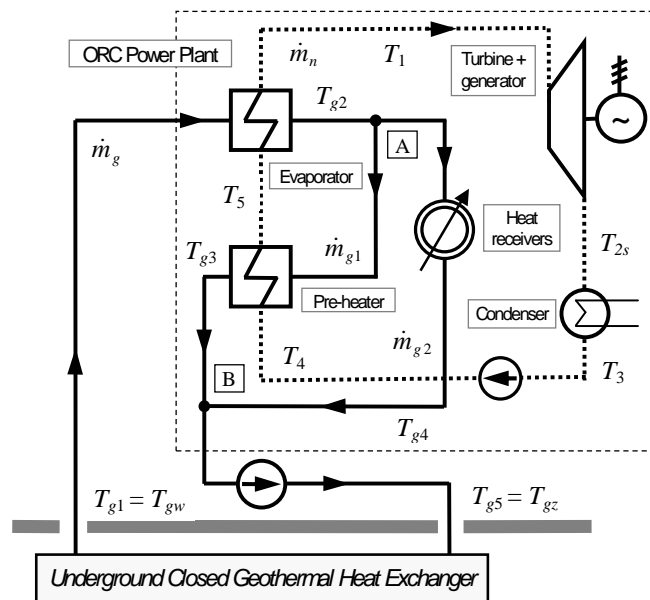


Fig. 4. Schematic of geothermal heat and power installation

In the considered power plant the so called dry organic substance has been considered where the entropic index $I < 1$. That means that if the beginning of expansion in turbine is located on the vapour saturation line, then the state after expansion is in the region of superheated vapour (Fig. 5).

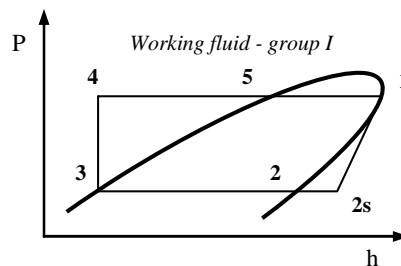


Fig. 5. Sequence of thermodynamical processes of working fluid from group I in C–R cycle realised in the region of superheated vapour

It has been assumed in the analysis that all processes realized in the cycle are reversible and the entire cycle is consistent with the C–R cycle for the saturated vapour. In case of dry fluids the Clausius – Rankine cycle consists of isobaric heat supply encompassing heating process (4–5) and liquid evaporation (5–1), isentropic expansion of working fluid vapour in the turbine (1–2s), isobaric heat removal during vapour condensation (2s–2) and its condensation (2–3) as well as isentropic compression of the condensate (3–4).

The starting point for the analysis of operation of power/heat and power plant was construction of thermal-hydraulic characteristics of extraction of geothermal energy in the underground closed geothermal heat exchanger (node 2, Fig. 3) as well as development of temperature characteristics of the evaporator, heater and condenser, depicting temperature field of network water and organic working fluid (Fig. 6).

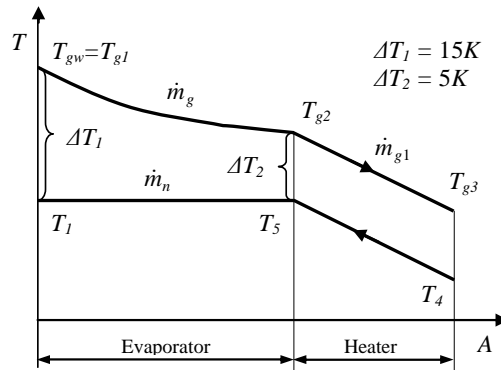


Fig. 6. The temperature fields of heat exchangers

In accomplished thermal-hydraulic calculations of the power/heat and power plant the following relations were utilized:

- energy balance for the evaporator:

$$\dot{Q}_{ev} = \dot{m}_g c_g (T_{g1} - T_{g2}) = \dot{m}_n (h_1 - h_5). \quad (10)$$

Eq. 10 enables determination of the flow rate of fluid circulating in the power plant loop:

$$\dot{m}_n = \frac{\dot{m}_g c_g (T_{g1} - T_{g2})}{h_1 - h_5}, \quad (10a)$$

- energy balance of the heater:

$$\dot{Q}_{hr} = \dot{m}_{g1} c_g (T_{g2} - T_{g3}) = \dot{m}_n (h_5 - h_4) = \dot{m}_n c_n (T_5 - T_4). \quad (11)$$

Eq. (11) enables determination of the flow rate of network water (heating water) directed to the heater assuming equal rates of heat capacity $\dot{m}_{g1} c_g = \dot{m}_n c_n$:

$$\dot{m}_{g1} = \dot{m}_n \frac{h_5 - h_4}{c_g (T_{g2} - T_{g4})}, \quad (11a)$$

- rate of heat acquired in geothermal heat exchanger:

$$\dot{Q}_g = \dot{m}_g c_g (T_{gw} - T_{gz}) = \dot{m}_g c_g (T_{g1} - T_{g5}), \quad (12)$$

- rate of heat spent for technological or heating purposes:

$$\dot{Q}_{co} = \dot{m}_{g2} c_g (T_{g2} - T_{g4}), \quad (13)$$

– where the flow rate of network water supplied to the heat receivers can be determined from the relation: $\dot{m}_{g2} = \dot{m}_g - \dot{m}_{g1}$.

- rate of heat supplied to the C–R cycle:

$$\dot{Q}_{s-ORC} = \dot{Q}_{1-4} = \dot{m}_n (h_1 - h_4), \quad (14)$$

- rate of heat removed in the condenser:

$$\dot{Q}_{cond} = \dot{Q}_{2s-3} = \dot{m}_n (h_{2s} - h_3) \quad (15)$$

– thermal efficiency of $C-R$ cycle:

$$\eta_{C-R} = \frac{h_1 - h_{2s}}{h_1 - h_4}, \quad (16)$$

– power of $C-R$ cycle:

$$N_{CR} = \dot{m}_n (h_1 - h_{2s}), \quad (17)$$

– overall efficiency of the geothermal heat and power plant:

$$\eta_{EC} = \frac{N_{CR} + \dot{Q}_{CO}}{\dot{Q}_g} \quad (18)$$

Indispensable thermal and calorific parameters of the particular states of the $C-R$ cycle for particular working fluids have been determined using the physical property calculation software REFPROP [19].

3. RESULTS OF CALCULATIONS

Utilising developed earlier mathematical models and relevant relations accomplished were calculations of the power/heat and power plant for selected organic fluids. Obtained results of calculations have been presented in tables 1 and graphically in Fig. 7 and Fig. 8.

Table 1. Results of calculations of the geothermal heat and power plant with different working fluids

Working fluid	T_{g1} (T_{gw}), °C	T_{g5} (T_{gz}), °C	\dot{m}_s , kg/s	\dot{Q}_g , kW	\dot{m}_{g1} , kg/s	\dot{m}_{g2} , kg/s	\dot{m}_n , kg/s	N_{C-R} , kW	η_{C-R} , %	\dot{Q}_{CO} , kW	η_{EC} , %
RC318	88	46.02	9.0	1579.9	1.37	7.63	4.865	64.12	10.29	956.8	64.73
R236fa	88	46.45	9.0	1563.7	1.07	7.93	3.364	60.96	10.71	994.4	61.59
R245fa	88	46.85	9.0	1548.1	0.79	8.21	2.368	56.76	10.95	1029.5	70.17
PFP	88	46.08	9.0	1576.6	1.33	7.67	4.927	59.32	9.65	961.8	64.77

$T_{s2} = 78$ °C; $T_{s3} = 35$ °C; $T_{s4} = 48$ °C; $T_p = 73$ °C; PFP – perfluoropentane.

Presented results of calculations regard different low-boiling point fluids accomplished at the assumption that same flow rates of heat carrier flows through heat exchangers and same outflow temperatures from geothermal exchanger are present.

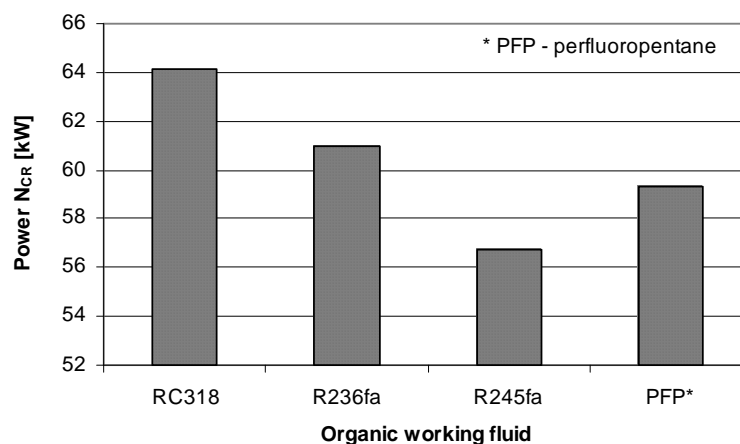


Fig. 7. Comparison of the total power of $C-R$ cycles in case of different working fluids for constant temperatures of heat carrier at outlet from the UCGHE

The results of calculations for different temperatures of network water at outflow from underground closed geothermal heat exchanger have been presented in table 2.

Table 2. Results of calculations for geothermal heat and power plant with RC318 for different temperatures of network water at outflow from a UCGHE [13]

T_{s1}	T_{s2}	\dot{m}_s	\dot{m}_{s1}	\dot{m}_{s2}	\dot{Q}_g	\dot{m}_n	N_{C-R}	η_{C-R}	\dot{Q}_{co}	η_{EC}
°C	°C	kg/s	kg/s	kg/s	kW	kg/s	kW	%	kW	%
85	75	3	0.45	2.55	564.3	1.58	16.65	8.70	373.07	69.05
95	85	3	0.51	2.49	689.7	1.74	22.94	10.39	468.37	71.23
105	95	3	0.59	2.41	815.1	1.99	30.94	11.85	554.06	71.77

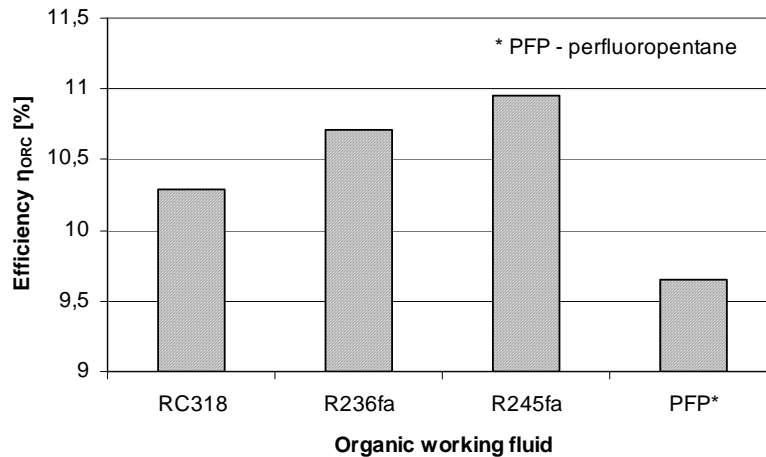


Fig. 8. Comparison of efficiency of C–R cycle for different working fluids for the same temperatures of heat carrier at outlet from the UCGHE

On the basis of conducted analysis of the results of calculations the following conclusions can be drawn:

- with the decrease of working fluid temperature at outflow from the UCGHE efficiency and power of C–R cycle decreases,
- increase of the flow rate of heat carrier supplied to UCGHE renders reduction of its outflow temperature at the inlet one remaining unchanged,
- decrease of temperature at inlet to UCGHE renders temperature drop at outlet at the same rate of heat of the heat carrier.

4. CONCLUSIONS

Accomplished analysis allows to conclude that effectiveness of extraction of geothermal energy is influenced by the type of applied geothermal heat exchanger and its thermal-hydraulic characteristics, whereas the effectiveness of utilization of geothermal energy is governed by the kind of applied geothermal exchanger as well as applied installation and the kind of working fluid in the installation.

Additionally, it results from the analysis that despite the fact that the efficiency of considered heat and power plants is relatively high but the drawback of presented design is a small share of acquired power of the C-R cycle with respect to the rate of heat for central heating purposes. Therefore, in order to improve the effectiveness of installation operation with the view to increase available power of C-R cycle with respect to rate of heat spent for central heating there ought to be applied a different configuration of the heat and power plant (for example with a multi-pass power plant or installations of combined production of electricity and heat).

Acknowledgments

The work has been carried out in the frame of the project No. N513 419334 financed by the Polish Ministry of Science and Higher Education.

References

1. Górecki W. *Atlas Geothermal Energy Resources in Polish Lowland*. GEOS, Kraków 1995.
2. Nowak W., Sobański R, Kabat M., Kujawa T. *Systems of Acquisition and Utilisation of Geothermal Energy*. Publishing: Technical University of Szczecin, Szczecin, 2000.
3. Nowak W., Stachel A. *State of the Art and Perspectives of Utilization of the Some Renewable Sources of Energy in Poland*. Publishing: Technical University of Szczecin, Szczecin, 2004 (in Polish).
4. Čeremenskij G.A. *Geotermija*, NEDRA, Leningrad: 1972 (in Russian).
5. Nowak W., Stachel A., Borsukiewicz-Gozdur A. *Applying of Renewable Sources of Energy*. Publishing: Technical University of Szczecin, Szczecin, 2004 (in Polish).
6. Kujawa T., Kaczmarek R. Heat flow characteristics of underground closed geothermal heat exchanger // *13 Symp. "Nutzung Regenerativer Energiequellen und Wasserstofftechnik"*, Stralsund, 2–4.11.2006. Pp. 45–51.
7. Morita K. One possible way to utilize abandoned deep wells – the application of the DCHE // *Technika Poszukiwań Geologicznych*. 2001. No. 5. Pp. 129–148.
8. Nowak W. *Theory of underground closed-loop geothermal heat exchanger*, Unpublished internal report of Department of Heat Engineering, TU of Szczecin, 2003 (in Polish).
9. Nowak W., Stachel A. Die Möglichkeiten der Nutzung der Geothermalen Energie als einer einspeisenden Energiequelle für ein Heizkraftwerk // *XXXVII Kraftwerkstechnisches Kolloquium, TU Dresden*, 18–19.10.2005, Vorträge V-38.
10. Plewa M., Plewa S. Analysis of possibilities of utilisation of geothermal energy of dry hot rocks in Poland // *Konferencja: Możliwości wykorzystania wód geotermalnych w Polsce*. AGH Kraków, 1990. Pp. 171–181.
11. Wolff H., Möller F., Besser T., Schmidt S., Oppelt J., Treviranus J. *Ansätze fortschrittlichen Bohr- und Komplettierungstechnik für die Errichtung eines Untertrügig Geschlossenen Geothermischen Wärmetauscher. Projekt „Untertägig Geschlossener Geothermischer Wärmetauscher“ BMU – ZIP 0327506*. 20 Jahre Tiefe Geothermie in Deutschland, 7. Geothermische Fachtagung, 06–08.11.2002, Waren (Müritz).
12. Wolff H., Schmidt S., Möller F., Legarth B., Oppelt J., Treviranus, J. *Geothermische Stromerzeugung Projekt „Untertägig Geschlossener Geothermischer Wärmetauscher“ BMU – ZIP 0327506, Status-Quo*, Juni 2002, Vortrag, Symposium "Geothermische Stromerzeugung", Landau 20/21 Juni 2002.
13. Nowak W., Stachel A. Geothermic heat and power station with a single component power cycle with organic working medium // *Acta Metallurgica Slovaca, R-13*. 2007. No. 3 Pp. 251–256.
14. Nowak W. Analytical calculation model of underground closed geothermal heat exchanger // *Archives of Thermodynamics*. 2005. Vol. 26, No. 2. Pp. 49–66.
15. Nowak W., Stachel A. Assessment of operation of underground closed geothermal heat exchanger // *Inzhenerno-Fizicheskii Zhurnal*. 2005. Vol. 78, No. 1. Pp. 131–137.
16. Čarnyj I.A. O prodvizenii granicy izmenenija agregatnogo sostojania pri ochlaždenii ili nagrevanii tel // *Izw. OTN AN SSSR*. 1948. No. 2 (in Polish).
17. Čarnyj I.A. Nagrevanie prizabojnoj zony pri zakačke gorjačej vody w skvažinu // *NCh*. 1953. No. 3 (in Polish).
18. Nowak W., Kaczmarek R. Assessment of the influence of application of active insulation in the extracting part of underground closed geothermal heat exchanger on its influence // *Proc. of XIII Symp. on Heat and Mass Transfer, Koszalin-Darłówek*, 2007. Vol. 2 Pp. 745–752 (in Polish).
19. National Institute of Standards and Technology, Standard Reference Database 23, Reference Fluid Thermodynamic and Transport Properties – Refprop 7.0, US, 2002.
20. Djadkin Ju.D., Gendler S.G. *Processy teplomassoperenosa pri izwlečenii geotermalnoj énergii*, LGI, Leningrad: 1985 (in Russian).

HEAT EXCHANGE DURING EVAPORATION OF OZONE SAFE REFRIGERANTS R134A AND R407C ON SMOOTH AND DEVELOPED SURFACES OF HEAT EXCHANGE APPARATUSES OF HEAT PUMP PLANTS AND REFRIGERATING UNITS

Anatoly V. Ovsyannik, Aleksandr V. Shapovalov, Tatsiana S. Yufanova, Nikolay A. Valchenko

Department of Industrial Heat Power Engineering and Ecology

P.O.Sukhoi State Technical University of Gomel

Pr.Octiabria, 246746, Gomel, Belarus

Tel.: (375 232) 48 35 79

Abstract

The work presented includes the results of the study of the process of heat exchange during boiling of R134A on smooth technically rough and finned surfaces in wide ranges of saturation and input heat load parameters variation (at saturation pressures of $p = 0.4\text{--}0.8$ MPa ($t_s = 9.8\text{--}31.1$ °C) at heat flow density $q = 8\text{--}63$ kW/m²); of the process of heat exchange during evaporation of R407C on smooth and finned surfaces at saturation pressures of $p = 1.02\text{--}1.25$ MPa ($t_s = 18.7\text{--}26$ °C) at variations of input heat flow density of $q = 0.2\text{--}35$ kW/m², which resulted in establishing heat exchange rate increase during evaporation of refrigerants R134A and R407C on finned surfaces by 2–4 times as compared with the process rate during evaporation on smooth technically rough surface during developed bubble boiling.

KEYWORDS

Boiling, heat transfer, freon-134A, freon-407C, finned tube, criterion equation.

INTRODUCTION

Urgency of the work is stipulated by the fact that now more and more attention is paid to the use of ozone safe refrigerants as working medium in refrigerators and heat pumps. This is explained by not only the conditions of the Montreal Protocol but also by the intention to lower indirect and direct contribution of refrigerating and heat pump equipment to the Total Equivalent Warming Impact (TEWI). This can be achieved by selecting refrigerants having high energy efficiency and low potential of global warming. A number of single component and mix refrigerants (R134A, R407C, R404A and other) complies with such requirements. Research novelty consists in theoretical and experimental studies of heat exchange process during phase transitions of ozone safe refrigerants on developed surfaces of various types with different orientation in heat exchange equipment of refrigerating and heat pump units.

EXPERIMENTAL METHODS

Experiments were conducted at an experimental stand for the study of evaporation processes at boundary conditions of heat flow constant density. A schematic drawing of the stand is presented in Fig. 1.

Working evaporation chamber 1 is a cylinder closed with flanges 6 and 4. Flange 4 has a glass light port for lighting with a lamp. Connector 8 for connecting thermocouples is mounted on flange 6. In the middle of the chamber there is viewing port 9 for visual monitoring of the process of boiling on a sample surface. Water heat exchanger-condenser 2 represents a container with two coils installed and is designed for providing steady-state conditions for experimenting. Pressure vessel 3 is provided for working fluid storing. There is pressure gauge 10, safety valve 11 and valve 13 mounted on the working chamber for air supply to the chamber when checking airtightness, during sample replacement and working fluid vapor release.

Required pressure in the chamber is produced and maintained by means of regulation of heat load supplied to the chamber heater and also by means of condenser 2 cooling water discharge variation.

Experimental sample is set in the working evaporation chamber by means of flange connection. Heat flow is supplied to the surface under study by electric heater which is located inside the experimental sample. Temperature drop between heating surface and liquid is measured directly by differential thermocouples one thermal junction of which is in the sample and the other is in the liquid. Thermocouple conductors covered with varnish insulation and fluoroplastic insulation are laid in grooves on the experimental sample and covered with aluminum wire.

Saturation conditions in the experimental chamber are maintained by the regulation of the discharge of cooling water through the condenser. Saturation temperature is determined by two thermocouples located in the liquid and in vapor space. Saturation pressure is checked up with a standard pressure gauge.

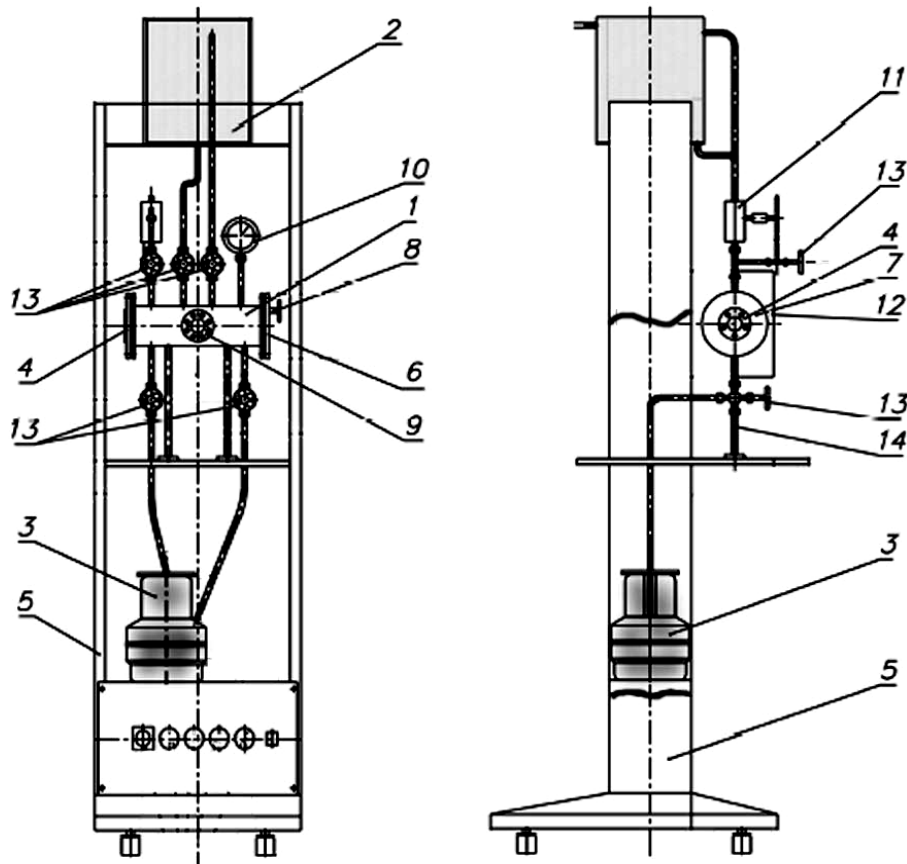


Fig. 1. Experimental stand for the study of the process of heat exchange during evaporation: 1 – working chamber, 2 – condenser, 3 – pressure vessel with liquid, 4, 9 – ports, 5 – frame, 6, 7 – flanges, 8 – thermocouple terminal, 10 – pressure gauge, 11 – safety valve, 12 – protecting shield, 13 – valve, 14 – working chamber foot

EXPERIMENTAL SAMPLES

Horizontal tubes with smooth and finned surfaces made of duralumin by milling and rolling were used as experimental samples.

Smooth tubes have the following dimensions: length – 310 mm, outer diameter – 25 mm, inner diameter – 16 mm. On the external surface of the tubes longitudinal grooves having width 0.5 mm, depth 1.5 mm and length 20–30 mm for thermocouple cabling are milled with 90 ° circumferential pitch.

Finned tubes (Fig. 2) are made with transverse fins having trapezoid profile. Tube length is 310 mm, fin height is 12.5 mm, fin width at the base of load-bearing surface is 4 mm and 2 mm at the top, spacing between the fins is 4 mm. Thermal junctions of thermocouples are cabled into the base, into the center, and into the top of the fin.



Fig. 2. Transversely finned tube with trapezoid profile fins

EXPERIMENT RESULTS

Heat exchange process during Freon R134A boiling on smooth technically rough surface was studied in the range of condition parameters: heat flow density variation within 8–63 kW/m², saturation pressure variations within 0.5–0.8 MPa ($t_s = 15.7$ – 31.1 °C). In this situation overheating of the surface varied within 3.7–10 °C. It is established that at the increase of heat flow density with saturation pressure increase heat transfer rate on smooth technically rough surface increases.

Heat exchange studying during Freon R407C boiling on smooth technically rough surface was provided in the range of the following condition parameters: heat flow density variation within 0.2–35 kW/m², saturation pressure variation within 1.02–1.25 MPa ($t_s = 18.7$ – 26.0 °C), overheating of the surface varied within 0.8...5 °C. In the range of heat flow density variations of 3.0–6.0 kW/m² an abrupt reduction of the surface overheating was observed and also an abrupt increase of heat transfer coefficient and the start of developed bubble boiling of liquid.

In Fig. 3 the comparison of heat transfer rate and temperature drop values for two ozone safe refrigerants (R134A and R407C) under study in the range of developed bubble boiling is presented. Comparison was provided at the same liquid saturation temperatures but at different pressure values, since heat and physical properties of the refrigerants particularly boiling temperature significantly differ (R134A: $t_s = -26.1$ °C, R407C: $t_s = -44$ °C, with $p = 101.3$ kPa).

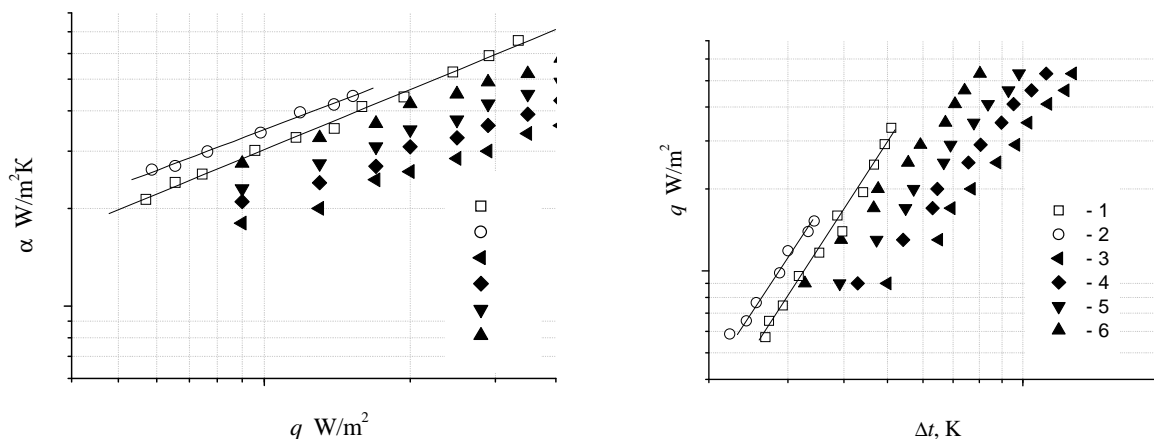


Fig. 3. Experimental dependencies $\alpha = f(q)$ and $q = f(\Delta t)$ during evaporation of Freons 134A and 407C in the range of developed bubble boiling (1 – R407C, $p = 1.15$ MPa, $t_l = 296$ K; 2 – R407C, $p = 1.25$ MPa, $t_l = 299$ K; 3 – R134A, $p = 0.5$ MPa, $t_l = 289$ K; 4 – R134A, $p = 0.6$ MPa, $t_l = 295$ K; 5 – R134A, $p = 0.7$ MPa, $t_l = 300$ K; 6 – R134A, $p = 0.8$ MPa, $t_l = 304$ K)

As it is seen from the graphs heat transfer rate during Freon R407 boiling is much higher than that during R134A boiling which will result in case of using R407C in the reduction of mass dimensional characteristics of the evaporator. However in designing equipment it is necessary to take into account the fact that the use of R407C will involve higher pressures into the process as compared with R134A.

The study of heat exchange during boiling of R134 and R407C Freons on finned surfaces was conducted in the conditions of free volume at saturation pressures of $p = 0,4\text{--}0.7$ MPa (R134A), $p = 1.15\text{--}1.25$ MPa (R407C) at heat flow densities of $q = 5\text{--}60$ kW/m².

During the experiments visual monitoring of the process of evaporation on the surface of the tubes under study was provided. It was observed that on smooth technically rough surfaces boiling started and stopped at higher values of heat loads than on finned tubes.

As it is seen from Fig.4 heat transfer coefficients during boiling on finned surface are much higher than on smooth one, i.e. during developed bubble boiling of R134A and R407C heat exchange on finned surfaces is 2-4 times more intensive than on non-developed one.

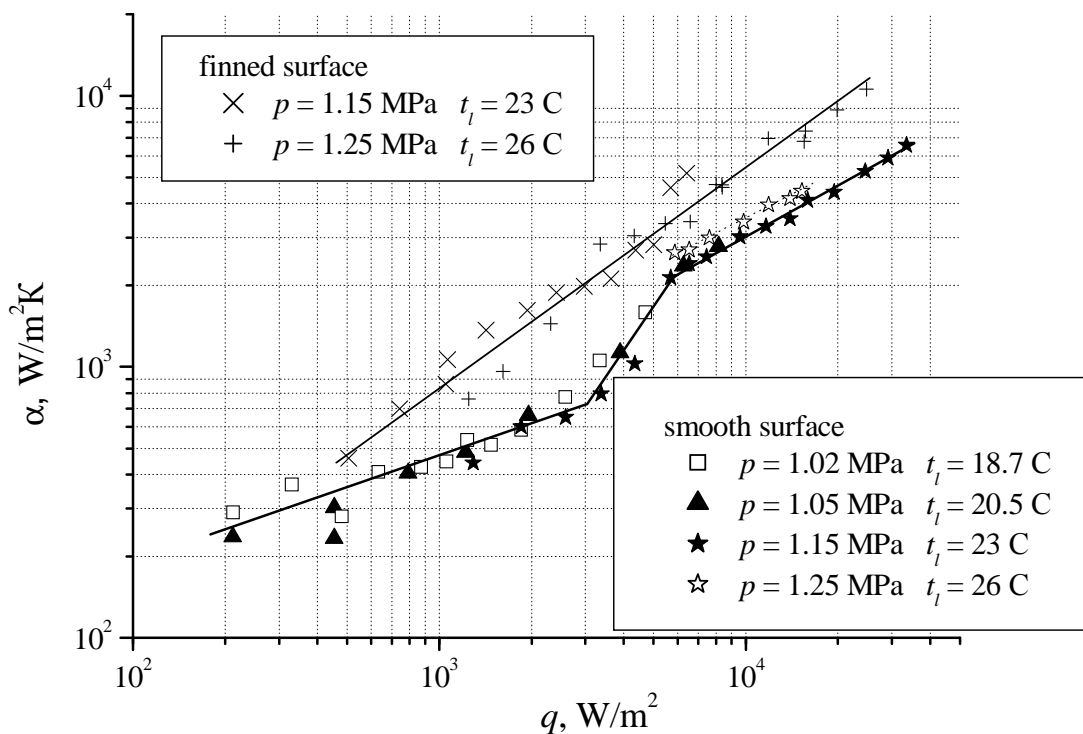


Fig. 4. Experimental dependencies of heat transfer coefficient on heat flow density during R407C boiling on smooth and finned surfaces

Specific features of heat exchange during boiling on the finned surfaces under study are preconditioned by the following facts. At the base of the fins the greatest overheating of liquid is observed and also local reduction of wettability due to the change of surface configuration and local stresses. On these surface areas undissolved gases are adsorbed which are the centers of evaporation in the beginning of the process and also vapor nuclei are entrapped during vapor phase detachment from the surface at steady boiling. Confining small volumes of liquid with the fins provides greater average overheating and improving the conditions of bubble growth. At comparable ratio of fin spacing and bubble detachment diameter the most intensive heat supply is provided not only from micro layer at the base of the fin as in the case of smooth surface but also from overheated thin layer of liquid confined between the bubble and the fin. More intensive evaporation in small volumes of liquid in inter fin space results in turbulent disturbance of boundary layer as compared with smooth surfaces.

The facts noted produce the reduction of temperature drop value at the same values of heat flow density and saturation pressure for finned tubes as compared with smooth ones.

Finning most significantly influences heat transfer coefficient at the initial stage of developed boiling at heat flow densities of up to 50 kW/m². At larger values of heat flow density ($q > 50$ kW/m²) active coalescence of vapor bubbles occurs and the conditions of removal of vapor phase out of inter fin areas are impaired. This causes a distinctive "steaming" of heat exchange surface and heat exchange deterioration. Consequently during boiling on finned surfaces with comparable ratio of fin spacing and detachment diameter of the bubble heat exchange rate is not dependent on finning dimensions (spacing, height, fin thickness). They are important for heat exchange process during boiling and should be considered in single-valuedness condition. Intensification of heat exchange process during R134 and R407C boiling on finned tubes was observed over the whole range of heat loads. The value of heat transfer coefficient during liquid boiling depends on pressure, the rise of which results in higher heat exchange rate and the degree of the influence of pressure manifests itself in different ways depending on heat-release surface type and heat and physical properties of liquid.

There is very little data on R134A boiling at various saturation pressure values published in the literature and this data has limited character while such information on R407C is not presented in the literature at all. It is established experimentally that during R134A Freon boiling at various saturation pressures on finned surfaces heat exchange rate does not depend on the fin profile and it is determined only by condition parameters, which is confirmed by the results obtained before during acetone and ethyl alcohol boiling on finned surfaces of various profile.

Heat transfer coefficient continuously increases with saturation pressure increase due to improving the condition of new vapor bubble inception on heat-release surface. When heat flow density increases the degree of saturation pressure influence is reduced due to the increase of overheating value necessary for liquid boiling and the reduction of the rate of growth of active evaporation centers.

With finned surfaces the influence of pressure on the intensity of the process of heat exchange manifests itself stronger than on smooth surface because of greater number of active centers of evaporation.

During R407 refrigerant evaporation in the range of condition parameters under study the increase of saturation pressures at heat flow density increasing has practically no influence on heat transfer rate on smooth technically rough and also on finned surface. Following the generalization of data based on S.S. Kutateladze theory empiric equations have been obtained enabling to correctly describe experimental data during freon R134A and R407C evaporation on smooth technically rough surfaces with the error of within 30% for R134A and within 15% for R407C.

$$\text{R134A:} \quad \alpha = 0.272 p^{0.4} \cdot q^{0.7}, \quad (1)$$

$$\text{R407C:} \quad \alpha = 0.351 p^{0.4} \cdot q^{0.7}, \quad (2)$$

where p – absolute pressure, MPa; q – heat flow, W/m².

CONCLUSION

The increase of heat exchange rate by 2–4 times during evaporation of R134A and R407C ozone safe refrigerants on transversely finned tubes as compared with heat exchange rate on smooth technically rough tubes in the range of condition parameters under study are established experimentally.

Empirical relations enabling to define heat transfer coefficients at R134A and R407C Freon evaporation during developed bubble boiling on smooth tubes are obtained.

Design dependencies and recommendations of the work can be practically used for designing up-to-date highly efficient evaporator heat exchangers with developed heat transfer surfaces with applying ozone safe refrigerants for improving ecologic, heat engineering and mass dimensional parameters of refrigerator and heat pump equipment.

Nomenclature

l – liquid, p – pressure, Pa; q – heat flux, W/m²; t – temperature, K; α – heat transfer coefficient, W/(m²·K). Subscripts: s – saturation.

UTILIZATION OF THE HEAT CAPACITY OF RESERVOIR WATER IN THE EXTRACTION OF COAL BED METHANE TO SURFACE

E. A. Patskov

Scientific-Technical Center "Development hydrocarbon Deposits "Gazprom promgaz"
Russia, 117420, Moscow, Nametkina st., 6

Tel: 8(495)504-4360, fax: 8(495)504-4370, e.patskov@promgaz.ru

Abstract

Creating technology for disposal of produced water, utilized to the surface during extraction of coal bed methane is purpose to work. The borehole for extraction coal bed methane has tubing through which a submersible pump is extracted brine water to create a depression in the bottom hole.

Created by an engineering method for calculating the station heat pump, allowing calculate the geometric characteristics of the ground heat exchanger and temporal characteristics of the coolant. The base - is the solutions of two non-stationary differential equations modeling the temperature distribution inside the heat exchanger and the environment. Are received the analytical dependences of the geometrical characteristics of the soil heat exchanger from the conversion coefficient of the heat pump, the refrigerant temperature, soil properties, the properties engineering systems in the heated rooms.

Are calculated the main parameters of the heat pump station and study of the costs of various kinds of organic fuels and electricity for heating and hot water.

In the Kuzbas, where the main energy source is coal, and all other energy sources (except for electricity) are imported, economically are viable use of heat pumps of the bivalent scheme.

KEYWORDS

Coal bed methane, ground heat exchanger, the heat pump station, the coal, non-stationary differential equations.

Multiple increase in the cost of extraction and produced energy resources, depletion of traditional fossil fuels and environmental effects of its combustion, more stricter requirements for environmental friendliness technological process and environment - in result in the Western countries, the USA, Japan the widespread are used of energy-saving equipment - the heat pumps (HP) and the technologies based on them. In recent decades there has been some interest to the technology, based on the heat pumps in many developed countries. In Russia, with its cold winters, of the most promising area of implementation of heat pumps - is to warm of the population, utilities and industry, air conditioning facilities in the summer. For the effective operation of heat pumps need is a stable source of the low-grade heat, which are the underground waters.

Currently in Russia begins the active extraction methane coal bed, reserves wich in the Kuzbass, are estimated at 35 trillion. m³. The extraction methane is accompanied by extraction water at a stable temperature of 15–20 °C and high flow rate. The degassing of coal seams is one of the most urgent problems to ensure the safety of mining operations and cost reduction of coal production by increasing the load. The solution of the indicated issues is accompanied by significant improvement of ecological situation in the coal mining regions. The coal reserves in Russia significantly exceed the reserves of natural gas and oil, and the share of coal in the fuel and power balance of Russia in the near future will increase.

The extraction of coal bed methane in Russia, which are classified as one of the gas-bearing in the world, could significantly compensate the mining of natural gas from major gas fields in Russia, witch are characterized by declining production.

The objective of this study was to create a method for calculating heat pump station, including the solution of problems of no stationary heat transfer of vertical ground heat exchanger with the environment (external and internal problems). Was created an engineering method for calculating the vertical heat exchangers, are made examples of calculations, recommendations for optimizing the costs of using heat pumps with vertical heat exchangers.

In this paper we study the cost various types of energy for heating of industrial enterprises, facilities and utilities and the public. We considered the various energy sources (Table 1), an alternative which is the thermal energy from heat pumps.

№	The kind of energy source	The price of 1 kW·h of thermal energy (ruble/kW·h)	
		Population	Industry
1	A Steam Coal	0,11	
2	Heat Pumps	0,38	0,5
3	Liquefied hydrocarbons (LPG)	0,85	
4	Diesel fuel	1,95	1,6
5	Electricity	1,32	1,75
6	Natural Gas	1,95	1,6
7	Heat energy (FTS) ^{*)}		0,49
	^{*)} FTS - Federal Tariff Service		

Therefore, in the Kuzbas, where the main energy source is coal, and all other energy sources (except for electricity) are imported, the application of heat pumps is economically justified. The cost of 1 kW·h heat supplied thermal power station, almost equal to cost of thermal energy, which can be obtained by using heat pumps. In these calculations do not take into account the environmental component. The latter factor is important for Kuzbas, where ecological situation are not very enabling due to the large number of enterprises that use coal. The success of the heat pump depends on the low-temperature heat source and method of space heating - water or air. For all types of thermal pumps characterized by a number of features:

- heat pump justifies itself only in well-warmed room;
- the more temperature difference between coolant in the input and output contours, the lower the conversion factor of heat (φ);
- if necessary to get the hot water the power of HP decreases and increases electricity consumption;
- to improve the efficiency of heat pump exploitation is practiced in a pair of HP with the additional heat generator - bivalent heating scheme.

The gas wells contain a casing pipes, inside which is placed lined tubing. Through the annulus between the casing pipe and lined tubing is extracted gas. The lined tubing is the groundwater heat exchanger, in which moves in water in the non-isothermal conditions.

The paper presents the two solutions of no stationary problems of heating of heat exchanger and of heat transfer with the environment.

Calculation of temperature distribution inside the heat exchanger

Considered unlimited cylinder of radius R with an initial temperature T_m . At the initial time a cylinder is placed in an environment with constant temperature $T_0 < T_m$ ($T_0 > T_m$). Solution of the problem is also valid for a limited cylinder under the condition that its length is much greater than the radius $L_C \gg R$. Heat transfer between the surface of the cylinder and the environment is carried out by Newton's law and the initial time the heat flow is equal to:

$$q = \alpha_k (T_0 - T_m), \quad (1)$$

where α_k – coefficient of heat transfer, kJ/(m²·hr·deg).

Necessary to find distribution of temperature inside the cylinder along the radius at any given time with a significant excess of of the radial temperature gradient coefficient on the vertical. In the case of the symmetric problem the heat equation for an unbounded cylinder is as follows:

$$\frac{\partial T}{\partial t} = a \left(\frac{\partial^2 T}{\partial r^2} + \frac{1}{r} \frac{\partial T}{\partial r} \right) \quad (2)$$

Boundary conditions:

$$T(r, 0) = T_m, \quad (3)$$

$$\frac{\partial T}{\partial r} + \frac{\alpha}{\lambda} (T(R, t) - T_0) = 0, \quad (4)$$

$$\frac{\partial T(0, t)}{\partial r} = 0. \quad (5)$$

The solution of equation (2) is obtained with the boundary conditions (3)–(5) the use of Laplace transform [1]:

$$E(r, t) = \frac{T_m - T(r, t)}{T_m - T_0} = 1 - \sum A_n J(\mu_n \frac{r}{R}) e^{-\mu_n^2 \varphi}, \quad (6)$$

where: $\varphi = a\tau/R^2$ - a criterion for Fourier, $a = \frac{\lambda}{\rho \cdot c_p}$ - thermal diffusivity, m²/h; τ - the characteristic

time, h; λ - thermal conductivity, J/(m·hr·deg); ρ - density, kg/m³; C_p - heat capacity, J/(kg·deg).

Coefficients

$$A_n = \frac{2\mu_n J_1(\mu_n)}{J_0^2(\mu_n) \left(\mu_n^2 + \frac{\alpha^2 R^2}{\lambda^2} \right)}, \quad (7)$$

where $J_0(z)$ – Bessel function of zero order, $J_1(z)$ – Bessel function of first order, Z – argument.

Solution (6) is a rapidly converging series, which allows the calculations use only the first terms of the series. The values of coefficients $\mu_1, \mu_2, \mu_3, \mu_4$ depend on the value number $Bi = \alpha R / \lambda$ and are determined from the recurrence relation:

$$\mu_n J(\mu_n) = Bi \cdot J(\mu_n). \quad (8)$$

Heat transfer of vertical ground heat exchanger with the environment

It is assumed that the inside of the heat exchanger is a cylinder with inner of radius R_1 , the temperature $T(t) = T_m \div T_0$, outer radius R_2 , the temperature T_{cr} , t – time of heating (cooling) of coolant. Heating (cooling) during the time coolant by heat conduction from the environment and offers the following differential equation

$$B_m \cdot C_p \cdot \frac{dT}{dt} = q \cdot S_1 \quad (9)$$

$$\text{Initial conditions: } \left. \begin{array}{l} t = 0, T = T_m \\ t \rightarrow \infty, T = T_0 \end{array} \right\} \quad (10)$$

where: B_m, C_p – weight (kg) and heat capacity of coolant (kJ/(kg·deg)); q – convective heat stream supplied to the heated surface S_1 .

The convective heat transfer coefficient α_k is given by $\alpha_k = Nu \cdot \lambda_{mc} / (R_2 - R_1)$,

where $Nu = 0,023 Re^{0,8} Pr^{0,4}$.

Reynolds number for the heat exchanger: $Re = w(R_2 - R_1)/\nu$,

where w, ν – velocity and the kinematic viscosity of the coolant, Prandtl number is $Pr = 0,7$.

The solution of equation (14) with initial conditions (15) has the form:

$$T(t) = T_0 - \frac{T_0 - T_m}{\exp(\beta \cdot t)} \quad (11)$$

where $\beta = \frac{S_1 \cdot \alpha_r}{B_m \cdot C_p}$, $S_1 = \pi \cdot R_2^2 \cdot L$, L – height of the heat exchanger.

The solution of the internal (6) and external (11) heat transfer problem of a cylinder with the environment will create an engineering method calculating of heat pump stations with ground heat exchangers great length.

For the calculation of the vertical ground heat exchangers necessary to install an analytical dependence of the temperature in a heat exchanger circulating fluid, the conversion coefficient of heat pump and the refrigerant temperature at the outlet of the evaporator.

The values of these parameters can be set arbitrarily, since they are interrelated with each other because of the design features of heat pumps.

As is known, the criterion for the effectiveness of the heat pump serves as a conversion factor φ , whose value is determined by the ratio of thermal capacity of the heat pump to power the electric compressor. The conversion factor of the heat pump is a function of the boiling refrigerant in the evaporator and condensing in the condenser. With regard to heat pumps «water-water» use temperature refrigerant at the outlet of the evaporator and coolant temperature at the outlet of the condenser.

A generalization of data in the literature for the production of refrigerating machinery and the thermal pumps «water-water» [2, 3] were allowed to obtain the analytical dependence of the conversion coefficient of the heat pump on the temperature of refrigerant at the evaporator outlet and the coolant temperature at the outlet of the condenser. The length of the vertical ground heat exchanger (VGT) is dependent on properties of the ground and characteristics of the heat pump system. We consider the 2 options:

1. Brine water is extracted to the surface, gives up its heat capacity and back under the ground.
2. Brine water is extracted to the surface, gives up its heat capacity and then removed at the surface.

The intensity of the heat transfer in the ground is influenced by its properties: the temperature t_g ; density ρ ; thermal conductivity λ ; thermal diffusivity a ; relative humidity of ground w . The length of the vertical of ground heat exchanger L_c is determined by its equivalent diameter D_e and the heat output Q of the heat pump. In the case of a vertical of ground the heat exchanger (VGT) to dissipate heat in the air conditioning mode to take into account the cooling capacity Q_c and electrical power compressor N . The intensity of heat transfer in soil is largely determined by the temperature of heat carrier at the inlet and outlet of a vertical ground heat exchanger VGT. The temperature at the outlet of the condenser is defining in determining the transformation coefficients of the heat pump φ and refrigeration coefficient ε , which are characterized by the energy efficiency of the system. The calculation is complicated by the fact that the ground is unsteady heat transfer due to the vertical and horizontal temperature gradients. Coolant rises through the feed pipe to the surface of the earth's depths, where the temperature reaches the bottom – $t_b = 40^\circ \text{C}$, and the temperature at the ground surface during winter $t_s = 2^\circ \text{C}$. In the process of lifting the coolant to the surface carries out its heat exchange with the surrounding rock, having a temperature below the temperature at the bottom. Varying the temperature at the surface of the vertical ground heat exchanger alters the temperature profile of the heat carrier inside the heat exchanger.

The calculation is based on the physical dependence of the heat flux q on the length of the borehole L_c , ground temperature t_g , the temperature of the fluid circulating in the VGT t_w and linear (referred to 1 m of the borehole) of the thermal resistance of heat transfer of R ground to the liquid resulting from Newton's law convective heat transfer cylinder to the environment. Most problematic is in determining the magnitude of the linear thermal heat transfer resistance R , because heat transfer occurs in the no uniform field under no stationary conditions. Was obtained an expression of the total length of borehole L_c depending on the average annual magnitude of the heat flux from the ground, the magnitude of the thermal resistance of ground, the thermal power of heating system and others parameters. The vertical exchangers can be used for the transfer in the summer in the soil heat of condensation from the system conditioning. The method has the information on the thermal conductivity and thermal diffusivity of the sandy and clay soils. All other types of the ground are considered as a combination of different proportions of sand and clay, and the corresponding values determined by interpolation. The values of thermal loads, as well as the ground temperature are taken by data this project.

Coolant temperature and refrigerant is calculated from a set value from the conversion coefficient and the coolant temperature in the heating system. Coolant temperature at the outlet of the vertical ground heat exchangers are taken at the 5 °C above.

The reliability of the algorithm was tested on the examples of calculation.

1. The duration of the heating period is 170 days, ground temperature at the location of the VGT at a depth of 600 m $t_g = 30$ ° C. Metal pipe $D_p = 60$ mm - a vertical heat exchanger, installed in the borehole diameter $D_{bh} = 150$ mm. Characteristics of the ground: density $\rho = 1318$ kg/m³, moisture content 15 %, thermal conductivity = 2,076 W/(m·K), thermal diffusivity $a = 0,087$ m²/day. The peak thermal power the system of the heating $qH = 50$ kW. The annual heat consumption for heating and hot water supply $Q = 367$ GJ. The system of the heating is designed taking into account the coolant temperature at the outlet of the condenser = 50 ° C. The coefficient of the conversion is taken $\varphi = 3,5$. The average per year power of the heat flux q_a from the ground to the heat pump without demand for a cold is 8.3 kW. The electrical power the engine the heat pump is determined from of maximum heat output of heating system $q = 50$ kW and the magnitude of the coefficient transformation $\phi = 3,5$ and is equal $q = 14.3$ kW. The mass flow of water through the borehole is $q = 1,7$ kg / s (6,120 kg / h). The velocity of the water through the tube is $w = 0,56$ m/s. The linear thermal resistance R_b borehole with given its occupation the thermally conductive bentonite $R_b = 0,03$ m·K/W. The coefficient of averaging the maximum heat load is equal to 0,5. The total length of borehole in the absence of adjacent boreholes affecting the heat transfer is equal to 480 m. Power of the heat flow from the ground to the VGT is the difference between heat and electrical power of a heat pump: $Q_{gr} = 50 - 14.3 = 35.7$ kW. The specific value of the heat flux, attributed to one meter VGT, is $Q_{gr} = 74.5$ W/m.

2. The total length of the vertical heat exchangers is significantly affected by the magnitude of thermal resistance R_b . According to available data, the value of thermal resistivity with of the borehole with DN = 60 mm is equal $R_b = 0,04 \div 0,095$. Minimum value of $R_b = 0,04$ corresponds to variant 1. For the option 2 calculations were performed for $R_b = 0,085$ m·K/W. The total length of the boreholes is equal to 560 m. The value of heat flow, referred to 1 m VGT is equal $Q_{gr} = 64$ W/m. The calculations confirm the correctness of calculation methods.

CONCLUSION

1. The heat pump is justified only in well-insulated buildings with heat loss no more than 100 W/m².
2. To achieve greater efficiency of heat pump is advisable to use them in a bivalent scheme – with an additional heat source (boiler), includes at the maximum heat demand.
3. In the Kuzbas, where the main energy source is coal, and all other energy sources (except for electricity) are imported, the application of heat pumps is economically justified.
4. The presented method of design of heat pump stations contain a solution of 2 the problems simulating of the heat exchanger with the environment and the temperature distribution inside the heat exchanger, as well as an engineering method of calculating heat pump station.
5. The design of the heat exchangers it is necessary the availability information of the characteristic of the ground at the construction site.
6. Engineering the system facilities (heat and cold) should be calculated the optimal to exclude of excess capacity
7. Not recommended the heat pumps with a coefficient of transformation of less than $3,5 \div 4$.

References

1. Lykov A.V. The thermal conductivity of non stationary processes. GEI, Moscow-Leningrad, 1948. Pp. 232.
2. Gorshkov V.G. "Heat Pumps. Analytical review, Handbook of industrial equipment. 2004. No. 2.
3. Popov A.V., Bogdanov A.I., Pazdnikov A.G. Experience in designing and creating lithium bromide absorption heat pump // Industrial Energy. 1999. No. 8. Pp. 38÷43.

HEAT PUMPS FOR HEAT SUPPLY OF INDUSTRIAL ENTERPRISE AND DISTRICT HEATING

Alina A. Potapova, Ildar A. Sultanguzin

Industrial Thermal Engineering Systems Department
Moscow Power Engineering Institute (Technical University)
Krasnokazarmennaya Street, 14, Moscow, 111250, Russian Federation
+7-495-362-7217; SultanguzinIA@mpei.ru

Peter A. Shomov

Limited Liability Company Scientific and Technical Center "Industrial Power Engineering"
Semenovskogo Alleyway, 10, Office 503, Ivanovo, 153000, Russian Federation
+7-4932-301488; Shomov@list.ru

Tatyana P. Shomova

Industrial Thermal Engineering Department, Ivanovo Power Engineering University
Rabfakovskaya Street, 34, Ivanovo, 153003, Russian Federation

Abstract

Different thermal engineering systems are examined for making use of low-potential waste energy to supply heat and cold to an integrated steelworks. The article also examines the use of vapor compression heat pumps operating on the return water of industrial combined heat and power plants to supply district heating. It demonstrates the energy efficiency of combining the positive characteristics of vapor compression heat pumps and absorption heat pumps to supply heat and cold to the enterprise and the city.

KEYWORDS

Absorption heat pump, vapor compression heat pump, metallurgical combine, low-potential waste energy, refrigerant, cold supply, heat supply.

INTRODUCTION

Different thermal engineering systems are examined for using of low-potential waste energy to supply heat and cold to an integrated steelworks. The report also considers the use of vapor compression heat pumps (VCHP) operating on the return water of industrial combined heat and power plant (CHPP) for district heating. It demonstrates the energy efficiency of combining the positive characteristics of VCHP and absorption heat pumps (AHP) to supply heat and cold to the industrial enterprise and the city. Heat-pump units (HPU) can be used for different sources of energy: low-potential waste heat in the form of steam and hot water; circulating mains water in heat supply systems; process water in circulating water supply systems; the exhaust gases of boilers and production equipment; effluent; sea water and river water; soil and ground water. One important problem is making efficient use of HPU, including AHP and VCHP.

IMPORTANCE AND PURPOSE

Industrial enterprises (integrated steelworks, petrochemical plants, etc.) are large consumers of thermal and electrical energy and have their own combined heat and power plants. These plants often supply heat and electric power not only the enterprise but also nearby residential and municipal buildings. In addition to heat and electric power, the administrative buildings of the site and nearby public buildings also need to be cooled during the summer months.

The rising costs of energy sources is forcing large industrial concerns to become more efficient in energy generation. Their need for energy and their expenditures on outside energy purchases can both be reduced by

using low-potential waste energy or secondary energy resource (SER). Such resources are already available at almost every industrial site.

Heat-pump units (HPU) can be used for different sources of energy: low-potential waste energy as steam or hot water; return water of heat supply systems; process water in circulating water supply systems; the exhaust gases of boilers and furnaces; sewage; sea water and river water; soil and ground water, etc. [1–4]. The important problem is efficient using of HPU, including absorption heat pumps (AHP) and vapor compression pumps (VCHP) (Fig. 1). Both types of HPU are successfully apply in Europe, USA, and Japan to cover the loads on systems designed for supplying hot water (HWS), heating, and air conditioning.

The main prerequisite to the efficient use of HPU is the presence of a low-potential waste energy with a temperature not lower than 15–20 °C. Modern heat pumps are capable of heating a heat carrier to temperatures as high as 90 °C, thus making it fit for use in a local heating system.

HPU connected to a heating system near consumers allows to increase the amount of heat energy generated by CHPP. The temperature of the return water from the heating system decreases in this case. It also saves fuel by reducing the amount of generated heat or increasing the output of heat and electric power. An analysis shows that the most efficient HPU could be installed for replace of electric boilers. Modern heat pumps are capable of heating a heat carrier to temperatures as high as 90°C, thus making it fit for use in a local heating system.

APPLICATION OF ABSORPTION HEAT PUMPS

The largest consumer of energy in an HPU is the compressor (see Fig. 1, *b*). Electric power costs can be reduced by using an AHP. In addition to the standard components (condenser, evaporator), an AHP has its own absorber, pump, and regenerator. It is also possible to make use of an intermediate heat exchanger or rectifier (see Fig. 1, *a*). An AHP operates on the basis of the principle of the ability of a solution of an absorbent to absorb water vapor that is at a lower temperature than the solution [1–3].

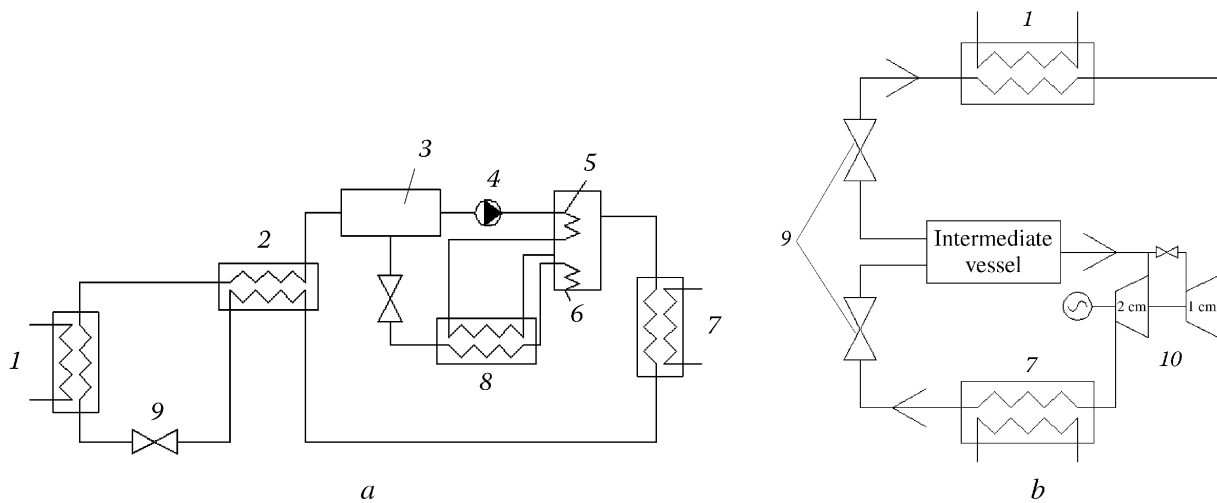


Fig. 1. Diagrams of AHP (*a*) and SCP (*b*): 1 – evaporator, 2 – intermediate heat exchanger, 3 – absorber, 4 – pump, 5 – rectifier, 6 – generator, 7 – condenser, 8 – liquid heat exchanger, 9 – choke valve, 10 – compressor

An AHP operates in the following manner: low-temperature water is delivered to the tube space of evaporator 1, where it is cooled as a result of boiling (vaporization) in a vacuum. The water enters the space in the form of a film that flows through the spaces between the tubes. The water vapor that is formed is absorbed by an aqueous solution of lithium bromide that flows through the intertubular space in absorber 3. This heats the lithium bromide solution, and to maintain its absorption capacity the heat of absorption is removed by water that flows inside the tubes of the absorber. Thus, heat is transferred from the low-temperature level in

the evaporator to the level of higher temperatures in the absorber. In the course of absorbing the water vapor, the solution of lithium bromide becomes weak – its concentration is reduced. The weak solution is regenerated by sending it through heat exchanger 8 to generator 6, where it is evaporated (concentrated) by heat from a certain heat source (such as steam).

The newly concentrated solution is sent through heat exchanger 2 to the absorber. The water vapor obtained in the generator is sent into the intertubular space of condenser 7 and in condensed form proceeds through choke 9 to evaporator 1. The water is directed in succession to the absorber and condenser, where it is heated to the necessary temperature and sent to the customer. All the processes that occur inside the machine take place in a vacuum.

Since the mixture of the liquid absorbent and the refrigerant is nearly incompressible, the power costs of the pump are negligible (compared to an HPU), and the only primary energy source is the heat supplied to the steam generator – which always has the highest temperature in the cycle. The heat given off in the absorber is added to the heat from the condenser, so that the heat coefficient of performance (COP) for the cycle μ_t is always greater than 1.

EXAMPLE OF THE USE OF AHP IN BY-PRODUCT COKE PLANT

Coke is produced in high-productivity coke ovens heated by a low-calorie (blast-furnace gas) or high-calorie (coke-oven gas, etc.) gas. The raw material for coking is a mixture of special grades of hard coal that are capable of agglomeration. The gas formed during the coking operation contains the following (g/nm^3): water vapor 250–450; resin vapor 100–120; benzene hydrocarbons 30–40; ammonia 8–13; hydrogen sulfide 5–30. The hot (700–800 °C) gas is cooled in a gas collector by spraying water into the latter (until the gas is at 80–90 °C). It is then further cooled (to 25–35 °C) in primary gas coolers (PGC). The condensate is separated into ammonia water and coal-tar pitch, and the cooled gas is carried off by powerful gas blowers and sent to a system built to remove and clean coke-oven gas.

The system that is currently used to cool and transport gas is often far from perfect. Disturbances of the prescribed temperature regime in the pipelines result in the formation of various deposits in the pipes. These deposits reduce the cross-sectional area of the lines, which in turn increases the load on the blowers. To avoid this, the actual temperature of the coke-oven gas at the outlet of the PGC should not be allowed to exceed the specification (which is on the order of 30–35 °C). In addition to increasing the consumption of electric power, having the gas at an excessively high temperature increases the load on the steam generator, the cost of providing make-up water to maintain the prescribed temperature of the process water in the coolers' circulation loop, the losses of resinous matter in the acid distillation equipment, and the losses of H_2SO_4 , benzene hydrocarbons, and caustic soda. For example, the specification in Germany for the temperature of coke-oven gas leaving the PGC is 25 °C because the lower this temperature, the cleaner the coke-oven gas.

In actuality, at certain Russian integrated steelworks the temperature of the coke-oven gas has exceeded 40 °C during the winter months: in accidents occurring on PGC, the temperature of the coke-oven gas after the coolers was found to have reached 55 °C. Allowing the gas to be at such a high temperature has had many negative effects: excessive consumption of electric power for the coke-oven-gas blowers, significant losses of benzene and resinous matter, deposition of naphthalene in the pipelines that carry coke-oven gas throughout the combine, fouling of the burners in power and production equipment, etc. The associated financial losses total tens and hundreds of millions of rubles.

The circulating water supply systems are also failing to adequately cool the circulating water used in the PGC. For example, the temperature of the circulating water leaving the cooling towers reaches 30–35 °C in the summer, although the norm is 25 °C.

In the winter, these heat pumps can be used in the heat supply system of the combine and produce up to 8.3 MW of heat energy [4]. The energy source for these AHP is waste heat steam from the coke plant. This steam, at a pressure of 0.5 MPa, is consumed by the heat pumps at a rate of 7.4 tons/h. A significant portion of the steam is not being efficiently used at present, and a considerable amount of it is lost altogether during the summer months.

Absorption heat pumps often use mixtures of water and lithium bromide or water and ammonia. Operation of the pumps requires steam for heating, water for cooling, and electric power. At coke and coal chemicals plants where ammonia is one of the products, it is preferable to use a water-ammonia mixture.

However, there are certain shortcomings to its use: ammonia produces a vapor with an excessively high pressure and leads to the corrosion of copper, and ammonia vapors are also toxic.

Proceeding on the basis of calculations performed to ensure that the prescribed temperatures of the circulating water and coke-oven gas are maintained during the summer, planners are proposing the installation of two lithium-bromide absorption heat pumps of the type ABTN-3000P [2, 5] (made by the Teplosibmash company in Novosibirsk). These pumps have a refrigerating capacity of up to 3.2 MW. Their specifications are as follows:

Thermal capacity/usable heat, kW	8300/3200
Consumption:	
hot steam, kg/h	7400
heated water/ coolant water, m ³ /h	225/550
electric power, kW	14

In the winter, these pumps can be used in the heat supply system of the combine and produce up to 8.3 MW of heat energy. The energy source for these AHP is recycled steam from the By-product Coke Plant. This steam, at a pressure of 0.5 MPa, is consumed by the heat pumps at a rate of 7.4 tons/h. A significant portion of the steam is not being efficiently used at present, and a considerable amount of it is lost altogether during the summer months. The COP that characterizes heat transformation by the AHP, determined on the basis of the ratio of the amount of heat that is produced to the amount of hot steam that is consumed, is equal to

$$\mu_t = Q_t / Q_{\text{steam}} = 8300 \text{ kW} / 4917 \text{ kW} = 1.69.$$

The cooling coefficient of performance of the AHP is

$$\varepsilon_r = Q_r / Q_{\text{steam}} = 3200 \text{ kW} / 4917 \text{ kW} = 0.65.$$

The nominal parameters of the heat carriers for ABTN-3000P are the temperatures of the water as it enters and leaves the system:

- coolant water – 30/25 °C;
- heated water – 40/70 °C.

THE USE OF VAPOR COMPRESSION HEAT PUMPS

We consider the example of VCHP using for district heating. It is investigated the feasibility of using heat pumps which employ heat from return water that is in close physical proximity to the customer (water located at central heating points, in peaking boilers, etc.) [6]. This is water that is returned to the heat and power plant from the central heat supply system.

One of the most important advantages of such a scheme is that it would lower the temperature of the circulating water, which would in turn make it possible to increase the cogeneration of electric power at the heat and power plant in accordance with the ongoing demand for heat. Such a possibility becomes even more important when one considers that the temperature of the return water continually rises due to various factors beyond normal system operation. In two such different cities as Krasnodar (in southern Russia) and Krasnoyarsk (in northeast Russia), it has been observed that water temperature in the return line of these cities' heat supply systems exceeds the norm by 5–8 °C in the winter.

A large two-stage VCHP [7] has been proposed for practical use (see Fig. 1, *b*) in a mountainous region with a growing heat load. It is proposed that the pump be installed on the return water line of the heat and power plant operated by a metallurgical combine in that area.

The heat pump was designed to operate on the basis of the heat in the return line under the condition that the temperature of the refrigerant in the condenser be 90 °C and that temperature in the evaporator be 40 °C [8, 9]. Some of the mains water that enters the heat supply system from the return line is directed to the evaporator, where it is cooled from 58 to 46 °C and then returned to the heat and power plant. Water from the return line that is used in the inner loop of the customer's local heating system is sent to the condenser of the heat pump and heated from 58 to 88 °C for return to the customer.

The heat pump was operated with coolant R-134a ($\text{CH}_2\text{F}-\text{CF}_3$), which does not affect the ozone layer. The refrigerant is used at a temperature of 101.08°C , and it has a pressure of 40.603 bars at the critical point. The decrease in temperature in the return line is negligible. If we consider that this temperature often increases, then the installation of an VCHP on the return line can serve as an additional means of protecting the line from overheating and keeping the boiler in a safe operating mode.

Figure 2 shows the p - H diagram of the thermal processes which take place during the operation of a heat pump on the return water of heating system.

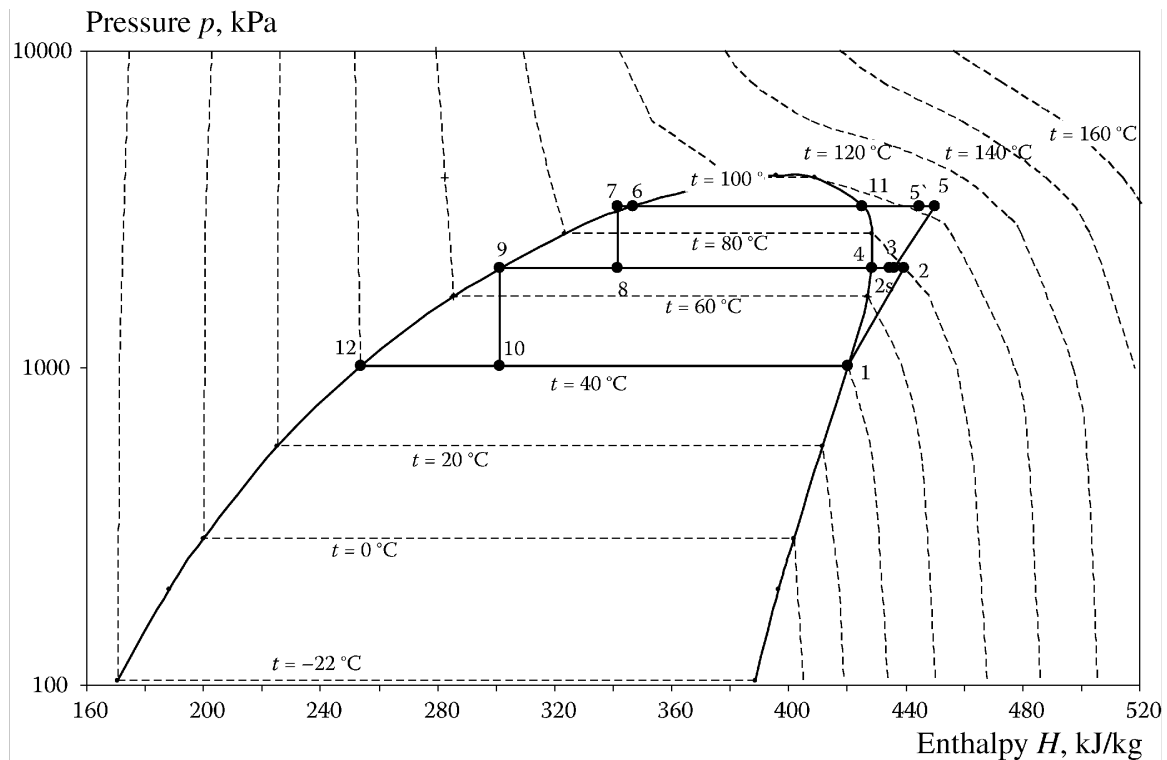


Fig. 2. p - H -diagram of the thermal processes in the operation of a two-stage heat pump operating on return water with the use of R-134a refrigerant

If the thermal capacity of the condenser $Q_{cond} = 17000$ kW, the amount of electric power needed for the drive of the compressor will be $N_e = 4050$ kW and the heat coefficient of performance – $\mu_t = Q_{cond}/N_e = 4.20$. During the summer, the pump can produce 10000–12000 kW of cold for the air-conditioning systems of office buildings and trade and business centers located within a 1-km radius of the VCHP. It can also cover the load for the HWS. Here, the refrigeration coefficient of performance is $\epsilon_r = Q_{evp}/N_e = 2.5$ –3.5.

In deciding on specific sites for installing heat pumps and their most efficient mode of operation in a centralized heat supply system, it is necessary to establish a scale of priorities that shows values of pump efficiency from the economic and energy standpoints. Heat pumps should first of all be used in place of electric and hot-water boilers whose operation entails the use of organic fuels. Here, there should be no reduction in the cogeneration of electric power by the heat and power plant to satisfy the existing thermal load. If the percentage of steam used in the turbines of the plant is increased – with the steam being brought up to the pressures corresponding to the district-heating loads (0.05–0.25 MPa) and dispatched to heat the water used in the heat supply system (from 58 to 90°C) – the amounts of electricity and heat energy obtained by cogeneration will increase. That will in turn reduce the amount of electricity generated by condensation because it will decrease the amount of steam that is reduced to the pressure which exists in the condenser (0.004 MPa). The heat of the steam inside the condenser will be lost to the environment. If a heat pump is installed near one of the customers using the heat energy and the pump makes use of the heat of the return-line water, then we have

the situation shown above: the temperature of the return water will decrease (from 58 to 46 °C). That will increase cogeneration in the turbines of the plant as long as the additional steam is used to heat the water and the amount of steam consumed in the condenser is reduced.

Absorption heat pumps and vapor compression heat pumps often end up competing with one another [3], and it is necessary to determine which is best for a given situation. The effectiveness of each type of heat pump depends on many conflicting factors (the availability of low-potential waste energy, the current cost of electrical and thermal energy, the temperature gradients, etc.). We believe that instead of having the two types of pumps compete against one another it is best if the most attractive qualities of each are put to practical use [4]. This can be done by developing new equipment and systems that will take advantage of the benefits of each type of pump and use them together (Fig. 3).

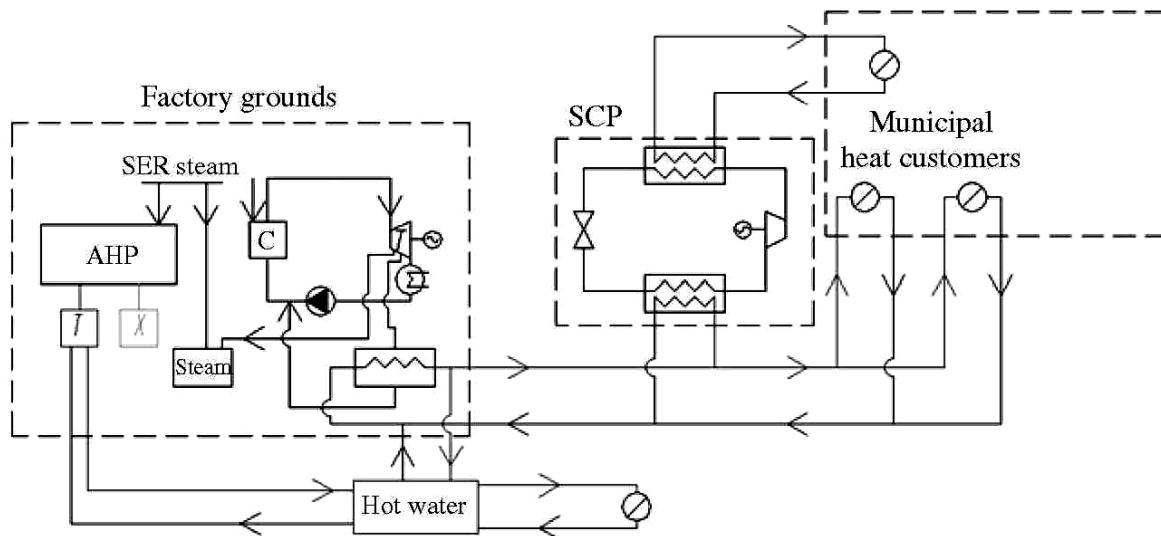


Fig. 3. The use of heat pumps in the heat supply system of a metallurgical combine and city

To sum up, although absorption heat pumps and vapor compression heat pumps last 20–25 years and pay for themselves in about 5–7 years even when the capital investment is substantial, AHP cannot compete with heat and power plants in terms of productivity. However, they can generate heat and cold with the use of low-potential sources whose energy often goes completely unused.

CONCLUSIONS

1. The use of absorption heat pumps (AHP) is most effective at factories that have a large number of low-potential waste energy. In winter, the heat coefficient of performance of an AHP with steam heating is $\mu_t = 1.6\text{--}1.8$; in summer, the refrigeration coefficient of performance of the same AHP is $\epsilon_r = 0.6\text{--}0.7$.
2. The use of vapor compression heat pumps is most effective near large municipal customers that can use the heat from the water in the return mains of heat and power plants. The same applies to customers for cold (residential and office buildings and new trade and business centers).
3. Calculations show that a vapor compression heat pumps can heat hot water to 85–90 °C and that it has a heat coefficient of performance $\mu_r = 4.0\text{--}5.0$ when using mains water. The exact values of these two parameters depend on the temperature of the refrigerant in the evaporator.

References

1. Sokolov E. Ya., Brodyanskii V. M. *Energy Principles of the Transformation of Heat and Cooling Processes*, Energoizdat, Moscow, 1981 (in Russian).

2. Gorshkov V. G. Heat Pumps. Analytical Survey: *Handbook of Industrial Equipment*, No. 2, 2004. Pp. 47–80 (in Russian).
3. Ogurechnikov L. A. Comparative analysis of steam-compression and absorption heat pumps // *Kholodilnaya Tekhnika (Refrigerating Engineering)*. 1996. No. 8. Pp. 8–9 (in Russian).
4. Potapova A.A., Sultanguzin I.A. Use of heat pumps in the heat supply system of a factory and a city // *Metallurgist*. 2010. Vol. 54, Nos. 9-10. Pp. 635–640.
5. Bykov A. V., Kalnin I. M., Kruze A. A. *Refrigerators and Heat Pumps*, Moscow: Agropromizdat, 1988 (in Russian).
6. Nikolaev Yu. E., Baksheev A. Yu. Determination of the efficiency of heat pumps that use the heat of water in the return mains of heat and power plants // *Promyshlennaya Energetika (Industrial Power Engineering)*. 2007. No. 9. Pp. 14–17 (in Russian).
7. Bailer P., Pietrucha U. District heating and district cooling with large centrifugal chiller – heat pumps // *Proc. 10th Int. Symp. on District Heating and Cooling*, Hanover, Germany, September 3–5, 2006.
8. Sultanguzin I.A., Potapova A.A. High-temperature high power heat pumps for a heat supply // *Novosti Teplosnabzheniya (News of a Heat Supply)*. 2010. No. 10. Pp. 23–27 (in Russian).
9. Sultanguzin I.A., Albul A.V., Potapova A.A., Govorin A.V. Heat pumps for Russian cities // *Energoberezheniye (Energy Saving)*. 2011. No. 1. Pp. 22–26 (in Russian).

RETROFITTING OF POWER PLANT CONDENSERS WITH HEAT PIPE HEAT EXCHANGER: A CASE STUDY

T. Mallikharjuna Rao

Central Power Research Institute
TRC, Koradi, Nagpur-441 111, India
Mobile Phone: 91 9422826022
E-mail: tmrao@cpri.in, vsld_1999@yahoo.com

S. S. Rao

Mechanical Engineering Dept
National Institute of Technology
Warangal – 506 004, INDIA
Mobile Phone: 91 9490165357
E-mail: sneni@nitw.ac.in

Abstract

This paper explores the feasibility of using the heat pipe for power plant condenser. Power Plant Condenser, which is a vital component in the power plant, consists of thousands of non-ferrous tubes. A huge number of tubes are required to condense steam entering into the power plant condenser. Power plant people were facing number of operational and maintenance problems because of these huge number of condenser tubes. Also a large quantity of cooling water is required for this conventional condenser. In this paper an attempt made to replace thousands of condenser tubes by hundreds of heat pipes. This paper describes comparison between, the conventional condenser and heat pipe heat exchanger for condensing the given amount of steam. Comparison is also made between the required cooling water quantities in the both cases.

This paper is also describes the design details of heat pipe that is material of heat pipe, heat pipe length, diameter of heat pipe for condensation purpose. Justification is also given for the type fluid and quantity of fluid used in the heat pipe. Angle of inclination of heat pipe is discussed in detail. Mathematical calculations are described for the pressure drops across the heat pipe. The feasibility study was carried out for smooth operation of the heat pipe that is without ceasing during operation. Experimental setup to conduct laboratory experiments is also described in this paper.

Detailed discussion presented for the suitability of designed heat pipe for practical applications of power plant condensers. A brief description is given to the method of "retrofitting the heat pipes" into an existing power plant condenser.

KEYWORDS

Wickless heat pipe, thermal syphon, steam condenser, heat transfer coefficient.

INTRODUCTION

Historical Development of heat pipes dates back 1942 when the first Patent for a heat pipe employing a capillary wick for pumping liquid against gravity was applied by Gaugler (1942). In the words of Grover (1963, 1964) who along his co-workers reinvented the 'heat pipe' in 1963, a heat pipe is a "... synergistic engineering structure which is equivalent to a material having thermal conductivity greatly exceeding that of any known metal...". In other words, a heat pipe is a passive two-phase heat transfer device capable of transferring large quantities of heat with minimum temperature drop. In 1964, RCA was the first commercial organisation to perform heat pipe research. Due to the its commendable ability to transport heat energy the use of heat pipe becoming popular, starting from space shuttles to electronic industry (14).

The special features of heat pipes have made them attractive for use as heat pipe heat exchangers (HPHE). The use heat pipes in modern heat exchangers reviewed by Leonard L.Vasiliev (15). But all these application are for energy recovery, air to air, air to gas exchanges and liquid to liquid only. Till now no application is made to condensate the steam using heat pipes, especially in the thermal power plants.

Condenser, which is a vital component in the power plant consists of thousands of non-ferrous tubes. Mostly, these condensers are shell and Tube heat exchangers. The steam will be in shell side and cooling water flows through the tubes. The transfer of heat energy will be due to cooling water temperature rise only (single phase heating). Hence there will be huge number of tubes employed in these condensers. Due to a large number of tubes there will be lot of operational and maintenance problems. Hence an attempt can be made to replace thousands of condenser tubes by comparatively less number of heat pipes.

CONCEPT OF THE PROPOSAL

In the conventional condensers of the power plant the, turbine outlet steam enters the condenser and incidents on the tube surfaces. The cold water flows inside the tubes and maintains the tube surface below the saturation temperature of steam. Hence the steam condenses on the tubes surface. Temperature of cooling water in the tubes will rise due to latent heat of steam condensation on the tube surface. There will be phase change of steam into condensate and cooling water will undergo only sensible temperature rise. Due to this reason, large area of heat transfer required, in turn more of tubes, that is thousand of tubes required.

In the present proposal, phase change of the cooling water is proposed. Because of higher latent heat of vaporization of the cooling water, the heat carrying capacity will be increased and hence, there will be reduction of heat transfer area, that is number of tubes in the condenser.

To achieve this phase changer of cooling water, the heat pipes will be employed. The cooling water in the heat pipe will be maintained under vacuum, hence the lower boiling temperature of the cooling water.

The process of heat transfer shown in the Fig. 1. The steam incidents on the heat pipe evaporator surface at 46 °C. The evaporator will heaving the water at a pressure of 0.07 bar. At this pressure the boiling temperature of the water is 39.02 °C. Therefore the ΔT will be (46–39.02) 6.98 °C. For 0.07 bar, ΔT_{chf} is equal to 14 °C, which is greater than Δt in the present case. Hence nucleate boiling will occur.

So the vapors from the evaporator regions enters the condenser portion of heat pipe. This portion is maintained at a surface temperature of 27 °C with help of inlet cooling water. So the vapors which reached the top portion of the heat pipe will condense on side surface of the heat pipe by releasing heat gained at evaporator section to the cooling water. The condensate will flow down due to gravity. The cycle repeats as the process go on.

CASE STUDY

The details of Condenser of a Thermal Power plant for this case study conducted are as follows.

Sl. No	Parameter	Numerical value
1	Unit Load	200 MW
2	Condenser Steam inlet temperature	46 ° C
3	Condenser steam inlet pressure	0.102 bar
4	Condenser cooling water inlet Temp	27 ° C
5	Condenser cooling water outlet Temp	43.45 ° C
6	No of Condenser Tubes	24398
7	Condenser Tube OD	31.75 mm
8	Condenser Tube ID	30.3276 mm
9	Condenser Tube Length	14.73 m
10	Load on Condenser	25367508 kcal/hr 29503 kW
11	Cooling water Flow	2428 t/hr 675 kg/s
12	Tube velocity	0.077 m/sec

DETAILS OF REPLACEMENT PROPOSAL FOR THIS CONDENSER WITH HPHE

Sl. No	Parameter	Numerical value
1	No of Heat Pipes in HPHE (Dimensions of Heat pipe given in justification)	6400
2	Arrangement of Heat pipes in HPHE	Staggered , 80x80
3	Length of Heat Pipe	4.3 m
4	Material of Heat Pipe	Copper
5	Vacuum inside the Heat Pipe	0.07 bar
6	Working fluid inside heat pipe	Distilled water
7	Saturation temperature of water inside the heat pipe	39.02 °C
8	Wick material	Wickless heat pipe

THE DETAILS AND THERMAL ANALYSIS OF HEAT PIPE TO BE USED IN HPHE

The line diagram of the heat pipe which are to be placed in the HPHE shown in Fig. 2.

Length of the Heat pipe $L = 4.3\text{m}$

Length of evaporator section $L_e = 2\text{m}$

Length of the condenser section $L_c = 2\text{m}$

Length of the adiabatic section $L_a = 0.3\text{ m}$

Tube is 'K' type Nominal Standard Size is 2 inch

Outside diameter of the heat pipe $d_o = 2.125\text{ inch} = 0.053975\text{ m}$

Inside diameter of the heat pipe $d_i = 1.959\text{ inch} = 0.0497586\text{ m}$

Thickness of the heat pipe wall $t = 0.083\text{ inch} = 2.1082 \cdot 10^{-3}\text{ m}$

The heat pipe is a wickless, gravity assisted that is strictly it is a two phase closed thermo syphon

Vacuum inside heat pipe 0.07 bar

Hence Saturation temperature for water inside heat pipe 39.02 °C.

HEAT TRANSPORT LIMITATIONS OF THE PROPOSED HEAT PIPE

The working fluid is selected as distilled water according to ref (1, 9).

As per Amir Faghri (2), the compatible material for water is Copper, stainless steel, Nickel, Titanium. Here for this case Copper is selected.

Now, Aspect Ratio (AR)

$$L_e / d_i = 2/0.0497586 = 40.19 \approx 40. \quad (1)$$

Calculation for the working Fluid inventory

The total Heat pipes proposed are 7225

Condenser load in this case 29503 kW \approx 30,000 kW

Assuming that all heat pipes in the heat exchanger takes load equally

Thermal load on each heat pipe $Q_1 = 30000/6400 = 4.6875\text{ kW}$

As per Amir Faghri (2), the the total volume of the working fluid in the heat pipe

$$V_t = [4/5(L_c + L_e) + L_a][3Q_1\mu_1(\pi d_i)^2 / \rho_l^2 g h_{fg}]^{1/3}$$

$Q_1 =$ Thermal load on each heat pipe in $W = 4687.5\text{ W}$

μ_1 = liquid viscosity inside the heat pipe = $663 \cdot 10^{-6}$ kg/(m·s)

g = acceleration due to gravity = 9.81 m/s²

h_{fg} = latent heat of evaporation of water inside heat pipe J/kg = $2408 \cdot 10^3$ J/kg

ρ_l = liquid density inside heat pipe = 992 kg/m³

Hence , $V_t = [4/5(2+ 2) + 0.3][3 \cdot 4687.5 \cdot 663 \cdot 10^{-6} \cdot (\pi \cdot 0.0497586)^2 / (992)^2 \cdot 9.81 \cdot 2408 \cdot 10^3]^{1/3} = 7.487 \cdot 10^{-5}$ m³.

This fluid quantity is sufficient to handle the load of heat load on each heat pipe. But however it is proposed to have 8.35 times of this quantity of fluid to have maximum capability of heat pipe (3, 15).

Hence quantity of water inside the proposed heat pipe $7.487 \cdot 10^{-5} \cdot 8.35 = 6.25 \cdot 10^{-4}$ m³.

Hence the Filling Ratio (FR) = Volume of the Working Fluid / Volume of the Evaporator section

$$= 6.25 \cdot 10^{-4} / \pi (0.0497586)^2 \cdot 2 = 0.16 \text{ or } 16 \% . \quad (2)$$

BOILING LIMIT

As per Gorbis, Z. R & Savchenkov, G. A (1976) the maximum heat transfer Q_2 from boiling point of view is given by,

$$Q_2 = Ku \{ h_{fg} \rho_v^{0.5} [\sigma g (\rho_l - \rho_v)]^{0.25} \},$$

$$Ku = 0.0093 (AR)^{-1.1} [d_i/L_e]^{-0.88} (FR)^{-0.74} (1 + 0.03Bo)^2.$$

Bo = Bond Number = $d_i \{ g (\rho_l - \rho_v) / \sigma \}^{1/2}$

σ = surface tension N/m = $69.6 \cdot 10^{-3}$ N/m

Applying numerals for the inside conditions of the heat pipe

$Bo = 0.0497586 \{ 9.81 \cdot (992 - 0.05) / 69.6 \cdot 10^{-3} \}^{1/2} = 18.6$

$Ku = 0.0093 (40)^{-1.1} [0.0497586/2]^{-0.88} (0.16)^{-0.74} (1 + 0.03 \cdot 18.6)^2 = 0.0391$

Hence,

$$Q_2 = Ku \{ h_{fg} \rho_v^{0.5} [\sigma g (\rho_l - \rho_v)]^{0.25} \} = 0.0391 \{ 2408 \cdot 10^3 \cdot 0.05^{0.5} [69.6 \cdot 10^{-3} \cdot 9.81 (992 - 0.05)]^{0.25} \} =$$

$$= 107079.9 \text{ W} = 107 \text{ kW} . \quad (3)$$

FLOODING LIMIT

As per Amir Faghri (2)

Maximum heat transfer limit from the boiling point of view, Q_3 will be given as

$$Q_3 = K h_{fg} A_{\text{cross}} [g \sigma (\rho_l - \rho_v)]^{0.25} \times [\rho_v^{-1/4} + \rho_l^{-1/4}] .$$

Now $K = [\rho_l / \rho_v]^{0.14} \tanh (Bo)^{1/4}$.

Applying Numericals, $K = 3.756$. And

$$Q_3 = 155 \text{ kW} . \quad (4)$$

Summarizing the above results in a tabular form

Sl.No	Parameters	Desired requirements of Heat Pipes in the proposed HPHE	Designed Heat pipes characteristics as per different calculations
1	Maximum heat transfer limit from the Boiling point of view	4.6875 kW	107 kW from (3)
2	Maximum heat transfer limit from the Flooding point of view	4.6875 kW	155 kW from (4)

Hence the designed heat pipe qualifies the desired heat transfer requirements and can be used in the HPHE. The laboratory model of the heat pipe is under laboratory trials and actual results will be discussed in the seminar.

HPHE Condenser Calculations

The line diagram of the proposed HPHE condenser is shown in Fig 3.

Steam inlet entry to the condenser will be from the both sides as shown in the above figure. The cooling water will be entered inside the condenser just above separator plate and exited from the top portion. The condensate will be flooded to the bottom of the condenser. The heat pipes will be arranged in 80x80, vertical, staggered arrangements. The plan of the arrangement of heat pipes is shown in Fig. 4

Now Thermal Calculations of the Heat Pipe Condenser

Steam inlet conditions into the condenser = 46 °C, 0.102 bar

Condenser load for 200 MW turbine = 29503 kW \approx 30,000 kW

Proposed Heat pipes in the condenser = 6400.

Calculation of Heat Transfer Coefficient (h_1) for the portion of heat pipe which is exposed to inlet steam

t_{sat} = steam inlet temperature = 46 °C

Steam inlet pressure $p = 0.102$ bar

μ_{11} = viscosity of condensed water = $9.69 \cdot 10^{-6}$ kg/(m·s)

h_{fg1} = heat of vaporization of inlet steam = 2390 KJ/kg

The saturated water temperature inside of heat at at evaporator section = 39.02 °C = t_s

Hence the outside film temperature $t_f = (39.02 + 46)/2 = 42.51$ °C = 315.5 K

The modified heat of vaporization $h_{fg1} = h_{fg1} + 0.68C_{pl}(t_{sat} - t_s) = 2390 + 0.68 \cdot 4.179 \cdot (46 - 39.02) = 2409.8$ KJ/kg

Mass of the condensate on each heat pipe $m^* = 4.6875/2409.8 = 1.95 \cdot 10^{-3}$ kg/s

Reynold number for condensate, $Re_1 = 4m^*/p \mu_{11}$

p = outside perimeter of het pipe

$$Re_1 = (4 \cdot 1.95 \cdot 10^{-3}) / \{\pi \cdot (0.053975) \cdot 9.69 \cdot 10^{-6}\} = 4747.4.$$

Hence the flow on heat pipe is turbulent. From the literature, for condensation on vertical tubes is given by, which are near to experimental values.

$$h_1 = 0.0076 Re_1^{0.4} \{ k_f^3 \rho_f (\rho_f \rho_g) g / \mu_f^2 \}^{1/3}$$

$$k_f = 634 \cdot 10^{-3} \text{ W/(m·K)}$$

$$\mu_f = 631 \cdot 10^{-6} \text{ kg/(m·s)}$$

$$\rho_f = 991.1 \text{ kg/m}^3, \rho_g = 0.056 \text{ kg/m}^3.$$

$$\text{Hence, } h_1 = 4116.8 \text{ W/(m}^2 \cdot \text{K)}.$$

Calculation of Heat Transfer Coefficient (h_4) for the portion of heat pipe which is exposed to water Pool

The heat transfer coefficient for portion of heat pipe immersed in the cooling water pool can be calculated based on correlations suggested by Whitakar(7) and Zhukaushas A (8).

The Nusselt number for this, situation is,

$$Nu = C Re_{2,max}^m Pr^{0.36} (Pr/Pr_s)^{1/4}. \quad (5)$$

For $Nu \geq 20$, $0.7 < Pr < 500$, $1000 < Re_{max} < 2 \cdot 10^5$.

Cooling water inlet temperature $t_{c,in} = 27$ °C

Cooling water inlet velocity $V_{in} = 0.085$ m/s

S_L = Longitudinal pitch = 0.063975

$S_T = \text{Transverse pitch} = 0.063975$

$$V_{\max} = \{S_T/(S_T-d_o)\}V_{in} = 0.544 \text{ m/s.}$$

Out let cooling water temperature $t_{c,o} = 27 + (30000/675 \cdot 4179) = 37.6 \text{ }^\circ\text{C}$.

Hence average cooling water temperature $= (27+37.6)/2 = 32.3 \text{ }^\circ\text{C} = 305.3 \text{ K}$

$Pr = 5.20$, $Pr_s = 4.39$, $\mu_c = 769 \cdot 10^{-6} \text{ kg/(m}\cdot\text{s)}$, $\rho_c = 995 \text{ kg/m}^3$

$Re_{2,\max} = \{\rho_c V_{\max} d_o\} / \mu_c = 3.8 \cdot 10^4$.

Hence the constants for Equation (5), $C = 0.35$, $m = 0.60$

Applying numerical to Equation (5) $Nu = 369.75$

Hence, $h_4 = kNu / d_o = 4246.7 \text{ W/(m}^2\cdot\text{K)}$.

Calculation of Heat Transfer Coefficient (h_2) for the evaporator section, inside of heat pipe.

The heat transfer coefficient for evaporator section inside heat pipe can be calculated based on correlations suggested by Imura (1979) et. al.

$$h_2 = 0.32[(\rho_l^{0.65} k_l^{0.3} c_{p,l}^{0.7} g^{0.2} q_e^{0.4}) / (\rho_v^{0.25} h_{fg}^{0.4} \mu_l^{0.1})][p_{sat}/p_a], \quad (6)$$

$\rho_l = \text{liquid density inside heat pipe} = 992 \text{ kg/m}^3$, $c_{p,l} = 4178.5 \text{ J/(kg}\cdot\text{K)}$

$q_e = \text{heat flux at evaporator section from outside} = 4687.5 / (\pi \cdot 0.053975 \cdot 2) = 13821.9 \text{ W/m}^2$

$\rho_v = 0.05 \text{ kg/m}^3$, $h_{fg} = 2408 \cdot 10^3 \text{ kg/m}^3$, $\mu_l = 663 \cdot 10^{-6} \text{ kg/(m}\cdot\text{s)}$

therefore, applying numerals to equation (6), $h_2 = 3400 \text{ W/(m}^2\cdot\text{K)}$.

Calculation of Heat Transfer Coefficient (h_3) for the evaporator section, inside of heat pipe

The Reynold for condensate flow inside heat pipe is given by,

$$Re_3 = Q / \pi \cdot d_o \mu_l h_{fg} = 4.6875 / \pi (0.0497586) \cdot 9.59 \cdot 10^{-6} \cdot 2408 = 1296.$$

Hence the flow is laminar and the heat transfer coefficient for condenser section inside heat pipe can be calculated based on correlations suggested by Rohsenow, 1956,

$$h_3 = 0.943 \{ \rho_l g k_l^3 (\rho_l - \rho_v) [h_{fg} + 0.68 c_{p,l} (T_{sat} - T_w)] / (\mu_l L_c (t_{sat} - t_w)) \}^{1/4}, \quad (7)$$

$t_w = \text{surface wall temperature at condenser section}$ } $= (27+37.6)/2 = 32.3 \text{ }^\circ\text{C} = 305.3 \text{ K}$
that is part of heat pipe immersed in the water pool }

the physical properties are evaluated taken at this wall temperature.

$\rho_l = 995 \text{ kg/m}^3$, $\rho_v = 0.034 \text{ kg/m}^3$, $K_l = 620 \cdot 10^{-3} \text{ W/(m}\cdot\text{K)}$

$h_{fg} = 2426 \cdot 10^3 \text{ J/kg}$, $c_{p,l} = 4178 \text{ J/(kg}\cdot\text{K)}$, $\mu_l = 769 \cdot 10^{-6}$

Applying these numericals to the equation 7,

$$h_3 = 4561.65 \text{ W/(m}^2\cdot\text{K)}$$

Overall Thermal Resistance.

By definition, the overall heat transfer coefficient for a single heat pipe is (Amir Faghri)

$$U_p = 1/R_p. \quad (8)$$

Where R_p is the thermal resistance of a single heat transfer element in the HPHE, which is defined as the sum of individual resistances in the element. The expression for this is,

$$R_p = R_h + R_{f,h} + R_{w,h} + R_{w,i,e} + R_{i,e} + R_{i,c} + R_{w,i,c} + R_{w,c} + R_{f,c} + R_c. \quad (9)$$

$R_h = \text{Resistance due to steam condensation at evaporator section of the heat pipe} = 1 / (h_1 \pi d_o) L_e = 7.14 \cdot 10^{-4}$.

$R_{f,h}$, $R_{f,c}$ are fouling resistance due to corrosion or oxidation at the outer surfaces of the heat pipes or

thermalsyphons. These resistances are typically neglected, but incases when HPHE is operating in a corrosive environments, they can be significant and should be accounted for with an additional conduction resistance through the corrosion layer. In the present case these are neglected.

$$R_{w,h} = \text{resistances due to the pipe wall at evaporator section} = \ln(d_o/d_i)/(2\pi k_w L_e) = 1.64 \cdot 10^{-5}$$

K_w is the thermal conductivity of copper

$$R_{w,c} = \text{resistances due to the pipe wall at condenser section} = \ln(d_o/d_i)/(2\pi k_w L_c) = 1.64 \cdot 10^{-5}$$

K_w is the thermal conductivity of copper

$R_{wi,e}$, $R_{wi,c}$ are resistance terms occur due to heat through the liquid saturated wick which is zero in the present case.

$$R_{i,e} = \text{resistance which occur due to the phase change at evaporator section} = 1/(h_2 \pi d_i L_e) = 9.19 \cdot 10^{-4}$$

$$R_{i,c} = \text{resistance which occur due to the phase change at condenser section} = 1/(h_3 \pi d_i L_c) = 6.85 \cdot 10^{-4}$$

$$R_c = \text{Resistance due to convection of water pool at condenser section of the heat pipe} = 1/(h_4 \pi d_o) L_c = 6.9 \cdot 10^{-4}$$

Applying these numerical values to Equation (9), (8)

$$R_p = 7.14 \cdot 10^{-4} + 1.64 \cdot 10^{-5} + 1.64 \cdot 10^{-5} + 9.19 \cdot 10^{-4} + 6.85 \cdot 10^{-4} + 6.9 \cdot 10^{-4} = 3.0408 \cdot 10^{-3}$$

Over all Heat transfer coefficient of single heat pipe $U_p = 1/R_p = 328.86 \approx 329$.

LMTD calculation of Heat Pipe Condenser (As per Fig. 5).

Steam entry temperature = 46 °C, and steam is condensating at this temperature. Cooling water inlet temperature = 27 °C. Cooling water outlet temperature 37.6 °C

$$LMTD = (37.6 - 27)/\ln \{(46 - 27)/(46 - 37.6)\} = 12.99$$

$$\text{Total Heat transfer area of single heat pipe } A = \pi (d_o L_e + d_i L_e + d_o L_c + d_i L_c) = 1.3 \text{ m}^2$$

Let N be number of heat pipes in the HPHE $Q = U_p N A (LMTD)$

$$30000000 = 329 \cdot N \cdot 1.3 \cdot 12.99 \text{ implies, } N = 5399 \approx 5400$$

That is the Number of heat pipes required for the assignment is 5400. But the assumption made is 6400 tubes. The extra tubes will take care dirt factor and act like cushion of heat pipes.

Experimental Set for Laboratory Experiment

The line diagram of the laboratory model of HPHE is shown in Fig. 6.

Different Parameters for the experimental set up

No heat pipes = 36, exactly as shown in Fig 2.

The outlet steam conditions of 200 MW turbine is simulated by arrangement of a miniature steam generator whose capacity will be 200 kW. At starting point of steam pipe line a throttle and temperature indicator fixed. The condensate is collected at bottom tank.

The cooling water is supplied from a overhead tank. The inlet and out let temperature of cooling water is determined by thermometers.

This experimental set up is under laboratory trails and results will be presented during the seminar.

THE ECONOMICS OF RETROFITTING.

This heat pipe condensers can be retrofitted economically as described in the following table. This is valid for the case of 200 MW power plant, which is under consideration.

1	Heat pipe loaded condenser	No heat pipes are only against 24,398 copper tubes of original conventional condenser. The shell dimensions are also small as compared to the conventional shell and tube condenser. Hence the cost Heat pipe condenser will 50 % cost of the original condenser.
2	Area comparison	The conventional condenser having a total volume of 250 m ³ . But the Heat pipe condenser for this job will be only 125 m ³ . The conventional condenser will be horizontal, but this heat pipe condenser will be vertical and can be retrofitted at old condenser place.
3	Cost for Piping	In the conventional condenser directly to the outlet of turbine exhaust. But for this heat pipe condensers, the exhaust steam is to distributed into two steam for two side entrance. This may cost around Rs. 30 lakh Indian Rupess (INR)
3	Cost for Cooling water	The existing cooling water supply is sufficient and with little modification in the plumbing work the water arrangement can be made. The expenditure for this will be around RS. 5 Lakh Indian Rupees.
4	Air removal from the condenser	The existing system can be utilized for this and expenditure will be around Rs. 15 lakh Indian rupees.
5	Cooling towers	The existing cooling towers can be utilized with a little modifications. The expenditure for this will be around Rs. 20 lakh Indian rupees.

CONCLUSIONS

1. The calculations made how the wickless heat pipe can be used for condensation of steam of power plant, the latest usage of heat pipes.
2. The paper also brings out how a huge conventional condenser can be replaced by a comparatively smaller heat pipe condenser which contains less number and less number of heat pipes. This reduce the maintenance problems of condenser.
3. The paper also addressed the cost retrofitting of this condenser in place of conventional condenser.
4. The laboratory experiment results will be presented in the seminar proceedings.

ACKNOWLEDGEMENTS

The authors would like to thank M/s. Central Power Research Institute for sponsoring the experimental expenditure and gave permission to publish this article.

Nomenclature

Explained in the running text.

References

1. Seshan S. and Vijayalakshmi D. Heat Pipes – concepts, Materials, and Applications. Energy MANAGEMENT. Vol. 26. 1986.
2. Faghri Amir. Heat Pipe Science and Technology. Taylor and Francis, Washington Dc, USA, 1995.
3. M.R. Sarmasti Exami, Noie S.H. & Khoshnoodi M. Effect of Aspect Ration and Filling Ration on Thermal performance of an inclined Two Phase closed Thermosyphon, Iranian Journal of Science & Technology. Vol. 32, No. 31, Feb. 2008.
4. Park Y.J., Kang H.K & Kim C.J. Heat Traansfer Characteristics of Two Phase Closed Thermosyphon to the Fill Fill charge Ratio // Int J. of Heat and Mass Tranfer. 2002. Vol. 45. Pp. 4655–4661.
5. Gorbis Z. R. & Savchenkov G. A. Low Temperature Two Phase Closed Thermosyphon investigation // 7th International Heat Pipe conference. 1976. Bologna, Italy, Pp. 37–45.

6. Shiraishi M., Kim Y., Murakami M. & Terdtoon P. A correlation for the critical Heat transfer rate in ITPCT // Proceedings of 5th International Heat Pipe Symposium. 1996. Pp. 248–254.
7. Zhukaushas A. Heat Transfer from Tubes in Cross Flow in J.P. Hartnett and T.F. Irvine, Jr. Eds Advances in Heat Transfer. Vol. 8. Academic Press, New York, 1972.
8. Whitaker S. AI chE J. 18, 361, 1972.
9. Heat Pipes, Second Edition, P. Dunn and D.A. Reay, Pergamon Press.
10. "Predicting Heat Transfer in Long, R-134a, Filled Thermosyphons" by M.H.M. Grooten, C.W. M. Van del Geld. Department of Mechanical Engineering, Technische Universities Eindhoven, Postbus 513, 5600 MB, Eindhoven, Netherlands.
11. Fundamentals of Heat and Mass Transfer. F. P. Incropera, D. P. Dewitt / Third edition, John Wiley & Sons.
12. Performance Analysis of Power Plant Condensers. By Dr. P.V. Subba Rao, IIT, Delhi.
13. Heat pipe Activity in the Americas, LA-UR-97-155, Robert S. Reid, New Mexico.
14. Review Heat Pipes in modern Heat Exchangers, Leonard L. Vasiliev. Applied Thermal Engineering. 25 (2005) 1–19.
15. Thermal Performance of a Two Phase Closed Thermosyphon using Aqueous Solution. M. Karthikeyan, S. Vaidyanathan, B. Sivaraman, International urnal of Engineering Science and Technology. 2010, 2(5), 913–918.
16. Computational Study of Thermosyphon heat exchanger for water heating using flue gas from rice husk combustion. Chaiwat Wannagoist and Piyanun Charoensawan. As. J. Energy Env. 2010, 11(01), 10–18.
17. Air heat Exchangers with long heat pipes Experiments and predictions. H. Hagens et. Al. Applied Thermal Eng. 27(2007) 2426–2434.
18. Process Heat Transfer, D. Q. Kern.

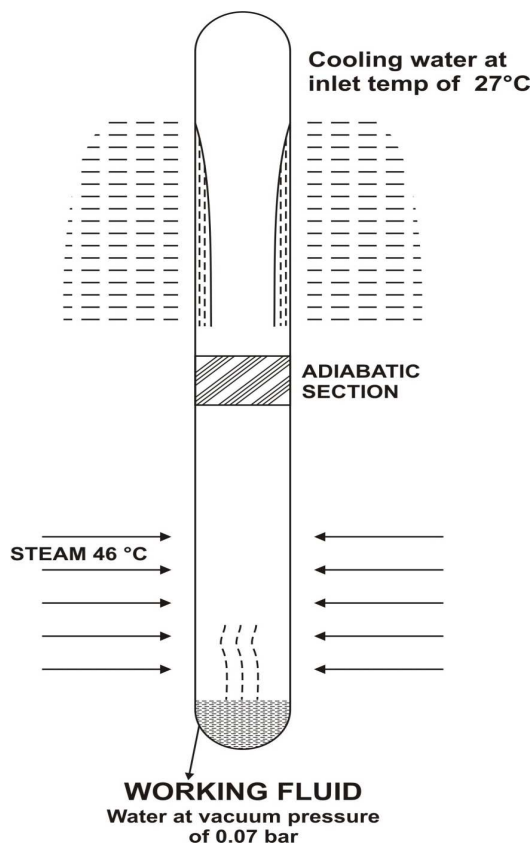


Fig. 1

PROPOSED HEAT PIPE

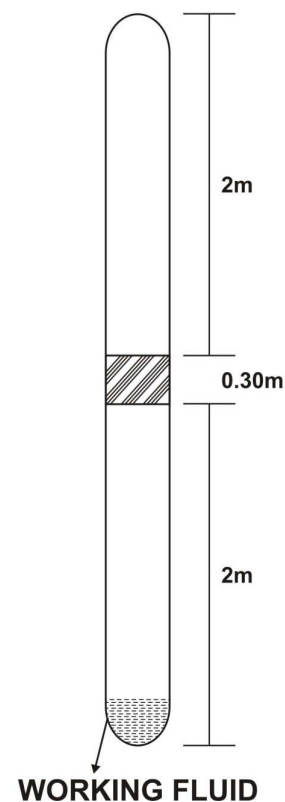


Fig. 2

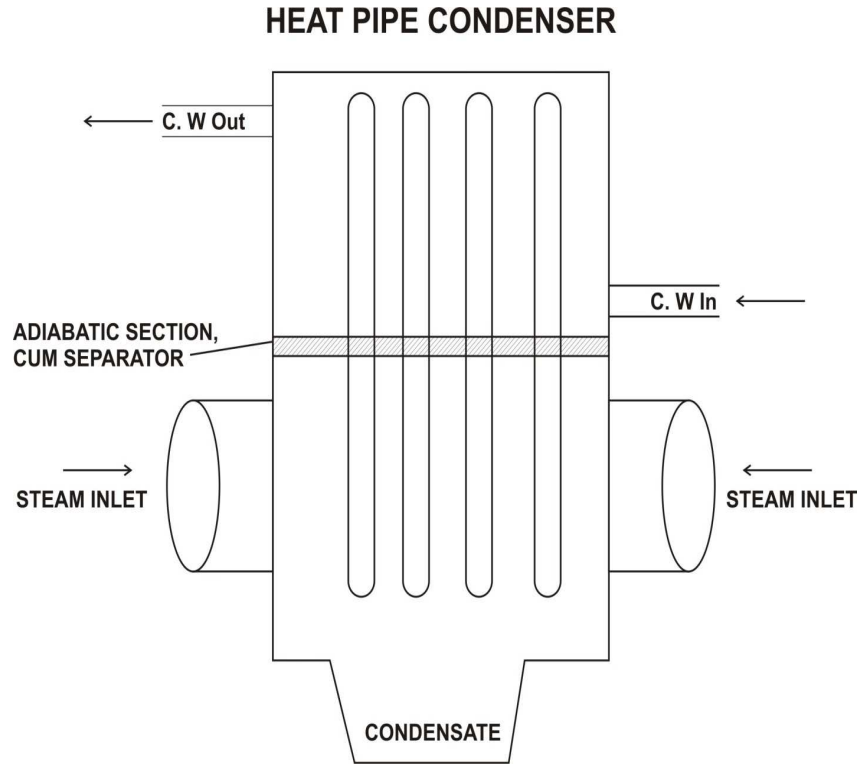


Fig. 3

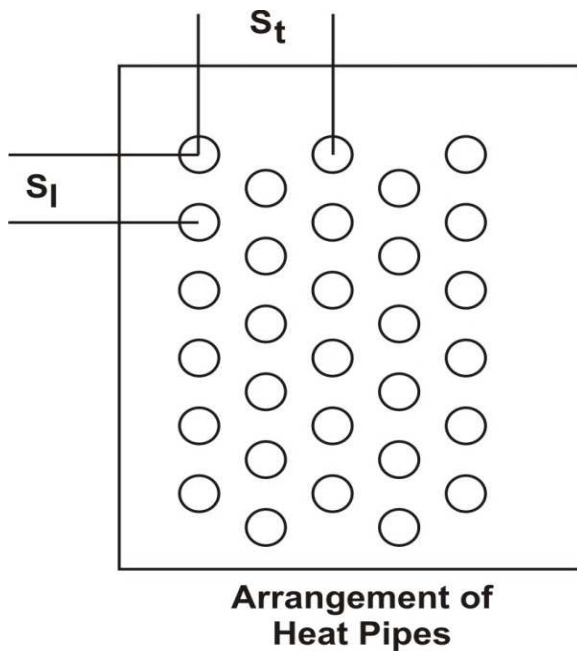


Fig. 4

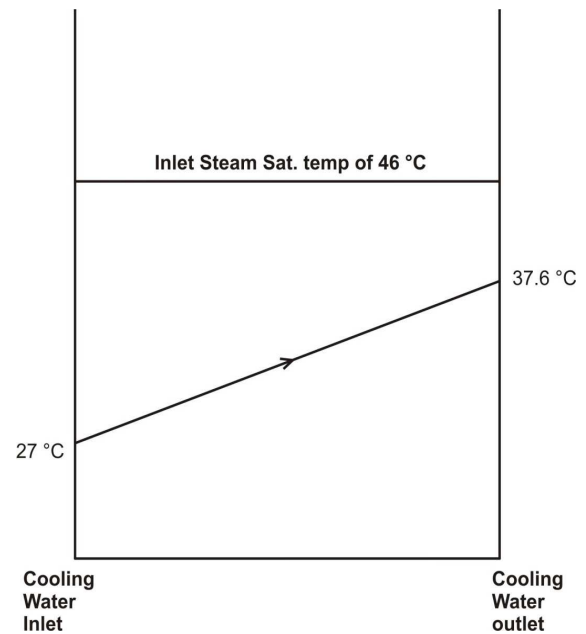


Fig. 5

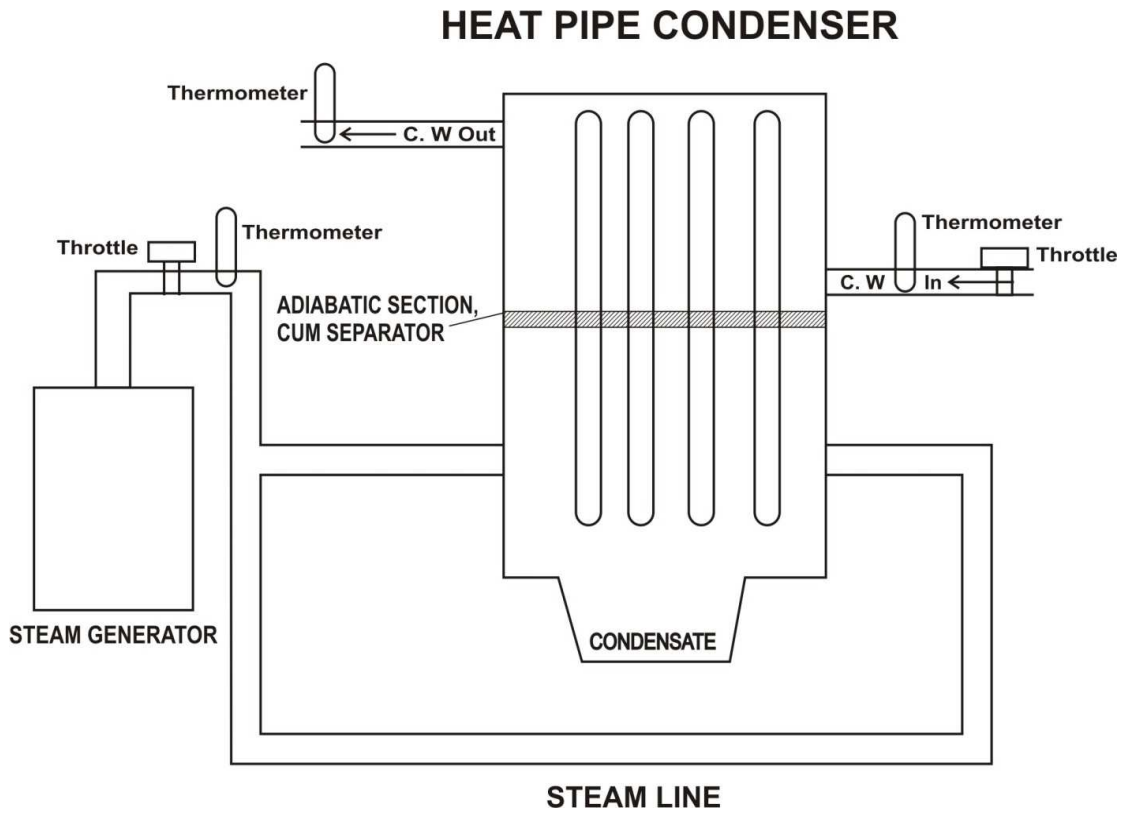


Fig. 6

DESIGN AND CHARACTERIZATION OF OBSTACLED BIPOLAR PLATES

Mehmet Sankır*, İbrahim Türkmen, Talha Camcı, Levent Semiz, Nurdan Demirci Sankır

Micro and Nanotechnology Graduate Program
TOBB University of Economics and Technology
Söğütözü C. No 43 06560, Ankara, Turkey
Tel +90 312 2924332 msankir@etu.edu.tr

Ertan Açar and Derek Baker

Mechanical Engineering
Middle East Technical University
06531 Ankara, Turkey

Abstract

Proton Exchange Membrane Fuel Cell (PEMFC) was built using COMSOL Multiphysics® software. The goal was to check if the model responded correctly to reactant species concentration changes in terms of polarizations. Rectangular shaped obstacles inside the flow channels of the bipolar plates were located at various heights to decrease concentration polarizations and make more reactant species react due to the obstacles. Different reactant gas velocity values were used as inlet boundary conditions. Additionally, different pressure values were used as outlet boundary condition to investigate the effect of pressure. The results of the study indicate that increasing outlet pressure, inlet velocity and depth of the obstacles through the channels results in better cell performance. Bipolar plates with moderate height obstacles and no-obstacles (straight) were manufactured and their electrochemical performances were tested under both dry and humidified environment. It was observed that obstacles lowered the performances at mass transport region for dry conditions. Similarly, obstructed bipolar plates resulted lower performances at lower reactant rates at humidified conditions. However, when flow rates of reactants were increased, the cell performances of obstructed plates resulted with the best performances. It was significantly increased up to 1.1 A/cm^2 at 0.5 V . It was concluded that obstacles results significant improvements on performances if there is enough flow rates provided.

KEYWORDS

PEM Fuel Cell, COMSOL Multiphysics, Bipolar Plate, Electrochemical Cell Performances, Polarization Curves.

INTRODUCTION

Fuel cells are electrochemical cells which convert the chemical energy of a fuel directly into useful electrical energy. In particular, proton exchange membrane fuel cells (PEMFCs) which already have commercial availability in some countries are one of the most promising types of fuel cells for transportation and residential applications. In terms of energy conversion efficiency, when compared to combustion engines and turbomachines, fuel cells can achieve higher efficiencies since they do not operate according to a cycle between a heat source and a heat sink and therefore are not limited by the Carnot efficiency. PEMFCs use hydrogen as a fuel and oxygen or air as the oxidant. Since the only product of the oxidation reaction of hydrogen is water, fuel cell vehicles have zero tailpipe emissions, which have made them attractive for transportation applications for the last two decades as the governments of the industrialized countries push for reducing the carbon footprint of vehicles. After the first usage of fuel cells for space applications, PEMFCs emerged as the leading fuel cell type for portable and automotive applications due to its low operating temperatures, comparative simplicity in construction, high power density and ease of operation [1]. However, some major obstacles still inhibit the adaptation of this technology, namely the excessive cost, lackluster performance at high current densities, and durability over an extended period of time [2].

Computational engineering has become a major technique for designing better engineering products over the last several decades. For instance, computational fluid dynamics (CFD) analyses have enabled

researchers to design more efficient engines without the need of manufacturing and testing at every design step. CFD is also a useful and necessary tool for modeling of fuel cells; however the complete modeling of a fuel cell requires a multi-physics approach. In order to obtain a meaningful performance evaluation of a fuel cell, not only is CFD modeling of the momentum transport inside the reactant flow channels required, but also the modeling of the electrochemical phenomena and the resulting mass transport by diffusion and convection, or in other words reactant species consumption, is necessary.

Agar built a two-dimensional, one-phase and isothermal fuel cell model using COMSOL Multiphysics [3]. The model included the mathematical background coupling the electrochemical, mass transport and momentum transport phenomena in a single PEMFC. Agar applied pressure inlet and outlet boundary conditions in their models and found that at low operating voltages, low pressure gradients inside the gas flow channels result in an unexpected species depletion problem and the current density goes to zero. Agar stated that this may be a problem occurring at the mid-cells of a fuel cell stack. Ekiz also demonstrated a similar two-dimensional PEMFC model in their thesis work [4] utilizing velocities as inlet boundary conditions and pressures as outlet boundary conditions. By providing sufficient reactant flow inside the channels, Ekiz overcame the problem of species depletion and produced realistic polarization curves.

Bipolar plates of a fuel cell function as both reactant supplier to the active layers and current collector. Fluid flow, heat and mass transport processes in the channels of bipolar plates have significant effects on fuel cell performance, particularly on the mass transport losses [2]. The current computational model accounts for all the mentioned physical phenomena. The resulting output of the work is the polarization curves of the models, which directly determine the performance of a fuel cell. In order to detect the effect of different reactant gas flow channel designs and operating conditions on cell performance, polarization curves were plotted and interpreted.

NUMERICAL MODELING

The aim of this modeling work is to obtain the polarization, or performance, curve of the fuel cell, using a 2D computational model and accounting for the significant role species depletion plays on this curve. To observe the species depletion and to obtain the polarization curve, parallel-to-flow cross section of a unit fuel cell was modeled (Fig. 1). The domain has subdomains to represent the flow space of the channels, GDLs (gas diffusion layers) and the MEA (membrane electrode assembly) where the active layers are assumed to be one-dimensional boundaries. The thicknesses of a flow channel, GDL and MEA are 0.75 mm, 0.25 mm and 0.1 mm, respectively. Three different heights in obstacles were utilized. The qualitative heights were named as 1, 2, 3, with a greater number having a greater height. The model is two-dimensional and steady-state conditions were applied. Also, hydrogen and air, or fuel and oxidant and product gas are always in the gas phase. It is assumed that permeability, porosity and conductivity properties of the electrodes and the channels were isotropic. Gas transport is by diffusion and convection. On the other hand, temperature-driven diffusion is neglected and the flow of species is incompressible flow.

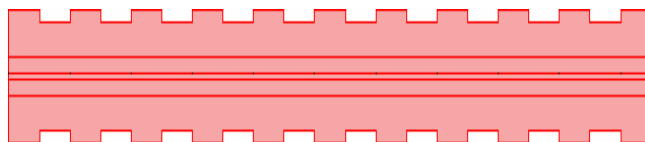


Fig. 1. Rectangular obstacles in flow channel. The purpose of these rectangular obstacles is to direct the reactants to the active layers

FUEL CELL TESTING

Bipolar plates used in this study were machined based on most of the criteria set during modeling. Bipolar plates with middle-sized rectangular obstacles (rectangular obs. 2) were fabricated (Fig. 2). Fuel cell tests were performed using a FuelCon Test Station®. Membranes were conditioned prior to performance tests. Performance tests were performed under both dry (room temperature) and humidified (50 %)

environments. Hydrogen and air were utilized during performance tests. Hydrogen and air flow rates were 1.2 and 2.0, respectively. Only cathode was humidified at 53 °C where cell temperature was 70 °C.

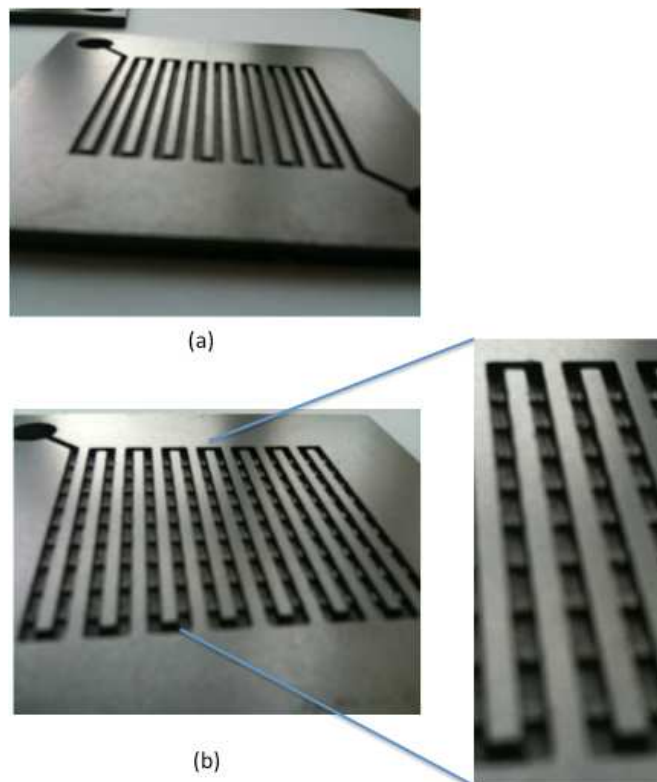


Fig. 2. Bipolar plates (16 cm² active area): *a* – without obstacles, *b* – with obstacles

RESULTS AND DISCUSSION

The model with rectangular obstacles resulted better performance than straight channel (no-obstacle) model. The highest obstacles was always showed the best performance. As intended, the obstacles forced more reactant species to react by directing them through the GDL to the active layer, therefore greater current densities were produced compared to no-obstacle model.

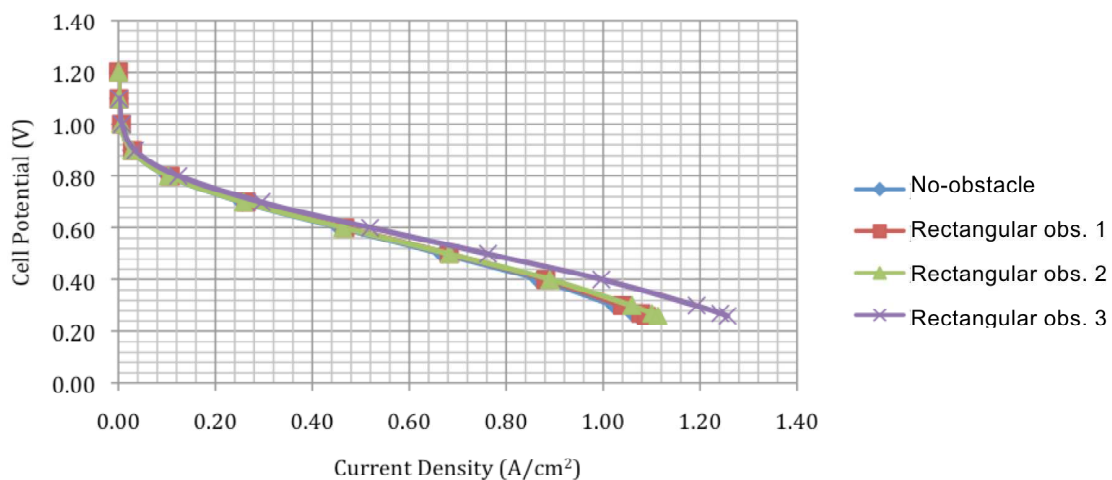


Fig. 3. Performance curves for rectangular obstructed channel and no-obstacle straight channel models

The increase in performance of the obstructed model was encouraged us to manufacture bipolar plates having rectangular obstacles at moderate heights. Typical electrochemical polarizations curves of PEMFC having straight and obstructed bipolar plates were obtained both under dry and humidified conditions. As seen in Fig. 4, performances due to the obstructed plates were not much changed in both activation and ohmic polarization regions. However, there was a slight difference in performances of mass transport region. Obstacles slightly cause to have worse performances in mass transport region. This was most probably because of the fully dried test condition where limiting current was easily achieved because of mass transport limitations. On the other hand, our computational model including humidification consistently showed better performances.

Later, influence of bipolar plates on performance were tested for various flow rates under 50 % relative humidity with the cell temperature of 70 °C. As one can easily concludes that performances of all bipolar plates regardless of existence of obstacles were improved a lot with humidification (Fig. 5). As flow rate increases performances of the PEMFC having straight bipolar plates were lowered (Fig. 5.2 and 3). Since the amount of reactant directing to catalyst layer was not increased much, but most probably caused drying with increasing flow rate, which probably reduced the cell performance. On the other hand, obstructed bipolar plates at lower flow rates of reactants caused to decrease in cell performances, although they showed very little ohmic polarization. Unlike to PEMFC with straight channels (no-obstacle), the amount of the reactants directing to catalyst layer in obstructed channels was probably not enough. Therefore, performances were lowered with very low limiting current in mass transport region, but performances at ohmic polarization regions were quite high. Conversely, when flow rates of reactants were increased, it was assumed that reactants directed to catalyst layer increased significantly. The cell performance was increased significantly up to 1.1 A/cm² at 0.5 V. It can be concluded that obstructed plates showed better performances at higher flow rates as model predicted.

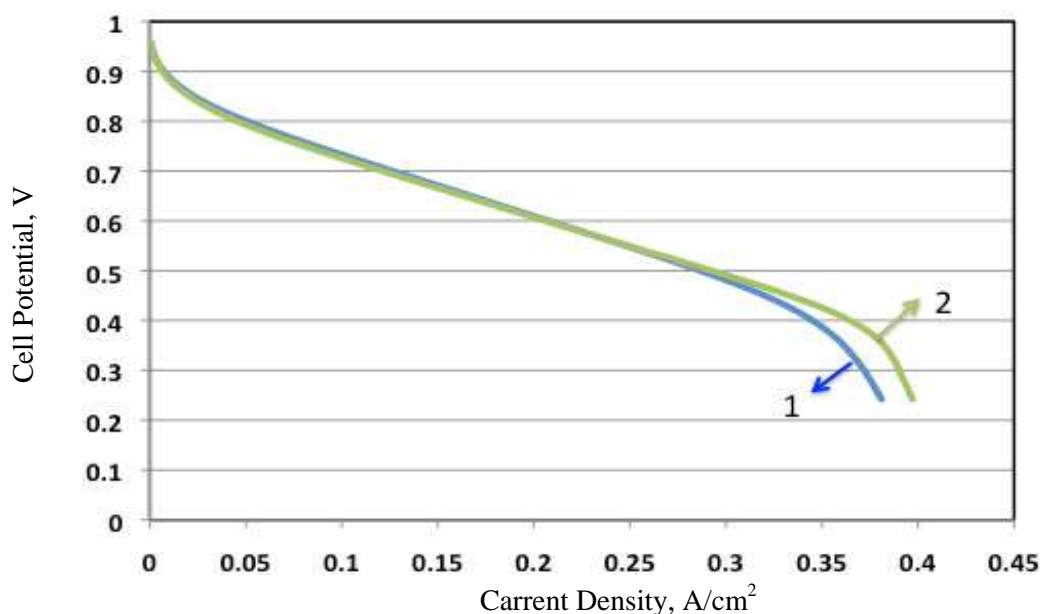


Fig. 4. Performance curves at room temperature without external humidification for (1) PEMFC having bipolar plates with obstacles (2) without obstacles

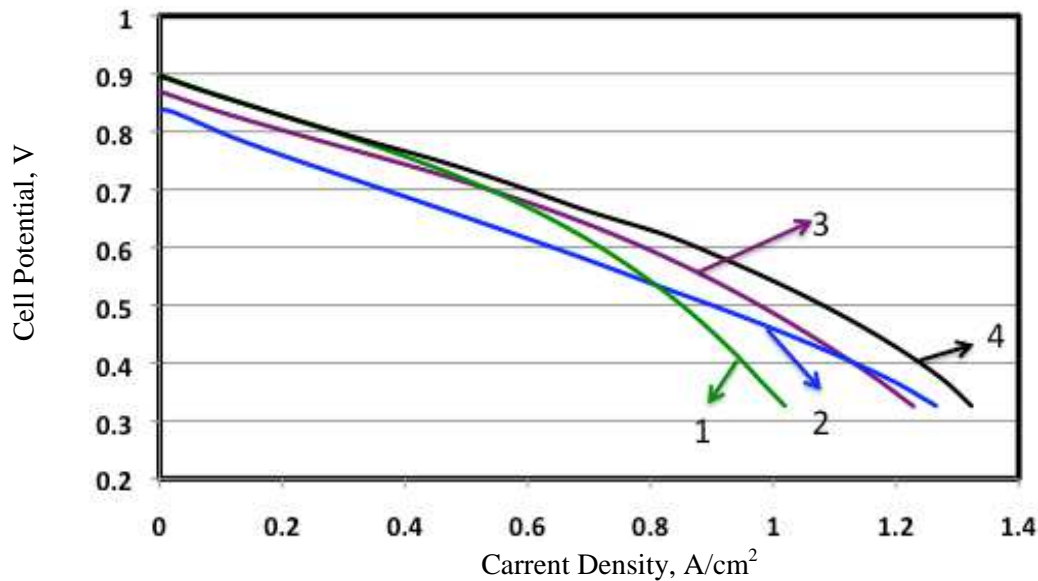


Fig. 5. Performance curves: 1 – obstructed (Hydrogen – 0.24 L/min, Air – 0.60 L/min) ; 2 – No-obstacle (Hydrogen – 0.36 L/min, Air – 0.90 L/min) ; 3 – No-obstacle (Hydrogen – 0.24 L/min, Air – 0.60 L/min) ; 4 – Obstructed (Hydrogen – 0.36 L/min, Air – 0.90 L/min)

CONCLUSIONS

The influence of placing obstacles with various heights along the flow plate channels was investigated with the intention of decreasing the concentration gradient through the GDL and increasing the reactant concentration at the catalyst layer. As expected with obstacles, a greater amount of reactant species interacted with the active layers, decreasing the concentration polarizations, and more reactant species were consumed. This effect culminated in greater generated current densities, meaning better cell performance. It was demonstrated that increasing flow rates was lowered cell performance of straight channels. However, this improved the performances of PEMFC with obstructed bipolar plates at higher flow rates by directing more reactants to catalyst layer as predicted in the model.

Acknowledgments

Financial support from Ministry of Industry and Trade: General Directorate of Industrial Research and Development under the contract #00277.STZ.2008-1 is gratefully acknowledged.

References

1. Akhtara N., Qureshib A., Scholtaa J., Hartniga Ch. Messerschmidta M., Lehnerta W. Investigation of water droplet kinetics and optimization of channel geometry for PEM fuel cell cathodes // *Inter. J. of Hydrogen Energy*. 2000. Vol. 934. Pp. 3104–3111.
2. Boddua R., Marupakulaa U.K., Summersa B., Majumdar P. Development of bipolar plates with different flow channel configurations for fuel cells // *J. of Power Sources*. 2009. Vol. 189. Pp. 1083–1092.
3. Agar E. *2-D Modeling of a Proton Exchange Membrane Fuel Cell*. Master's thesis, Middle East Technical University, Ankara, Turkey, 2010.
4. Ekiz A. *Modelling of Bipolar Plates for Proton Exchange Membrane Fuel Cells*. Master's thesis, TOBB University of Economics and Technology, Ankara, Turkey, 2010.

MOLYBDENUM THIN FILMS FOR HIGH TEMPERATURE PHOTOVOLTAIC FABRICATION PROCESS

Nurdan Demirci Sankir*, **Erkan Aydın**, **Hülya Ünver**
Micro and Nanotechnology Graduate Program
TOBB University of Economics and Technology
Sogutozu Cad. No:43 06560 Sogutozu Ankara/TURKEY
Phone:+90 312 2924331, Fax:+90 312 2924121,
*email:nsankir@etu.edu.tr

Demiral Akbar, **Sinan Bilikmen**
Department of Physics
Middle East Technical University
Universiteler Mahallesi,
Dumlupinar Bulvari No:1
06800 Cankaya Ankara/TURKEY
Phone:+90 312 2103283, Fax: +90 312 2105099

Abstract

In this study, we are proposing optimized process conditions for the deposition of molybdenum (Mo) thin films on various substrates for high temperature photovoltaic applications. Mo thin films have been deposited on various substrates using RF magnetron sputtering technique. Morphological and structural properties of the Mo thin films have been investigated via scanning electron microscopy (SEM) and X-ray diffraction (XRD) analysis, respectively. Well-adhered Mo thin films with low electrical resistivity have been obtained for both glass and polyimide substrates. Most of the photovoltaic device fabrication processes include high temperature and oxidative production steps. With this motivation, film forming properties, electrical conductivity and reflectance of the Mo thin films after heat treatment has been studied. Soda lime glass and Kapton HN films suffered from crack formation and loss of electrical conductivity after heat treatment. Hence, chemical and plasma treatments prior to metallization were applied. Although, chemical treatment improved the electrical conductivity of as deposited samples, after heat treatment Mo thin films were damaged severely and lost their conductivities. On the other hand, plasma treated polyimide samples retained their electrical conductivities even after heat treatment, which was a very promising result for the flexible photovoltaic device applications.

KEYWORDS

Molybdenum, Thin Films, Electrical Conductivity, Surface Treatment, Plasma Treatment, Flexible Photovoltaic Devices, High Temperature Fabrication.

INTRODUCTION

Photovoltaic devices convert the solar energy into electricity by means of a quantum mechanical process known "photovoltaic effect". Thin films have been extensively used in photovoltaic devices due to less material need and ease of manufacturing techniques compared to the bulk materials. Thickness of the thin film layers for photovoltaic devices can be ranged from a few nanometers to tens of micrometers. Hence, the material cost, which is almost the fifty percent of overall device cost, can be reduced dramatically. Copper indium gallium diselenide (CIGS) and copper indium disulfide (CIS) thin films are promising candidates to be replaced with bulk silicon for photovoltaic applications. CIGS and CIS thin films offer high absorptivity, high diffusion length and better solar-to-electricity conversion efficiency [1, 2]. Therefore, these materials have been used in the solar cells as absorption layer. In a typical solar cell back and front metal contacts act as the current collector. Film properties of the contact metal dramatically affect the conversion efficiency of the solar cell. Metal back contact thin film should be pinhole free and mechanically stable especially for the high temperature photovoltaic fabrication processes. Moreover, there should be ohmic contact between back contact and the absorber layer. Molybdenum (Mo) thin films are used as back contact of CIGS and CIS

photovoltaic devices due to ohmic contact formation, low electrical resistance, high chemical and thermal stability.

There are very limited studies on thermal, mechanical and electrical stability of Mo thin films for photovoltaic devices [3, 4]. Hence, there is a very strong need for detailed studies on high temperature stability of Mo thin films deposited onto different substrates. In this study, we reported the optical, electrical and morphological properties of Mo thin films before and after temperature treatments for photovoltaic applications.

EXPERIMENTAL

Mo thin films were deposited on soda lime glass and two different types of polyimide substrates (Kapton HN, Dupont and Upilex S, UBE Industries) using Vaksis PVD-MT/2M2T system. Prior to Mo deposition all substrates were ultrasonically cleaned in acetone bath for 10 minutes. Morphology of the Mo thin films was characterized using FEI Quanta 200 FEG. Electrical resistivity of the Mo thin films was measured via Lucas Lab S-302-4 four point probe analyzer equipped with Keithley 2400 source-measure unit. Perkin Elmer Lambda 650 G with 150 mm Integrating Sphere were used to measure the reflectance of the thin films. Reflectance measurements were conducted over the wavelength range of 200–800 nm at room temperature. In order to confirm the crystal structure of the films, Pananalytical MPD X-Ray system was used. Thermal treatment of the samples were conducted at 300 °C and atmospheric conditions. During the thermal treatment water was sprayed on the samples to mimic the spray or chemical deposition techniques. Table 1 summarizes the sample name and their deposition conditions used in this study.

Table 1. Information of the samples used in this study

Sample Name	Substrate	Deposition Time (min)
S1	Upilex S	15
S2		30
S3	Kapton HN	15
S4		30
S5	Soda Lime Glass	15
S6		30

RESULTS AND DISCUSSION

As can be seen in Fig. 1, as deposited Mo thin films were homogenous and showed good adherence. It is also worth to mention here that bending Kapton HN and Upilex S substrates did not caused visual crack formations.

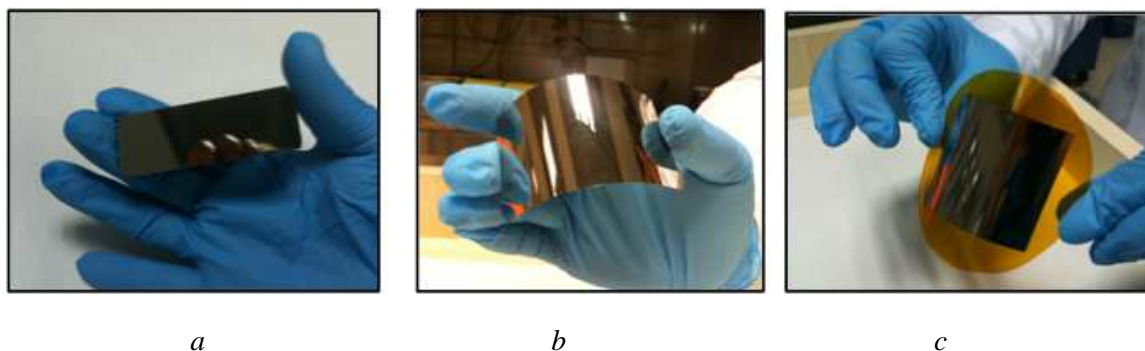


Fig. 1. Pictures of Mo thin films deposited on (a) soda lime glass, (b) Upilex S and (c) Kapton HN

Fig. 2 shows the surface SEM images of the Mo thin films. As can be seen in this figure, all films were homogenous and pinhole/crack free. SEM images also indicated that there has been no significant effect of substrate on morphology of Mo thin films. The thickness of the Mo thin films was measured from cross sectional SEM images. Regardless of the substrate, average thickness of the Mo thin films deposited for 15 and 30 minutes was 260 and 460 nm, respectively.

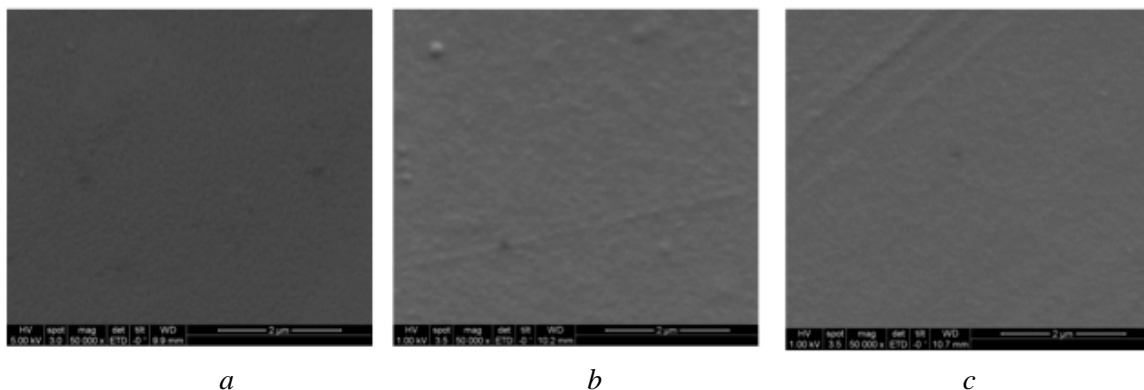


Fig. 2. SEM images of Mo thin films deposited on (a) soda lime glass, (b) Kapton HN and (c) Upilex S

Fig. 3 shows the XRD diffraction pattern of Mo thin films. As can be seen in this figure all samples have crystal peaks at around similar 2θ values. These peaks are comparable to the previously reported Mo thin film crystal peaks [3, 4]. Therefore, peaks around 40° could be attributed to the (110), 60° was for the (200), and 70° could be assigned to the (211) Mo peaks. It has also observed that the intensity of the Mo thin films deposited on soda lime glass was higher than that of Mo thin films deposited on both Kapton HN and Upilex S. This is most probably due to the better crystal formation on soda lime glass compare to the polyimide substrates.

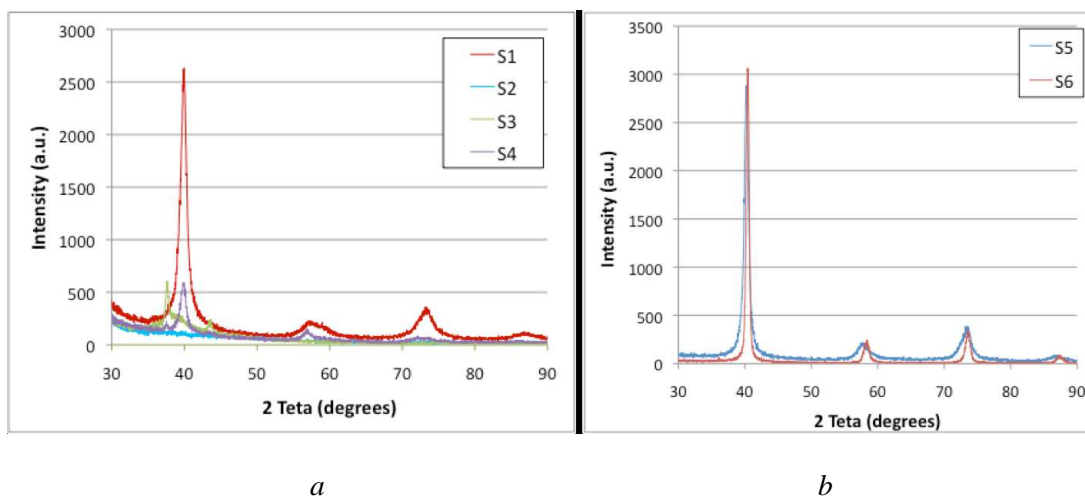


Fig. 3. XRD patterns of Mo thin films deposited on (a) polyimide (Kapton HN and Upilex S) and (b) soda lime glass

Electrical conductivity of the Mo thin films affects the performance of photovoltaic devices directly. Hence, the electrical performances of the Mo thin films were tested using 4-point probe technique. Table 2 summarizes the sheet resistivity of the Mo thin films on different substrates. All resistivity values reported here are high enough to be used as back contact layer for photovoltaic cells. Also, it is very interesting that, resistivity of the Mo thin films deposited on polyimide substrates were lower than the resistivity of the thin films deposited on glass substrates. This could be related with the interface interaction, and therefore,

different oxidation rates of Mo coated polyimide and soda lime glass substrates. Moreover, Mo thin films deposited for 30 minutes had higher conductivity. This is most probably due to more material deposition with longer time. Our group is currently working on the interface interaction of the Mo thin films on various substrates.

Table 2. Sheet resistivity of the Mo thin films

Sample Name	Substrate	Deposition Time, min	Sheet resistivity, Ohm/square
S1	Uplex S	15	7
S2		30	3
S3	Kapton HN	15	12
S4		30	4
S5	Soda Lime Glass	15	75
S6		30	29

Aforementioned photovoltaic device fabrication may include high temperature and oxidative production steps. Hence, the back contact layer should be both mechanically and electrically stable during these processes. For this purpose, Mo thin films were annealed at 250 and 300 °C. During heat treatment samples were also subjected to the water. Fig. 4 indicates the sheet resistivity of the Mo thin films before and after heat treatment. Kapton HN samples lost their electrical conductivity after heat treatment. Also, crack formation occurred for some of the glass substrates. On the other hand, Uplex S samples were homogenous and electrically conductive after heat treatment. As can be seen in Fig. 4, Uplex S samples with 15 minute Mo coating showed the lowest sheet resistivity after 300 °C annealing. Conversely, the sheet resistivity of the Uplex S substrates with 30 minutes Mo thin film coating dramatically increased after 300 °C heat treatment. Unlike Uplex S, resistivity of the glass substrates decreased with heat treatment.

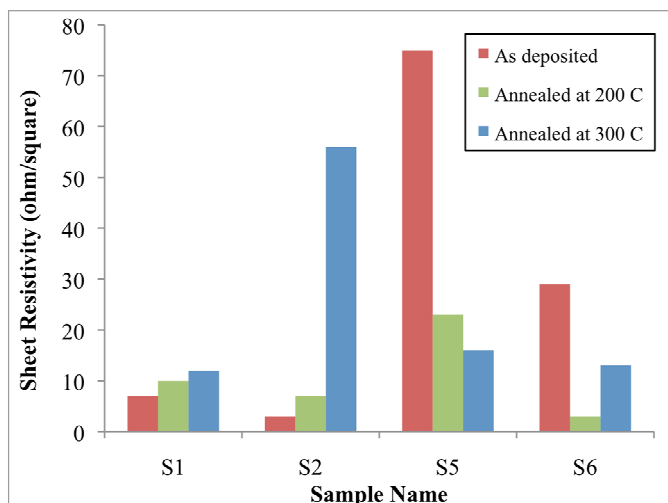


Fig. 4. Sheet resistivity of the Mo thin films before and after heat treatment

As can be seen in Fig. 5 after heat treatment S2 samples were cracked, which explains the increase in sheet resistivity. On the other hand S1, S5 and S6 samples were still homogenous after heat treatment. As indicated from electrical conductivity and SEM images, Mo deposition on Uplex S for 15 minutes and on

soda lime glass for 30 minutes is proper for back contact layer for high temperature photovoltaic applications.

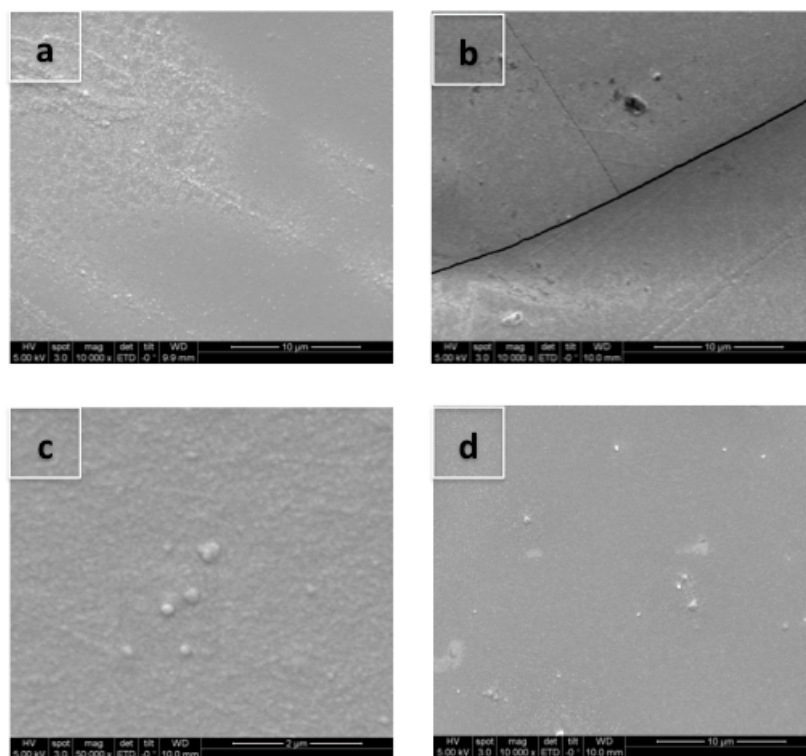


Fig. 5. SEM images of Mo thin films deposited on after heat treatment (a) S1, (b) S2, (c) S5 and (d) S6

It has been known that physical properties of the thin films, such as adhesion and electrical conductivity can be improved by making surface treatment prior to metallization [5–7]. Both chemical and plasma treatments can be used to tailor surface properties. Generally, surface treatment either increases the roughness or makes the surface chemically available for binding. Our initial study on chemical treatment of Upilex S and Kapton HN indicated that surface of the polyimide films can be modified using potassium hydroxide solution. It has been previously reported that the potassium hydroxide treatment opens the imide rings on the surface and results the formation of polyamide [5]. Fig. 6 shows the optical microscope pictures of Upilex S and Kapton HN films before and after potassium hydroxide treatment. As can be seen in this figure, surface of the Upilex S film did not change significantly with chemical treatment. On the other hand, surface of the Kapton HN became rough.

Surface modification of the Kapton HN and Upilex S films can also be investigated by measuring the total reflectance. As can be seen in Fig. 7, total reflectance of the Mo thin films deposited on chemically treated samples were lower than the total reflectance of untreated samples. This may indicate increase in the surface roughness with chemical treatment. Here, the effect of heat treatment on chemically treated Upilex S and Kapton HN was also investigated. It was observed that after annealing process Mo thin films deposited on chemically treated samples were severely damaged. They lost their adhesion and electrical conductivity. There are two most probable reasons for this performance decay. First, there might be potassium residual on the surface lowering the adhesion of Mo thin films. Second, polyamide surface did not adhere very well to the Mo layer. Although, chemical treatment enhanced the electrical resistivity prior to the annealing process, after heat treatment all samples lost their electrical conductivity. Therefore, we investigated the effect of plasma treatment. For this purpose, nitrogen and argon gasses have been used as plasma atmosphere. Table 3 summarizes the plasma conditions of the samples. Sheet resistivities of the Mo thin films have been measured before and after heat treatment (Fig. 8). Unlike the chemical treatment, adhesion of the Mo thin film on plasma treated samples was very good. Additionally, no crack formation has been observed.

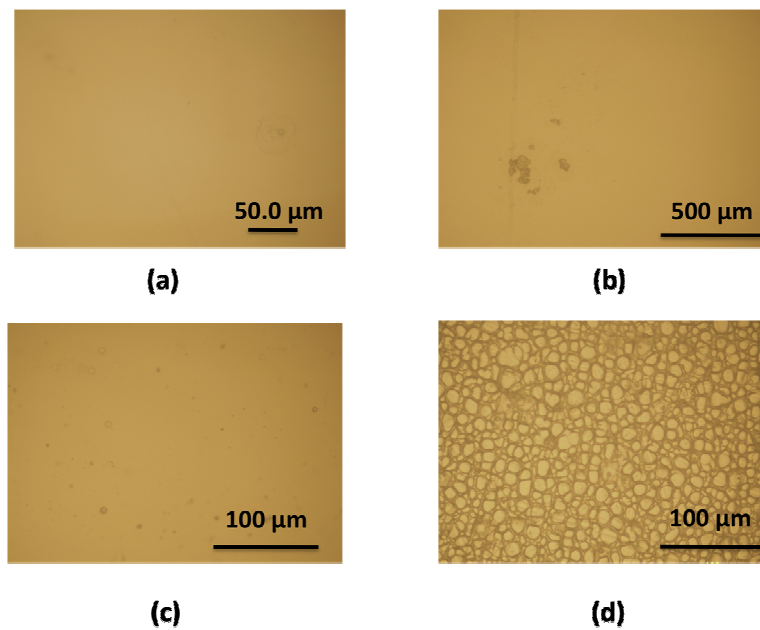


Fig. 6. Optical microscope pictures of the (a) untreated Upilex S, (b) potassium hydroxide treated Upilex S, (c) untreated Kapton HN and (d) potassium hydroxide treated Kapton HN

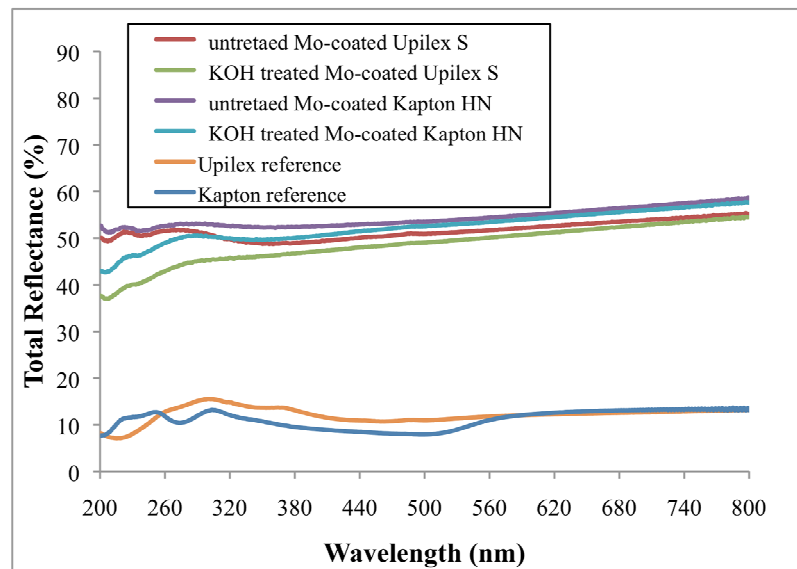


Fig. 7. Total reflectance versus wavelength plots of Kapton HN, Upilex S reference samples and also Mo thin films deposited on both chemically treated and untreated polyimide substrates

Except the samples treated under Argon atmosphere at 100 W for 30 minutes, sheet resistivities increased slightly after plasma treatment. Treatments performed under nitrogen atmosphere at 100 W for 30 minutes resulted the best electrical conductivity after annealing. Similarly, samples treated under argon atmosphere at 100 W for 15 minutes had the lowest sheet resistivity. It is possible to conclude that plasma treatment improves the quality of Mo thin films on the Upilex S substrates resulting the better electrical conductivity even at high temperatures. Detailed studies on mechanical and structural effects on plasma treatment on Mo thin films are among the purposes of our ongoing work. We are also aiming to determine the effect of Mo thin film layer on photovoltaic devices performances as a future work.

Table 3. Sample information of plasma treated Upilex S

Sample Name	Plasma Atmosphere	Power, W	Time, min
S7	Nitrogen	100	30
S8		200	15
S9		100	15
S10	Argon	100	15
S11		100	30
S12		200	15
S13		100	30

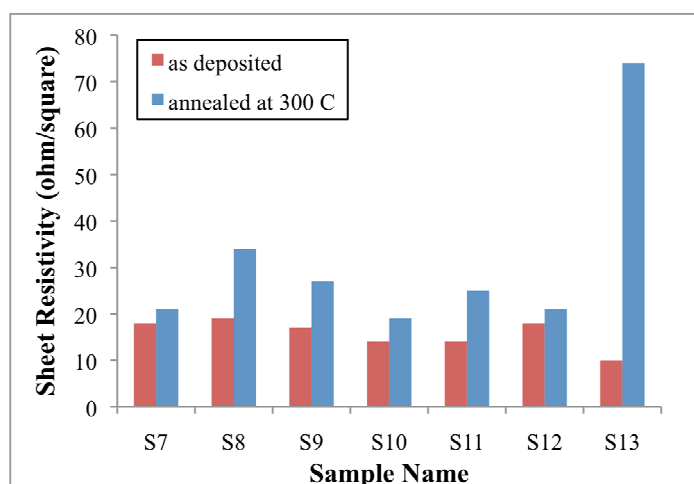


Fig. 8. Sheet resistivity of the Mo thin films deposited on plasma treated Upilex S

CONCLUSIONS

Molybdenum thin films successfully have been deposited on soda lime glass, Kapton HN and Upilex S substrates via RF magnetron sputtering technique. As deposited Mo thin films adhered very well and have high electrical conductivities. SEM images indicated that there has been no significant effect of substrate on morphology of Mo thin films. XRD analysis revealed that all our samples had typical crystal peaks of Mo. Intensity of the Mo thin films deposited on glass was higher than that of Mo thin films on polyimide. This was clue for better crystallinity of Mo thin films on glass. After 250 and 300 °C heat treatment, Mo thin films deposited on Kapton HN were peeled off. Some crack formation was also observed for the glass substrates. 15 minute Mo coated Upilex S films retained their mechanical stability and electrical

conductivity, which was about 10 ohm/square. In order to improve the film properties of both 260 and 460 nm thick Mo films, surface treatments have been performed. Although, the electrical conductivity of potassium hydroxide treated samples improved, their film forming properties failed after heat treatment. On the other hand, plasma treatment prevent the crack formation for 30 minute Mo coating on Upilex S and made it possible to retain electrical conductivity of the Mo thin films after heat treatment. Therefore, we are proposing an optimized process condition for the deposition of Mo thin films on various substrates for high temperature photovoltaic applications.

References

1. Neelkanth G. D. Present status and future prospects of CIGSS thin film solar cells // *Solar Energy Materials & Solar Cells*. 2006. Vol. 90. Pp. 2181–2190.
2. Romeo A., Terheggen M., Abou-Ras D., Batzner D. L., Haug F.-J., Kalin M., Rudmann D., Tiwari A. N. // Development of Thin-film Cu(In,Ga)Se₂ and CdTe Solar Cells // *Progress in Photovoltaics: Research And Applications*. 2004. Vol. 12. Pp. 93–111.
3. Jubault M., Ribeaucourt L., Chassaing E., Renou G., Lincot D., Donsanti F. Optimization of molybdenum thin films for electrodeposited CIGS solar cells // *Solar Energy Materials & Solar Cells*. 2011. Vol. 95. Pp. S26–S31.
4. Assmann L., Bernede J. C., Drici A., Amory C., Halgand E., Morsli M. Study of the Mo thin films and Mo/CIGS interface properties // *Applied Surface Science*. 2005. Vol. 246. Pp.159–166.
5. Yu W., Ko T-M. Surface characterizations of potassium-hydroxide-modified Upilex-S polyimide at an elevated temperature // *European Polymer J*. 2001. Vol. 37. Pp. 1791–1799.
6. Kim C., Jeong D., Hwang J., Chae H. Argon and nitrogen plasma surface treatments of polyimide films for electroless copper plating // *J. of the Korean Phys. Soc.* 2009. Vol. 54. Pp. 621–627.
7. Lin Y-S., Liu H-M., Chen H-T. Surface modification of polyimide films by argon plasma for copper metallization on microelectronic flex substrates // *J. of Appl. Polymer Science*. 2006. Vol. 99, Pp. 744–755.

PREDICTION OF PHYSICAL AND CHEMICAL PARAMETERS OF FLUOROPROPYLENE AS POTENTIAL REFRIGERANTS FOR HEAT PUMPS

Peter A. Shomov

Limited Liability Company Scientific and Technical Center "Industrial Power Engineering"
Semenovskogo alleyway, 10, Office 503, Ivanovo, 153000, Russian Federation
+7-4932-301488; Shomov@list.ru

Agadzhan M. Gyulmaliev

Laboratory of Catalytic Synthesis and Petrochemical Processes name A.N. Bashkirov
A.V.Topchiev Institute of Petrochemical Synthesis of Russian Academy of Sciences (TIPS RAS)
Leninsky prospect 29, Moscow, 119991, Russian Federation
+7 495 955-42-64 9; Gyulmaliev@ips.ac.ru

Ildar A. Sultanguzin, Andrey V. Albul, Alina A. Potapova,

Industrial Thermal Engineering Systems Department
Moscow Power Engineering Institute (Technical University)
Krasnokazarmennaya street, 14, Moscow, 111250, Russian Federation
+7-495-362-7217; SultanguzinIA@mpei.ru

Abstract

The report purpose is calculation of thermodynamic functions of fluorinated propylene's by the methods of quantum chemistry. It is necessary for determination of equilibrium structure of synthesis reaction, and calculation of spectral characteristics for their identification.

KEYWORDS

Fluorinated propylene, refrigerant, thermodynamic functions, quantum chemistry, statistical thermodynamic, infra-red spectrum (IRS), nuclear-magnetic resonance (NMR), NMR spectrum ^1H , ^{13}C , ^{19}F .

INTRODUCTION

Fluorinated propylene's represent the potential refrigerants of new generation. According to the literary data fluorinated propylene's are almost same effective refrigerants in comparison with applied now in the industry on the one hand, and with another – they, practically don't create greenhouse effect and in atmosphere decay on environmentally safe components. Thereupon, for their estimation refrigerative properties and working out of optimum methods of synthesis, it is necessary to establish temperature dependence of their thermodynamic functions which in literature are absent generally.

THERMODYNAMIC CHARACTERISTICS OF FLUORINATED PROPYLENE'S

The results of calculations of thermodynamic functions by the non-empirical quantum-chemical Hartree-Fock (HF) method in the basis of STO 3-21G [1] for fluorinated propylene's are displayed in this paper (enthalpy H , entropy S , Gibbs energy G , heat capacities C_V and C_P , null-oscillation energy H_0). The results are shown on the Table 1.

Table 1. The values of thermodynamic functions of fluorinated propylene's

Molecule	C_v , cal/(mole·K)	C_p , cal/(mole·K)	H_0 , kcal/mole	H , kcal/mole	S , cal/(mole·K)	G , kcal/mole
CF ₃ CF=CH ₂	21.95	23.94	4.71	37.33	82.99	12.59
CF ₃ CH=CH ₂	19.11	21.10	4.10	40.86	75.84	18.24
CF ₂ HCH=CH ₂	16.43	18.42	3.76	45.79	71.96	24.33
CFH ₂ CH=CH ₂	14.13	16.12	3.34	50.20	67.38	30.11
CH ₃ CH=CH ₂	12.66	14.65	3.14	54.32	63.29	35.45
s-CF ₃ CH=CFH	21.13	23.11	4.58	36.68	83.45	11.80
t-CF ₃ CH=CFH	21.50	23.49	4.58	36.49	80.96	12.36

The temperature dependences of thermodynamic functions are calculated on the basis of using methods of statistical thermodynamics. Temperature dependences of thermodynamic functions are defined on the basis of calculation results of quantum chemistry methods. The algorithm of calculation is resulted more low.

$$Q = Q_{tr} \cdot Q_{rot} \cdot Q_{v/b}, \quad (1)$$

where Q_{tr} – the sum of transmitting movement condition, Q_{rot} – the sum of rotary motion condition, $Q_{v/b}$ – the sum of oscillating (vibrating) motion conditions.

After a number of transformations it is possible to write following dependences (2)–(4):

$$Q_{tr} = A \cdot T^{3/2} \quad (2)$$

$$Q_{rot} = B \cdot T^{3/2} \quad (3)$$

$$Q_{v/b} = \prod_{i=1}^{3N-3-n} \left(\frac{1}{1 - e^{-\frac{h\nu_i}{kT}}} \right) \quad (4)$$

Having defined values of constants A and B we will receive dependences (5)–(7):

$$Q_{tr} = \frac{Q_{tr}^{298.15}}{5148.1622} \cdot T^{3/2}, \quad (5)$$

$$Q_{rot} = \frac{Q_{rot}^{298.15}}{5148.1622} \cdot T^{2/3}, \quad (6)$$

$$Q_{v/b} = \prod_{i=1}^{N_{v/b}} \left(\frac{1}{1 - e^{-T_{v/b,i}/T}} \right), \quad (7)$$

$$T_{v/b,i} = \frac{h\nu_i}{k}.$$

The values Q_{tr} , Q_{rot} , $T_{v/b}$ are calculated by methods of quantum chemistry.

Results of calculation temperature dependence of thermodynamic functions of a molecule 3,3,3,2-tetrafluoropropyne (CF₃CF=CH₂) are presented in Table 2.

Table 2. Temperature dependences of thermodynamic functions of molecule
3,3,3,2-tetrafluoropropyne calculated by formula's (1–7)

T , K	U , kcal/mol	S , kcal/(mol·K)	H , kcal/mol	G , kcal/mol	C_p , kcal/(mol·K)
300	36.780	83.156	37.376	12.429	24.037
310	37.003	83.952	37.619	11.593	24.517
320	37.230	84.738	37.866	10.750	24.989
330	37.463	85.514	38.118	9.899	25.452
340	37.699	86.281	38.375	9.040	25.906
350	37.941	87.038	38.637	8.173	26.351
360	38.187	87.787	38.902	7.299	26.786
370	38.437	88.526	39.172	6.417	27.213
380	38.691	89.258	39.446	5.528	27.631
390	38.950	89.981	39.725	4.632	28.040
400	39.212	90.696	40.007	3.729	28.440
410	39.479	91.403	40.294	2.818	28.832
420	39.749	92.102	40.584	1.901	29.214
430	40.023	92.794	40.878	0.976	29.588
440	40.301	93.478	41.176	0.045	29.953
450	40.582	94.156	41.477	-0.893	30.310
460	40.867	94.826	41.782	-1.838	30.658
470	41.156	95.488	42.090	-2.790	30.999
480	41.448	96.145	42.402	-3.748	31.331
490	41.743	96.794	42.717	-4.713	31.655
500	42.041	97.437	43.035	-5.684	31.971
510	42.342	98.073	43.356	-6.661	32.281
520	42.647	98.703	43.680	-7.645	32.582
530	42.954	99.326	44.008	-8.635	32.877
540	43.264	99.943	44.338	-9.632	33.163
550	43.578	100.554	44.671	-10.634	33.444
560	43.894	101.160	45.007	-11.643	33.717
570	44.212	101.759	45.345	-12.658	33.983
580	44.534	102.352	45.686	-13.678	34.243
590	44.857	102.940	46.030	-14.705	34.498
600	45.184	103.521	46.376	-15.737	34.746
610	45.513	104.098	46.725	-16.775	34.988
620	45.844	104.669	47.076	-17.819	35.224
630	46.177	105.234	47.429	-18.868	35.455

T , K	U , kcal/mol	S , kcal/(mol·K)	H , kcal/mol	G , kcal/mol	C_p , kcal/(mol·K)
640	46.513	105.794	47.785	-19.923	35.679
650	46.851	106.349	48.143	-20.984	35.899
660	47.191	106.899	48.503	-22.050	36.114
670	47.534	107.443	48.865	-23.122	36.324
680	47.878	107.983	49.229	-24.199	36.529
690	48.224	108.518	49.596	-25.282	36.729
700	48.573	109.048	49.964	-26.370	36.925

The temperature dependences of thermodynamic functions are calculated on the basis of using methods of statistical thermodynamics. For $\text{CF}_3\text{CF}=\text{CH}_2$ compound the comparison of calculated values of specific heat capacity with experimental data [4] (see Fig. 1) shows that the error is no more than 0.9%.

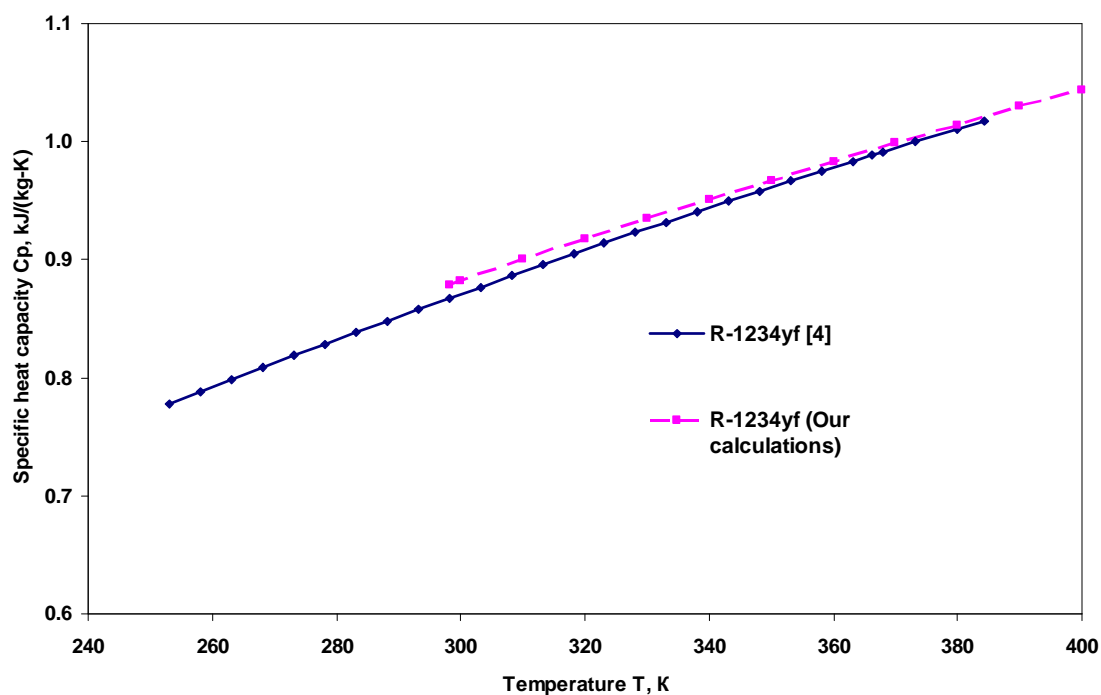


Fig. 1. Comparison of calculated values of specific heat capacity depending on temperature of R-1234yf with experimental data [4]

Lower in Table 3 the calculated values of heat of formation of refrigerants are resulted by methods of quantum chemistry: PM3, AM1 and MNDO. As appears from the table, with experiment will better be coordinated given received by method MNDO. It is necessary to note, what even essential discrepancies in values ΔH_{298} influences results of calculation of equilibrium structure of reaction a little. On it, ΔH_{298} is possible to consider settlement values are quite comprehensible.

Table 3. Heat of formation of refrigerants

Molecules	ΔH_{298} , kcal/mol			
	Experiment [3]	PM3	AM1	MNDO
$\text{CF}_3\text{-CF=CF}_2$	-266.2	-275.5	-277.6	-273
$\text{CF}_3\text{-CH=CF}_2$	–	-273.2	-240	-233
$\text{CF}_3\text{-CH=CFH}$	–	-188.2	-192.9	-186.1
$\text{CF}_3\text{-CH=CH}_2$	–	-143.8	-144	-138.1
$\text{CF}_2\text{H-CH=CH}_2$	–	-84.6	-91.2	-87.7
$\text{CFH}_2\text{-CH=CH}_2$	–	-32.2	-41.1	-39.6
$\text{CH}_3\text{-CH=CH}_2$	4.88	6.3	6.5	5.08

SPECTRUM CHARACTERISTICS OF 3,3,3,2-TETRAFLUOROPROPYLENE

Spectral characteristics of a molecule 3,3,3,2 tetrafluoropropylene (Fig. 2) paid off on not empirical method HF in basis 6-311G. Results of calculation are presented on Figs. 3–6.

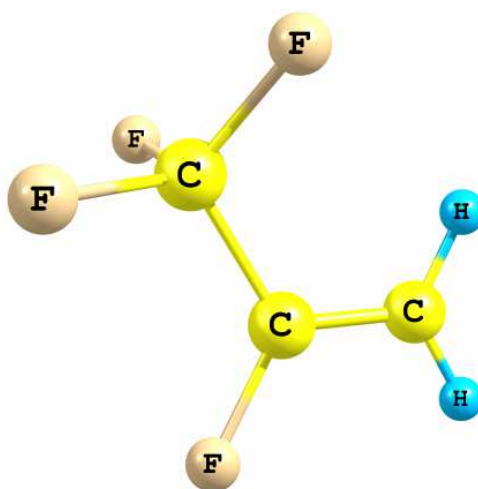


Fig. 2. Structure of molecule 3,3,3,2-tetrafluoropropylene

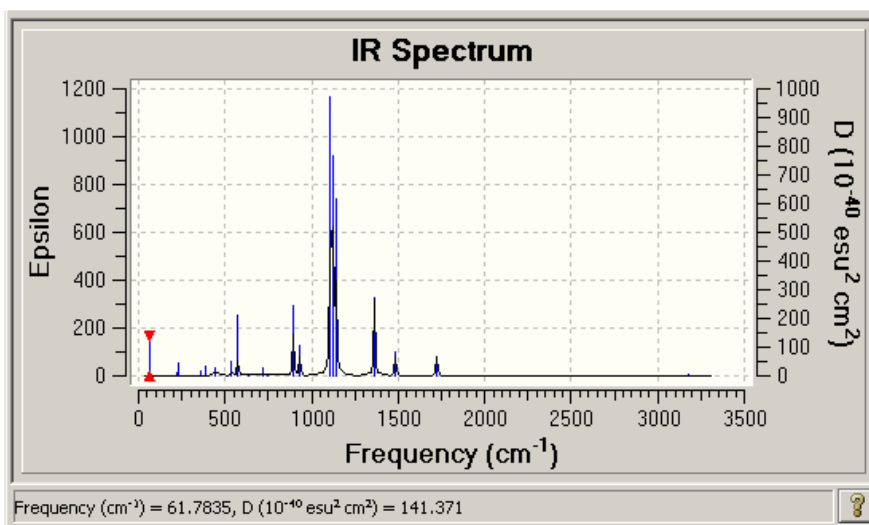


Fig. 3. Infra-red spectrum of 3,3,3,2-tetrafluoropropylene

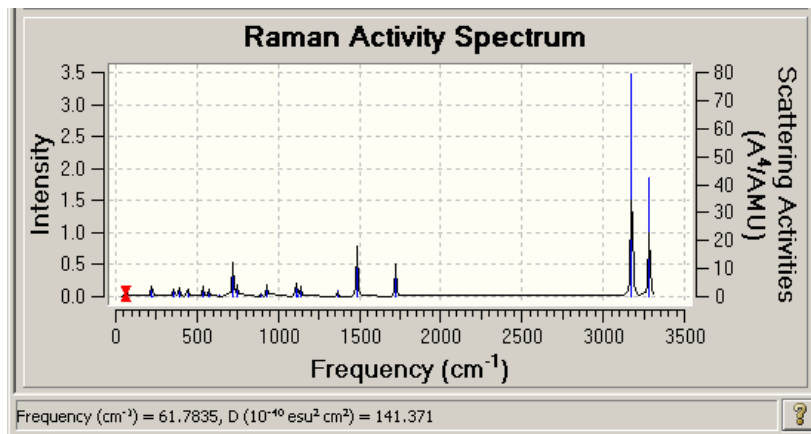


Fig. 4. Roman active spectrum of 3,3,3,2-tetrafluoropropylene

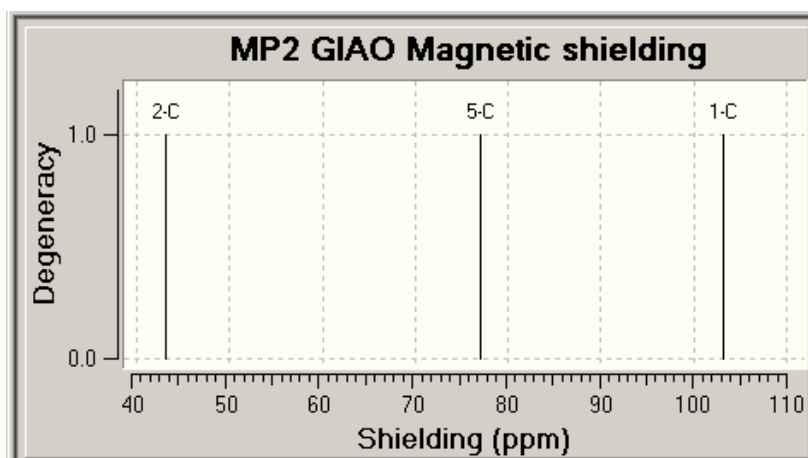


Fig. 5. NMR spectrum ¹³C of 3,3,3,2-tetrafluoropropylene

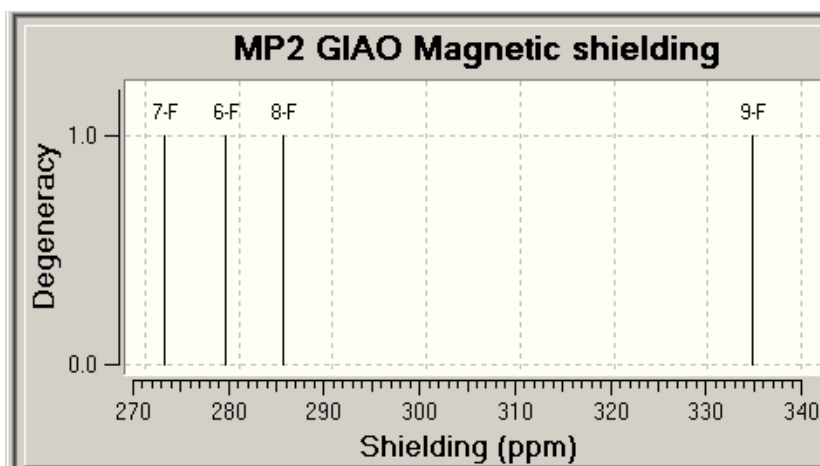


Fig. 6. NMR spectrum ¹⁹F of 3,3,3,2-tetrafluoropropylene

Let's notice that the received spectra are necessary for identification of separate refrigerants. For example, on Fig. 7 the experimental infra-red spectrum is presented for 3,3,3,2-tetrafluoropropylene [5]. Its comparison with settlement IRS (Fig. 3) shows that these spectra are almost identical in infra-red area of greenhouse radiation with the maximum peak at frequency of 1200 cm⁻¹.

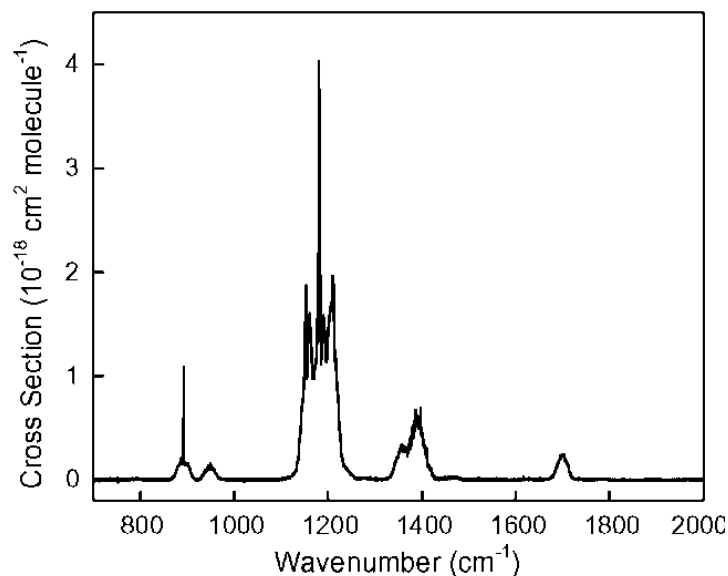


Fig. 7. Experimental IRS of 3,3,3,2- tetrafluoropropylene [5]

In [5] it has been defined that term of life of 3,3,3,2-tetrafluoropropylene in atmosphere makes 11 days, and the global warming potential is equal $GWP = 4$ that is essential less than 150, borders defining refrigerants with the minimum influence on global warming [6].

The similar analysis for others fluorinated propylene's with calculation of thermodynamic functions by methods of quantum chemistry and with calculation of spectral characteristics shows that they also concern group of substances with the minimum influence on global warming. The next years they can find of themselves application as new refrigerants in heat pumps, automobile and stationary air-conditioners, refrigeration machines, and also as fire fighting means and building foam.

The obtained results could be used for calculations of steady-state concentrations of fluorinated propylene's with chemical thermodynamics methods during their synthesis process in dependency from temperature and pressure. It is very important for selective leading of the process and also for evaluating their different refrigerant properties.

It should be noticed that the quantum chemical methods allow to calculate NMR ^{13}C , ^1H and ^{19}F specters of refrigerants, which are required during their identification.

References

1. Tsirelson V.G. *Quantum Chemistry of Molecule, Molecular Systems and Solid Bodies*, BINOM, Moscow, 2010. 496 p. (in Russian).
2. Levich V.G. *Introduction in Statistical Physics*, State Publishing Company of Technical and Theoretical Literature, Moscow, 1954. 528 p. (in Russian).
3. Stall D., Vestram E., Zinke G. *Chemical Thermodynamics of Organic Compounds*, Mir, Moscow. 1971. 807 p.
4. Leck T.J. Evaluation of HFO-1234yf as a potential replacement for R-134a in refrigeration applications // *Proc. 3rd IIR Conference on Thermophysical Properties and Transfer Processes of Refrigerants*, Boulder, CO, 2009. Paper 155.
5. Nielsen, O.J., Javadi M.S., Sulbaek Andersen M.P. et al. Atmospheric chemistry of $\text{CF}_3\text{CF}=\text{CH}_2$: Kinetics and mechanisms of gas-phase reactions with Cl atoms, OH radicals, and O_3 // *Chemical Physical Letters*. 2007. Vol. 439. Pp. 18–22.
6. Directive 2006/40/EC of The European Parliament and of the Council of 17 May 2006 relating to emissions from air-conditioning systems in motor vehicles and amending Council Directive 70/156/EC, 2006 // *Official Journal of the European Union*. <http://tinyurl.com/lxw8nm>.

THE GRAIN LAYER DRYING APPROXIMATED MODEL

H. F. Smirnov, E. V. Voskresenskaya

Department of Food Processes and Apparatuses
Odessa National Academy of Food Technologies
112 Kanatnaya Str., 65044, Odessa, Ukraine

Tel.: +38-048 712-41-29 (off.), +38048 2-40-23-44, +38048 267-14-70 (home), +38-050-333-63-71 (mob)
E-mail: g.smirnov@e-mail.ua ; genrikh@blacksea.net.ua ; icpa2006@mail.ru

Abstract

An approximated model of the grain layer drying for a thermomechanical rotating apparatus is presented. The main assumptions are the division of the entire process into specific transfer processes and the key role of transient heat conduction, especially for the initial stage of drying process. The results presented are related to this initial stage.

KEYWORDS

Drying model; two-phase thermosiphon; grain layer; thermal conductivity, transient process.

INTRODUCTION

Simulations of such a complex physical process as the grain layer drying are based, as a rule, on the well-known approach developed by A. V. Luikov and his colleagues. Despite the considerable achievements in this field, a comprehensive understanding of the different complex connections between separate stages of the process is lacking.

The authors consider the process as highly unsteady with significant changes occurring throughout the process stages. It is necessary to account for variations both in the process parameters and in the process physical nature. Thus, the bases of the approach suggested are as follows:

1. Transient heat conduction from the rotating heating of a thermosiphon wall is the initial key stage of the entire process.

2. The ratio between the heated and quasi-isothermal layers changes substantially. This ratio should be taken into account in solving the for transient heat conduction equation.

3. As the first approximation, the real complex geometry of the grain layer can be replaced by a uniform plane layer having some equivalent properties such as the specific heat capacity, thermal conductivity, equivalent thickness, etc. [1].

4. The time interval needed for heating the first half of the raw grain determines the initial moment of the developed heating. Thus, the drying process is established after this initial moment.

5. In this moment, the external surface of the initial part of the grain layer is in equilibrium and a real evaporation process is initiated.

6. At this stage, water evaporates occurs only from the external surface of the grain layer into the volume of internal pores. The "driving force" process represents a difference between the partial water pressure on the external grain surface of the overheated part of the layer and the partial pressure of steam inside the internal volume of the pores.

7. The concentration (partial pressure scale) of moisture and air within this part of the pore volume is determined by taking into account the following considerations: on one side "air is removed" with the evaporating moisture. The average rate of air removal is determined in terms of vapor and air filtration from the pore volume. This filtration is carried out under the influence of a pressure gradient proportional to the "driving pressure". On the other hand, there is air diffusion from the environment to the pore volume. The balance of these "influences" determines the dynamics of corresponding partial pressure change inside the pore volume for the active (significantly overheated) part of the layer.

MODEL STATEMENT

These assumptions can be used based on the solution of the following equations:

$$W_1 \cdot \left(1 - \frac{P_A}{P_{00}}\right) \cdot \overline{\rho_A} = -D_{PA} \cdot \frac{d[P_{00} \cdot (1 - P_A / P_{00})]}{dZ}, \quad (1)$$

where

$$W_1 = \frac{\Delta P_{10}}{\Delta L} \cdot \frac{K_f}{\mu_{VG}}; \Delta P_{10} \equiv \Delta P_{VH} \quad (2)$$

As mentioned above, it is necessary to determine the initial moment, when the evaporation process from the external surface of the internal pore volume begins.

It was also assumed that, first of all, evaporation saturated with vapor the internal volume of the pores. When the heating zone of the grain layer approaches the initial temperature $T_1 = T_{10}$, the vapor density inside the pore volume equals the reversible value ρ'' ($T_{10} = T_{S0}$). It means that the following amount of the vapor mass should be evaporated:

$$\Delta M_{10} = V_{10} \cdot \varepsilon \cdot K(\tau) \cdot [\rho''(T_{S0}) - \rho''(T_{EM0})]. \quad (3)$$

Here V_{10} is the entire volume of the grain layer; ε is the layer porosity; $K(\tau)$ is a part of the grain layer overheated at the present time; $\rho''(T_{S0})$ is a vapor density at the given initial moment; $\rho''(T_{EM0})$ is the vapor density at the surrounding temperature.

The calculation of above-mentioned equivalent thermophysical properties (heat capacity, thermal conductivity, density, etc.) can be carried out using the data from [2].

The following dimensionless equation suggested in [3] can be applied to heat and mass transfer processes inside the pore volume:

$$Nu = const \cdot Re^m \cdot Pr^n \quad (4)$$

Accounting for the actual ranges of variation of the following numbers;

$$Re_E = 4w/S_V v_1, \quad (5)$$

$$Nu_E = 4\alpha_V \varepsilon / \lambda_1 S_V, \quad (6)$$

$$Pr = v_1 / a_1, \quad (7)$$

$$Pr_D = Sc = v_1 / D_1 \quad (8)$$

yields:

$$\text{at } 0.01 \leq Re_E \leq 2 \quad Nu_E = 0.515 Re_E^{0.85} Sc^{1/3}, \quad (9)$$

$$\text{at } 2 \leq Re_E \leq 30 \quad Nu_E = 0.725 Re_E^{0.47} Pr^{1/3}, \quad (10)$$

$$\text{at } 30 \leq Re_E \leq 3 \cdot 10^4 \quad Nu_E = 0.4 \cdot Re_E^{0.64} Sc^{1/3}. \quad (11)$$

Here $w, S_V, v_1, a_1, D_1, \lambda_1, \alpha_V$ and Sc are the average filtration velocity, specific volumetric surface of the porous media, kinematic viscosity, thermal diffusivity, diffusion coefficient, thermal conductivity, specific volumetric heat transfer coefficient, and Schmidt number, respectively.

After calculation of the heat transfer coefficient $\overline{\alpha_{out}}$, one can determine the following dimensionless parameter:

$$Y_{11} = \frac{(\overline{\alpha_{out}}) \cdot \sqrt{a_E \cdot \tau}}{\lambda_E}. \quad (12)$$

Thereafter, an important calculation step is connected with correct determination of the average partial vapor pressure in the internal pore volume. We suggest the following assumptions:

1. The approximate reversible partial vapor pressure inside the internal pore volume can be determined as follows:

on the one hand, the air state inside the pores is connected with the air being removed from the volume under the action of some pressure gradient, on the other, there is the diffusion process determined by the action of the partial pressure gradient. The balance between these two processes provides an approximate reversible vapor partial pressure inside the pore volume for each given moment.

2. These considerations yield the following key equations:

$$\rho_A \cdot \left(1 - \frac{P_{VH}}{P_0}\right) \cdot W_0 = -D_p \cdot \frac{d[P_0(1 - P_{VH}/P_0)]}{dZ}, \quad (13)$$

$$W_0 = \frac{\Delta P_{10}}{\Delta L} \cdot \frac{K_f}{\mu_{VG}}; \Delta P_{10} \cong \Delta P_{VH}. \quad (14)$$

Combining Eqs (13) and (14), we obtain

$$\rho_A \cdot \left(\frac{P_0 - P_{VH}}{P_0}\right) \cdot \frac{\Delta P_{10}}{\Delta L} \cdot \frac{K_f}{\mu_{VG}} = -D_p \cdot \frac{d[P_0 - P_{VH}]}{dZ}. \quad (15)$$

Here ρ_A , P_{VH} , P_0 , W_0 , D_p , K_f , μ_{VG} and $\frac{\Delta P_{10}}{\Delta L}$ are the average air-vapor mixture density, vapor partial pressure inside the pore volume, entire pressure inside the pores, the air-vapor mixture filtration velocity through the porous volume, the diffusion coefficient for partial pressures, the permeability coefficient for filtration through the grain layer volume, the vapor-air mixture dynamic viscosity, the pressure gradient being formed in vaporization inside the pores, i.e., the "driving force" of the actual filtration. Solution of the differential equation (15) yields

$$\frac{d[P_0 - P_{VH}]}{P_0 - P_{VH}} = -\frac{K_f}{\mu_{VG}} \cdot \frac{\Delta P_{10}}{\Delta L} \cdot \frac{\rho_A}{P_0 \cdot D_p} \cdot dZ; \ln[P_0 - P_{VH}] = -\frac{K_f}{\mu_{VG}} \cdot \frac{\Delta P_{10}}{\Delta L} \cdot \frac{\rho_A \cdot Z}{P_0 \cdot D_p} + const. \quad (16)$$

The *const* value can be determined on the basis of the boundary condition $Z = 0$, $P_{VH} = P_{EN}$.

Then

$$\ln \frac{P_0 - P_{VH}}{P_0 - P_{EN}} = -\frac{K_f}{\mu_{VG}} \cdot \frac{\Delta P_{10}}{\Delta L} \cdot \frac{\rho_A \cdot Z}{P_0 \cdot D_p}; P_0 - P_{VH} = [P_0 - P_{EN}] \cdot \exp\left\{-\frac{K_f}{\mu_{VG}} \cdot \frac{\Delta P_{10}}{\Delta L} \cdot \frac{\rho_A \cdot Z}{P_0 \cdot D_p}\right\}. \quad (17)$$

The permeability coefficient is calculated by using the Kozeny – Carman equation:

$$K_f = const \cdot \frac{\varepsilon^3 \cdot d_0^2}{(1 - \varepsilon)^2}. \quad (18)$$

Here ε , d_0 and *const* are the grain layer average porosity, the main pore size, and the empirical constant, respectively. Following [2, 3], $\varepsilon = 0.7$, $d_0 = 0.3$ mm, $const = 1/140$, were selected for further calculations. The previously done experimental study of the process employed a rotating thermosiphon as a main heat source. The details of the experimental conditions, methods, and key results are presented in [4, 5].

EXPERIMENTATION AND RESULTS

The sketch of a rotating thermosiphon is shown in Fig. 1.

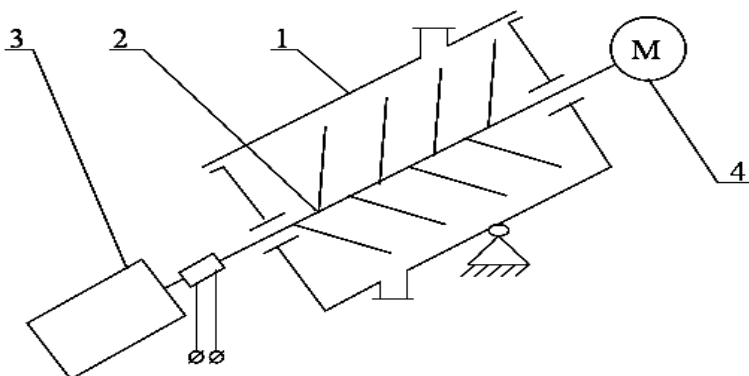


Fig. 1. Experimental setup with a rotating thermosiphon [4, 5]: 1 – container; 2 – rotating thermosiphon; 3 – electric motor. 4 – manometer for measurement of the saturation pressure inside the thermosiphon

The internal volume was filled with a heat carrier (water). The vapor pressure moves the heat carrier to the inclined condenser tubes. Due to the heat exchange between the wall and cold grain layer volume, the heat carrier condenses, while the grain layer volume is heated and dried. The key results of this experiment are presented in Figs. 2 and 3. Also, for the initial time (0...10 minutes) it was possible to compare the experimental results with calculations based on the above-presented theoretical approach.

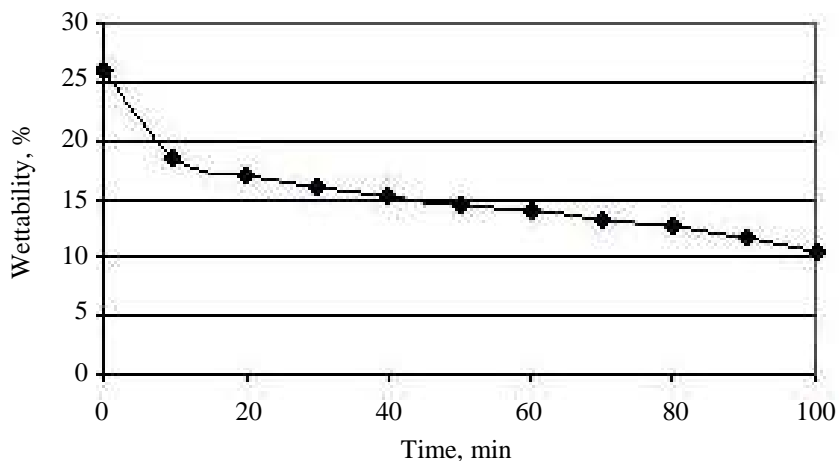


Fig. 2. Typical experimental results

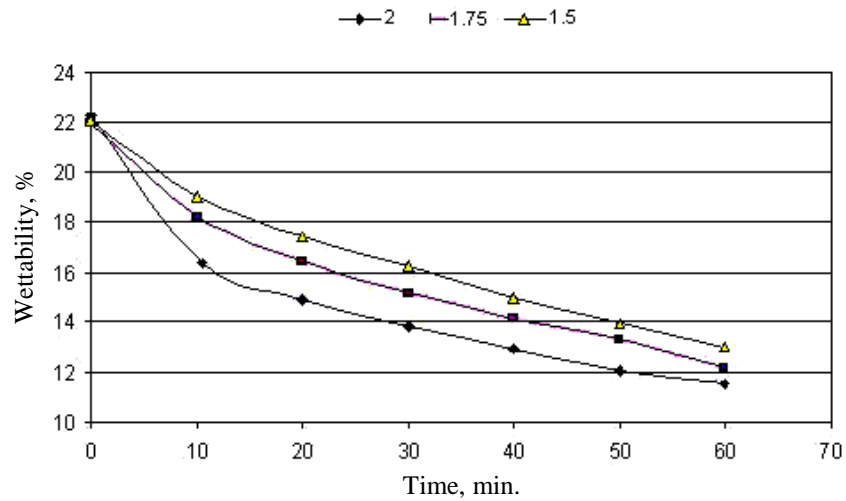


Fig. 3. Typical experimental results on grain layer drying: 2 – the internal water vapor pressure is equal to 2 bar; 1.75 – the internal water vapor pressure is equal to 1.75 bar; 1.5 – the internal water vapor pressure is equal to 1.5 bar

COMPARISON BETWEEN THE MODEL CALCULATIONS AND EXPERIMENTAL RESULTS

The model calculations were based on the following assumptions:

1. The grain layer mixing effect on the porous parameters and key process values can be neglected.
2. The entire surface of the overheated grain layer volume takes part uniformly in vaporization.
3. The empirical dimensionless heat and mass transfer correlations obtained for different conditions can be applied for quantitative estimations of the internal mass transfer.
4. The internal vaporization is not taken into account. This mechanism is significant only for the final time intervals.
5. The pressure gradient is considered constant and independent of other process parameters.

The typical results of comparison are presented in Fig. 4.

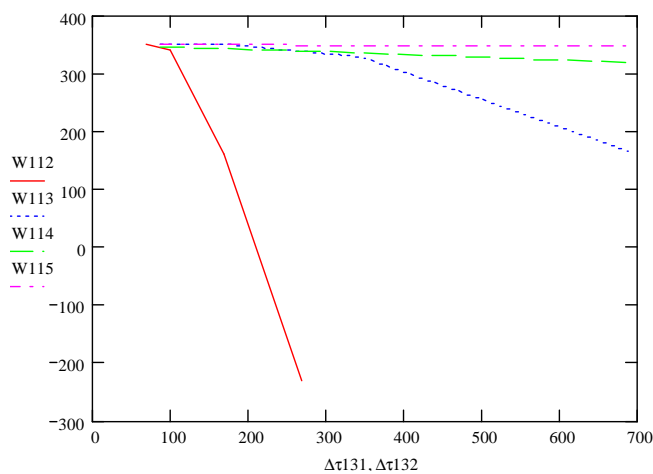


Fig. 4. Changing entire of the grain layer moisture. The vertical axis represents changes in the layer moisture in grams. The horizontal axis is the time interval in seconds. At the pressure gradient equal to 10 Pa per meter: W112 – the maximum estimation of the initial value of the partial pressure at the inner grain layer surface; W113 – the minimum estimation of the initial value of the partial pressure at the inner grain layer surface. At the pressure gradient equal to 20 Pa per meter: W114 – the minimum estimation of the initial value of the partial pressure at the inner grain layer surface. W115 – the experimental results on the initial value of the partial pressure at the inner grain layer surface

CONCLUSIONS

The authors consider that it is necessary to imagine some experimentation statement required for correct process understanding. For instance:

1. Interrelations between the “driving force” of the vapor-air mixture removed from the internal grain layer volume, the pressure gradient from the internal volume to the surroundings and other process parameters;
2. Connections between the structural parameters of the porous volume and such an important thermo–hydrodynamic regime parameters as the rotation frequency, geometric sizes of the rotating thermosiphon, etc.
3. Study of the existence of different moisture forms inside the porous volume and their influence on the process characteristics.
4. The study of moisture distribution both on the other pore surface, and on the internal grain volume, etc.
5. The determination of the effect of the ambient parameters onto the entire process characteristics.
6. Changes of the dynamic equilibrium parameters, etc.

Nevertheless, the present approach can be useful especially for the development of the new methods improving understanding of the physical nature of drying. In the nearest future this approach will be used for further developments.

Reference

1. Kreith F., Bohn M.S. *Principles of Heat Transfer*. 5th ed., West Publishing Company, 1993. 720 p.
2. Stankevich G.M., Strachova T.V., Atanazevich V.I. *The Grain Drying*, Publishing House “Lebed”, 1997. 352 (*in Russian*).
3. Aerov M.I., Todes O.M. The hydrodynamic and thermal fundamentals of Apparatuses with steady and pseudo – liquidize layers performance, Publ. House “Chemistry”, 1968. 457 p.
4. Bezbach I.V., Voskresenskaya E.V., Maracheva S.A. The boiled pea drying inside an apparatus with rotating thermosiphon: ONAFT Science works / Odessa, 2007. Issue 30. Vol. 1. Pp. 226–229 (*in Russian*).
5. Voskresenskaya E.V. The cereal crop drying inside rotating mechanical thermosiphon apparatuses dynamic: ONAFT Science works / Odessa, 2009. Vol. 1 (36). Pp. 79–82 (*in Russian*).
6. Luikov A.V. *The Theory of Drying*, Publishing House “Energy”, Moscow, 1968. 470 p. (*in Russian*).

PLOTTING OF *P-H* AND *T-S* DIAGRAMS OF FLUOROPROPYLENES

Ildar A. Sultanguzin, Andrey V. Albul, Alina A. Potapova

Industrial Thermal Engineering Systems Department
Moscow Power Engineering Institute (Technical University)
Krasnokazarmennaya street, 14, Moscow, 111250, Russian Federation
+7-495-362-7217; SultanguzinIA@mpei.ru

Summary

The report addresses issues of plotting the pressure-enthalpy and temperature-entropy diagrams of fluoropropylenes as potential refrigerants, that do not influence global warming. These diagrams are required for the calculation of thermodynamic cycles in heat pumps. The Peng-Robinson equation of state is used to plot predictive diagrams of state of new refrigerants. It is defined and applied constant heat capacity of the substance to improve the accuracy of the equation of state in the area of saturation during the calculation of enthalpy and entropy.

KEYWORDS

Fluoropropylenes, pressure-enthalpy diagram, temperature-entropy diagram, Peng-Robinson equation of state, heat capacity, refrigerants, heat pumps.

INTRODUCTION

The goal of the present work is plotting the pressure (*P*) – enthalpy (*H*) and temperature (*T*) – entropy (*S*) diagrams of state of fluoropropylenes as potential refrigerants, that do not affect the global warming, that are required to calculate thermodynamic properties of heat pump cycles. It is required to define equation of state in order to build these diagrams for new refrigerants.

CHOOSING THE EQUATION OF STATE

The thermodynamic properties of working agents used in heat pumps are calculated by the unified equation of state [1]. Alongside with multivariable interpolated equations of state with virial coefficients (e.g. the Benedict-Webb-Rubin equation [2]), cubic equations based on van der Waals' model are widely used also. The equations of state written by Lee-Kessler [3], Boyarsky-Podchernyaev [1, 4] etc. require three additional parameters. It improves the accuracy of the equation of state for well-known agents, but for little-studied compounds the accuracy of determining of these parameters is unknown.

When many properties of substances are unknown, one of the most effective calculation methods which uses a wide range of variation of parameters (pressure, temperature) could be the Peng-Robinson equation of state [5]. The advantage of this equation is that it's one of the most accurate in the area close to the critical point and also that it's simple: in order to solve this equation only 2 additional parameters (*a* and *b*):

$$P = \frac{RT}{V-b} - \frac{a(T)}{V(V+b) + (V-b)^2}, \quad (1)$$

where *P* – pressure, *T* – temperature, *V* – molar volume, *R* – gas constant.

At present the properties of tetrafluoropropylenes such as R-1234yf [6, 7] and R-1234ze(E) [8] are well studied. But the properties of other fluoropropylenes such as R-1234zf [9] or R-1234ye(E) [10] are insufficiently explored.

PLOTTING THE PRESSURE-ENTHALPY DIAGRAMS

During the calculation of enthalpy *H* and entropy *S* it is important to know the value of the specific heat capacity of ideal gas *C_p* [2, 11]. For insufficiently known substances the heat capacity could be determined based on the quantum-chemical calculations of electronic structure of the molecule [12].

For already known substances R-1234yf (Fig. 1) and R-1234ze(E) (Fig. 2) the comparison has been made for the saturation line on P - H and T - S diagrams based on published data [6–8] and diagrams based on the Peng-Robinson equation of state.

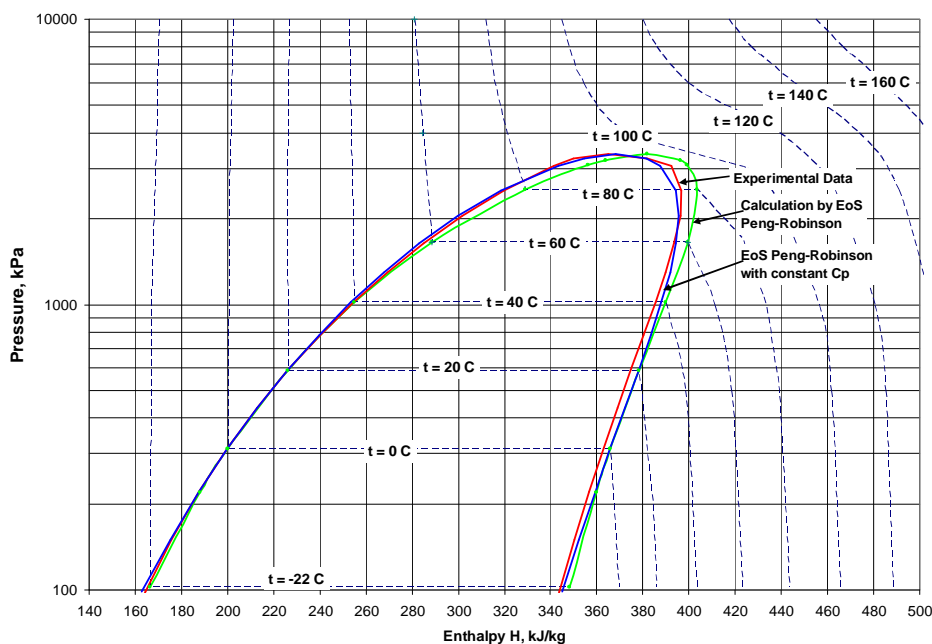


Fig. 1. P - H diagram of refrigerant R-1234yf

It was found that the calculated saturation lines near the critical point were shifted to the right by 13.5 kJ/kg (3.7%) in enthalpy on P - H diagram and by 0.04 kJ/(kg·K) (2.7%) in entropy on T - S diagram.

IMPROVING ACCURACY OF THE STATE DIAGRAMS

It is known that heat capacity, the acentric factor and the critical temperature affect the saturation line shifting [13].

An optimization task has been formulated to minimize least-squares deviation of enthalpy and entropy between the calculated saturation line and the saturation line based on published data. The coefficients of polynomial of heat capacity dependence from temperature, acentric factor and critical temperature have been chosen as optimization parameters.

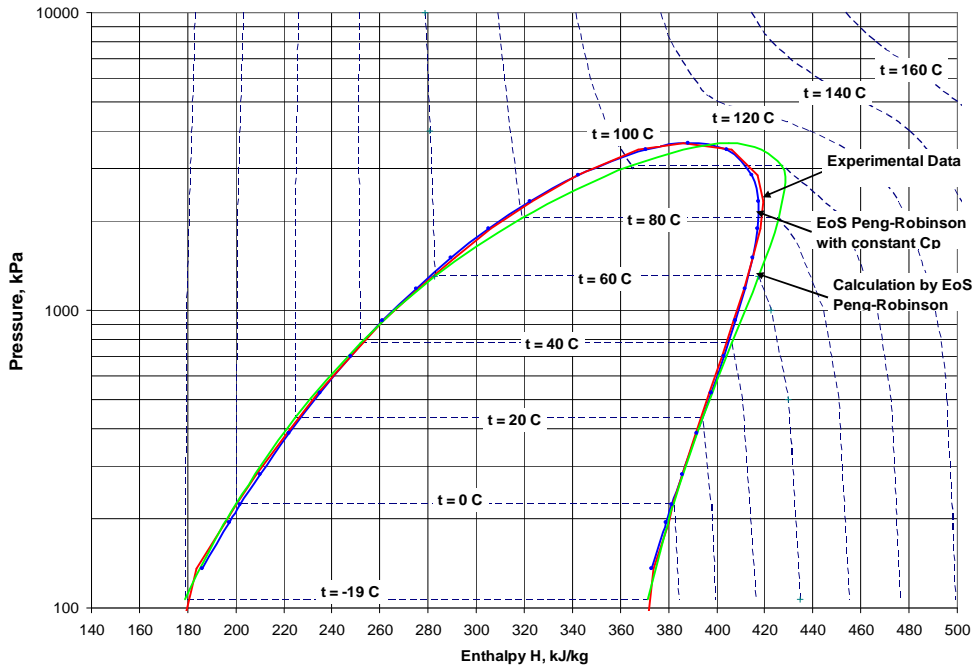


Fig. 2. P - H diagram of refrigerant R-1234ze(E)

The direct search of feasible directions (DSFD) algorithm and software has been used for optimization [14]. The calculations showed that the largest affect on saturation line shifting has been done by heat capacity.

For R-1234yf the dependence of heat capacity from temperature was defined by the following equation (2), kJ/(kg·K) [6]:

$$C_p = 0.2334 + 1.825 \cdot 10^{-3} T + 3.516 \cdot 10^{-6} T^2 - 1.125 \cdot 10^{-8} T^3 + 1.061 \cdot 10^{-11} T^4 - 3.483 \cdot 10^{-15} T^5. \quad (2)$$

Another important result is that the selection of constant heat capacity instead of polynomial dependence does not significantly lower the accuracy of calculations. Only the constant is determined but other coefficients are equal zero. It is found that for R-1234yf the heat capacity is chosen by temperature which is on 8.9% more ($T_{Cp} = 265.5$ K) than the normal boiling point (NBP) $T_b = 243.8$ K [6] (Fig. 3). The accepted value of heat capacity for R-1234yf was equal to 0.803 kJ/(kg·K).

The value of $T_{Cp} = 276$ K for R-1234ze(E) is on 8.7% more than its NBP ($T_b = 253.92$ K [8]). The accepted value of heat capacity for R-1234ze(E) was equal to 0.766 kJ/(kg·K).

In consecutive forecast calculations the heat capacity was determined by saturation temperature on 8.8% more than NBP at 760 mm Hg. The accepted constant value of heat capacity for R-1234zf was equal to 0.859 kJ/(kg·K).

PRESSURE-ENTHALPY AND TEMPERATURE-ENTHALPY DIAGRAMS

These data have been used to plot forecast P - H and T - S diagrams for other fluoropropylenes R-1234zf (Figs. 4 and 5) and R-1234ye(E) as potential refrigerant agents, which do not significantly affect to the global warming. The described above correction for heat capacity could be used to plot the saturation line calculated by Peng-Robinson equation of state which close to the real saturation line.

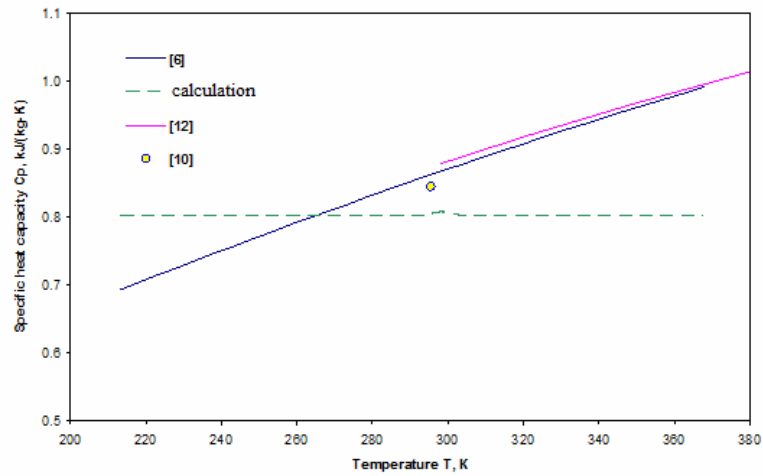


Fig. 3. Heat capacity of refrigerant R-1234yf

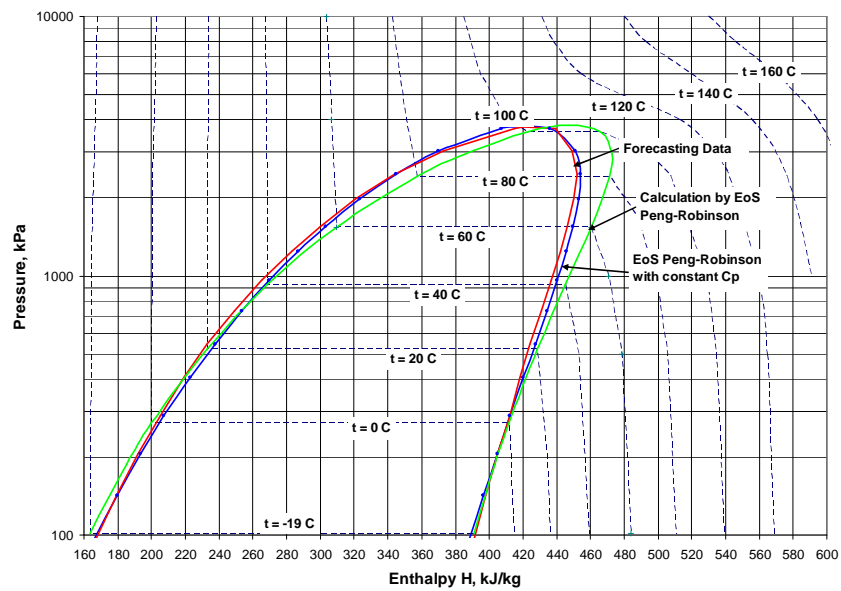


Fig. 4. P - H diagram of refrigerant R-1243zf

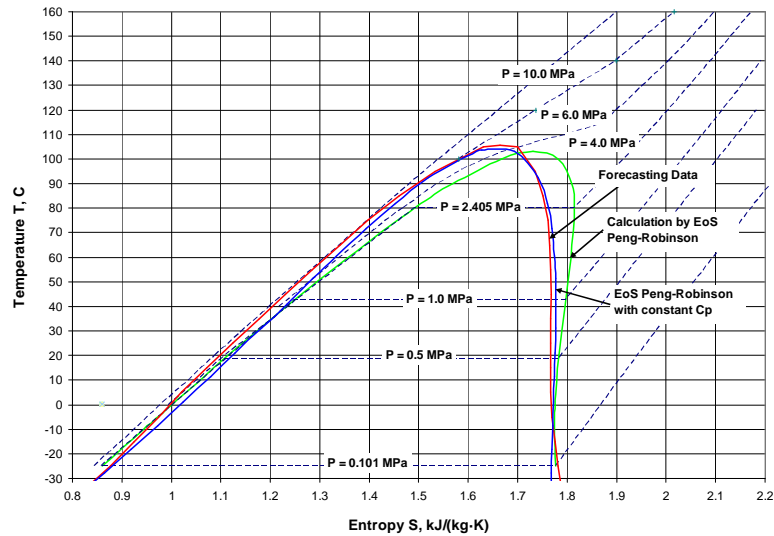


Fig. 5. T - S of refrigerant R-1243zf

CORRECTION ON HEAT CAPACITY FOR SUPERHEATED VAPOR AND LIQUID

However for calculation of heat pumps it is necessary to have calculated dependences, P - H and T - S diagrams of refrigerants not only on a saturation line, but also in the field of superheated vapor and liquid. In this case it is appropriately to use the correction for heat capacity of refrigerant R-1234yf in the form of (3):

$$\Delta C_p = c \cdot (T - T_s), \text{ [kJ/(kgK)]}, \quad (3)$$

where T_s is refrigerant temperature on a saturation line at pressure P_s , T – temperature of a coolant in the field of superheated vapor or a liquid at pressure P_s , the factor $d = 1.807 \cdot 10^{-3}$ is defined on linear regression of a heat capacity of gas as temperature dependence (2) [6] for R-1234yf in the form of (4):

$$C_p = c + d \cdot T = 0.328 + 1.807 \cdot 10^{-3} \cdot T, \text{ [kJ/(kgK)]}, \quad (4)$$

with the determination coefficient close to 1 $R^2 = 0.9992$ for a range of temperatures 273–369 K.

Similarly the coefficients d were found for refrigerants: R-1234ze(E) $d = 2.050 \cdot 10^{-3}$ (under the data [8]) and for R-1243zf $d = 2.054 \cdot 10^{-3}$ (by data on the basis of the approach offered in [12]). Constant values and the corrections on a heat capacity in the field of superheated vapor and liquid allow use forecasting P - H and T - S diagrams of new refrigerants for calculation of high-temperature heat pumps.

References

1. Boyarsky M. Yu., Podchernyayev O. N., Zulkarneyeva Yu. R. Choice of an optimal structure of unitary equations of state // *Holodilnaya Tekhnika (Refrigerating Engineering)*. 1996. No. 8. Pp. 26–27 (in Russian).
2. Walas S. M. *Phase Equilibria in Chemical Engineering*. Boston: Butterworth Publisher. 1985.
3. Kesler M. G., Lee B. I., Sandler S. I. A Third Parameter for Use in Generalized Thermodynamic Correlation // *Ind. Eng. Chem. Fundam.* 1979. Vol. 18, No. 1. Pp. 49–54.
4. Boyarsky M. Yu., Podchernyayev O.N. Calculation of properties of working agents by means of a particular accuracy cubic // *Holodilnaya Tekhnika (Refrigerating Engineering)*. 1991. No. 7. Pp. 13–16 (in Russian).
5. Peng D.-Y., Robinson D.D. A New Two-Constant Equation of State // *Ind. Eng. Chem. Fundam.* 1976. Vol. 15. Pp. 59–64.

6. Leck T. J. Evaluation of HFO-1234yf as a Potential Replacement for R-134a in Refrigeration Applications // *Proc. 3rd IIR Conf. on Thermophys. Properties and Transfer Proc. of Refrigerants, Boulder, CO, 2009*. Paper 155.
7. Akasaka R., Tanaka K., Higashi Y. Thermodynamic property modeling for 2,3,3,3-tetrafluoropropene (HFO-1234yf) // *Int. J. of Refrigeration*. 2010. Vol. 33. Pp. 52–60.
8. Akasaka R. An application of the extended corresponding states model to thermodynamic property calculations for trans-1,3,3,3-tetrafluoropropene (HFO-1234ze(E)) // *Int. J. of Refrigeration*. 2010. Vol. 33. Pp. 907–914.
9. Zernov V. S., Kogan V. B., Lyubetsky S. G., Duntov F. I. An equilibrium liquid – vapour in a system ethylene - trifluoropropylene // *Zhurnal Prikladnoi Himii (J. of Appl. Chem.)*. 1971. No. 3. Pp. 683–686 (*in Russian*).
10. Brown J. S., Zilio C., Cavallini A. Thermodynamic Properties of Eight Fluorinated Olefins // *Int. J. of Refrigeration*. 2010. Vol. 32. Pp. 235–241.
11. Elliot J. R., Lira C. R. Introductory Chem. Eng. Thermodyn. *Prentice Hall, Upper Saddle River, New York*, 1999. – 660 p.
12. Shomov P. A., Gulmaliev A. M, Sultanguzin I. A. et.al. Prediction of physical and chemical parameters of fluoropropylene as potential refrigerants for heat pumps // *VIII Minsk International Seminar "Heat Pipes, Heat Pumps, Refrigerators, Power Sources"*, Minsk, Belarus, 12–15 September, 2011 (Report in this book).
13. Brown J. S., Didion D. Identification and Evaluation of Working Fluids for High Temperature Heat Applications (Including Replacements for R-114) // *AHSRAE Final Report 1308-TRP*, Atlanta, Georgia, 2008. – 321 p.
14. Pappas M., Moradi J.Y. An Improved Direct Search Mathematical Programming Algorithm // *J. of Eng. for Industry, Transactions of the ASME, Series B*. 1975. Vol. 97, No. 4. Pp. 1305–1310.

PREDICTION OF CRITICAL PARAMETERS OF FLUORO OLEFINS AS POTENTIAL LOW GLOBAL WARMING REFRIGERANTS FOR HEAT PUMPS

Ildar A. Sultanguzin, Alexandre V. Govorin, Alina A. Potapova
Industrial Thermal Engineering Systems Department
Moscow Power Engineering Institute (Technical University)
Krasnokazarmennaya street, 14, Moscow, 111250, Russian Federation
Tel./fax: +7-495-362-7217; SultanguzinIA@mpei.ru

Agadzhan M. Gyulmaliev
Laboratory of Catalytic Synthesis and Petrochemical Processes name A. N. Bashkirov
A.V. Topchiev Institute of Petrochemical Synthesis of Russian Academy of Sciences (TIPS RAS)
Leninsky prospect 29, Moscow, 119991, Russian Federation
+7 495 955-42-64; Gyulmaliev@ips.ac.ru

Peter A. Shomov
Limited Liability Company Scientific and Technical Center "Industrial Power Engineering"
Semenovskogo alleyway, 10, Office 503, Ivanovo, 153000, Russian Federation
+7-4932-301488; Shomov@list.ru

Abstract

The aim is prediction of the critical properties and the normal boiling point at atmospheric pressure of fluorinated unsaturated hydrocarbons (olefins) as potential low global warming refrigerants for heat pumps, based on an analysis of the elemental composition of molecules. In the study results and proposed dependence of the normal boiling point and critical parameters (temperature, pressure, volume) of the molecular structure of fluorinated olefins, in particular on the number of carbon and fluorine atoms in the molecules of substances with high coefficients of determination (over 98%).

KEYWORDS

Fluorinated olefins, the critical temperature, critical pressure, critical volume, normal boiling point, forecasting, refrigerants, heat pumps, carbon, fluorine atoms, the structure of molecules.

INTRODUCTION

It is proposed recently new refrigerant for automotive air conditioners based on tetrafluoropropylene R-1234yf [1] with minimal impact on global warming, as an alternative refrigerants such as R-134a, does not affect the ozone layer, but have a global warming potential (GWP) 1430 once greater than CO₂. It is need to find new fluorinated olefins and their isomers, which could be used as refrigerants in heat pumps, refrigerating machines, stationary air condition systems, which have a minimal impact on global warming. For these new agents it is need to predict their critical properties. Universal methods for prediction the critical properties of substances (e.g., group contribution methods) used for a wide range of analyzable matters have insufficiently high accuracy. It is necessary to predict the properties of the critical point and normal boiling point at atmospheric pressure over a narrow range of substances related to fluorinated olefins.

METHOD OF PREDICTING THE CRITICAL PROPERTIES

Typically it is requires knowledge of several fundamental parameters (e. g., critical temperature, critical volume, acentric factor, and others). However, there are situations when besides the chemical formula is no reliable parameters. We can assume that in the near future it will be possible to identify fundamental parameters and all other properties on the knowledge of only the molecular structure of matter. It will be

possible to predict of thermodynamic and thermophysical properties of new substances chemical on the basis of methods of electronic structure calculations.

Group contribution methods for prediction of the substances critical properties [2–6] have the less accurate than the wider range of analyzable matters: saturated hydrocarbons, unsaturated and aromatic hydrocarbons, with chlorine, iodine, fluorine, oxygen atoms, etc.

FLUORIDE ANALYSIS OF PROPERTIES OF UNSATURATED HYDROCARBONS

These results show that the universal methods of predicting the critical properties of substances are the less accurate than the wider range of analytes, such as: limit, unsaturated, aromatic hydrocarbons with chlorine, iodine, fluorine, etc.

Our main quest aimed primarily at the critical properties of fluorinated olefins.

In [7] there is presents the thermophysical properties of the most extensive list of hydrocarbons and many other chemicals. The critical parameters for certain substances are differed according to some sources, for example, properties of trifluoropropylene R-1243zf in [7–9]. Were added the parameters of refrigerants R-1234yf [1, 10, 11] and R-1234ze (E) [12, 13], recently obtained from experimental studies. In [14] there are analyzed predicted critical properties of 8 fluoropropylene isomers, including pentafluoropropylene's R-1225ye (E), R-1225ye (Z), R-1225zc and tetrafluoropropylene R-1234ze (Z).

Thus, an analysis of groups of 127 fluorinated olefins and unsaturated hydrocarbons with the carbon atoms of N_C from 2 to 20 has been done. With an increasing number of C atoms in olefins the normal boiling point, the critical temperature and critical volume increase, and the critical pressure falls.

Molecules with a carbon number of N_C from 8 to 20 are offered by unsaturated hydrocarbons and olefins with one atom of fluorine. The molecules with less carbon atoms (from 2 to 7) are presented by perfluoroolefins (with a full replacement of hydrogen atoms by fluorine atoms), and molecules with a large number of fluorine atoms N_F (from 2 to 5). The large number of fluorine atoms influence to the dispersion of the critical and normal parameters. Consequently, they should be analyzed separately for each group of substances depends on fluorine atoms in each group.

There is interesting the relationship of the normal boiling point T_b (K) and critical temperature T_c (K) of the investigated substances. Let us analyze the relationship, depending on the number of fluorine atoms in the molecules of compounds with carbon number from 2 to 5 (see Fig. 1).

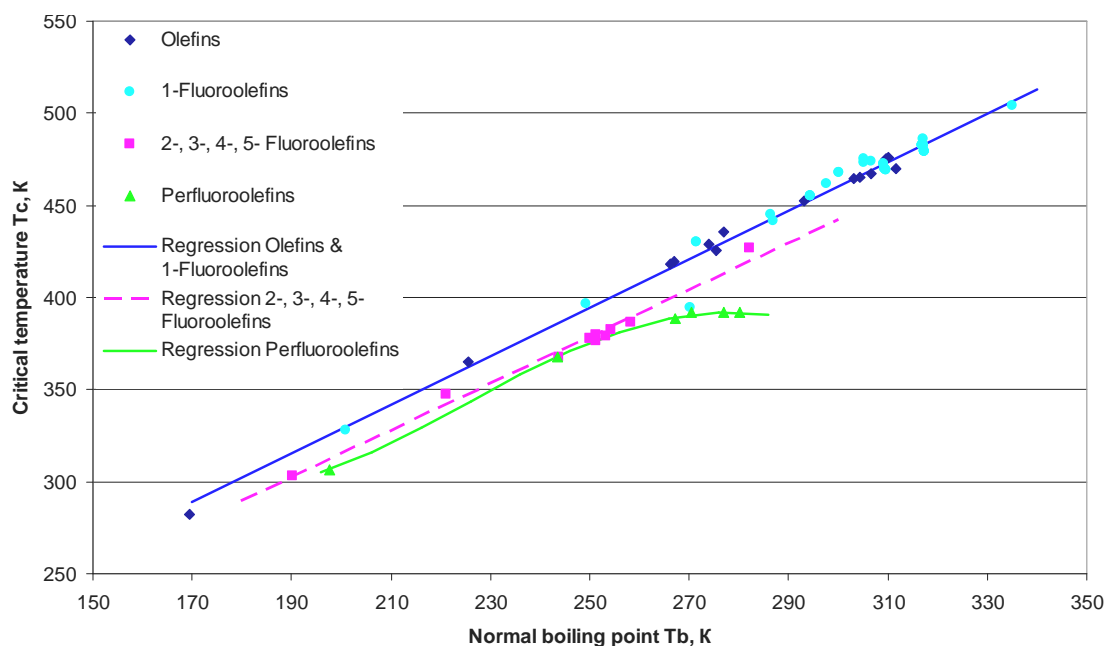


Fig. 1. Interrelation of critical temperature and normal boiling point of fluorinated olefins

There are three groups of unsaturated fluorinated hydrocarbons:

- 1) unsaturated hydrocarbon and fluoroolefins with one atom of fluorine (60 substances);

- 2) di-, tri-, tetra- and penta- fluoroolefins (10 substances);
- 3) perfluoroolefins (5 substances).

Regression relationships (1)–(3) have been obtained for each of these groups:

$$T_c = 64.81 + 1.3187 \cdot T_b \text{ (with a coefficient of determination } R^2 = 98.37\%); \quad (1)$$

$$T_c = 60.24 + 1.273 \cdot T_b \text{ (} R^2 = 98.59\%); \quad (2)$$

$$T_c = 13401 + 120.96 \cdot T_b - 0.088917 \cdot T_b^2 - 2384.9 \cdot T_b^{0.5} \text{ (} R^2 = 99.89\%). \quad (3)$$

The relationship of the critical molar volume and critical pressure of the substances studied presents on Fig. 2. It is evident that this relationship differs for hydrocarbon olefins and fluorinated olefins with a fluorine atom on the one hand, and for fluorolefins with the number of fluorine atoms of 2 or more (in this case, the number of fluorine atoms up to 8).

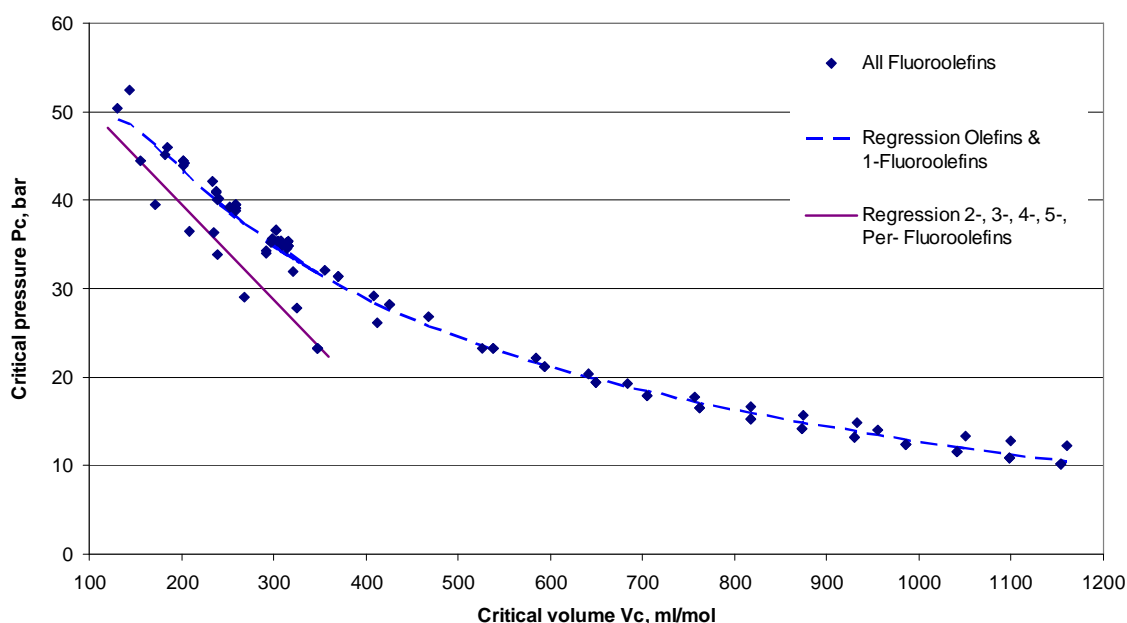


Fig. 2. Interrelation of critical pressure and critical volume of fluorine olefins

The nonlinear regression dependence eq. (4) has been obtained for unsaturated hydrocarbons and fluorinated olefins with 1 atom of fluorine and carbon atoms from 2 to 20 (116 substances):

$$P_c = 10.174 - 0.006973 \cdot V_c + 10199 / V_c - 65275 / V_c^2 \text{ (} R^2 = 95.45\%). \quad (4)$$

The linear regression dependence eq. (5) has been received for di-, tri-, tetra-, penta-, trans-fluoroolefins with the number of fluorine atoms from 2 to 8 (16 substances) (see Fig. 5):

$$P_c = 61.18 - 0.1082 \cdot V_c \text{ (} R^2 = 90.78\%). \quad (5)$$

The linear regression dependence for olefins and fluoroolefins with 1 atom of fluorine and carbon atoms from 2 up to 5 (60 substances) presents on formula eq. (6):

$$P_c = 61.915 - 0.0868 \cdot V_c \text{ (} R^2 = 96.6\%). \quad (6)$$

There is a relationship for different groups of fluorinated olefins between critical pressure and normal boiling point eqs. (7)–(9):

for olefins and fluorolefins with a 1 fluorine atom (60 substances) -

$$P_c = 75.84 - 0.1281 \cdot T_b \quad (R^2 = 86.22\%); \quad (7)$$

for di-, tri-, tetra-, penta- fluorolefins (10 substances) as a linear regression -

$$P_c = 81.45 - 0.1845 \cdot T_b \quad (R^2 = 76.41\%); \quad (8)$$

for perfluoroolefins (6 substances) as a linear regression -

$$P_c = 77.71 - 0.1954 \cdot T_b \quad (R^2 = 95.33\%). \quad (9)$$

The relationship between the critical volume and normal boiling point established on (10)–(12):
for olefins and fluorolefins with a 1 fluorine atom (60 substances)

$$V_c = -155.3 + 1.4584 \cdot T_b \quad (R^2 = 87.16\%); \quad (10)$$

for di-, tri-, tetra-, penta-fluorolefins (10 substances) as a linear regression -

$$V_c = -130.7 + 1.474 \cdot T_b \quad (R^2 = 83.74\%); \quad (11)$$

for perfluoroolefins (6 substances) as a linear regression -

$$V_c = -193.0 + 1.901 \cdot T_b \quad (R^2 = 92.11\%). \quad (12)$$

However, the accuracy of the dependencies in eqs. (1)–(12) is insufficient for a reliable determination of the critical properties of fluorinated olefins. It was necessary to find a different principle for constructing the required dependencies.

DEPENDENCE OF CRITICAL PROPERTIES OF FLUORINATED OLEFINS ON NUMBER OF ATOMS OF CARBON AND FLUORINE IN MOLECULE

In the study results and proposed dependence of the normal boiling point and critical parameters (temperature, pressure, volume) of the molecular structure of fluorinated olefins, in particular on the number of carbon atoms N_C and N_F fluorine in the molecules of substances with higher coefficients of determination R^2 .

The highest precision founds for the dependence eq. (13) of the critical volume upon the number of carbon atoms N_C and the number of fluorine N_F atoms with coefficient of determination $R^2 = 99.96\%$:

$$V_c = 13.014 + 57.049 \cdot N_C + 19.517 \cdot N_F - 0.97944 \cdot N_F \cdot N_C - \frac{5.4676 \cdot N_F^2}{N_C} \quad (13)$$

This dependence presents on Fig. 3.

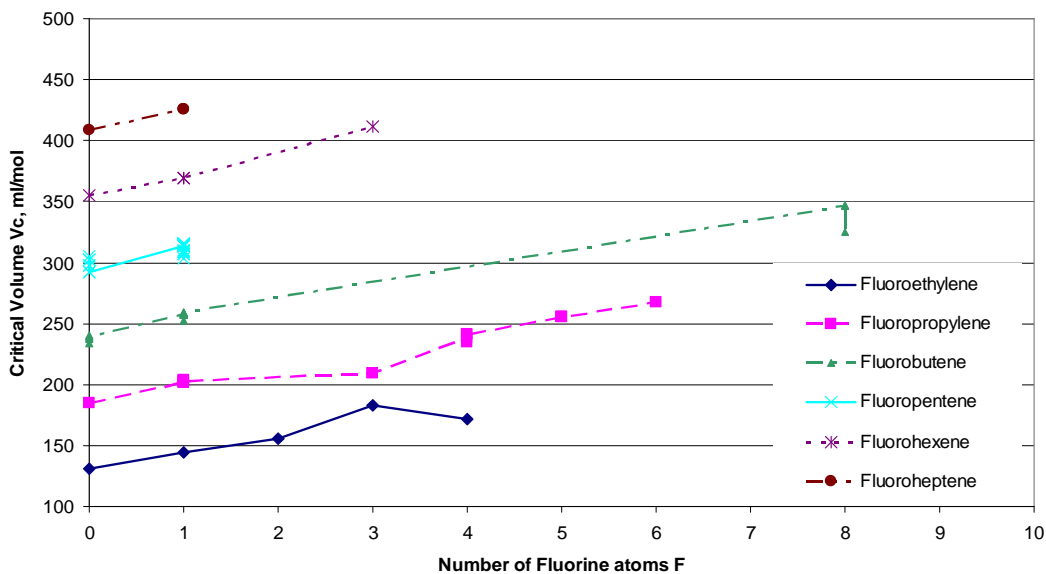


Fig. 3. Dependence of critical volume of fluorine olefins on number of fluorine atoms

Similar relationships have been established in eqs. (14)–(16) (see Figs. 4–6):

- The normal boiling point at atmospheric pressure ($R^2 = 99.22\%$):

$$T_b = 33.6657 + 0.1861N_c^2 - \frac{1.56N_c}{N_F + 1} + 124.943\sqrt{N_c}; \quad (14)$$

- Critical temperature ($R^2 = 98.74\%$):

$$T_c = -41.482 - 50.873N_c + 0.91105N_c^2 + \sqrt{N_c} - 0.24545N_F^2 - \frac{6.0109N_F^2}{N_c^2}; \quad (15)$$

- Critical pressure ($R^2 = 98.6\%$):

$$P_c = 17.476 - 0.68928N_c - \frac{7.347N_F}{N_c} + \frac{133.68}{N_c} - \frac{119.25}{N_c^2}. \quad (16)$$

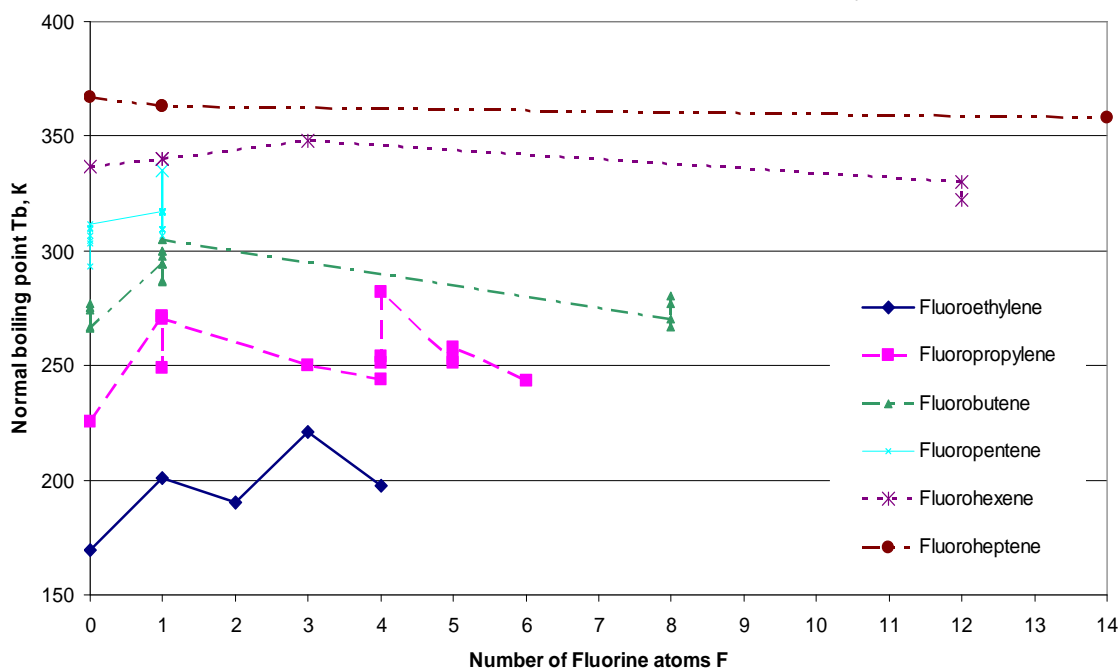


Fig. 4. Dependence of normal boiling point of fluorine olefins on number of fluorine atoms

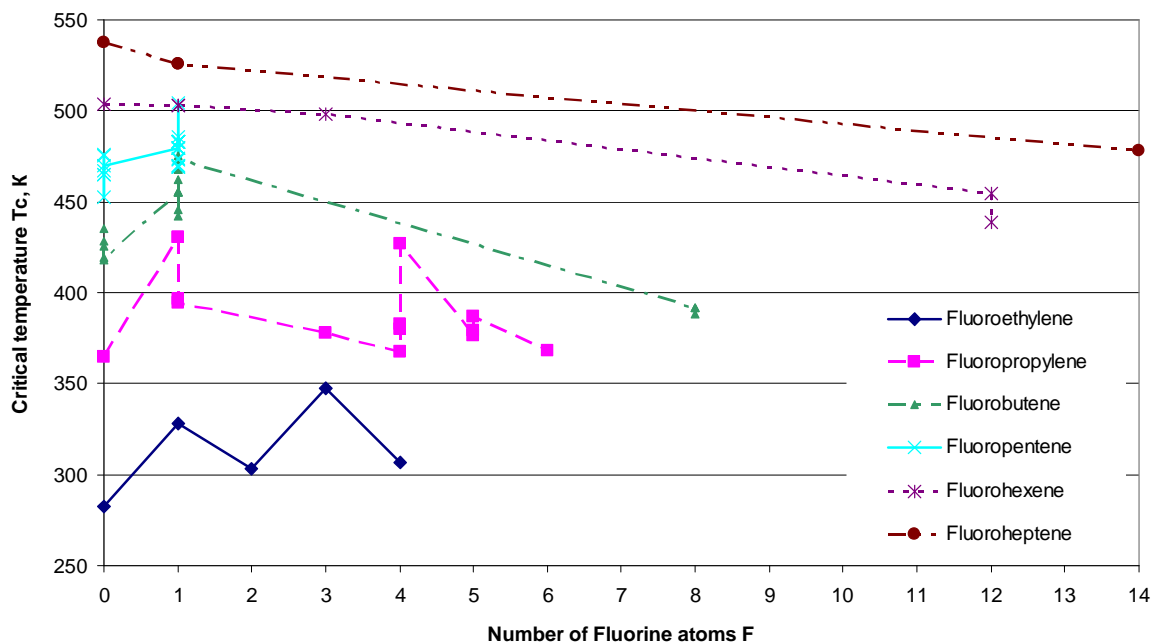


Fig. 5. Dependence of critical temperature of fluorine olefins on number of fluorine atoms

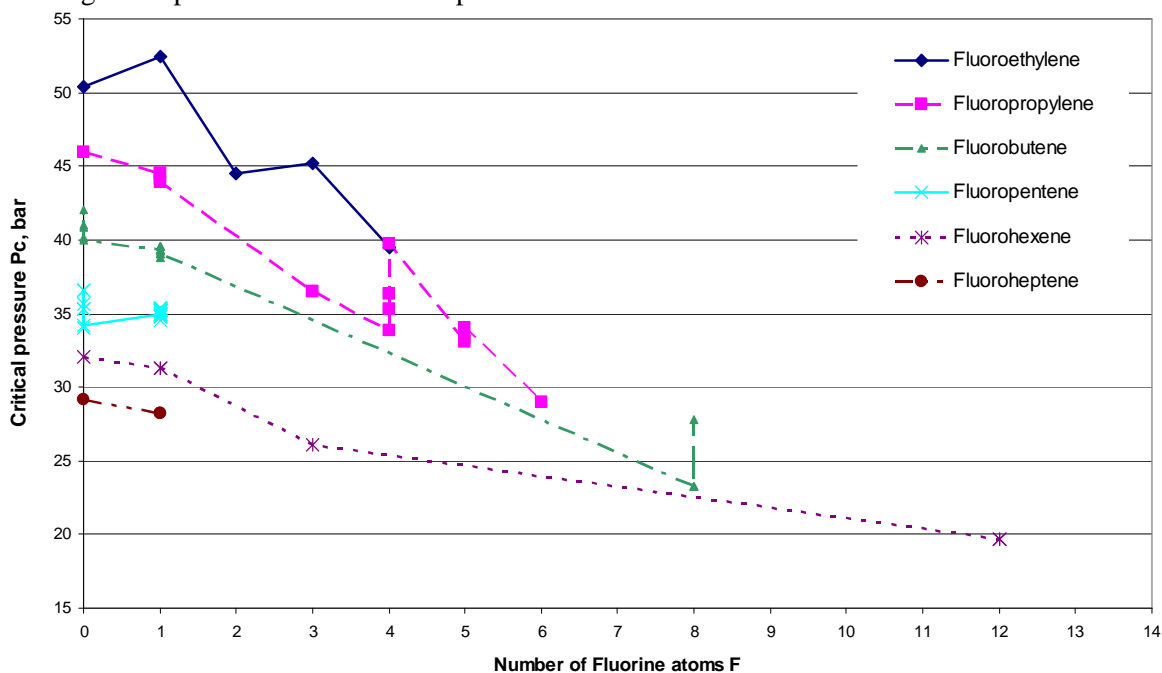


Fig. 6. Dependence of critical pressure of fluorine olefins on number of fluorine atoms

The obtained dependences could be used to predict the thermodynamic properties (P-H and T-S diagrams), thermal physicochemical properties of potential refrigerants with low GWP, based on fluorinated unsaturated hydrocarbons in heat pumps, refrigerating machines, air condition systems.

References

1. Leck T. J. Evaluation of HFO-1234yf as a Potential Replacement for R-134a in Refrigeration Applications // *Proc. 3rd IIR Conf. on Thermophys. Properties and Transfer Proc. of Refrigerants*, Boulder, CO, 2009. Paper 155.

2. Poling B. E., Prausnitz J. M., O'Connell J.P. Pure Component Constants: *The Properties of Gases and Liquids*, 5th ed., New York: McGraw-Hill, 2001. Pp. 2.1–2.38.
3. Prediction and Correlation of Physical Properties: *Perry's Chem. Eng. Handbook*, 8th ed. / Eds. R. H. Perry, D. W. Green, McGraw-Hill, New York, 2008. Pp. 2.463–2.517.
4. Joback K. G. Obtain the Best Physical Property Data // *AIChE Chem. Eng. Progress*. May 2009. Vol. 105, No. 5. Pp. 30–39.
5. Nannoolal Y. *Development and Critical Evaluation of Group Contribution Methods for the Estimation of Critical Properties, Liquid Vapour Pressure and Liquid Viscosity of Organic Compounds* // PhD thesis, University of Kwazulu-Natal, Durban Campus, 2006.
6. Filippov L. P. *Prediction of Thermophysical Properties of Liquids and Gases*, Moscow: Energoatomizdat, 1988. Pp. 109–160 (in Russian).
7. Yaws C. L. Critical Properties and Acentric Factor – Organic Compounds: *Thermophysical Properties of Chemicals and Hydrocarbons*. New York: William Andrew Inc. 2008. Pp. 1–95.
8. Zernov V. S., Kogan V. B., Lyubetsky S. G., Duntov F. I. Equilibrium liquid–vapor in an ethylene–trifluorinepropylene system // *Zhurnal Prikladnoi Himii (Journal of an Applied Chemistry)*. 1971. No. 3. Pp. 683–686 (in Russian).
9. Marsh K. N., Abramson A., Ambrose D., et al. Vapor–Liquid Critical Properties of Elements and Compounds. 10. Organic Compounds Containing Halogens // *J. Chem. Eng. Data*. 2007. Vol. 52. Pp. 1509–1538.
10. Akasaka R., Tanaka K., Higashi Y. Thermodynamic property modeling for 2,3,3,3-tetrafluoropropene (HFO-1234yf) // *Int. J. of Refrigeration*. 2010. Vol. 33. Pp. 52–60.
11. Di Nicola G., Polonara F., Santory G. Saturated Pressure Measurements of 2,3,3,3-tetrafluoroprop-1-ene (HFO-1234yf) // *J. Chem. Eng. Data*. 2010. Vol.55. Pp. 201–204.
12. Grebenkov, A. J., Hulse, R., Pham, H., Singh R. Physical Properties and Equation of State for Trans-1,3,3,3-Tetrafluoropropene // *Proc. of 3rd IIR Conf. on Thermophysical Properties and Transfer Processes of Refrigerants, Boulder, CO, 2009*. Paper 61.
13. Higashi Y., Tanaka K. Critical Parameters and Saturated Densities in the Critical Region for trans-1,3,3,3-Tetrafluoropropene (HFO-1234ze(E)) // *J. Chem. Eng. Data*. 2010. Vol. 55. Pp. 1594–1597.
14. Brown J. S., Zilio C., Cavallini A. Thermodynamic Properties of Eight Fluorinated Olefins // *Int. J. of Refrigeration*. 2010. Vol. 32. Pp. 235–241.

THERMAL CONTROL SYSTEM OF THE PRECISION INSTRUMENT BOARD INTEGRATED INTO METEOROLOGICAL SATELLITE

D. V. Tulin, I. D. Tulin, K. A. Goncharov, A. Yu. Kochetkov

Lavochkin Association

24 Leningradskaya, Khimki, 141400, Moscow region, Russia

E-mail: ival@laspace.ru

Meteorological geostationary satellite "Electro-L" was successfully launched on 21 January 2011. In this paper there will be presented precision instrument board thermal control issues and in-flight temperatures.

The satellite main parts are as follows:

- target equipment complex that provides for obtaining, processing and transmitting of multi-spectral pictures and heliogeophysical environment data at the altitude of the spacecraft orbit, execution of telecommunication functions;
- complex of the service systems supporting operation of the target equipment and spacecraft as a whole in accordance with the requirements.

The main part of the payload is information system that represents multiregional scanning device of hydrometeorological hardware (MRSU-HMH).

All equipment of the satellite is designed for operation in outer space without keeping it in the sealed gas filled container. Payload, MRSU-HMH, star sensors and command gyoinstrument, located on the special precision instrument board on the base THP to maintain the specified precision characteristics.

The payload represents two multiregional scanning devices of hydro meteorological hardware, gyroscopic gage of angular velocity vector and three star sensors. For payload normal operation it is required to keep its temperature within a narrow range.

The THP design represents honeycomb panel with embedded ammonia axial grooved heat pipes (AGHP) which functions simultaneously as a support frame for installation of the equipment units and heat sink device of the TCS. Hereinafter this structure is referred to as a thermal honeycomb panel.

The THP design consists of two aluminum surface sheets and aluminum honeycombs filling the gaps between the heat pipes bodies.

On the THP surfaces there are to be mounted collector ammonia axial grooves heat pipes perpendicular to the THP embedded heat pipes. The collector heat pipes are purposed for heat power distribution between the THP heat pipes and collect of heat flows for heat power further transfer to heat sink.

Onto the collector heat pipes there is to be mounted with LHP evaporator

The LHP is purposed to transfer heat flow collected by the collector to the heat sink – radiation heat exchanger (RHE). Heat is supplied to the LHP evaporator which body is made of a steel tube. To ensure heat supply, the aluminum contact saddle is welded to the steel tube. The contact saddle shape ensures the minimum temperature gradient between the heat supply surface and evaporator body.

The LHP content propylene like a fluid with freezing temperature minus 187oC and consists of the following components:

- capillary pump (evaporator) that represents a cylindrical body with threaded internal surface fitted on a capillary-porous wick;
- compensation chamber connected with evaporator from the side of the condenser and freely communicating with internal (absorbed) surface of capillary-porous wick;
- transport channels for vapor and liquid (vapor line and liquid line);
- condenser-radiator, that represents system of lines conductively connected with radiating sheet. Radiator is designed as a honeycomb panel from aluminum alloy with embedded condensers lines.

The heat power generated in the THP equipment is rejected by axial grooved heat pipes embedded into the THP, collector heat pipes and then by LHP to the operating surface of the RHE from which it is radiated to environment. To decrease uncontrolled heat exchange with the environment the precision instrument

board and the equipment (excepting for operation surfaces of multi-region scanning devices and star sensors) are covered with multi-layer insulation (MLI).

If intrinsic heat power generated by the THP equipment is minimal, the LHP will control the heat flow to the radiator from the THP by using pressure regulator or TEC.

The LHP is controlled by two methods: passive (by means of pressure regulator and bypass line) and active (by means of TEC).

The passive method is a primary one applied under normal operation as there is no need electric power supply. The active method is a redundant one applied only in case of pressure regulator failure.

If heat generated by the equipment is minimal, the heat rejected from the THP through the equipment surfaces uncovered with MLI will be compensated by the electrical heaters mounted to the THP and switched on/off in accordance with the temperature sensors telemetry data.

In this paper there will be discussed some issues of thermal conditions mathematical modeling for precision devices platform and thermal vacuum tests of the TCS.

The authors will present the results of heat calculations and temperature measurements obtained during TCS thermal vacuum tests and in-flight tests. The comparison of estimated, experimental and in-flight temperatures will be also given.

DYNAMIC STUDY OF AN ADSORPTION HEAT TRANSFORMER

Janna V. Veselovskaya, Mikhail M. Tokarev, Alexandra D. Grekova, Larisa G. Gordeeva

The Laboratory of Energy Accumulating Processes and Materials

Boreskov Institute of Catalysis SB RAS

Pr. Lavrentieva 5, Novosibirsk, Russia, 630090

Tel/Fax: +7383-3309573; E-mail: jvv@catalysis.ru

Abstract

By means of Large Temperature Jump (LTJ) method the dynamics of ammonia sorption was investigated for loose grains of the "BaCl₂/vermiculite" and "BaCl₂/BaBr₂/vermiculite" composites which are promising materials for adsorption air conditioning. The influence of the grain size, the adsorbent composition and the adsorbent load was studied. The heat transfer coefficients for the adsorbent-heat exchanger configuration studied were calculated for adsorbents with different grain sizes. The results of LTJ experiments were used for modeling of the adsorption air-conditioning cycle. Appropriate recommendations on optimization of the adsorbent composition and load are made.

KEYWORDS

Adsorption, dynamics, composite, barium chloride, barium bromide, vermiculite, ammonia, performance.

INTRODUCTION

Performance of an adsorption heat transformer (AHT) is essentially affected by dynamics of adsorption and desorption stages of its working cycle [1]. It was revealed that gas-solid reactions between ammonia and inorganic salts (BaCl₂, SrCl₂, CaCl₂, MnCl₂, NiCl₂) require a certain driving force to proceed with a reasonable rate [2-9]. For isobaric desorption, the driving force is a difference ΔT between the temperature of the heat source T_{reg} and the equilibrium temperature of reaction $T_r(P_c)$: $\Delta T = T_{reg} - T_r(P_c)$. In [4] ΔT was called as the temperature equilibrium drop; in this work it will be named as the driving temperature difference (DTD). Accordingly, for isobaric adsorption, the DTD can be introduced as $\Delta T = T_r(P_e) - T_{hs}$, where T_{hs} is the heat sink temperature.

Recently the composite ammonia adsorbent «BaCl₂/vermiculite» has been presented as a promising material for adsorption cooling [10]. This composite has a high sorption ability (up to 0.24 g/g) which is due to the fact that ammonia is sorbed by barium chloride confined to the vermiculite pores, and one mole of the salt absorbs 8 moles of ammonia:



with the heat release of 36.7 kJ per 1 mol of ammonia [11].

Dynamics of ammonia sorption on 1-2 mm grains of «45 wt.% BaCl₂/vermiculite» composite was measured by the LTJ method under conditions which closely imitated the isobaric stages of AHT units. In this method sorption and desorption of the refrigerant were initiated by a sharp change of the temperature of a metal plate supported adsorbent [12].

It was revealed that experimental conversion x obeyed a simple exponential evolution on time t :

$$x(t) = 1 - \exp(-kt), \quad (2)$$

where k was the rate constant of adsorption process. This constant depends linearly on the DTD:

$$k = 1/\tau = \frac{\alpha \cdot S}{\Delta H \cdot \Delta N} \cdot \Delta T = C \cdot \Delta T, \quad (3)$$

where ΔH is the reaction heat, ΔN is the total amount of adsorbed ammonia, α is the heat transfer coefficient between the grains and the metal plate, S is the area of heat exchange. The heat transfer coefficient α equals $90 \text{ W}/(\text{m}^2 \cdot \text{K})$ and does not depend on pressure, temperature and salt content. The $\Delta H_r \cdot \Delta N / S$ expression is the energy density per unit area of the heat exchanger [12]. Thereby, the higher are the heat transfer coefficient and DTD and the lower is the energy density the faster is adsorption process.

The composite «BaCl₂/vermiculite» was experimentally tested in a lab-scale prototype of an ammonia adsorption chiller with plate heat exchanger [13]. Adaptability of the kinetic model defined by eqs. (2) and (3) to simulating the dynamics of adsorption processes and the performance of the AHT prototype was demonstrated using the results of the composite testing. It was shown that the new material provided effective AC operation using a low regeneration temperature $T_{reg} = 80\text{--}90 \text{ }^\circ\text{C}$ giving Coefficient of Performance $\text{COP} = 0.54 \pm 0.01$ and Specific Cooling Power SCP ranging from 300 to 680 W/kg. The SCP depended strongly on the DTD and the cycle duration. Optimization of the ratio of adsorption and desorption stages duration leads to the increase in SCP up to 690-860 W/kg. Although the measured values of SCP and COP are rather encouraging, a room for improvements still exists.

The aim of this study was further improvement of the dynamic characteristics of AC cycles. According to eq. (3) the rate constant k can be increased by the rise of the heat transfer coefficient α and DTD and by diminishing the energy density per unit area of the heat exchanger. In [14] it was revealed that heat transfer coefficient α between the metal plate and an adsorbent layer was increased from 50 to $120 \text{ W}/(\text{m}^2 \cdot \text{K})$ by the lowering the grain size of the adsorbent from 1.6–1.8 mm to 0.4-0.5 mm. DTD depends on the equilibrium temperature T_r of the reaction (1), which can be changed by confinement of a binary salt system, which forms a solid solution inside pores of the matrix [15]. The energy density can be diminished by decreasing the total amount ΔN of adsorbed ammonia, which depends on the mass of the adsorbent loaded in the AHT. Therefore, in this work we investigated these three ways to intensify ammonia sorption, namely, variation of the adsorbent grains size, optimization of the adsorbent load and shift of the reaction equilibrium temperature.

EXPERIMENTAL

Composite adsorbents preparation

The composites were synthesized by dry impregnation [10, 15] of expanded vermiculite with an aqueous BaCl₂ solution (Samples 1, 2) and with a mixed aqueous solution of BaCl₂ and BaBr₂ (Sample 3) followed by the drying at $160 \text{ }^\circ\text{C}$. The samples of the composite ammonia adsorbents studied are described in Table 1. The sample of the composite adsorbent that was previously studied in [12] is referenced in Table 1 as Sample 0. Note, that the molar content of Barium in the Samples 0, 1 and 3 was the same while in the Sample 2 it was half as great.

Table 1. Characteristics of the composites studied

	Sample 0	Sample 1	Sample 2	Sample 3
Active salt(s)	BaCl ₂	BaCl ₂	BaCl ₂	BaCl ₂ and BaBr ₂
Salt content	45 wt.%	45 wt.%	45 wt.%	23 wt.% BaCl ₂ , 25 wt.% BaBr ₂
Grain size	1–2 mm	0.5–1 mm	0.5–1 mm	1–2 mm
Mass of the adsorbent	0.833 g	0.833 g	0.416 g	0.925 g

Measurements of ammonia adsorption kinetics

The kinetics measurements were performed by the LTJ method using an experimental rig schematically shown in Figure 1. The loose adsorbent particles were placed in a measuring cell on a metal plate which was surrounded by water jacket in order to provide a needed plate temperature. The surface area of the metal plate that served as the heat exchanger was $S = 1.96 \cdot 10^{-3} \text{ m}^2$. The cell was connected by pipes and valves with a buffer volume, a liquid ammonia vessel and a vacuum line for the set-up evacuation. Two liquid thermostats connected to the water jacket through the 3-way valves were used to maintain the temperature of the

measuring cell. This temperature was changed in a step-wise mode by switching the liquid flow between the thermostats. These thermostats served as a heat sink at adsorption run and as a heat source for regeneration of the adsorbent. The pressure over the sample was measured by a gauge within ± 0.01 bar accuracy; the temperatures of the metal plate and the buffer volume were measured by J-type thermocouples within ± 0.1 °C accuracy. An analog-to-digital converter and a personal computer were used for data acquisition.

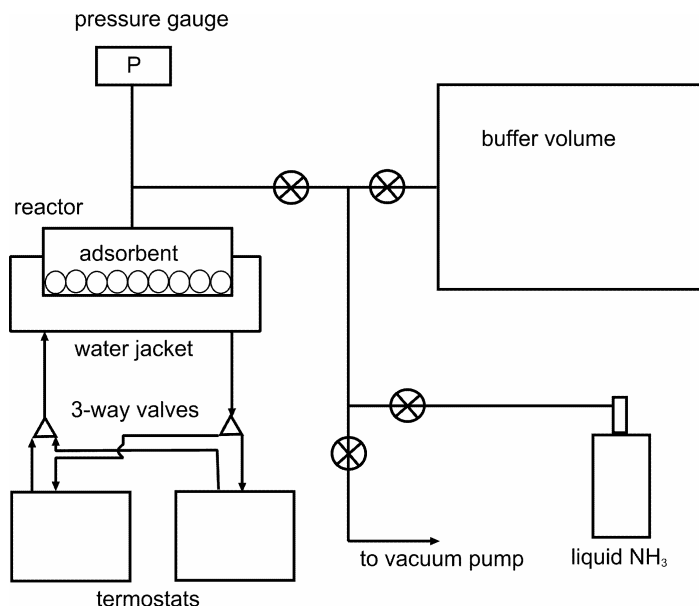


Fig. 1. Scheme of the experimental rig for dynamic measurements (see the text for details)

The volume of the gas buffer $V = 5.2 \cdot 10^{-4}$ m³ and the mass of the adsorbent loaded were selected in a way that provided the pressure change due to the ammonia adsorption of 5–10% of the initial pressure. Thus, the ammonia adsorption occurred in quasi-isobaric conditions.

Before the kinetics measurements, granules of the composite were placed on the metal plate, then heated up to 90 °C and evacuated at $P \approx 10^{-3}$ mbar during 2 h. The measuring cell was connected with the liquid ammonia vessel and ammonia pressure was maintained at $P = 5.8$ bar that correspond evaporator temperature $T_e = 10$ °C. After reaching the equilibrium the ammonia source was disconnected from the measuring cell. Then the temperature of the metal plate was changed in a step-wise way by switching the heat carrier flow from one thermostat to another.

The drop of temperature down to a temperature of heat sink T_{hs} initiated ammonia adsorption, and a time dependence $P(t)$ of the ammonia pressure over the adsorbent was registered each 1 s. The duration of adsorption runs was approximately 1 h that was enough for reaching the sorption equilibrium. In order to regenerate the adsorbent we heated the metal plate again up to the temperature of the heat source $T_{reg} = 90$ °C. The temperatures of heat sink varied from 15 to 40 °C.

The time dependence of conversion $x(t)$ was calculated from the evolution of pressure $P(t)$ and temperature of the buffer tank $T(t)$ using the Soave-Redlich-Kwong equation of state [16] for ammonia:

$$x(t) = \frac{V_m(T_{fin}, P_{fin}) \cdot [V_m(T_{in}, P_{in}) - V_m(T(t), P(t))]}{V_m(T(t), P(t)) \cdot [V_m(T_{in}, P_{in}) - V_m(T_{fin}, P_{fin})]}, \quad (4)$$

where $V_m(T, P)$ was the molar volume of ammonia at T and P , indexes *in* and *fin* corresponded to initial and final states of the run, respectively.

RESULTS AND DISCUSSION

Characteristic times of ammonia adsorption

The dependences of conversion on time $x(t)$ for all the experiments presented in Fig. 2 obey the exponential equation (2). Characteristic times of adsorption process ($\tau = 1/k$) are displayed in Table 2. The relative error in the characteristic time determination was about 5%, whereas coefficient of determination R^2 for fittings was not less than 0.99. One can see that lowering of the heat sink temperature always enhances the rate of ammonia adsorption. This confirms that the increase in driving temperature difference leads to the rise of the solid–gas chemical reaction rate.

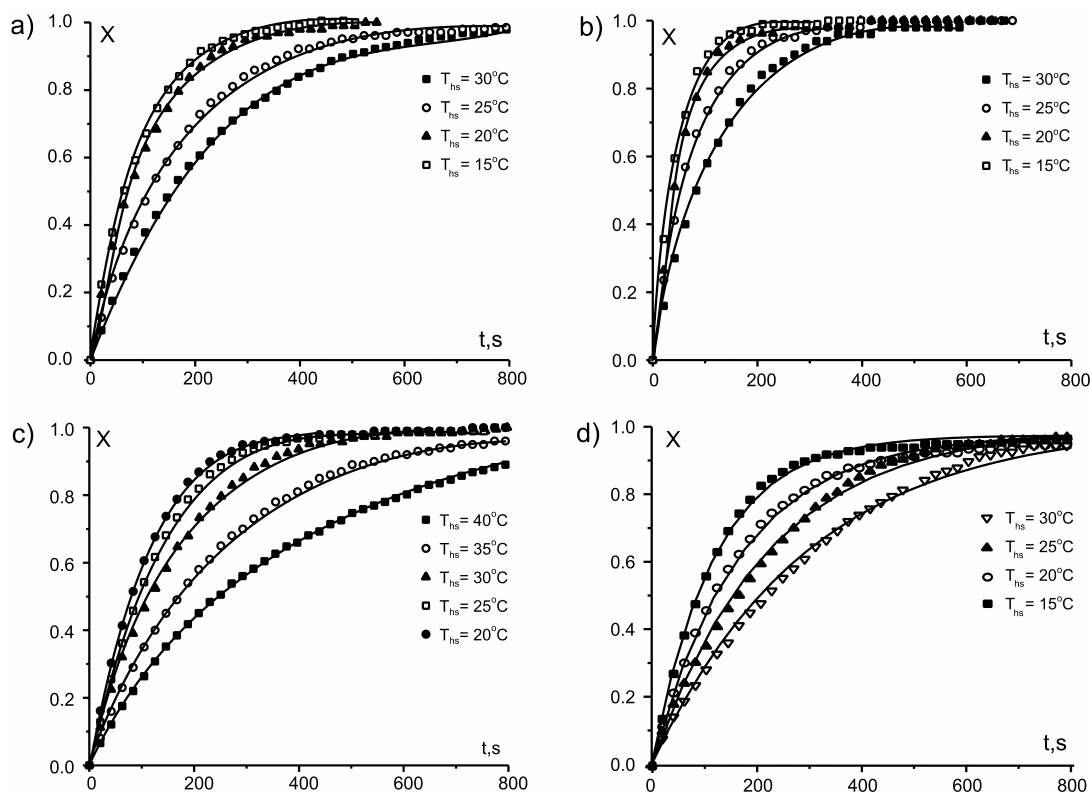


Fig. 2. The dependences of conversion on time (symbols) and its exponential fits (line) for a) Sample 1, b) Sample 2, c) Sample 3. Data for Sample 0 (d) is taken from [12]

Table 2. Characteristic times τ of ammonia adsorption at $P = 5.8$ bar

$T_{hs}, ^\circ\text{C}$	Characteristic time τ , s			
	Sample 0	Sample 1	Sample 2	Sample 3
15	140	94	47	-
20	170	113	57	109
25	220	161	78	126
30	330	225	112	162
35	-	-	-	224
40	-	-	-	366

The lowering of the adsorbent grain size from 1–2 mm down to 0.5–1 mm (Samples 0 and 1) leads to decrease in characteristic time of adsorption. Reduction of the adsorbent load (and, consequently, the total amount of ammonia exchanged) in two times (Samples 1 and 2) results in halving of τ that agrees with eq. (3). It is worth noting that the area of heat exchange surface was equal for Samples 1 and 2, thus the thickness of the adsorbent layer was lesser for Sample 2. The rate of ammonia adsorption on the composite based on binary salt system (Sample 3) was higher as well in comparison with the single salt composite (Sample 0). The amount of ammonia adsorbed and the sizes of the grains for these samples were the same, therefore the reduction of the characteristic time is caused only by the chemical nature of the active component.

Heat transfer coefficients

The data obtained allows evaluation of the initial heat power W_0 released due to chemical reaction (1):

$$W_0 = \Delta H_r \cdot \Delta N \cdot \left. \frac{dx(t)}{dt} \right|_{t=0} = \frac{\Delta H_r \cdot \Delta N}{\tau} \quad (5)$$

where ΔH_r is the enthalpy of reaction (1) (36.7 kJ/mol [11]), ΔN is maximal amount of ammonia adsorbed, which corresponds to stoichiometric adsorption capacity of the composite [10].

The value of W_0 appears to be a linear function of temperature of heat sink (Fig. 3) that agrees well with the data of [12] where it was shown that the values of W_0 linearly depended on the DTD:

$$W_0 = \alpha \cdot S \cdot (T_r - T_{hs}) \quad (6)$$

The heat transfer coefficient α was estimated as 115 ± 5 W/(m²·K) from eq. 6 for the grains size of 0.5–1 mm (Samples 1 and 2). The heat transfer coefficient for 1–2 mm grains (Sample 3) turned out to be $\alpha = 90 \pm 5$ W/(m²·K) that equals to α for Sample 0 (1–2 mm grain size) [12]. Thus, it was demonstrated that the coefficient of heat transfer depended only on the grain size. The adsorbent load (see Fig.3, Samples 1 and 2) and the chemistry of the active component did not affect the heat transfer coefficient.

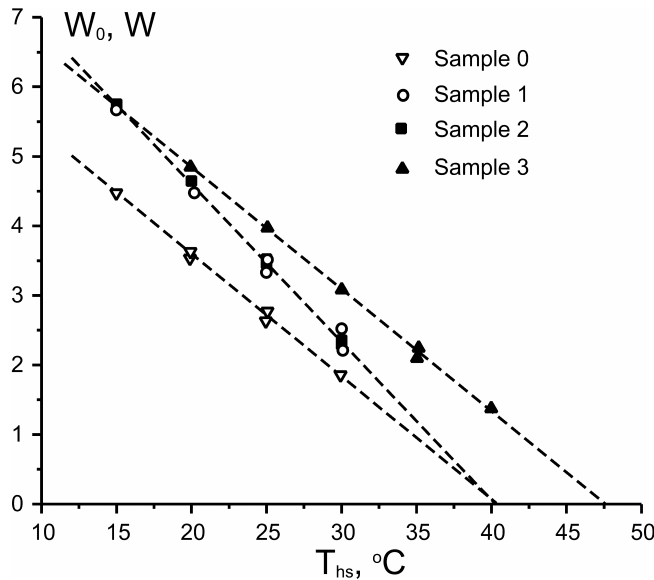


Fig. 3. Dependence of the initial heat power W_0 on the temperature of heat sink T_{hs} .

It is worth nothing that the approximation lines (Fig. 3) cross the axes of abscissa at point $T = 40$ °C for Samples 0, 1 and 2 that corresponds to the equilibrium temperature T_r of the reaction (1) at $P = 5.8$ bar (eq. (6)). On the contrary, for Sample 3 the approximation line intersects the abscissa at $T = 48$ °C. Consequently, the equilibrium reaction temperature shifted to the higher level. The reason of this alteration of the reaction temperature was shown to be the formation of the solid solution of the barium chloride and barium bromide inside pores [15]. The rise of the temperature T_r resulted in the increase in DTD: $\Delta T = T_{hs} - T_r$. That's why at the same T_{hs} Sample 3 adsorbs ammonia faster than Sample 0.

Simulation of AHT dynamic characteristics

All the kinetic data obtained are in a good agreement with kinetic model defined by eqs. (2) and (3). This model was developed for simulation of the main AHT characteristics (COP and cooling power related to unit mass of the adsorbent SCP_m) [12]:

$$COP = \frac{\Delta H_{ev} \cdot \Delta N \cdot x(t_a)}{\Delta H_r \cdot \Delta N \cdot x(t_d) + C_p \cdot m_s \cdot (T_{hs} - T_{reg})}, \quad (7)$$

$$SCP_m = \frac{\Delta H_{ev} \cdot \Delta N \cdot x(t_a)}{t_c \cdot m_s}, \quad (8)$$

where ΔH_{ev} is the ammonia evaporation heat (23.3 kJ/mol), C_p is the effective heat capacity of the composite adsorbent under ammonia pressure (1.49 J/(g·K)), m_s is the adsorbent mass, t_c is the total cycle duration, t_a and t_d are durations of adsorption and desorption stages, respectively. The optimal ratio of adsorption and desorption stages durations is the subject of optimization [12].

To find out the effect of the adsorbent load (and, consequently, the energy density per unit area of the heat exchanger) it is reasonable to relate the cooling power per unit of the surface area of the heat exchanger (S):

$$SCP_S = \frac{\Delta H_{ev} \cdot \Delta N \cdot x(t_a)}{t_c \cdot S} = SCP_m \cdot \rho, \quad (9)$$

where ρ is the adsorbent load density: $\rho = m_s/S$. From the practical point of view this parameter is more significant and indicative than SCP_m because usually the surface area of a heat exchanger of the AHT is fixed. Note that here we consider a basic cooling cycle without heat and mass recuperation and do not take into account thermal losses due to the inert thermal masses.

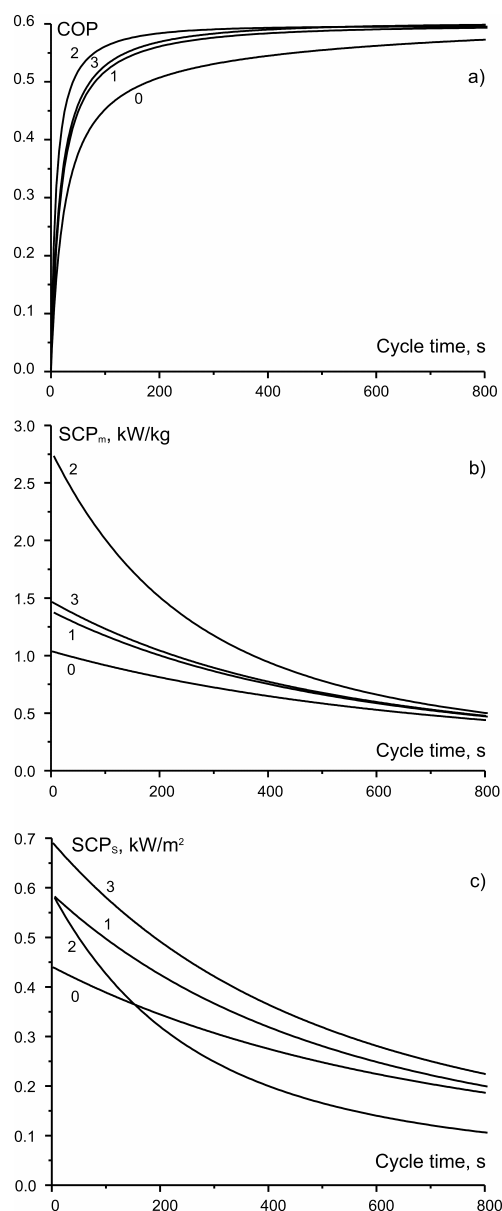


Fig. 4. Dependence of COP (a), SCP_m (b) and SCP_S (c) on the cycle time. $T_e = 10^\circ\text{C}$, $T_{hs} = 30^\circ\text{C}$ and $T_{reg} = 90^\circ\text{C}$ for Samples 0, 1, 2 and 3

Using eqs. (2), (3), (7)–(9) the COP, SCP_m and SCP_S dependences on the total cycle time were calculated for Samples 0, 1, 2 and 3 under conditions of air-conditioning cycle ($T_e = 10^\circ\text{C}$, $T_{hs} = 30^\circ\text{C}$ and $T_{reg} = 90^\circ\text{C}$). One can see (Fig. 4) that lowering the grain size down to 0.5–1 mm (Sample 1) increases the values of both SCP_m and SCP_S in comparison with Sample 0 (1–2 mm size). Another effect of reducing the grains size is that COP rises faster with the increase in the cycle duration and at $t_c = 100$ s reaches COP = 0.52. This value is 15% higher than that for the sample with twice larger grains (Sample 0).

One more possibility to accelerate the adsorption is reducing the adsorbent load. Thus, halving of the adsorbent mass (Sample 2) leads to a drastic increase in SCP_m that becomes almost twice higher than that for Sample 1. At the same time the specific cooling power related per unit area of the heat exchanger (SCP_S) becomes lower than that for higher adsorbent load. This effect is not surprising taking into account that the total amount of the ammonia exchanged in this case becomes twice lower. Nevertheless the benefit of the lowering of the adsorbent load is that COP increases with cycle time rapidly and reaches COP = 0.56 at $t_c = 100$ s. Thus, lessening the adsorbent load can be recommended for applications that require high COP and very short cycle times. The disadvantage of adsorbent load reducing is lowering of the cooling power per unit area of the heat exchanger.

The effect of shifting the equilibrium reaction temperature (Sample 3) on COP and SCP_m turned out to be similar to the effect of reducing the adsorbent grains size (Sample 1). On the other hand the adsorbent containing binary salt system demonstrates the highest SCP_S among all the samples studied. Indeed, this sample demonstrates the highest initial adsorption rate at $T_{hs} = 30^\circ\text{C}$ (Fig. 3). Thus, this adsorbent turned out to be the closest to the optimal one for air conditioning cycle with $T_e = 10^\circ\text{C}$, $T_{hs} = 30^\circ\text{C}$ and $T_{reg} = 90^\circ\text{C}$. Moreover, it is evident that the dynamic characteristics for composite adsorbent based on binary salt system $\text{BaCl}_2\text{-BaBr}_2$ can be further improved by reduction of the adsorbent grain size.

Thus, augmentation of both COP and SCP of the AHT cycle can be reached by using smaller grains of the adsorbent and by proper shift of equilibrium temperature of reaction. On the other hand, the optimal adsorbent load and cycle duration should be found as a compromise between the COP and SCP.

CONCLUSIONS

The dynamics of ammonia adsorption on the composite materials based on BaCl_2 and $\text{BaCl}_2+\text{BaBr}_2$ as active components and expanded vermiculite as a porous matrix was investigated in the quasi-isobaric conditions by LTJ method. It was shown that all the experimental kinetic curves obeyed an exponential function with one characteristic time. The influence of the grain size, the equilibrium reaction temperature and the adsorbent load were studied. The heat transfer coefficients for the adsorbent-heat exchanger configuration studied were calculated to be $90 \text{ W}/(\text{m}^2\cdot\text{K})$ for 1–2 mm grain size and $115 \text{ W}/(\text{m}^2\cdot\text{K})$ for half grain size. The results of LTJ experiments were used for modeling and optimization of the air-conditioning cycle. It was revealed that both COP and SCP of the AHT can be increased by using smaller grains of the adsorbent and by the proper shift of equilibrium temperature of reaction. The optimal adsorbent load and cycle duration is a subject of a compromise between the COP and SCP.

Acknowledgments

This research activity is supported in part by the Russian Foundation for Basic Researches and the Royal Society (Grants 09-03-00916a and 09-08-92604-KOa). The authors thank Prof. Yu.I. Aristov for fruitful discussion and valuable comments.

References

1. Critoph R.E., Metcalf S.J. Specific cooling power intensification limits in ammonia carbon adsorption refrigeration system // *Appl. Therm. Eng.* 2004. Vol. 24. Pp. 661–678.
2. Stitou D., Goetz V., Spinner B. A new analytical model for solid – gas thermochemical properties of the reactive medium, *Chem. Eng. Process.* 1997. Vol. 36. Pp. 29–43.
3. Goetz V., Marty A. A model for reversible solid-gas reactions submitted to temperature and pressure constraints: simulation of the rate of reaction in solid-gas reactor used as chemical heat pump // *Chem. Eng. Sci.* 1992. Vol. 47. Pp. 4445–4454.
4. Lepinasse E., Goetz V., Crosat G. Modelling and experimental investigation of a new type of thermochemical transformer based on the coupling of two solid-gas reactions // *Chem. Eng. Process.* 1994. Vol. 33. Pp. 125–134.
5. Lebrun M., Spinner B. Models of heat and mass transfers in solid-gas reactors used as chemical heat pumps // *Chem. Eng. Sci.* 1990. Vol. 45. Pp. 1743–1753.
6. V. Goetz, A solid-gas thermochemical cooling system using BaCl_2 and NiCl_2 // *Energy*. 1997. Vol. 22. Pp. 49–58.
7. Huang H.J., Wu G.B., Yang J., Dai J.C., Yuan W.K., Lu H.B. Modeling of gas-solid chemisorption in chemical heat pumps // *Sep. Purif. Technol.* 2004. Vol. 34. Pp. 191–200.
8. Diawara B., Dufour L.-C., de Hartoulari R. Solid ammonia systems and affinity thermal machines: a kinetic study of the $\text{CaCl}_2\cdot 8\text{NH}_3\text{-NH}_3\text{-CaCl}_2\cdot 4\text{NH}_3$ system // *React. Solid.* 1986. Vol.2. Pp. 73–83.
9. Lebrun M. Simulation for the development of solid—gas chemical heat pump pilot plants, Part II. Simulation and optimization of discontinuous and pseudo-continuous operating cycles // *Chem. Eng. Process.* 1990. Vol. 28 Pp. 67–77.
10. Veselovskaya J.V., Tokarev M.M., Aristov Yu.I. Novel ammonia sorbents "porous matrix modified by active salt" for adsorptive heat transformation: 1. Barium chloride in various matrices // *Appl. Therm. Eng.* 2010. Vol. 30. Pp. 584–589.
11. Touzain Ph. Thermodynamic values of ammonia-salts reactions for chemical sorption heat pumps, // *Proc. of the Int. Sorption Heat Pump Conf., Munich, Germany*, 1999. Pp. 225–238.
12. Veselovskaya J.V., Tokarev M.M. Novel ammonia sorbents "porous matrix modified by active salt" for adsorptive heat transformation: 4. Dynamics on quasi-isobaric sorption and desorption on BaCl_2 /vermiculite // *Appl. Therm. Eng.* 2011. Vol. 31. Pp. 566–572.

13. Veselovskaya J.V., Critoph R.E., Thorpe R.N., Metcalf S., Tokarev M.M., Aristov Yu.I. Novel ammonia sorbents "porous matrix modified by active salt" for adsorptive heat transformation: 3. Testing of "BaCl₂/vermiculite" composite in the lab-scale adsorption chiller // *Appl. Therm. Eng.* 2010. Vol. 30. Pp. 1188–1192.
14. Glaznev I.S., Aristov Yu.I. // The effect of cycle boundary conditions and adsorbent grain size on the water sorption dynamics in adsorption chillers // *Int. J. of Heat and Mass Transfer*. 2010. Vol. 53. Pp. 1893–1898.
15. Gordeeva L.G., Grekova A.D., Krieger T.N., Aristov Yu.I. Binary salt systems – an efficient tool for designing composite sorbents "salt inside porous matrix" // *Proc. of IMPRES 2010, Singapore, 2010*. Pp. 3–10.
16. Soave G. Equilibrium constants from a modified Redlich-Kwong equation of state // *Chem. Eng. Sci.* 1972. Vol. 27. Pp. 1197–1203.

NUMERICAL STUDY OF THERMOACOUSTIC COUPLING IN NEAR-CRITICAL NITROGEN

Peng Zhang, Biao Shen, Ruzhu Wang
Institute of Refrigeration and Cryogenics
Shanghai Jiao Tong University
Shanghai, 200240 China
Tel: +86-21-34205505
Fax: +86-21-34206814
Email: zhangp@sjtu.edu.cn

Abstract

Strong thermoacoustic coupling exists near the liquid-gas critical point, known as the piston effect, due to the exceptionally high compressibility and low thermal diffusivity. Heat is transferred efficiently by means of thermoacoustic waves instead of heat conduction. We carry out a numerical study of both the short-time and long-time thermoacoustic behaviors in near-critical nitrogen, using the explicit MacCormack-FCT method and the finite volume-based SIMPLE algorithm, respectively. Two contributing factors in the generation of thermoacoustic waves are identified and examined, namely, the rapidity of the external heating and the inherent thermophysical properties of the fluid. The wave pattern changes significantly under their influences, which involves various complex implications. At an isothermal boundary, the reflection of a thermoacoustic pulse might create "cold spots" in the extreme case of impulsive heating. The results obtained over four decades of reduced temperatures along the critical isochore suggest the nonlinear waveform distortions in connection with the initial criticality to be of a transient nature. On a much longer timescale, the lasting effect of the thermoacoustic process helps trigger thermal plumes under gravity, which then leads to hydrodynamic instability.

KEYWORDS

Thermoacoustic waves; Piston effect; Thermal plumes; Hydrodynamic instability; Numerical simulation.

INTRODUCTION

Near the liquid-gas critical point (CP), fluid properties experience dramatic changes. Strong divergence is expected of the isothermal compressibility κ_T , the isobaric thermal-expansion coefficient α_p , and the specific heat at constant pressure C_p . The resulting vanishingly low thermal diffusivity D prompted the assumption of a critical slowing down, which predicts that it could become increasingly difficult for heat to dissipate through conduction when approaching the CP. However, a micro-gravity experiment performed with confined near-critical SF_6 produced puzzling results of extremely fast thermalization. Several groups independently proposed the theory of piston effect (PE) to explain the unusual anomaly [1–3]. Driven by thermoacoustic wave motion on the acoustic timescale (denoted by $t_a = L/c$, with L the characteristic length, and c the sound velocity), the PE causes adiabatic and homogeneous temperature changes in the bulk of the fluid, whereas thermal diffusion is largely limited inside thin thermal boundary layers. On a much longer timescale, the thermal and mechanical equilibration is dominated by the interplay between the PE and

gravity-induced natural convection. The excess of entropy accumulating near the heated boundary can rise up under gravity in the form of thermal plumes [4, 5].

In this paper, we present a numerical study of the thermoacoustic effect in nitrogen near its CP. The generations of both thermoacoustic waves on the short timescale and thermal plumes under gravity on the long timescale are investigated, with some interesting features revealed.

THERMOACOUSTIC BEHAVIOR ON THE SHORT TIMESCALE

Mathematical formulation

The thermoacoustic effect near the CP can be modeled by the complete Navier-Stokes description for an isotropic, Newtonian, compressible, and dissipative (viscous and heat-conducting) fluid. For a one-dimensional (1D) configuration, the governing equations are given as

$$\frac{\partial \rho}{\partial t} + \frac{\partial}{\partial x}(\rho u) = 0, \quad (1)$$

$$\frac{\partial}{\partial t}(\rho u) + \frac{\partial}{\partial x}(\rho u^2) = \frac{\partial}{\partial x} \left(\frac{4}{3} \eta \frac{\partial u}{\partial x} \right) - \frac{\partial P}{\partial x}, \quad (2)$$

$$\frac{\partial}{\partial t}(\rho C_V T) + \frac{\partial}{\partial x}(\rho C_V T u) = \frac{\partial}{\partial x} \left(\lambda \frac{\partial T}{\partial x} \right) + \frac{\partial}{\partial x} \left(\frac{4}{3} \eta u \frac{\partial u}{\partial x} \right) - \frac{\rho(C_P - C_V)}{\alpha_p} \frac{\partial u}{\partial x}, \quad (3)$$

where η is the shear viscosity, λ is the thermal conductivity, and C_V is the specific heat at constant volume. Equations (1)–(3) describe the evolution of fluid density ρ , velocity u , and temperature T with space variable x and time variable t , respectively. Note that we ignore the effect of gravity for the moment as gravity is of limited importance on the acoustic timescale. To complete the above equations, a real-fluid equation of state has been added, which reads

$$\delta P = \frac{1}{\rho \kappa_T} \delta \rho + \frac{\alpha_p}{\kappa_T} \delta T, \quad (4)$$

relating the change in pressure P with density and temperature variations. We employ the high-order explicit MacCormack-FCT method [6] to solve the equations, combined with a special formulation of boundary conditions proposed by Poinot and Lele [7]. Using the same numerical method [8], we successfully verified the experimental observation of thermoacoustic waves by Miura *et al.* [9]. The following results are obtained on two sets of uniform meshes of size $\Delta x = 5 \cdot 10^{-6}$ and $1 \cdot 10^{-5}$ m, with a matching time-step of $\Delta t = 2 \cdot 10^{-10}$ and $5 \cdot 10^{-9}$ s.

Under various rates of external heating

First we examine the effect of the rapidity of the boundary heating on the generation of thermoacoustic waves. Consider thermally-balanced and motion-free near-critical nitrogen confined in a 1D cell ($L = 10$ mm) bounded by rigid walls. The initial condition is $T_i = 126.5$ K and $P_i = 3.5$ MPa. At $t > 0$, the right wall is kept at the initial temperature, while a time-varying thermal load is imposed at the left boundary in the form of

$$T_L = f(t) = T_i + \Delta T \left[1 - e^{-t/(Ht_a)} \right]. \quad (5)$$

In eq. (5), ΔT is 10 mK, and H denotes the rate of temperature rise. The impulsive heating corresponds with $H = 0$. With larger H , the heating becomes more gradual and smooth. In Fig. 1, we plot the boundary pressure variations during the first 50 μs since the heating starts, under different H values. For $H = 0$, the violent pressure surge is quickly resolved within only several microseconds, which indicates particularly strong yet transient boundary layer expansion. As H increases, more stable pressure buildups emerge at the boundary while the continuous expansion of the thermal boundary layer is being maintained by the gentler heating.

The local pressure fluctuations at the boundary emit thermoacoustic waves, whose propagation in the fluid is depicted in Fig. 2. Under the impulsive heating ($H = 0$), the transient pressure oscillation at the boundary (see Fig. 1) creates a thermoacoustic pulse, which imposes successive compressive (due to the rising edge of the pulse) and expansive (due to the falling edge of the pulse) effects on the local fluid as it travels. By analogy, the solely compressive nature of the thermoacoustic wave for $H = 100$ is evidenced in the plateau waveform, as the figure shows. The steady boundary pressure gradient (see Fig. 1) gives rise to the continuous expansion of the boundary layer, which in turn compresses the rest of the fluid.

Figure 3 shows the reflection patterns at the right boundary with $H = 0$ and 100, respectively. It is interesting to note that a singular temperature “dip” appears near the boundary after the reflection of the thermoacoustic pulse [Fig. 3 a], which can be explained through the bifurcation of the waveform. When the pulse first arrives at the isothermal wall, a heat outflow is required by the first law of thermodynamics to balance the effect of the incoming fluid due to the strong compression. Similarly, during the expansion, the isothermal boundary demands a heat inflow from the surroundings to counteract the cooling effect caused by the departing fluid so that the local thermodynamic equilibrium can be preserved. Thus, the temperature temporarily drops below the initial value as a result. Since the thermal diffusivity is vanishingly small close to the CP, the relaxation of such temperature inhomogeneities is expected to take a rather long time.

At various initial distances to the CP

Next we turn to the effect of the fluid properties on the thermoacoustic process. The initial condition is given by

$$T(x, t = 0) = T_i = T_c (1 + \varepsilon), \quad P(x, t = 0) = P_i, \quad \rho(x, t = 0) = \rho_i = \rho_c, \quad u(x, t = 0) = 0, \quad (6)$$

where the subscript c represents the critical state ($T_c = 126.192$ K, $\rho_c = 313.3$ kg/m³). The degree of criticality is modeled through the reduced temperature ε , which represents the distance to the CP. We include a wide range of ε from order 10^{-4} to 1 along the critical isochore, with which the thermophysical properties vary considerably. Now consider a constant heat flux $q_b = 100$ W/m² applied at the left end of a 1D slab, while the right boundary maintains thermally insulated.

The boundary heating with a constant heat flux essentially prescribes a nonlinear boundary temperature growth varying as $t^{1/2}$. We plot in Fig. 4 the corresponding boundary pressure variations in response to such a temperature rise. Salient features of nonlinearity associated with ε are present. Because the thermal diffusivity tends to zero close to the CP, the boundary temperature variation is growing increasingly diminished with smaller ε . Consequently, the pressure response becomes gradually dampened. On the other hand, as time elapses, the rate of the temperature increase shows signs of deceleration (as the power law $t^{1/2}$ implies). We find that accordingly the pressure starts to decrease quickly after peaking, which evidently occurs at an earlier

instant the further from the CP. Fig. 5 depicts the spatial profiles of the resulting thermoacoustic waves with different ε values at $t = t_d/2$. The strong nonlinearity exhibited in the boundary pressure relaxation accounts for the apparent waveform variations. For small ε , the slowly varying pressure at the boundary (Fig. 4) produces a smooth wave profile; whereas with large ε , the transient pressure fluctuation (Fig. 4) generates a steep shockwave-like wave shape. The evolution of waveform from the former to the latter with intermediate ε can also be observed in the figure.

Here we define a coefficient of energy efficiency,

$$\zeta = \frac{\Delta E_{bulk}}{Q_{input}} = \frac{\int P \delta \rho / \rho dx}{\int q_b dt}, \quad (7)$$

so as to evaluate the amount of mechanical energy converted from the heat input. Fig. 6 illustrates the distributions of ζ along the critical isochore at different times. We also include the theoretical values based on a linearized model [9] for comparison. We find that a convergence between the numerically obtained ζ and the theoretical prediction slowly emerges as the time goes on. The transient nonlinear effects at all distances to the CP seem to be ultimately smeared out.

INTERACTION WITH GRAVITY-INDUCED CONVECTION

On a long timescale, the thermoacoustic effect can be definitely felt even in the presence of gravity-induced convection. The onset of convection near the CP shows evidence of a crossover from the classical Rayleigh criterion to the Schwarzschild criterion [4-5]. We set to investigate the mechanism of convection very close to the CP in a Rayleigh-Bénard geometry. Specifically, we consider a 2D rectangular cell (of length $L = 10$ mm and height $H = 2.5$ mm) heated from below with a constant heat flux $Q = 1.0$ W/m². The cell is filled with nitrogen at the initial state $T_i = T_c(1+\varepsilon)$ and $\rho_i = \rho_c$ (assuming no severe density stratification). The top wall is maintained at the initial temperature, and both of the side walls are thermally insulated. After introducing non-dimensional variables $\rho^* = \rho/\rho_i$, $P^* = P/P_i$, $T^* = T/T_i$, $u^* = u/U$, $v^* = v/U$, $x^* = x/L$, $y^* = y/L$, $t^* = tU/L$, the conservation equation of mass, momentum, and energy are formulated as,

$$\frac{\partial \rho}{\partial t} + \frac{\partial}{\partial x}(\rho u) + \frac{\partial}{\partial y}(\rho v) = 0, \quad (8)$$

$$\frac{\partial}{\partial t}(\rho u) + \frac{\partial}{\partial x}(\rho uu) + \frac{\partial}{\partial y}(\rho uv) = -\frac{P_i}{\rho_i c^2} \frac{\partial P^{(1)}}{\partial x} + Re^{-1} \left(\frac{4}{3} \frac{\partial^2 u}{\partial x^2} + \frac{\partial^2 u}{\partial y^2} + \frac{1}{3} \frac{\partial^2 v}{\partial x \partial y} \right), \quad (9)$$

$$\frac{\partial}{\partial t}(\rho v) + \frac{\partial}{\partial x}(\rho uv) + \frac{\partial}{\partial y}(\rho vv) = -\frac{P_i}{\rho_i c^2} \frac{\partial P^{(1)}}{\partial y} + Re^{-1} \left(\frac{\partial^2 v}{\partial x^2} + \frac{4}{3} \frac{\partial^2 v}{\partial y^2} + \frac{1}{3} \frac{\partial^2 u}{\partial x \partial y} \right) - \frac{gL}{U^2} \rho, \quad (10)$$

$$\frac{\partial}{\partial t}(\rho T) + \frac{\partial}{\partial x}(\rho u T) + \frac{\partial}{\partial y}(\rho v T) = Pe^{-1} \left(\frac{\partial^2 T}{\partial x^2} + \frac{\partial^2 T}{\partial y^2} \right) + \frac{P_i \kappa_T}{T_i \alpha_p} \left(1 - \frac{1}{\gamma} \right) \rho \frac{dP}{dt}, \quad (11)$$

where the superscripts have been dropped for the sake of brevity. In the above equations, the characteristic fluid velocity is $U = \eta/(\rho_i H)$, the Reynolds number is $Re = \rho_i L U / \eta$, and the Peclét number is $Pe = \rho_i C_p U L / \lambda$. In

deriving the equations, a low Mach-number approximation has been applied to filter out acoustic waves [10]. Note that the high-order pressure term $P^{(1)}$ remains in eqs. (9) and (10), while the leading-order term P regarded as a function of time only contribute to the temperature evolution in eq. (11). The numerical simulation is performed on a staggered uniform grid of 201×101 with the use of the SIMPLE algorithm. The time-step is kept at a constant value of $5 \cdot 10^{-3}$ s.

Shown in Fig. 7 and 8 are the preliminary results obtained for $\varepsilon = 7.92 \cdot 10^{-4}$ and $3.96 \cdot 10^{-2}$, respectively. The generation of convection appears to differ significantly between the two cases. For $\varepsilon = 7.92 \cdot 10^{-4}$, at $t \approx 7.1$ s, the PE results in a homogeneously heated bulk and the formation of thermal boundary layers at both of the bottom and top walls, which seem almost symmetrical. At $t \approx 9.7$ s, first the hot diffusive layer turns unstable, releasing thermal plumes upwards; At $t \approx 11.4$ s, the rising thermal plumes appear to have disintegrated halfway through the fluid layer, while the cold diffusive layer starts to exhibit instability and downward Rayleigh-Taylor-type thermal plumes are visible [11]. Due to the resulting cooling PE, the bulk temperature decreases [see Fig. 7 b]. At $t \approx 13.6$ s, a strong thermal mixing seems to dominate at the center of the cell, which would lead to a final equilibrium state. By contrast, for $\varepsilon = 3.96 \cdot 10^{-2}$, huge thermal plumes are generated from the hot diffusive layer as shown in Fig. 8, while no plume-type flow can be observed at the cold end. Apparently, the local temperature difference within the top boundary layer is considerably smaller than that within the hot boundary layer, owing to the weaker PE relatively far from the CP. As a result, the bulk temperature does not seem to be affected by the cooling PE until the thermal plumes reach the top wall around $t \approx 13.8$ s [see Fig. 8 b].

CONCLUSIONS

We have conducted a numerical study aimed at exploring the thermoacoustic features in energy transport near the CP both on a short timescale and on a long timescale. The simulations describe the generation of thermoacoustic waves and the onset of thermal plumes in near-critical nitrogen, which have been found to be strongly influenced by various external and internal factors.

Acknowledgments

This research is supported by the National Natural Science Foundation of China under Contract No. 50976068. Biao Shen acknowledges financial support by the Scholarship Award for Excellent Doctoral Student granted by Ministry of Education.

References

1. Onuki A., Hao H., Ferrel R. Fast adiabatic equilibration in a single-component fluid near the liquid-vapor critical point // *Physical Review A*. 1990. Vol. 41. Pp. 2256–2259.
2. Boukari H., Shaumeyer J., Briggs M., Gammon R. Critical speeding up in pure fluids // *Physical Review A*. 1990. Vol. 41. Pp. 2260–2263.
3. Zappoli B., Bailly D., Garrabos Y., Neindre B. Le, Guenoun P., Beysens D. Anomalous heat transport by the piston effect in supercritical fluids under zero gravity // *Physical Review A*. 1990. Vol. 41. Pp. 2264–2267. – 144301.
4. Chiwata Y., Onuki A. Thermal plumes and convection in highly compressible fluids // *Physical Review Letters*. 2001. Vol. 87.

5. Amiroudine S., Zappoli B. Piston-effect-induced thermal oscillations at the Rayleigh-Bénard threshold in supercritical ^3He // *Physical Review Letters*. 2003. Vol. 90. – 105303.
6. Fletcher C. A. J. *Computational technique for fluid dynamics*. Berlin: Springer-Verlag. Vol. II, 1988.
7. Poinsot T. J., Lele S. K. Boundary conditions for direct simulations of compressible viscous flows // *J. of Computational Physics*. 1992. Vol. 101. Pp. 104–129.
8. Zhang P., Shen B. Thermoacoustic wave propagation and reflection near the liquid-gas critical point // *Physical Review E*. 2009. Vol. 79. 060103(R).
9. Miura Y., Yoshihara S., Ohnishi M., Honda K., Matsumoto M., Kawai J., Ishikawa M., Kobayashi H., Onuki A. High-speed observation of the piston effect near the gas-liquid critical point // *Physical Review E*. 2006. Vol. 74. 010101(R).
10. Paolucci S. On the filtering of sound from the Navier-Stokes equations, SAND 92-8257, Livermore, CA, 1982. Pp. 3–22.
11. Amiroudine S., Bontoux P., Larroudé P., Gilly B., Zappoli. Direct numerical simulation of instabilities in a two-dimensional near-critical fluid layer heated from below // *J. of Fluid Mechanics*. 2001. Vol. 442. Pp. 119–140.

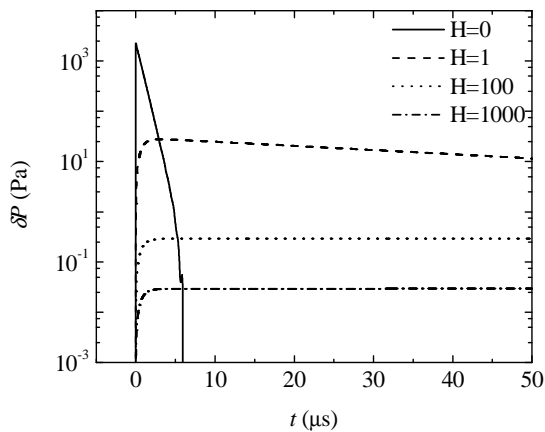


Fig. 1. Pressure variations at the left wall for different heating parameters H on a semi-log scale. As H increases, the pressure surge at the boundary becomes more stable

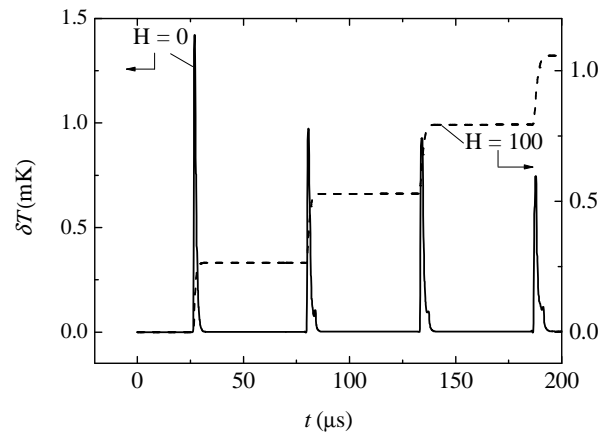


Fig. 2. Temperature evolutions at the cell center $x = L/2$, for $H = 0$ and $H = 100$

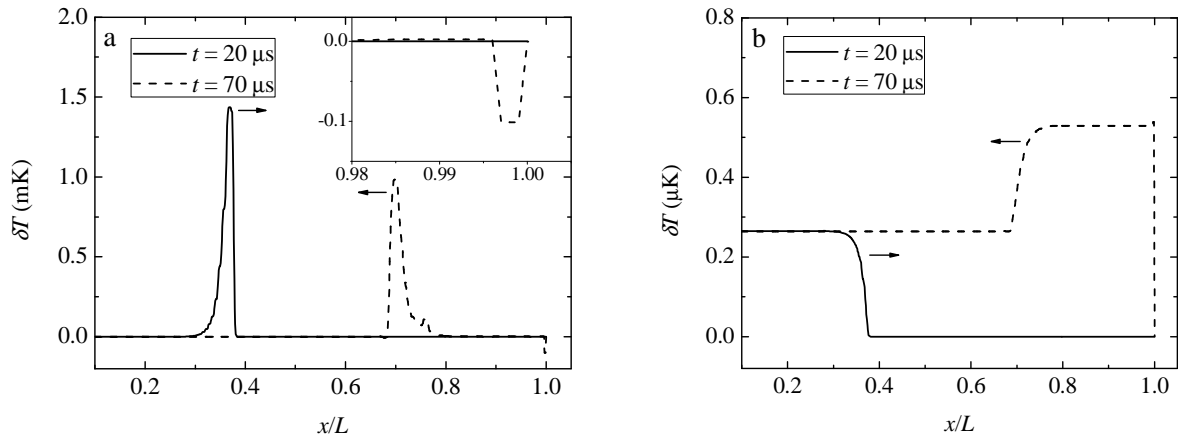


Fig. 3. Reflection patterns of thermoacoustic waves at the isothermal right boundary for (a) $H = 0$, and (b) $H = 100$. In (a), there seems to be a “dip” right next to the cold boundary after the reflection. The arrows indicate the direction of the wave propagation. The horizontal axes have been scaled by L

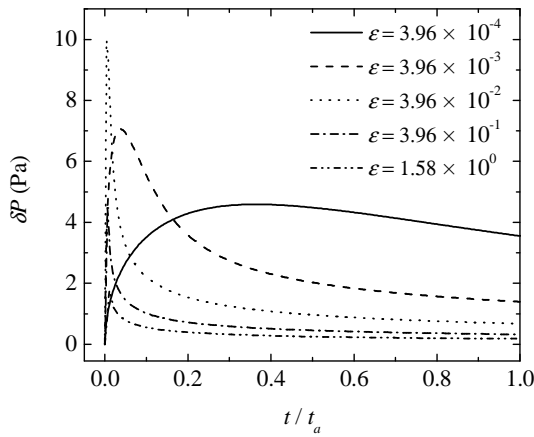


Fig. 4. Pressure variations at the left wall for different reduced temperatures ε . The horizontal axis has been normalized by $t_a = L/c$. Strong nonlinear effects are present

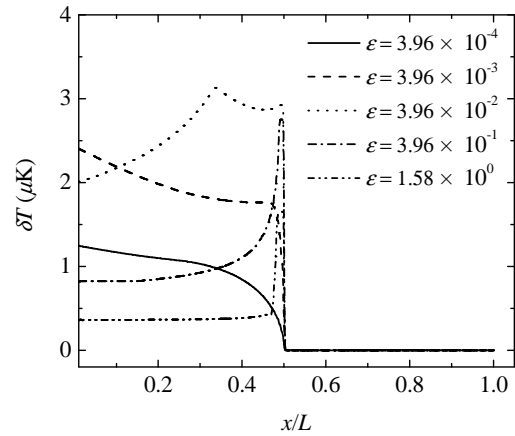


Fig. 5. Temperature profiles at $t = t_a/2$ for different reduced temperatures ε . The horizontal axis has been scaled by L

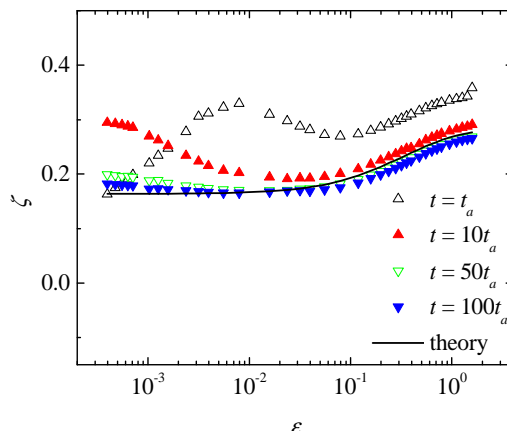


Fig. 6. Time evolution of the energy efficiency ζ versus reduced temperature ε . The results are presented on a semi-log scale. As time passes, a convergence between the calculations and the theoretical values begins to emerge

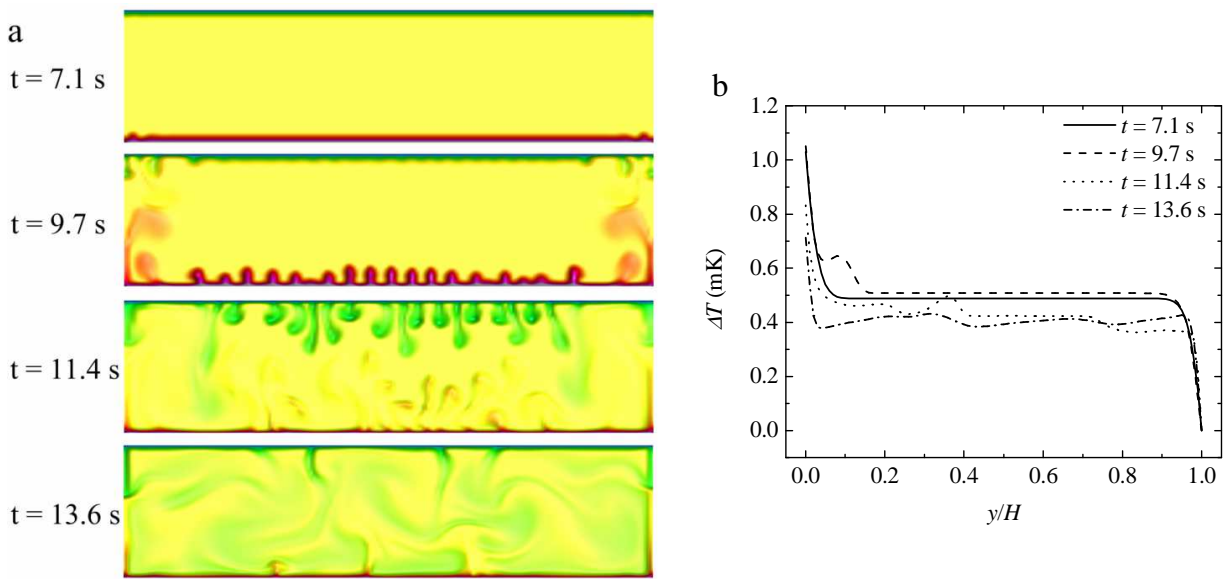


Fig. 7. Onset of convection at $\varepsilon = 7.92 \cdot 10^{-4}$. (a) Two-dimensional temperature distribution at various times. Both the top and bottom boundary layers exhibit increasing instability. (b) Corresponding vertical temperature differences across the cell $x/L = 0.5$. After the initiation of thermal plumes at the cold end, the bulk temperature drops due to the cooling PE

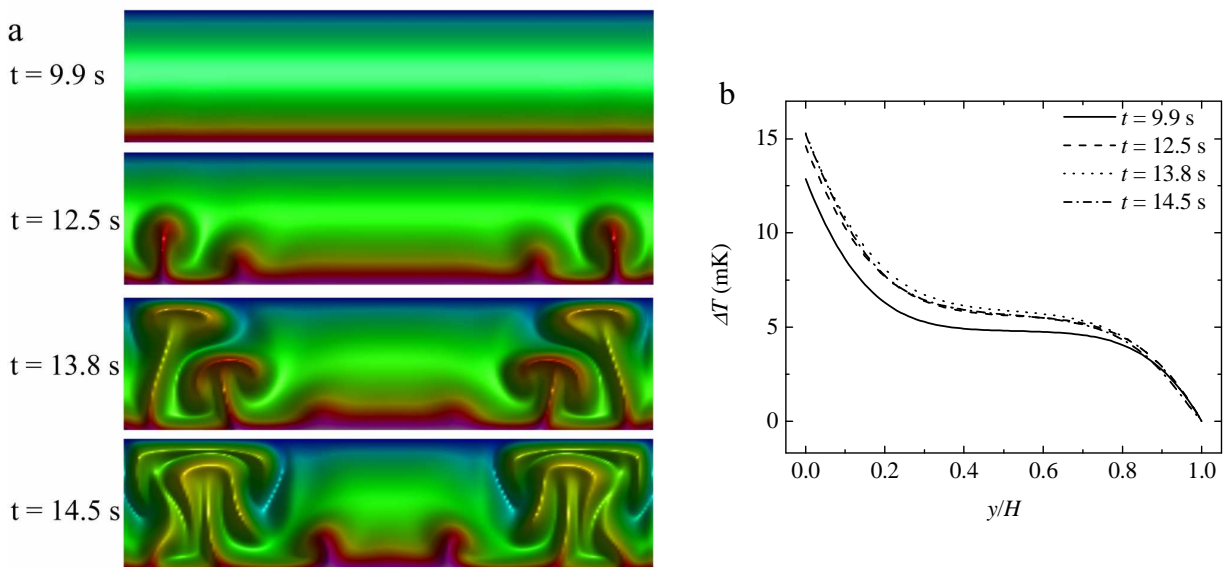


Fig. 8. Onset of convection at $\varepsilon = 3.96 \cdot 10^{-2}$. (a) Two-dimensional temperature distribution at various times. Thermal plumes rise up from the bottom end. (b) Corresponding vertical temperature differences across the cell at $x/L = 0.5$. The bulk temperature decreases after the ascending thermal plumes arrive at the top end

APPLICATION OF ULTRA HIGH MODULAR THERMAL CONDUCTIVE CARBON PLASTIC IN THE DESIGN OF THERMAL HONEYCOMB PANELS

A. Khmel'nitsky

Research and Production Enterprise "Technologiya"
Obninsk, Kaluga region, Russia

K. Goncharov

TAIS Ltd., Khimky, Moscow region, Russia

Results of application of carbon plastic skins made of ultra high modular thermal conductive carbon fibers and used for the development of thermal panels with Aluminum embedded heat pipes are presented in this paper.

Due to different thermal expansion coefficient values of carbon plastic skins and metallic embedded elements, the main problem to be solved when designing thermal honeycomb panels with carbon plastic skins and metallic embedded elements is providing of effective and stable mechanical and thermal interface between the skins and embedded elements.

After choice of skin material and determination of skin design the skin was optimized by carrying out its structural and thermal calculations taking into account the requirements to panel manufacturability.

Numerous specimens were investigated for estimation of skin composite materials characteristics. Material with thermal expansion coefficient in one direction close to the value of thermal expansion coefficient of Aluminum alloys was developed. Calculation results show that skins made of carbon plastic have advantageous stiffness and weight parameters in comparison with Aluminum skins.

Analytical results determine configuration of thermal panel for space application that mostly meet wide range of constructive and thermal requirements. Such panel consists of carbon plastic skins, Aluminum honeycombs and Aluminum embedded heat pipes.

Application of traditional carbon fillers together with carbon plastic skins is unacceptable due to their negligibly small thermal conductivity. However, new composite materials developed during last years have advanced constructive parameters and high thermal parameters as well. For example, thermal conductivity of carbon plastics reinforced by mono crystal carbon fibers with thermal conductivity more than 1100 W/(m·K) is more than 400 W/(m·K). Thus, traditional opinion on poor thermal conductivity of plastic panels reinforced by carbon fibers is not correct now.

First demonstration engineering panel was developed, manufactured and successfully tested in Russia. There was carried out checking of thermal conductivity and constructive operation ability of demonstration engineering panel when thermal cycling. Different samples of honeycomb panel with carbon plastic skins passed tests for lap shear strength, flexural strength, flatwise strength, mass loss when degassing, determination of thermal and mechanical parameters.

After choice of optimum design, experimental specimen of thermal panel with dimensions 1900×900 mm was manufactured. The specimen passed thermal vacuum tests and mechanical tests for static load. Mass of experimental thermal panel with carbon plastic skins is less by 1.5 kg (20%) in comparison with its metallic analogue. It can be assumed that for the panels with smaller dimensions mass effectiveness will be substantially higher as mass part of metallic carcass of small panels is substantially higher.

Specially manufactured sample of thermal panel with carbon plastic skins with the same dimensions and design (Fig. 1) successfully passed thermal cycling (50 cycles in the temperature range from minus 20 °C to plus 60 °C and one cycle in the temperature range from minus 40 °C to plus 80 °C). Temperature measurements were done at the skin surface nearby heat pipes. There was not detected deterioration of gluing joint (carbon skin/ heat pipes) that proves reliability of manufacturing method and possibility of using epoxy glues with specific mass less than 100 g/m².

Carbon plastic skins that twice exceed aluminum skins in thermal conductivity and twice less in mass

were developed. Task of carbon plastic skins compatibility with aluminum embedded heat pipes and load-bearing elements was solved.

Thermal panels with carbon plastic skins of high thermal conductivity allow lighten honeycomb panels by 20% and are recommended for use in the structures of perspective spacecrafts.

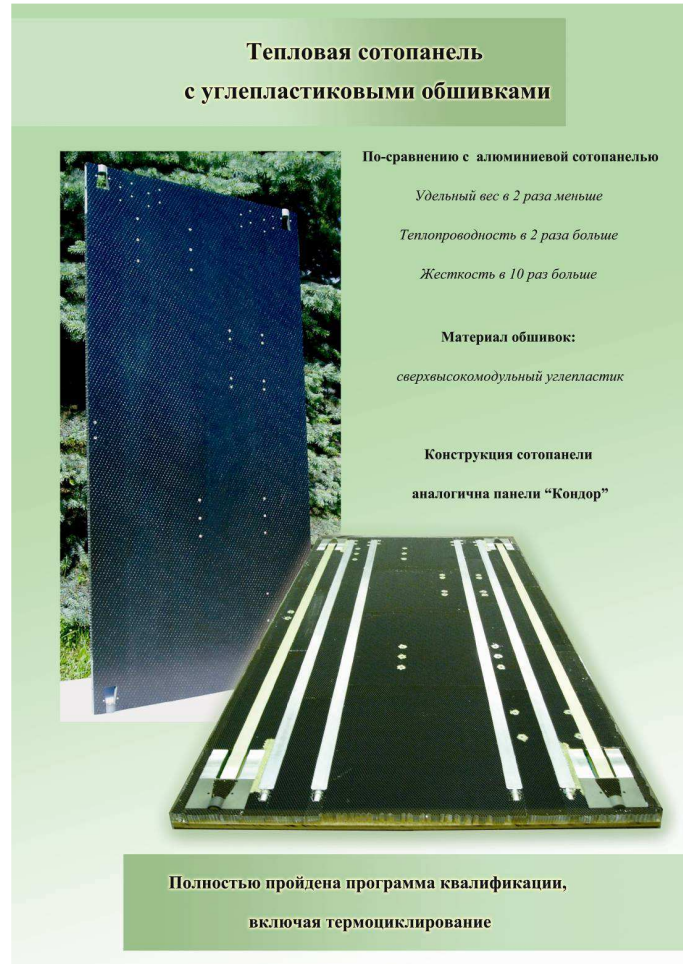


Fig. 1. Thermal honeycomb panel with carbon plastic skins

CONTINUOUS OPERATING EXPERIENCE OF NICKEL-HYDROGEN STORAGE BATTERIES 18NH-100 WITH INDEPENDENT THERMAL CONTROL SYSTEM USING HEAT PIPES WITHIN SPACECRAFT "YAMAL-200"

V.Y. Lapshin, Y.M. Shevchenko (JSC «Saturn», 6, Solnechnaya Str., 350072, Krasnodar, Russia
e-mail: ikc@zit.kuban.ru; Phone: (861) 252-39-90; Fax: (861) 252-39-73, 252-39-43)

K.A. Goncharov (TzTT NPO named after S.A. Lavochkin, 24 Leningradskoye road, city of Khimky,
Moscow region, Russia, Phone/Fax (495) 573-63-74; e-mail: heatpipe@berc.rssi.ru)

G.V. Noskin, O.V. Surguchev, A.P. Elchin (RKK "Energia", 4a, Lenina Str., Korolev, Moscow region,
141070, Russia)

Abstract

Application of heat pipes (HP) for thermal control system (TCS) of nickel-hydrogen storage battery (NHSB) used in spacecraft (S/C) improves mass characteristics both of NHSB and TCS, and makes possible different modifications of S/C assembly. Heat transport organization from NHSB directly by means of HP is provided in S/C «Yamal-200», «BelKA», «KazSat-2» and in NHSB 17NH-95. There have been shown stability of TCS work and charge-discharge characteristics during continuous operation of S/C «Yamal-200».

KEYWORDS

Heat pipes, nickel-hydrogen storage battery, spacecraft, thermal control system.

INTRODUCTION

Temperature range of NHSB operation, providing optimal combination of high energy and life time characteristics, is from 0 to 15 °C. At the same time most of the S/C equipment operates at ambient temperature. Autonomous TCS is used more and more frequently to create comfortable thermal conditions for NHSB operation.

Heat pipes application expanded the possibilities of heat transport organization and made it possible to select the most optimal scheme for the given conditions. The most comfortable temperature conditions during continuous operation allowed to obtain the stability of charge-discharge characteristics.

Variants of autonomous TCS for NHSB

TCS of NHSB has an effect not only on thermal conditions of the battery, which ensures optimal charge-discharge characteristics, but on its design, and as a consequence on energy density, which is one of the main characteristics of the storage batteries used in S/C.

Among different variants of autonomous TCS design for NHSB we will consider the two basic ones:

1) traditional variant used in S/C "KazSat", where heat released from NHS goes to the bottom of the NHSB body and then to the radiator mounted directly on the bottom (fig. 1a);

2) variant used in S/C "Yamal-200", where heat released from NHS goes to the perimeter of NHSB body to the axial grooved heat pipes and then through the loop heat pipes it goes to the radiator (fig. 1b).

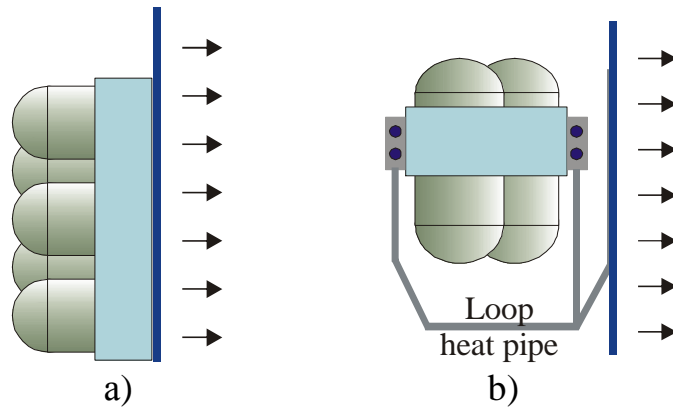


Fig. 1. Heat transport schemes for NHSB in S/Cs «KazSat» and «Yamal -200»

In the first variant thermal control is accomplished by heaters, located close to radiator.

In the second variant thermal control, according to the basic scheme, is provided automatically by pressure regulator in loop heat pipes (this regulator is adjusted for the required temperature during manufacturing) or according to the reserve scheme by heating and/or cooling of corresponding elements of loop HP. Thus the reliability of TCS rises and energy balance of S/C becomes economical.

Advantages of axial heat pipes application

One of the main characteristics of NHSB is energy density – ratio of accumulated energy volume to mass.

Application of heat pipes located along the NHSB perimeter (variant 2) allows to make radial heat transport to the perimeter of NHSB housing and decrease noticeably its mass by “cutting off” its bottom. This is illustrated in Figure 2. At radial heat transport NHSB height is equal to the height of electrodes’ stack – heat-generating part of NHC. In case of axial heat transport to the bottom of NHSB – housing height increases.

Furthermore, the advantage of radial heat transport is the relatively small length of current collectors from electrodes’ stack to terminals, located at the top (Figure 2). Apart from mass saving this decreases internal resistance and, consequently, decreases heat generation and increases energy storage. In its turn lower heat generation requires smaller radiator area.

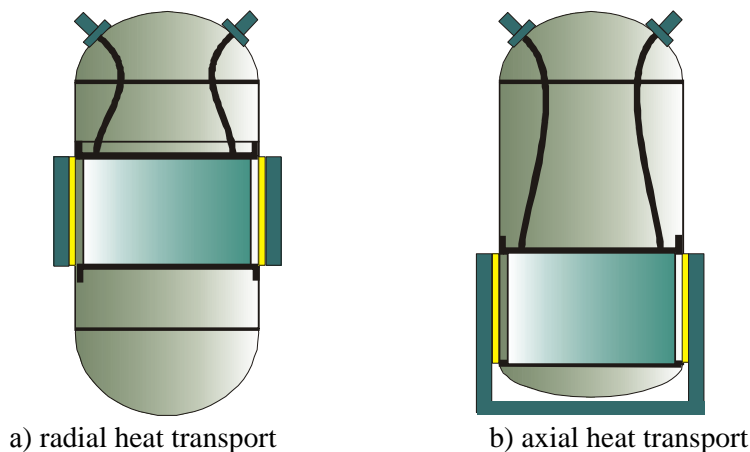


Fig. 2. Current collection dependence on heat transport

Eventually advantages of heat pipes application outbalance their drawback – additional mass.

Advantages of loop heat pipes application

In case, when spacecraft configuration does not allow installing NHSB in close proximity to radiator, heat pickup from NHSB may be accomplished either by means of fluid cooling, or by means of heat pipes.

Fluid cooling is feasible, if common TCS ensures thermal conditions for all the equipment of the S/C. For autonomous TCS fluidal path with hydraulic pump will load it impermissibly. Therefore, in case, when NHSB and its radiator are separated in space, the most acceptable option is to use heat pipes, especially loop ones, like it is implemented in S/C «Yamal-200» and «BelKA» (Figure 1 b), and is foreseen to be used in the development of NHSB and TCS for the People's Republic of China.

As soon as loop heat pipes may be rather long, thin and flexible, NHSB may be located in any suitable place, independent of radiator location.

Besides, loop heat pipes have lower mass as compared to the other ones.

The other advantage of loop heat pipes is the possibility of thermal resistance regulation. This fact makes it possible to exclude from TCS powerful heaters, which are used in other schemes for maintaining the required temperature at small loads, and, consequently, at small heat-generation.

NHSB 18NH-100 with autonomous TCS with axial and loop heat pipes

NHSB 18NH-100 is shown on Figure 3. Axial U-type HP is installed along the perimeter of NHSB housing. To increase reliability it consists of two parallel loops. At the ends of axial HP there are places for loop HP evaporators' installation (are protected by red covers for transportation).



Fig. 3. NHSB 18NH-100 for S/C «Yamal-200»

The scheme of the autonomous TCS is shown in Figure 4, and its performance principles – in Figure 5.

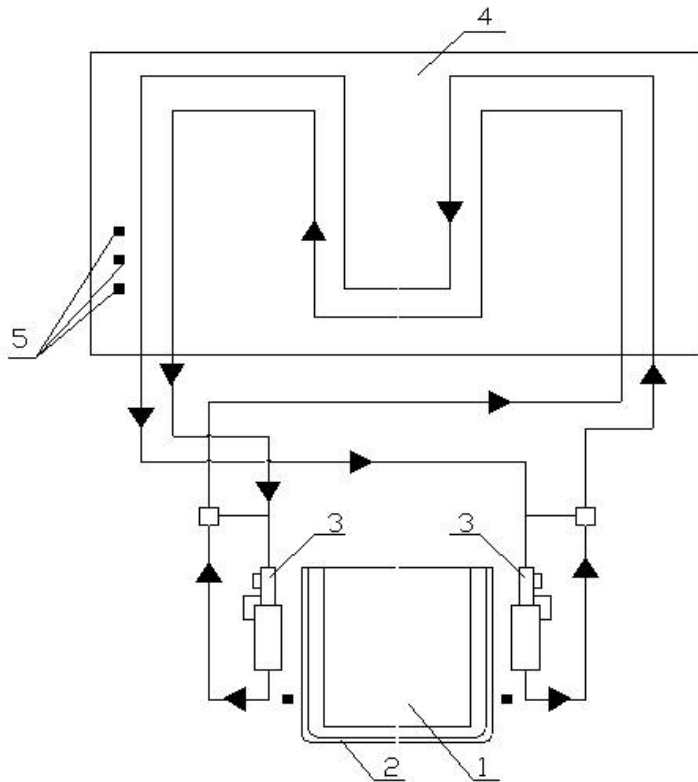


Fig. 4. NHSB 18NH-100 scheme with autonomous TCS (1 - NHSB, 2 – axial HP, 3 – loop HP, 4 - Radiator, 5 - Thermal sensors)

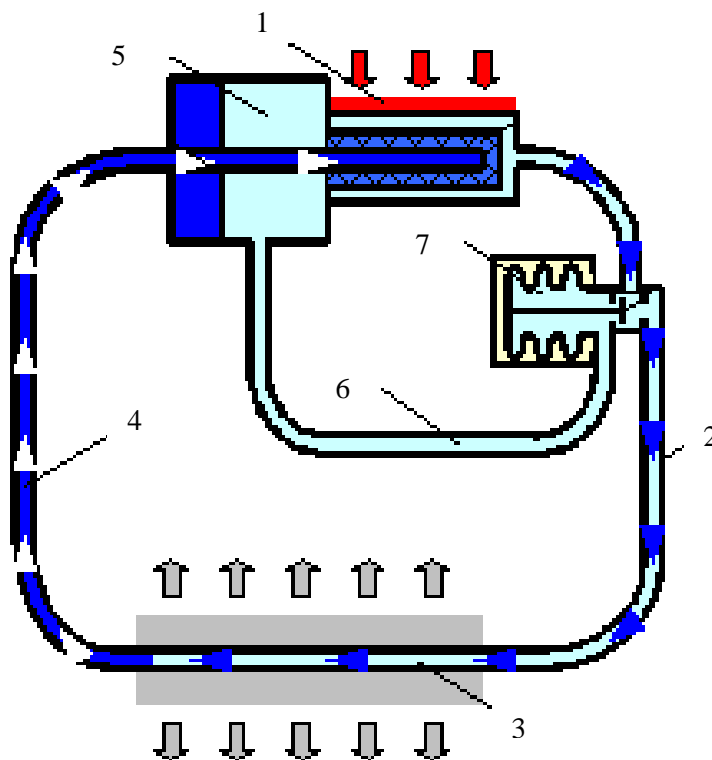


Fig. 5 – Principles of loop HP operation (1 – evaporator; 2 – vapor line; 3 – condenser; 4 – condenser line; 5 – reservoir; 6 - bypass; 7 – pressure regulator)

Automatic thermal control is provided by pressure regulator.

In case when NHSB temperature is higher than the adjusted temperature, the pressure in reservoir rises and moves the stock, which opens vapor line and closes bypass line, and the whole heat current flows to the radiator.

In case when NHSB temperature is lower than the adjusted temperature, the vapor line closes and bypass line opens. At that heat current across the radiator decreases, and NHSB temperature increases.

For the active management of loop HP a heater is installed on the compensatory reservoir, and Peltier cooling element –between the reservoir and evaporator.

The thermal control is made according to the following scheme. In case NHSB temperature is lower than the adjusted temperature a signal appears to turn on the compensatory reservoir heater. At that difference in vapor pressure between compensatory reservoir and evaporator decreases, and circulation inside the loop stops.

In case NHSB temperature is higher than the adjusted temperature, the heater is turned off by a command, and circulation inside the loop is renewed.

For guaranteed startup of loop HP and its active management Peltier cooling elements are used. Peltier cooling elements are installed on the evaporator by hot solder. Thermal bus is fixed to the cold solder of Peltier cooling elements, connecting it to the compensatory reservoir housing.

When direct voltage is applied to Peltier cooling elements, they start to heat evaporator basement and cool the housing of compensatory reservoir. At that the difference in vapor pressure between evaporator and compensatory reservoir increases, and circulation inside the loop stops.

In case of reverse voltage in Peltier cooling elements, the evaporator is cooling and compensatory reservoir is heating. The difference in vapor pressure between evaporator and compensatory reservoir decreases and circulation inside the loop stops.

Continuous operating experience of NHSB 18NH-100 within S/C «Yamal-200»

The launch of two «Yamal-200» S/Cs took place on November 24, 2003. Each S/C has two NHSBs with independent TCS, in which two types of HPs are applied: axial and loop ones.

The telemetry information on NHSB temperature and pressure during operation in flight is shown in Figures 8 – 11.

The hydrogen pressure in NHC, generating at charge, is proportional to charge capacity, so difference between maximum and minimum pressure in test-recovery cycles (TRC) characterizes NHSB total capacity.

The stability of NHSB thermal control and capacity one can see in comparison of temperature and pressure telemetry of TRC in 2004 and 2011. The comparison of these characteristics is also represented in the table below.

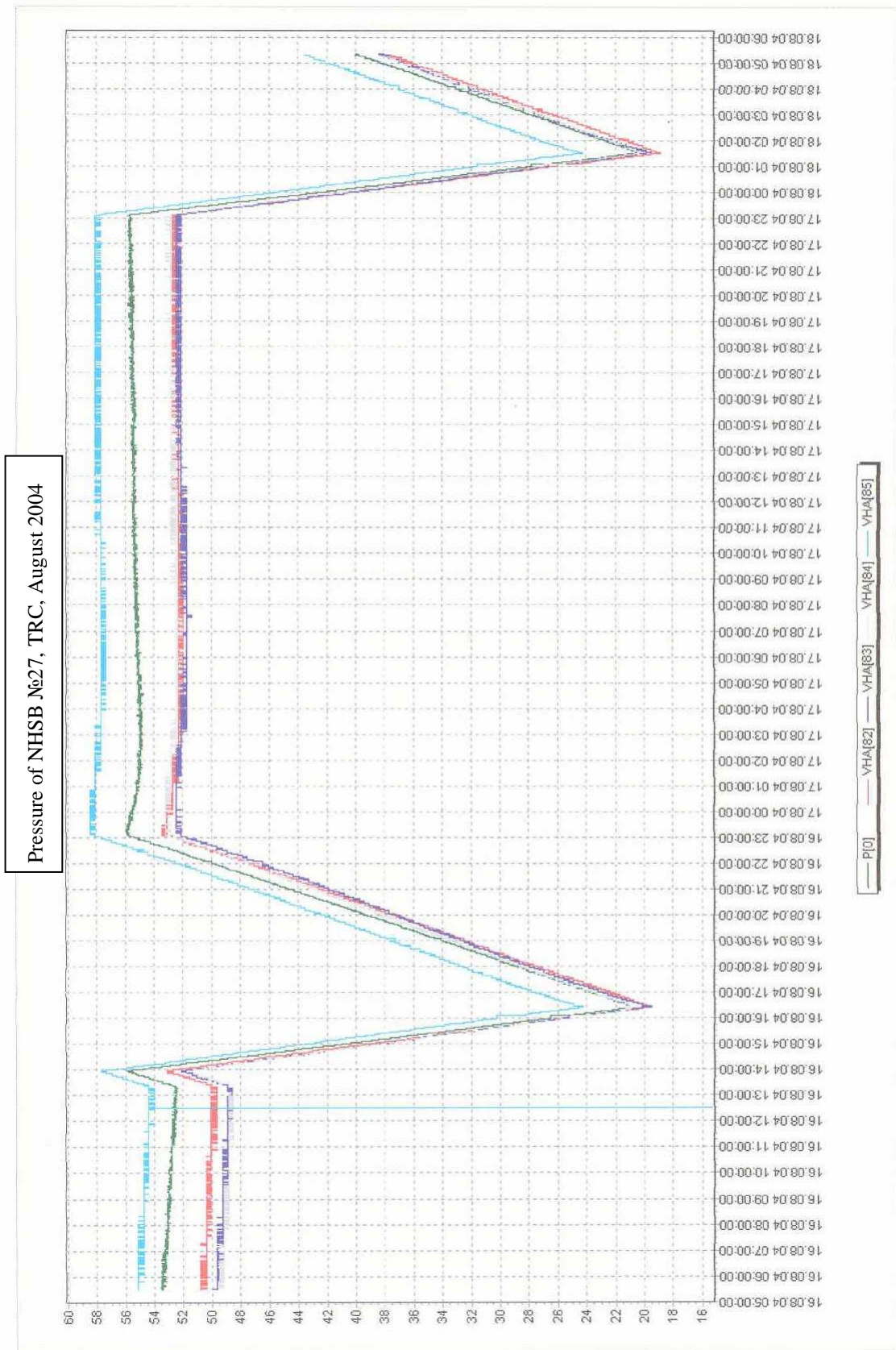


Fig. 6. Telemetry of NHSB № 27, TRC, August 2004

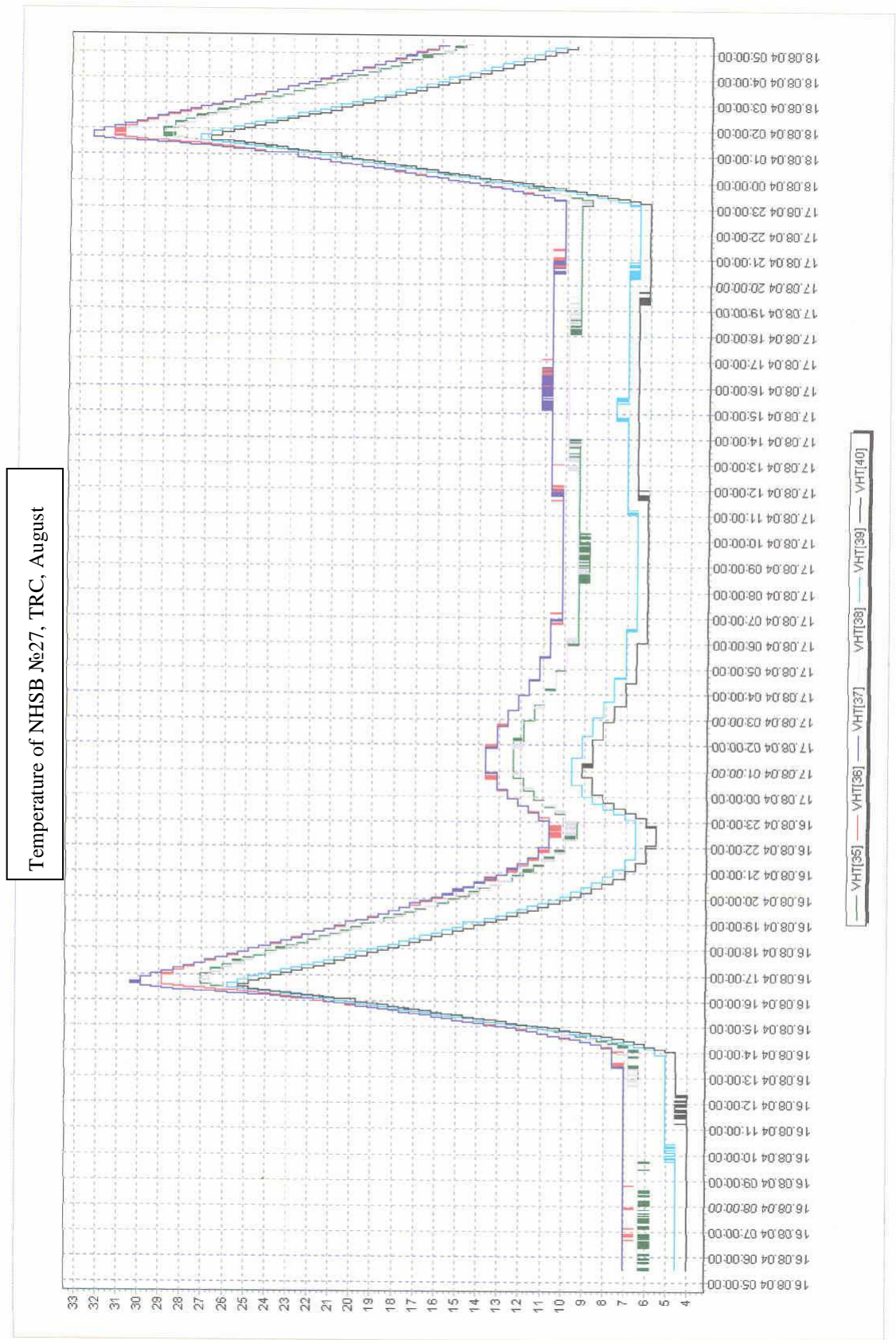


Fig. 7. Telemetry of NHSB № 27, TRC, August 2004

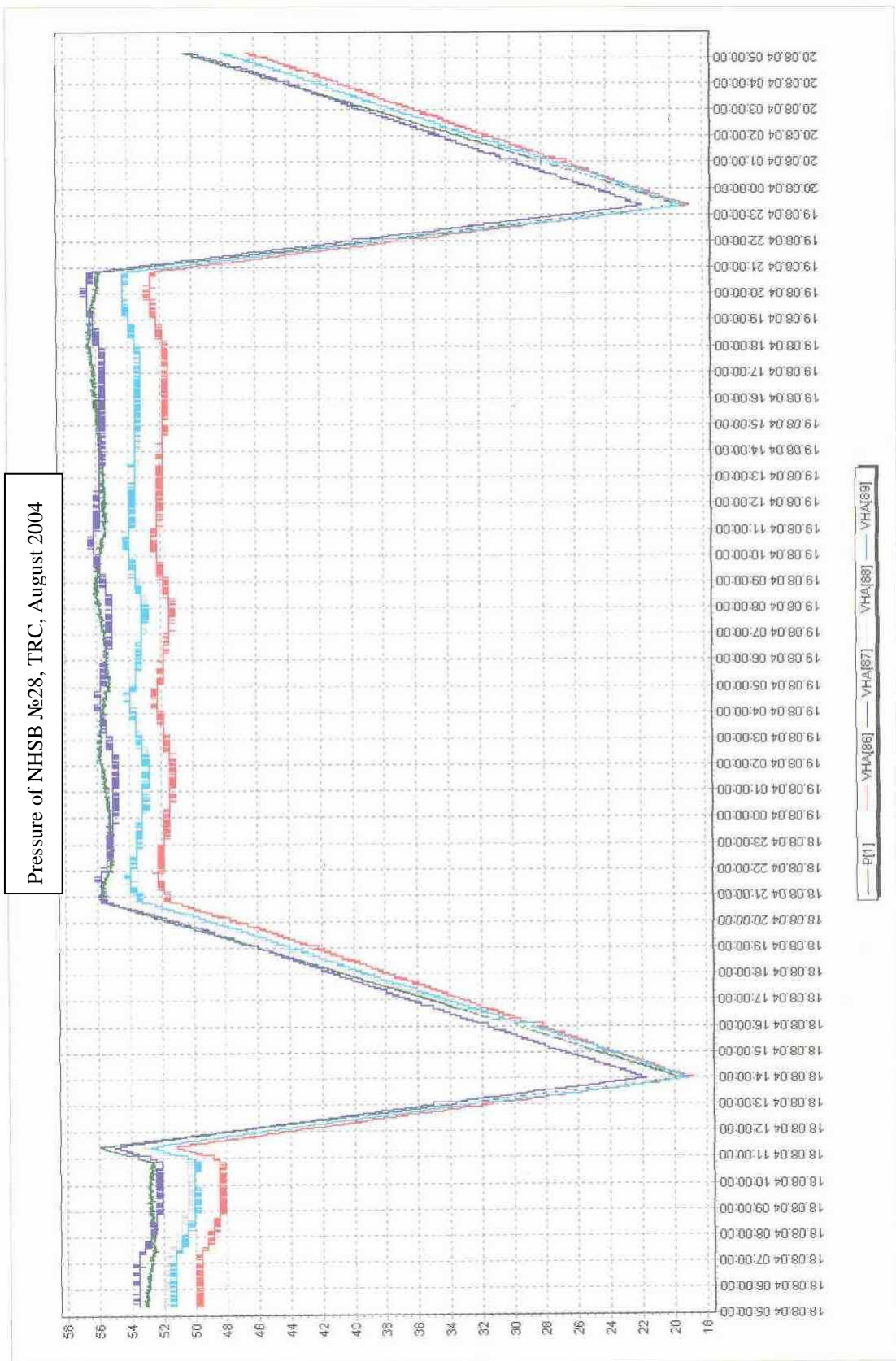


Fig. 8. Telemetry of NHSB № 28, TRC, August 2004

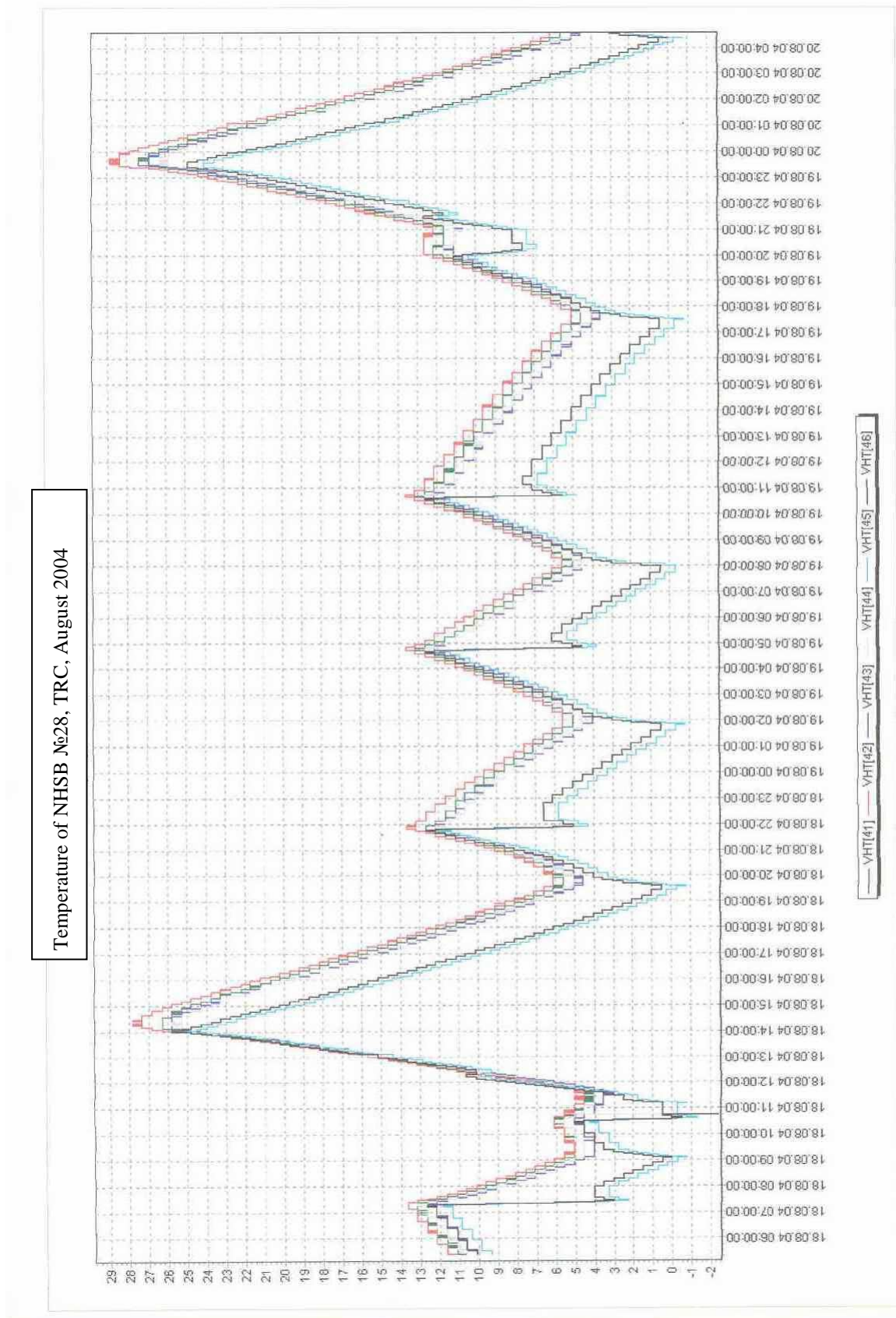


Fig. 9. Telemetry of NHSB № 28, TRC, August 2004

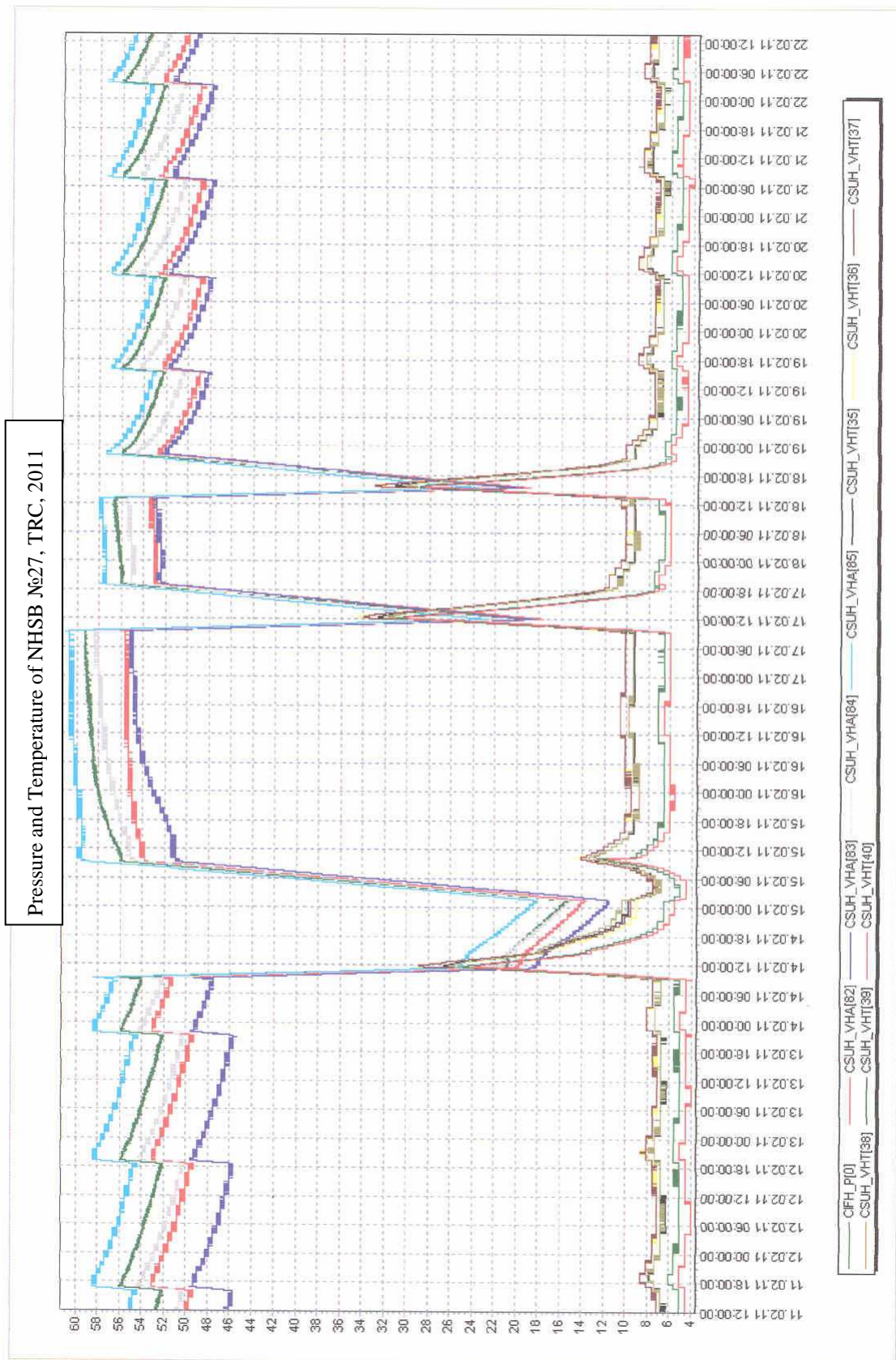


Fig. 10. Telemetry of NHSB № 27, TRC, February 2011

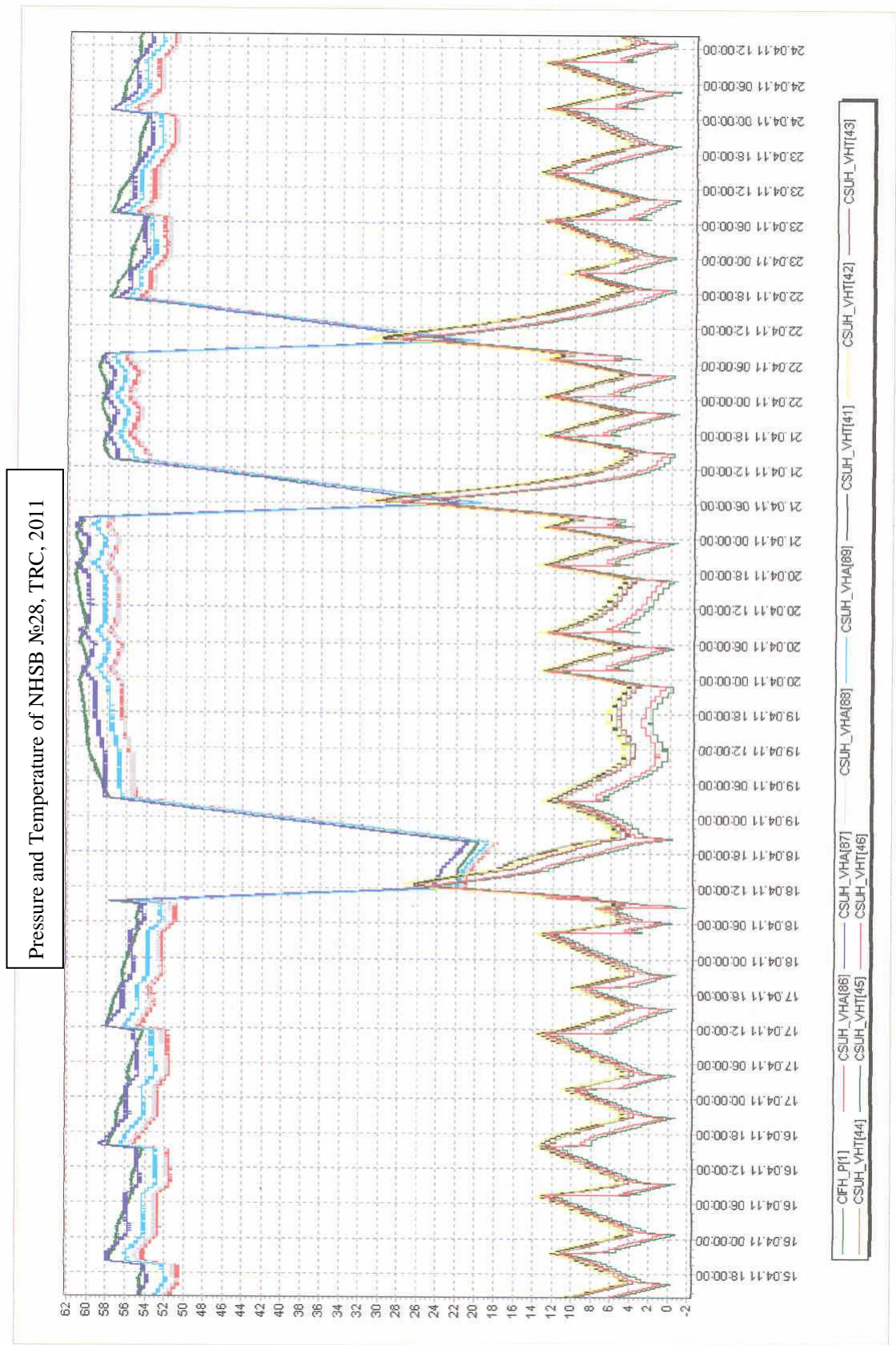


Fig. 11. Telemetry of NHSB № 28, TRC, February 2011

Table

Telemetry	NHSB	TRC in August 2004	TRC in February 2011
End of charge (EOC) temperature, °C	№ 27	8±2	8±2
	№ 28	6±7	7±7
Pressure difference in test cycle, atm	№ 27	33±1	33±1
	№ 28	33±1	33±1
Pressure difference in recovery cycle, atm	№ 27	35±1	39±1
	№ 28	34±0,5	39±1

SB heating at charge, when heat generation capacity exceeds that of TCS more than by order, is not considered in the analysis as discharge duration is small and SB temperature in the end of discharge is within operation range. Further follows cooling and maintenance of SB EOC temperature in the given range.

Analyzing telemetry data it should be taken into account that thermal control of SB №27 was made automatically by pressure regulator with accuracy to $\pm 2^{\circ}\text{C}$, and that of SB №28 – by means of heating and/or cooling of compensatory reservoir and evaporator. Due to inertance of this thermal control method the accuracy of SB temperature maintenance is $\pm 7^{\circ}\text{C}$.

As can be seen in the telemetry thermal control in the process of continuous autonomous operation is effected with high reliability – stability of the given temperature mode maintenance both in the main and bypass schemes of thermal control has been demonstrated.

NHSB discharge capacity also demonstrates stability – difference between maximum and minimum pressures in test cycles does not change and that in the recovery cycles - increases slightly. With account for some degradation of average discharge voltage, NHSB energy density has not exceeded 5%.

CONCLUSION

Thus, NHSB with independent TCS on the base of HPs applied in S/C "Yamal-200" has demonstrated not only high energy density, but also high lifetime capability.

According to telemetry information for more than 7.5 years of flight operation TCS work is stable, and NHSB energy volume degradation has not exceeded 5%.

FLIGHT EXPERIENCE OF AXIAL HEAT PIPES AT SPACECRAFT EXPRESS-MD1

Y.N. Vinokurov, E.V. Pavlova, V.A. Shabanov

Thermal design department
DB "Salyut" Khrunichev Space Center
Russia, Moscow, Novozavodskaya 18
Tel. +7-(499)-749-52-30, Email: salut@khrunichev.com

The report presents the results of thermal mode monitoring at the existing communication spacecraft Express-MD1, were launched in January 2010. The spacecraft thermal control system is based on the ammonia heat pipes with axial Ω -shaped grooves. Heat pipes have been developed and delivered by the Heat Pipe Center of Roscosmos (Lavochkin Association).

Thermal resistance of typical heat pipes joints at the spacecraft was estimated. Thermal resistance values were obtained from results of ground and flight tests.

The spacecraft thermal mode analysis confirmed the stability of heat pipe performances during ground and flight operation.

LOOP HEAT PIPES APPLICATION FOR UPPER STAGE BLOCK "FRIGATE-SB"

V. Luzhenkov, K. Goncharov, Yu. Panin, A. Kochetkov

Lavochkin Association
Khimki, Moscow reg. Russia

LHP was used for cooling of electric motor and electric pump of servo unit mounted on board upper stage block "Frigate-SB". Cooling is being performed by conductive rejection of heat power from plate, located under servo unit, to LHP evaporator. Evaporator of LHP is located on the plate and uses transport lines for transfer of heat power to condenser that is located on "cold" fuel tank with temperature less than 23 °C. Contact surface of condenser body has spherical shape like tank spherical surface.

The system includes two LHP for cooling each of two servo units. The temperature of servo unit and evaporator of LHP must be less than 75°C. The LHP must transfer heat power 150 W on distance more than 1 m in normal gravity and micro gravity conditions. Start up power is less than 10 W. Working fluid is ammonia. LHP mass is 250 grams only! Thermal resistance of LHP is less than 0.2 K/W.

Presentation includes LHP calculation made with EASY2.1 software package; results of LHP qualification tests including thermal, strength and lifetime tests.

Efficiency of LHP was confirmed by telemetry data received on January 20, 2011 when putting in orbit meteorological spacecraft "Electro-L" by upper-stage block "Frigate-SB". The telemetry data is presented in the paper.

Main requirements to LHP design objectives and LHP design procedure are described.

Calculations of thermal conditions of servo unit electric motor and electric pump are made for different alternative methods of their thermal control. Comparative analysis of obtained calculation results is presented.

RESEARCH OF THE UNPACKAGED HEAT STORAGE IN VACUUM

V. A. Alexeev, L. V. Karaban, A. E. Karabin

Thermal conditions Laboratory
Open Joint Stock Company "Research Institute of Precision Instruments"
51 Dekabristov st., Moscow, 127490
Tel. (499) 202-95-27, fax (499) 204-93-63
e-mail: Vladimir.Alekseev@niitp.ru

V. A. Evseeva, M. A. Shashkina

Composite materials Laboratory
Federal State Enterprise "All-Russian Aviation Material Institute"
17 Radio st., Moscow, 105005
Tel. (499) 263-88-02

Abstract

The present work is dedicated to the experimental study of behavior of unpackaged heat storages (HS) based on form-stable V-HSM-50 material in vacuum environment. The problem of this study was to determine the serviceability of the unpackaged HS in vacuum for the purpose of their application in the radio-electronic instruments, mounted in unpressurized compartments of spacecraft.

KEYWORDS

Vacuum, heat storage (HS), phase-transition material (PTM), melting filler, heat-storage material (HSM), unpackaged HS, form-stable PTM, energy source (ES), radio-electronic equipment (REE), spacecraft (SC).

INTRODUCTION

In space hardware heat storages (HS) are applied for absorption of heat dissipated by radio-electronic instruments during short-time communications sessions. Removal of the accumulated heat is accomplished during more prolonged time intervals in the pauses between the repeated sessions. As a rule, a structure consisting of the HS together with a powerful energy source is part of some instrument. Heat exchange between the instrument and the environment in SC is carried out through conduction with the mounting surface and radiation on the adjacent surfaces of unpressurized spacecraft compartment. Usually pressure in the spacecraft compartment of this type varies in the limits from $133 \cdot 10^{-2}$ to $133 \cdot 10^{-6}$ Pa. This circumstance compelled to conduct an additional study connected with the serviceability of the unpackaged HS in the vacuum.

OBJECT AND MODES OF VACUUM TESTS

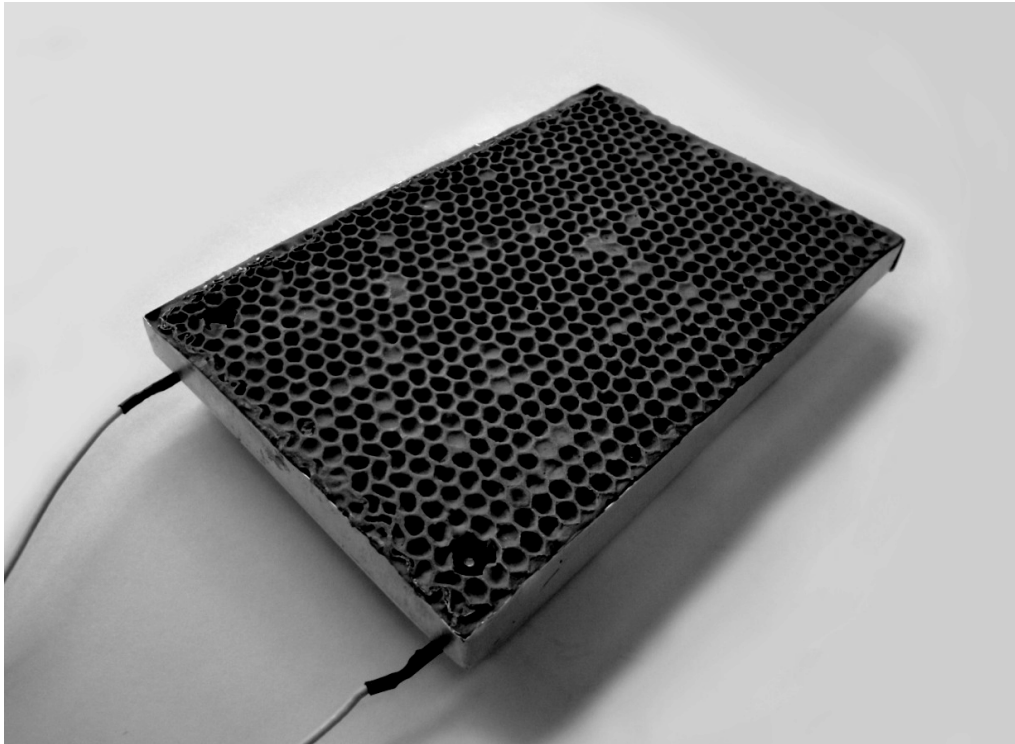
The questions connected with creating form-stable PTM and their operation in REE at normal pressure were taken up at two previous scientific workshops [1, 2].

V-HSM-50 heat-storage material with melting temperature of 53 °C was used as PTM in the unpackaged HS. As it was published earlier in [1], it represented a composition consisting of P-2 paraffin melting filler and a polymer base from ethylene propylene rubber with vulcanizing group [3].

Vacuum tests of the samples were implemented on the facilities of the OJSC "Research Institute of Precision Instruments" equipped with the necessary measuring stocks for measuring pressure, electric parameters and temperature of tested samples.

For vacuum tests the following items were used:

- four unpackaged HS, consisting each of its ES and integrated with its fasteners and form-stable PTM, communicated with the vacuum environment of the test chamber;
- a sample, consisting only of V-HSM-50 blank part. One of such samples is presented in Fig. 1 [4].



a



b

Fig. 1. HSM-04-03 experimental sample (two views)

Temperature measurements in the vacuum chamber were carried out only for this sample.

The tests were accomplished during a one-year period at pressure level from $133 \cdot 10^{-2}$ to $133 \cdot 10^{-6}$ Pa (from 10^{-2} to 10^{-6} mm Hg) in the vacuum chamber. All initial parameters necessary for analyzing tests results were measured before placing the samples in the chamber and after termination of the tests in the vacuum.

Besides, during the tests the HS samples were originally kept in vacuum environment without turning on the ES for 10 months. After that for 2 months the samples' ES were cyclically turned on and samples' parameters were cyclically measured.

After staying the samples in the vacuum their weight were measured (lost) and physico-mechanical properties of the heat-storage material were studied. These results are presented in Table 1.

Table 1. Physical-mechanical properties of heat-storage material before and after staying in vacuum

Weight, g		Weight loss, %	Physical-mechanical properties			
Initial	After staying in vacuum		Initial parameters		After staying in vacuum	
			Tensile strength at break, MPa	Elongation at break, %	Tensile strength at break, MPa	Elongation at break, %
5.54	5.49	0.99	12.5	98.0	20.2	72.0

The represented data confirms that after staying in the vacuum weight loss was slight and didn't exceed the specified norms. Moreover, with increase of time of staying in vacuum the weight decreased. The physical-mechanical properties of HSM obviously improved. Both facts were connected with driving away volatile products generated during material vulcanization.

STUDY OF VACUUM INFLUENCE ON ENERGY CAPACITY OF UNPACKAGED HS

The main efficiency indicator of the heat-storage material is its ability to accumulate thermal energy. When checking PTM energy capacity, two effects of heat accumulation are realized: phase transition effect and thermal capacity effect in the area of high temperatures of the material. A calorimetric method was used for estimating total heat absorption effect of the material. The method provided for heating and staying the tested sample in the heat chamber at a temperature of 100 °C. After that the sample was placed in a water calorimeter for transmission of stored heat to water. Due to constant temperature control, the termination moment of heat transmission from the sample to water was determined. Quantity of heat transmitted to the water was defined by the difference between initial and final temperatures of the water taking into account its thermal capacity and volume. This characterizes the thermal absorption of the material.

The results of the vacuum influence study on thermal absorption of the samples (energy capacity) are presented in Table 2.

Table 2. Heat absorption of the samples before and after staying in vacuum

Sample No.	Heat absorption, kJ/kg		Note
	Initial	After staying in vacuum	
HSM blank part	100	102	PTM without the structure
HSM-04-02	75	80	HS integrated into the structure with ES
HSM-04-03	280	305	

It follows from Table 2 that the total effect of heat absorption of the samples even improved after their staying in vacuum. This fact can be explained by two factors:

- stabilization of samples' material structure after driving away the volatile products which led to improvement of the thermal contact between touching surfaces of the structure and the PTM;
- by certain difference of initial temperatures before and after the tests.

STUDY OF SERVICEABILITY OF THE HS WITH ENERGY SOURCES

The following main purposes were set before the tests:

- functional test of the HS for providing the required thermal conditions of the energy sources used in on-board REE of SC in vacuum environment;
- definition of the vacuum influence on the HSM parameters;
- comparison of the received results with corresponding values at normal environmental pressure.

The procedure of the tests are as follows:

- all the samples were placed in the vacuum chamber (VC);
- thermocouples and heating elements with capacity of 24 W were mounted on the HSM-04-03 sample;
- heating elements (HE) were turned on twice a week and in HS control points the relation of change in temperature (from the initial to assigned temperature levels) with time was determined on the honeycombed panel (90 °C);
- during the tests the pressure in the chamber was measured;
- the samples were weighted before and after termination of the tests in breaks between repeated switching on the energy sources.

STUDY RESULTS

In Fig. 2 one of the typical graphs of temperature change of the component parts of the HSM-04-03 honeycombed panel fragment, filled with V-HSM-50, against the time of switching on the thermal load is presented.

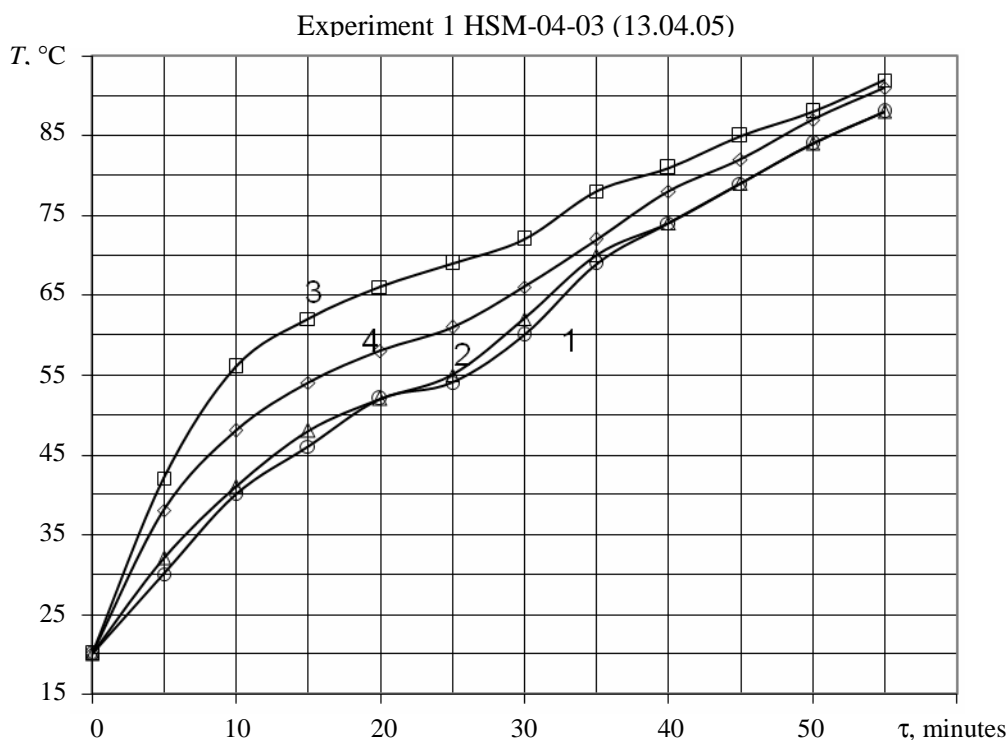


Fig. 2. Typical dynamics of temperatures change of the sample components: 1, 2 – temperature along the PTM thickness; 3 – ES; 4 – honeycombed panel structure

The thermophysical processes in the HS can be presented as follows.

During the heat supply from the ES the temperature of the structure and the HSM located in honeycombed panel cells and contacting with aluminum corrugations, is rising. Further the HSM is heated up and the stage of pre-melting of the working medium prior to the beginning of phase transition at a level of

(40–45) °C starts, characterized in deceleration of temperature increase rate. This is connected with the additional energy expenditures for softening and expanding the volume of the melting filler. Afterwards phase transition of the HSM at a temperature of 53 °C and appreciable decline in the HS temperature increase rate occur. The complete stabilization of the temperatures of HS component parts doesn't occur here because of the poor thermal conductivity of working medium but it is observed the smoothing the temperatures of all component parts of the HS. After the termination of melting process, the rate of temperature increase of the HS is noticeably lower than that at heating-up the solid phase of the melting filler. This is explained by the fact that the specific heat capacity of liquid phase from the beginning of melting to the level of (90–100) °C steadily increased from 2.1 to 3.0 kJ/(kg·K) [1]. Therein lays the additional thermal-capacitive effect of the heat absorption in the unpackaged heat storages.

The presented dependences of temperature change of the HSM-04-03 sample components, taken within the last 2 months of the vacuum tests were practically identical (there were 15 tests in all).

For obviousness the averaged dependence of the honeycombed panel temperature is presented in Fig. 3. The presented dependence confirms the stability of thermal mode of the HS, and consequently the serviceability of the V-HSM-50 heat-storage material in the vacuum.

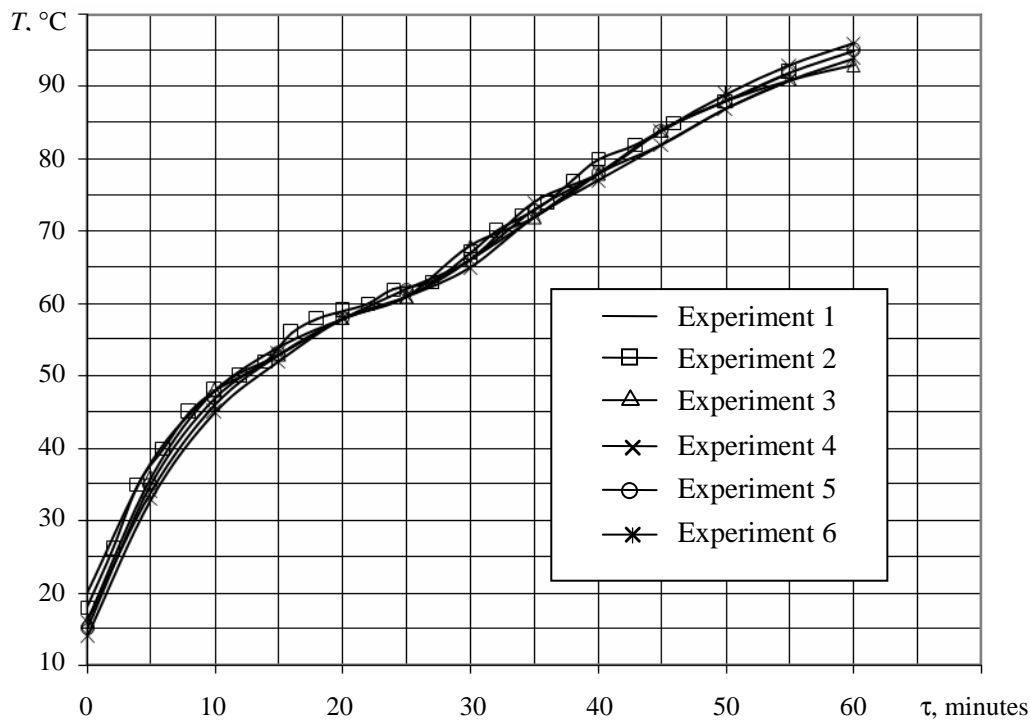


Fig. 3. Averaged dependence of honeycombed panel temperature change at multiple switching on the ES (results of 6 experiments of staying HSM-04-03 sample in the vacuum for the last two months)

Results of weighing all four HS samples before and after tests in the vacuum chamber are presented in Table 3.

The results of the experimental studies of the unpackaged HS in the vacuum have been presented in scientific and technical reports of the OJSC "Research Institute of Precision Instruments", but they have not been published. During the subsequent years the obtained results became a basis for introduction of the HS into space hardware. At present a practical interest appears in terms of implementation of functional tests in vacuum of previously investigated HSM-04-03 sample after its storage within 5 years at normal environmental pressure. For these purposes the same conditions were reproduced in the vacuum chamber, which were supported earlier. Results of newly implemented tests in the vacuum confirmed the coincidence of temperature values of the HS components almost with accuracy of errors from thermocouples and measuring instruments. It is visually presented in Fig. 4.

Table 3. Change of components weight before and after staying in the vacuum

HS samples	Before vacuum tests		After vacuum tests	
	HSM, kg	HS and ES structure	HSM, kg	HS and ES structure
HSM-04-01	0.0067	0.0194	0.0066	0.0193
HSM-04-02	0.0394	0.1634	0.0389	0.1629
HSM-04-03	0.1206	0.1603	0.1189	0.1586
HSM-04-04	0.3383	0.8209	0.3342	0.8168

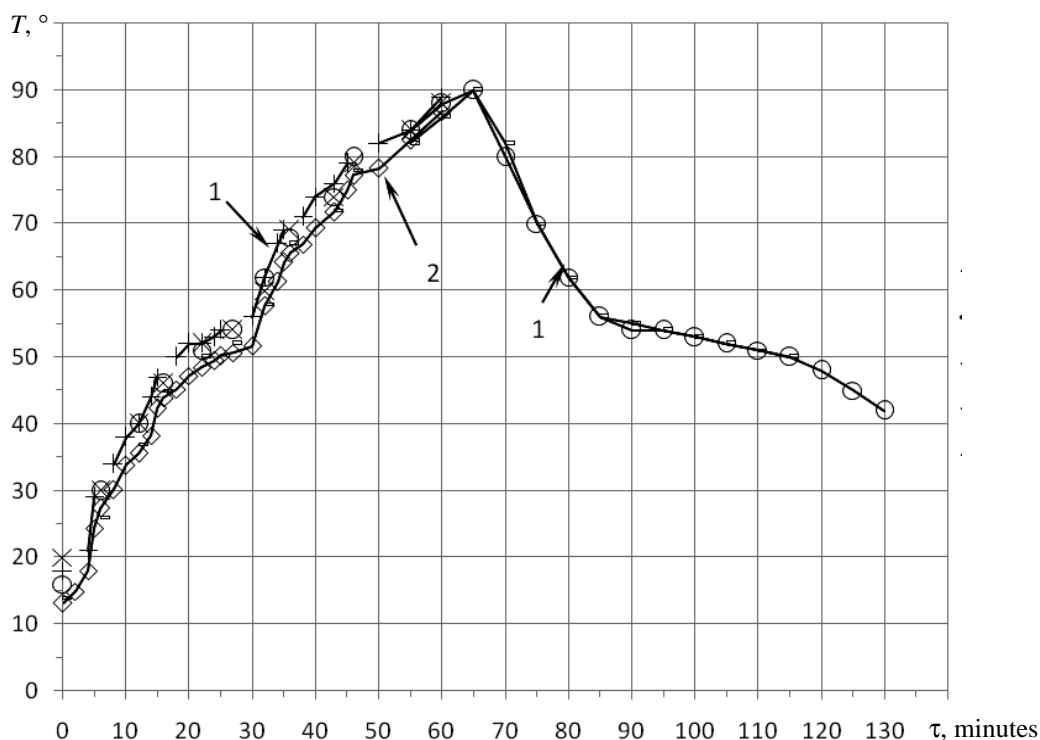


Fig. 4. Checking stability of thermal-physic properties of V-HSM-50 as a part of HSM-04-03 sample in vacuum after storage at normal environmental pressure within 5 years: 1 – tests conducted in April 2005 at $P = 24 \text{ W}$ and 10^{-5} mm Hg ; 2 – tests conducted on 24.11.10 at $P = 24,3 \text{ W}$ and 10^{-6} mm Hg

CONCLUSIONS

1. The conducted studies of the unpackaged HS in the vacuum where the V-HSM-50 heat storage material was used as a working medium, has shown that after driving away the volatile products generated during vulcanization of the material a slight loss of its weight occurred (about 1%).
2. Physical-mechanical properties of the material have improved and remained stable under the exposure of the reduced pressure in the chamber within limits from $133 \cdot 10^{-2} \text{ Pa}$ to $133 \cdot 10^{-6} \text{ Pa}$ after staying in it within 1 year.
3. We were convinced that it would be efficient if the technological process of manufacturing the material before its installation in the structure with the ES should include vacuum processing of the HSM blank part for driving away the volatile products after vulcanization.

4. The conducted tests have shown that the V-HSM-50 heat storage material in the structure, consisting of the unpackaged HS with the energy sources is efficient in vacuum from $133 \cdot 10^{-2}$ Pa to $133 \cdot 10^{-6}$ Pa (from 10^{-2} to 10^{-6} mm Hg) and can be applied in unpressurized compartments of spacecraft.

References

1. Alexeev V. A., Shishanov A. V., Donskoy A. A., et al. Heat storages based on shape-stable phase-transitional material // *Proc. of VI Minsk Intern. Seminar "Heat Pipes. Heat Pumps. Refrigerators"*, Minsk, Belarus, 2005. Pp. 133–138.
2. Alexeev V. A., Karabin A. E. Study of the heat exchange processes in heat storages with shape-stable composite phase-transitional material // *Proc. of VII Minsk Intern. Seminar "Heat Pipes. Heat Pumps. Refrigerators"*, Minsk, Belarus, 2008. Pp. 360–366.
3. Pat. 2199656.
4. Pat. 2306494.

INVESTIGATION OF THE GUIDE INSERTIONS INFLUENCE ON THE CONDENSATION OF WATER IN A NARROW GAP CONDENSER OF A LOOP HEAT PIPE

E. Bartuli, M. Chernysheva, S. Vershinin, Yu. Maydanik

Institute of Thermal Physics, Ural Branch of the Russian Academy of Sciences,

Ekaterinburg, 620016, Amundsen st. 106

Tel. 7(343)267-87-91, Fax. 7(343)267-87-99, e-mail: ebartuli@gmail.com

Abstract

The results of heat transfer and hydrodynamics investigation in the time of water vapor condensation in a narrow gap condenser of a loop heat pipes. The length of the condenser is 80 mm. A cross-section is 40x1.1 mm. Instrumental investigations and visual observations of a condensation process of a condenser with longitudinal guide insertions and without them was carried out. The investigations were conducted at the condenser cooling temperature varied from 60 to 95 °C. At all operating parameters there was a stratified flow regime of a two-phase flow and a film type of condensation. A temperature field in the condenser and the coefficient of heat transfer were measured. Heat transfer coefficients for the condenser without the insertions are in a range of 21 to 46 kW/(K·m²), and with the insertions - from 42 to 88 kW/(K·m²).

KEYWORDS

Loop heat pipe, gap condenser, condensation, heat transfer coefficient, thermal resistance.

INTRODUCTION

Heat-transfer processes in the condenser of a loop heat pipe (LHP) affect significantly the operating characteristics of the device [1, 2], and yet up to now they have not been adequately studied. The LHP condenser must have generally small sizes and at the same time remain sufficiently effective [3]. One of the main characteristics of the LHP effectiveness is a total thermal resistance, calculated on the following formula:

$$R = \frac{T_{ev} - T_{cond}}{Q}, \quad (1)$$

where Q is a transferred heat load, T_{ev} , T_{cond} – the temperature of the evaporator and the condenser respectively. It includes a thermal resistance of the evaporator R_{ev} , a resistance of the vapor line R_{vl} , connecting the evaporator and the condenser, and a resistance of the condenser R_{cond} :

$$R = R_{ev} + R_{vl} + R_{cond}. \quad (2)$$

A resistance R_{vl} is usually small and it can be neglected.

The article [4] shows that for miniature LHP (mLHP) in a value R the resistance of the condenser plays the important role, which can exceed the resistance of the evaporator in several times. Therefore, one of the main issues in the development of a LHP becomes the increase of the condenser efficiency. A R_{cond} value is determined by the difference of vapor temperature at the inlet of the condenser and the ambient temperature, cooling the condenser, related to a heat load Q :

$$R_{cond} = \frac{T_v - T_{cool}}{Q}. \quad (3)$$

For the analysis of R_{cond} the other formula is used:

$$R_{cond} = \frac{1}{S_{cond} \cdot \alpha_{cond}}, \quad (4)$$

according to which the decrease of the condenser thermal resistance can be achieved both by the increasing

of the intensity of heat transfer α_{cond} , and by the increasing of its heat-exchange surface S_{cond} . The latter is quite difficult to do, taking into account size limitations of a LHP. A gap type of the condenser in view of its geometry can be quite compact, and at the same time, have a relatively large heat-exchange surface, which is well correlated with different heat sinks.

This work is aimed at the intensification of heat-exchange processes in a narrow gap condenser by means of special guide insertions.

DESCRIPTION OF EXPERIMENTAL SETUP

An experimental setup for investigating heat transfer in the gap condenser of an LHP is presented in Fig. 1. The setup has a system for the pumping (1) and a module for clearing and degassing the working fluid (2). Heat to the evaporator (3) is supplied from an electric heater (4). To cool the condenser, use is made of running thermostatted water (5). Experimental data were registered with the help of a data acquisition unit Agilent 34970A (6). All readings of the thermocouples as well as the information of the optical apparatus are then input into the computer (7) for further the data processing and analysis. Photography and filming are used for visual observations (8).

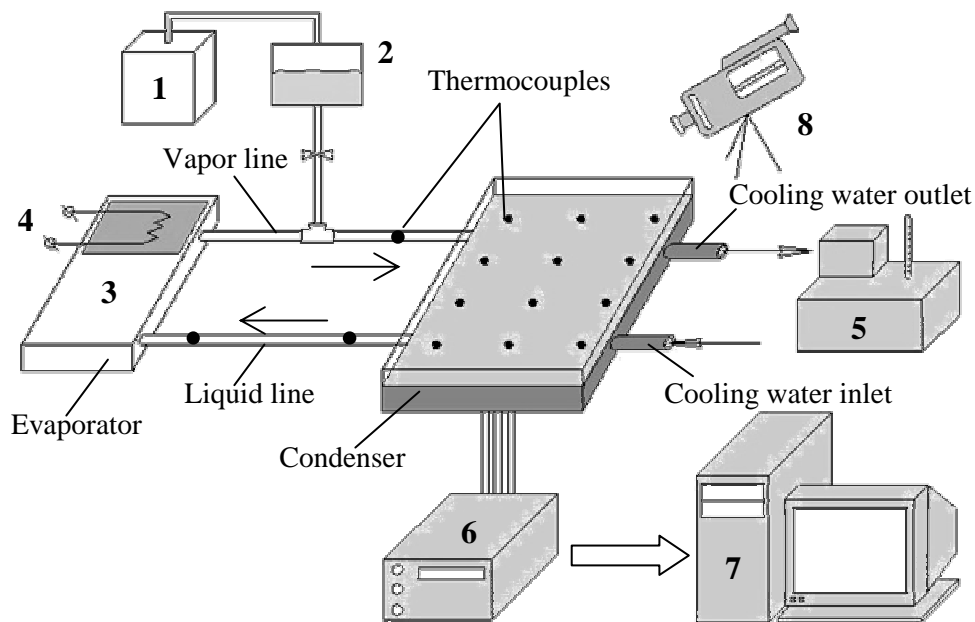


Fig. 1. Scheme of the experimental setup

Investigations were carried out with a copper-water LHP, which was located horizontally and had a flat evaporator. The heating area was 40x40 mm. The length of a vapor line was 550 mm, the length of a liquid line was 250 mm, and the internal diameters were 3 mm and 4 mm respectively. The outer surfaces of the evaporator, heater and pipelines were thermally insulated.

A design of the test section as it is shown in Fig. 3 was represented as a multi-layer package. Between the lower copper and the upper glass plate there was a rubber seal in the form of a frame with a rectangular opening measuring 80x40 mm. The seal ensured the air-tightness of the test section and formed the lateral surfaces of a gap channel. The channel thickness was determined by the degree of the rubber seal compression, which was controlled by the bolts on the flange. In our case the thickness was 1.1 mm. The flange was located above and also had a rectangular centered opening measuring 80x40 mm. Such an assembly of the test section allowed visual observations, photography and filming of the condensation process. The low side of the copper plate was in contact with "a cold plate", cooled by running water from a thermostat. Cooling temperature varied from 60 to 95 °C. The inlet and the outlet of the condenser were located at its opposite corners.

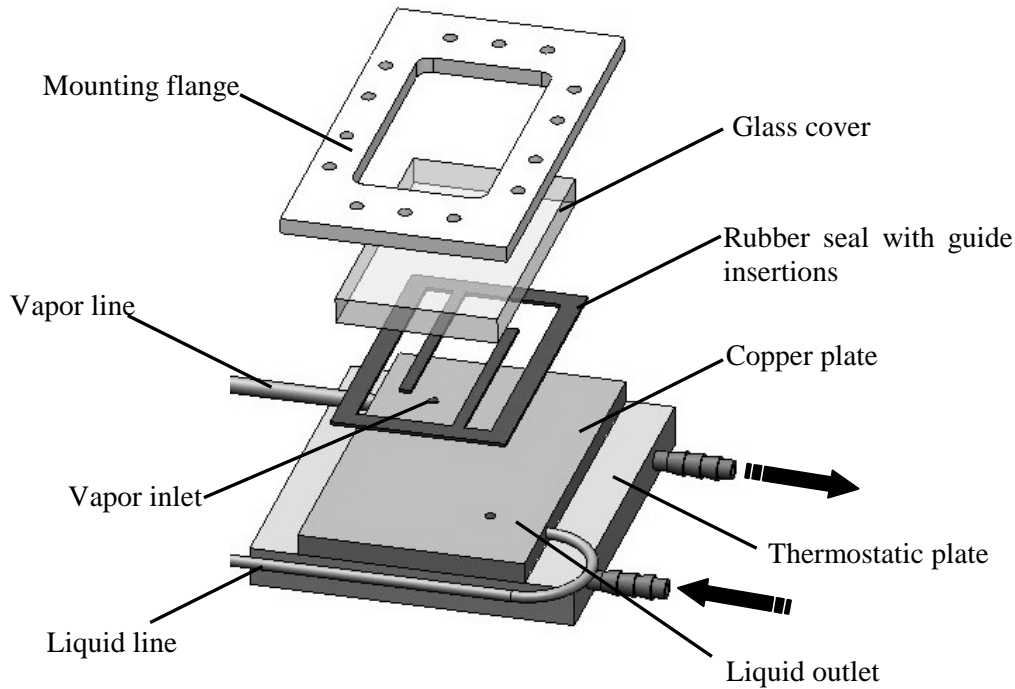


Fig. 2. Scheme of the test section

The vapor condensed on the lower cold surface. The temperature on the condensation surface was measured at 12 points. Their positions are shown in Fig. 1. Copper-constantan thermocouples were used for the temperature measurement. In the course of experiments records were also kept of the vapor temperature in the vapor line, the condensate temperature at the exit from the condenser and the entrance into the evaporator, the control of the temperature difference of cooling water at the entrance into the "cold plate" and at the exit from it was held.

TESTING PROCEDURE

An experiment began with preparation of the working fluid and the loop heat pipe for investigations. Such a procedure was carried out to exclude the effect of permanent gases, air and impurities on the LHP operation as a whole, and also on the condensation process. This stage of the work included the cleaning and degassing of water, and also the pumping and filling of the LHP. Then the condenser cooling system and the evaporator heating were switched on. The indications of the thermocouples were recorded after the completion of transient processes in the LHP, i.e. during a stationary operation of the heat-transfer device. The optical apparatus was located just above the condenser to record the working fluid flow and condensation situation. The area of the condensation zone was determined from photographs. Investigations were conducted with different mass flow rates of the working fluids entering the condenser. The flow rate was controlled by the heat load Q delivered to the evaporator and calculated with account of the heat loss from the heater, evaporator and vapor line into the outside ambient Q_{amb} , as well as heat Q_1 , spent for the heating the cold liquid that enters the evaporator with a temperature T_1 , to the vapor temperature T_v :

$$\dot{m} = \frac{Q_{ev}}{h}, \quad (5)$$

where $Q_{ev} = Q - Q_1 - Q_{amb}$, h is the heat of vaporization.

The value of Q in experiments varied from 50 W to 500 W.

TEST RESULTS

Visual studies of condensation process

The aim of the work consisted in investigation of the guide insertions influence on the heat transfer intensity during the condensation. Fig. 3 presents the photographs of the condensation process at the cooling temperature of 80°C for the condenser with insertions and without them.

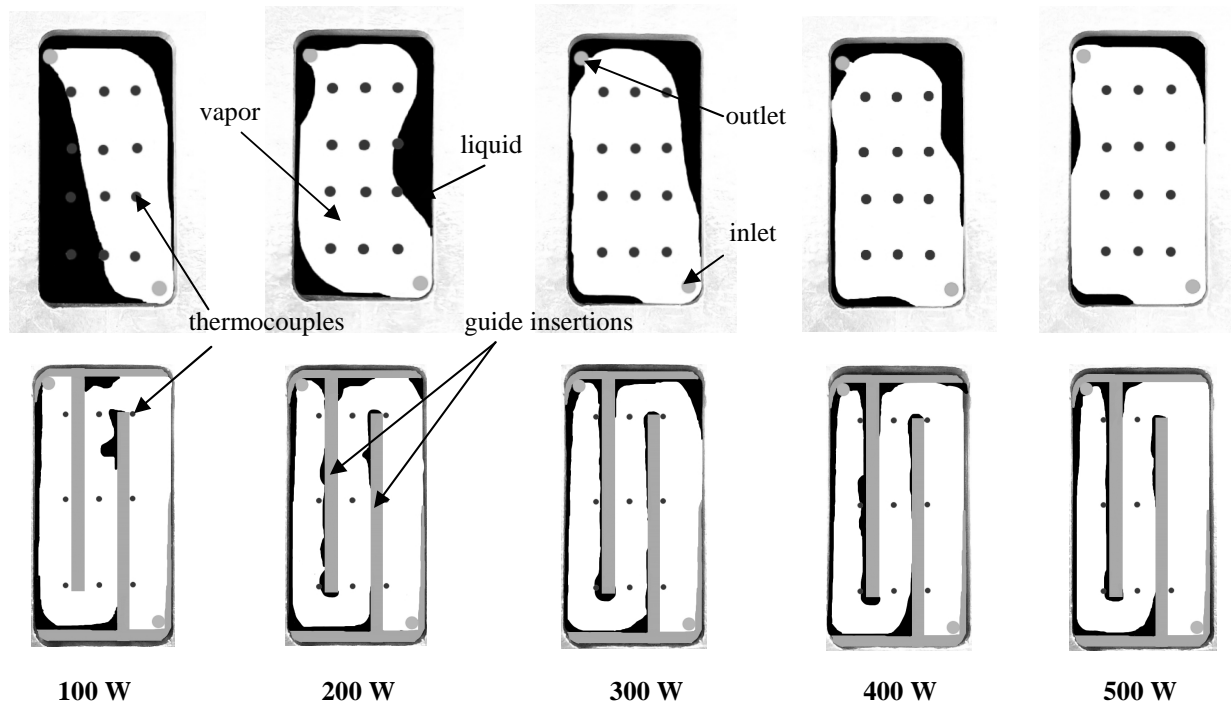


Fig. 3. Photographs of the condensation process with guide insertions and without them

To reduce the uncertainty of the measurement results some photographs ($n \geq 4$) made at the different times but with invariable mode parameters Q and T_{cool} were used for further computer processing. The average area was calculated by the formula:

$$\bar{S}_{\text{cond}} = \frac{1}{n} \cdot \sum_{i=1}^n S_{\text{cond } i}, \quad (7)$$

where \bar{S}_{cond} – an average area of the condensation zone, $S_{\text{cond } i}$ – an area of the condensation zone for a moment of time at the same regime parameters.

It was found that there was a multi-layer flow regime of a two-phase flow and a filming type of the condensation process. The heat load dependence of a relative area of the condensation zone is presented in Fig. 4. It was calculated by the formula:

$$S^* = \frac{\bar{S}_{\text{cond } i}}{S_{\text{total}}}, \quad (8)$$

where $\bar{S}_{\text{cond } i}$ – an average area of condensation zone for the i -heat load, S_{total} - the total area of active condensation zone. The figure shows that the area of the condensation zone, for the condenser with guide insertions, practically does not change with increasing heat load and is independent of the cooling temperature. It remains the maximum in the entire range of heat loads. The redistribution of a liquid between the condenser and the compensation chamber wasn't fully observed.

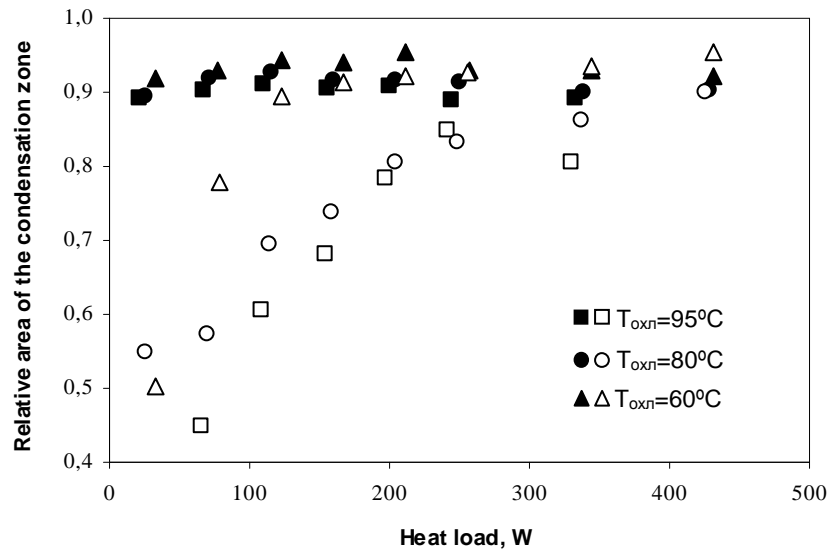


Fig. 4. Heat load dependence of a relative area of the condensation zone:
■ ● ▲ - with guide insertions, □ ○ △ - without insertions

The area of the condensation zone was about a half of the total area of the condenser zone in the condenser without the guide insertions at minimal heat load. An active release of the condenser from the liquid and the increase of the condensation area to the maximum value took place at the load increase to 200–250 W. Further the condensation area didn't practically change and was about 99% from the total area of the condenser [5].

Heat exchange in the condensation zone

The average temperature at the condensation surface was determined by readings of the thermocouples that were located in the condensation zone:

$$\bar{T}_{\text{cond}} = \frac{1}{N} \cdot \sum_{i=1}^N T_{\text{cond } i}, \quad (9)$$

where $T_{\text{cond } i}$ is the local value of the temperature, N is the number of thermocouples in the condensation zone.

The dependence of an average heat-transfer coefficient in the condensation zone $\bar{\alpha}$ on the heat flux Q_{cond} at different cooling temperatures is shown in Fig. 5.

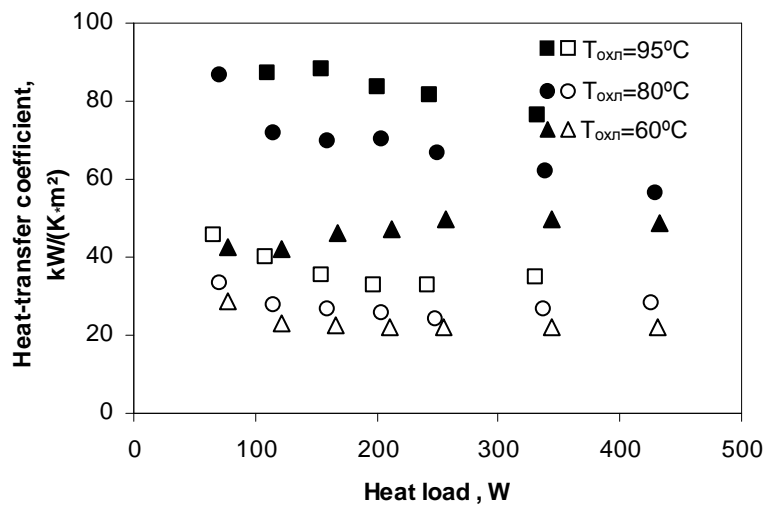


Fig. 5. Heat load dependence of the heat-transfer coefficient:
■ ● ▲ - with guide insertions, □ ○ △ - without insertions

The graph presents that heat-transfer coefficients for the condenser without insertions are in the range from 21 to 46 kW/(K·m²), but with insertions – from 42 to 88 kW/(K·m²). This fact says about that the use of the guide insertions allow increasing the intensity of heat-transfer processes in the condenser in about two times. Apparently one of the reasons of the increasing of the heat-transfer intensity is the growth of the vapor velocity in the condenser. It is connected with the decrease of the cross-section of the channel. Moreover a serpentine-shaped form of the channel, which leads to the turbulezation of the vapor flux, influences the intensification of the heat-transfer processes.

Thermal resistance of a condenser

Heat exchange processes during condensation are considerably determined by the thermal resistance of the condenser. The thermal resistance associated with the condensation process can be defined by the formula:

$$R_{\text{int}} = \frac{1}{S_{\text{cond}} \cdot \alpha_{\text{cond}}} = \frac{T_v - \bar{T}_{\text{cond}}}{Q}, \quad (10)$$

where T_v is a vapor temperature at the entrance into the condenser, \bar{T}_{cond} - an average temperature of the active area of the condensation zone, which was calculated by 12 thermocouples placed in the condenser, as it is shown in Fig. 3. It is clear seen from Fig. 6 that the thermal resistance is two times less with the insertions than without them at the same cooling temperature. One of the main mechanisms of a thermal resistance decrease is a thickness reduction of a film, covered the condensation surface. By means of capillary forces a liquid moves from the centre of a channel to its edges and the guide insertions. It moves to the exit from the condenser owing to a pressure drop. In this case the denseness of a liquid flow in the condenser doesn't change.

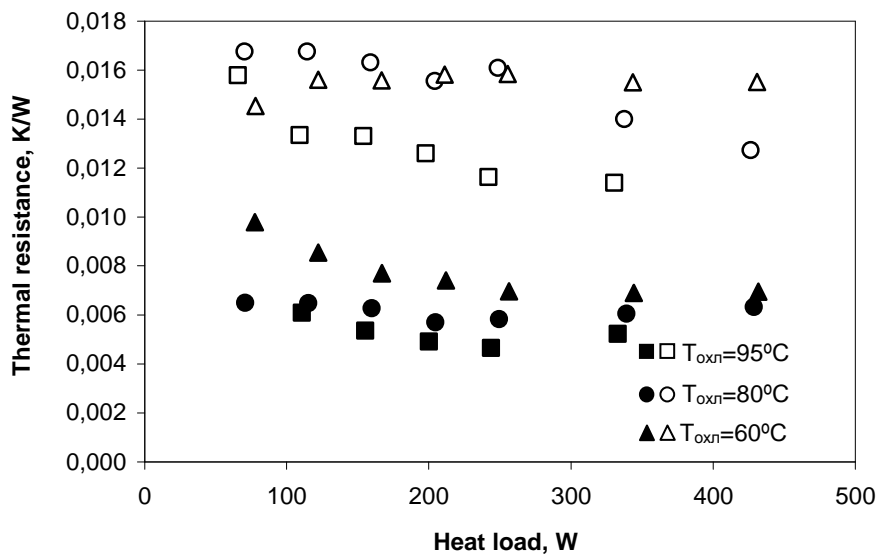


Fig. 6. Heat load dependence of the condenser thermal resistance:
■ ● ▲ - with guide insertions, □ ○ △ - without insertions.

CONCLUSION

The tests of the LHP condenser with the longitudinal guide insertions and without them were carried out at different cooling temperatures. The film type of condensation was observed at all regime parameters. It is found that the use of the longitudinal guide insertions in the condenser of a LHP increases the density of heat-exchange processes at condensation in 1.5–2 times. It is connected with:

- the growth of a local vapor velocity;
- vapor flow turbulezation;
- removal of the liquid film from the active heat-exchange by means of capillary forces.

NOMENCLATURE

T – temperature, °C

Q – heat load, W

S – area of the condensation zone, m²

α - heat-transfer coefficient, W/K·m²

Subscripts

amb – ambient

ev – evaporator

cond – condenser

cool – cooling water

int – initial

l – liquid

v - vapor

vl – vapor line

Acknowledgements

This work was supported by the Russian Foundation for Basic Research, Grant № 11-08-00369-a.

Reference

1. Miscevic M., et al. Condensation in capillary-driven two-phase loops // *International Journal for Microgravity Research and Applications*, 2007, V. 19, Issue 3-4, pp. 116-120.
2. Mishkinis D., Ochterbeck J.D. Analysis of tubeside condensation in microgravity and earth-normal gravity // *Proc. of the 5th International Seminar "Heat Pipes, Heat Pumps, Refrigerators"*, Minsk, Belarus, 2003, pp. 36-53.
3. Майданик Ю.Ф. Достижения и перспективы развития контурных тепловых труб // *Труды IV Российской национальной конференции по теплообмену*, Москва, 2006, Т.1, с. 84-92.
4. Maydanik Yu.F., Vrshinin S.V. Development and tests of ammonia miniature loop heat pipes with cylindrical evaporators // *Applied Thermal Engineering*, 2009, V. 29, pp. 2297-2301.
5. Чернышова М.А., Бартули Э.Ф., Майданик Ю.Ф. Теплообменные процессы в щелевом конденсаторе медь-водяной контурной тепловой трубы // *Тепловые процессы в технике*, 2010, Т. 2, № 8, с. 354-363.

THE ENERGY SAVING PROBLEM SOLUTION FOR NUCLEAR POWER STATION, USING HEAT PIPE HEAT EXCHANGERS, BASED ON SPECIAL COILED FORM OF IT DESIGN

I. Chadzobied¹, H. F. Smirnov², V. S. Kirov¹, P. Ya. Pavlishin³

¹Nuclear Power Station Department
Odessa National Polytechnic University
T. Schevchenko ave 1, 65044, Odessa, Ukraine
Tel.: 38-048 734-86-88 (off.), 38-048 263-17-56
E-mail: vskir@mail.ru

²Food Technology Processes and Apparatus Department
Odessa National Academy of Food Technology
Kanatnaya str. 112; 65084, Odessa, Ukraine
Tel.: 38-048 712-41-75 (off.), 38-048 240-23-44
E – mail: g.smirnov@e-mail.ua

³Government Industrial Nuclear Power Energy Commission "Energoatom"
"Rovno Atomic Power Station"
Kuznetzovsk, 265921, Rovno Region, Ukraine
Tel.: 38 036 363 24 75 (off.), 38 036 366-45-72
E-mail: pavpj@rnpp.atom.gov.ua

Abstract

There are presented the different investigations, devoting new direction of energy saving – energy saving in Nuclear Power Station (NPS). Studying the typical schemes of these stations was shown many sources of waste low – potential heat existence. It was proposed to use these sources most preferable form – to replace may be only part of the vapor selection from turbine by heat from the mentioned sources. It was suggested to use for the mentioned goal to apply as most effective thermal connections between waste heat sources and turbine regenerative system heat exchangers special form of heat pipe heat exchangers, based on coiled their forms.

It was proposed the approach to the selection optimal parameters determination, including as the turbine thermal schematic parameters both mentioned heat exchangers ones. There were produced all necessary calculations for typical turbine schematic with respect to use as mentioned thermal connections on the base as auxiliary heat carrier in the mentioned heat exchanger any low – temperature liquid such as n-butane.

The calculations were made for different possible ratio between cost of energy saving unit and used heat exchangers surface price. The results are presented in the graphic form.

KEYWORDS.

Nuclear power station; heat pipe heat exchanger; vapor turbine; regenerative system; waste heat; energy saving; coiled form; thermal siphon.

INTRODUCTION

The information about some waste heat sources into the Nuclear Power Station (NPS) with (for example water cooled nuclear reactors with power 1000 MW) auxiliary system is discovering a lot great possibilities, including also using these possibilities for partially removing of the low-temperature steam extraction and obtaining for it the additional electric power getting. Naturally, it is appearing the question: How could it be better done?

There are existing now a lot different heat transfer apparatuses, which could be used to the problem solving. The authors are considering, that it is most perspective to use the goal two – phase heat transfer exchangers, such as heat pipes heat exchangers, thermal siphons heat exchangers or pulsating heat pipes heat exchangers too. It is seemed, that the best variant of some of these exchanger design for pointed goal to use

their separate form, when the heating and cooling zones are presented as two separate exchangers, connected each other with vapor and condensate lines [1, 2].

There are becoming the energy saving problems statement the more and more important in the different fields of modern technology. The next auxiliary nuclear power station systems can be related to the perspective from the mentioned point of view: 1. the automatic systems protection blocks cooling; 2. the cooling ponds; 3. the different cooling systems of bleed water and etc.

There aren't known the energy – saving systems, relating NPS, problems such analysis and representative discussion and statement. There are absent right knowledge and imagination about the energy potential of these possible waste heat sources in NPS and most perspective forms of their using. The important problem in the theme is such systems optimal parameters determination.

There is considered in the paper any approach to the problem statement and its solution initial step.

THE PROBLEM STATEMENT

It is possible to state the NPS waste heat saved energy system optimal parameters determination by the next view. The optimal parameters have to ensure the minimum general expenditures for energy saving. It is possible to imagine the value of the mentioned expenditures by the next way:

$$Z_0 = -K_1 \cdot (F_E + F_C) + K_2 \cdot N_E. \quad (1)$$

Here, Z_0 is a general expenditures for the energy saving and waste low-temperature heat using; K_1 , K_2 , F_E , F_C , – special cost coefficients caused by installed heat exchanger area values correspondingly and N_E – an additional energy, obtained for account of this energy saving form using.

The total economy for the saving energy system application can be determined by the next way:

$$Z_E = K_E \cdot \tau_0 \cdot \sum_{i=1}^{i=n} (G_i \cdot \Delta I_i). \quad (2)$$

Here Z_E , K_E , τ_0 , G_i , ΔI_i are total profit for the energy saving system application; specific electricity cost; the saving energy system whole working time per one year; the turbine selection vapor flow rate, removed with using some of mentioned waste heat sources; the specific enthalpy production for it account, respectively. The next important index is the pay – back time T_τ . It can be defined by the next way, using above mentioned parameters:

$$T_\tau = Z_0 / Z_E. \quad (3)$$

The lower the value is, the better from the economic point of view. So, it means, that it will be comfortable to take as the first step any initial value of T_τ . For example, it could be one month or some months.

THE OPTIMAL PARAMETERES DETERMINATION ON THE SUGGESTED APPROACH BASE

Let's to consider the problem at the first approximation. It will be taken as the object of optimization the saturation temperature in the heat pipe heat exchanger with separate zones (heating and cooling). It will be using for determination some real values of the real NPS with real nuclear reactor type (we took WWR-1000 design and thermal schematic parameters). The calculation whole schematic is the next:

- 1) the inlet condensate temperature in the turbine regenerative system is 31 °C,
- 2) the feed water flow rate is as for turbine K – 1000 – 60/50 ... 890 kg/s. [3],
- 3) the low-potential waste heat inlet temperature is 60 °C,
- 4) the pointed waste heat flow rate is equal 20.8 kg/s. [4].

There were taken the next optimization objects: 1) the heated condensate or feed water in the additional heat exchanger outlet temperature; 2) a working surface of this heat exchanger; 3) the utilized low-potential heat quantity. The optimization criteria (goal function) was taken the whole expenditures minimum. The whole calculation schematic has the next view:

The thermal power, transferred over the heat pipe heat exchanger was defined as the next:

$$Q = G1 \cdot C1 \cdot (t_{22} - t_{21}) \quad (4)$$

Here $Q, G1, C1, t_{22}, t_{21}$ – a thermal power, transferring in the heat pipe heat exchanger (HPHE) based on the thermal siphon; heat carrier flow rate value; its specific heat capacity, its inlet and outlet temperatures, correspondingly.

$$t_{12} = t_{11} + Q / (G2 \cdot C2), \quad (5)$$

where $t_{12}, t_{11}, G2, C2$ – the feed water or condensate inlet and outlet temperatures in HPHE; its flow rate; its specific heat capacity, correspondingly. It was taken in the calculations, that specific heat capacities for waste water flow and feed water (or condensate) are equal, that is:

$$C1 = C2 = 4190 \text{ J}/(\text{kg} \cdot \text{K}) \quad (6)$$

Besides it, there were taken into the account the next important heat transfer processes characteristics:

$$F1 = \frac{Q}{\Delta T1} \cdot \frac{1}{k1}; \quad F2 = \frac{Q}{\Delta T2} \cdot \frac{1}{k2}; \quad \overline{\Delta T1} = \frac{(t_{22} - t_{21})}{\ln \frac{(t_{22} - t_s)}{(t_{21} - t_s)}}, \quad \overline{\Delta T2} = \frac{t_{12} - t_{11}}{\ln \frac{(t_s - t_{11})}{(t_s - t_{12})}} \quad (7)$$

The total heat transfer coefficients in HPHE k_1, k_2 were taken for preliminary calculations to be equal 1000 W/(m²·K) and 500 W/(m²·K) correspondingly. The waste flow rate and feed water (or condensate) flow rate were taken on the base of the known turbine regenerative system schematic thermodynamic calculations for energy block WWER-1000. They were equal, correspondingly: $G1 = 20.8$ kg/s., $G2 = 890$ kg/s. The specific electric energy addition, obtained for account of partial removing of the turbine lower vapor selection was determined as 195.5 KJ/kg.

Then the whole profit of the HPHE application with account expenditures on the exchanger production, installation, performance and additional expenditures for its service and commonly with taken into consideration the payment for the additional electric energy could be defined with respect the specific energy cost is equal 0.14 grivna per 1 kW·hour with pay-back time will be taken one month, that is 750 hours, approximately. The all pointed conditions gave possibility to calculate the profit for the proposed form of save energy solution and presented it in the graphic form, as dependency of the profit in grivna on the waste flow in HPHE outlet temperature.

There was determined the equation for the HPHE internal saturation temperature. It has the next view:

$$t_{s0} = \frac{[(k1/k2) \cdot (t_{22} + t_{21}) - (t_{12} + t_{11})]}{2 \cdot [(k1/k2) - 1]} - \sqrt{\left\{ \frac{[(k1/k2) \cdot (t_{22} + t_{21}) - (t_{12} + t_{11})]}{2 \cdot [(k1/k2) - 1]} \right\}^2 - \frac{\{[(k1/k2) \cdot t_{22} \cdot t_{21} - t_{11} \cdot t_{12}]\}}{[(k1/k2) - 1]}} \quad (8)$$

Therefore, on the prescribed base the calculations were done and their results in the graphic form are given in the Figs. 1 and 2.

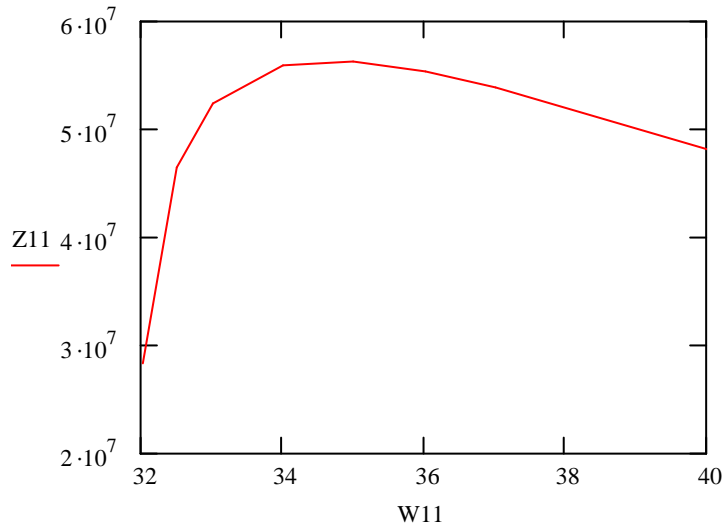


Fig. 1. The dependency optimization function Z11 (grivna per year) on the waste flow outlet temperature from HPHE in grad C (W11).

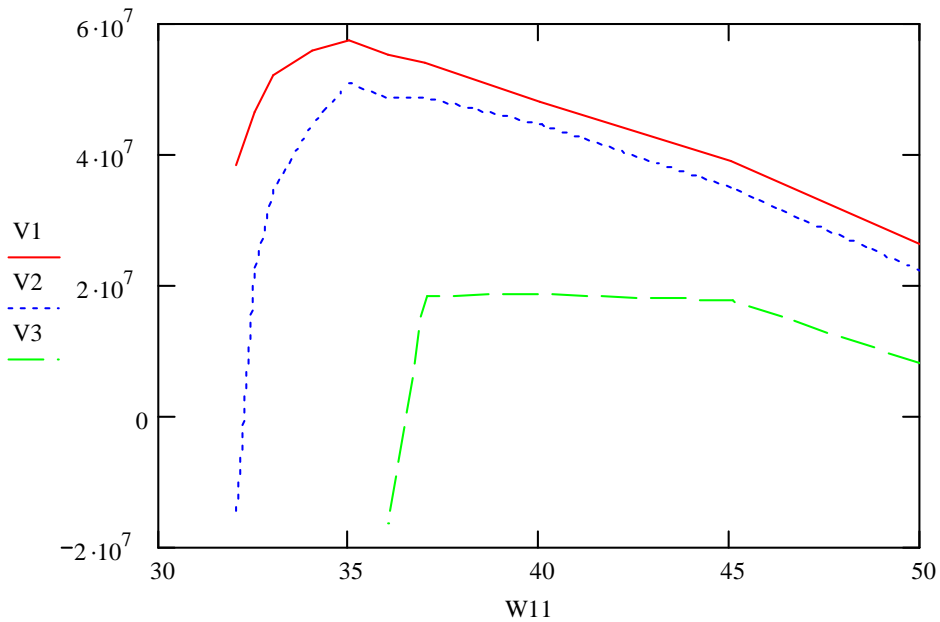


Fig. 2. The dependency optimization function V1, V2, V3 (grivna per year) on the waste flow outlet temperature from HPHE in grad C (W11) for different cost ratio between specific electric energy cost and specific cost of total HPHE expenditures. V2 has it ratio in two times lower, than for V1; and as V3 it ratio in ten times lower, than the mentioned one.

It is seen from the Figs. 1 and 2 that there do exist the outlet temperature from HPHE clear optimum. It is essentially depend on the ratio between obtained addition electric energy during pay-back time cost and the HPHE total expenditures per the same time. It means, that there are possible realize such conditions, when the considered form of energy saving will not have a sense.

The calculations also gave information about the HPHE surface scale and possible scale of the additional energy dependencies on the mentioned factor the waste flow outlet temperature from HPHE in °C. The results can be presented in the graphic form in the Figs. 3 and 4.

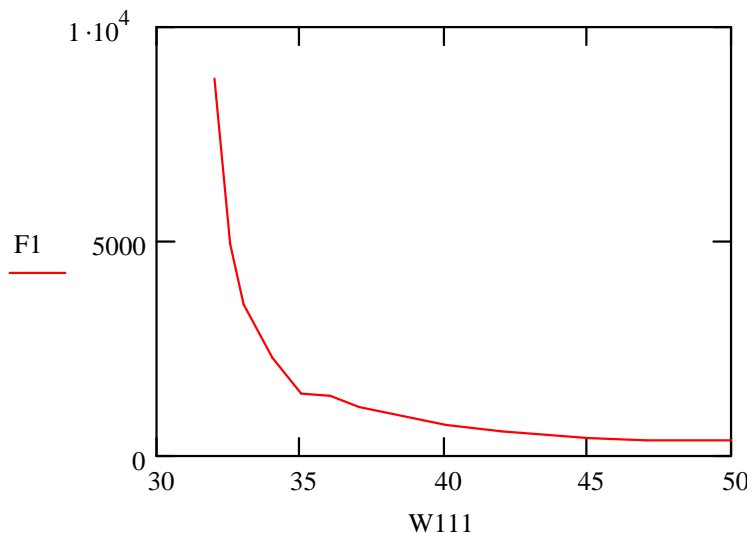


Fig. 3. The HPHE surface $F1$ (m^2) dependency on the waste flow outlet temperature from HPHE in $^{\circ}C$ ($W111$).

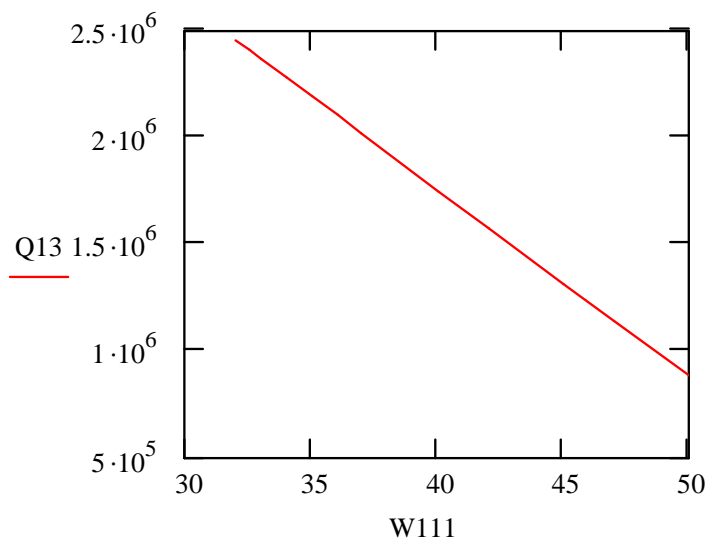


Fig. 4. The additional energy power $Q13$ ($kW \cdot hour$) obtained during pay-back time dependency on the waste flow outlet temperature from HPHE in grad C ($W111$).

Naturally, it is necessary to account by the more detailed calculations many of the circumstances, which were not take into consideration, including those as the heat transfer coefficients in the condensation and evaporation zones dependency on the heat flux intensity, on the thermal regimes, technology and geometry factors too and etc. Finally, it will be necessary to take into consideration also the turbine thermal regimes peculiarities, connected with power load changing. It is necessary in this case to account essential changing in all turbine selections parameters. It has to be leading to many changing in the HPHE heat transfer conditions and as it result to the corresponding changing in the mentioned save energy final profit estimation. But the problem is required a serious additional work, what is far coming for present work limitation. The last problem will be the subject of the future investigations.

CONCLUSIONS

1. The defined optimal parameters have to be considered as some first approximation, what help to estimate the order and scale of these real values. These results are not considered to be final and are not required discussion and correction.

2. It is useful to widen this investigation, accounting whole other thermal regimes peculiarities, including as steady power load both unsteady too.

3. The suggested in the paper approach can be considered as rather perspective and that is why, it could be recommended to continue and next development.

4. The problem important moment, what has to be accounted, is the necessity to take into consideration the main cost input values ratio.

References

1. Bezrodny M.K., Volkov S.S., Moklyak V.F. *Two-Phase Thermal Siphons in Industrial Thermal Engineering*, "Vischa shkola" Publishing House, Kiev, 1991. 226 pp. (in Russian).
2. Smirnov H.F. The thermal industrial engineering problems of heat pipes heat exchangers calculations // *Teploenergetika (Heat-Power Engineering)*. 1988. No. 7. Pp. 51–54 (in Russian).
3. Troyanovsky B.M., Fillipov G.A., Bulkin A.E. *The Nuclear Power Station Vapor and Gas Turbines: Tutorial for Institutes of Higher Education*, Energoatomizdat, Moscow, 1985. 256 pp. (in Russian).
4. Tevlin C.A. *Atomic Electric Power Stations with WWER-1000 Nuclear Reactors: Tutorial for Institutes of Higher Education*, Publishing House of Moscow Power Engineering Institute. 2008. 358 pp. (in Russian).

A TWO-PHASE REVERSE THERMOSYPHON WITH TWO WORK-AGENTS

Yuri Dobriansky, Michal Duda, Daniel Chludzinski

Faculty of Technical Sciences

University of Warmia and Mazury in Olsztyn

ul. Oczapowskiego 11, 10-736 Olsztyn, Poland

Tel. +4889 523-4932, fax. +4889 523-3603, email: dobr@uwm.edu.pl

Abstract

A new kind of two-phase reverse thermosyphon with liquid water as a heat carrier and with vapour of refrigerant as a pumping agent will be presented in this paper. The best properties of the each work agent are used in this case. In particular, water and its solutions has the best properties as a heat carrier, and refrigerants keep pressure above the atmospheric pressure inside of devices if temperature lies in the range from 0 to 100°C. It considerably improves operating characteristics of the device and allows to eliminate mechanical transporting pump out of loop with circulation directed opposite to natural convection. The main news consist in adding second work agent and performing of heat carrying and pumping of the heat carrier with help of two different work agents. A few copies of the two-phase reverse thermosyphon loop with two work agents were successfully tested under laboratory conditions and in combination with an experimental solar installation.

KEYWORDS

Reverse thermosyphon, passive heat transfer, downward, two-phases, two work agent.

INTRODUCTION

The task of heat transfer downward is often met in engineering practice. Ordinary liquid (one-phase) reverse thermosyphons with pump powered by electricity are usually an widely used for this purpose. One-phase or two-phase thermosyphons are used for heat transfer upward. These devices operate autonomously, without external energy supply. It is very desirable to design self-acting reverse thermosyphon for passive heat transfer downward. It is a lot attempts to make such devices. Review of concepts of self-acting circulation loops for heat transfer downward is given in [1]. Unfortunately, such devices are not used in practice because they need for its operation either using great quantity of costly and harmful refrigerants, or keeping pressure below atmosphere pressure inside installation, if water is used as a work agent. Is it possible to use useful properties of both work agents mentioned above?

PRINCIPLES OF OPERATION AND SCHEME OF THE DEVICE

Water and its solutions is the best liquid heat carrier. Vapour is even better heat carrier, but pressure of saturated vapour is less than atmospheric pressure, and such devices must be absolutely leak-tight, what is difficult practical task. Therefore liquid water is preferable for reverse thermosyphons. Calculating shown, that heat stream density transported by water liquid and vapour are enough similar [1], and liquid water would be acceptable heat carrier.

If thermosyphon circulation loop will operate cyclically, only a moderate volume of vapour (about 1 dm³) and small quantity of low-boiling pumping agent (about 10 g) is needed to force circulation in the loop with 1 kW heat flux [2].

If it is wanted that low-boiling substance was used as an additional pumping work agent, this substance must be incapable to dissolve in the heat carrier, its vapour pressure must be greater then atmospheric pressure in temperature range from 0 to 100°C, and preferably the density of the pumping substance must be less than the density of the heat carrier. Such hydrocarbons as butane or pentane enough satisfactorily meet these requirements.

The reverse two-phase thermosyphons with two work agents must also comprise technical means intended for vapour condensation of the pumping substance as well as technical means intended for transport of the condensate from the condensation area to the evaporation area.

Schematic diagram and stages of action of the device are shown in the Fig. 1.

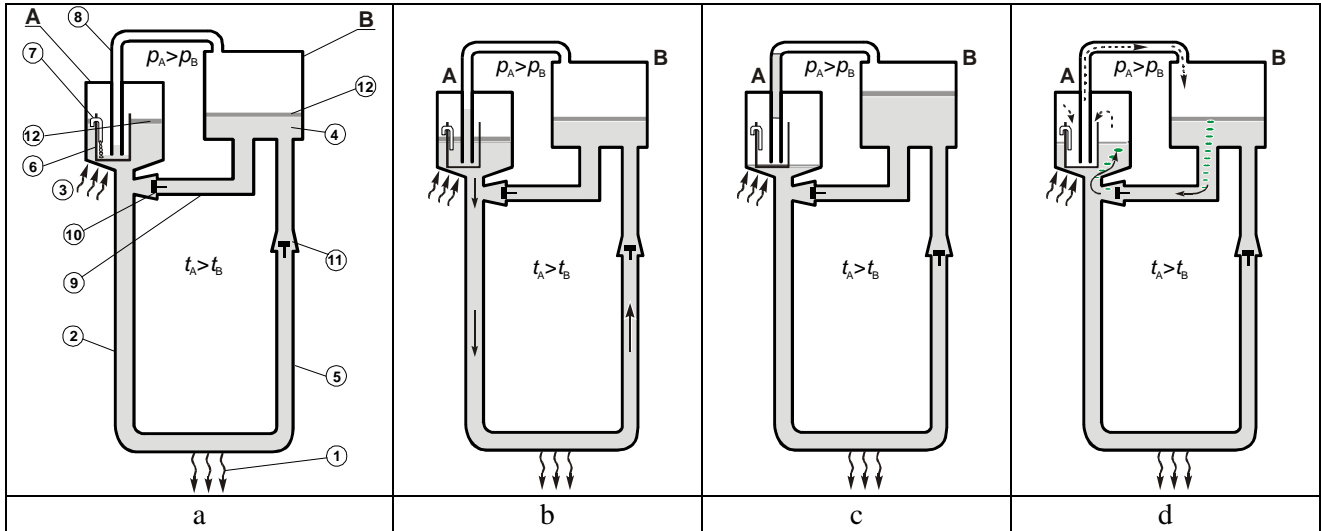


Fig. 1. Schematic diagram and stages of action of the device: A – hot vessel, B – cold vessel, 1 – cooler, 2 – hot falling pipe, 3 – source of heat, 4 – liquid heat carrier, 5 – cold lifting pipe, 6, 7, 8 – control valve (liquid seal), 9 – intermediate canal, 10, 11 – check valves, 12 – additional pumping agent, a – initial conditions, b – pumping stage (hot liquid moves downward), c – opening of control valve, d – pouring off stage (cold liquid moves to hot branch)

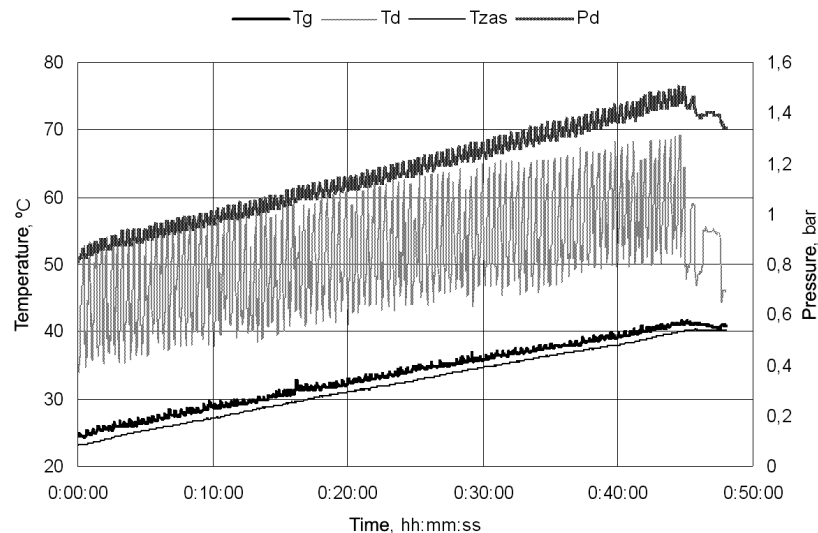


Fig. 2 Water temperature (T_d) and vapour pressure (P_d) in hot vessel A, water temperature in storage tank used as a cooler (T_{stor}), water temperature in cold vessel B (T_t) for heat stream 840 W

A few copies of the two-phase reverse thermosyphon loop with two work agents were successfully tested under laboratory conditions and in combination with an experimental solar installation. Operating temperature and pressure of experimental setup for 840 W heater is shown in Fig. 2.

CONCLUSION

The insertion an additional work agent into circulation loop allows to perform the heat carrying and the pumping of the heat carrier with help of different substances. It allows to use better properties of water and low-boiling substance simultaneously. Two-phase reverse thermosiphon with two work agents has noticeably better operating characteristics in comparison with other known devices for passive heat transfer downward.

References

1. Dobriansky Y. Concepts of self-acting circulation loops for downward heat transfer (reverse thermosiphons) // *Energy conversion and management*. 2011. Vol. 52. Pp. 414–425.
2. Dobriansky Y., Yohanis Y. G. Cyclical reverse thermosiphon // *Archives of Thermodynamics*. 2010. Vol. 31, No.1. Pp. 3–32.

THE USE OF HEAT PIPES FOR ELECTRONICS BLOCK THERMOSTATING OF MAGNETIC MEASUREMENT SYSTEM FIXED ON SPACE VEHICLE

S. A. Grishin, A. L. Petsiuk, S. S. Grishin

Laboratory of optoelectronic and magnetic measurements
State Scientific Institution

The B.I.Stepanov Institute of Physics

68 Prospekt Nezavisimosti, Minsk BY-220072, Republic of Belarus

Tel/Fax: +375 (17) 281-34-13. E-mail: srbas@open.by

V. V. Doctorov, V. V. Maziuk

Research laboratory of capillary-porous materials

State Scientific Institution

The Powder Metallurgy Institute

41 Platonov Street, Minsk BY-220005, Republic of Belarus

Tel/Fax: +375 (17) 293-98-36. E-mail: maziuk@tut.by

Abstract

The report examines the use of heat pipes in magnetic measurement system designed for installation on the spacecraft to monitor the state of Earth's magnetic field and the magnetic environment near the modules and blocks of spectrometric equipment complex. A numerical simulation is made in order to select type of heat pipe and determine optimum design parameters of the elements of the heat sink. Installation on the basis of chamber for heat and a cold for carrying out thermal tests of onboard equipment is described. The automated multisensor network system of temperature measurement is considered. The results of thermal testing of the electronics magnetic measurement system are discussed. The expediency in heat pipes for thermostating blocks of onboard scientific equipment is shown.

KEYWORDS

Heat pipe, heat sink, thermostating system for onboard equipment, magnetic measurement system, spacecraft, numerical modeling of thermal processes, automated system for measuring temperature, chamber for heat and cold.

INTRODUCTION

Traditional field of low-temperature heat pipes (HPs) systems are the thermal conditions support systems for equipment of spacecraft. The effective heat removing is made with the help of HPs on spacecraft and thermoregulation and thermostating of onboard scientific instruments is made too.

HP is a device designed to effectively remove heat from the heating element [1]. Coefficient of thermal conductivity of HP is about a hundred times more than the highest heat conducting metals: silver and copper. HP is completely self-contained unit which requires no supply of electricity or cooling liquid.

Miniature HPs developed by the Institute of Powder Metallurgy are capable of transmitting heat flows up to several tens of watts on a distance up to ten centimeters [2]. Such HPs are designed to remove heat to the radiator which is far away from heating device to evenly distribute heat over the radiator. Also, HP can be used to provide the same temperature of the set of elements. The use of HP makes heat removal and transfer much easier, reduces the sizes of radiators and improves the device characteristics. HP can efficiently solve the following technical tasks:

- the division between heat source and discharge that is the arranged supply and removal on sites which are considerably remote and are arbitrarily orientated in space in relation to each other;
- ensuring high thermal conductivity of heat transfer systems;
- heat flow density transformation, i.e. concentration or deconcentration in wide heat flow range at heat fall site in comparison with heat supply site;
- temperature field leveling and smoothing of temperature peaks;

- adjustment and stabilization of objects' temperature.

Application of HPs makes it possible to maintain a nearly constant temperature over the entire surface of the cooling element, it eliminates uneven heating and implements effective discharge of heat to the platform. This greatly improves the reliability of onboard equipment as modern semiconductor devices used in it are very sensitive to temperature changes. Thus, reducing the operating temperature of a semiconductor device by 20% gives a reduction in failure by 3 times.

The report examines the use of HPs in magnetic measurement system (MMS) (Fig. 2), developed by the Institute of Physics, National Academy of Sciences [3]. MMS is designed for installation on the spacecraft and allows you to monitor the Earth's magnetic field and the magnetic environment near the modules and blocks of spectrometry instrumentation to study the complex relationships between the state of the magnetic field and the flows of space particles. MMS can also be used in stabilization and orientation of spacecraft.

INSTALLATION FOR THE TEMPERATURE TEST

To conduct thermal testing of MMS blocks, the installation was made the structure scheme of which is shown in Fig. 1. The main component is a chamber for heat and cold (CHC). The chamber allows you to specify within the working volume temperature range from minus 50 to plus 80 °C.

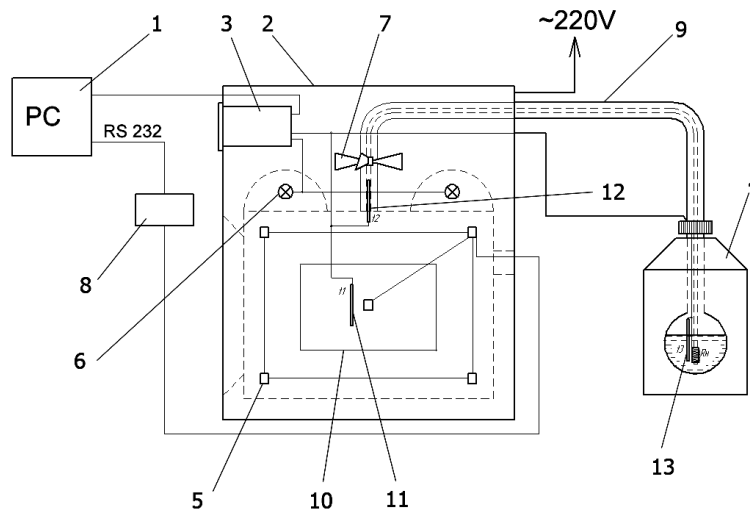


Fig. 1. Installation for the thermal test: 1 – personal computer, 2 – chamber for heat and cold, 3 – controller, 4 – Duar vessel with liquid nitrogen, 5 – system of digital temperature sensors inside the CHC to determine the temperature heterogeneity, 6 – heating lamps, 7 – ventilation system, 8 – adapter to connect the thermal sensors to the PC via interface RS232, 9 – thermally insulated pipe for supplying nitrogen, 10 – magnetic measurement system under testing, 11 – feedback thermosensor №1 installed in the heart of the working volume of the chamber, 12 – feedback thermosensor No. 2 installed on the channel outlet of nitrogen, 13 – feedback thermosensor № 3 immersed in liquid nitrogen Duar vessel

The control system is based on controller "Sosna-002", which is connected to a personal computer (PC) via interface RS232. This allows you to remotely manage the work of CHC, to visualize the process of temperature measurement in both graphical and tabular forms and to store the data on your computer. Heating up in the CHC occurs due to the work of heating lamps of heating system, cooling occurs due to supply of the vapor of liquid nitrogen from Duar vessel inside the chamber. Temperature distribution uniformity is provided by the ventilation system.

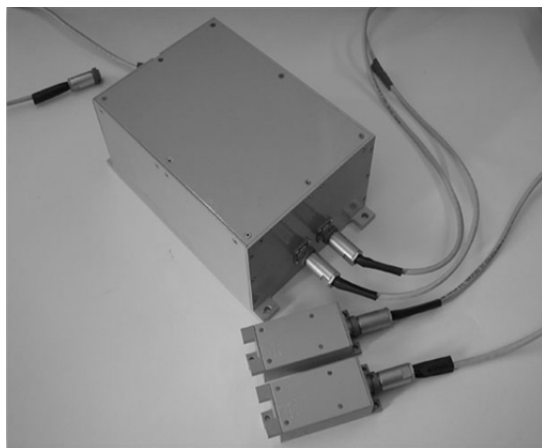
CHC control is performed using feedback by temperature. Feedback is implemented on the basis of three sensors (11, 12, 13, Fig. 1) installed in the center of the working volume of the CHC at the channel outlet of nitrogen vapors and in the Duar vessel. Thermoresistors are used as thermosensors.

To determine the heterogeneity of the temperature inside the chamber, ten digital thermosensors are installed at given points within volume. (5, Fig. 1). Semiconductor digital temperature sensors of company Maxim / Dallas DS1820 (measuring range from -55 to 125 °C, accuracy of measurement $\pm 0,5$ °C) are used as thermosensors, these sensors have a serial 1-Wire interface which allows you to connect all the sensors, using only a two-wire bus. Thermosensors are mounted on a flexible frame carcass and they are connected sequentially with the help of a cable. The system of temperature sensors is connected to a PC via RS232 or USB ports by means of an adapter.

MMS (10, Fig. 1) is placed inside the chamber on a platform that simulates the spacecraft's board. The platform has its own thermostating system that ensures constant temperature maintenance regardless of ambient temperature.

DESCRIPTION OF TEST OBJECT

Test object (Fig. 2) is MMS. MMS contains in its structure magnetometers for primary and backup channels and electronics block (EB). The structure of EB includes a voltage transducer module, processor module (CPC304, PC/104 Processor board), the current channels module with the help of which one can specify currents in the coils included into magnetic field compensation system and into the system of dampening and orientation of spacecraft.



Technical characteristics of MMS

- number of magnetic field components under measurement – 3
- number of current channels – 3
- number of temperature channels – 3
- range of magnetic field under measurement ($\pm 60\ 000$) nT
- channel for digital information transmission spacecraft – RS422
- outer power supply voltage – 27V
- power consumption: magnetometer -100 mA@5V, module for current channels -0,4A@12V, processor board -1,5@5V

Fig. 2. Magnetic measurement system

The hardware part of MMS is executed under the scheme with an unloaded reserve ("cold" back up). The most energy saturated block of MMS is EB. Electronics block must be mounted directly on the space platform during the operation. The temperature of the platform is supported in a given temperature range (extreme temperature values of platform minus 20 °C and plus 40 °C).

Heat from the EB is conducted through metal body made of aluminium alloy. Fig. 3 shows how the heat from the radiator of the processor module is dropped with the help of HP to the bottom of the device, which

has contact with the spacecraft platform. A given thermal regime for EB is maintained by automatic thermal regime system. That system consists of autonomous means of electrical heating, thermo-optical covering, HPs, temperature sensors, radiation surfaces on the casing of device to discharge excess amounts of heat into the surrounding space, screen-vacuum insulation to prevent the leakage of heat.

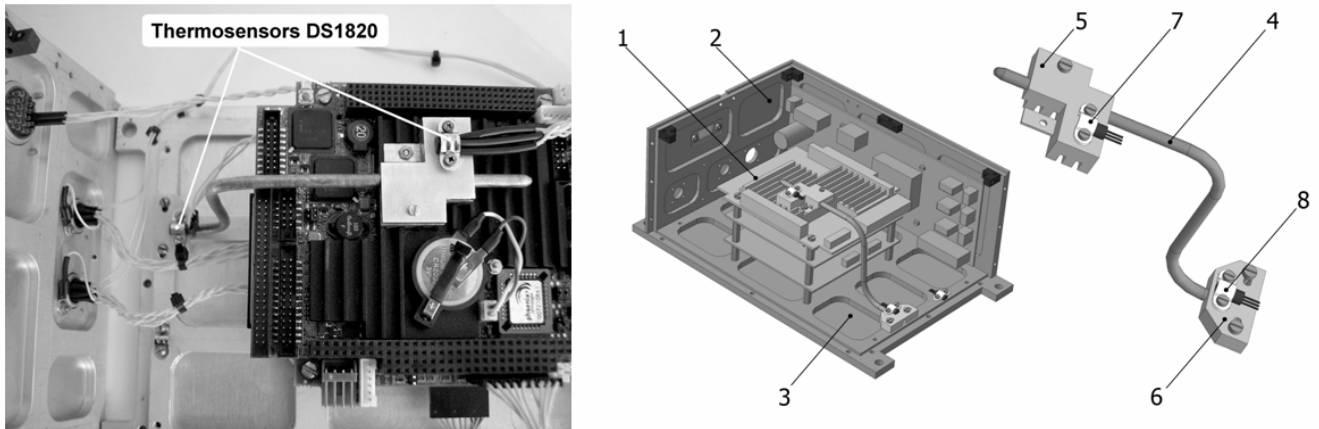


Fig. 3. The design of heat sink for processor module: 1 – cooled processor board, 2 – case of EB MMS, 3 – EB's base, 4-heat pipe, 5 – evaporator radiator, 6-condenser radiator, 7, 8 – thermosensors DS1820

Maximum power dissipation of the processor module (CPC304) – 7,5 Watt. Thermal paste is used for better thermal contact with the surface when installing the radiator for evaporator, radiator for condenser.

Digital thermal sensors connected to the network are installed inside the body of EB of MMS (Fig. 3). Temperature sensors are installed on the evaporator radiator of processor board (thermosensor 7 in Fig. 3), on the condenser radiator (thermosensor 8 in Fig. 3), on the voltage transducer and body surfaces of EB. The system of temperature sensors is connected to a computer via the serial interface. Structure scheme and the appearance of an automated multisensor network system for temperature measurement are shown in Fig. 4.

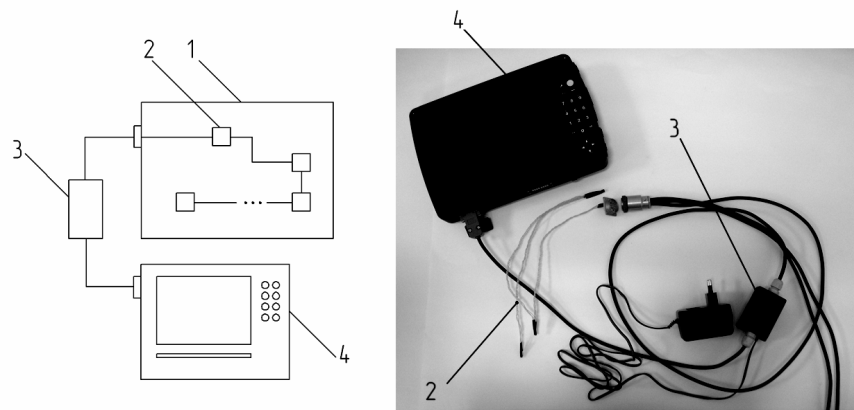


Fig. 4. Automated multisensor network system for temperature measurement: 1 – electronics block, 2 – digital thermosensors, 3 – adapter for connecting sensors to a computer via USB or RS232 ports, 4 – computer

Semiconductor digital temperature sensors are connected sequentially between each other, the number of sensors may vary depending on the task.

To visualize the process of temperature change and to save the results of measurements the developed program TempView was used.

HEAT DISTRIBUTION SIMULATION

Calculation methods

To carry out thermal calculations, a specially developed method of determining the thermal resistance of HPs was used [4]. The method allows you to calculate temperature in the zone of heat supply from the processor module, depending upon changes in outer conditions (heat transfer coefficient and ambient temperature), the geometric design parameters (coefficient of fins), and upon the thermal properties of HPs (thermal resistance).

Initial data for calculations

Heat sink from the EB is carried out conductively through the base. Fig. 5 shows how the heat from the radiator of processor module with the help of heat pipe is dropped to the bottom of the device, which has close contact with the spacecraft platform.

Power emission from processor board – 7,5 W. The contact area of basis of EB with a board of spacecraft is 340 cm². EB’s basis is executed from an aluminum alloy with thickness of 8 mm. The developed evaporator radiator which is installed on processor board CPC304 and condenser radiator have the parameters listed in table 1.

Table 1. Parameters of evaporator and condenser radiators

Parameter	Evaporator radiator	Condenser radiator
Material	aluminium alloy	aluminium alloy
Mass	14 g	6 g
Total surface area	3992 mm ²	1620 mm ²
Contact area with heat pipe	345 mm ²	100 mm ²
Contact area with processor module radiator / EB’s base	1183 mm ²	336 mm ²

The HP installed on processor board radiator is depicted in Fig. 5. HP evaporator is attached to processor board radiator with the help of additional element – evaporator radiator. Heat from processor board radiator is removed to the base of EB MMS. Condenser radiator performs the functions of fixing and heat transfer from HP to the base of EB.

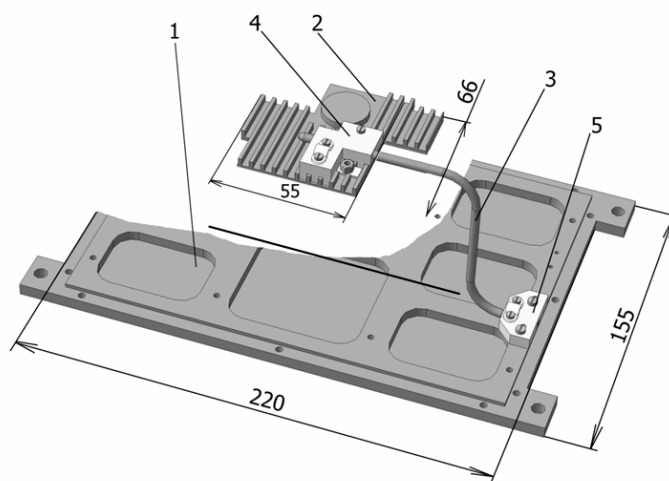


Fig. 5. Constructive heat transfer system parameters: 1 – base of EB MMS, 2 – processor board radiator, 3 – heat pipe, 4 – evaporator radiator, 5 – condenser radiator

The choice of heat pipe

HP for heat removing from the processor module of MMS must correspond to the following requirements:

- sufficient heat transferring capability;
- minimal temperature difference between heat supply and heat removal zones;
- capable to work under vacuum conditions as well as under weightlessness;
- small dimensions and weight;
- high reliability;
- great work resource.

The main parameters for HPs are presented in Table 2. The pipe sites, where the cold agent evaporation and condensation occurs, are in contact with radiators via thermal paste layer.

Table 2. Main heat pipe parameters

Parameter	Value
Outer / internal body diameter	4 mm / 3 mm
Total length / Steam channel length	171 mm / 171 mm
Evaporator length / Condenser length	27 mm / 14 mm
Artery diameter / average size of pores	1 mm / 25 μ m
Heat pipe body material / Heat carrier	Copper / Water
Heat pipe thermal resistance	0.1 K/W
Heat transfer in boiling and condensing areas	50 000 W/(m·K)
Maximal transferred heat flows	15 W

Results of calculations

Results of modeling a temperature distribution are indicated in Fig. 6.

Temperature difference in evaporation and condensation zones will have the value:

$$\Delta T_{\text{evaporation}} = 23,02 - 22,71 = 0,31 \text{ }^{\circ}\text{C},$$

$$\Delta T_{\text{condensation}} = 20,82 - 20,60 = 0,22 \text{ }^{\circ}\text{C},$$

$$\Delta T_{\Sigma} = 23,07 - 20,60 = 2,47 \text{ }^{\circ}\text{C} \text{ (Temperature difference between the cold end of HP and the hot one.)}$$

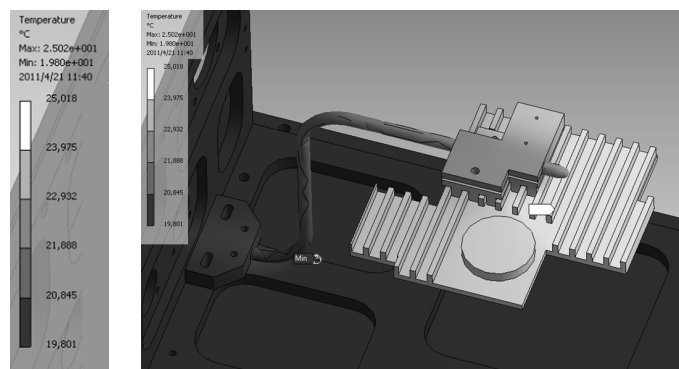


Fig. 6. Results of modeling a temperature distribution

In accordance with conducted simulation, the EB’s heat state assessment has been performed. The obtained calculation results allow us to select HPs in the best possible way, to identify their structure and location in accordance with the ranges in expected temperatures on EB’s structure elements.

RESULTS OF TEMPERATURE TESTS

The process for the conduction of MMS temperature tests is depicted in Fig. 7. The test results are shown in form of curves in Fig. 8.

The total average time for one test was 3,5 hours. MMS cooling from 26 °C up to -42 °C lasted 72 minutes. The radiator temperature for processor board reached -30 °C. After seasoning in chamber, MMS inclusion was made as well as its functioning check up.

During the tests, EB body cooling velocity as well as velocity for processor board CPC304 inside CHC constituted approximately 1,2 °C per minute. The further heating occurred at a velocity equal to 0,74 °C/min. The heating continued during 2 hours. EB MMS base temperature rose up to 47,9 °C. The temperature changes in evaporator radiator and condenser radiator during tests are shown in Fig. 8.



Fig. 7. The process for the conduction of MMS temperature tests

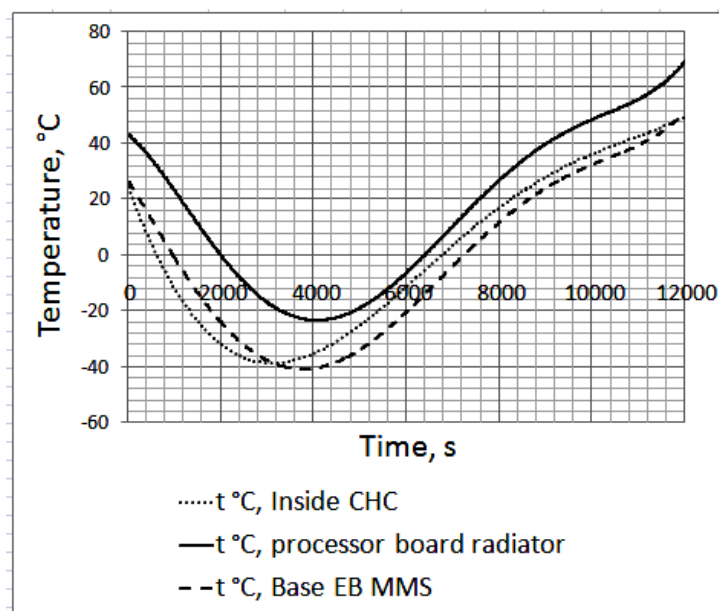


Fig. 8. The results of MMS temperature tests

The curve on the relationship between processor board radiator temperature and EB MMS base temperature was built on the obtained data (Fig. 9).

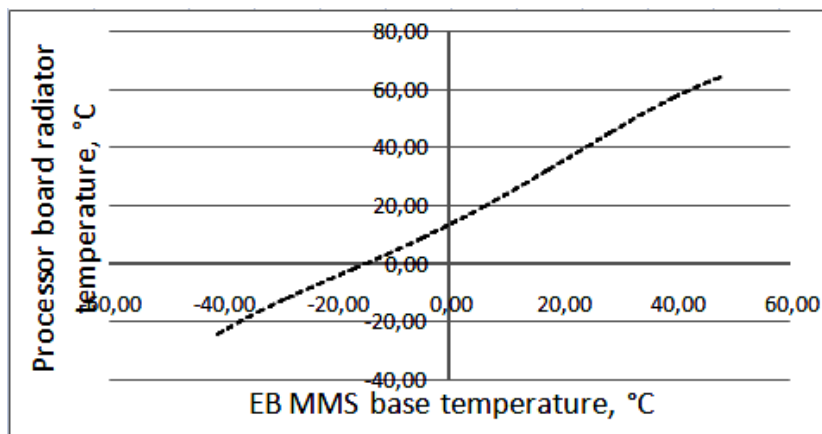


Fig. 9. The relationship between processor board radiator temperature and EB MMS base temperature

CONCLUSIONS

The conducted calculations allowed us to determine the type, location and constructive heat pipe parameters. In accordance with calculation results, the structure was developed and samples for heat sinks for MMS processor board were made. EB MMS tests in chamber for heat and cold demonstrated the efficiency in using heat pipes as a heat sinks of electronic device, they also confirmed the simulation results. The temperature tests have shown magnetic measurement system work capacity under low and high temperatures.

Designations

- EB – Electronics block
- CHC – Chamber for heat and cold
- MMS – Magnetic measurement system
- HP – Heat pipe
- PC – Personal computer.

References

1. Vasilev L. L. *Low Temperature Pipes and Porous Heat Exchangers*, Minsk: Nauka i Tekhnika, 1977 (in Russian).
2. Mazyuk V. V., Rak A. L., Doktorov V. V. Capillary and porous powder materials and heat exchange devices on their base. The development and production: *50 Years of Powder Metallurgy of Belarus. History, Achievements, Perspectives* / Eds. A. F. Ilyuschenko et al., Minsk, 2010. Pp. 321–327 (in Russian).
3. Grishin S. A., Melnikov V. P., Nedvetskiy N. S., Grishin S. S., Petyuk A. L., Batishchev A. G., Naumov P. Yu. Magnetic spectrometry equipment measurement system // *Modern Information and Electron Technologies: Materials of 11 Intern. Scien. and Pract. Conf. "MIET-2010", Odessa (Ukraine), 24-28 May, 2010* / Polytechperiodika, Odessa, 2010. Pp. 172 (in Russian).
4. Maziuk V., Kulakov A., Rabetsky M., Vasiliev L., Vukovic M. Miniature heat pipe thermal performance prediction tool – software development // *Appl. Therm. Eng.* Vol. 21. 2001. Pp. 559–571.

CALCULATION OF EFFICIENCY OF POROUS CHANNELS OF ROUND CROSS SECTION AT A TRANSITION REGIME OF A MOTION OF A LIQUID COOLANT IN COMPARED CANALS WITH SMOOTH WALL AND UNDER THE BOUNDARY CONDITIONS OF THE FIRST TYPE

A. P. Lukisha

The Polyakov Institute of geotechnical mechanics
of National Academy Sciences of Ukraine
49005 Dnepropetrovsk, Simpheropolskaja str., 2a
E-mail: lukisha@ukr.net

Abstract

The important problem of the present time is the making of unobstructive heat exchangers, with high efficiency. One of methods of magnification of efficiency of heat exchangers is application of porous materials with a high heat conductivity. Along with obvious advantage - high efficiency of heat transfer due to high heat conductivity of porous insert material, there is also a disadvantage - high hydraulic resistance of porous structures. The purpose of this work was to discover parameter space of porous heat exchangers, where gain in heat transfer would exceed hydraulic losses. Smooth-wall tube was taken as a surface of comparison. Computation of comparative efficiency was carried out for metal-felt porous materials, at a transition regime of a motion of incompressible fluid – water - and at boundary condition of first-type. The accounts showed, that the maximal positive effect is reached at a small diameter of the channel - about 3 mm, value of Reynolds number of a transition regime of flow in the smooth channel – $Re_{sm} \approx 4000$, meanings of porosity about $0,8 \div 0,9$ and relative length of channel about 20.

KEYWORDS

Porous materials, coefficients of effectiveness, transition area of motion of incompressible fluid- water, first-type boundary condition.

INTRODUCTION

One of the important ways of development of warm energetics in modern time is the application of highly effective inventory with saving of power. One of elements of a similar sort of devices can be porous canals of transmitting of heat, which are made from materials with high thermal conductivity. However, together with the explicit advantage of such porous elements - high efficiency of the heat transfer, there is also a deficiency - high hydraulic resistance of porous structures. The problems of numerical research of efficiency of porous channels of round cross section at a laminar and turbulent motion of a liquid coolant in compared channels with smooth wall and at boundary conditions of the first type in articles [1] and [2] were explored. Thus was obtained result, that showed, that the best values of effectiveness ratio can be reached at the end of a laminar regime of a motion of a coolant in compared smooth - wall pipe. At a turbulent regime the results were obtained a little worse. Therefore has appeared interest to explore transition area $2300 \leq Re_{sm} \leq 10000$ of motions of the liquid coolant in compared smooth-wall channels. The given article is dedicated to study of this problem at the first-type boundary conditions.

FORMULATION OF THE PROBLEM

The calculation of effectiveness of porous canals was conducted using the methodology of Guhman A.A., presented in [3]. This methodology compares three parameters - quantity of transferred heat Q , power consumed for heat carrier pumping N , and area of lateral surface of channels F . At the same time, any two of three parameters mentioned above are considered to be constant, and comparison is performed basing on the

third one. Therefore, there can be three coefficients of effectiveness ratio - $k_Q = Q_p/Q_{sm}$ (thermal coefficient); $k_N = N_p/N_{sm}$ (power coefficient) and $k_F = F_p/F_{sm}$ (surface or dimensional coefficient). Since a smooth-wall tube was taken as a reference surface for comparison, the indices of the three coefficients given above represent p - porous and sm - smooth-wall cylindrical channel. If the diameters of channels are identical, $k_F = k_\xi = (\xi_p/\xi_{sm})$, where $\xi = x/d$ - dimensionless length of channel, x - the coordinate along the axis of the channel, d - diameter of the channel.

The calculation of coefficients of effectiveness was carried out at a transition area of motion of incompressible fluid - water - and first-type boundary condition. The quantity of heat, transmitted by the channel with smooth wall, was calculated with the use of the average coefficient of a convective heat exchange over the length of the channel. This coefficient was calculated under the formula of V. Gnielinski [4].

The quantity of heat transferred by the porous channels was conducted with the use of the average temperature of a fluid over the cross-section of a channel on an exit of the channel. The expression for the average temperature of a liquid over a cross-section of a porous channel under the first-type boundary condition was derived by V.A. Majorov and co-authors [5]. The relationships of S.S. Kutateladse and H. Blasius were used for the calculation of hydraulic resistance in the smooth-wall channels, and the modified equation of Darcy was used for the porous channels. The resulting system of equations for calculating the coefficients k_Q , k_N and k_F is written as follows:

$$\frac{\mu c_p}{4d} \cdot \text{Re}_p \cdot [1 - 4 \cdot \sum_{i=1}^{\infty} \frac{1}{2\mu_n} \exp(-4\mu_n^2 \cdot \xi_p / \text{Pe}_p (1 + 4\mu_n^2 / \gamma^2))] \cdot (T_w - T_0) = \alpha_i \cdot \xi_{sm} \cdot (T_w - \bar{T}_i) \quad (1)$$

$$\text{Re}_p^3 + \frac{\alpha d}{\beta} \cdot \text{Re}_p^2 - \frac{\xi'_{ot}}{2d\beta} \cdot \text{Re}_{sm}^3 \cdot \frac{\xi_{sm}}{\xi_p} = 0 \quad (2)$$

at $\gamma^2 \leq 10^3$, and

$$\frac{\mu c_p}{4d} \text{Re}_p [1 - 4 \sum_{i=1}^{\infty} \frac{1}{2\mu_n} \exp(-B'_n \xi_p)] = \alpha_i \cdot \xi_{sm} \cdot (T_w - \bar{T}_i), \quad (3)$$

where $B'_n = [(Pe/2)^2 + 4\mu_n^2]^{1/2} - Pe/2$

$$\text{Re}_p^3 + \frac{\alpha d}{\beta} \cdot \text{Re}_p^2 - \frac{\xi'_{ot}}{2d\beta} \cdot \text{Re}_{sm}^3 \cdot \frac{\xi_{sm}}{\xi_p} = 0 \quad (4)$$

at $\gamma^2 > 10^3$

Combined equations (1), (2) are written down for $\gamma^2 \leq 10^3$, and combined equations (3)–(4) are written for $\gamma^2 > 10^3$.

Here $\gamma^2 = (h_v \cdot d^2) / \lambda_p$ - parameter which characterizes intensity of heat exchange inside of porous material; h_v - the intensity of volumetric heat exchange inside of porous material; λ_p - the coefficient of the thermal conductivity of porous material; \bar{T}_i и α_i - the average temperature of a liquid over a length of a smooth-wall channel and coefficient of a convective heat exchange gained on i-th a step of iteration at calculation with the help of a method of successive approximations and with use of the formula of V. Gnielinski; ξ'_{ot} - coefficient of hydraulic resistance in the smooth-wall channels at transition regime of motion of single-phase liquid flow.

In equations (1) and (3) the following designations are accepted: Re_p and Re_{sm} - Reynolds number in the porous and smooth-wall channels; $\text{Pe}_p = \text{Re}_p \cdot \text{Pr}_p = (G \cdot d \cdot c_p) / \lambda_p$ - Pekle's number of a porous channel; Pr_p - Prandtl's number of porous channel; $G = \dot{m} / F_{cs}$ - specific mass rate of flux of a coolant; F_{cs} - cross-sectional area; \dot{m} and c_p - rate of flux and heat capacity of a fluid; μ_n - the sequential roots of the equation $I_0(\mu) = 0$, ($n = 1, 2, 3 \dots, (\mu_1 = 2,4048)$), I_0 - the Bessel function of the first kind, zero degree. In this case, the expression

in the brackets on the left side of equations (1) and (3) is the average dimensionless temperature of a fluid on an entrance of the porous channel:

$$k = 1 - \bar{\vartheta} = (\bar{t} - t_0)/(t_w - t_0) \quad (5)$$

Here \bar{t} – is average temperature of a liquid on an exit from the porous channels; indices «w» and «0» refer to the temperature of a liquid on the wall and at the channel inlet respectively.

In equations (2) and (4), the parameters α and β designate the viscous and inertial coefficients of resistance of a porous material.

The calculation of the parameter h_v in the expression for γ^2 is performed through the criterial equations of the form:

$$Nu = a \cdot Re^b \cdot Pr^c, \quad (6)$$

where the coefficients a , b and c are taken from the experimental data for a concrete type of porous material and the heat transfer medium .

Nusselt's criterion in this equation is calculated using the formula $Nu = (h_v \cdot (\beta/\alpha)^2)/\lambda_1$, and Reynolds number is calculated from the relationship $Re = (G \cdot (\beta/\alpha))/\mu$, where λ_1 – thermal conductivity of heat transfer medium, μ - coefficient of dynamic viscosity.

The obtained system of equations is the system of nonlinear algebraic equations with the variable coefficients. Solving the problem in this setting is reduced to the search for the combination of the parameters of the porous structure and the smooth-wall channel: porosity θ , the diameter of the channels d , relative length of the smooth-wall channel $\xi_{sm} = x/d$, temperature of the wall of the channels (T_w) and the Reynolds number in the smooth-wall channel Re_{sm} , where the obtained system of equations (1), (2) or (3), (4) has the best solution – the maximum value of the coefficients k_Q ; k_N and k_F .

SOLUTION

The calculations of the effectiveness coefficients were performed for the metal-felt, prepared from the fibers of copper with a diameter of 200 μm for the following calculated parameters: porosity: $\theta = 0,3; 0,4; 0,5; 0,6; 0,7; 0,8; 0,9$; Reynolds number of the smooth channel: $Re_{sm} = 2,3 \cdot 10^3; 3,0 \cdot 10^3; 4,0 \cdot 10^3; 6,0 \cdot 10^3; 8,0 \cdot 10^3; 1,0 \cdot 10^4$; the relative length of the smooth-wall channel of $\xi_{sm} = x/d = 2; 5; 20; 50; 100; 500; 1000$; the diameter of channel $d = 1, 2, 3, 4, 5, 10, 20, 50$ mm.; the temperature of the wall $T_w = 25; 30; 40; 70; 100$ °C; the temperature of liquid at the channel inlet $T_0 = 20$ °C.

The calculation of the coefficient of thermal conductivity of the porous material λ_p used the relationship obtained in [6] that agreed with the experimental data according to [7]. The calculation of the intensity of heat exchange inside of porous materials was performed with the aid of the criterions equation [5], which was obtained experimentally for the porous material prepared from the fibers:

$$Nu = 0,007 Re^{1,2}. \quad (7)$$

For calculating of the parameters α and β the following relationships [7] were used:

$$\alpha = 2,57 \cdot 10^8 \cdot \theta^{-3,91} \quad (8)$$

$$\beta = 0,91 \cdot 10^3 \cdot \theta^{-5,33} \quad (9)$$

As it was above mentioned , the calculation of average on length of a smooth-wall pipe of coefficient of a convective heat exchange was carried out with use of the equation of V. Gnielinski [4].

$$\overline{Nu} = \frac{\overline{\alpha}d}{\lambda} = \frac{(\xi/8) Pr(Re-1000)}{1 + 12,7\sqrt{\xi/8}(Pr^{2/3} - 1)} \left[1 + \left(\frac{l}{d} \right)^{-2/3} \right] \quad (10)$$

This equation is obtained by betterment of dependence of Petuhov B.S. and Kirillov V.V., which was obtained for turbulent Reynolds numbers $10^4 \leq Re \leq 5 \cdot 10^6$ and values of Prandtl's numbers $0,5 \leq Pr \leq 200$

$$Nu = \frac{(\xi/8) Re Pr}{k + 12,7\sqrt{\xi/8}(Pr^{2/3} - 1)} \quad (11)$$

where $\xi = (1,82 \lg Re - 1,64)^2$; $k = 1,07$.

According by the data [9] the equation (10) is validly in the following criteria area $2300 < Re < 10^6$, $0,5 \leq Pr \leq 200$ and $l/d \geq 1$.

At calculation of coefficient of a convective heat exchange under the formula of V. Gnielinski (10) as determining temperature, the average temperature over the length of the channel was taken. This temperature was determined by a method of successive approximations under the given formula.

In the beginning of calculations as determining temperature, the average temperature of a fluid \bar{T}_1 between temperature of a wall T_w and temperature of a fluid on an inlet T_0 was taken. In further coefficient of a convective heat exchange under the formula (10) and quantity of heat transferred by the channel with a smooth wall under the formula (12) were calculated.

$$Q_{\alpha} = \alpha \cdot (T_w - \bar{T}_1) \cdot F, \quad (12)$$

here F is lateral area of the channel.

After that the relation (12) was equated to expression of quantity of heat calculated on the formula (13)

$$Q_{\bar{T}} = \dot{m} \cdot C_p \cdot (\bar{T}_{ex} - T_0) \quad (13)$$

and value of quantity \bar{T}_{ex} in further was defined. Average temperature of a fluid in the channel under a relation $\bar{T}_2 = \frac{T_0 + \bar{T}_{ex}}{2}$ in further was calculated and the calculation was iterated again as long, as the successive approximations of average temperature did not differ on quantity $\Delta \approx 15\%$.

The calculation of thermal physics properties of a fluid at this temperature was done under an interpolation formula of Lagrange with use of 10 base points in an interval of temperatures 0–100 °C. At calculation of coefficient of hydraulic resistance of a pipe with a smooth wall at $2200 \leq Re_d \leq 4000$ the formula of Kutateladse S.S. [10] was used:

$$\xi'_{ot} = 6,3 \cdot 10^{-4} Re^{0,5} \quad (14)$$

At values of Reynolds numbers in transition area $4000 \leq Re_d \leq 10000$ the relation of H. Blasius [11] was used

$$\xi'_{ot} = 0,3164 \cdot Re_d^{-1/4}, \quad (15)$$

In relations (14) and (15) Re_d - Reynolds criterion calculated on a diameter of the channel.

Calculations were carried out for the entire field of parameters, what composed 11760 points. Further the procedures of calculations of each of effectiveness ratio - k_Q ; k_N and k_F are considered.

Coefficient k_Q . At calculation of coefficient k_Q , using requirements $N_p = N_{sm}$ and $\xi_p = \xi_{sm}$, we gain and solve the cubic equation Cardano (2) or (4) concerning variable Re_{sm} . Further we substitute the received value variable Re_p and known value $\xi_p = \xi_{sm}$ in the equation (1) or (3) and we calculate coefficient k_Q , as the attitude of the left-hand part of the equation to the right part. Thus, at substitution of values α_i and T_i d in the given equations, we use a method of iterations, as mentioned above. Table 1 present a fragment of calculations of coefficients k_Q for the parameters of $T_w = 25^\circ C$; $d = 0,003m$; $\xi_{sm} = x/d = 20$.

Table 1. $k_Q = f(Rep, \theta)$ $T_0 = 20^\circ C$; $T_w = 25^\circ C$; $x/d = 20$; $d = 0,003m$.

$\theta \backslash Re_{sm}$	2300	3000	4000	6000	8000	10000
0,3	0,110	0,120	0,136	0,145	0,153	0,160
0,4	0,207	0,221	0,246	0,259	0,270	0,279
0,5	0,324	0,343	0,379	0,395	0,410	0,423
0,6	0,462	0,486	0,536	0,555	0,575	0,591
0,7	0,620	0,652	0,715	0,738	0,762	0,782
0,8	0,800	0,839	0,917	0,940	0,962	0,976
0,9	0,999	1,039	1,115	1,095	1,069	1,038

Coefficient k_N . At calculation of this coefficient, taking into account, that $k_F=1$, i.e. $\xi_p=\xi_{sm}$, we solve the nonlinear algebraic equation (1) concerning quantity Re_p by sorting out this variable from 0 up to Re_{sm} . After finding of variable Re_p at which is satisfied condition $Q_p=Q_{sm}$ and after substitution of this value in the equation (2), there is easy opportunity to calculate coefficient k_N :

$$k_N = \frac{2d\beta \cdot (Re_p^3 + \frac{\alpha d}{\beta} Re_p^2)}{\xi'_{ot} \cdot Re_{sm}^3} \quad (16)$$

Table 2 present a fragment of calculations of coefficients k_N for the parameters of $T_w=25^\circ C$; $d=0,003m$; $\xi_{sm}=x/d=20$.

Table 2. $k_N=f(Re_p, \theta)$ $T_0=20^0C$; $T_w=25^0C$; $x/d=20$; $d=0,003m$.

$\theta \backslash Re_{sm}$	2300	3000	4000	6000	8000	10000
0,3	0,007	0,007	0,008	0,007	0,007	0,007
0,4	0,029	0,029	0,033	0,032	0,032	0,033
0,5	0,079	0,082	0,096	0,095	0,099	0,102
0,6	0,179	0,190	0,225	0,230	0,241	0,252
0,7	0,350	0,379	0,456	0,475	0,504	0,531
0,8	0,620	0,681	0,828	0,875	0,926	0,960
0,9	1,010	1,117	1,344	1,330	1,278	1,179

Coefficient k_F . At calculation of coefficient k_F at first is necessary to express ξ_p and γ^2 from the equations (2) and (7) as function Re_p :

$$\xi_p = \frac{\xi'_{ot}}{2d\beta} \cdot Re_{sm} \cdot \xi_{sm} \cdot \left(\frac{1}{Re_p^3 + \frac{\alpha d}{\beta} \cdot Re_p^2} \right) \quad (17)$$

$$\gamma^2 = 0,07 \cdot Re_p^{1,2} \cdot \left(\frac{\lambda_1}{\lambda_p} \right) \cdot \left(\frac{d}{\beta \alpha} \right)^{0,8} \quad (18)$$

and to substitute them in the left-hand part of the equation (1). In a result we shall receive the nonlinear algebraic equation concerning a variable Re_p . This equation can be easily decided numerically by sorting out of values Re_p from 0 up to Re_{sm} or in the inverse order. After a determination of magnitude Re_p from the equation (2), it is possible to find magnitude k_F :

$$k_F = \frac{\xi_{sm}}{\xi_p} = \frac{2d\beta \cdot (Re_p^3 + \frac{\alpha d}{\beta} Re_p^2)}{\xi'_{ot} \cdot Re_{sm}^3} \quad (19)$$

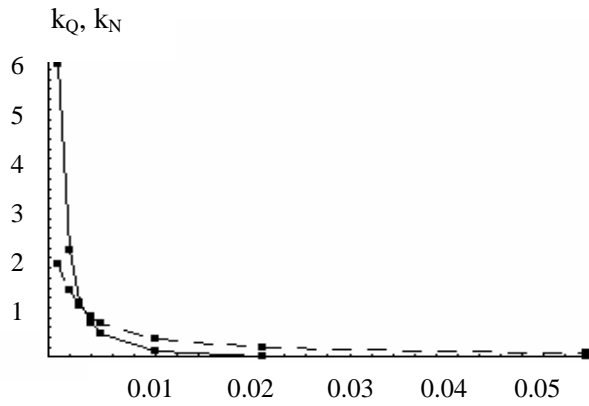
The data of calculation of magnitude k_F are submitted in the table 3.

Table 3. $k_F=f(Rep, \theta)$ $T_0=20^0C$; $T_w=25^0C$; $x/d=20$; $d=0,003m$.

$\theta \backslash Re_{sm}$	2300	3000	4000	6000	8000	10000
0,7	5,706	5,998	6,700	4,443	*	*
0,8	13,165	10,629	9,099	6,057	4,475	3,447
0,9	11,137	8,158	6,278	3,601	2,368	1,666

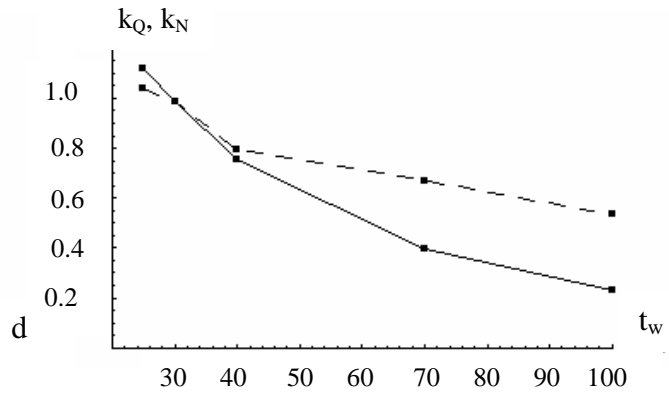
* in the table 3 means, that the solution of a problem at the given combination of calculated parameters does not exist.

Figs. 1–4 present the graphs of a change of the coefficients k_Q and k_N , depending on the diameter of a channel (m), the temperature of the channel wall ($^{\circ}\text{C}$), the Reynolds number of the compared smooth-wall channel Re_{sm} and the porosity. The following points were the initial parameters for the graphs: porosity $\theta = 0,9$; Reynolds number of the smooth - wall channel: $Re_{sm} = 3000$; the relative length of the channel $\xi_{sm} = x/d = 20$; diameter of the channel $d = 3\text{mm}$; the wall's temperature $T_w = 25^{\circ}\text{C}$; temperature of the fluid at the inlet of a channel $T_0 = 20^{\circ}\text{C}$.



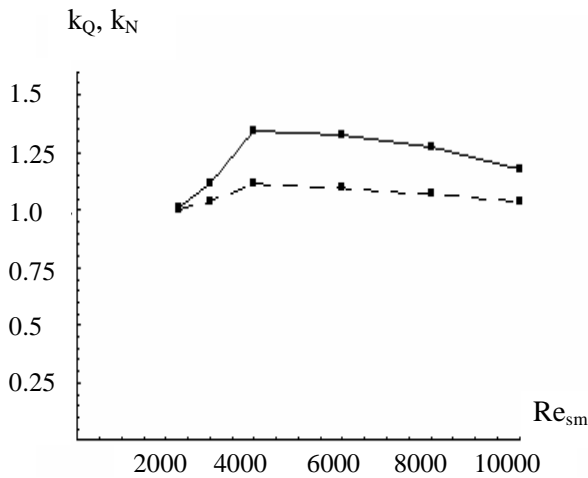
$Re_{sm}=3000$; $\xi_{sm}=20$; $T_0=20^{\circ}\text{C}$; $T_w=25^{\circ}\text{C}$; $\theta=0,9$
- - - - k_Q ; ——— k_N

Fig. 1. Dependence of coefficients k_Q and k_N from diameter of a channel.
 $k_Q; k_N = f(d, m)$



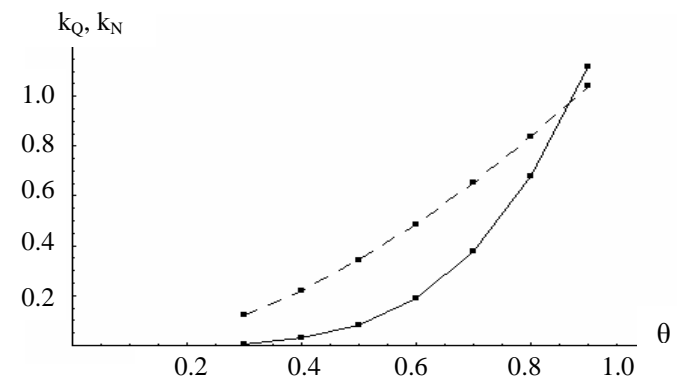
$Re_{sm}=3000$; $\xi_{sm}=20$; $T_0=20^{\circ}\text{C}$; $\theta=0,9$; $d=3\text{mm}$
- - - - k_Q ; ——— k_N

Fig. 2. Dependence of coefficients k_Q and k_N from temperature of a wall.
 $k_Q; k_N = f(t_w, ^{\circ}\text{C})$



$\xi_{sm}=20$; $T_0=20^{\circ}\text{C}$; $T_w=25^{\circ}\text{C}$; $d=3\text{mm}$; $\theta=0,9$
- - - - k_Q ; ——— k_N

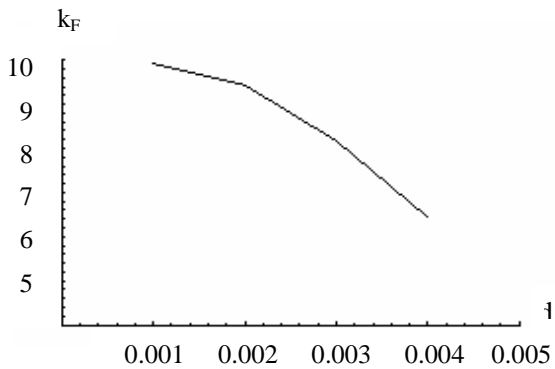
Fig. 3. Dependence of coefficients k_Q and k_N from Reynolds number of a channel with smooth wall
 $k_Q; k_N = f(Re_{sm})$



$Re_{sm}=3000$; $\xi_{sm}=20$; $T_0=20^{\circ}\text{C}$; $T_w=25^{\circ}\text{C}$; $d=3\text{mm}$;
- - - - k_Q ; ——— k_N

Fig. 4. Dependence of coefficients k_Q and k_N from porosity of a channel
 $k_Q; k_N = f(\theta)$

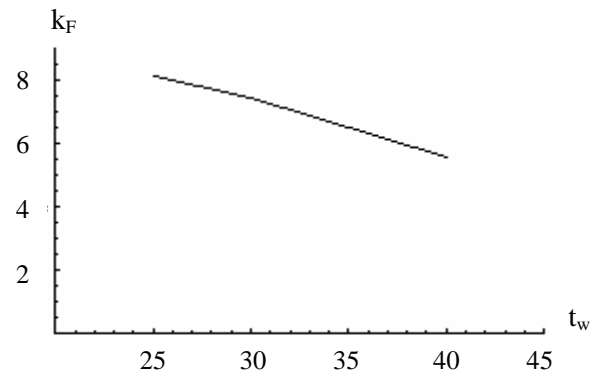
The behaviours of coefficient k_F depending on a diameter of the channel (m), the temperature of the channel wall ($^{\circ}\text{C}$), Reynolds number of the compared smooth-wall channel Re_{sm} and the porosity are submitted in figs. 5–8. Initial parameters for calculation of these diagrams were the same points, as for the diagrams of coefficients k_Q and k_N .



$Re_{sm}=3000; \xi_{sm}=20; T_0=20^{\circ}C; T_w=25^{\circ}C; \theta = 0,9$

Fig. 5. Dependence of coefficient k_F from diameter of a channel.

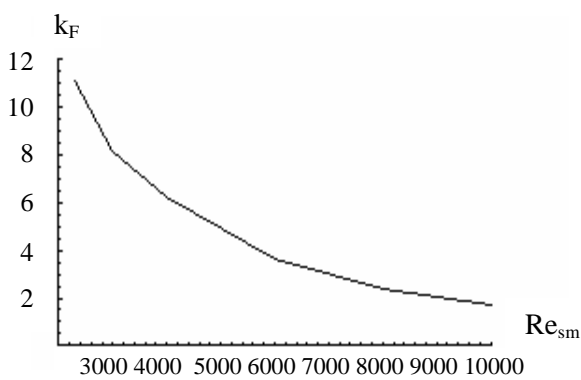
$$k_F = f(d, m)$$



$Re_{sm}=3000; \xi_{sm}=20; d=3mm; T_0=20^{\circ}C; \theta=0,9$

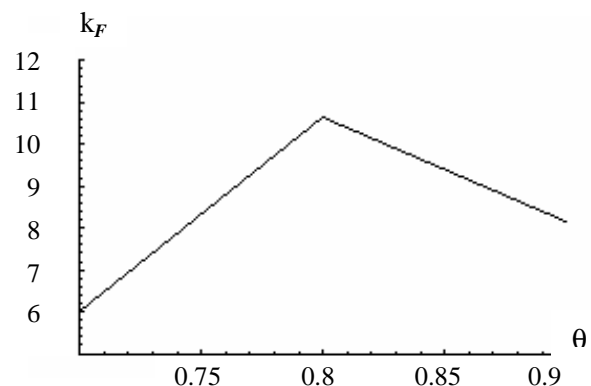
Fig. 6. Dependence of coefficient k_F from temperature of a wall.

$$k_F = f(t_w, ^{\circ}C)$$



$\xi_{sm}=20; T_0=20^{\circ}C; T_w=25^{\circ}C; d=3mm; \theta=0,9$

Fig. 7. Dependence of coefficient k_F from Reynolds number of a channel with smooth wall $k_F = f(Re_{sm})$



$Re_{sm}=3000; \xi_{sm}=20; T_0=20^{\circ}C; T_w=25^{\circ}C; d=3mm;$

Fig. 8. Dependence of coefficients k_F from porosity of a channel.

$$k_F = f(\theta)$$

CONCLUSION

In article the influence of parameters of regime and design of porous channels of round cross-section on their efficiency is explored. The area of parameters of porous heat exchangers are set, where the scoring in a heat transfer exceed losses on hydraulic resistance.

The analysis of the calculations of the effectiveness coefficients of porous structures k_Q ; k_N and k_F showed a general behavioral tendency with a change in the model's parameters. The values of the indicated coefficients vary inversely proportionally to a change of the diameter of a channel d , of difference of temperatures $t_w - t_0$ and of the length of the compared smooth-wall channel ξ_{sm} . The effectiveness coefficients k_Q and k_N vary directly proportionally to a change of the porosity θ . The dependence of coefficient k_F from a porosity of the channel has extreme view. The dependence of coefficients k_Q and k_N from Reynolds number in compared smooth-wall channel has extreme view too.

The behaviour of coefficient k_F depending on a Reynolds number in compared smooth-wall channel has inversely proportionally character.

The carried out calculations have shown, that the greatest values of effectiveness ratio k_Q , k_N and k_F can be reached at big values of a porosity ($\theta = 0,8-0,9$), at values of Reynolds numbers in the channel with smooth wall $Re_{sm} \approx 4000$.

In this case the quantity of heat, transmitted by the porous channel, in comparison with the quantity of heat, transmitted by the channel with smooth wall, at identical power, spent on press (pumping) of coolant through the channels, is incremented by 12 %.

At comparison of powers, spent on press (pumping) heat transfer medium through the channels (at identical quantity of heat, transmitted by the channels), it is possible to achieve magnification of effectiveness ratio in 1,34 times.

The value of dimensional coefficient of effectiveness ratio in this area of parameters reaches magnitude $k_F \approx 9 \div 10$.

During calculations a considerable increase of the effectiveness coefficients with the decrease of the diameter of a channel was shown too.

On the basis of the given data it is possible to make a inference, that the application of porous channels at a transition regime of a motion of a liquid coolant is expedient at removal of low of potential heat, at use of porous channels of a small diameter.

The obtained data testify to necessity of the further searching of parameters, in which there are the energy scoring of porous channels in comparison with traditional channels with a smooth wall.

NOMENCLATURE

c_p , J/(kg·K) – heat capacity of a fluid; d , m – diameter of the channel; F , m^2 – lateral area of the channel; F_{cs} , m^2 – cross-sectional area of the channel; G , kg/($m^2 \cdot s$) – specific mass rate of flux of a coolant; h_v , W/($m^3 \cdot K$) – intensity volumetric heat exchange inside of porous material; k_Q – thermal coefficient of effectiveness ratio; k_N – power coefficient of effectiveness ratio; k_F – surface (dimensional) coefficient of effectiveness ratio; \dot{m} , kg/s – Rate of flux of a fluid; N , W – power consumed for press (pumping) heat transfer medium through the channel; Nu – Nusselt number; Pe – Peclet number; Pr – Prandtl number; Q , W – quantity of transferred by the channel heat in unit of time; Re – Reynolds number; t , K – average temperature of a fluid on an output(exit) from the porous channel; \bar{T} , K – average temperature of a fluid on an output(exit) from the smooth-wall channel; x , m – coordinate along an axis of the channel; \bar{T}_i , K – the average temperature of a liquid over a length of a smooth-wall channel gained on i -th a step of iteration.

Special characters: α , m^{-2} -viscous coefficient of resistance of a porous material; α_i , W/($m^2 \cdot K$) – coefficient of a convective heat exchange gained on i -th a step of iteration; β , m^{-1} -inertial coefficient of resistance of a porous material; $\gamma^2 = h_v d^2 / \lambda_p$ – parameter, which characterizes intensity of heat exchange inside of porous material; λ_p , W/(m·K) – thermal conductivity of a porous material; λ_f , W/m·K – thermal conductivity of a fluid; μ , kg·m/s-coefficient of dynamic viscosity; ξ -dimensionless length of the channel; ξ'_{ot} – coefficient of hydraulic resistance in the smooth-wall channels.

Subscripts: cs – cross section; p – porous channel; sm – smooth-wall channel; w – wall; 0 – inlet.

References

1. Prisnyakov V.F. and Lukisha A.P. Computation of efficiency of porous heat exchangers with high heat conductivity applied in the structure of power plants. // *HEFAT 2008. 6th Intern. Conf. on Heat Transfer, Fluid Mechanics and Thermodynamics. 30 June–2 July 2008, Pretoria, South Africa.* Paper number: PV2.
2. Prisnyakov V.F. and Lukisha A.P. Calculation of efficiency of porous cylindrical channels at a turbulent motion of a liquid coolant and under the boundary conditions of the first type // *Proc. of the VII Minsk Intern. Seminar Heat Pipes, Heat Pumps, Refrigerators, Power Sources.* Minsk, Belarus, 8–11 September, 2008, Pp.430–437.
3. Guhman A.A. Intensifikatsija konvektivnogo teploobmena i problema sravnitelnoj otsenki teploobmennyh poverhnostej // *Teploenergetika.* 1977. No4. s. 5–8.
4. Gnielinski V. Neue Gleichungen für den Wärme-und Stoffübergang in turbulent durchströmten Rohren und Kanälen // *Forsch. Ing.* 1975. - B. 41, No 1. S.8.
5. Poljaev V.M., Majorov V.A., Vasiljev L.L. *Gidrodinamika i teploobmen v poristyh elementah konstruksij letatelnyh apparatov.* M.: Mashinostroenie, 1988. – 168 s.
6. Singh B.S., Dybbs A., Lyman F.A. Experimental study of the effective thermal conductivity of liquid saturated sintered fiber metal wicks. // *Int. J. Heat and Mass Transfer.* – 1973. - No 16. Pp. 1–12.
7. Kostornov A.G. *Pronitsaemye metallitsheskie voloknovye materialy.* – K.: Tehnika, 1983.
8. Petuhov B.S., Kirillov V.V. K voprosu o teploobmene pri turbulentnom techenii shidkosti v trubah // *Teploenergetika,* 1958, No. 4, s.63.
9. Petuhov B.S., Genin L.G., Kovalev S.A. *Teploobmen v jadernyh energeticheskikh ustanovkah.* M.: Energoatomizdat, 1986. – 472 s.
10. Kutateladse S.S. *Teploperedacha i gidravlicheskoje soprotivlenie.* M.: Energoatomizdat, 1990. – 367s.
11. Dejch M.E., Zarjankin A.E. *Gidrogazodinamika.* M.: Energoatomizdat, 1984. – 384 s.

EXPERIMENTAL STUDY OF THE INFLUENCE EFFECTS OF VIBRATION AND ANGLE TO THE HORIZONTAL ON THE DYNAMICS OF START-UP AND TRANSIENT REGIMES OF THE HEAT PIPE

V. I. Lutsenko, V. I. Eliseyev

Department of Mechanics of Machines and Processes of Processing Mineral Raw Materials
The Polyakov Institute of Geotechnical Mechanics
of National Academy of Science of Ukraine
Simpheropolskaya, 2A, Dnepropetrovsk, 49005, Ukraine
+38(0562) 460151; E-mail: nanu@igtm.dp.ua

Abstract

Heat pipes with metal-fibrous capillary structure was studied. Frequency range studied was 10–4000 Hz, the vibration level from 0 to 100 m/s². Rotation of the pipe with respect to the horizon at any angle had. Ten thermocouples on the outer surface of the pipe in the heating zone, and three thermocouples on the outer surface of the cooling zone were established. Portholes of glass at the ends of the heat pipe were made. The start-up the heat pipe was studied. Effect of vibration and tilt angles of the heat pipe on its parameters are shown. Determined that the slope of the heat pipe $\alpha = +30^\circ$ is optimal. Vibration increases the temperature drop. It was established that the dynamic properties of the cooling system with heat pipe are determined by external boundary conditions. Heat Pipe responds quickly to changes in external boundary conditions, and its thermal resistance varies widely.

KEYWORDS

Heat pipe, start up, transition mode, temperature, vibration, experiment, heating, cooling.

INTRODUCTION

Since the publication of books [1–7] many years have passed. The processes of heat and mass transfer in heat pipes at all times intensively studied. At the present time, these processes are well known for classic designs of heat pipes and conventional conditions. The influence of external force fields on the processes of heat and mass transfer in heat pipes and heat exchange systems based on them continues to be actively studied. Vibration field is such a field, and occurs in all technical devices. Problem of the influence of vibrations on heat and mass transfer, including those in heat pipes, have been studied in [8] and later publications, carried out under the supervision of Professor VF Prisnyakova, for example [9–11]. Ambiguity effect of vibration on heat and mass transfer, is shown in these papers. Further studies are needed, including experiments.

The results of experiments to study the combined effect of vibration and gravitational fields on the surface temperature of the heat pipe during startup and transient conditions are presented below.

THE EXPERIMENTAL MODEL

For the experiments we used apparatus consisting of vibrating table VEDS-400, the device of measurement of vibration parameters, analog-digital converter and personal computer. This construction of was used in [10] and described it in more detail.

Studied the heat pipe on the water 0,3 m in length, outer diameter of 0,035 m. The body and the capillary structure of the pipe were made of copper. Pipe wall thickness $1.25 \cdot 10^{-3}$ m, the thickness of the porous structure $1 \cdot 10^{-3}$ m, the porosity of the wick 81%, fiber diameter $50 \cdot 10^{-6}$ m. At each end of the heat pipe were fixed portholes of glass for visual monitoring of processes on the surface of the capillary structure and the vapor channel. It was possible to rotate the pipe at any angle relative to horizontal. For supplying heat to the heating zone of the heat pipe used heater of nichrome wire. Heating zone was insulated from the environment with glass wool. Heat pipe is cooled by convection and radiation. Ten thermocouples were

located on the outer surface of the pipe in the heating zone and three in the cooling zone. The geometry of the working area and the location of the thermocouples are shown in Fig. 1.

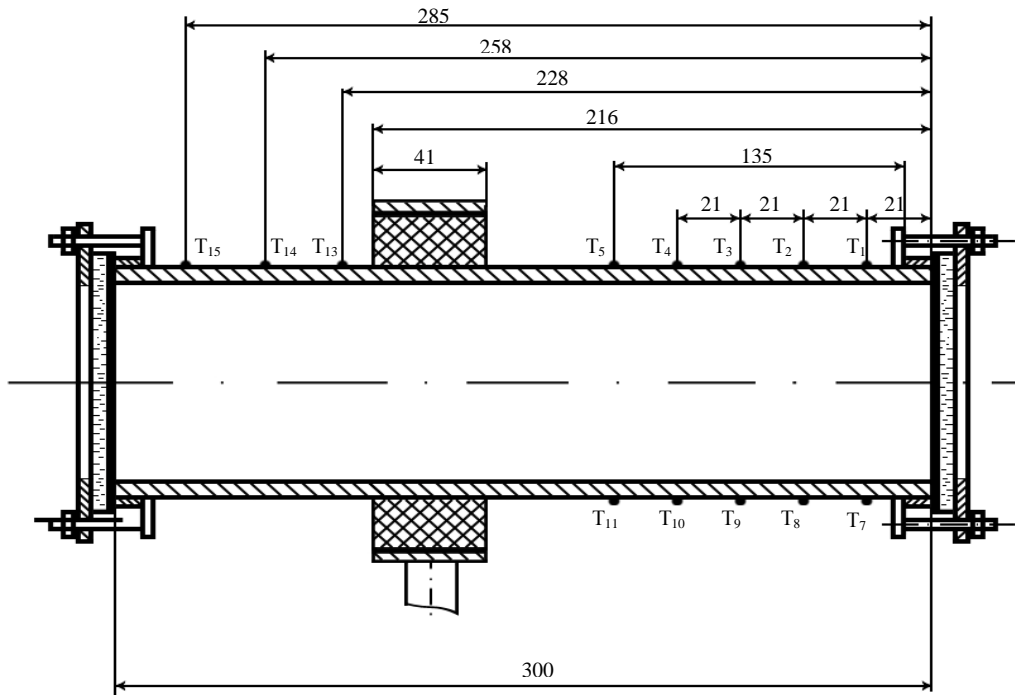


Fig. 1. Arrangement of thermocouples

GENERAL COMMENTS ON EXPERIMENT

Design features of the heat pipe led to a restriction on the maximum allowable temperature in the heating zone. Therefore, electrical power was limited. It is not possible to examine all regime of heat pipe. In fact, the radial heat flow in the heating zone does not exceed the value $2 \cdot 10^3 \text{ W/m}^2$, which corresponds to the evaporative regime of the heat pipe. The maximum value of axial heat flow was about $5 \cdot 10^4 \text{ W/m}^2$, and speed of vapor at the outlet of the evaporation zone was less than 1 m/s at the initial time and decreased to 0.025 m/s at maximum temperature. The methodology of the experiments was chosen such that a constant value was supplied to the pipe, electric power and the variable parameters were the frequency of vibration, acceleration and angle of the heat pipe with respect to horizon. We studied various options of start up the heat pipe. Was studied start up without vibrations at different orientations of the pipe in the gravity field. In these experiments, to a heat pipe, was first fed only electrical power. Vibration were added after the release of the heat pipe at the stationary state. Cases, when vibration was imposed simultaneously with the application of electrical power, were considered also. Angles of the heat pipe to the horizon line changed from -90 degrees (zone of heating from above) to $+90$ degrees (zone of heating from below). For angles -90° and -45° the stationary states were not achieved due to exceeding the maximum allowable temperature in the heating zone. The range of frequencies that were studied was 10–4000 Hz, the range of vibroaccelerations 0–100 m/s^2 . Poll of each thermocouple was been 16 measurements per second. For one thermocouple recorded about 100 thousand of values during each experiment. To reduce the data set was collected every 16 value. As a result, the data array contains data of thermocouples at intervals of 1 second.

EXPERIMENTAL RESULTS

In experiments was conducted video and photography of the internal surface of capillary-porous structure and the vapor channel of the heat pipe, and also visual observations. For an example, on Fig. 2 shows photos of the capillary structure in the evaporation zone (a), (b) and vapor channel (c). In the photographs are clearly visible differences in appearance of the surface of the porous structure is no working (a) and working (b) heat pipe. During the work, the surface of the heating zone looks shiny and sometimes observed phenomena similar to the bursting of bubbles. Condensing vapor is noticeable in the vapor channel in the cooling zone. Observations have not detected any changes associated with the action of vibration. In experiments on single capillaries [9], we have observed emission of single drops of fluid from the surface of the liquid meniscus in the vapor zone. In these experiments, similar phenomena were not observed.

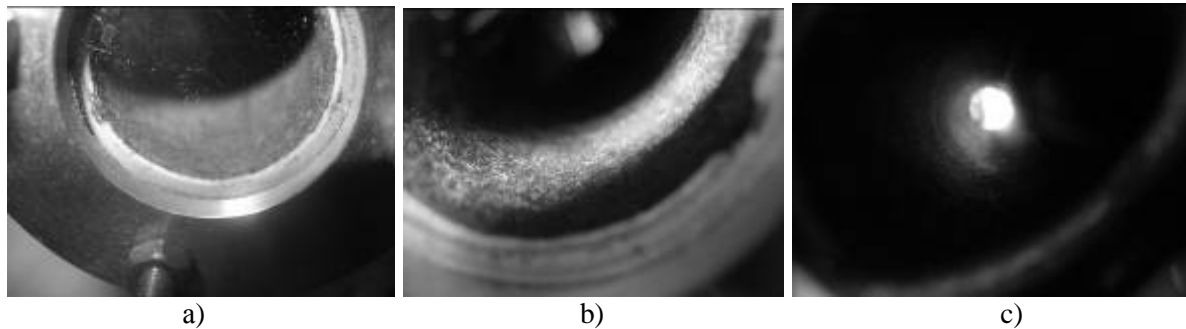


Fig. 2. The inner surface of the capillary structure and the vapor channel of the heat pipe

After averaging and sampling of experimental points, the schedules of change of temperatures of points of a surface of the heat pipe in time have been constructed. The temperature drop on length of a heat pipe was defined on the maximum temperature difference between the zones of heating and cooling. These data is shown in Figs. 3–9. In order not to clutter the drawings, shows the data of three thermocouples T_1 , T_3 , T_5 , in the evaporation zone and three T_{13} , T_{14} , T_{15} in the condensation zone.

The results of determination effect of low-frequency vibrations on the temperature field of a horizontal heat pipe (experiment 9) are shown in Fig. 3.

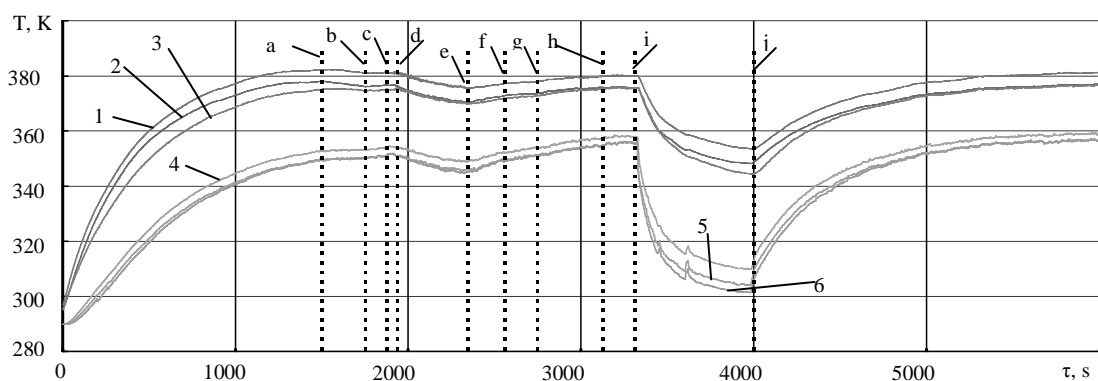


Fig. 3. The dependence of the surface temperature of the heat pipe on time at low-frequency vibrations. Horizontal position (experiment 9): 1 – thermocouple T_3 ; 2 – T_1 ; 3 – T_5 ; 4 – T_{13} ; 5 – T_{14} ; 6 – T_{15} .

0-a – $F = 0$; a-b – $F = 50$ Hz, $a = 60$ m/s²; b-c – $F = 100$ Hz, $a = 60$ m/s²; c-d – $F = 0$; d-e – $F = 25$ Hz, $a = 60$ m/s²; e-f – $F = 0$; f-g – $F = 10$ Hz, $a = 36$ m/s²; g-h – $F = 200$ Hz, $a = 62$ m/s²; h-i – $F = 0$; i-j – $F = 0$, forced cooling; j-6000 – free convection

On an the interval 0-a pipe was heats without vibration. In a point vibration by frequency of 50 Hz and vibroacceleration 60 m/s^2 have been established. Temperature field did not change almost. Temperature T_3 decreased slightly. Temperatura T_1 decreased more due to the increased heat removal from the glass illuminator. At point b the frequency was increased to 100 Hz. Acceleration is not changed. At the c point of vibration exposure was removed, and the point d again let down with a frequency of 25 Hz and the vibration acceleration 60 m/s^2 . On an interval d-e appreciable drop of temperature is visible. In a point e vibrations have been switched off, and in a point f are included, but with frequency of 10 Hz and vibration acceleration 36 m/s^2 . The slope of the curves changed slightly. At the point g vibration frequency was increased to 200 Hz, and the vibration acceleration of up to 60 m/s^2 . At the point h vibrations were turned off and after reaching the stationary state at the point i forced cooling was turned on. At the j point forced cooling was turned off. Gradually, the stationary temperature level was established, corresponding to the level at the i point. This experiment showed that low-frequency vibrations at specified frequencies and accelerations have little effect on the temperature field of heat pipes in a horizontal position, with the exception of the frequency of 25 Hz.

Vibration frequency Influence on the temperature surface of the heat pipe in horizontal position (experiment 18) are shown in Fig. 4. In this experiment more high-frequency range was used. Start up the pipe was carried out with imposing of a vibrating field by frequency of 50 Hz and the vibration acceleration 60 m/s^2 . At the a point vibration was turned off and on the a-b section the heat pipe works without vibration. At the b point has been turned on vibrating field at 50 Hz. This experiment confirmed that the vibration exposure, except for the frequency of 25 Hz, no significant effect on the temperature field of the external surface of the heat pipe.

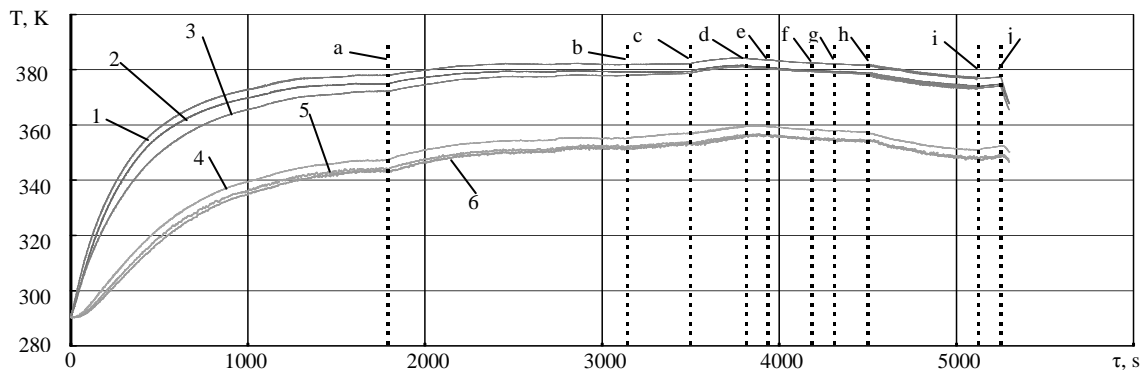


Fig. 4. The dependence of the surface temperature of the heat pipe from time to time at different frequencies. Horizontal position (experiment 18): 1 – thermocouple T_3 ; 2 – T_1 ; 3 – T_5 ; 4 – T_{13} ; 5 – T_{14} ; 6 – T_{15} .

0-a – $F = 50 \text{ Hz}$, $a = 60 \text{ m/s}^2$; a-b – $F = 0 \text{ Hz}$; b-c – $F = 50 \text{ Hz}$, $a = 58 \text{ m/s}^2$; c-d – $F = 200 \text{ Hz}$, $a = 64 \text{ m/s}^2$; d-e – $F = 400 \text{ Hz}$, $a = 58 \text{ m/s}^2$; e-f – $F = 1000 \text{ Hz}$, $a = 60 \text{ m/s}^2$; f-g – $F = 2000 \text{ Hz}$, $a = 60 \text{ m/s}^2$; g-h – $F = 4000 \text{ Hz}$, $a = 60 \text{ m/s}^2$; h-i – $F = 25 \text{ Hz}$, $a = 60 \text{ m/s}^2$; i-j – $F = 0 \text{ Hz}$, $a = 6000 - N = 0$

Effect of inclination angle of the heat pipe to the horizon on her work shown in Fig. 5 (experiment 25). Start up has been in an upright position with the supply of heat from below and vibration. Pipe entered the stationary regime at time b. At this point the vibrations were turned off. For angle $+30^\circ$ temperature in a heating zone is minimal (zone c-d). Safe operation of a heat pipe with $\alpha = -90^\circ$ could not be achieved without the action of vibration (zones e-f and h-i). Limit the temperature in the heating zone at a safe level was due to vibration (zone g-h).

After determining the most effective frequency of exposure and the optimum angle of inclination, was studied the effect of acceleration on the work of the heat pipe (Fig. 6, experiment 27).

In this experiment, the angle of the pipe has not changed and was equal to $+30^\circ$. Start up of the heat pipe was carried out under the action of vibration of $F = 25 \text{ Hz}$, $a = 60 \text{ m/s}^2$.

Stationary state was reached at time a, and vibration have been disabled. Temperature field stabilized at a new higher level (b point). At time b were again included vibration with the same frequency and amplitude. Temperatures dropped to previous levels. After stabilizing the temperature at the point c, the vibration acceleration was increased to 100 m/s^2 . Temperature at all points of the pipe down. In the cooling zone the decrease was more pronounced. Thus, increasing the acceleration has led to a decrease in temperature. This is natural, as it increases the amplitude of the surface, which intensifies the process of cooling.

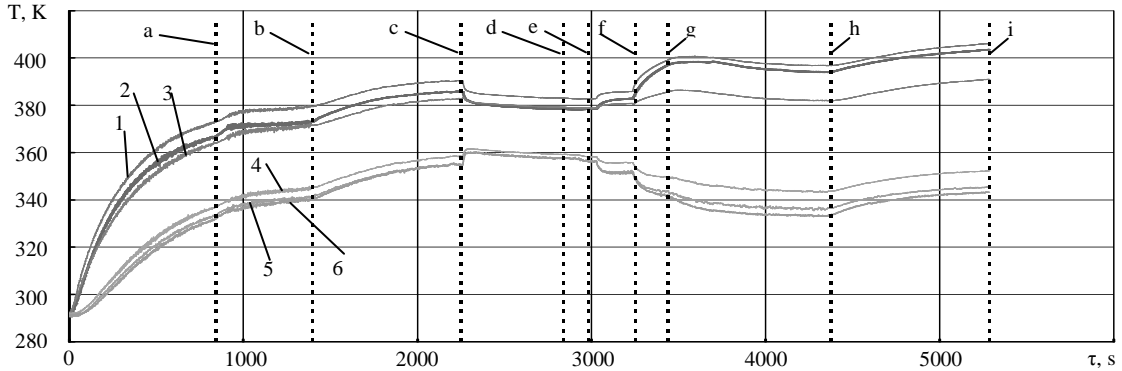


Fig. 5. The dependence of the surface temperature from time at different angles of inclination of the heat pipe (experiment 25): 1 – thermocouple T_3 ; 2 – T_1 ; 3 – T_5 ; 4 – T_{13} ; 5 – T_{14} ; 6 – T_{15} .
0-a – $\alpha = +90^\circ$, $F = 25 \text{ Hz}$, $a = 60 \text{ m/s}^2$; a-b – $\alpha = +90^\circ$, $F = 25 \text{ Hz}$, $a = 60 \text{ m/s}^2$; b-c – $\alpha = +90^\circ$, $F = 0$; c-d – $\alpha = +30^\circ$, $F = 0$; d-e – $\alpha = +20^\circ$, $F = 0$; e-f – $\alpha = 0^\circ$, $F = 0$; f-g – $\alpha = -90^\circ$, $F = 0$; g-h – $\alpha = -90^\circ$, $F = 25 \text{ Hz}$, $a = 60 \text{ m/s}^2$; h-i – $\alpha = -90^\circ$, $F = 0$

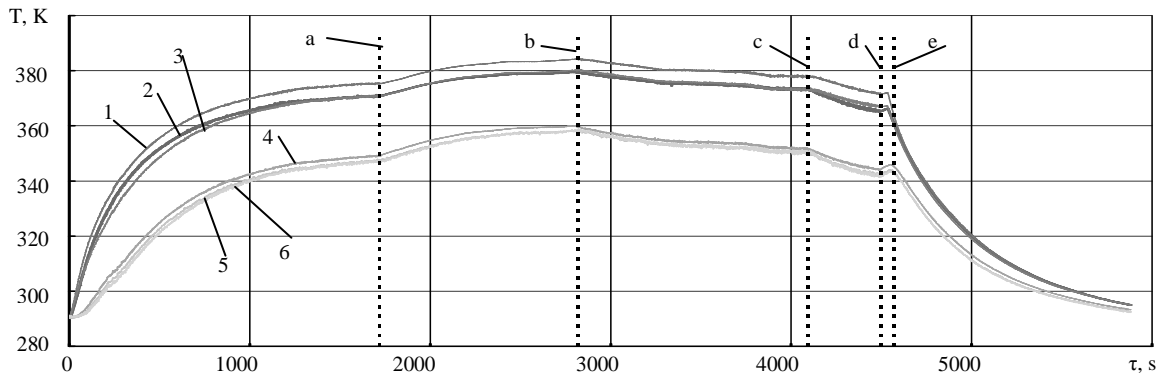


Fig. 6. Dependence of change surface temperature to time for different values of acceleration (experiment 27): 1 – thermocouple T_3 ; 2 – T_1 ; 3 – T_5 ; 4 – T_{13} ; 5 – T_{14} ; 6 – T_{15} . $\alpha = +30^\circ$.
0-a – $F = 25 \text{ Hz}$, $a = 60 \text{ m/s}^2$; a-b – $F = 0$; b-c – $F = 25 \text{ Hz}$, $a = 60 \text{ m/s}^2$; c-d – $F = 25 \text{ Hz}$, $a = 100 \text{ m/s}^2$; d-e – $F = 0$; e-5800 – $N = 0$

From the graphs in Figs. 3–6, we can conclude that the change in the slope, causing a sharp change in temperature. Position with an angle of about 30° is optimal. Vibration have a milder effect and the temperature field varies smoothly. Frequency of 25 Hz was the most effective in these experiments.

In next three Figures 7–9 are shown the data on the change on time of maximum temperature difference $\Delta T_{3-15} = T_3 - T_{15}$ along the length of the heat pipe. Figure 7 shows the change of difference temperature for

experiment 9. The behavior of the difference temperature differs from the distribution of the absolute temperature (Fig. 3). The temperature difference increases up to time about 400 s, and then begins to decrease. But, if on the interval d-e absolute temperature decreases (Fig. 3), the difference it is insignificant, but increases. Hence, vibrations by frequency of 25 Hz have lowered the general level of temperatures, but haven't lowered the thermal resistance of heat pipe. In the interval e-i the difference temperature continued to decrease, although heat pipe at this time was under the influence different effects of vibration, and its temperature at all points only continued to increase. At the moment of time i, was included forced cooling. Absolute temperature dropped sharply at all points, but the temperature difference on the contrary increased twice and stayed at a new level. Probably, this is due to the presence of non-condensing gas in the vapor channel.

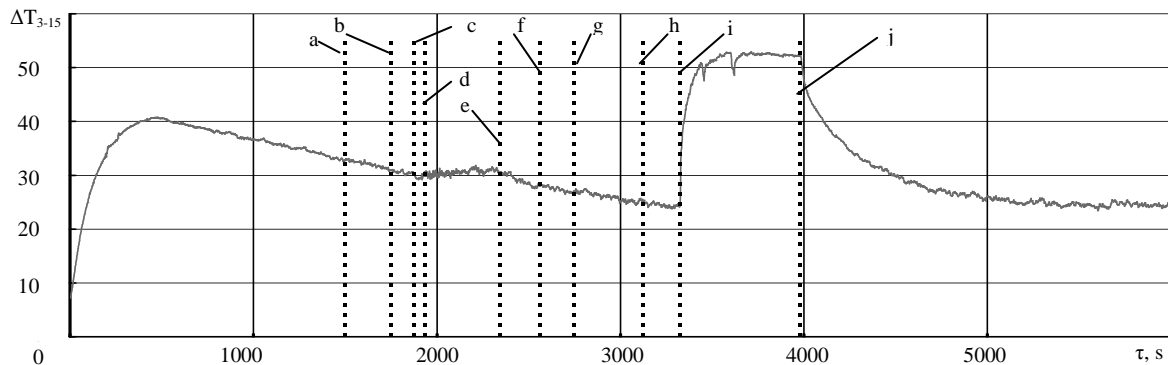


Fig. 7. Effect of low-frequency vibrations on the behavior difference of temperature between the zones of heating and cooling. Experiment 9: 0-a – $F = 0$; a-b – $F = 50$ Hz, $a = 60$ m/s²; b-c – $F = 100$ Hz, $a = 60$ m/s²; c-d – $F = 0$; d-e – $F = 25$ Hz, $a = 60$ m/s²; e-f – $F = 0$; f-g – $F = 10$ Hz, $a = 36$ m/s²; g-h – $F = 200$ Hz, $a = 62$ m/s²; h-i – $F = 0$; i-j – $F = 0$, forced cooling; j-6000 – free convection, $N = 34$ W

The following fig. 8 shows the data of the experiment 18 (see Fig. 4). In this experiment, the pipe also was in a horizontal position, but more high-frequency range of vibrations was investigated. In the frequency range 50–400 Hz are observed decrease in the difference of temperature. In the range 400–4000 Hz, influence of vibration not considerably. As in the previous figure, the difference of temperature increases at vibration frequency of 25 Hz.

Finally, in Fig. 9 shows the results of the experiment 25 (see Fig. 5), which studied the effect of vibration and angles of tilt of the heat pipe at its parameters. Here it is interesting to notice that the change in the angle of slope from $\alpha = +90$ to $\alpha = +30^\circ$ without influence of vibrations has led to sharp decrease of the temperature drop along the heat pipe, and horizontal position of heat pipe has led to increase the difference of temperature on 10 K. The maximum temperature difference observed at negative angles.

As a whole on these figures we can say that the temperature difference between the zones of heating and cooling in the heat pipe depends on the frequency of vibration and the angle of inclination of the heat pipe to the horizon in a complicated manner. Dependence on the angle is more sharply is expressed. The smallest temperature difference was observed at an inclination of 30 and It was equal 25 K.

In conclusion, we note that the temperature differences between pairs of diametrically opposite points pretty quickly adopt the steady value of about 6 K and further fluctuate about this value. Short-term deviations of the temperature difference at change of inclination angle heat pipe were observed.

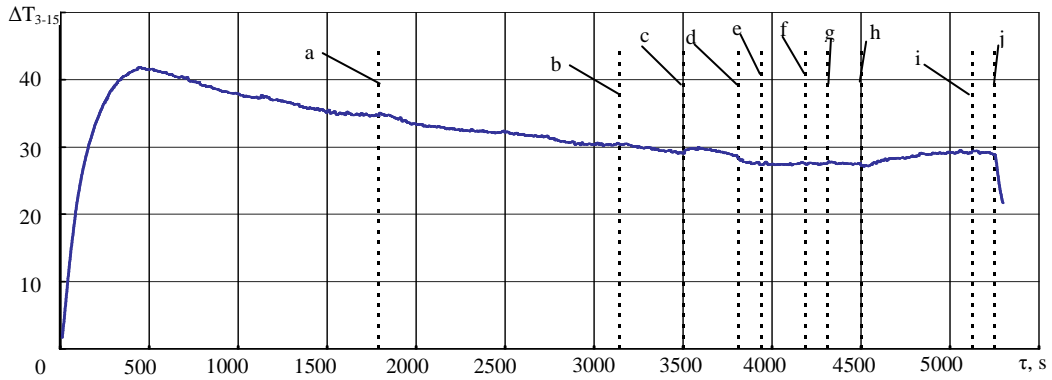


Fig. 8. Effect of vibrations on the behavior difference of temperature between the zones of heating and cooling. Experiment 18:1 – $\Delta T_{3-15} = T_3 - T_{15}$
 0-a – $F = 50$ Hz, $a = 60$ m/s²; a-b – $F = 0$; b-c – $F = 50$ Hz, $a = 58$ m/s²; c-d – $F = 200$ Hz, $a = 64$ m/s²; d-e – $F = 400$ Hz, $a = 58$ m/s²; e-f – $F = 1000$ Hz, $a = 60$ m/s²; f-g – $F = 2000$ Hz, $a = 60$ m/s²; g-h – $F = 4000$ Hz, $a = 60$ m/s²; h-i – $F = 25$ Hz, $a = 60$ m/s²; i-j – $F = 0$, j-6000 – $N = 0$ W

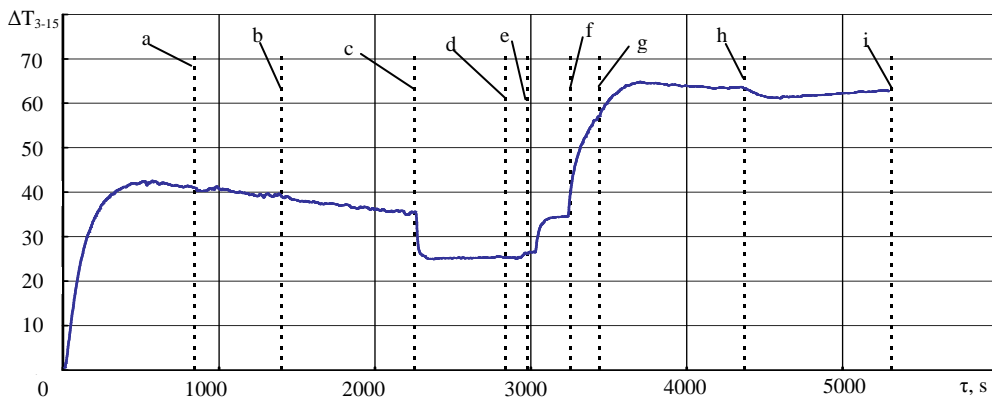


Fig. 9. Effect of inclination angle of the heat pipe to the horizon on the behavior difference of temperature between the zones of heating and cooling (experiment 25): 0-a – $\alpha = +90^\circ$, $F = 25$ Hz, $a = 60$ m/s²; a-b – $\alpha = +90^\circ$, $F = 25$ Hz, $a = 60$ m/s²; b-c – $\alpha = +90^\circ$, $F = 0$; c-d – $\alpha = +30^\circ$, $F = 0$; d-e – $\alpha = +20^\circ$, $F = 0$; e-f – $\alpha = 0^\circ$, $F = 0$; f-g – $\alpha = -90^\circ$, $F = 0$; g-h – $\alpha = -90^\circ$, $F = 25$ Hz, $a = 60$ m/s²; h-i – $\alpha = -90^\circ$, $F = 0$

CONCLUSION

1. The best condition of capillary transport (angle $\alpha = +90^\circ$) don't provide a minimum level of temperatures. The temperature in the heating zone was minimal when the angle of inclination $\alpha = 30^\circ$. This angle is optimal for a given heat pipe. Vibration, except for frequencies 25 Hz, no significant effect on the temperature field of the heat pipe, which we studied. Vibration with a frequency of 25 Hz reduces the temperature level at all points of the pipe.

2. Thermal resistance of heat pipe at a stationary state depends on the frequency of vibration and the angle inclination of pipe to the horizontal. Dependence on the angle of inclination has been expressed more

sharply. The minimum temperature difference was observed at an inclination of the heat pipe to the horizon of $+30^\circ$ and was 25 K. Work at negative angles leads to a significant increase in temperature difference. Vibration with a frequency of 25 Hz and vibration acceleration 100 m/s^2 leads to a increase the temperature difference between the zones of heating and cooling by 18%.

3. Time of an establishment of a stationary temperature field of an external surface was equal 1500–1800 s in the time of start up of heat pipe. The thermal resistance of the heat pipe has increased to the maximum value 42 K in a time of about 500 s and then smoothly decreased to stationary value.

4. In working order, the heat pipe is sufficiently responsive to changes in external boundary conditions, and its thermal resistance varies widely.

References

1. *Low-temperature heat pipes* / Ed. L.L. Vasilieva, Minsk: Nauka i Technology, 1976. – 136 pp.
2. Ivanovskiy M.N., Sorokin V.P., Yagodkin I.V. *Physical principles of heat pipes*. Moscow: Atomizdat. 1978. – 256 pp.
3. Dan P., Ray. D. *Heat Pipes*. Moscow: Energy 1979. 272 pp.
4. Semena M. G., Gershuni A. N., and Zaripov V.K. *Heat pipes with metal-fibrous capillary structures*, Kiev: Visha Shola, 1984. 215 pp.
5. Kovalev S.A, Soloviev S.L. *Evaporation and condensation in heat pipes*. Moscow: Nauka, 1989. – 112 pp.
6. Tolubinskiy ., Shevchuk E.N. *High temperature heat pipes*. Kiev: Naukova Dumka, 1989. – 168 pp.
7. Prisniakov V.F., Lutsenko V.I., Navruzov Y.V. *Processes heat and mass transfer in heat pipes.*, Kiev: Naukova Dumka, 1992. – 160 pp.
8. Prisniakov V., Bondarenko S., Lutsenko V. *Heat and Mass Transfer and vibration* / Und. the gen. ed. V.F Prisniakova. Neptune Technology, Odessa, 2001. – 208 pp.
9. Eliseyev V. I., Lutsenko V. I., Prisniakov V. F. The phenomena of the hysteresis in capillaries // *VII Minsk Int. Seminar "Heat Pipes, Heat Pumps, Refregerators, Power Sources"*, Minsk: ITMP, Belarus, 2008. Pp. 388–394.
10. Prisniakov V. F., Marchenko O. L., Prisniakov K. V. Influence Of External Factors On Starting And An Operation Of Heat Pipes As A Component Of The Space Propulsion Systems // *The 59th Int. Astronautical Congress, Glasgow, Scotland, 29 September-3 October 2008, Paper-Nr: IAF-08-C4.3.2.* 15 pp.
11. Prisniakov K., Marchenko O., Melikaev Yu., Kravetz V., Nikolaenko Yu., Prisniakov V.. About the complex influence of vibrations and gravitational fields on serviceability of heat pipes in composition of the space-rocket systems // *Acta Astronautica*, 2004. Vol. 55. Pp. 509–518.

TWO-PHASE FLOW ENTROPY GENERATION IN MICROCHANNELS WITH VARIABLE CROSS SECTIONS

A. Nouri-Borujerdi

Islamic Azad University, south Tehran Branch
Tehran, Iran

Abstract

This work has been focused on modeling and optimization of two-phase forced convective flow in a rectangular microchannel with variable cross section under a constant heat flux. The procedure is based on the minimization of entropy generation resulting from viscous fluid effects and heat transfer for a homogeneous two-phase flow of a pure fluid to determine the overall performance of the microchannel. The entropy generation rate is obtained by using the conservation equations for mass and energy with the entropy balance. The channel is minimized in terms of channel aspect ratio, fin efficiency, outlet vapor quality and total mass flow rate. The contributions of thermal resistance include conductance resistance in the fin, convective resistance at the solid-fluid interface and fluid resistance. Contribution of heat transfer, pressure drop and phase-change process are determined by using the mixture model. The findings indicate that the location of the lowest entropy generation moves toward the higher aspect ratio for higher outlet vapor qualities. In addition, the slope of the entropy gradient is much steeper for aspect ratios smaller than the critical one. This is because of more effect of pressure contribution on the entropy generation than that of the heat transfer for smaller aspect ratios.

KEYWORDS

Microchannel, variable cross section, two-phase flow, entropy generation.

INTRODUCTION

Two-phase flow in a microchannel fabricated using micromachining technologies has become very important in many micro-scale devices such as micro heat pipe, fuel cell, Lab-on-chip technology, medical and aircraft industries. For instance, a micro heat pipe is a triangular cross section or other cross section with sharp corners and that has a diameter between about 100 μm and 2 mm. It uses the sharp corner regions instead of a wick to return the working fluid from the condenser to the evaporator. Or, performance gains in proton exchange membrane fuel cell can be attained by utilizing microchannels in the range of 0.05–1 mm to improve gas routing. Optimization of microchannels is promising because it requires less pumping power and high heat transfer rate due to an increase in surface area and a decrease in the convective resistance at the solid/fluid interface. In order to successfully design such devices, understanding of flow physics in micro scale and their engineering modeling are necessary. The behavior of gas-liquid two-phase flows in mini and microchannels is often different from those in macrochannels. One reason for this difference is the ratio of the gravitational effects to the surface tension, $gd^2\Delta\rho/\sigma$ as reported by N. Brauner et al. [1].

S. G. Kandlikar and W. J. Grande [2] investigated the need for enhanced plain rectangular microchannels and obtained the water cooling limits of the microchannels for high heat flux dissipation. They described a simplified and well-established fabrication process to fabricate three dimensional microchannels. They also demonstrated the efficacy of the fabrication process in fabricating complex microstructures within a microchannel. W. A. Khan et al. [3] studied an entropy generation minimization procedure to optimize the overall performance of microchannel heat sinks. They assessed the combined effects of thermal resistance and pressure drop simultaneously as the heat sink interacts with the surrounding flow field. A new general expression was developed for the entropy generation rate by considering an appropriate control volume and applying mass, energy, and entropy balances. They also explored the effect of channel aspect ratio, fin spacing ratio, heat sink material, Knudsen numbers and accommodation coefficients on the entropy generation rate in the slip flow region. K. Chen [4] used the second law of thermodynamics to optimize microchannels by considering heat conduction in the flow direction and

neglecting the entrance effects and friction losses. E. Galvis and G. R. Culham [5] presented a procedure that allowed the channel width in microheat exchanger to be optimized for a prescribed microheat exchanger size and channel depth. The procedure was based on the minimization of entropy generation resulting from viscous fluid effects and heat transfer for laminar and developed fluid flow. The optimum channel aspect ratio for the study cases showed a linear behavior with the channel depth and similar results were observed for isothermal and isoflux boundary conditions. By two different approaches, R. Revellin et al. [6] estimated local entropy generation rate for diabatic saturated two-phase flow of a pure fluid. These two approaches are the separated flow model using the classical vapor flow quality, and the mixture model, using the thermodynamic vapor quality. They proposed two distinct expressions for the local entropy generation. The contribution of heat transfer, pressure drop and phase-change process are determined using the mixture model. The developed formulation is applied to analyze the thermodynamic performance of enhanced heat transfer tubes under different conditions. They concluded that enhanced tubes may be a relevant solution for reducing entropy generation at low mass velocities whereas smooth tubes remain the best solution at higher ones. I. Papautski et al. [7] conducted some experiments with single phase gas flow in a microchannel. They discussed that the data of the friction factor of slip flow had approximately been reduced 60% compared to macroscale theory at the same Reynolds number. G. Ibáñez and S. Cuevas [8] analyzed a thermally fully developed flow in a parallel plate microchannel under conducting walls of finite thickness conditions. The flow is produced by a Lorentz force created by a transverse magnetic field and an injected electric current as occurs in a magneto-hydrodynamic micropump. The entropy generation rate is used as a tool for the assessment of the intrinsic irreversibilities present in the microchannel owing to viscous friction, heat flow and electric conduction. They minimized the global entropy generation rate by using velocity, temperature and current density fields in the fluid and walls for specific values of the geometrical and physical parameters of the system. They also calculated Nusselt number for different conditions under which to determine optimized conditions that lead to a minimum dissipation consistent with the physical constraints demanded by the microdevice.

This paper aims to study the optimization of thermal and hydraulic resistances of two-phase flow in microchannels with variable cross section. The complicated physics of two-phase flow in microchannels with variable cross section has not received any attention yet. All relevant design parameters including geometric parameters and material properties are optimized simultaneously by minimizing the entropy generation rate.

PROBLEM STATEMENT

A steady state homogeneous forced convective boiling model is considered in a plain rectangular microchannel ($a \times b \times L$) with variable side b , (Fig. 1). The top, left and right side surfaces are insulated and the bottom surface is uniformly heated. A two-phase flow passes through the microchannel along the z -axis and takes heat away from the heat dissipating electronic component attached below with an inlet temperature T_{sat} . The microchannel is taken from a collection of N channels.

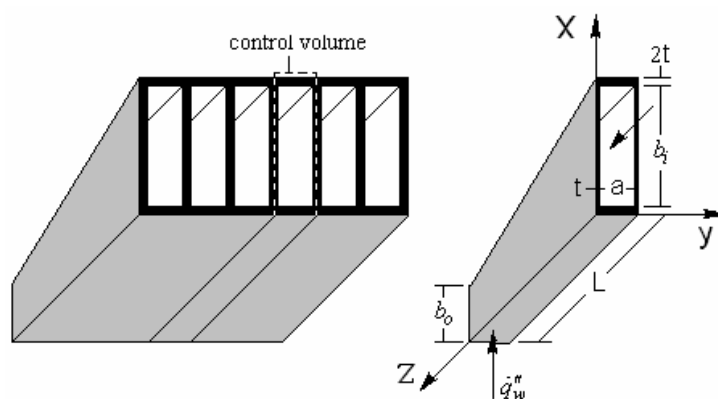


Fig. 1. Schematic diagram of a microchannel with variable cross section

The irreversibility of this system is due to friction and to heat transfer across the finite wall-bulk fluid temperature difference. The liquid-vapor two-phase heat transfer is characterized by a finite wall-bulk fluid temperature difference ΔT and a finite frictional pressure gradient. Using the second law of thermodynamic, the rate of entropy generation for a control volume of a saturated two-phase flow in the microchannel will be

$$dS_{gen} = \dot{m}ds - \frac{\delta\dot{q}_w}{T_{wo}}. \quad (1)$$

On the other hand, for any simple compressible substance, the second law of thermodynamics is

$$ds = \frac{h_{fg}dx}{T_\infty} - \frac{\vartheta}{T_\infty}dP. \quad (2)$$

Heat transfer in the control volume (Fig. 1) is a conjugate and that is combination of heat conduction in the fin and convection to the cooling fluid. Applying the energy and the momentum equations to the same control volume, we have respectively

$$\delta\dot{q}_w = \dot{q}_w''(a + 2t)dz = \dot{m}h_{fg}dx, \quad (3)$$

$$\dot{m}^2 d\left[\frac{\vartheta}{A}\right] = -AdP - \tau_w p_w dz, \quad (4)$$

where t , x and h_{fg} are the wall thickness, mass fraction of the vapor and heat transfer coefficient of the two-phase mixture respectively.

Replacing wall shear stress in terms of the two-phase frictional pressure drop, the momentum equation changes to:

$$\dot{m}^2 d\left[\frac{\vartheta}{A}\right] = -AdP - \frac{f_{TP} p_w \rho u^2}{2} dz, \quad (5)$$

$p_w = 2(a + b)$ is the wetted perimeter and $A = A_i(1 - \gamma z)$, in which $A_i = ab_i$ is the inlet cross sectional area and $\gamma = (b_i - b_o)/b_i$ is slope of the channel length.

Inserting Eqs. (2), (3), (5) into Eq. (1), the final result yields

$$d\dot{S}_{gen} = \frac{(a + 2t)\dot{q}_w'' dz}{T_\infty \left[1 + \frac{T_\infty}{\Delta T}\right]} + \frac{\dot{m}}{T_\infty} \left\{ \frac{f_{TP} p_w u^2}{2A} dz + \frac{\dot{m}^2}{2} d\left[\frac{\vartheta}{A}\right]^2 \right\}. \quad (6)$$

The temperature difference ΔT can be written as

$$\Delta T = T_{wo} - T_\infty = (T_{wo} - T_{wi}) + (T_{wi} - T_{sat}) + (T_{sat} - T_\infty). \quad (7)$$

To calculate $T_{wi} - T_{sat}$ and $T_{sat} - T_\infty$, we apply the heat transfer between the wall and the two-phase mixture inside the microchannel and the global energy equation as follows:

$$\dot{q}_w''(a + 2t) = h_{TP} [a + \eta(2b + a)](T_{wi} - T_{sat}), \quad (8)$$

$$\dot{q}_w''(a + 2t)L = \dot{m}C_p(T_{sat} - T_\infty), \quad (9)$$

where $\eta = \tanh[m(b + 0.5a)]/m(b + 0.5a)$ is fin efficiency and $m = \sqrt{h_{TP}/tk_w}$.

The temperature difference between inside and outside of the channel wall is

$$T_{wo} - T_{wi} = \frac{2t \dot{q}_w''}{k_w}. \quad (10)$$

Inserting Eqs. (8), (9), (10) into Eq. (7), we get

$$\Delta T = T_{wo} - T_\infty = \left[\frac{2t}{k_w} + \frac{a + 2t}{h_{TP} [a + \eta(2b + a)]} + \frac{L(a + 2t)}{\dot{m} C_p} \right] \dot{q}_w''. \quad (11)$$

When a liquid pump or a condenser is employed in the cooling system, it is common to have a single phase saturated liquid at the inlet. If vapor quality at the exit is x_o , integration of Eq. (3) is led to $dz/dx = L/x_o$. Introducing this result along with Eq. (11) into Eq. (6), the final result in a dimensionless form is obtained as:

$$d \left[\frac{T_\infty S_{gen}}{La \dot{q}_w''} \right] = \frac{\dot{m}^3}{2aL \dot{q}_w''} \left\{ \frac{f_{TP} P_w L \vartheta^2}{x_o A^3} dx + d \left[\frac{\vartheta}{A} \right]^2 \right\} + \frac{(1 + \frac{2t}{a}) \frac{dx}{x_o}}{1 + \frac{T_\infty h_{TP}}{\dot{q}_w''} \left[\frac{2th_{TP}}{k_w} + \frac{a + 2t}{a + \eta(a + 2b)} + \frac{L(a + 2t)h_{TP}}{\dot{m} C_p} \right]^{-1}}. \quad (12)$$

Under the boundary condition of $S_{gen}(x = 0) = 0$ and a constant heat flux, the integration of the above equation is:

$$\begin{aligned} \frac{T_\infty S_{gen}}{La \dot{q}_w''} = & \frac{\dot{m}^3 \vartheta_f^2}{2aL \dot{q}_w'' A_i^2} \left\{ L \int_0^{x_o} \frac{f_{TP} P_w}{A_i A^{*3}} \left[1 + x \frac{\vartheta_{fg}}{\vartheta_f} \right]^2 dx + \left[(1 + x_o \frac{\vartheta_{fg}}{\vartheta_f}) / (1 - \gamma) \right]^2 - 1 \right\} \\ & + \frac{1 + \frac{2t}{a}}{x_o} \int_0^{x_o} \frac{dx}{1 + \frac{T_\infty h_{TP}}{\dot{q}_w''} \left[\frac{2th_{TP}}{k_w} + \frac{a + 2t}{\eta(a + 2b)} + \frac{L(a + 2t)h_{TP}}{\dot{m} C_p} \right]^{-1}}. \end{aligned} \quad (13)$$

After integration of Eq. (5) and some manipulation, the pressure distribution in dimensionless form is

$$\frac{P}{P_i} = 1 - \frac{\vartheta_f \dot{m}^2}{P_i A_i^2} \int_0^{x_o} \frac{1}{A^{*3}} \left[\frac{\vartheta_{fg}}{\vartheta_f} + \frac{\gamma}{x_o} + \frac{f_{TP} P_w L}{2x_o A_i} (1 + x \frac{\vartheta_{fg}}{\vartheta_f}) \right] dx, \quad (14)$$

$A^* = 1 - \gamma z/L$, $\dot{m} = (a + 2t)L \dot{q}_w'' / x_o h_{fg}$ and $\vartheta = \vartheta_f + x \vartheta_{fg}$ is the two-phase mixture specific volume.

The two-phase heat transfer coefficient can be calculated by the following expression.

$$h_{TP} = \frac{3.5}{\sqrt{X}}, \quad (15)$$

where X is called Martinuelli parameter and is defined by:

$$X^2 = \left[-\frac{dP}{dz} F \right]_f / \left[-\frac{dP}{dz} F \right]_g = \left[\frac{\mu_f}{\mu_g} \right]^n \left[\frac{1-x}{x} \right]^{2-n} \frac{\vartheta_f}{\vartheta_g}, \quad (16)$$

$n = 1$ is used for a laminar flow and $n = 0.25$ is used for a turbulent one.

The required f_{TP} may be calculated based on the single friction factor formula for a rectangular channel. For a laminar developed flow and non-slip flow is obtained closely by the following empirical equation provided by R. K. Shah and A. L. London [9] with short side a , long side b , and a channel aspect ratio defined as $\eta = a/b$.

$$f_{TP} \text{Re}_D = C \left(1 - 1.3553\eta + 1.9467\eta^2 - 1.7012\eta^3 + 0.9564\eta^4 - 0.2537\eta^5 \right), \quad (17)$$

$C = 24$, $\text{Re}_D = 4\dot{m}/p_w\mu_{TP}$ and $D = 2ab/(a + b)$.

Hidrovo et al. claim that the value of C is higher than those predicted by theory for fully developed single phase flow in rectangular channels of aspect ratio 10:1, which is 85. Several factors contribute to this discrepancy including entrance length effects and the bends in U-shape among others, all of which lead to higher effective $f \cdot \text{Re}$ values.

SOLUTION TECHNIQUE

To obtain the optimum sizes of the microchannel in order to increase heat transfer rate and to decrease the pressure drop, the entropy generation of the two-phase flow is to be minimized. For this purpose, we plot the above equation as a function of the aspect ratio when the height changes and the other side remain constant.

RESULTS AND DISCUSSION

In this study, the saturated water-vapor two-phase flow is simulated in a rectangular microchannel under a constant wall heat flux in the range of $100 < \dot{q}_w'' < 1000 \text{ kW/m}^2$ from below surface. Saturated liquid water enters a microchannels at pressure $P_i = 2 \text{ atm}$ with width $a = 50 \text{ }\mu\text{m}$, depth $b = 500 \text{ }\mu\text{m}$, length $L = 24 \text{ mm}$ and thickness $t = 100 \text{ }\mu\text{m}$. Numerical solution of the equations leads to evaluation of the pressure drop, heat transfer, entropy generation and optimum size of the microchannel which can be used in design calculations.

Fig. 2 shows the entropy generation versus the aspect ratio for a heat flux $\dot{q}_w'' = 1000 \text{ kW/m}^2$. The contribution of the heat transfer and the pressure drop on the entropy generation are also illustrated. There is an optimum aspect ratio by which the lowest entropy generation rate occurs. The result indicates that increasing the aspect ratio larger than the critical one contributes to enhance entropy generation by heat transfer, because larger channel width allows for more heat transfer rate. In contrast, increasing the aspect ratio contributes to decrease entropy generation by pressure drop and also the relationship between the entropy and aspect ratio is a nonlinear function. Fig. 3 reproduces the aforementioned figure but for different wall heat fluxes. It is seen that increasing the wall heat flux increases the entropy generation significantly for aspect ratios larger than 0.25 and the location of their lowest entropy generation does not change. Fig. 4 exhibits the distribution of the entropy generation as a function of the aspect ratio for different vapor qualities. The findings indicate that the location of the lowest entropy generation moves toward the higher aspect ratio for higher outlet vapor qualities. In addition, the slope of the entropy gradient is much steeper for aspect ratios smaller than the critical one. This is because of more effect of pressure contribution on the entropy generation than those of heat transfer for smaller aspect ratios. Fig. 5 indicates the profile of the pressure drop versus the aspect ratio for different vapor qualities. Similar to the previous plot, the gradient slope of the pressure drop is much steeper for very low aspect ratios especially at high vapor quality. This gradient vanishes gradually and approaches nearly a constant value at high aspect ratios.

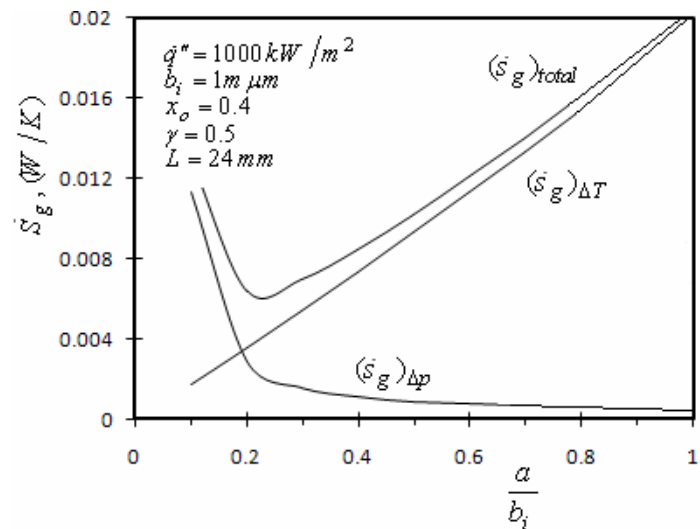


Fig. 2. Entropy generation in the microchannels versus aspect ratio

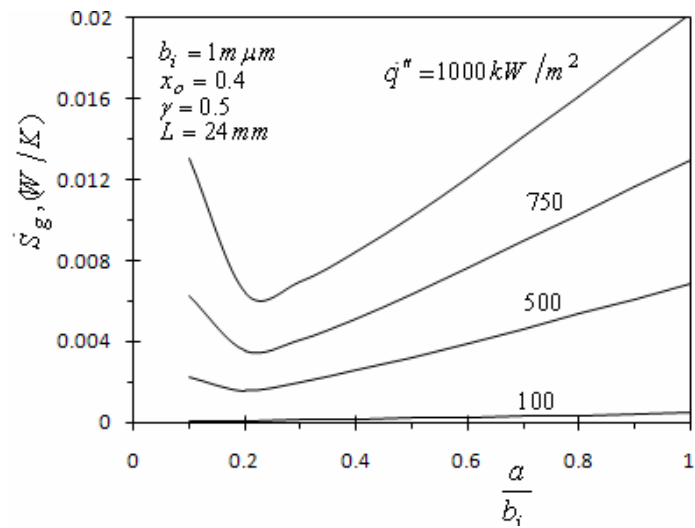


Fig. 3. Entropy generation in the microchannels versus aspect ratio for different wall heat fluxes

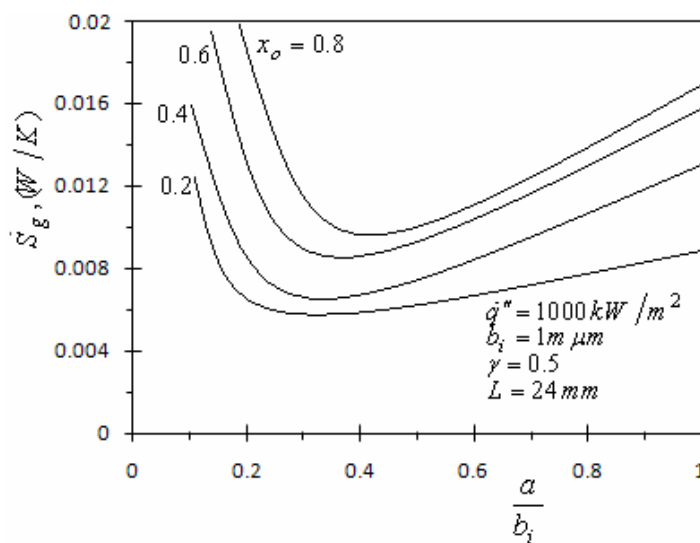


Fig. 4. Entropy generation in the microchannels versus aspect ratio for different vapor qualities

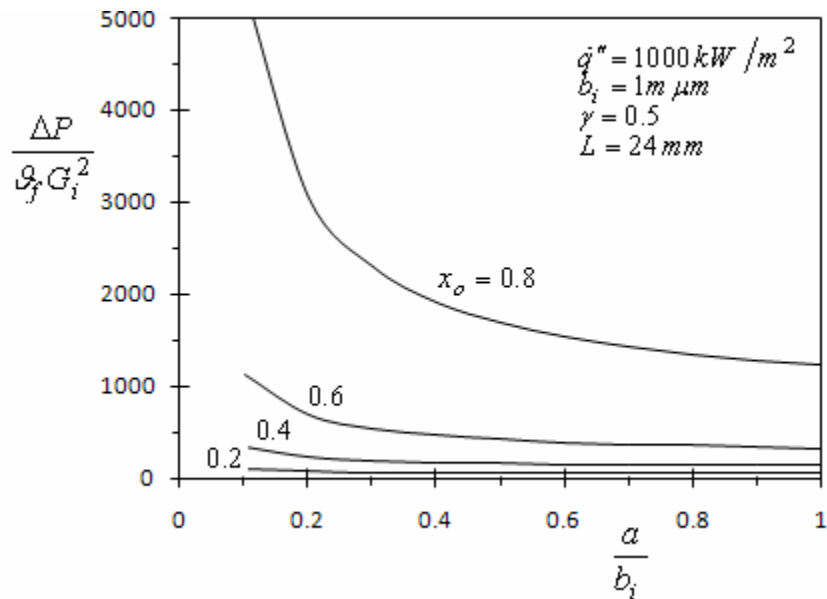


Fig. 5. Pressure drop versus aspect ratio for different vapor qualities

CONCLUSIONS

Optimization of two-phase forced convective flow is modeled in a rectangular microchannel with variable cross section. The procedure is based on the minimization of entropy generation resulting from viscous fluid effects and heat transfer for a homogeneous two-phase flow of a pure fluid. Several effects which are normally neglected in conventional channel are important in microchannels. The entropy generation rate is obtained by using the conservation equations for mass and energy with the entropy balance. The channel is minimized in terms of channel aspect ratio, fin efficiency, outlet vapor quality and total mass flow rate. The contributions of thermal resistance include conductance resistance in the fin, convective resistance at the solid-fluid interface and the fluid resistance. The present results show that the entropy generation rate is a strong function of the channel sizes. The findings indicate that the location of the lowest entropy generation moves toward the higher aspect ratio for higher outlet vapor qualities. In addition, the slope of the entropy gradient is much steeper for those of aspect ratios smaller than the critical one. This is because of more effect of pressure contribution on the entropy generation than that of the heat transfer for smaller aspect ratios.

Nomenclature

a	channel width
A	cross section area
b	channel depth
D	diameter
f	friction coefficient
h	enthalpy, heat transfer coefficient
k	Thermal conductivity
L	channel length
\dot{m}	mass flow rate
P	Pressure, wetted perimeter
q''	heat flux
Re	Reynolds number
S	entropy
u	axial velocity
t	thickness

T	temperature
x	vapor quality
z	coordinate system.

Greek Symbols

Δ	difference
ϕ^2	friction multiplier
γ	Slope of channel
μ	viscosity
η	Aspect ratio, b/a
ϑ	specific volume
ρ	density.

Subscripts

f	liquid
fg	two-phase mixture
g	gas
gen	generation
h	hydraulic
i	inlet
o	outlet
sat	saturation
TP	two-phase
w	wall, wetted perimeter
∞	ambient.

Superscripts

*	dimensionless
---	---------------

References

1. Brauner N., Moalem-Maron D. Identification of the range of small diameter conduits regarding two-phase flow pattern transition // *Int. Commun. Heat Mass Transfer*. 1992. Vol. 19. Pp. 29–39.
2. Kandlikar S. G., Grande W. J. Evaluation of single phase flow in microchannels for high flux chip cooling - thermohydraulic performance evaluation and fabrication technology // *Heat Transfer Engineering*. 2004. Vol. 25, No. 8. Pp. 5–16.
3. Khan W.A. Yovanovich M.M., Culham J.R. Optimization of Microchannels Heat Sinks Using Entropy Generation Minimization Method // *23th Annual IEEE Semiconductor Thermal Measurement and Measurement Symp., Dallas, TX, USA, 2006*.
4. Chen K. Second law analysis and optimization of microchannels flows subjected to different thermal boundary conditions // *Int. J. of Energy Research*. 2005. Vol. 29, No.3. Pp. 249–263.
5. Galvis E., Culham G.R. Lower entropy generation in microchannels with laminar single phases flow // *3rd Joint US-European Fluids Engineering Summer Meeting and 8th Int. Conf. on Nanochannel, Microchannels and Minichannels, Montreal, Canada, 2004, August 1–5*.
6. Revellin R., Lips S., Khandekar S., Bonjour B. Local entropy generation for saturated two-phase flow // *Energy*. 2009. Vol. 34. Pp.1113–1121.
7. Papautsky I., Ameel T., Frazier A. A review of laminar single-phase flow in microchannels // *Proc. of ASME, Int. Mechanical Engineering Congress and Exposition, 2001*. Vol. 2. Pp. 3067–3075.
8. Ibáñez G., Cuevas S. Entropy generation minimization of a MHD (magnetohydrodynamic) flow in a microchannels // *Energy*. 2010. 35. Pp. 4149–4155.
9. Shah R. K., London A. L. *Laminar Flow Forced Convection in Ducts, Supplement 1 to Advances in Heat Transfer*, Academic Press, New York, 1978.

THE INTENSIFICATION OF HEAT-TRANSFER CHARACTERISTIC OF HEAT PIPES

Arkady V. Seryakov¹, Aleksander V. Konkin²

¹Scientific Laboratory, ²22 Department,
Special Relay System Design and Engineering Bureau,
Nekhinskaya Street, 55, 173021, Veliky Novgorod, Russia.
E-mail: seryakovav@yandex.ru , E-mail: konkin_a_v@mail.ru

Vyacheslav K. Belousov

³Computational laboratory,
Joint Stock Company SPLAV,
Nekhinskaya Street, 61, 173021, Veliky Novgorod, Russia.
E-mail: bel_vk@mail.natm.ru

Abstract

The work presents a part of the complex rated experimental research of the heat-transfer characteristic intensification of the heat pipes of medium temperature range. At the butt (axial) direction of heat flow at the inlet into the heat pipe a possibility of the jet nozzle with a specified jet direction appears that intensifies heat transfer under the low heat loads and increases the heat pipe efficiency. The heat tube steam channel realization as a whole as a gas dynamics confuser-diffuser nozzle analogous to the Laval nozzle and surrounded by a capillary porous insertion, layer along the whole length, increases the parameter limit and heat transfer factor of the heat pipe.

KEYWORDS

Heat pipe of the medium temperature range, capillary porous insertion, capillary steam injectors, Laval nozzle, steam flow twist.

INTRODUCTION

In this work results of the rated experimental modeling of the heat pipes of medium temperature range is presented. The problem of the heat-transfer characteristic intensification of the heat pipes of medium temperature range used for cooling of the heat-loaded elements of electronic technique is at present exceptionally urgency.

The heat transfer and operating efficiency of the heat pipes with capillary porous insertions are defined by a closed rotational motion of the working body undergoing to the fluid-steam phase transition with heat liberation in the condensation zone and fluid return through the capillary porous insertions into the evaporation zone of the heat pipe.

At the butt (axial) direction of the heat flow at the inlet into the heat pipe a preferable constructive solution is a flat evaporator made of capillary porous material tightly adjoining to the flat bottom cap.

With small diameters of the heat pipes made of stainless steel the application of the flat caps are possible because of their moderate thermal resistance, simplicity and technological effectiveness of manufacturing. The Fig. 1 shows the heat pipe scheme with the flat evaporator, confuser-diffuser steam channel and turbulator.

The steam phase transfer analysis was carried out by a turbulent gas dynamics model.

The steam phase transfer proceeds through the steam channel arranged along the central axis of the capillary porous insertion, which in its turn is tightly set and mechanically fixed in the thin-walled cylindrical body of the heat pipe with top and bottom caps.

The central location of the steam channel, which is made as a gas dynamics confuser-diffuser nozzle, surrounded with a capillary porous insertion layer along the whole length of the heat pipe, allows to realize a considerable reduction of heat loss. Without the capillary porous insertion layer the steam nozzle is becomes supersaturated. As a result of the normal behaviour of the steam jet outflow is broken: in the flow in the diffuser zones near the critical section a premature large amount of microdrops of the working fluid condensate appears.

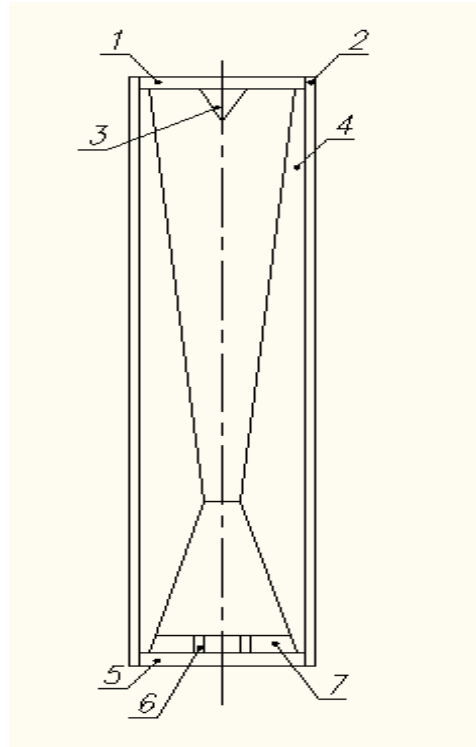


Fig.1. 1 – top cap, 2 – cylindrical body of the heat pipe, 3 – conic turbulator, 4 – capillary porous insertion, 5 – bottom cap, 6 – capillary injection channels, 7 – bottom flat capillary porous evaporator

Simultaneously an important expansion steam jet divergence and fastening of this jet on the walls of the capillary porous insertion takes place that reduces maximum permissible parameters of the heat pipe heat transfer. The condensation jumps being formed in the extending part of the nozzle is followed by heat evolution and under the influence of two factors (heat and geometrical once) loose stability. The variable section of the capillary porous insertion with a maximum thickness value near the critical section of the nozzle and a decreasing thickness in the evaporation and condensation zone protects the steam flow from supercooling in such a manner, that the maximum condensation takes place on the inner surface of the heat pipe top cap, at the steam jet braking temperature exceeding the condensation temperature. The compression ratios and degrees of expansion of the gas dynamics confuser-diffuser nozzle are selected the same as by the Laval nozzle, the confuser part estimated profile is performed concave in such a manner, that the reflected steam jets converge to the critical section center of nozzle.

Overheating $\Delta\dot{O}$ of the steam flow on going out of the nozzle depended on the temperature exceeding against the working fluid boiling point in the heat pipe evaporator is rated by means of introduction of the heat condensation effective value in accordance with the formula [1]:

$$r_{eff} = r + C_p^{//} \cdot \Delta T \quad (1)$$

where : r_{eff} – heat condensation effective value, J/kg ; r – heat condensation value, J/kg ; $C_p^{//}$ – steam heat capacity, J/(kg·K); ΔT – difference of the overheated steam temperatures, K, and its saturation temperature at given pressure. The overheating value $\Delta\dot{O}$ under high heat loads on the heat pipe reaches 50 K.

In the preliminary experiments with model equipment it is determined that the condensation intensity of the broadening steam jet on the perpendicular surface of heat exchange is proportional to the steam flow forticity.

The motion type of the condensate microdrops in the two-phase dispersed flow is complicated, drops can be accelerated get additional energy owing to what not only coagulation but also crushing of drops into still smaller ones [2, 3]. The increase of condensation nucleus amount of supersaturated steam promotes the

steam condensation intensification both on the heat exchange surface and on the drops. The heat and mass exchange within heat pipes is determined not only by hydraulic and gas dynamics features of steam and condensate motion, but by interaction with solid body surfaces as well in order to increase the heat transfer coefficient from the steam flow to the inner surface of the top cap and the intraphase mass exchange of the condensate film, the heat pipe top cap is made with a taper turbulator.

The turbulator surface, and the top cap inner surface are covered with elongated grooves [4–6], the longitudinal axes of which in the azimuthal plane are turned concerning the longitudinal axis of the steam channel at specified angle, which provides maximum twist of the steam wet flow with condensate microdrops. The twist value effects on the thermal resistance of the layer adjoining to the walls including a viscous sublayer.

For the steam generation intensification in the evaporation zone under low heat loads some injecting steam outlet channels are used piercing the bottom flat insertion capillary porous insertion tightly adjoining the flat bottom cap of the heat pipe. The injection channel diameter reaches 1 mm, and reduced capillary pressure results in temperature lowering of boiling and steam generation of the working fluid in these channels that was found as very important under low heat loads of the heat pipe. Fig.2 shows the calculation result of velocity distribution at the steam injecting channels over the bottom flat insertion of the capillary porous insertion under low heat load. The injectors are especially effective with small heat flows and accordingly with low initial velocities of the steam flow over the evaporator.

Fig. 3 shows the same calculation result, but under high heat load on the evaporation butt surface of the heat pipe, when operation effects of the jet injectors virtually become not apparent and steam generation becomes uniform on the whole section of the nozzle confuser part. The injecting capillary channels are made as Laval nozzles that increases the fluid working body supply to them on the capillary porous insertion layer along the bottom, the inner surface of which is additionally covered with radial and circular grooves. The groove profile is selected as a dihedral angle. Realization of the steam channel of the heat pipe wholly as a gas dynamics confuser nozzle analogous to the Laval nozzle and surrounded with a capillary porous insertion layer results in the flow velocity increase of the steam turbulent jet.

To illustrate the application effectiveness of the confuser-diffuser nozzle as a steam channel of the heat pipe, Fig. 4 shows differences of velocity, m/s, steam jet flow in the steam channels of two structures – as a confuser-diffuser nozzle and in a standard cylindrical channel, in both cases without use of the injecting capillary steam channel. The steam jet velocities were calculated at a height of the nozzle critical section, the nozzle diameters in the broad part and of the cylindrical steam channel are the same. The axial heat flow and initial steam velocities over the evaporators are the same as well.

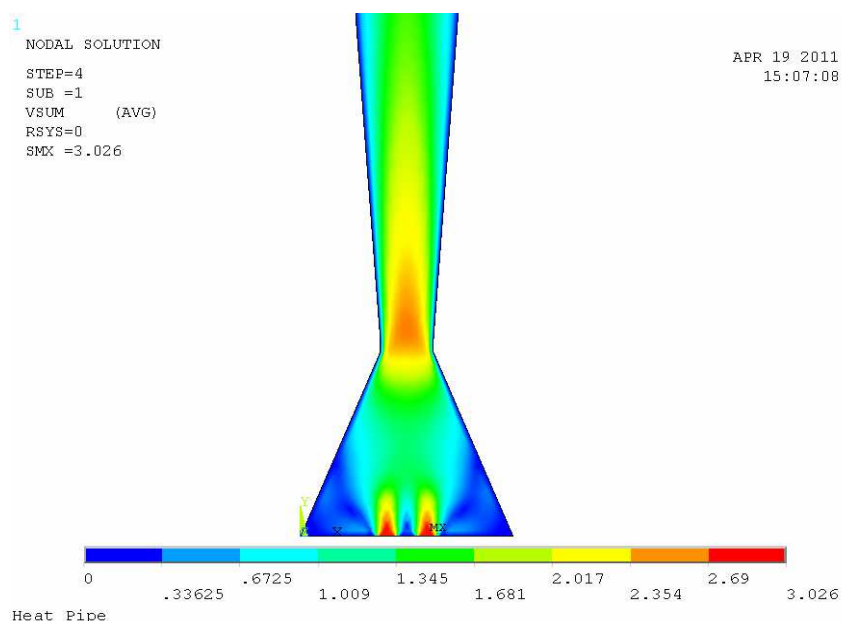


Fig. 2. Steam velocity distribution, m/s, over the steam injecting channels in the evaporation part of the heat pipe under low axial heat load

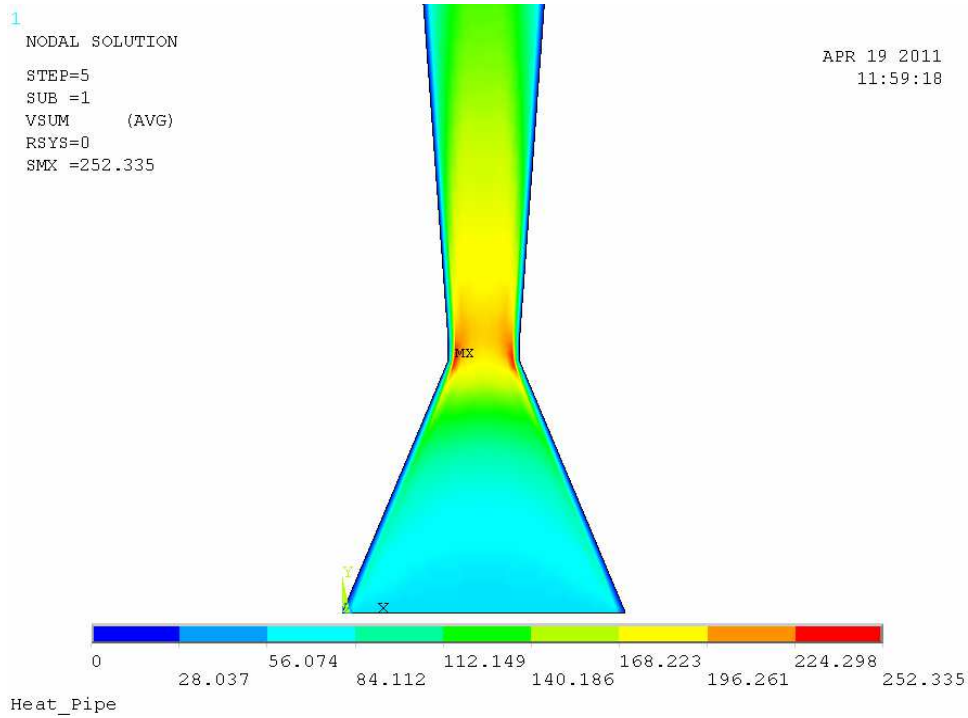


Fig. 3. Steam velocity distribution, m/s, over the steam injecting channels above the evaporator of the heat pipe under high axial heat load

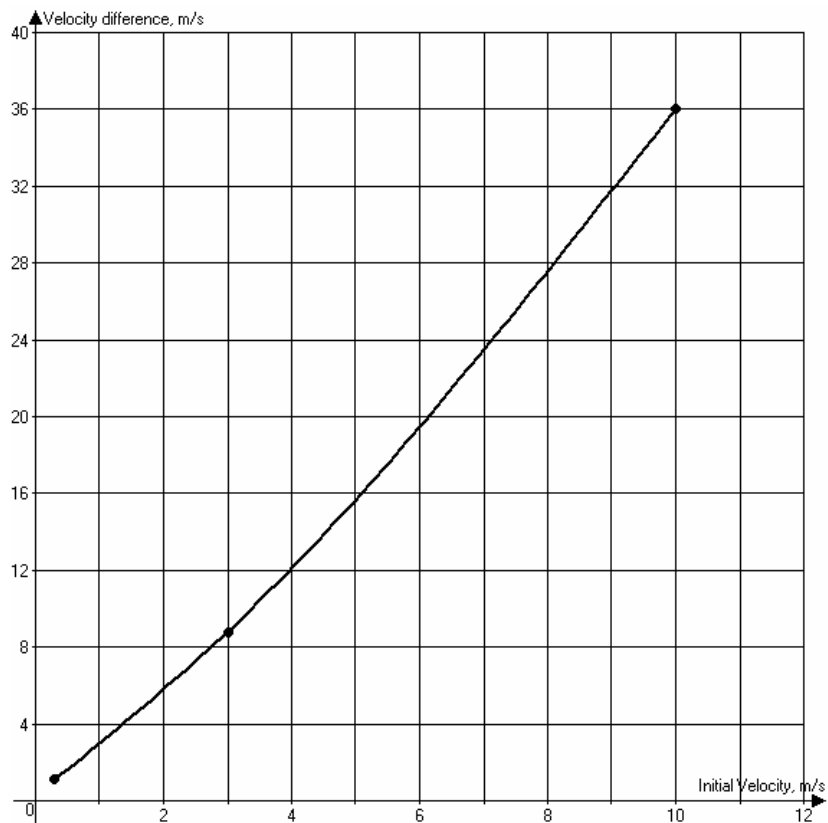


Fig. 4. Velocity differences, m/s, steam jet flow in the nozzle critical section and in the standard cylindrical steam channel depending on the initial steam velocity over the evaporators (Reynolds numbers of evaporators)

The pressure differences, Pa, of the confuser-diffuser steam channel and standard cylindrical steam channel calculated on the height of the nozzle critical section is shown in the Fig. 5. One can see that the nozzle is found as a very effective accelerator of the steam flow under low axial heat loads.

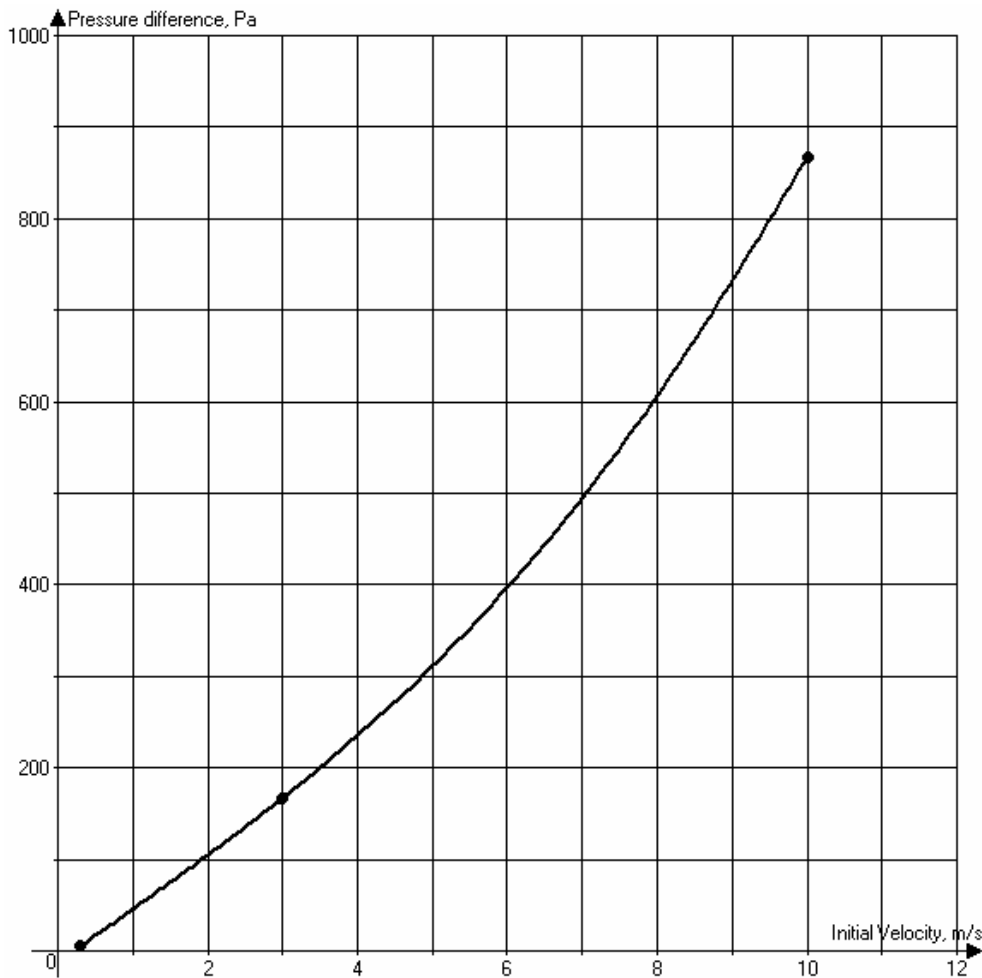


Fig. 5. Pressure difference, Pa, in the critical section of the steam channel as a confuser-diffuser nozzle and a standard cylindrical steam channel, depending on the initial steam velocity over the evaporators (Reynolds numbers of evaporators)

The steam channel made as a confuser-diffuser nozzle possesses a distance action that results in the velocity exceeding of the steam flow in comparison with the standard cylindrical steam channel in the frontal point of the turbulator when come nearer to the heat pipe condensation zone. The Fig. 6 shows the velocity differences, m/s, of the steam jet flow in the frontal point of the turbulator in the channel with the confuser-diffuser nozzle, and in the standard cylindrical steam channel. The Fig. 7 shows the pressure difference, Pa, of the steam jet flow in the frontal point of the turbulator in the channel with the confuser-diffuser nozzle, and in the standard cylindrical steam channel.

A complex nature of the pressure behaviour in the frontal point of the turbulator, depending on the initial velocity of the steam flow over the evaporators (Reynolds numbers Re of evaporators), shows a presence of some modes of the steam flow in this point, depending on the heat load on the evaporator and the heat pipe.

This fact means a necessity of some supplementing each other arrangements of the condensation intensification on the turbulator including the steam flow twist.

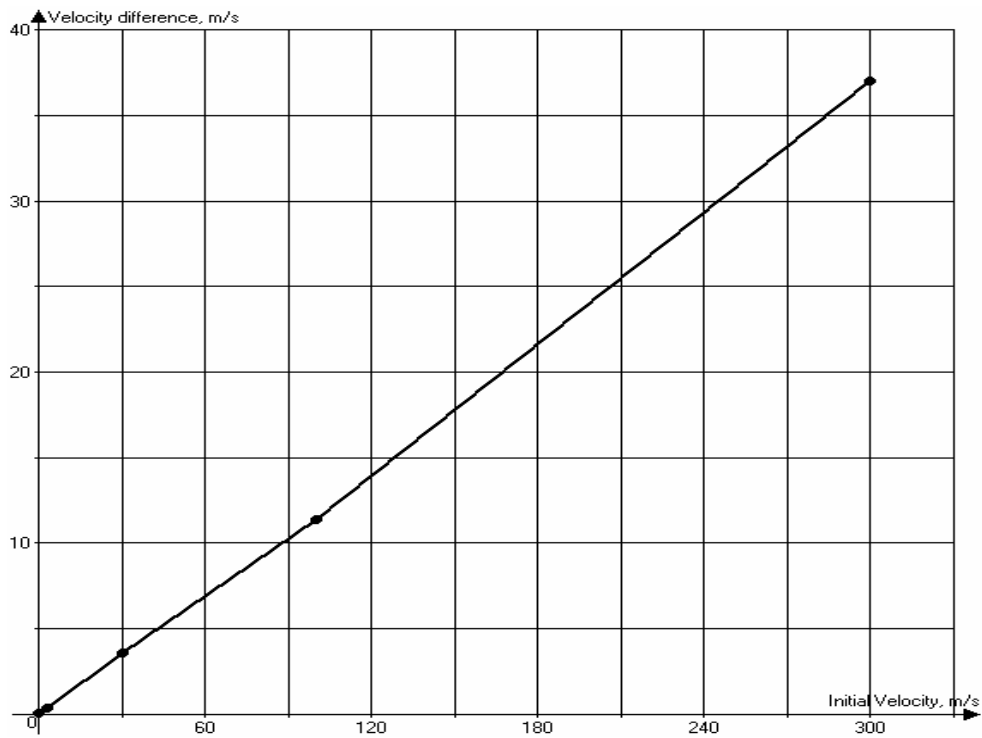


Fig. 6. Velocity differences, m/s, of the steam flow in the turbulator frontal point in the confuser-diffuser steam channel and in the standard cylindrical steam channel, depending on the initial steam velocity over the evaporators (Reynolds numbers of evaporators)

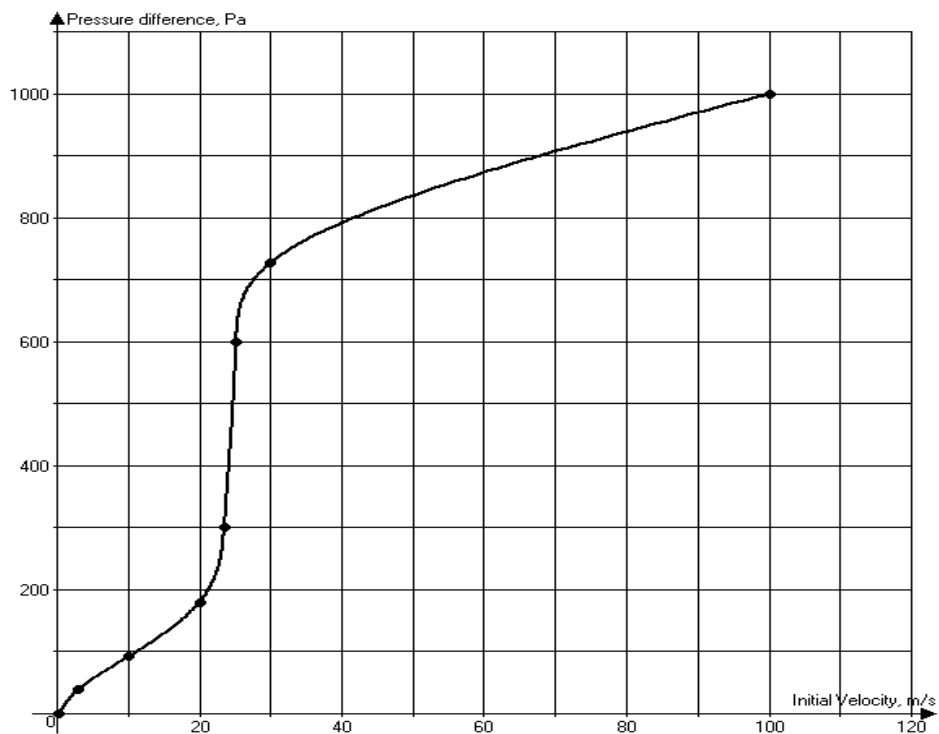


Fig. 7. Pressure difference, Pa, in the turbulator frontal point in the confuser-diffuser steam channel and in the standard cylindrical steam channel, depending on the initial steam velocity over the evaporators (Reynolds numbers of evaporators)

An additional dynamic pressure of the condensate at the input into the top edge of the capillary porous insertion enlarges the limiting parameters of the heat pipes.

The condensate return is realized by the capillary porous insertion, the transient characteristics of which are expanded by introducing the longitudinal microcapillary channels passing along the whole length of the pipe, the average diameter of which doesn't exceed 10 μm .

The layers of the sintered granulated material adjoining the microcapillary channels form the additional porous channels passing along the whole length of the capillary porous insertion as well.

The estimated evaluations of the heat mass transfer of the heat pipe carried out with programs CF Design (Blue Ridge Inc., USA) and ANSYS and also model analytic evaluations show increase of the heat - transfer factor of the heat pipe of the selected design.

References

1. Kutateladze S. S. Heat transfer and hydrodynamic resistance: *Handbook* / Energoatomizdat Publ., Moscow, 1990. – 307 p. (*In Russian*).
2. Frenkel Ya. I. *Kinetic theory of fluids*, Nauka Publ., Moscow, Leningrad Branch, 1975. – 592 p. (*In Russian*).
3. Sternin L. E. *Gas dynamics fundamentals of two- phase flows in nozzles*, Mashinostroenie Publ., Moscow, 1974. – 212 p. (*In Russian*).
4. Leontyev A. I., Olimp'ev V. V., Dilevskaya E. V., Isaev S. A. Mechanism essence of heat exchange intensification on surface with spherical groves // *Proceedings of the Russian Academy of Sciences. Energetics (Izvestiya Rossijskoj AN. Energetica)*. 2002. No. 2. Pp. 117–133. (*In Russian*).
5. Leontyev A. I., Olimp'ev V. V. Power economy potential of different methods of flow twist and discrete rough channels // *Proceedings of the Russian Academy of Sciences. Energetics (Izvestiya Rossijskoj AN. Energetica)*. 2010. No. 1. Pp. 13–49. (*In Russian*).
6. Gortyshov Y. F., Popov I. A. Scientific fundamentals of estimation of high-effective compact heat exchanger with rational heat emission intensificators // *Heat-Power Engineering (Teploenergetica)*. 2006. No. 4. Pp. 2–14. (*In Russian*).

CRITICAL HEAT FLUXES IN HEAT PIPES

A. A. Shapoval

Department of permeable materials
Frantsevich Institute for Problems of Materials Science,
Ukraine National Academy of Sciences,
Krzhyzhanovsky St., 3, 03142, Kiev, Ukraine
Tel/fax: 044-424-15-71; E-mail: ash48@rambler.ru

Abstract

Researches of influence of porous capillary structure characteristics on parameters of critical heat fluxes in the conditions typical for functioning of heat pipes and thermosyphons is important thermophysical a problem. Some experimental results of influence of porosity, heat conductivity and thickness of fiber-porous structures at boiling water in conditions which are characteristic for work of thermosyphons, received by the author, are presented in this report.

KEYWORDS

Critical heat flux, two-phase heat transfer, boiling, heat pipes, thermosyphons, metal-fiber, porous, capillary structures

INTRODUCTION

There are some specific features in two-phase heat transfer in heat pipes (HP) and thermosyphons heating zones with porous capillary structures (PCS) in comparison with the similar processes occurring on technical smooth. The porous materials used in heat pipes as capillary structures, have a set of physical characteristics, such as porosity Θ_{cs} , heat conductivity λ_{cs} , thickness δ_{cs} , that can have an essential influence on the critical heat fluxes q_{cr} in heat supply zones. The limiting (critical) heat fluxes researches are vital thermophysical issues, actual for the two-phase heat transfer theory, in particular, for liquid boiling processes on surfaces with porous capillary materials (structures). The vaporization and heat evacuation mechanisms typical for the "working" conditions of technical smooth and the mechanisms typical for surfaces with porous structures can essentially differ [1–4].

Current state of a problem

The most researches in the heat pipe application domain are carried out to determine the alarm levels of the heat flows Q_{max} transmitted by pipes at their various orientation in space. It is necessary to distinguish the critical phenomena in the HP heating zone, occurring in conditions with a overliquid-heat-carrier (HP operating mode; «thermophysical» crisis), and the phenomena occurring in the conditions of a deficit liquid transported to liquid heating zone (HP operating mode, "hydrodynamical" crisis). Different forms of heat transfer crises for conditions typical for heat and mass transport processes inside thermosyphons and heat pipes, are full enough presented in monographies [5]. However, the influence of the main characteristics of metal-fiber capillary structures (porosity Θ_{cs} , heat conductivity λ_{cs} , thickness d_{cs}) on the critical heat fluxes q_{cr} , arising on the surfaces with PCS at their superfluous liquid filling, is not presented in [5].

The experimental equipment and technique

The solution of this problem is carried out in the following way: 1) the experimental equipment was created for the heat transfer researches at boiling on surfaces with porous covering and structures (Fig. 1) in free liquid movement and capillary liquid transport conditions; 2) the series of the researching PCS samples were made with following characteristics: porous structures are made from thin discrete fibers; the PCS-material is copper and stainless steel; porosity $\Theta_{cs} = 40\text{--}90\%$; thickness $\delta_{cs} = 0,2\text{--}10,0\text{ mm}$; skeleton heat conductivity $\lambda_{cs} = 0,1\text{--}70\text{ W/(m}\cdot\text{K)}$. The block-heater allowed to reach the values $q_{max} = 260\cdot 10^4\text{ W/m}^2$. The calibration of testbed system is carried out by water and ethanol boiling research on technical copper smooth.

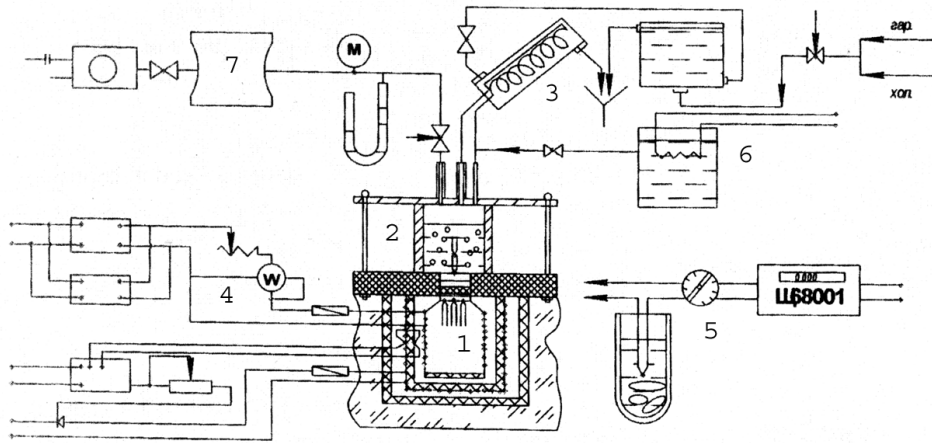


Fig. 1. The test bed system scheme for the researches of critical heat fluxes at boiling on surfaces with porous capillary structures: 1 – block-heater to the sample of porous capillary structure; 2 – liquid boiling zone on a surface with porous capillary structure; 3 – system of pair condensation; 4 – system of electric power and heating regulation and measurement; 5 – system of temperature measurement (with thermocouples); 6 – system of condensate cooling; 7 – system of vacuum pumping and saturation pressure support

The experimental technique consisted of the following. The researching PCS sample was sintered to a round copper lining, which had been previously placed with set of the thermocouples inside. This sample was soldered to the butt end of the copper block-heater. Then the block-heater was turned on and the heat flux was discretely increased to the limiting values q for this PCS sample. The values q and the difference of temperatures Δt were measured between the surface of lining and a boiling liquid. The moment of crisis approach was fixed on a sharp change temperature jump of a lining; afterwards the heater was disconnected.

THE RESULTS OF THE EXPERIMENTAL RESEARCHES AND THEIR DISCUSSION

Considerable modifications of the critical phenomena are observed on porous surfaces with metal-fiber capillary structures (MFCS) as distinct from boiling on a technical smooth. The main differences consist in the following:

- 1) the size of critical values of q essentially depends on basic PCS characteristics;
- 2) the crises of heat transfer can be carried out either in steps or smoothly depending on thickness, porosity and heat conductivity of PCS;
- 3) limiting values of q_{cr} on porous surfaces with metal-fiber PCS can exceed to a certain extent (in 2–3 times) similar values of q_{cr} typical for technical smooths.

Some results of researches received by us at water boiling on surfaces with metal-fiber PCS, are presented in fig. 2–4.

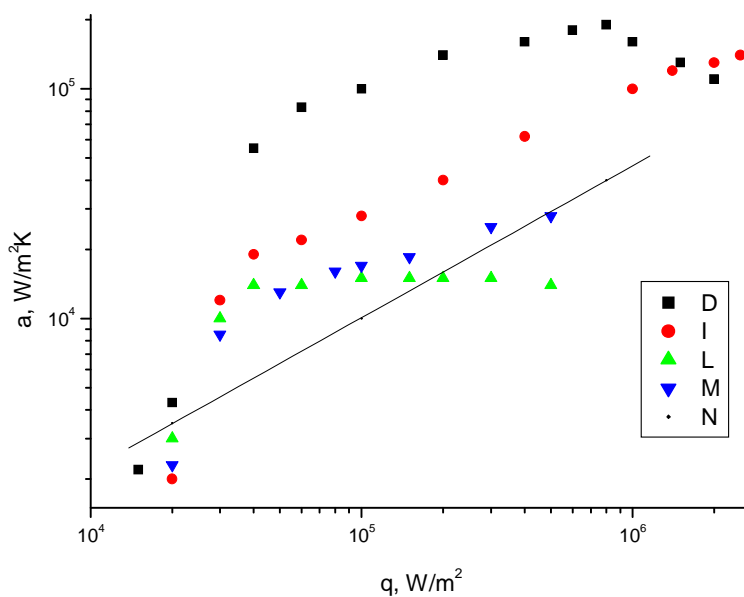


Fig. 2. Influence of porosity and heat conductivity of concerning "thin" MFCS on heat transfer intensity at boiling; thickness of CS $\delta = 0.8$ mm; copper CS: D – $\Theta = 40$ %; I – $\Theta = 84$ %; CS from stainless steel: L – $\Theta = 59$ %; M – $\Theta = 88$ %; N – boiling of water on a smooth

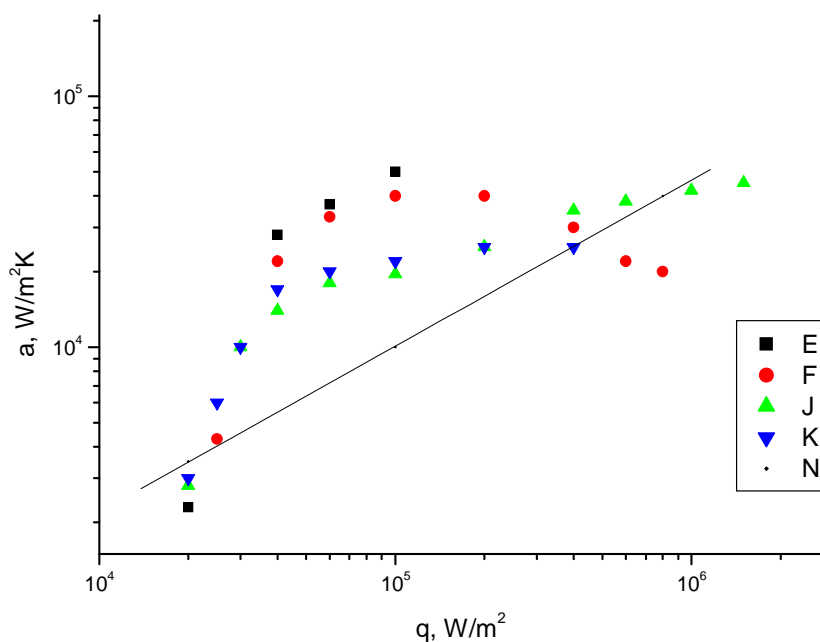


Fig. 3. Influence of porosity and heat conductivity of concerning "thick" MFCS on heat transfer intensity at boiling; copper CS; porosity $\Theta = 40$ %; CS thickness δ : E – 2.0 mm; F – 4.0 mm; $\Theta = 84$ %; CS δ : J – 2.0 mm, K – 4.0 mm; N – boiling of water on a smooth

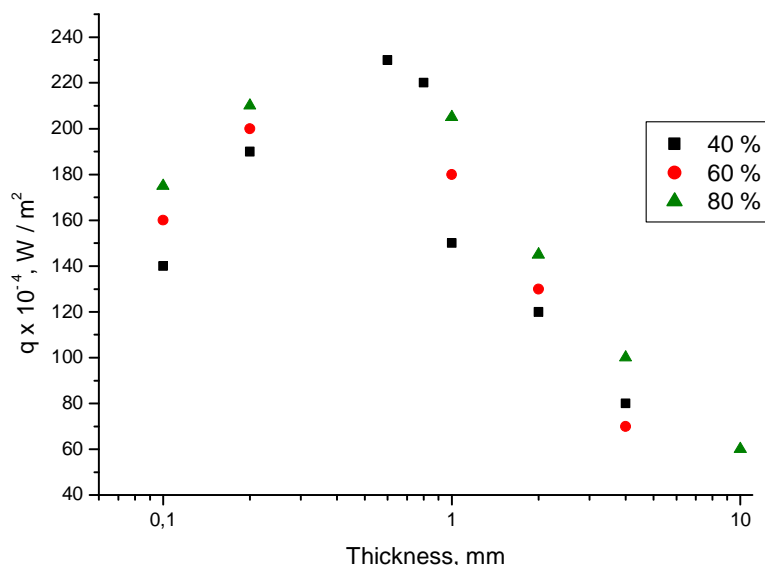


Fig. 4. Influence of copper MFCS thickness on critical heat fluxes at water boiling (atmospheric pressure)

The analysis of experimental data allows ascertain the following.

1. There is an "optimum" MFCS thickness, equal $\sim 0.4-0.8$ mm for water, at which
2. values of the first critical flux q_{cr1} reach maximal values – 2–3 times exceeding similar values of q_{cr1} , typical for technical smoothes (fig. 2).
3. The high-porosity metal-fiber copper structures (at $\Theta_{cs} = 80\%$) provide the greatest values of q_{cr1} .
4. MFCS made from low-heat-conduction materials (stainless steel) with small sizes of frame heat conductivity λ_{cs} accordingly, do not provide the augment of q_{cr1} critical values, typical for smoothes. At some combinations of basic PCS characteristics they give the values of heat transfer coefficients a [$W/(m^2 \cdot K)$] and q_{cr1} , which are even smaller, than similar values a and q_{cr1} , typical for smoothes (Fig. 3).

It is possible to explain received experimental results according to the following hypotheses.

1. The porous capillary structures change significantly the heat-conducting path mechanisms, typical for liquid boiling on smoothes. The PCS "modify" hydro dynamical and thermal boundary layers of liquid, adjoining with both the PCS and «CS-plane» smooth simultaneously.
2. Discrete fibrous CS elements well connected to a smooth (in our case), carry out a role of "microribes", which can essentially change the boundary conditions of heat supply to formed steam-blebs. The steam-germs, surrounded by the high-heat-conductivity fibers, enlarge much more quickly, than in case of the top parts washing of their "calottes" with relatively cold liquid (in case of a smooth).
3. Considerable quantity of the potential centers of steam-germ formation on porous surfaces is much more bigger in comparison with technical smoothes. The steam-germs exist in both the fiber-butting places of smooth and in most fibers. Furthermore, such steam-germs are faster activated on high-heat-conductivity elements (fibers) of the CS.
4. Porous structures possess considerable capillary properties. Laplas capillary forces are the greatest in small pores. The pores of this type capable to keep a liquid-micropellicle from merging into one greater pellicle. Thus, up to the certain values q_{cr1} , the small pores prevent from great pellicle "domains" formation, typical for the technical smoothes, and this pores realize stunted growth of boiling crisis.

The PCS thickness increasing ($\delta_{cs} > 1-2$ mm) makes hydraulic resistance of steam evacuation grow. It leads to the increasing influence of two-phase flow hydrodynamic factors and finally to the rapid decrease of q_{cr} value. In this case the temperature of surface increases slowly (or smoothly), and it is possible to talk not about critical, but about "limiting" values of heat flux q .

We receive the empirical formula which generalizes influence of the main characteristics of metal-fiber PCS on the values of the first critical heat fluxes at water boiling in conditions of free movement. The formula has a following form:

$$q_{cr} = c \cdot q_{cr1} \cdot \Theta_{cs}^{0.1} \lambda_{cs} \delta_{cs}^n \cdot D_{ef}^{0.2}, \quad (1)$$

where q_{cr1} – the value of first critical heat flux at water boiling on smooth (at atmospheric pressure).

The results of calculations realized under the formula (1) are presented in Fig. 4. The satisfactory coordination of calculation results with received experimental results is accomplished.

We didn't lead experiments with other liquids, however, by known data from the literature, it is necessary to expect a certain analogy with results on the water. There is a good reason to think, how the organic liquids also could increase the values of a heat flux 2–3 times at boiling on MFCS surfaces.

CONCLUSION

The following facts are established as a result of the lead experimental researches of water boiling on surfaces with metal-fiber porous structures (MFCS) in the wide range of MFCS main characteristics changes (porosity, thickness and heat conductivities):

1. The magnitudes of critical heat fluxes at water boiling in conditions of free movement (a mode typical for thermosyphons with porous capillary structures) essentially depend on basic physical PCS characteristics.

2. The high-porous-fiber structures with thickness ~0,4-0,8 mm created from high-heat-conductivity metals (for example copper) and qualitatively sintered to the heating surfaces, are capable to increase the critical heat fluxes in 2–3 times in comparison with technical smooth.

References

1. Costello C.P., Frea W.J. The roles of capillary wicking and surface deposits in the attainment of high boiling burnout heat fluxes // *AICHE J.* 1964. Vol. 10, No. 3. Pp. 393–398.
2. Nikolaev G., Tokalov J. Crisis of boiling on porous covering surfaces // *Eng.-Phys. J.* 1974. Vol. 26, No. 1. Pp. 5–9 (*in Russian*).
3. Tehver J., Tunik A. About heat transfer crisis at boiling on a surface covered with a porous material // *Bulletin of Estonian Academy of Sciences (Izvestia Estonskoi Akademii Nauk). Ser. Phys.-Math.* 1977. Vol. 26, No. 2. Pp. 195–198 (*in Russian*).
4. Kovalyov S., Solovyov S. Heat transfer and critical heat fluxes at boiling on a porous surface: *Two-Phase Flows: Heat transfer and Hydrodynamics*, Nauka Publ., Leningrad, 1987. Pp. 3–6 (*in Russian*).
5. Bezrodny M., Pioro I., Kostyuk T. *The two-phase processes in thermosyphon systems*, Fact, Kiev, 2003. – 480 p. (*in Russian*).

AUTONOMOUS THERMOSIPHON SYSTEM FOR WWER-1000 PRESSURIZER COOLDOWN

Igor Sviridenko

Sevastopol State Technical University
99053, Ukraine, Sevastopol, University str., 33
Phone: +380692 543086, fax: +380692 456 019, e-mail: i.sviridenko@mail.ru

Dmitry Shevielov

Department of thermal hydraulics analyses and emergency transients,
Sevastopol branch of scientific and technical support of OP STC NAEK «Energoatom»
99033, Ukraine, Sevastopol, Academic Kurchatov str., 7
Phone: +0380692 710420; e-mail: am5x86@mail.ru

Abstract

Autonomous passive residual heat removal system (RHRS) for the Pressurizer of NPP with WWER-1000 cooldown presented. The residual heat removed via heat exchangers composed from two-phase thermosiphons. The method provides effective pressure decrease in the primary circuit due to activation of natural circulation of Pressurizer coolant through emergency gas removal system to thermosiphon heat exchanger and further returning of the condensate back to the primary circuit. The results of carried out designed modeling showed that the suggested passive system provides timely injection of boric acid solution from hydroaccumulators and thus sufficient subcriticality during the entire emergency process simultaneously with keeping subcooling of coolant in the core.

The results of analytical modeling of emergency cooldown of the reactor installation during complete, long-term blackout event presented. It is proved that proposed passive heat removal system provides efficient heat sink and decreasing of primary pressure. That provides conditions for actuation of ECCS hydro-accumulators (ECCS HA) and maintains adequate subcriticality during the transient along with maintaining subcooling conditions of the primary coolant in reactor core.

INTRODUCTION

One of the most dangerous beyond design basis accidents (BDBA), leading to severe reactor core damage, is long-term blackout with loss of all emergency power sources. Loss of emergency power at Fukushima NPP in March 2011 led to loss of cooling capabilities of reactor cores and spent fuel pools. Overheating, steaming and further loss of coolant led to fuel uncover, overheating and fuel cladding failure, core meltdown, and to the reactor vessel and containment degradation. As a result large radioactive material releases to the environment occurred that was rated as INES Level 7 (maximum) accident.

For WWER 1000 NPPs the danger of such an accident is the loss of feed water flow to SGs and loss of primary – to – secondary heat sink, and also loss of possibility to inject boron into the primary circuit. As the result, the primary pressure starts to grow, initiating loss of primary coolant (LOCA) through pressurizer safety valve eventually leading to core uncover with the consequent core meltdown at high primary pressure conditions.

A method to decreasing primary pressure due to natural circulation (NC) of vapor from Pressurized (PRZ) through emergency gas removal system (EGRS) pipelines, with its subsequent cooldown in a heat exchanger and returning of the condensate to the primary circuit is proposed to prevent such an accident.

To provide reliable heat sink from the reactor core and primary circuit during blackout accident with the full scope, long term loss of all power, an autonomous [passive residual heat removal system \(RHRS\)](#) composed of low temperature two phase thermosiphons (DTS) has been proposed [1, 2]. Analytical modeling of residual heat removal by the RHRS has proved its efficiency [3].

However, the problem of WWER–440 and 1000 core recriticality due to significant negative coolant and fuel reactivity effect along with the positive coolant density coefficient (at the end of fuel cycle), when the primary temperature drops below about 220 °C, requires boron injection into the primary circuit.

Analysis of analytical modeling of residual heat transfer of WWER-1000 with the autonomous RHRS has shown that without boron injection the reactor may reach recriticality at coolant temperature about 225 °C [4]. It happens at 16850 s. after SCRAM actuation (14440 s. after actuation of the RHRS). Therefore, introduction of the RHRS in scope of WWER safety systems requires additional actions to guarantee reactor subcriticality during cooldown.

PASSIVE COOLDOWN SYSTEM FOR PRESSURIZER

Passive system for Pressurizer cooldown may be important during an emergency with complete long-term blackout, to speed up depressurization of primary circuit to the ECCS HA actuation setpoint. Pressurizer is cooled down simultaneously with RHRS operation. Fig. 1 shows the WWER 1000 RI with autonomous RHRS and Passive cooldown system for Pressurizer (PRZ-PCS).

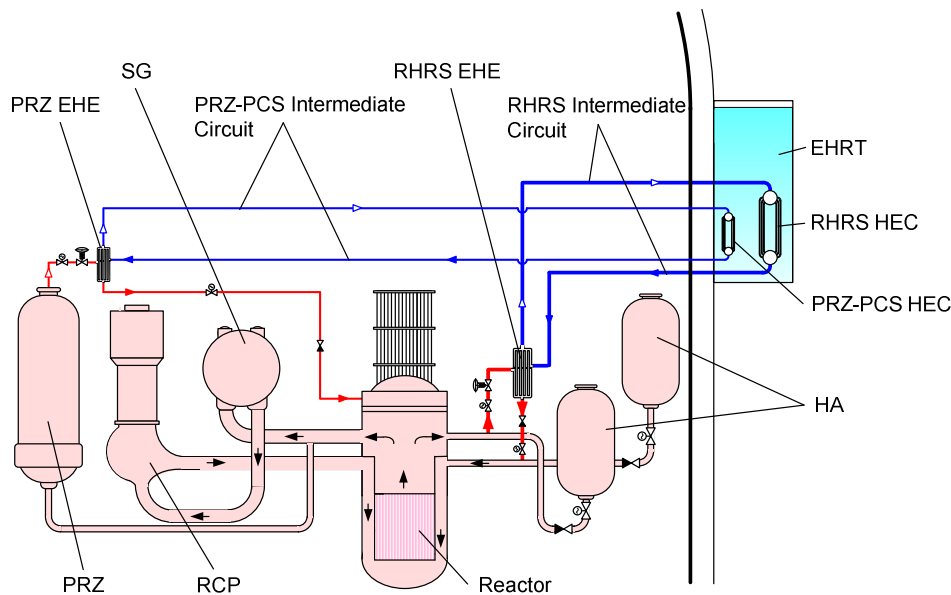


Fig. 1. RI WWER with autonomous RHRS and passive cooldown system for Pressurizer (PRZ-PCS)

RHRS and PRZ-PCS are built of low temperature two-phase thermosiphons (TPTS). Water serves as intermediate TPTS coolant. RHRS is composed of convective primary coolant loop with natural circulation (NC), thermosiphon-based emergency heat exchanger (EHE), two-phase intermediate heat removal circuit that runs out of the Containment and connects EHE to Heat Exchanger – Condenser (HEC). HEC is placed into emergency heat removal tank (EHRT) which provides heat removal to the final heat repository – EHRT water. PRZ-PCS consists of thermosiphon emergency heat exchanger PRZ-EHE, steam line that connects Pressurizer to EHE, condensate line connecting EHE to Reactor Head, two-phase intermediate circuit that connects EHE to HEC located in the EHRT.

Passive RHRS has four independent cooldown trains, PCS – two. Design of Heat Exchangers for RHRS and PCS is similar; the difference is only in heat transfer surface. Passive actuation of PRZ-PCS is based on the same principle that PHRS [1]. Working principles of PHRS and PCS are also similar. The difference is that heat transfer to the thermosiphon PHRS EHE is provided by convective cooldown circuit, and the cooldown of PRZ – with two-phase cooldown. PRZ-PCS acts as condenser of primary steam coming from pressurizer. After being cooled down in the EHE, the condensate flows down to the reactor, where is mixing with the primary coolant. Part of the coolant, via the primary hot leg and pressurizer surge line, again comes to the pressurizer, evaporates and again flows to the EHE.

There is a check valve upstream the PRZ EHE, which prevents injection of the colder coolant from the reactor to PRZ via EHE in case of inadvertent opening of isolation valves when RCPs are in operation. Downstream – isolation valves with the same purpose [1].

In this way, due to permanent cooldown of the steaming PRZ coolant, the passive PRZ cooldown and primary depressurization and cooldown are provided.

INITIAL STATUS OF THE REACTOR AND INITIAL CONDITIONS

Analytical modeling of activation and operation of the PRZ-PCS of WWER-1000/V320 reactor installation has been performed for BDBA with the Initiating Event (IE) – complete long-term blackout using the WWER-1000/V320 model of Khmelnitsky NPP Unit 1, with the failure of all the emergency DGs and failure to provide external power. Modeling has been performed on RELAP5/MOD3.2.

Diameter of the connecting piping to upper part of the PRZ was assumed as Du 32 mm, relative elevation of the upper (inlet) EHE nozzle is 5 meters above the upper part of the PRZ. The connecting options were chosen based on existing design, with possibility to be connected to existing EGRS piping of PRZ and Reactor. Heat exchanging surface of the PRZ EHE has been assessed based on preliminary thermal calculations of heat to be removed – about 1.5 Mw in existing range of primary parameters that provided required depressurization rate.

IE (total blackout) occurs at 20s s. of the transient. Analytical modeling was made for three modes of PRZ-PCS actuation, presenting possible «bounding» modes of the PCS connection to the PRZ:

– Mode "1": opening of the PRZ-PCS isolation valve takes place 10 s. before the IE. This mode is modeling inadvertent opening of PRZ-PCS valve. The aim is to analyze reaction of primary side under inadvertent opening of PRZ-PCS isolation valve. The check valve in this case remains in closed position until the RCPs are in operation.

– Mode "2": opening of PRZ-PCS isolation valve at 600 s. after opening of PHRS Main Isolation Valve (MIV), e.g. at 3020 s. of the transient ($20+2400+600 = 3020$ s.). The mode is modeling conditional "delay" (10 min.) of PRZ-PCS valve actuation compare to actuation of PHRS MIV. That provides understanding of conditions of the primary circuit under conditionally earlier actuation of PCS to PRZ (our understanding is that the mode has to be considered as basic).

– Mode "3": opening of PRZ-PCS isolation valve at 3000 s. after the blackout and after 1800 s. after opening of PHRS MIV, that means at 4220 s. of the transient ($20+2400+1800 = 4220$ s.). The mode is modeling essential "delay" of PRZ-PCS valve actuation. That provides understanding of conditions of the primary circuit under delayed connection of PCS to the PRZ compare to PHRS.

RESULTS OF ANALYTICAL MODELING

Analytical modeling has been performed for 42000 sec. of the transient. Analyses show that the proposed PRZ-PCS provides timely discharge of ECCS Hydro Accumulators (ECCS HA) and adequate subcriticality margin during the whole transient, at the same time maintaining subcooling of the reactor coolant. At the same time, the efficiency of the system remains quite high and there are no negative effects, under wide range of the system actuation – from "early" actuation, at the time of IE, and to "delayed", in 30 min. after actuation of PHRS.

Despite small amount of the heat removed by PRZ-PCS from primary coolant during the cooldown, compare to that removed by PHRS, which makes about 5 to 15 % (Fig. 2), PCS is fully capable to perform the required function – it provides efficient primary depressurization to the ECCS HA actuation setpoint (6.0 ± 1.0 MPa).

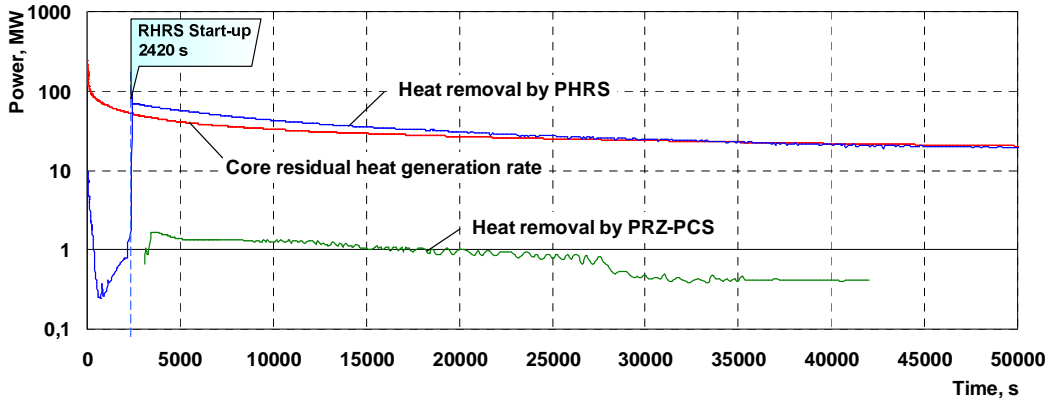


Fig. 2. Heat balance curves: RI, heat removal by PHRS and PRZ-PCS

This is the main advantage of the proposed system – passive depressurization with simultaneous maintaining the conditions, preventing introduction of positive reactivity. This advantage is presented by primary parameter's behavior (Figs. 3–6).

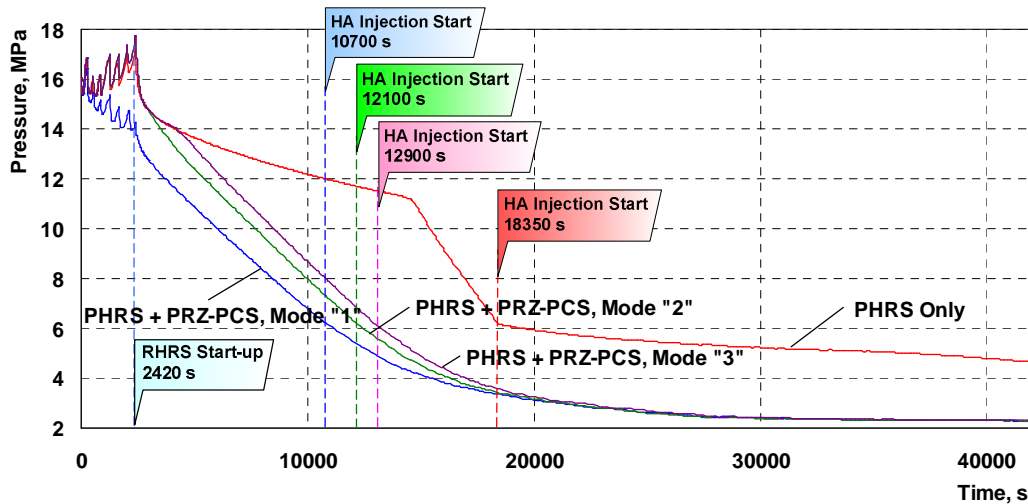


Fig. 3. Primary depressurization in different PRZ-PCS actuation modes

Also, during the whole transient prior actuation of ECCS HA, in all the three considered modes, subcooling margins remain quite high: 15...44 Centigrade – for mode "1"; 15...50 Centigrade – for mode "2" and 16...54 Centigrade – for mode "3". A criterion of safe core cooldown for the considered modes is stable decrease of fuel rod's cladding temperature (TVEL) (Fig. 7).

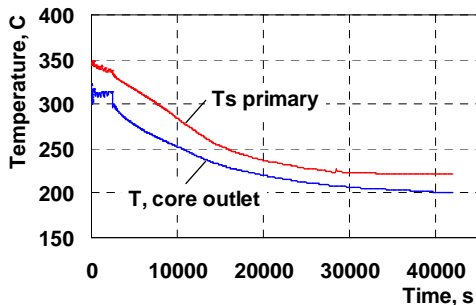


Fig. 4. Coolant temperature above Reactor Core (mode "1")

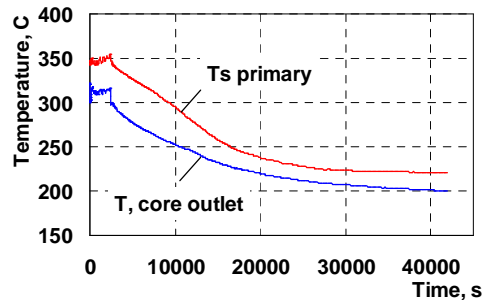


Fig. 5. Coolant temperature above Reactor Core (mode "2")

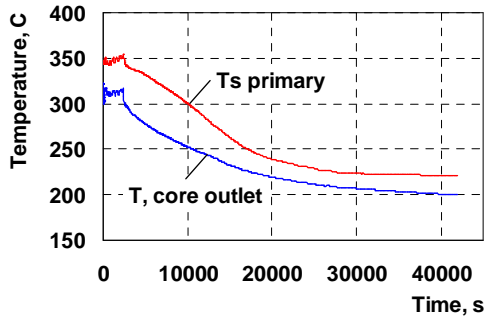


Fig. 6. Coolant temperature above Reactor Core (Mode "3")

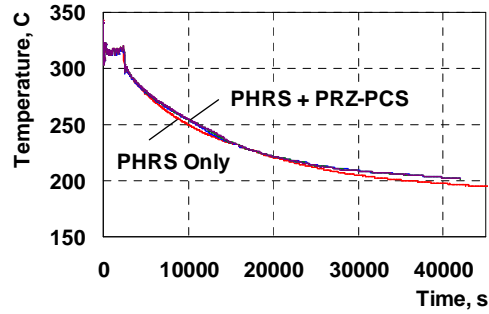


Fig. 7. Fuel Rod Cladding temperature in different modes of PRZ-PCS actuation

Efficient depressurization due to PRZ cooldown provides possibility of earlier actuation of ECCS HA to the Primary Circuit (Fig. 8). Compare to RI cooldown only with PHRS (actuation of ECCS HA at 18350 sec), in the considered modes ECCS HA actuation with complementary PRZ cooldown occurs, accordingly, for 7650, 6250 and 5450 sec earlier. Earlier ECCS HA actuation provides sooner PRZ level restoration (Fig. 9).

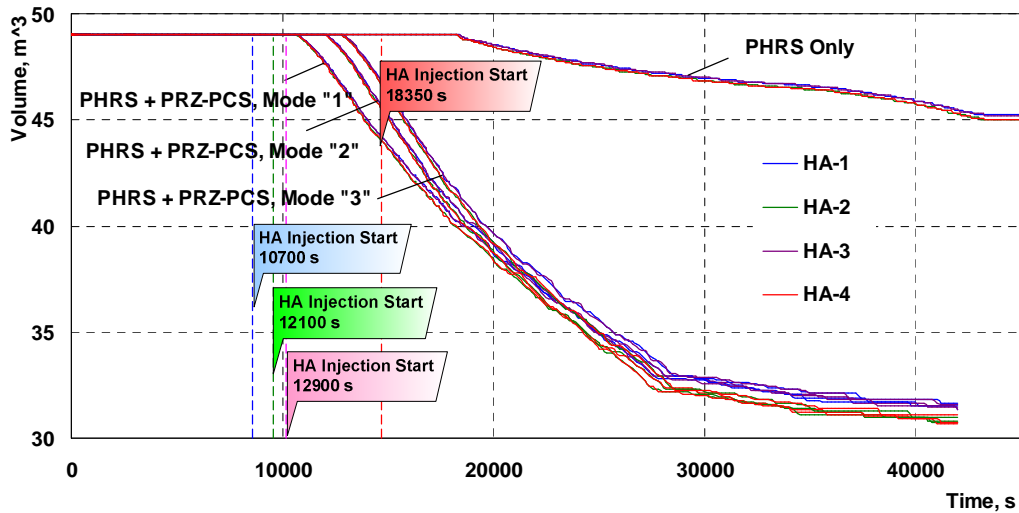


Fig. 8. ECCS HA discharge time for different modes of PRZ-PCS actuation

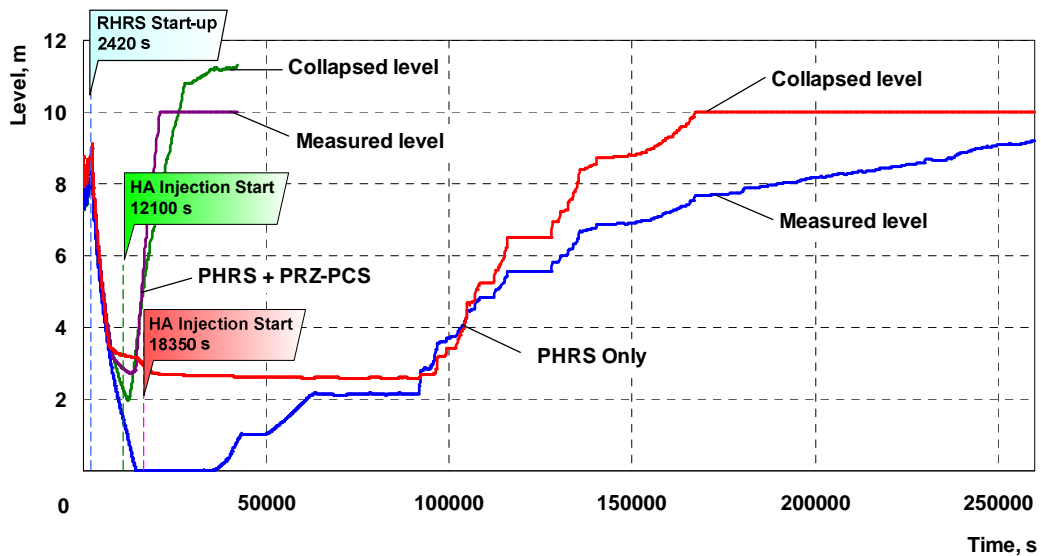


Fig. 9. Comparison of PRZ level restoration after ECCS HA actuation

Fig. 10 presents reactivity evolution for different modes of PRZ-PCS cooldown. Prior ECCS HA actuation the characteristics practically do not differ. After start of boron injection some differences became evident, reflecting insignificant difference in time when $1/\beta_{\text{eff}}$ Starts decreasing. The character of that decrease is practically similar.

Extrapolating upraising part of reactivity curve (at Fig. 10 is marked by a dashed line), we can reach the criticality line approximately at 17500 s. That corresponds to a cooldown mode with PHRS, when RI, without additional boron injection, can reach positive criticality at 16850 s. [5]. Therefore, the presented RI model with PRZ cooldown does not contradict to known nuclear physics of WWER.

Except that, analyzed cooldown mode with intact primary circuit presents the worst case from subcriticality prospective. The explanation is that maximum boron flow from ECCS HA to the primary circuit is bounded by comparatively small steam volume of PRZ. Nevertheless, the reactor is subcritical during the whole cooldown process (Fig. 10).

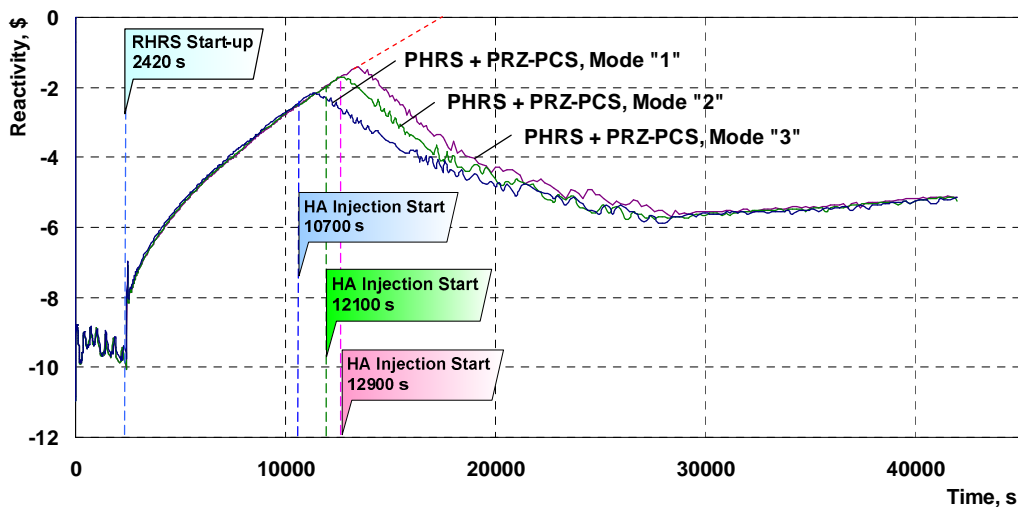


Fig. 10. Subcriticality evolution for different PRZ-PCS actuation modes

Figs. 11-14 present primary circuit flow through PRZ heat exchanger for all three modes of PCS actuation during the transient. The modes "2" and "3" are practically identical and can be considered as stable. Mode "1", where PCS is connected to PRZ in 10 sec prior the IE, has specific instability related to more intensive primary depressurization (Fig. 6). Nevertheless, this mode with premature opening of PRZ-PCS isolation valve under blackout conditions (Fig. 12), provides efficient RI depressurization and necessary subcriticality (Fig. 10) for safe reactor core cooldown.

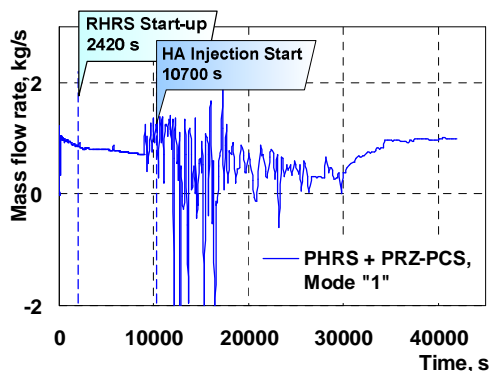


Fig. 11. Flow via PRZ-PCS (mode 1)

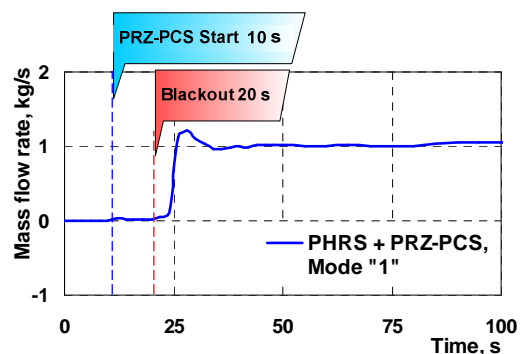


Fig. 12. Actuation of PRZ-PCS in 10 sec prior IE

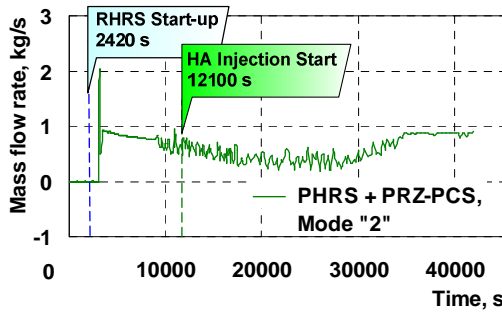


Fig. 13. Flow via PRZ-PCS (mode "2")

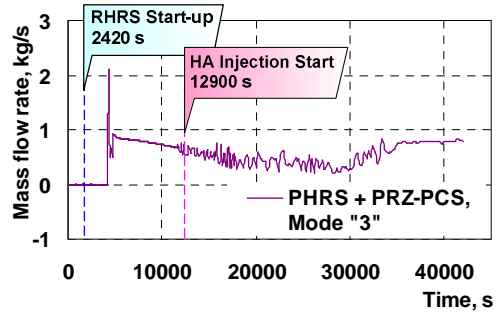


Fig. 14. Flow via PRZ-PCS (mode "3")

The proposed system provides conditions for earlier actuation of ECCS HA and more intensive increase of Boron concentration into the primary circuit (Fig. 15), for safer primary cooldown.

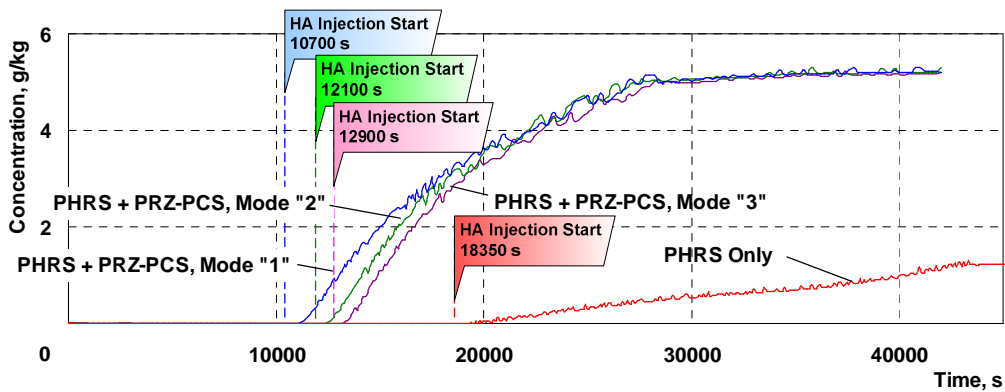


Fig. 15. Comparison of H_3BO_3 concentration curves into the primary circuit with operation of PHRS and different modes of connection of PCS to PRZ

Identified fluctuations of steam flow from PRZ to PCS Heat Exchanger have no impact to stability of the primary cooldown and do not lead to fluctuations of Fuel Cladding temperature. All three modes of PRZ-PCS actuation in different stages of the blackout transient may be considered as satisfying from the point of view of safe reactor core cooldown and prevention of increase of positive reactivity and returned criticality of the reactor.

SUMMARY

Proposed passive cooldown system for Pressurizer (PRZ) of NPP with WWER-1000 reactors provides efficient primary depressurization due to remove of the heat of condensed steam from the steam volume of PRZ. That provides conditions for advanced primary depressurization compare to primary cooldown, at the same time maintaining sufficient subcooling rate in the reactor core. That prevents increase of positive reactivity during residual heat removal by autonomous PHRS and provides maintaining of safe core conditions up to actuation of the ECCS HA.

Results of analytical modeling prove possibility of proposed scheme for PRZ cooldown by autonomous thermosiphon PCS and may be proposed as basis for development of similar passive systems for NPPs with WWER-1000 reactors without necessity to up-rate existing SCRAM systems or to install additional systems for reactivity control.

References

1. Pat. No. 81419. Ukraine. Passive System of Rejection of an Excess Heat Generation / Sviridenko I. I., 2008 (in Ukrainian).
2. Sviridenko I. I. Heat exchangers based on low temperature heat pipes for autonomous emergency WWER cooldown systems // *Applied Thermal Engineering*, 2008. Vol. 28, Iss. 4. Pp. 327–334.
3. Sviridenko I. I. Dynamic characteristics of independent system Residual Heat Removal with thermosiphon heat-exchange equipment // *Safety Assurance of NPP with VVER. An accident prevention of nuclear power plants with WWER. Materials of 5th Int. Scientific and Technical Conf., Podolsk (Russia), OKB "Gidropress"*. Electronic Resource. Access Mode: <http://www.grpress.podolsk.ru/publications/conferences/mntk2007/disc/documents/f07.pdf#search> (in Russian).
4. Sviridenko I. I., Shevielov D. V. Reactor facility accident prevention with independent PRHR system at refusal of absorber injection system: *Collected Scientific Proc. of SNUNE&I*, 2008. Pp. 31–39 (in Russian).

INVESTIGATIONS REGARDING THE WETTING BEHAVIOUR OF PROPANE ON THE SURFACES OF GEOTHERMAL HEAT PIPES

Tom Weickert, Thomas Grab, Thomas Storch, Ulrich Gross

Institute of Thermal Engineering, Technische Universität Bergakademie Freiberg
09596 Freiberg, Germany

Tel. 0049-3731-392164; fax 0049-3731-393963; e-mail tom.weickert@iwtt.tu-freiberg.de

Abstract

The efficiency of geothermal heat pipes shall be improved due to complete wetting. So main aim of the present investigations is to identify tube materials which are long-lasting and easy to process having optimized wetting characteristics for propane. For the research an experimental facility was developed; the setup and function principle are described. The facility was designed for operation at saturation pressure of propane. On solid samples, the wetted area of a single drop containing a defined volume is determined and it serves as criterion for wetting. This area is documented optically by a camera and it is evaluated by means of image analysis software. First results are presented. Observation showed that a liquid propane drop spreads after it is impinged on a sample because of its low surface tension. The wetted area and therefore the contact angle are time-dependent. On the treated materials propane showed a very well wetting. On the basis of the actual and coming results it is expected to evolve new surfaces for geothermal heat pipes.

KEYWORDS

Geothermal heat pipe, Experiment, Wetting, Propane, Visual Observation.

INTRODUCTION

Propane heat pipes constitute a relatively new technology for the use of near-surface geothermal energy (down to 400 m depth) for heating applications being more effective than conventional U-tube heat exchangers. Caused by heat transfer to a heat pump, propane vapour is liquefied inside the head of the heat pipe. A liquid film is formed which flows downwards the inner tube surface where it is vaporized step-by-step due to heat extraction from the ground. Because of its lower density the vapour arises and condenses again on the heat exchanger of the heat pump. The design of the probe is similar to that of CO₂-heat pipes (cf. [1]), so corrugated pipes or welded segments of tubes are used. This means the principle is a wickless heat pipe working gravity driven.

In falling film evaporators a closed thin film is required for effective heat and mass transfer. Scientific research at existing geothermal heat pipes showed that various technical problems can appear during operation yielding a reduction of the performance. Especially incomplete wetting of the inner tube wall leads to a strong decrease of the achievable heat extraction due to the smaller phase interface and thus lower heat transfer area. In such a case the unwetted parts of the probe are not useable and the heat pumps coefficient of performance decreases.

Causes for wetting problems in geothermal heat pipes can be of various types:

- Dry out by falling below the critical film thickness.
- Counter-current flooding with subsequent reduction of the liquid flow [2].
- Impurities and bad wetting surface of the inner probe surface.
- Asymmetric film distribution through inclination of the probe.

Therefore the investigation of wetting behaviour of liquid propane in geothermal heat pipes is in the focus of interest. It's especially important to know on the one hand the location of liquid film break up in existing probes [3], in dependence of the extraction performance. On the other hand new materials and surface characteristics should be investigated to improve the wetting characteristics of the probe-surface.

The minimum liquid film thickness (MLFT) defines the value below which a liquid film breaks up into rivulets [4]. Dry patches form if the mass flow is too low or the surface wets badly. Various mathematical models have been reported for predicting MLFT [4–7]. All of them are based on the knowledge of the equilibrium contact angle. Because of its very low surface tension (7.5 mN/m at 20 °C [8]) the contact angle

of propane on steel is predicted to be below 10° . At present no exact values for the edge angle on any substrate can be found in the literature. Without the contact angle, MLFT and also the location of film dry out cannot be calculated adequately.

Main aim of the current research is the direct and quantitative comparison of various materials concerning wetting by liquid propane. Hence first of all it was necessary to develop a laboratory facility.

EXPERIMENTAL

Wetting is essentially influenced by the surface material, i.e. its characteristic and structure [9]. This was motivation for design and construction of an experimental apparatus, which allows wetting experiments on various solids.

Description of Experimental Setup

The experiments are done with saturated propane at room temperature and the corresponding vapour pressure of about $p_{\text{abs}}=8.3$ bar (see Fig. 1). Propane also is highly flammable. In face of these facts the facility is designed to be pressure resistant and the components are explosion-proof.

Fig. 2 shows a scheme of the experimental setup which is constructed and build under consideration of:

- Ordinance on Industrial Safety and Health,
- Pressure Equipment Directive (PED) and
- Explosion protection guideline.

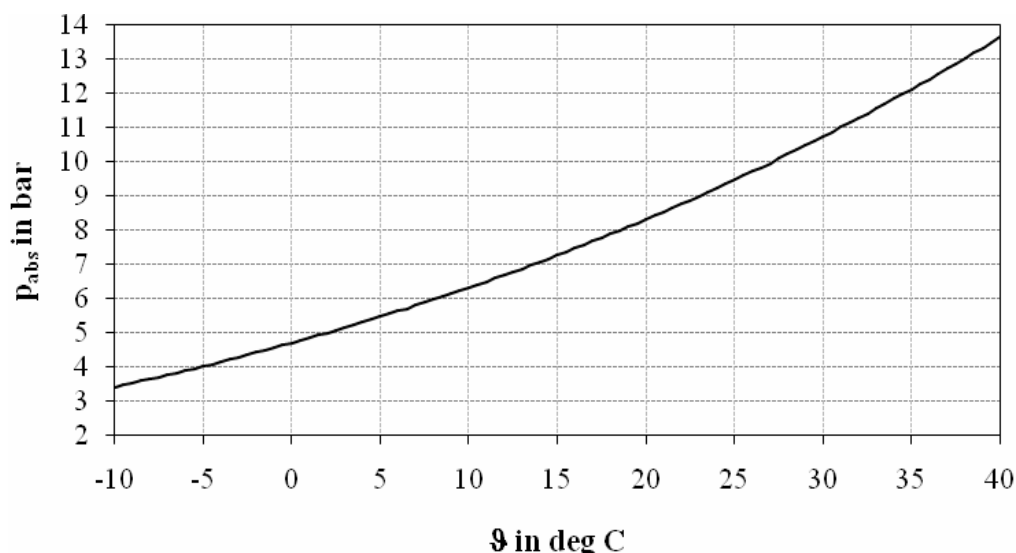


Fig. 1. Vapour pressure of propane as a function of temperature (data taken from [8])

The key component is a $12 \cdot 10^{-3} \text{ m}^3$ pressure vessel ("autoclave"), see Fig. 2 and 3. Two different gas types are used for the experiments: propane 2.5 (purity 99.5 %) and technical nitrogen for inerting after the tests. Liquid propane is supplied from a bottle that is installed bottom up. For final inert purging, nitrogen is added through a float-type flowmeter.

Before liquid drops can be deposited on the surface of the samples a saturated vapour atmosphere has to be generated. Afterwards liquid drops are dripped onto the samples through a capillary tube and two needle valves. The samples are located on an object slide that is moveable. For observation, lighting and photographic documentation, two sight glasses are implemented on the top and the left side of the autoclave. A CCD camera allows taking pictures of the drops.

For safety reasons a gas trough is installed below the apparatus. In case of leakage propane would sink down because its density is larger than that of air. A gas sensor generates an alarm sound if the concentration exceeds 20 vol. % of the lower explosion limit (LEL). Furthermore, the maximum pressure is limited to 13.7 bar by installation of a safety valve and backflow of propane is avoided by an additional check valve. The system can be evacuated by means of a vacuum pump. All valves are operated manually. The saturation state can be identified by means of the temperature and pressure sensor (Fig. 1).

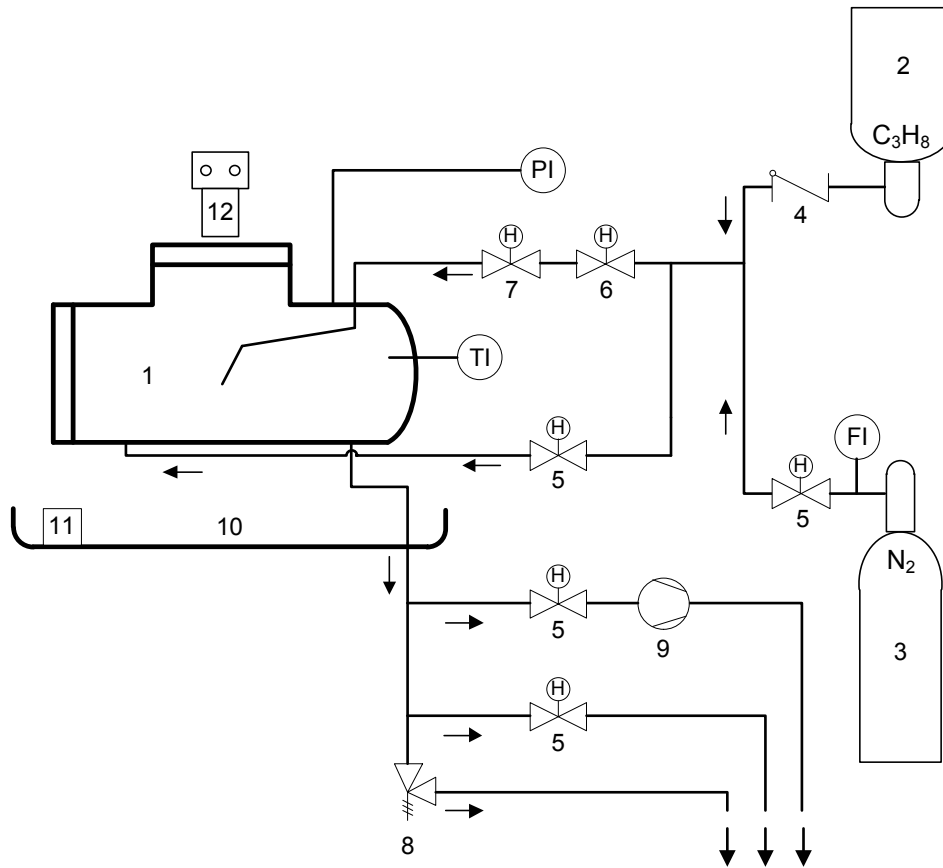


Fig. 2. Scheme of the experimental setup: 1 – autoclave, 2 – propane bottle, 3 – nitrogen bottle with pressure reducer, 4 – check valve, 5 – ball valves, 6 – lock needle valve, 7 – low-flow metering valve, 8 – safety valve, 9 – vacuum pump, 10 – gas trough, 11 – gas detector propane, 12 – CCD camera and LED-light, PI – pressure indicator, FI – float-type flowmeter, TI – temperature indicator

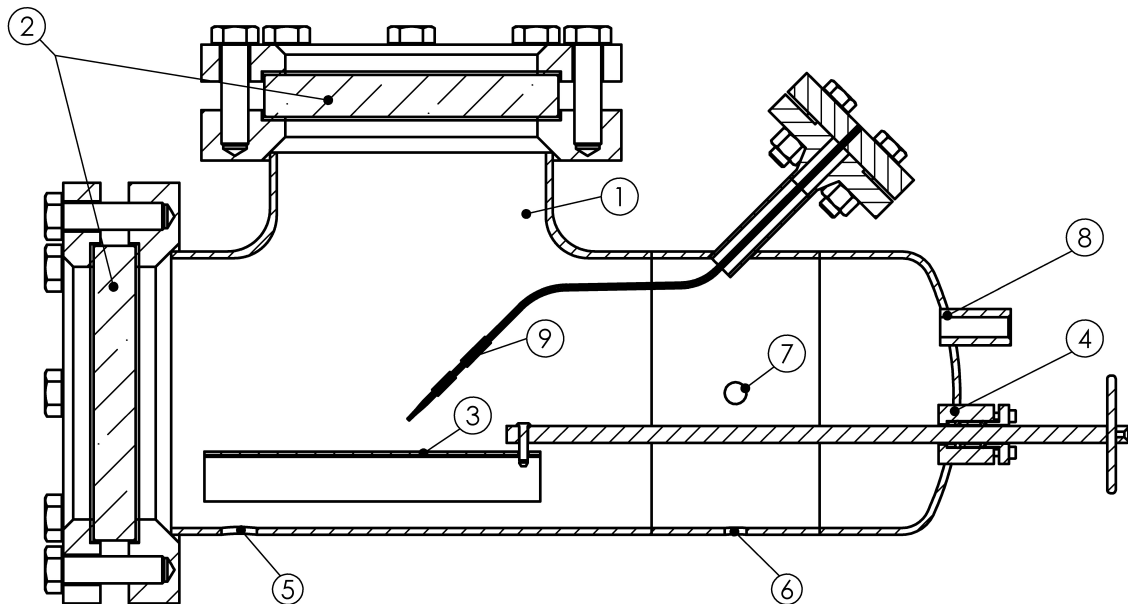


Fig. 3. Autoclave (cross-sectional view) with moveable object slide and sight glasses: 1 – autoclave, 2 – sight glasses, 3 – horizontal moveable object slide, 4 – slideway, 5 – gas inlet, 6 – connection to outlet, vacuum pump, 7 – connection pressure sensor, 8 – connection thermocouple, 9 – capillary for drop generating

Experimental Procedure

The aim is to identify materials and treated surfaces which have a good wettability by liquid propane. This is examined with single droplets with a defined volume of about $5.6 \cdot 10^{-9} \text{ m}^3$. The surface area wetted by a liquid droplet on the sample is defined as the wetting criterion. The larger this area, the better the wetting.

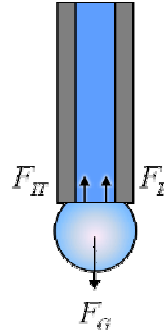


Fig. 4. Balance of forces of a pendant droplet on a capillary

The balance of forces on a pendant droplet (Fig. 4) is given by Eq. (1), where $F_{IT} = 2\pi r \sigma_{fl}$ is the Interfacial Tension Force, $F_B = V \rho_g g$ the buoyancy and $F_G = V \rho_{fl} g$ the gravitational force [10]. In these equations V is the drop volume, σ_{fl} the surface tension of the liquid, ρ_{fl} and ρ_g the densities of liquid and gas, g the gravitational constant and r is the radius of wetting.

$$F_{IT} + F_B = F_G \quad (1)$$

Therefore the volume can be calculated with Eq. (2) if the radius of the wetting on the capillary is known.

$$V = \frac{2\pi r \sigma_{fl}}{(\rho_{fl} - \rho_g) g} \quad (2)$$

As seen in the third picture of Fig. 6, the wetting radius is between the inner (0.325 mm) and outer (0.75 mm) radius of the capillary. Therefore the calculated drop volume lies between $3.3 \cdot 10^{-9}$ and $7.5 \cdot 10^{-9} \text{ m}^3$. The determination of the exact drop volume was carried out by dividing the defined volume of glass cylinder through the counted drops that were needed to fill it.

In the first part of the research, samples (100x20 mm) of actual geothermal heat pipes are investigated. After a cleaning process to remove oil-residues, the samples are put into the autoclave. Subsequently a saturated propane atmosphere is generated and a single liquid drop is applied on the sample.

A next step constitutes the optical documentation of the drop perpendicular from above by the CCD camera and evaluation of the wetted area by image analysis software. The contour line of the drop has to be framed manually; the software then calculates the wetted area from a defined scale. To determine this scale for the conversion of the measured pixel to an area, it is necessary that a rule is photographed with the sample (see Fig. 5). For comparability the curvature of all samples has to be equal. Therefore all investigated tubes have an inner diameter between 51 and 53 mm.

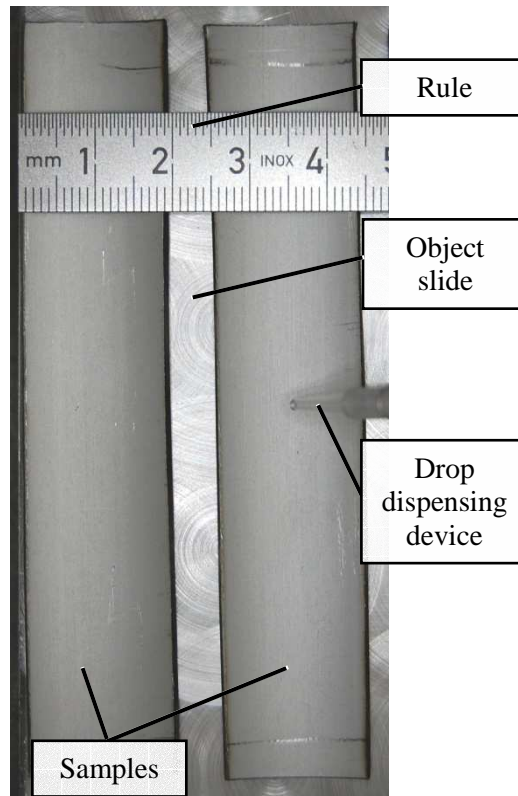


Fig. 5. Photo of the typical assembly with samples, object slide, rule and drop dispensing device

RESULTS AND DISCUSSION

During the experimental procedure a pendant drop forms on the lower end of the capillary and builds a necking. Fig. 6 shows the drop detachment. If the gravitational force exceeds the force by interfacial tension and buoyancy, the drop detaches from the capillary and falls down onto the sample. The drops height of fall is 5 mm.

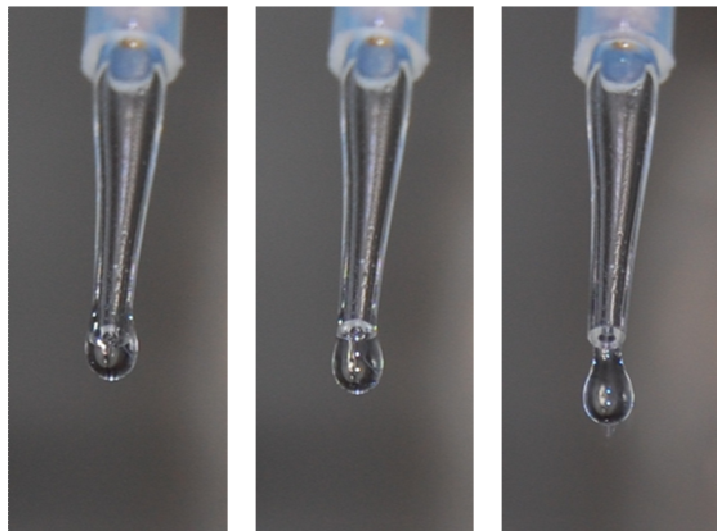


Fig. 6. Photo sequence of a detaching propane drop on a glass capillary

First investigations show, that once a propane drop impinges on a sample it builds a sessile drop. An important observation result was that the wetted area extends very strong with time, i.e. within the first

seconds. With rising drop age the spreading speed decreases. This general behaviour was observed on all examined materials. Fig. 7 shows exemplary the measured wetting-area in dependence of the drop age. Therefore not only the wetted area but also its time-dependent behaviour has always to be regarded.

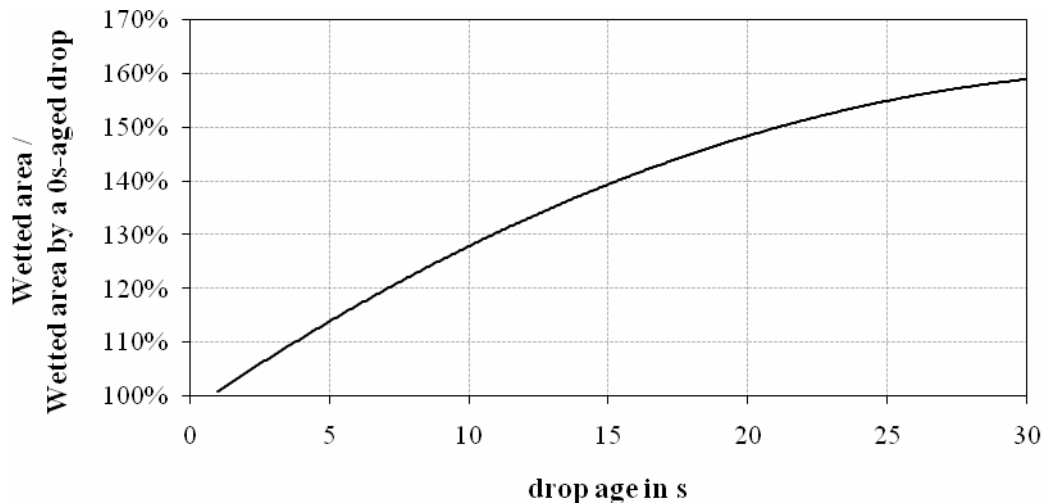


Fig. 7. Time-dependent wetted sample-area after dropping of a single propane drop

In consequence liquid propane has no static contact angle on the first examined materials and surfaces (steel, high grade steel, polyamide). The contact angle seems to be always dependent of the drop age.

Furthermore a noticeable contact angle as known from water does not occur. The appearing angle is very small and thus not measureable with conservative methods.

Further investigations are concentrated on the dynamic behaviour of liquid propane rivulets on inclined surfaces and inside of inclined tubes.

Acknowledgements

The support of the Federal Ministry of Economics and Technology on the basis of a decision by the German Bundestag is greatly appreciated. Special thanks are due to the company Multi Industrieanlagen GmbH in Aue (Germany) which manufactured the experimental apparatus.

Supported by:



on the basis of a decision
by the German Bundestag

References

1. Ochsner K. Carbon dioxide heat pipe in conjunction with a ground source heat pump (GSHP) // *Appl. Therm. Eng.* 2008. Vol. 28. Pp. 2077–2082.
2. El-Genk M., Saber H. Determination of operation envelopes for closed, two-phase thermosyphons // *Int. J. Heat Mass Transfer.* 1999. Vol. 42. Pp. 889–903.
3. Storch T., Grab T., Zieger C., Kupka M., Gross U., Wagner R.M. Visual observations inside a geothermal heat pipe // Proc. of 8th Minsk Intern. Seminar “Heat Pipes, Heat Pumps, Refrigerators, Power Sources”, Minsk, Belarus, 2011.

4. El-Genk M., Saber H. Minimum thickness of a flowing down liquid film on a vertical surface // *Int. J. Heat Mass Transfer*. 2001. Vol. 44. Pp. 2089–2825.
5. Hartley D. E., Murgatroyd W. Criteria for the break-up of thin liquid layers flowing isothermally over solid surface // *Int. J. Heat Mass Transfer*. 1964. Vol. 7. Pp. 1003–1015.
6. Hobler T. Minimum Surface Wetting // *Chemia Stosow*. 1964. Vol. 2B. Pp. 145–159.
7. Doniec A. Laminar Flow of a Liquid Rivulet Down a Vertical Solid Surface // *Can. J. Chem. Eng.* 1991. Vol. 69. Pp. 198–202.
8. VDI - Verein Deutscher Ingenieure. *VDI Heat Atlas*. 2nd ed., Springer, Berlin, 2010.
9. Xian J. Wettability of Rough Polymer. Metal and Oxide Surfaces as Well as of Composite Surfaces // *J. Adhes. Sci. Technol.* 2008. Vol. 22. Pp. 1893–1905.
10. Wakeham W., Assael M., Marmur A., Coninck J., Blake T., Theron S., Zussman E. Material Properties Measurement and Data: *Springer Handbook of Experimental Fluid Mechanics*/Eds. C. Tropea, A. Yarin, J. Foss, 2007. Pp. 85–177.

HEAT AND MASS TRANSFER FROM VAPOR – DUST – GAS FLOW INSIDE THERMAL SYPHON HEAT EXCHANGER

S. G. Tersiev, O. G. Burdo, H. F. Smirnov

Food Technology Processes and Apparatuses Department

Odessa National Academy of Food Technology

112 Kanatnaya street, 65090, Odessa, Ukraine

Phones: 038-048-712-41-75 (work); 038-050-6638-415 (mob), fax: 038 – 048 -

E-mail: terma@onaft.edu.ua; g.smirnov@e-mail.ua

Abstract

The food production manufacturing convective dryers usually have been working with great heat carriers flow rates. That is why, waste heat carrier requires a lot of energy. Besides it, the heat carrier brings a lot of food product particles, such as dry milk, coffee or sugar dust etc. There is presented in the paper the authors concept of the energy and product saving using combined system, what was based on the using of the possibility of heat pipe or thermal siphons heat exchanger (TSHE) as to transfer heat both to collect on their surface a lot of particles, which there are containing inside the vapor – gas flow. The idea is connected with the imagination, that vapor – gas flow contains the water. It was leading to the principal possibility to connect dust particles different physical nature with water and successfully to deposit them on the heat exchanger surface and as it result to clean the surface and to increase it heat transfer level and to be leading to the high and stable heat and mass transfer coefficients. There are presented in the paper authors theoretical suggestions about physical nature of the heat mass transfer intensity increasing in the mentioned conditions. They are based on the two main propositions: 1. The inter – phase limit equilibrium state existence; 2. Inter – phase mass interconnection existence too.

The authors are proposing the next: There are developing by vapor – dust – gas stream flowing over TSHE finned surface the next four processes: 1. The heat transfer from the hot stream to the cooled TSHE surface. 2. The vapor condensation, when there will be reached corresponding conditions. 3. The particles deposit commonly with water, appearing as the condensation result. 4. The dust and condensate flows interconnection. The analysis of the engineering realization of the experiments results shown, that the optimized designs of these energy and production saving system allowing to decrease energy expenditures on 12 – 15 % and to be compensated for the time lower than one year.

KEYWORDS

Waste heat carrier; dust; exhaust heat carrier flow; thermosiphon; vapor – dust – flow; heat and mass utilization exchanger; thermal siphon heat exchanger; condensation; heat mass transfer intensity.

INTRODUCTION

The whole food technologies are differing great energy consumption in all industrial countries. These production have to be developing very fast especially in the crisis times and to ensure considerable put in the government budget. The matter success is possible only if it will be realizing seriously changing in the whole chain of food technologies, including their significant improvement and modernization combining with new forms of energy monitoring and energy management [1]. However, these industry peculiarities, including it conservatism don't allow to reach it, don't allow to reach new innovation development. First of all it is relating to the ecology and energy saving problems successful solution. Unfortunately, the position in the industry field is considerable worse in the comparison with mentioned food technology production. Many forms and means of technology food equipment, extremely complex food products and raw materials structure are leading to appear as any serious barrier for using in the field many achievements, which were realized in the other industrial directions, including the possibility to use them for industrial processes intensity enhancement and energy consumption decreasing.

The most energy consumption process in the food technology is drying. Namely the process is determining the whole energy consumption in the most types of food technologies [1, 2]. There is spending a most part of whole energy expenditures during the drying. That is why the problem energy saving in the different food technologies is connected first of all with the problem successful solution for drying. It is spending in 2 – 3 times energy in the most food technologies processes, than it is requiring from the physical

point of view. The most comfortable method of energy saving for drying, is connected with known thermal siphon heat exchangers using for the goal of the heat in the waste heat carrier utilization.

THE SCHEMES WITH HEAT AND MASS UTILIZER EXCHANGER ON THE BASE OF A THERMOSIPHON

The peculiarity of many food technologies is connected with the waste flows are some mixtures of the burning products or air with some dusts obtained as products powders and partially with water vapor. The heat transfer from such complex flow has to take place over two-phase thermo siphon bundle exchanger to the additional heat carrier Fig. 1.

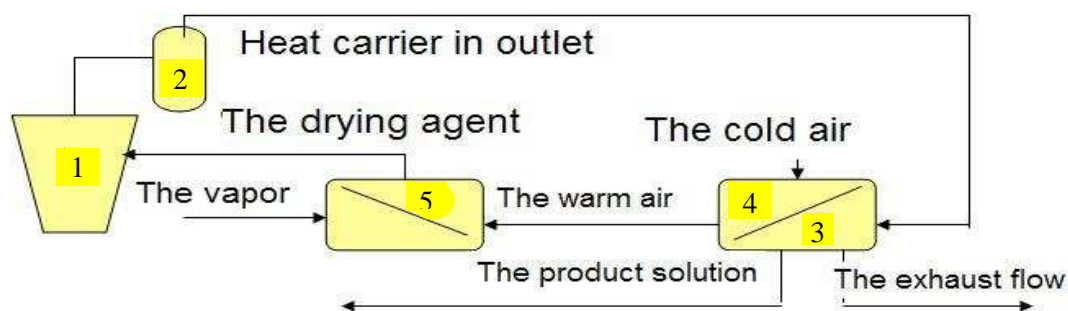


Fig. 1. The complex heat and dust utilization system with use of dryer aeroszole exhaust flow:
1 – dryer, 2 – cyclone, 3 – HMUS cooling section, 4 – HMUS heating section, 5 – vapor calorifer

The hot flow structure and temperature conditions determine as it character, both their thermal regimes and transfer processes intensity. The working out system of complex heat and waste products dust utilization base is special exchanger [3], which was named as a heat and mass utilize (TMU). The heat transfer modules are made as autonomous thermal siphons heat exchangers [4]. The exchanger key advantage is connected with high quality of surface cleaning from dust is reaching by it design and finned surface properties.

THERMALPHYSIC MODEL

The TMU working concept takes into consideration aerosols waste flow in many of food technologies, including some of combined heat and mass transfer processes peculiarities in the thermal siphon heat exchanger system [5]. The dust flow degree dustiness and heat and mass transfer surface of TMU determine the quantity and quality of the dust powder deposits on the heat and mass transfer surface. The kinetic and dynamic of food product dust particles movement into finned surface spaces are depending on the particle physical nature, their sizes and surface property and besides it is connected with any aerodynamic field into the exchanger. Simultaneously, it is possible to developing on the heat and mass transfer surfaces the water vapor partial condensation on the surface. It can be leading to the formation some mixtures or solutions of dust into water. During this flow draining over the finned surface takes place different interaction between drained flow and deposits besides it is take place interaction the solution with hot gas flow washing the surface. The dust from the hot gas flow can be partially dissolved and it means, that the surface can be considerable removed from dust. These processes are very tightly connected each other, they are taking place combined and simultaneously.

The thermal physic model of these interconnected processes block schematic is presented in Fig. 2.

The transfer processes organization into THMU has a very good influence on corresponding food technology development and it is leading to the positive effect. As the system and apparatus actions result the flow absolutely removing from the dust and water vapor. The formed solution is draining from the heat transfer finned surface accompanied by the surface cleaning. There are reaching three positive results:

1. The first – a cleaning product realized considerable ecology indexes of the processes.
2. The second – the expensive food product particles are trapped and returned into the process saving.
3. The third – the energy consumption reduced very high.

Besides, the apparatus work in the way is reaching to the good apparatus self cleaning. Therefore, it is reaching the apparatus work with best most attractive characteristics. It can be said, that there are reaching the apparatus with maximum positive indexes.

The gas – dust – vapor flow by streamline over the finned surface initiating next four actions: heat transfer from hot flow to the external surface of THMU; water vapor partial condensation from the moist air; the deposition of many small food product particles into the spaces of the heat transfer finned surface; the dust particles and condensate interaction. These processes understanding level is now very different [6–9]. The third and fourth now are requiring in the essential development improvement.

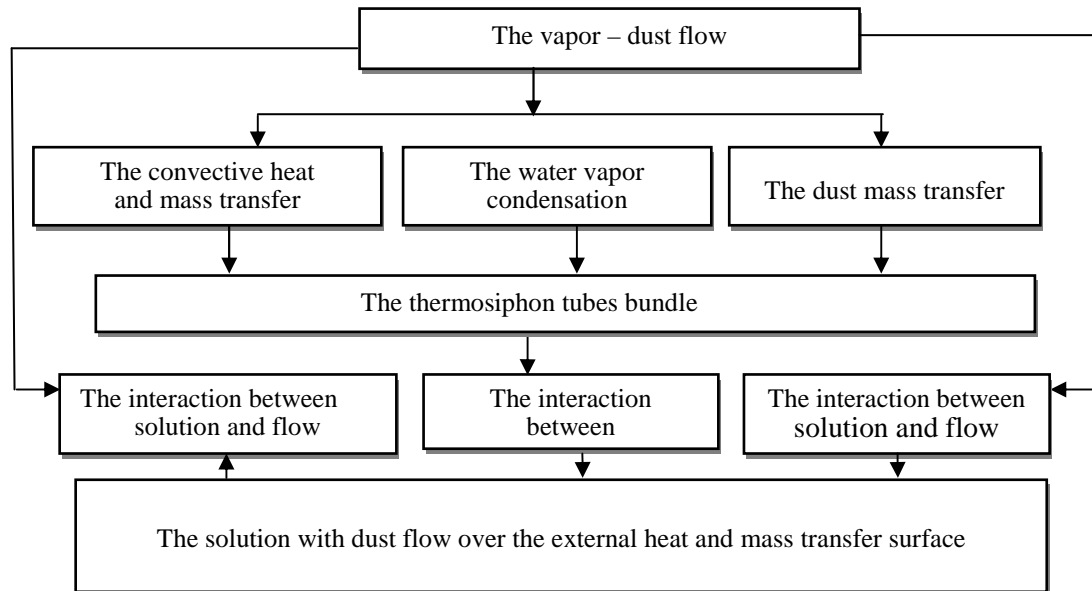


Fig. 2. The interconnected heat and mass transfer processes in Thermal Heat Mass Utilize exchanger (THMU)

THE INTERCONNECTED TRANSFER PROCESSES IN THERMAL HEAT MASS UTILIZE EXCHANGER MODELING

The authors were trying during some years to state and develop some initial steps in the theoretical modeling of the complex interconnected transfer processes in THMU exchangers on the two-phase thermosiphon base with external finned surface, including aerodynamic, heat, mass and dust particles transfer to the external surface and their deposition phenomena. Some key positions of their approach are presented in the paper.

The deposit layer formation model is based on imagination of the limit equilibrium of mass transfer existence.

On the point of view: the particles mass flow with rate of m is proportional the process velocity coefficient k , mass product particles concentration in the flow C , and running over velocity value w , mass accumulation on the surface value Δm and time performance value τ . The value Δm is determined as the difference between final mass of the deposit m_∞ and the deposit mass at the given moment τ .

So, there is in the boundary layer conditions the deposit layer growth law can be presented by the next form:

$$\delta = a\sqrt{\text{Re}} [1 - \exp(-kCw\tau)]. \quad (1)$$

The formula (1) has single independent variable τ , one design size, three flow parameters (C , w , v) and two empirical coefficienta (k and a). It was obtained on the mentioned imaginations base for soluble coffee technology the next law of the coffee powder layer growth as some deposit layer:

$$\delta = 0.63 \cdot 10^{-2} \cdot [1 - \exp(-75 \cdot 10^{-4} \tau)]. \quad (2)$$

The modeling next step was the description of the interaction of the food product dust layer with condensate. The most food products (sugar, coffee, dried milk and etc.) dust is very good solved by the water also condensate after partial condensation from the saturated gas (air) flow. That is why it will be caused under partial condensation influence the dust layer saturated by the water. The process model was presented as three zones model. There is take place in the first zone (consolidation) the contact (between product and THMU surface) spots area increasing, it is connected with the growth of the adhesion – cohesion forces. There is reaching the maximum adhesion forces on the border first and second zones. The second zone named as "relaxation" comes into third zone conditionally named as "fluidity". The model and these imaginations were confirmed on the experimentation base. There were obtained the quantitative dependences adhesion forces on the dust moisture content. The dust film thickness on the heat transfer surface at the third zone is determined by the common action of the inertia flow, adhesion (Pa) and surface tension σ forces. The final result of the theoretical model using was leading to the next criteria equation:

$$\Omega = \rho g Rn / \sigma = A (We)^n (P)^m \quad (3)$$

The empirical constants were found from the experimental data known method using treatment. They were determined for the some different products and are presented in the Table 1.

Table 1. Equation (3) constants

Product	A	n	m
Starch	$4 \cdot 10^{-4}$	-0.06	0.89
Sugar	$32 \cdot 10^{-3}$	-0.11	0.87
Coffee	$31 \cdot 10^{-4}$	-0.15	1.16

It was suggested to calculate the deposit film thickness from the value $\Omega = \rho g Rn / \sigma$, which can be determined from the equation (3). The value is determined as the difference of a film thickness Rn and the mentioned exchanger surface on the dependence number (We) and dimensionless ratio $P = PaRm / \sigma$, the last one meaning is the ratio adhesion and surface tension forces.

The interconnection heat and mass transfer inside THMU internal volume is the extremely complex separate problem to study. It is necessary to study the interaction of the draining on the thermo siphon surface condensate with aerosol flow. The reality it is required to determine interaction between vapor – gas – dust flow and the solution drops, which are reacting with dissolved in the condensate product dust particles. The mass transfer intensity in the process is characterized an influence of eleven parameters. There are the mentioned flow parameters: the velocity w ; the viscosity ν ; the density ρ ; the particles average diameter d_T and their concentration C_T ; the condensate drops parameters such as: their average diameter d_K , density ρ_K and their concentration C_K into in-tube volume. Besides them there are calculating the mass transfer intensity and diffusion coefficients β and D and take into consideration gravitational constant g . Using the similarity theory and dimensional analysis, including the π -theorem with some simplifications earlier the authors was obtained the next generalized experimentation formula, what is connected the flow and particles main parameters:

$$Sh = A (Pe_D)^k Re^n K^m. \quad (4)$$

The diffusion Peclet number $Pe_D = \nu d_T / D$ is characterizing the diffusion boundary layer formation and Reynolds number (Re) is characterizing the hydrodynamic position inside THMU. The complex K shows the flow dusting degree (C_T) and it washing - off degree (C_K) ratio. The equation (4) constants determination was requiring the wide experimentation conduction. It was recreating experimental set-up, including itself any gas loop with fan, electric heater, some devices with goal to organize dosing dust and condensate into the vapor – gas – dust flow and working element to experimental modeling of the thermosiphon external surface.

The experimental set – up allowed to change in the wide ranges main working regimes of proposed heat and mass transfer apparatuses. The set-up measurement system determined into the wide ranges such main parameters as inlet and outlet temperatures, surface temperatures t too, the main gas and vapor flow rate $G1$, the dust $G2$ and water $G3$ flow rate, which were incoming into the main flow.

TECHNO-ECONOMIC INDEXES OF THERMAL HEAT MASS UTILIZE EXCHANGER

The working out apparatus is acting simultaneously as dust filter, gas scrubber and heat and mass utilize exchanger. It is determining its high performance qualities. The apparatus high effectiveness is reaching, thanking by the thermosiphon principle using. It is allowing to organize inside the exchanger very effective counter – current both gas flows with cross streamline of the finned surfaces. As the result it is reaching inside the exchanger very high transfer intensity level and very high corresponding heat and mass transfer coefficients. Coefficients values relating to the tubes surface of the base are reaching such meanings as 100–150 W/(m²·K), inside conventional exchangers the same values usually are equal only 30–40 W/(m²·K).

The apparatus can be producing from the simple identical modules with cross – section finned thermo – siphon tubes. Such manufacturing technology is allowing to realize extremely simple and reliable design with very high heat transfer intensity especially for account cross finned tubes for both gas flow as for heating heat carrier both for the heated one. It is impossible for the conventional heat exchanger type. The life time of the apparatus can be more than sixty years. It is considerable more than for the traditional ones. The expenditures time is lower than one year only for account of the energy saving and the fuel consumption is decreasing. In the case of using also the waste product the time can be decreased even more and to reach lower than 3–6 months.

The self cleaning peculiarities of the technology open wide perspective it can be using in the different food technology processes, including such of them, which are containing itself the drying and stove equipment. The key idea is consisting in the using of the food technology natural property – existence inside waste food product flow water vapor commonly with the soluble food powder particles. Using of the thermosiphon exchangers unique advantages is allowing reaching new high level in the food technology considerable improvement. It means, that it is realizing the new type of very effective heat and mass exchanger with reliable self cleaning property. It gives some guarantees to stabilize during a lot of time the technology main positive indexes.

TECHNO-ECONOMIC INDEXES OF THERMAL HEAT MASS UTILIZE EXCHANGER USING AT THE DRYING TECHNOLOGY

Techno-economic indexes are given in Table 1.

Table 2. Techno-economic indexes

Indexes	Units	Production			
		Shugar	Dried milk		Concentrators
		Cylinder dryer	A1-OP4	P3-OCC	Absent
The drying agent temperature	°C	90	150	150	140
The exhaust heat carrier temperature	°C	55	80	75	100
The heat carrier flow rate.	m ³ /s	18.9	5.7	0.22	4.5
The heat carrier temperature after heat and mass utilizator	°C	40	52	50	52
The utilized heat flux	kW	272	140	5	140
The energy economy per year	Giga J	7850	4020	140	4095
The necessary electricity power.	W	450	130	5	110
The electric additional power per year	kW·hour	11650	3370	150	2800

Therefore the original transfer processes in food technologies organization is coming to the positive and perspectives in the food technologies different fields improvement.

CONCLUSIONS

It is shown, that new type of technology exchanger THMU using allow to considerable improve of important indexes in the different food technologies. As the result of combined interaction of much complex heat – mass transfer processes using it can be possible to use not only waste energy but waste product too commonly with of self cleaning of the exchanger external surface. These technical decisions allow reaching three positive results:

1. Cleaned gas – air flow to ensure the food technology the ecology high level.
2. The expensive food product particles are catching.
3. The energy consumption is decreasing essentially. Besides it, the apparatus work in the mentioned regime is leading to the appearance of such new the apparatus property as self cleaning. Therefore, there is realizing the unique new type of exchanger with great perspective in the different food technologies fields. The optimized design of the mentioned exchanger allows reducing energy consumption on 12–15%.
4. The reliable working time is considerable increasing.
5. The expenditures compensation time can be lower than one year and for the case with using waste product, it can be even more decreased up to some months.

References

1. Burdo O. G. *The food industry energy monitoring*, Poligraf Publishing House, Odessa, 2008. 244 Pp. (in Russian).
2. Burdo O. G. *The dryers manufacturing evolution*, Poligraf Publishing House, Odessa, 2010, 368 Pp. (in Russian).
3. Burdo O. G., Stanevsky O. L., Ida Amor. The aerosol flows transfer processes in the thermosiphon tubes bundle investigations // *Proc. of Intern. HMT Forum, Minsk, Belarus, 2000*. Vol. 10. Pp. 179–183 (in Russian).
4. Smirnov H. F. The refrigerant cooling system of electronic equipment with heat pipe application // *Proc. of Intern. Symp. "Heat pipe research and application"*, Shanghai, China, April 24–27, 1991. Pp. 417–426.
5. Burdo O. G., Terziev S. G., Peretyaka S. N. Energy-Saving Food Technologies on Heat Pipe Exchangers Basis. // *Proc. 9 th Int. Heat Pipe Conf., Albuquerk, USA, 1995*. Vol. 1. Pp. 219–224.
6. Burgo O.G., Gajda S., Knuish A.I. Heat aerodynamics reliability of the heat pipe exchangers // *Proc. 10-th Int. Heat Pipe conf., Stuttgart, Germany, 1997*. Pp. 101–106.
7. Burdo O.G., Terziev S.G., Peretyaka S.N. Heat mass transfer in the thermal utilizers of vapor – dust flow heat of food production exhaust flows // *Proc. of Minsk Intern. HMT Forum, Minsk, Belarus, 1996*. Vol. 10. Pp.173–178. (in Russian).
8. Burdo O. G., Terziev S. G., Zykov A. V., Bezbach I. V. The drying thermal technology improvements ways in the AIC // *Proc. of Internal. Practical Conf. "Modern Energy Saving Thermal Technologies"*, Moscow, Russia, 2002 (in Russian).
9. Burdo O. G., Terziev S. G., Zykov A. V. Optimization of Heat Pipes and Mass Recovery // *5th Intern. Seminar "Heat Pipe, Heat Pumps, Refrigerators"*, Minsk, Belarus, September, 8–11, 2003. Pp. 161–166.

INVESTIGATION OF THE EFFECT OF THE CONDENSER COOLING TEMPERATURE ON THE OPERATING CHARACTERISTICS OF A LOOP HEAT PIPE

S. Yushakova, S. Vershinin, Yu. Maydanik

Institute of Thermal Physics, Ural Branch of the Russian Academy of Sciences,
Ekaterinburg, 620016, Amundsen st. 106
Tel. 7(343)267-91-19, Fax. 7(343)267-87-99, e-mail: s.yushakova@gmail.com

Abstract

The results of developing and investigating the operating characteristics of a copper-water loop heat pipe with an effective length of 330 mm are presented. The pipe was equipped with a flat-oval evaporator 7 mm thick with an active zone measuring 30x30 mm and a condenser with a spiral finning and a cooling jacket. The tests were conducted at horizontal and vertical orientations of the device in the gravity field in a heat load range from 5 to 1400 W at water temperature, cooling a condenser, varying in the range from 10 to 80 °C. The dependence of parameters, characterizing the operating efficiency of a LHP, was studied in tests. The research on a start-up of the device at low and moderate heat loads was also carried out.

KEYWORDS

Loop heat pipe, evaporator, heat load, thermal resistance, start-up.

INTRIDUCTION

A loop heat pipe (LHP) is a high-performance heat-transfer device. The main parameters, characterizing the operation of these devices are a range of heat loads, a thermal resistance and an operating temperature. One of the factors, which influence the values of these parameters, is a condenser cooling temperature.

The results of the experimental studies of a copper-water LHP with a flat evaporator at the cooling temperature of the condenser by running water, varying in the range from 40 to 95°C, are presented in the paper [1]. In the range of heat loads from 100 to 500 W temperature dependences $T_{ev} = f(Q)$ have a linear form. It is also shown that at the same heat load the operating temperature of a LHP increases with the growth of the condenser cooling temperature.

There are few papers, describing a LHP start-up and factors, which influence its process. It particularly concerns copper-water devices. The paper [2] presents the research results of a start-up process of a copper-water LHP with a flat rectangular evaporator at heat load in the range from 10 to 300W. The authors note that the process of the device start-up at low heat loads is going with significant temperature oscillations. It is also noted that with increasing heat load the amplitude of these oscillations is reduced. In the paper [3] the influence of a wick barrier layer thickness of a copper-water LHP with a flat evaporator on the start-up process at heat loads of 6–8 W is studied. It is shown, that with the increase of a barrier layer thickness heat flow-over is decreasing in the compensation chamber. It is resulted in the reduction of the LHP operating characteristic and disappearance of the temperature oscillations during the startup process.

In this paper the influence of cooling temperature of the LHP condenser on the operational characteristics of the device in the range from 20 to 1400 W at horizontal and vertical orientations of the device in the gravity, and also the dependence of a start-up process from a heat load and a heat sink temperature.

DESCRIPTION OF AN EXPERIMENTAL DEVICE

Within the context of the paper a copper-water loop heat pipe, shown in Fig. 1, was designed and manufactured. The LHP was completely made of copper, including a wick with porosity of about 67% and a break-down pore radius of 21 microns, sintered from copper powder. A flat-oval evaporator measuring

80(L) x 42(W) x 7(H) mm was equipped with a thermal interface - a copper plate of 30x30x1 mm. The use of the thermal interface was explained by the necessity of temperature measurements right on the evaporator wall. For this purpose the plate had a groove 1 mm wide, where a thermocouple was placed. Comparatively short liquid and vapor lines 120 and 180 mm in length respectively, made it possible to minimize a hydraulic resistance and a thermal resistance of the LHP. A sufficiently long condenser, equipped with a spiral finning and a plastic water cooling jacket, was enable to remove heavy heat fluxes. The vapor line and the condenser had the same internal diameter of 5.4 mm, and the internal diameter of the liquid line was equal to 3.4 mm.

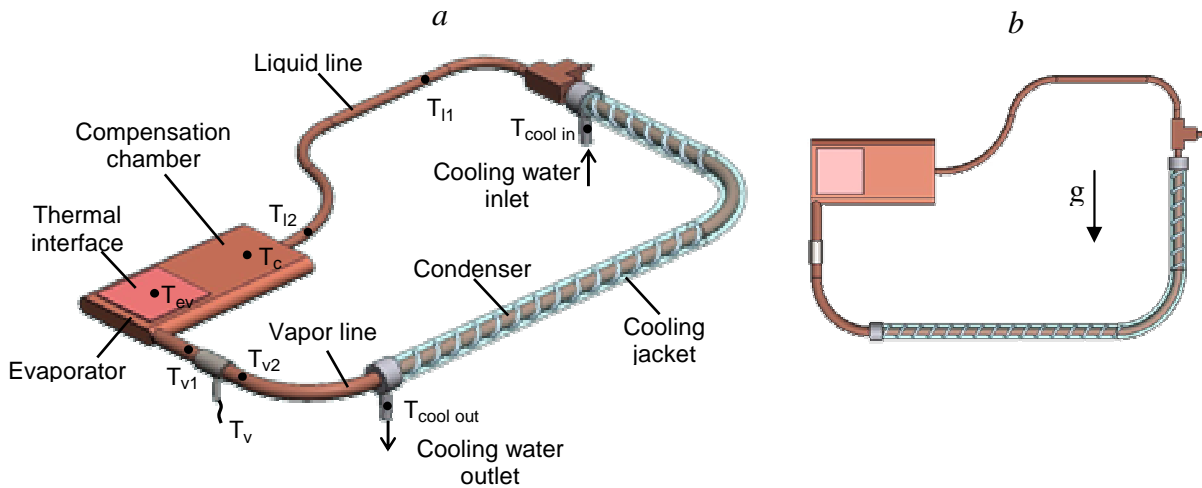


Fig. 1. Scheme of the copper-water LHP: *a* – horizontal position; *b* – vertical position.

TESTING PROCEDURE

The LHP tests were carried out at vertical and horizontal orientations of the device in the gravity field as it is shown in Fig. 1.

A copper cylindrical block, in which 6 heating cartridges with power of 250W each were positioned parallel to the longitudinal axis, was used as a heat source (Fig. 2). A heater had a square heating surface, which dimensions provided uniform distribution of heat load on the whole surface of the evaporator thermal interface. The whole copper block was in thermal insulation, limited from the outside by a thin-walled metal shell. Three thermocouples were located at the shell surface, and their readings made it possible to evaluate the heat losses from the heat source into the outside ambient. The electric power supplied to the heaters was measured by a wattmeter and changed stepwise with a step of 20 W to a value of 100 W, and then with a step of 100 W to the maximum magnitude. The magnitude of the maximum power was limited by the vapor temperature in the LHP equal to 110°C, at which the internal pressure reached 140 kPa. A further increase in the pressure was liable to cause deformation of the thin-walled body of the evaporator.

The LHP condenser was cooled by running thermostatted water. The tests at the LHP horizontal orientation were carried out at the cooling temperature of 10, 20, 40, 60 and 80°C, and at the vertical orientation at 10, 20, and 40°C.

The LHP operating temperature was measured with the help of copper-constantan thermocouples "OMEGA" TT-T-30, the placements of which is shown in Fig. 1. To measure the vapor temperature three thermocouples were used: two of them were placed on the external wall of the vapor line; one was inserted into the vapor line. The sufficiently large diameter of that line allowed doing it without any essential changes in the local hydraulic resistance to the vapor flow. Two thermocouples were also installed on the liquid line. The readings of the thermocouples were recorded by a data acquisition unit Agilent 34970A.

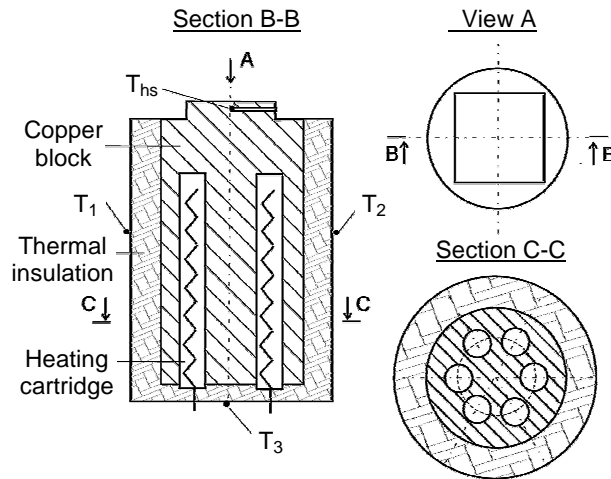


Fig. 2. Scheme of the heat source

To calculate the total thermal resistance of a LHP the following formula was used:

$$R_{LHP} = \frac{T_{ev} - (T_v + T_{ll}) / 2}{Q} \quad (1)$$

TEST RESULTS AND DESCRIPTION

In LHP tests a study was made of all the main thermal parameters that characterize the LHP operation at different condenser cooling temperatures and orientations in the gravity field. The heat load dependence of the evaporator temperature and also the total thermal resistance of the LHP were determined. Investigations were also made of the LHP behavior during start-up processes at low and moderate heat loads.

Operating characteristics

Horizontal orientation. The LHP operational characteristics in the form of heat load dependence of the evaporator's wall temperature for different condenser cooling temperatures are shown in Fig. 3. The values of heat load are presented with the heat loss from the heater and the vapor line into the environment.

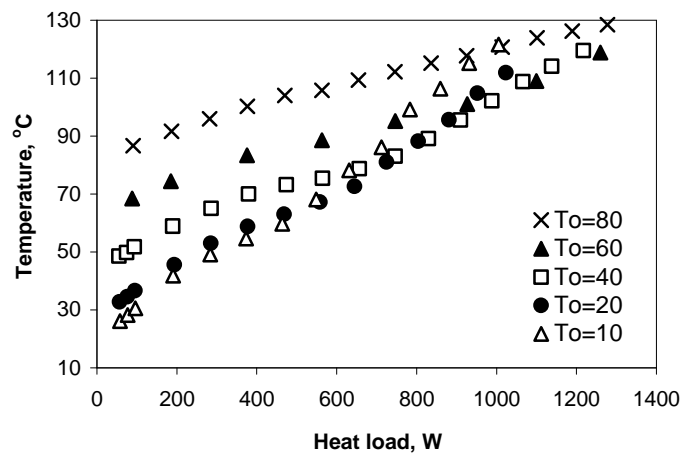


Fig. 3. LHP operating characteristics at a horizontal orientation

The test results show that with an increasing heat load a slope angle of dependence $T_{ev}=f(Q)$ is changed. It also can be seen that the LHP operation mode changes at heat loads above 500W.

In the first mode there is a gradual increase of the evaporator temperatures with an increase of the heat

load, and curves for different cooling temperatures are equidistant at that. The distance between them corresponds to the difference in the cooling temperatures of the condenser. There is an obvious dependence, showing that with an increase of the cooling temperature, the LHP operating temperatures are growing.

In the second mode of the LHP operation the type of the operating temperature dependence on the heat sink temperature changes. It can be seen that the LHP operating temperature increases when the temperature of the condenser cooling is falling. The intersection of the curves takes place at high heat loads, and there is an area in which the temperature of the evaporator wall has the same value at different heat loads and cooling temperatures of the condenser.

The change of the LHP operation mode is explained by the formation of the vapor phase in the compensation chamber and the redistribution of a working fluid in the LHP.

Vertical orientation. The heat load dependence of the LHP operational characteristics for different cooling temperatures of the condenser at a vertical orientation is shown in Fig. 4. The figure shows that all three curves have a quasihorizontal area, at which one the condenser temperature remains constant in a wide range of heat loads. The reason is that the surface of a vapor-liquid boundary in the condenser migrates with an increase of heat load, at the same time enlarging the condensation surface. The redundant working fluid is displaced in the compensation chamber, slightly lowering the temperature of the evaporator. After the compensation chamber is completely filled, the active surface of the condenser becomes constant, and a further increase of heat load leads to the rise of the LHP operating temperature.

The previously observed dependence of the operational characteristics on the condenser cooling temperature remains the same for a vertical orientation of the LHP. The direct dependence is observed at low and average heat loads: the lower a cooling temperature, the lower a LHP operating temperature. At high values of supplied load (from 500W) this dependence becomes opposite: the lower the cooling temperature of the condenser, the higher the operational characteristic of the LHP.

The maximum value of heat load reached in the LHP tests at a vertical orientation was 820W at the cooling temperature of the condenser of 40°C.

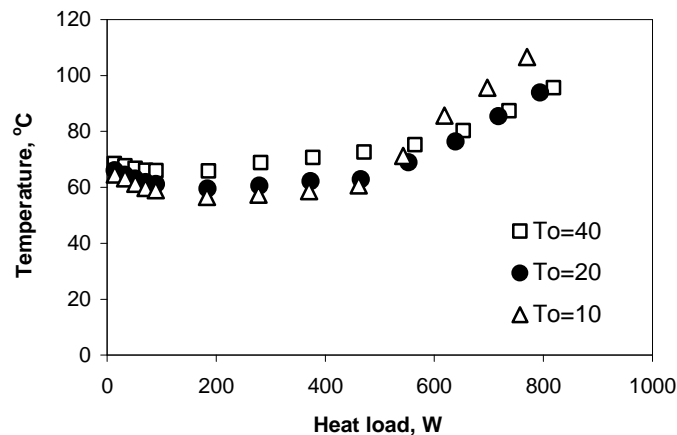


Fig. 4. LHP operating characteristics at a vertical orientation

Fig. 5 shows a comparison of the LHP operating temperature at the horizontal and vertical orientations of the device for the cooling temperature of the condenser of 20°C. The figure for the condenser cooling temperature of 10 and 40°C are the similar. It can be noticed that a LHP works at relatively high temperatures at the vertical orientation in the area of low heat loads. At this orientation, the condenser is inundated with a working fluid and for the start-up of the device it is necessary to produce a pressure that would not only compensate for losses during the movement of the working fluid on a vapor path, but the hydrostatic pressure of a working fluid column in the condenser.

One can see that there is a rather wide range of heat loads at which the operating temperature of the LHP is practically independent of an orientation.

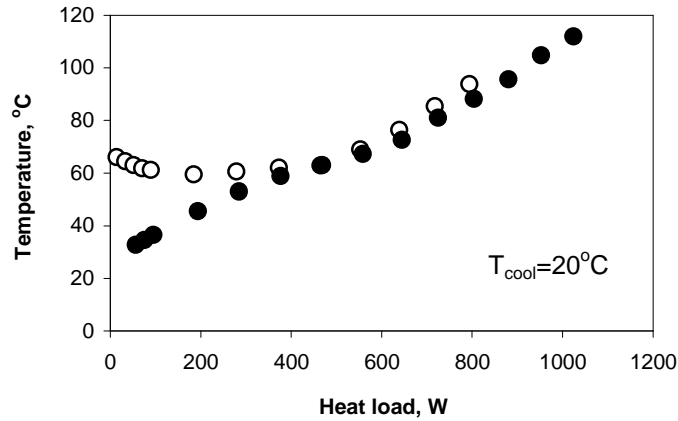


Fig. 5. LHP operating temperature vs heat load for different orientations ϕ in the gravity field: ● - $\phi = 0^\circ$; ○ - $\phi = +90^\circ$

Thermal resistance

The total thermal resistance of a LHP for different conditions of a condenser cooling at a horizontal orientation of the device is shown in Fig. 6. The figure shows that at the increase of the condenser cooling temperature the thermal resistance is lowering. This regularity is connected with the following: when at the increase of T_{cool} the raise of pressure in the LHP takes place, the vapor velocity reduces and, consequently, pressure losses at its movement. It results in the decrease of the temperature drop between the evaporator and the condenser. The minimal value of the LHP thermal resistance equal to $0.024^\circ\text{C}/\text{W}$ was obtained at heat load of 1278W and the cooling temperature of the condenser of 80°C .

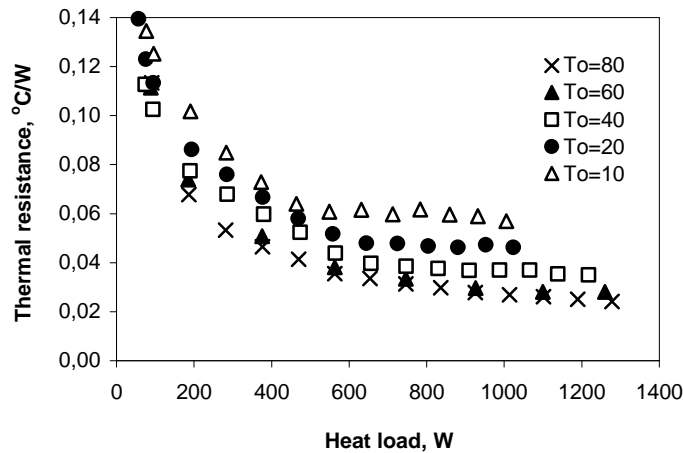


Fig. 6. Heat load dependence of the LHP thermal resistance at a horizontal orientation

The heat load dependence of the LHP total thermal resistance at a vertical orientation was shown in Fig. 7. At low heat loads it exceeds the similar value for the horizontal orientation in some times. However at heat loads above 700W the thermal resistances at horizontal and vertical orientations become practically the same. The minimal value of the total thermal resistance of the LHP equal to $0.039^\circ\text{C}/\text{W}$ was obtained at the heat load of 819W and the condenser cooling temperature of 40°C .

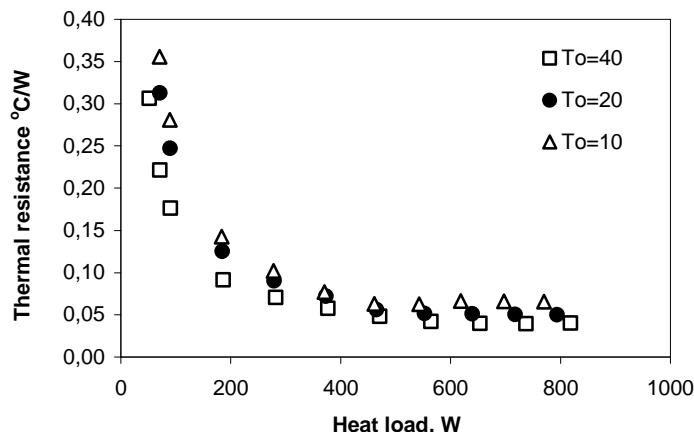


Fig. 7. Heat load dependence of the LHP thermal resistance at a vertical orientation

Заныск

Horizontal orientation. A start-up study was carried out at the condenser cooling temperatures of 10, 20 and 40°C. A start-up processes for a LHP horizontal orientation at heat loads of 5, 10, 20 and 100W, which correspond with heat load density of 0.6, 1.1, 2.2 and 11.1W/cm² are presented in Fig. 8. According to the criteria, suggested by the authors of the paper [4], the first three from them should be related to a low heat flux, the last one to the moderate heat flux.

In the analysis of start-up characteristics we can define the following features:

- The higher a heat load, the faster a heating and a next start-up of the device. For example, at a condenser cooling temperature of 10°C and the heat load of 5W, an actual start-up of the LHP begins in 1700 seconds and at 100W – in 90 seconds after the heat load supply.
- If the condenser cooling temperature is above the ambient temperature, a start-up is always going with overshoot. Actually, when the LHP condenser has a higher temperature, its release takes place since before the device start-up, a working fluid is displaced in the compensation chamber and the evaporator. Vapor-removal channels in the evaporator are submerged, and there is no ready-made vapor-liquid boundary. To make such a boundary it is necessary to boil-up the working fluid, which process is accompanied by overshoot. The start-up process is carrying according to the scenario described in [5]. However, the "absolute ceiling" of temperature overshoot for the evaporator for such cooling conditions remains approximately the same at different heat loads and is within 55-56°C.
- At the condenser cooling temperature which is lower than the ambient temperature there is no a definite regularity in the start-up nature. Both start-ups with the overheating and smooth start-ups are observed. This can be explained by the random nature of the distribution of a working fluid in the LHP. If the working fluid is distributed in such a way that the vapor-removal channels are free and there is a ready evaporation surface, the start-up takes place smoothly. If for some reason vapor-removal channels are filled, the start-up begins with overshoot.

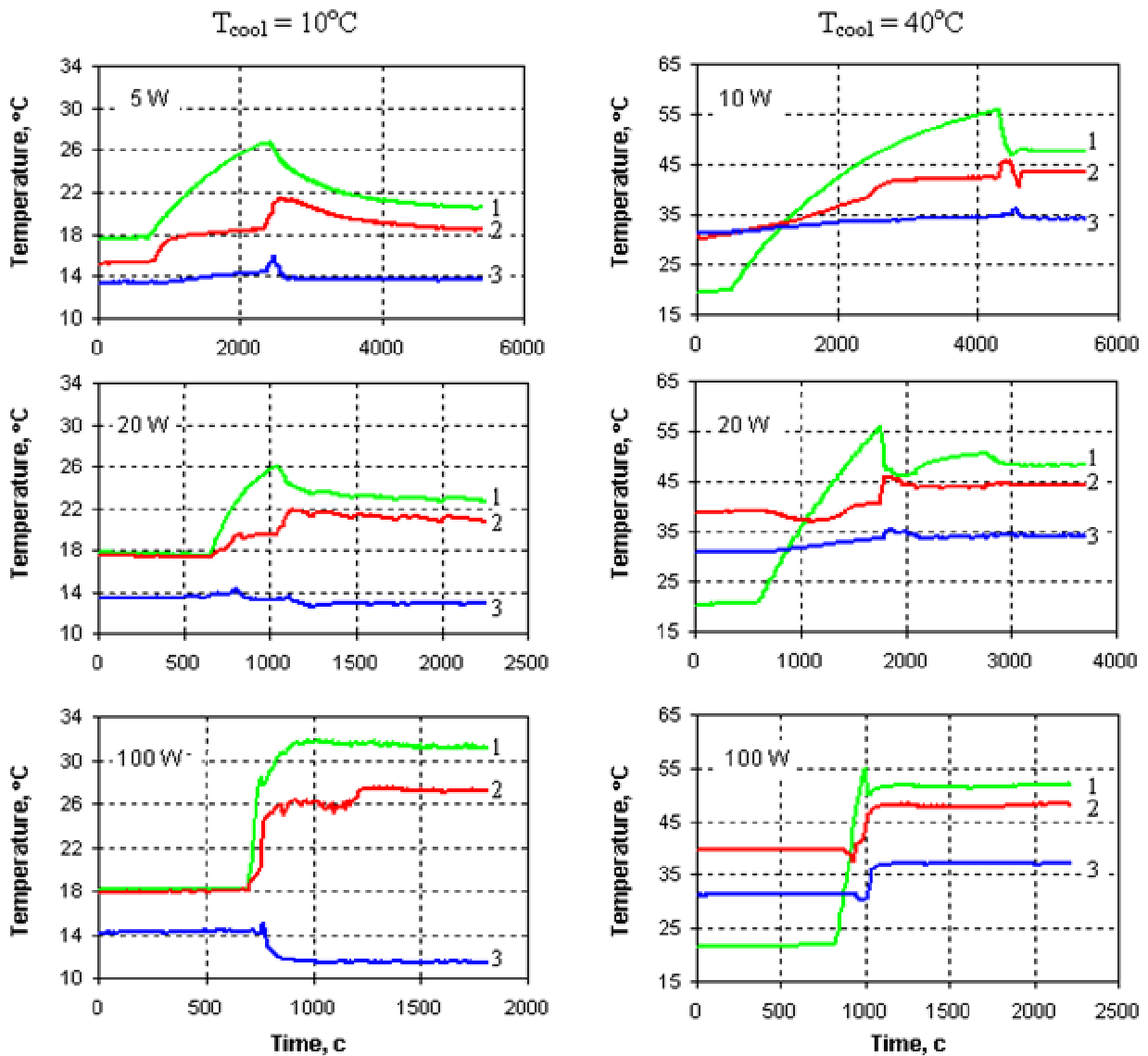


Fig. 8. Start-up of the LHP at a horizontal orientation: 1 – evaporator (T_{ev}), 2 – vapor (T_v), 3 – liquid (T_{li}).

Vertical orientation. Fig. 9 shows the process of the LHP start-up at a vertical orientation for the condenser cooling temperature of 10°C . Figures for the other cooling conditions have a similar form. As it can be seen from the figure, the startup process for all heat loads was coming smoothly, without overshoot. It confirms the above reason of smooth start-ups. Actually, at this orientation of a LHP in the gravitational field when the evaporator is placed above the condenser, all working fluid flows down and fills the condenser, at that vapor-removal channels are not submerged. Vaporization process begins immediately at a heat load supply to the evaporator.

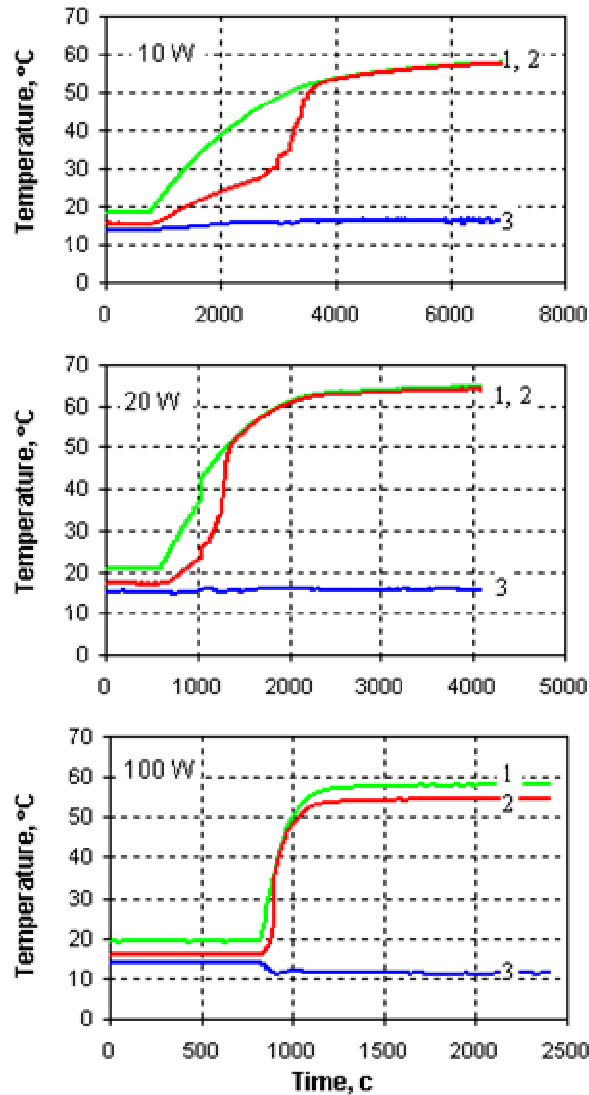


Fig. 9. Start-up of the LHP at vertical orientation:
1 – evaporator (T_{ev}), 2 – vapor (T_v), 3 – liquid (T_{ll})

CONCLUSION

A copper-water LHP equipped with a flat evaporator 7 mm thick with an active zone measuring 30x30 mm was developed and tested. All functional components of the device were entirely made of copper.

The tests of the device were carried out at horizontal and vertical orientation in the gravity field at the intensive condenser cooling by thermostatted water of 10, 20, 40, 60 and 80°C.

It is established that:

1. There is no an unambiguous dependence of an operational temperature on the condenser cooling conditions in the range of heat loads at both LHP orientations.
2. The LHP thermal resistance decreases with the increase of the cooling temperature of the condenser at all orientations of the device in the gravity field.
3. There is no an unambiguous dependence of a start-up process on the cooling temperature of the condenser at a LHP horizontal orientation. At the cooling temperature which is higher than the ambient temperature, the start-up at all heat loads passed with overshoot. When the cooling temperature was lower than the ambient temperature, both a smooth start-up, and a start-up with overshoot were observed.
4. At a LHP vertical orientation a start-up process passed smoothly, without overshoot at all heat loads and cooling temperature of the condenser.

NOMENCLATURE

H – height, mm;
L – length, mm;
Q – heat load, W;
R – thermal resistance, W/°C;
T – temperature, °C;
W – width, mm.

Subscripts

c – condenser;
cc – compensation chamber;
cool – cooling water;
ev – evaporator;
hs – heat source;
l – liquid;
v – vapor.

Acknowledgements

This work was supported by the Russian Foundation for Basic Research, Grant № 11-08-00369-a.

References

1. Чернышова М.А., Бартули Э.Ф., Майданик Ю.Ф. Теплообменные процессы в щелевом конденсаторе медь-водяной контурной тепловой трубы // *Тепловые процессы в технике*, 2010, Т. 2, № 8, с. 354-363.
2. Li J., Wang D., Peterson G.P. Experimental studies on a high performance Loop Heat Pipe with a square flat evaporator // *Applied Thermal Engineering*, 2010, Vol. 30, pp. 741-752.
3. Wang S., Zhang W., Zhang X., Chen J. Study on start-up characteristics of loop heat pipe under low-power // *International Journal of Heat and Mass Transfer*, 2011, Vol. 54, pp. 1002-1007.
4. Maydanik Yu., Vershinin S., Chernysheva M., Yushakova S. Investigation of a compact copper-water loop heat pipe with a flat evaporator // *Applied Thermal Engineering*, 2011 (in print).
5. Maydanik Yu., Solodovnik N., Fershtater Yu. Investigation of dynamic and stationary characteristics of a loop heat pipe // *Proceedings of the 9th Int. Heat Pipe Conference*, Albuquerque, USA, 1995, pp. 1002-1006.

COOLING SYSTEM FOR HERMETIC COMPRESSOR BASED ON THE LOOP THERMOSYPHON

V. A. Aliakhnovich, D. G. Kireichik, L. L. Vasiliev
S. V. Konev, A. B. Zikman

Luikov Heat and Mass Transfer Institute
National Academy of Sciences of Belarus
15, Str. P.Brovka, 220072 Minsk, Belarus
Tel: +375 17 2842133/ Fax: +375 017 2322513;
e-mail: leonard.vasiliev@gmail.com, aliakhnovich@gmail.com

Abstract

One of the simplest solutions to ensure the thermal control of a hermetic reciprocated refrigeration, or heat pumping compressor is related with the loop thermosyphon application. This paper presents experimental data obtained on two innovative loop thermosyphons - one with capillary structures and second without it. These thermosyphons are prime candidates for small hermetic compressor cooling solutions to replace typical oil-cooled and air-cooled systems, where commercially available heat exchangers cannot be used due to the high power and transport length limitations. The performance characteristics of two loop thermosyphons are discussed: (a) with vertical flat evaporator (one of its heat loaded wall has the sintered powder coating) and loop condenser, made from mini tube, sprayed by the cooling oil inside the compressor, and (b) horizontal mini tube evaporator embedded into the copper plate, two bendable transport lines and flat condenser (box) with fins on its outer surface. Air is the cooling media.

KEYWORDS

Cooling system, loop thermosyphon, hermetic compressor.

INTRODUCTION

When used for cooling and heating compressors, whether classified as positive displacement compressors or dynamic compressors, are used in air conditioning, refrigeration, and heat pump systems. As the key of these vapor compression system applications, the compressor raises the pressure of the working fluid so that it can be condensed to liquid at the heat sink temperature, expanded or throttled to reduce the pressure, and evaporated into vapor to absorb heat from the refrigerated source. In these systems, refrigeration compressors are a component in a closed loop system, which is tightly sealed (often hermetically) to prevent refrigerant loss. When used in air-conditioning, refrigeration, and heat pumps, they must be designed for a variety of refrigerants and compatible lubricants. Commonly used refrigerants include hydrochlorofluorocarbons such as R-22, or hydrofluorocarbons such as R-410A, R-407C, R-404A, and R-134a, or ammonia and various hydrocarbons. In the design of such compressors its thermal management is one of the most important components that determine overall performance and reliability. A proper understanding of heat transfer and the temperature distribution of various components in the compressor helps in determining the parts' geometry and materials selection. A small hermetic compressor usually is placed in the back of a refrigerator or air conditioner. R 134a and R600a are used as refrigerant. Typically the refrigerating capacity goes from 60 W to 350 W when these systems are operating at low evaporating temperatures (- 20°C to -35°C). In the past the industrial application of loop thermosyphons was considered in details by Piro L. S. and Piro I. L., 1997 [1] and Rossi, L., Polasek, F., 1999 [2]. The original design of "Vapor-dynamic" horizontal thermosyphon which has a split vapor and liquid (coaxial) liners was suggested in 1985 by L. Vasiliev et al. [3]. Extended electronics applications of heat pipes and thermosyphons require transport of the dissipated thermal energy in horizontal orientation or horizontally oriented evaporator and condenser surfaces, and, typically, capillary structures in the evaporators for the

heat transfer enhancement, Ptacnik J., Polasek F, 1999 [4]. The basic concepts related to the operation of vertical loop thermosyphons are well known and can be found, for example, in I. Rossi and F. Polasek (1999) [5]. The horizontal and vertical thermosyphons alternatives were considered in 1994 by L.L. Vasiliev [6]. Chu et al. (1999) [7] presented original test data for a traditional-design loop thermosyphons with flat vertically oriented evaporators. Garner and Patel (2001) [8] outlined in detail a number of electronics applications where use of loop thermosyphons would be technically and commercially appropriate. However, some further improvements and technical innovations are needed for a variety of loop thermosyphons to possibly become accepted as a standard by refrigeration and heat pumping industry.

Generally in the loop thermosyphon the heat transfer is considered to be affected by many factors, such as type of the working fluid, quantity of the working fluid, pipe diameter, pipe length, and ratio of cooled surface to heated surface, adiabatic length between heated and cooled sections, heat flux and operating temperature. The evaporator and condenser of the loop thermosyphon can be made of carbon-steel, copper, or aluminum. Propane, R 134a, R 600, or ammonia can be used as working fluid. When the copper is allowed to be applied water is the best working fluid. From the experimental data a reasonable filling ratio of working fluid and heat transfer coefficients for evaporator and condenser sections need to be obtained. In order to establish heat transfer correlations for the application in the design program for the loop thermosyphon heat exchanger, regression analysis could be applied to experimental data for heat transfer coefficients in evaporator and condenser. The review on heat pipe and thermosyphon heat exchangers was published by L.L.Vasiliev in 2005 [6]. There are many different types of thermally driven two-phase loops. They can be used in devices for the heat transfer like pumpless loop thermosyphons or Two Phase Loops (TPL) [7], which are working in a steady-state mode or in a periodic state if are gravity or antigravity assisted [8], in devices like as Pulsating Heat Pipes (PHP) and lastly in devices for the mass transfer like bubble pumps (BP), experimentally investigated by using different fluids in connection with the development of non-compression refrigeration systems. The application of miniature heat pipes and thermosyphons heat exchangers for compressor cooling was mentioned in [9]. In the loop thermosyphon, various types of flow instabilities occur depending on the system geometry, the working fluid filling ratios and the operating conditions, and often lead to abnormal behavior such as limit cycle oscillations or premature dry-out. Due to the coupling between momentum and energy transport the theoretical analysis of the loop performance is very complicate; therefore it is necessary that these problems be solved experimentally. There are several physical mechanisms restricting the "low-thermal-resistance" transport of the thermal energy from the evaporator to the condenser of the loop thermosyphon: (a) fluid circulation limitation, (b) capillary limitation in the evaporator, and (c) critical heat flux limitation in the capillary structure of the evaporator. The main thermal characteristics of the thermosyphon are the maximum capacity, the heat flux in the evaporation zone and thermal resistance. For the characteristic temperature one can use the temperature of the evaporator wall or the vapor. The thermal resistance of thermosyphon is usually written as:

$$R = \frac{T_e - T_c}{Q}, \quad (1)$$

where T_e and T_c are the mean wall temperatures of the evaporator and the condenser respectively, and Q is the heat flow transferred from the evaporator to the condenser. It is also necessary to know the temperature of the condenser wall.

1 EXPERIMENTAL SET-UP

The experiments with developed loop thermosyphons was carried out on the experimental set-up (Fig.1), which represented the heat pump with the demountable compressor. This set-up was performed to reproduce the mode of the device applications close to realistic.

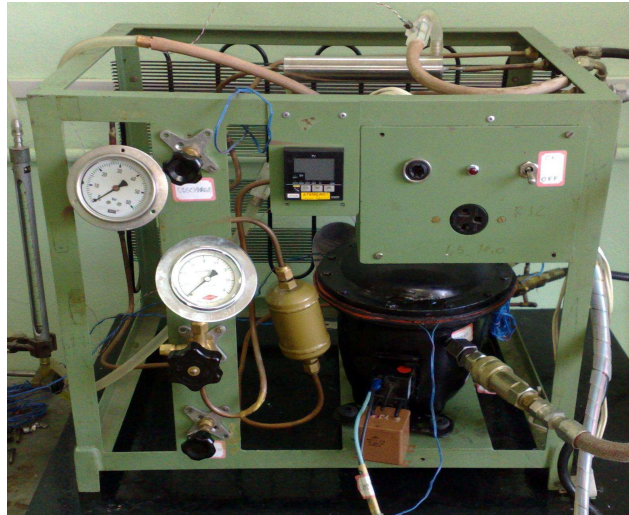


Fig. 1. Experimental set-up for the compressor cooling system testing

1.1 Loop thermosyphon (LTS) with sintered powder wick on the flat evaporator heat loaded wall

The photo of the thermosyphon is shown on Fig.2.

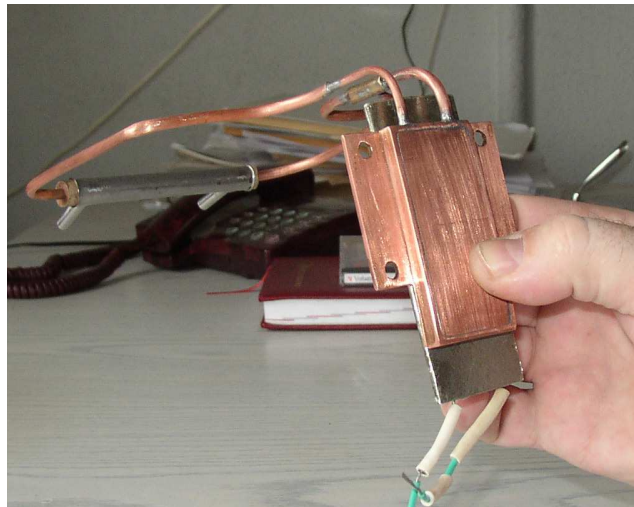


Fig. 2. Experimental loop thermosyphon with the electrical heater (on the evaporator) and the liquid heat exchanger on the condenser part

To determine the characteristics of LTS, the indoor tests consist of LTS, plate electric heater, voltage regulator, power supply, liquid heat exchanger (tube in tube) and data acquisition. The schematic diagrams of the experimental set-up is shown on Fig. 3. The loop LTS is made from a copper and has a flat evaporator with a thin layer (0.3 mm) of the copper sintered powder wick on the one of its inner surface. LTS evaporator and condenser were connected to each other by two small diameter (2mm) bendable tubes (one for vapor and second for liquid), Fig.2. The evaporator is contacted with the heat-loaded cylinder head of the compressor. Such type of porous coating ensures the heat transfer enhancement up to 5 times to compare with the plain tube thermosyphon. A vacuum pump was used to remove air from the inner space of the thermosyphon. No thermal insulation was used on the heater block to closely simulate the real operational conditions. The flat evaporator (Fig.2)

has a good thermal contact with a cylinder head of compressor, the condenser is cooled by the oil circulation inside the compressor shall. In the preliminary experiments the electric heater was used instead of the compressor cylinder head to calibrate the heat load of LTS. The flat thermal insulating block pressed the electric cartridge heater to the evaporator and a central hole for the thermocouple measuring the heated wall temperature.

The general aim of this experiment was to estimate the possibilities of the internal oil circulating cooling technology to reduce the temperature of the cylinder head :

- Determine the temperature distribution along the device for different heat loads;
- Estimate the device maximum heat transport capacity;
- Evaluate the dependency between the device thermal resistance and the rate of heat dissipation.

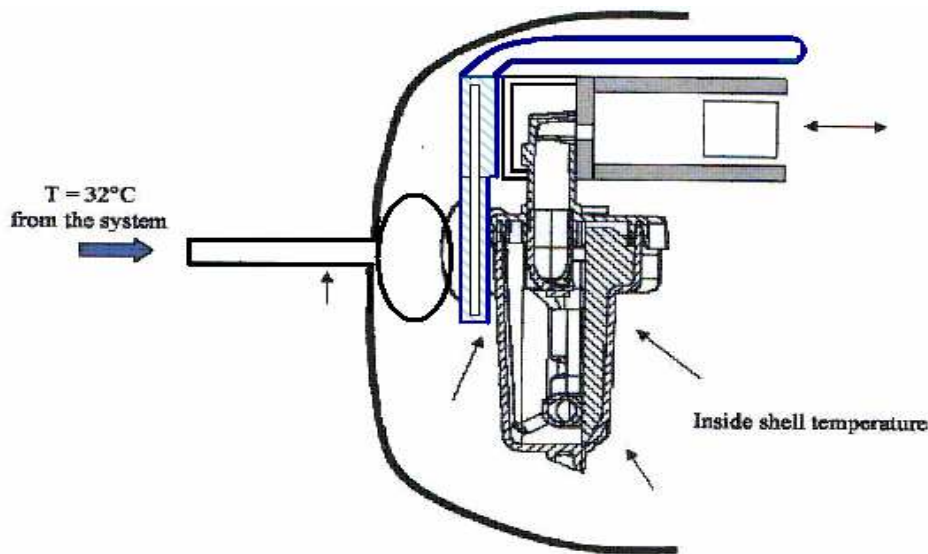


Fig. 3. Compressor body cross with LTS (blue color) as a cooler for the cylinder head.

The test data in terms of the characteristic temperatures of the copper block and LTS components are shown in Figs. 4, where the temperatures are plotted versus the time. To evacuate and fill-charge working fluid of the LTS, the three-way valve was installed. A kind of filling working fluid was water, ethanol (C₂H₅OH) and binary mixture of water and ethanol. The heat load was turned on from zero to the nominal level. The LTS started to work without a temperature overshoot typical for conventional thermosyphons. The temperatures of the heater block stabilized within five minutes after the heat load was turned on. During the calibrating tests the multi-rings (cylindrical coil) condenser was cooled by the water in the liquid heat exchanger. During the tests of LTS inside the compressor the oil spraying technology was used. The oil spraying cooling is not optimal and efficient and needs to be further redesigned to improve the intensity of condenser cooling. The calculation for the heat transfer between the condenser and the lubricating oil of the compressor is complex since the oil is circulated for lubrication purposes.

The flat copper evaporator with the footprint of 50 mm by 80 mm had a sintered copper capillary structure on the one inner surface that was 0.3 mm thick with the effective pore radius of about 50 μm. The heat transfer coefficient in the porous structure of the evaporator was 30 000 W/m²K, [9]. The thermal resistance of this thermosyphon was R = 0.03 K/W. Unfortunately the condenser cooling by the oil spray was not sufficient and limited the overall heat transfer rate through the thermosyphon, Fig.4.

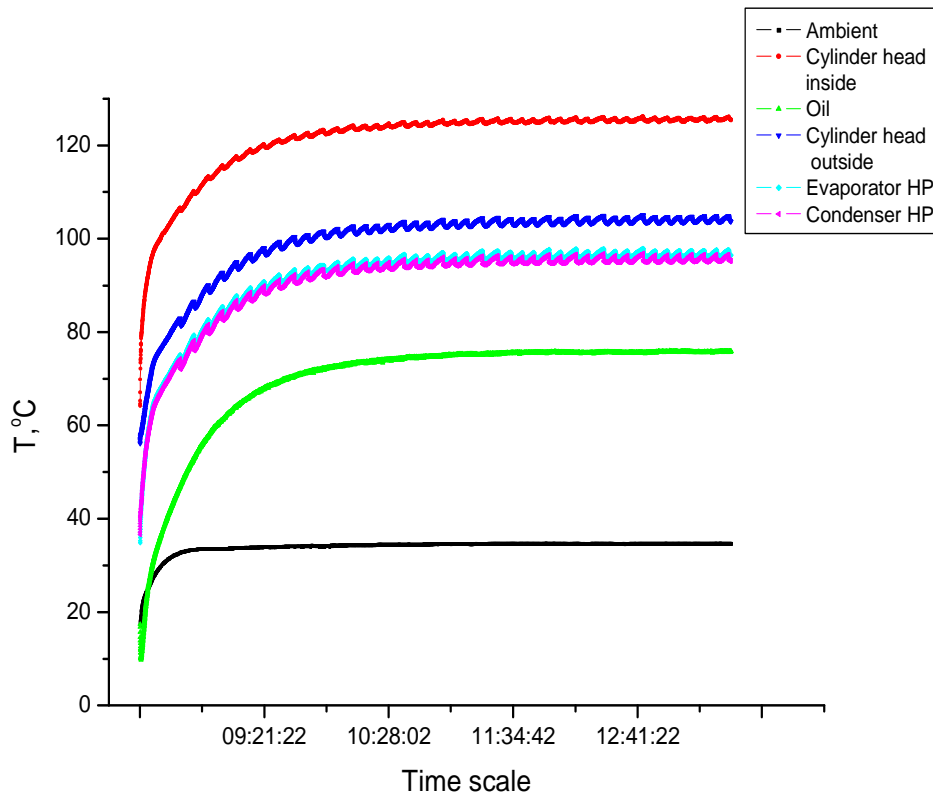


Fig. 4. Temperature evolution in the cylinder head, thermosyphon evaporator, thermosyphon condenser, evaporator of the cooling machine, gas in the sacking line of the compressor as a function of time

The experimental LTS after the preliminary tests was put in the compressor and all the necessary temperature measurements were performed. Fig. 4 shows us the temperature evolution on the cylinder head (inside and outside), thermosyphon evaporator, thermosyphon condenser, oil and ambient. The temperature difference between the evaporator wall and condenser wall was less than 1 °C. It means that the temperature drop and heat transfer resistance between the oil and the LTS is much more.

When we analyze the temperature difference between the thermosyphon evaporator and condenser and compare this difference with the temperature difference between the condenser and the oil, we can conclude, that the heat transfer intensity inside the thermosyphon is at least 100 times more., Fig.4. This is due to the low heat transfer between the condenser surface and the oil sprays. If the oil spray cooling technology will be improved the thermosyphon cooler could be considered as a good solution to improve the compressor thermal efficiency. The alternative is to use the additional heat exchanger between the thermosyphon condenser and the air outside the compressor.

1.2 Pulsating loop thermosyphon (PLT) as a compressor cylinder head cooler

The experiments with above mentioned loop thermosyphon testify that more efficient mean of compressor cooling is direct contact of the thermosyphon condenser with additional air heat exchanger (instead of the oil cooling inside the compressor), installed above the compressor shell. For such a case there is a possibility to use less expensive pulsating loop thermosyphon (PLT). The evaporator of thermosyphon is made from the capillary pipe embedded into the copper plate, Fig.5. The plate is contacting with the cylinder head.

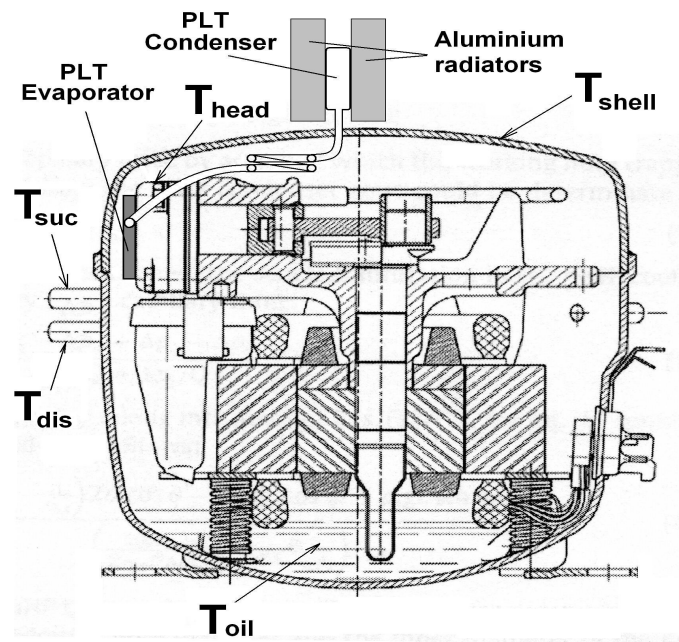


Fig. 5. Cross section of compressor with pulsating loop thermosyphon (PLT)

The design and parameters of PLT are described in [10-11]. Such PLT is made from the copper U-tube with the condenser box disposed on the upper part of vertical PLT, Fig. 6, 7.



Fig. 6. PLT evaporator and transport zone with two pipes for vapor and liquid transport between the evaporator and condenser

Two coils of vapor and liquid lines (as vibration isolator), Fig.6, prevents the PLT from destruction during the compressor vibrations. R-22 as the working fluid for the preliminary PLT tests was chosen. The thermophysical and thermodynamic properties of R-22 are close to propane and propylene – vacant fluids for PLT. The schematic of the PLT and its photo is shown on Fig.7. The vapor and liquid lines are

connecting the evaporator (inside the compressor) and the condenser box disposed outside the compressor. The compressor box is in good thermal contact with aluminum-finned plates, just forming the heat exchanger, Fig. 5, 8.

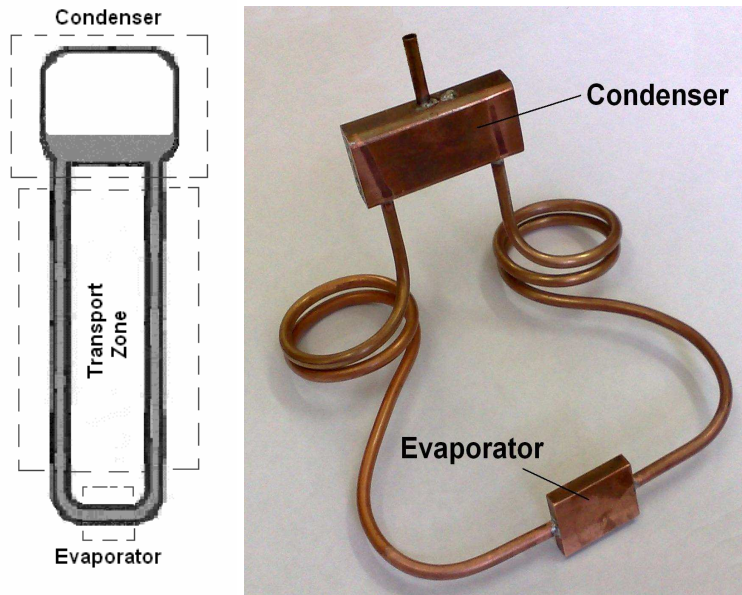


Fig. 7. Scheme and photo of PLT for the compressor cylinder head cooling

Two different tests of PLT as the cylinder head cooler were done. The first set of tests was realized using PLT cooled by natural convection of air (no fan), Fig.8a. The second set of experiments was devoted to the heat transfer enhancement between the PLT condenser and the ambient using the forced convection cooling technology, Fig.8b.

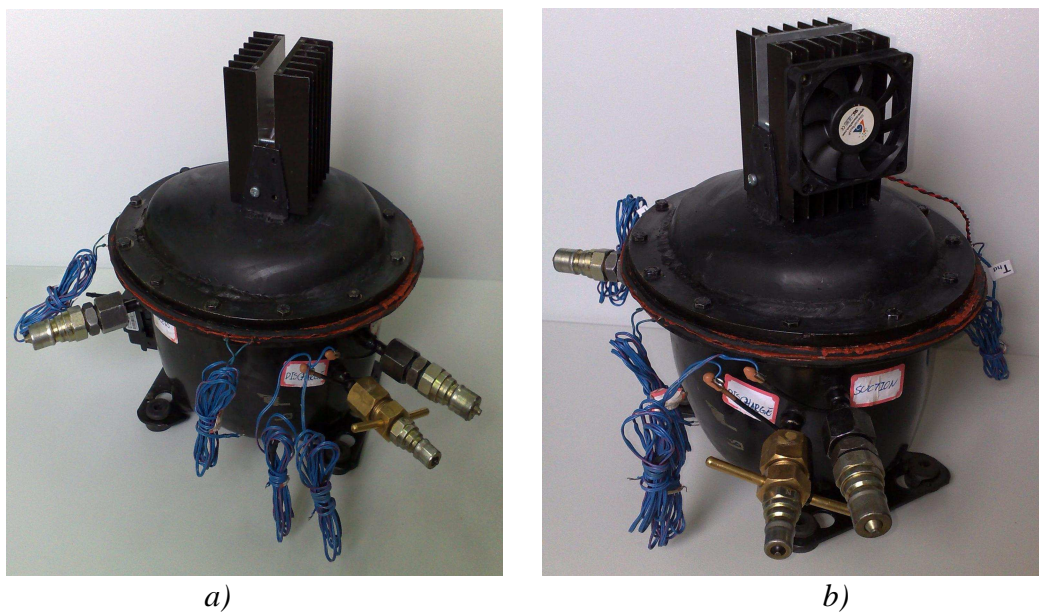


Figure 8. Photo of compressor with PLT: *a* – free convection cooling, *b* – cooling with fan

The PLT condenser consisted of the flat copper box with the footprint of 48 mm by 12 mm and 25 height without any capillary structure inside, connected with the evaporator by two bendable tubes. The smooth-wall transport lines were 2x38 cm long. The PLT was filled with 6.5 cm³ of the working fluid. Thermocouples were pressed into small diameter holes in the aluminum plates of the condenser. Thermocouples also were located in the middle of the vapor and liquid line of PLT. The test data are shown on Tables 1-2. Thermocouple number 6 was located on the top portion of the far end of the condenser. The tests of the compressor were performed with such parameters:

- ambient temperature – 26 °C;
- gas outlet pressure – 23 bar;
- gas sucking pressure – 1,5 bar;

An Agilent 34970A data acquisition system was used to record all temperature measurements. This device has a resolution of 0.02 °C. The data acquisition unit and T-type thermocouples were compared to a precision digital resistance temperature device with a rated accuracy of 0.03 °C. The system accuracy was found to be within 0.2 °C over the range being studied. In the steady state, the readings of the thermocouples fluctuate within 0.2 °C. The uncertainty of the electrical power through the power analyzer amounts to 0.5% of the reading.

The temperature measurements were made as:

- T_{head} – cylinder head;
- T_{shell} – compressor shell;
- T_{oil} – oil;
- T_{dis} – gas temperature at the compressor exit;
- T_{suc} – gas temperature at the compressor entrance;
- T_{con} – PLT condenser entrance;
- T_{evp} – PLT evaporator entrance;
- Q_{refr} – heat flow at PLT evaporator (cooling rate);

The experimental data were obtained for three different cases: traditional compressor cooling system, compressor cooling system with PLT (natural convection in the heat exchanger) and compressor cooling system with PLT and forced convection cooling of the heat exchanger. The summarized experimental data are recollected in the Tables 1-2.

During the experiment we can see on the monitor screen the data collected in the tables or the graphics, the temperature field at a given time or the dynamic of the temperature field change in time. The heat load Q of the PLT is determined by the computer program depending on the heater electric resistance. Q_{max} is determined as follows. For a fixed PLT orientation in space the electric heater is switched on. After some time the temperature field along a PLT becomes stationary and is recorded in the file. Then the PLT heat load is increasing by the step ΔQ and the temperature field along PLT is fixed once more. The Q_{max} is fixed when there is a non proportional dependency between the temperature change (thermocouples data disposed below the electric heater) and the heat load change. In this case we testify a sharp increasing of the temperature. For the precise measurements of this PLT crisis value we use a small step of the heat load ΔQ.

Table 1. The experimental data of the temperature distribution inside the compressor for three different modes of compressor cooling and three values of the cooling power

	T _{head} , °C	T _{shell} , °C	T _{oil} , °C	T _{dis} , °C	T _{suc} , °C	T _{cond} , °C	T _{evp} , °C	Q _{refr} , W
Without cooling	143.2	76.5	93.1	128.0	26.1	63.3	-7.9	136
With PLT cooling	119.5	75.2	89.5	117.6	26.0	60.1	-7.8	138
PLT with Fan	110.3	72.4	85.9	112.6	26.3	59.9	-8.1	137

Table 2. The temperature difference between the key parts of the compressor working without PLT and with PLT cooler

	$\Delta T_{\text{head}}, ^\circ\text{C}$	$\Delta T_{\text{shell}}, ^\circ\text{C}$	$\Delta T_{\text{oil}}, ^\circ\text{C}$	$\Delta T_{\text{dis}}, ^\circ\text{C}$
With PLT cooling	-23,7	-1,3	-3,6	-10,4
PLT with Fan	-32,9	-4,1	-7,2	-15,4

Following the data of the Table 1-2 it is interesting to apply the PLT cooler with fan to reduce the temperature of the cylinder heat down to 30 °C to compare with the traditional compressor oil cooling system. The results of this study could be applied to actual compressor design in industry and have resulted in improved compressor performance.

CONCLUSION

1. The heat transfer analysis aimed to predicting and experimentally check mean temperature of the principal heat loaded components of hermetic reciprocating refrigeration compressor was performed to decrease the temperature of the refrigerant and increase its density in the compressor piston.
2. Two loop thermosyphons, as a two-phase cooler was considered as the alternative to solve this problem.
3. The Loop Thermosyphon with porous coating of the evaporator (LTS) ensures the heat transfer enhancement up to 5 times to compare with the plain tube thermosyphon and started to work without a temperature overshoot typical for conventional thermosyphons.
4. The heat transfer coefficient in the porous structure of the LTS evaporator was 30000 W/(m² K). The thermal resistance of this thermosyphon was R = 0.03 K/W.
5. As an option to the loop thermosyphon (LTS) an advanced pulsating loop thermosyphon (PLT) was developed. This PLT was investigated on the experimental set-up and demonstrated the cylinder head temperature drop above 30 °C to compare with the traditional oil cooling.

References

1. Pioro L.S., Pioro I.L. Industrial Two-phase Thermosyphons. Begell House Inc., 1997.
2. Rossi L. and Polasek F. Thermal Control of Electronic Equipment by Heat Pipes and Two-Phase Thermosyphons. *Proc. 11th International Heat Pipe Conference, September 1999, Tokyo, Japan*, Keynote lecture, pp. 50-74.
3. Vasiliev L.L. et al. Heat transfer Device. US Patent No. 4.554.966, Nov. 26, 1985.
4. Ptacnik J., Polasek F. Present state of heat pipe technology in the Countries of Mutual Economic Assistance // *Proc. 3rd International Heat Pipe Symposium - Tsukuba, 12-14 September, 1988* / Ed. by Y. Kobayashi, Kanji Negishi, K. Oshima, pp. 13-30.
5. Garner S. and Patel C. Loop Thermosyphons and their Applications to High Density Electronics Cooling // *Proc. of IPACK'01 The Pacific Rim/ASME International Electronic Packaging Technical Conference and Exhibition, July 8 - 13, 2001, Kauai, Hawaii*. IPACK2001-15782.
6. Vasiliev L.L. Heat pipe technology in CIS Countries // *Proc. of the 4th International Heat Pipe Symposium-Tsukuba, 16-18 May, 1994* / Ed. by Y. Kobayashi and K. Oshima, pp.12-24.
7. Chu R., Simons R., and Chrysler G. Experimental Investigation of an Enhanced Thermosyphon Heat Loop for Cooling of a High Performance Electronics Module // *Proc. of the 15th IEEE SEMI-THERM Symposium, 1999*.

8. Vasiliev L.L. Heat Pipes in Modern Heat Exchangers, 2005 // *Applied Thermal Engineering*, 25, 1-19.
9. Possamai F.C., Setter I., Vasiliev L.L. Miniature heat pipe as compressor cooling devices // *Applied Thermal Engineering*, 29 (2009) 3218-3223.
10. Konev S., Aliakhnovich V. Investigation of Oscillating Heat & Mass Transfer in Capillary Heat Pipe // *13th Intern. Heat Pipe Conf., September 21-25, 2004*, Shanghai, China.
11. Konev S.V., Aliakhnovich V. Heat transfer device for microelectronic cooling // *MIF-VI, May 19-23, 2008*, Minsk, Belarus (in russian).

IMPROVEMENT OF OPERATION EFFECTIVENESS OF A CLOSED GEOHERMAL HEAT EXCHANGER DUE TO IMPLEMENTATION OF ACTIVE INSULATION OF THE EXTRACTION ELEMENT

Radomir Kaczmarek, Wladyslaw Nowak, Aleksander A. Stachel

Department of Heat Engineering
West-Pomeranian University of Technology
al. Piastow 17, PL 70-310 Szczecin, Poland,
e-mail: andrzej.stachel@zut.edu.pl

Abstract

The idea of construction of the so called underground closed geothermal heat exchanger presents an interesting concept of energy extraction from the resources contained in the Earth's crust. Such exchanger consists of a system of pipelines founded at a significant depth through which liquid is pumped extracting energy from surrounding rocks and transporting heat to the Earth's surface. It results from the accomplished analyses that the least efficient element from the efficiency point of view is the vertical part of such heat exchanger. As a result significant reduction of temperature of the energy carrier fluid at the outflow is observed leading to reduction of the overall efficiency of the heat exchanger.

Bearing in mind that application of the passive insulation in the extraction part of exchanger is technically difficult the authors proposed the concept of the active insulation. The idea is based on the formation in the extraction part of two concentrically positioned channels, namely the inner circular channel through which the principal flow rate of fluid flows and the external annular channel, where part of liquid flows serving as insulation layer.

In the paper, in brief presented is the calculation model with the active insulation enabling determination of the influence of the liquid flow rate in the external insulation channel on temperature distribution of the basic flow rate of the heat carrier flowing in the inner channel. That enabled conduction of the assessment of the influence of application of the active insulation on the improvement of the efficiency of operation of the entire geothermal heat exchanger.

KEYWORDS

Geothermal energy, utilisation of geothermal energy, underground closed geothermal heat exchanger, active insulation, active insulation of the extraction element.

INTRODUCTION

One of the ways of extraction of geothermic energy is application of closed or open installations enabling indirect or direct introduction of water into the Earth's crust as an energy carrier which receives heat from the surrounding rocks and transports it to the surface. It is estimated that in Poland the possibilities of acquisition of geothermic energy relate to the depths ranging from 2000 to 5000m and are greater than the possibilities of acquisition of geothermal energy contained in underground resources of hot water. Obtained in such a way heat can be used for heating purposes as well as production of electricity [1–3].

An interesting idea of a closed extraction installation has been developed at the Technical University of Berlin, where developed was the prototype of the so called underground closed geothermal heat exchanger, in brief UCGHE [4, 5]. The exchanger consists of a set of connected in series vertical and horizontal pipelines positioned at a significant depth through which the liquid receiving heat from the surrounding rocks is flowing and transporting it to the Earth's surface, where it is further distributed to the receivers of thermal energy. It is estimated that the present technical advancement enables construction of the UCGHE with the length of the horizontal part up to 15 km founded at the depth down to 5 km [6].

It results from the analysis of operation of specific parts of the underground closed geothermal heat exchanger accomplished at Department of Heat Engineering, West-Pomeranian University of Technology in Szczecin, using in-house calculation models [7–9] that from the thermal efficiency point of view the least efficient part is the extraction channel where reduction of temperature of heat carrying fluid from the exchanger is observed.

One of the ways to alleviate that issue is application of adequate insulation of the extraction part. Bearing however in mind that application of the passive insulation is technically problematic in the present

paper as well as in [1, 2, 7, 10] examined and analysed was the possibility of application of the active insulation, formed by a part of the liquid flow rate pumped through the exchanger and adequately modified design of the extraction channel.

In relation to that in the further part of the paper presented is (in an approximate manner) the analytical calculation model of such exchanger which enables determination of the influence of applied active insulation on temperature field of the heat carrier fluid used later for heating purposes. The calculations accomplished using that model show the possibilities of controlled influence on temperature distribution of the heat carrier fluid and in particular on its outlet temperature from the exchanger. That permits the analysis of the influence of application of active insulation on the improvement of the efficiency of operation of the entire UCGHE. Additionally, postulated design can be used for obtaining required temperature of the heat carrier, consistent with temperature of the network water supplying heat receivers.

UCGHE – UNDERGROUND CLOSED GEOTHERMAL HEAT EXCHANGER

Presented in Fig. 1 a horizontal closed geothermal heat exchanger consists of a set of pipelines founded as a significant depth through which liquid is pumped which is the heat carrier for extraction of geothermic energy from the surrounding rock bed.

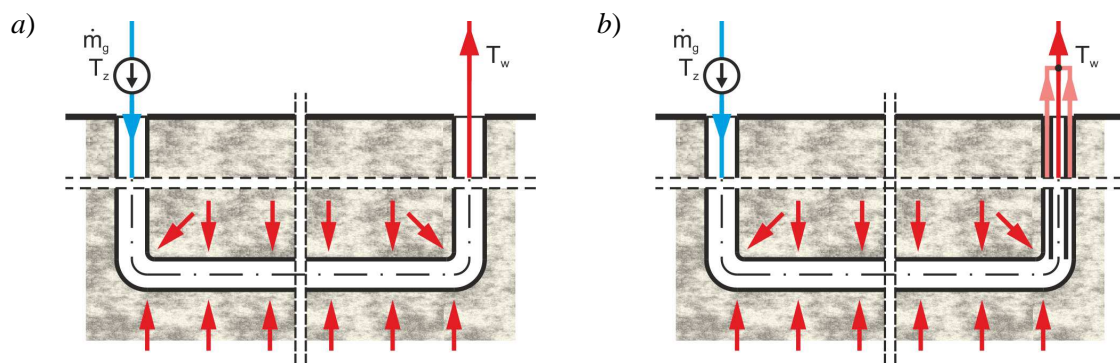


Fig. 1. Scheme of UCGHE without (a) and with (b) active insulation

Effectiveness of operation of such exchanger depends on several parameters of which the most important are:

- overall heat transfer coefficient,
- geometry of exchanger, related to the heat transfer surface,
- depth of location of the horizontal part of exchanger, related to temperature of surrounding rocks,
- flow rate of liquid through the exchanger,
- temperature of liquid pumped to the exchanger,
- energy losses in the extraction part of the exchanger.

In order to assess the influence of the above parameters on the effectiveness of energy extraction in underground closed geothermal heat exchanger the analytical calculation model has been developed, presented in detail in [8, 9]. The model regards the reference design presented schematically in Fig. 1.

In development of the model for each constituent part of the exchanger the relevant approach to determine the rate of heat transferred from the rock to the liquid has been applied. In order to determine elementary rate of energy taken up by the heat carrier from the rocks the following relation was used:

$$d\dot{Q} = k_z [T_s(h) - T_p(h)] dA \quad (1)$$

The common feature of the model is assumption for all parts of the UCGHE of a linear temperature change of the rock at a significant distance from the considered elements $T_s(h)$ as well as knowledge of varying in time overall heat transfer coefficient from the rock to the heat carrier k_z . Scheme of heat transfer

in particular channels of the exchanger together with temperature distributions of heat carrier fluid and rocks is presented in Fig. 2.

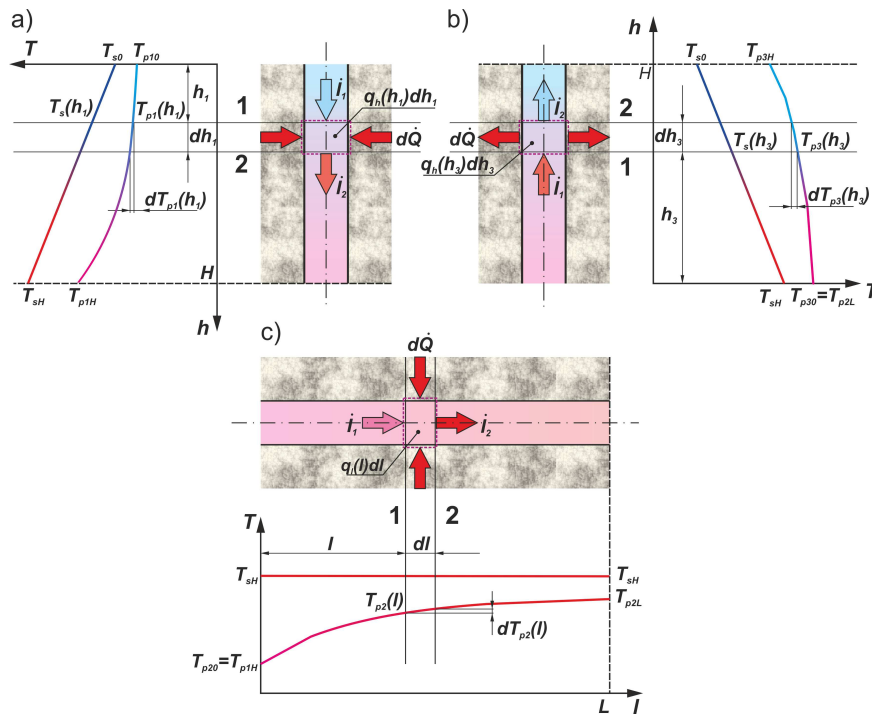


Fig. 2. Scheme of UCGHE with temperature distributions of heat carrier fluid in the a) pumping back, b) extraction, c) horizontal channels

Specific calculations of temperature distributions in the UCGHE have been presented in [7–9]. Presented below are only the final relations, which enable determination of temperature distributions for particular constituent elements of the exchanger. In that light the reduced temperature differences at inlet and outlet from the particular parts of UCGHE are determined from relations:

– for the case of vertical pumping back channel

$$\Theta_{1H} = \frac{T_{sH} - T_{p1H}}{T_{sH} - T_{p10}} = \frac{\varphi}{\varphi_n N_1} + \left[1 - \varphi \cdot \left(1 + \frac{1}{\varphi_n N_1} \right) \right] \cdot \exp(-\varphi_n N_1) \quad (2)$$

– for the case of horizontal channel

$$\Theta_{2L} = \frac{T_{sH} - T_{p2L}}{T_{sH} - T_{p1H}} = \exp(-\varphi_n \varphi_L n N_2) \quad (3)$$

– for the case of vertical extraction channel

$$\Theta_{3H} = \frac{T_{sH} - T_{p3H}}{T_{sH} - T_{p2L}} = \frac{\varphi}{\psi} + \exp(-\varphi_n N_3) - \frac{\varphi}{\psi \cdot \varphi_n N_3} \cdot [1 - \exp(-\varphi_n N_3)] \quad (4)$$

Therefore the relation describing adequately defined temperature difference at inlet and outlet from the UCGHE, which accounts for the influence of temperature of the fluid supplied to the exchanger (pumping temperature) assumes the form:

$$\Theta_{1H} \cdot \Theta_{2L} \cdot \Theta_{3H} = \Theta_{1H,2L} \cdot \Theta_{3H} \quad (5)$$

where

$$\Theta_{1H,2L} = \left\{ (1 - \varphi) \cdot \exp(-\varphi_n N_1) + \frac{\varphi}{\varphi_n N_1} \cdot [1 - \exp(-\varphi_n N_1)] \right\} \cdot \exp(-\varphi_n \varphi_L n N_2) \quad (6)$$

In relation to that

$$\Theta_{1H,2L,3H} = \frac{T_{sH} - T_{p3H}}{T_{sH} - T_{p10}} = \Theta_{1H,2L} \cdot \left\{ \frac{\varphi}{\Psi} + \exp(-\varphi_n N_3) - \frac{\varphi}{\Psi \cdot \varphi_n N_3} \cdot [1 - \exp(-\varphi_n N_3)] \right\} \quad (7)$$

or

$$\Theta_{1H,2L,3H} = \varphi + \Theta_{1H,2L} \cdot \exp(-\varphi_n N_3) - \frac{\varphi}{\varphi_n N_3} \cdot [1 - \exp(-\varphi_n N_3)] \quad (7a)$$

In the analysis equal rates of heat capacities were assumed as well as same diameters of pipelines and same heat transfer coefficients in particular parts of UCGHE. The meaning of particular quantities present in the above equations is presented in detail in [8, 11].

In order to determine temperature distribution of the heat carrier fluid through the exchanger indispensable is knowledge of the variable in time overall heat transfer coefficient k_z (1). In literature there can be found different relations enabling determination of that quantity [12]. On the basis accomplished calculations and analyses it can be concluded that the highest changes of the value of that coefficient occur in the initial period of installation operation. With the time lapse its value decreases and after passing of a specified period of time (about 1000 hours) it can be assumed that k_z stabilises and does not undergo significant changes.

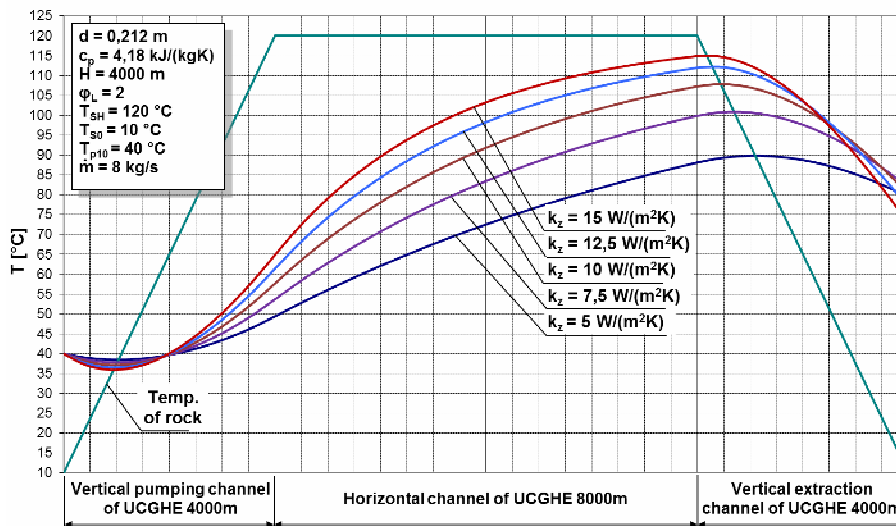


Fig. 3. Temperature distributions of heat carrier fluid for different values of the coefficient k_z

In Fig. 3 presented are the results of calculations of temperature distribution of heat carrier fluid in function of different values of the overall heat transfer coefficient k_z . It results from the diagram that this coefficient bears a significant influence on calculations of energy extracted in the geothermic heat exchanger. Therefore, bearing in mind variation in time of k_z , in the design process of the exchanger there ought to be envisaged its real values at a given rate of heat of the heat carrier fluid. In the case of too small rate of heat as well as significant losses of heat in the extraction pipeline there can arise a situation where the higher value of coefficient k_z renders extraction of a greater amount of energy in the pumping pipeline as well as in the horizontal part of exchanger as well as more energy is lost in the extraction pipeline. Due to that the total amount of energy acquired in the exchanger at the highest value of coefficient k_z is in effect smaller than in the case of the coefficient with the smallest value.

UCGHE WITH THE ACTIVE INSULATION OF THE EXTRACTION PART

It results from the analysis of temperature distributions of particular parts of UCGHE that the least efficient element, from the thermal point of view, is the extraction part of the exchanger (see Fig. 3). The process of heat transfer taking place there between hot fluid and colder rock surrounding the system renders reduction of temperature of the heat carrier fluid at outflow from the exchanger and reduction of effectiveness of operation of the entire exchanger. Therefore in order to improve effectiveness of energy extraction there ought to be reduced heat losses from the extraction part of the exchanger. Due to the fact that the use of typical thermal insulation is technically problematic hence the idea of application of so called active insulation [10] seems to be attractive alternative.

The idea is based on introduction to the extraction pipeline of the additional circular duct forming in effect the external annular channel serving as insulation layer with the aid of fluid flowing inside (Fig. 1 b). It ought to be noted that modification of UCGHE relates only to the extraction channel leaving the vertical pumping back part and horizontal part unchanged.

Modified extraction part of UCGHE consists of the extraction pipeline, where inside located is concentrically the additional duct with smaller diameter. As a result obtained is a tube-in-tube channel consisting of inner circular duct, carrying to the surface the predominant part of the heat carrier fluid, and the annular external part, which together with the fluid inside forms the active insulation layer to the principal flow rate of fluid in inside duct in the arrangement.

Values of flow rates flowing inside annular and inner channels are cross-correlated and equal in total to the amount of liquid pumped back to the UCGHE. Varying the proportions of flow rates in annular flow a d circular duct we can influence temperatures of both flow rates leaving the UCGHE. Due to that, after mixing of two flow rates possible is obtaining of required temperature of heat carrier fluid tailored to temperature of network water feeding the heat receivers.

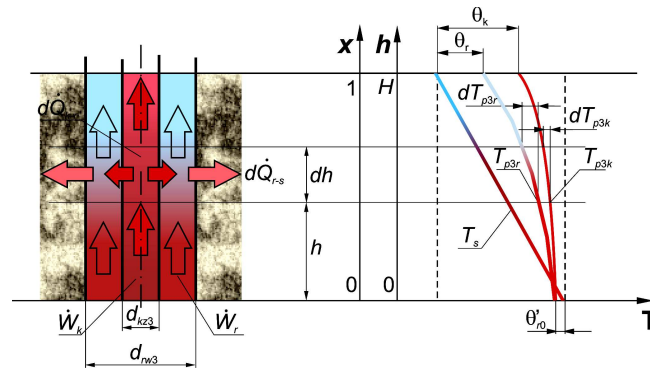


Fig. 4. Scheme of extraction part of UCGHE and temperature distributions of fluids

In order to show the effect of presence of active insulation on temperature of the fluid leaving the exchanger the model described in detail in [2, 10] has been applied. The model was developed based on energy balance equation for the fluid flowing in inner duct (Fig. 4):

$$\dot{W}_k dT_{p3k} = -K_{k-r} (T_{p3k} - T_{p3r}) dx \quad (8)$$

as well as the fluid flowing in external annular channel:

$$\dot{W}_r dT_{p3r} = K_{k-r} (T_{p3k} - T_{p3r}) dx - K_{r-s} (T_{p3r} - T_s) dx \quad (9)$$

where $x = \frac{h}{H}$, $K_{k-r} = k_{k-r} \pi d_{kz3} H$, $K_{r-s} = k_{r-s} \pi d_{rw3} H$, $\dot{W}_k = \dot{m}_k \cdot c_w$, $\dot{W}_r = \dot{m}_r \cdot c_w$

Following introduction of notation:

$$\theta_k = T_{p3k} - T_s, \quad \theta_r = T_{p3r} - T_s, \quad T_s = Ex + F, \quad a = -\frac{K_{k-r}}{\dot{W}_k}, \quad b = \frac{K_{k-r}}{\dot{W}_r}, \quad c = \frac{K_{k-r} + K_{r-s}}{\dot{W}_r}$$

the system of equations (8) and (9) can be reduced to the form:

$$\frac{d\theta_k}{dx} = a\theta_k - a\theta_r - E \quad (10)$$

$$\frac{d\theta_r}{dx} = b\theta_k - c\theta_r - E \quad (11)$$

The above system of equations has been solved using the d'Alambert method [8] and the details of solution are presented in [10]. In effect, the following functions describing temperature difference have been obtained:

$$\theta_r = \frac{C_1^* \exp(v_1^2 x) - C_2^* \exp(v_2^2 x) + EG}{R}, \quad (12)$$

$$\theta_k = C_1^* \exp(v_1^2 x) - \frac{q_1}{p_1} \left(\frac{C_1^* \exp(v_1^2 x) - C_2^* \exp(v_2^2 x) + EG}{R} \right) + \left(\frac{1 + \frac{q_1}{p_1}}{v_1^2} \right) E \quad (13)$$

Mathematical definitions of particular quantities present in equations (12) and (13) are given in Table 1. On the other hand the meaning of respective quantities is discussed in detail in [10, 11].

Table 1. Selection of auxiliary quantities

Symbol	Expression	Symbol	Expression
v_1^2	$\frac{-(c-a) + \sqrt{(c+a)^2 - 4ab}}{2}$	$\frac{q_1}{p_1}$	$\frac{v_1^2 - a}{b}$
v_2^2	$\frac{-(c-a) - \sqrt{(c+a)^2 - 4ab}}{2}$	$\frac{q_2}{p_2}$	$\frac{v_2^2 - a}{b}$
G	$\frac{(v_2^2 - v_1^2) \left(1 - \frac{a}{b}\right)}{v_1^2 v_2^2}$	R	$\frac{q_1}{p_1} - \frac{q_2}{p_2}$

Integration constants present in expressions (12) and (13) are indispensable in unanimous description of temperature field and are expressed in the form:

$$C_1^* = \left(1 + \frac{q_1}{p_1} \right) \left(\Theta_{20}' - \frac{E}{v_1^2} \right), \quad (14)$$

$$C_2^* = C_1^* - \Theta_{20}' R + EG. \quad (15)$$

These constants were determined using the appropriate boundary conditions ($\Theta_{2(x=0)} = \Theta_{20}'$; $\Theta_{1(x=0)} = \Theta_{2(x=0)}$).

RESULTS OF CALCULATIONS

Using the mathematical model presented above the appropriate calculations have been accomplished and the relevant diagrams depicting the influence of the active insulation on temperature of the heat carrier flowing out of the underground closed geothermal heat exchanger.

Calculations were calculated in such a way as the comparisons of the effectiveness of operation of the exchanger with and without insulation could be possible. With respect to that it has been assumed that the exchangers operate under comparable conditions and utilized were output data for construction of the

diagram in Fig. 3. Analysis has been referred to the case where highest temperature reduction of liquid was present in the extraction part of UCGHE ($k_z = 15 \text{ W}/(\text{m}^2 \cdot \text{K})$). Additionally in calculations were assumed the following quantities:

- inner diameter of annular extraction $d_{rw3} = 212 \text{ mm}$,
- external diameter of circular channel $d_{kz3} = 134.5 \text{ mm}$,
- overall heat transfer coefficient between fluid and rock $k_z = 15 \text{ W}/(\text{m}^2 \cdot \text{K})$,
- overall heat transfer coefficient between fluid in circular channel and fluid in annular channel $k_{k-r} = 30 \text{ W}/(\text{m}^2 \cdot \text{K})$.
- length of vertical extraction channel $H = 5000 \text{ m}$,
- length of horizontal part of exchanger $L = 8000 \text{ m}$,
- rock temperature at the depth of 4000 m $T_{sH} = 120 \text{ }^\circ\text{C}$,
- rock temperature at the Earth's surface $T_{s0} = 10 \text{ }^\circ\text{C}$,
- pumping back temperature $T_{p10} = 40 \text{ }^\circ\text{C}$,
- total mass flow rate of fluid flowing through the exchanger (total flow rate of fluid in annular and circular channels): $\dot{m} = 8 \text{ kg/s}$.

Obtained results of calculations have been presented graphically in subsequent figures. In Fig. 5 presented is the influence of flow rates flowing in circular and annular channels on outlet temperature from the exchanger. It stems from the diagram that in the considered case the highest outlet temperature was obtained when about 80% of the flow is present in the circular main channel. Remaining 20% flow inside the annular channel forming in that way the active insulation. Obtained proportions of flow rates are dependent on individual conditions and therefore the location of maximum change.

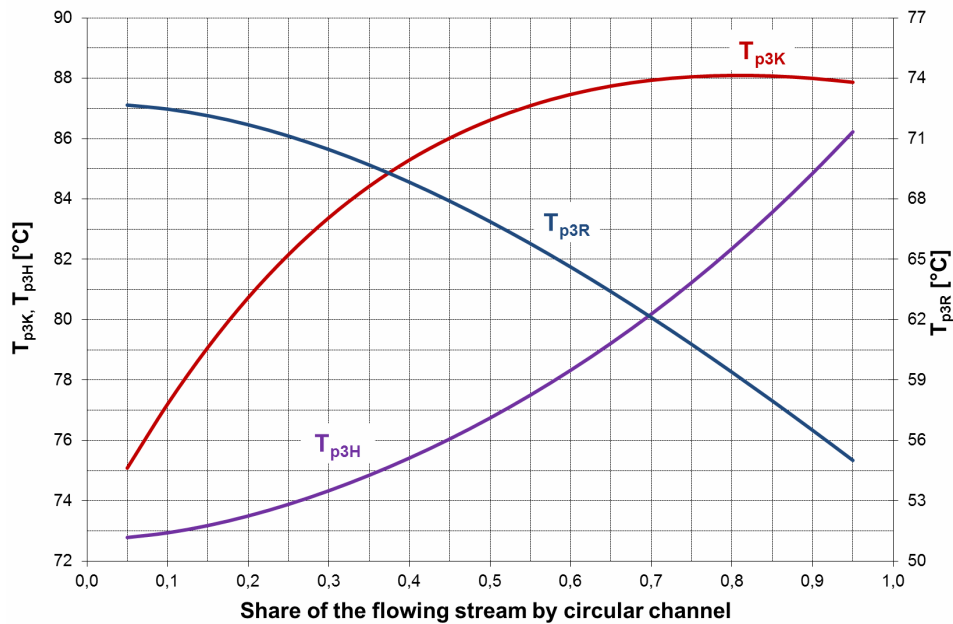


Fig. 5. Temperatures at outflow from the extraction part of UCGHE of fluids flowing in annular channel T_{p3R} , (insulation) and circular channels T_{p3K} together with fluid temperature after mixing of two flow rates T_{p3H} in relation to the flow rates of fluids in respective channels

On the other hand in Fig. 6 presented is temperature distribution of fluids in the best case, i.e. the one where highest liquid temperature of the fluid leaving the geothermal heat exchanger is found.

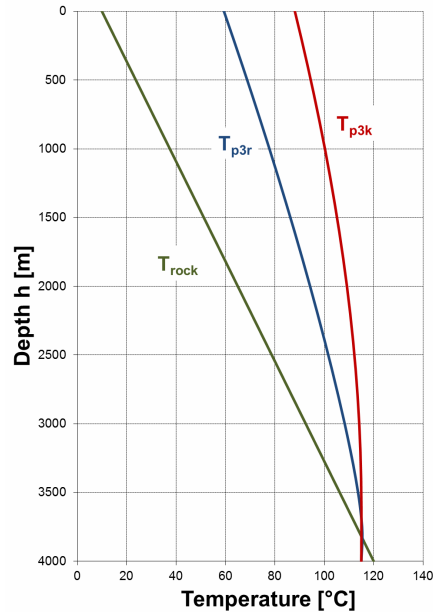


Fig. 6. Temperature distribution of fluids flowing in annular (T_{p3R}) and circular (T_{p3K}) channel for the case where highest temperature of the liquid leaving the heat exchanger is found

CONCLUSIONS

It results from the analysed case that by application of the active insulation the temperature of liquid leaving the exchanger can be increased. For example, in the case without insulation the liquid temperature at outlet was 72.7 °C. After application of the active insulation temperature of liquid increased to 88.1 °C. The increase of liquid temperature is at the expense of the part of the flow rate serving as insulation. Following the role of insulation that flow rate is directed back to the pumping back pipeline.

The above solution can be used in order to obtain required temperature of the heat carrier fluid tailored to the required temperature of network water supplying the heat receivers to obtain the balance between the rate of extracted heat and the rate of heat demanded by the heat receivers. In that case the flow rate flowing in the annular channel, serving earlier as active insulation, is used to obtain required temperature by mixing with the flow rate flowing in circular channel. Analysing the obtained results it can be concluded that varying proportions of the flow rates in annular and circular channels the temperature of fluids can be influenced. Therefore there can be found such a ratio of the flow rates at which the maximum temperature of the fluid in the circular channel (main channel) is obtained.

Nomenclature

- a_s – thermal diffusivity, m^2/s
- c_w – specific heat, $J/(kg \cdot K)$
- d – pipeline diameter, m
- H – length (depth) of vertical channel UCGHE, m
- k_z – overall heat transfer coefficient, $W/(m^2 \cdot K)$
- L – length of horizontal channel of UCGHE, m
- \dot{m} – mass flow rate of fluid, kg/s
- N – number of transfer units, -
- \dot{Q} – rate of heat, kW
- T – temperature, °C
- Θ – temperature difference, K
- \dot{W} – rate of heat capacity, W

Subscripts

- k, r – relates to fluid in the inner channel (k) or annular channel (r)
 s – relates to the rock

References

1. Kaczmarek R. *Analysis and Evaluation of Efficiency Extraction and Utilization Energy from Earth for Supplying Geothermal Power Plant / Heat and Power Plant* // PhD thesis. West-Pomeranian University of Technology in Szczecin, Szczecin, 2010 (*in Polish*).
2. Stachel A. A., Kaczmarek R. Evaluation of operation effectiveness of a heat plant supplied from underground geothermal heat exchanger equipped with an active insulation: *Balanced Development – Innovations*. Multi-author work / Ed. R. Grądzki, Łódź, 2009 (*in Polish*).
3. Stachel A.A, Kaczmarek R. Assessment of the effectiveness of a heating plant operation fed from a horizontal geothermal heat exchanger with a qualitative regulation // *Polish J. of Environ. Stud.* 2010. Vol. 19, No. 3. Pp. 539–546.
4. Wolff H., Schmidt S., Möller F., Legarth B., Oppelt J., Treviranus, J. *Geothermische Stromerzeugung Projekt „Untertägig Geschlossener Geothermischer Wärmetauscher“ BMU – ZIP 0327506, Status-Quo*, Juni 2002, Vortrag, Symposium "Geothermische Stromerzeugung", Landau 20./21. Juni 2002.
5. Wolff H., Möller F., Besser T., Schmidt S., Oppelt J., Treviranus J.: *Ansätze fortschrittlichen Bohr- und Komplettierungstechnik für die Errichtung eines Unterträngig Geschlossenen Geothermischen Wärmetauscher. Projekt „Untertägig Geschlossener Geothermischer Wärmetauscher“ BMU – ZIP 0327506*. 20 Jahre Tiefe Geothermie in Deutschland, 7. Geothermische Fachtagung, 06-08.11.2002, Waren (Müritz).
6. Kujawa T., Kaczmarek R. Heat flow characteristics of underground closed geothermal heat exchanger // *XIII Symposium: Nutzung Regenerativer Energiequellen und Wasserstofftechnik, Stralsund*, 2–4.11.2006. Pp. 45–51.
7. Nowak, W. *Theory of Underground Closed-Loop Geothermal Heat Exchange*. Unpublished internal report of Department of Heat Engineering, TU of Szczecin, 2003 (*in Polish*).
8. Nowak W. et al. *Thermal-Hydraulic Characteristics of Cooperation of Heat Receivers with Geothermal Heat Exchangers*. Final report from research project, No. 3 T10B 075 27, Szczecin, 2008 (*in Polish*).
9. Nowak W. Analytical calculation model of underground closed geothermal heat exchanger // *Archives of Thermodynamics*. 2005. Vol. 26. Pp. 49–66.
10. Nowak W., Kaczmarek R. Assessment of the influence of application of active insulation in the extracting part of underground closed geothermal heat exchanger on its influence // *Proc. of XIII Symp. on Heat and Mass Transfer, Koszalin-Darłówek*, 2007. Vol. 2. Pp. 745–752 (*in Polish*).
11. Nowak W., Kaczmarek R. Thermal-hydraulic analysis of horizontal closed-loop geothermal heat exchanger // *Proc. of XIII Symp. of Heat and Mass Transfer PAS. Koszalin-Darłówek*, 3–6.09.2007. Vol. 2. Pp. 753-762 (*in Polish*).
12. Nowak W., Sobański R., Kabat M., Kujawa T. *Systems of Acquisition and UTILISATION of Geothermal Energy*. Wydawnictwo Uczelniane Politechniki Szczecińskiej, Szczecin, 2000.